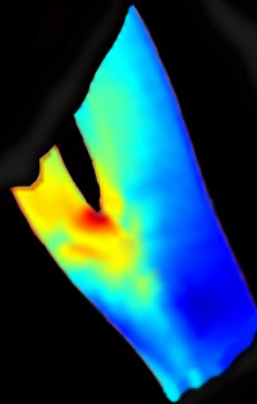# Integratie van medische beeldvorming en numerieke stromingsmechanica voor het meten van de bloedstroom in de halsslagaders

Integrating medical imaging and computational fluid dynmics for measuring blood flow in carotid arteries

ir. Fadi Paul Glor

Supervisors: Prof. Dr. Ir. Pascal R. Verdonck
Dr. Ir. Xiao Yun Xu

Imperial College London

IBITECH
Institute Biomedical Technology
GENT

Universiteit Gent
Faculteit Toegepaste Wetenschappen
Vakgroep Civiele Techniek
Laboratorium voor Hydraulica

Integratie van medische beeldvorming en numerieke stromingsmechanica voor het meten van de bloedstroom in de halsslagaders

Integrating medical imaging and computational fluid dynamics for measuring blood flow in carotid arteries

ir. Fadi Paul Glor

Supervisors: Prof. Dr. Ir. Pascal R. Verdonck
Dr. Ir. Xiao Yun Xu

Imperial College
London

IBITECH
Institute Biomedical Technology

Suggested citation: Glor Fadi Paul. Integrating medical imaging and computational fluid dynamics for measuring blood flow in carotid arteries. PhD thesis. Gent: Ghent University; 2004.

Preface:

A man is at his tallest when he stoops to help a child

The plan wasn't really to start a PhD. I had a number of things to do that day: work on the MSc thesis, attend some classes and maybe make the best of the good weather at the local beer garden. Starting a PhD was not on the list and wouldn't fit in. But I had an appointment. Of all days, why did I have to put the appointment with **Prof. P. Verdonck** today? Prof. Verdonck was responsible of the education called 'Advanced Studies in Biomedical and Clinical Engineering'. Could be interesting. So I went. The poor Professor had to work with a student who's vision of the rest of his life was bundled in the sentence: "I would like to do something with engineering and with medicine *and stuff*." This encounter initiated this PhD.

I started on the first of October 2000. My first task was to organise a karting event and - together with Kris - provide everybody with strong Belgian beers as a thank you for accepting us in the lab. I fitted in perfectly. Kris D, Peter D, Stefaan DM, Stijn VDB, Patrick S, Dirk DW, Sunny E, Koen M, Robert B, Ronny V, Erik D, Bart M, Martin VD, Stefaan B, Manuella DK, Kristien T, Ivo M and Marcel A created a nice work atmosphere. Meanwhile, I was enlightened on how to couple medical imaging and computational fluid dynamics. In that context, all credit goes to **Prof. J. Vierendeels** (FTW, UGent), **Mr. P. de Kermel** (ESI-group, Rungis, F) and **Dr. P. Groenenboom** (ESIbv, Krimpen aan den IJssel, NL) for teaching me how to use a workstation to obtain colourful drawings (CFD), and to **Dr. Ir. J. Westenberg** (Leids Universitair Medisch Centrum, Leiden, NL), who was desperately trying to explain how magnetic resonance imaging (MRI) works. The latter showered me with data and advice, and he was definitely one of the persons who carried this PhD through the early stages.

Due to *personifiable circumstances*, all funding ended after a year. When you work long enough in certain environments, you can tell why communism failed. This period was without doubt the toughest of the past four years. At that moment, it took a lot of courage to keep on supporting a PhD student like me. But only dead fish swim with the current. The support from supervisor and colleagues was invaluable here. A small e-mail to **Dr. Quan Long** was responded by an invitation to Imperial College London to come and talk to **Dr. X. Yun Xu**. She gave me a chance to continue my PhD in the very best of circumstances. I sincerely think this was better than winning the lottery. Thanks goes to Erasmus-Belgium who really helped me settling down in London. The irony is that now, looking back, I have to thank the

personifiable circumstances. Without them I would never have made it to London.

I started on the 9th of October 2001. One month later, I received a tie and cough-links as birthday gifts. I fitted in perfectly. It is not normal for an Arab with a burgundian Belgian life-style to fit in in England. Bulk of the credit goes to **Fadi and Rimoun Kasborsom**, for opening their house, and to **Dr. Alexander Augst**, for nailing every single nailable problem I encountered. Thanks to the variety of people at Imperial, the work atmosphere was very colourful. I thank the 414-crew: Pooi-Ling C, Guy G, Guido G, Shunzi Z, Ka-Wai L, Prashant V, Sayful, Lina H and James L, but also Dean B, Andy Z, Sheila B, Mark J, Simone P and Bassam K for the wonderful times in London. I still have the 414 good-bye gift in front of me every day. Professionally, I was backed by the insights of **Prof. A. Hughes**, the management of **Dr. S. Thom**, the witty jokes of Prof. K. Parker and the thorough supervision of Dr. Xu. Nothing could go wrong. Still, for a PhD, you need data. No data, no PhD. My MRI data came from **Dr. L. Crowe** at the Royal Brompton and the ultrasound data was the result of the extreme hard work of **Dr. Ben Ariff** at St Mary's hospital. Thanks Ben, hope you are better at the play-station meanwhile.

Thanks to some *kindly acknowledged interventions*, I was able to come back to Gent on the second of January 2003. The lab in Gent had lost some people and won some people. Ilse VT, Tom C, Edawi W, Stein-Inge R, Sebastian V, Liesbet DD, Lieve L, Guy M and Masanori N were the new colleagues who had to put up with me. I cooked bacon and eggs for everyone and was asked to organise a karting event. This time, I didn't win because I was tricked by the Verhoeven maffia. On this return, I was welcomed as if I never really left, and the work atmosphere was, if possible, even better than at the start of the PhD. Moreover, I sincerely thank Pascal V, Stijn VDB, Kris D, Ilse VT and Patrick S for their substantial help when I was stuck, or for making me halt when I was going too fast. I do not want to forget two students, Martin H and Mélissa B, who substantially contributed to the work presented in this book.

You can learn a lot on international meetings. You open up to the culture of a different city (Gent, Gent again, Calgary, Boston, Miami, Poitiers or Montpellier) and get to check out when the bars close (never, never, 3am, 1am, etc.). More importantly, I found it amazing to see how much you learn from simple discussions with colleagues. It is fair to say that my perception of the research field underwent severe changes after meeting **Ana I** and **Prof. D. Steinman** and his co-workers, of which I would like to mention Luca

**When you see me walking through it,
you may think there's nothing to it,
but I simply can not do it
alone!**

− Valma Kelly (Chicago, the musical)

Supervisors:

   Prof. Dr. Ir. Pascal R. Verdonck
   Dr. Ir. Xiao Yun Xu

Laboratorium voor hydraulica   Department of Chemical Engineering
Vakgroep Civiele techniek (TW15)   & Chemical Technology
Faculteit Toegepaste Wetenschappen (FTW)   South Kensington Campus
Universiteit Gent   Imperial College London
Sint-Pietersnieuwstraat 41   Exhibition Road
9000 Gent   London SW7 2AZ
BELGIE   UNITED KINGDOM

Members of the exam committee
Prof. Dr. Ir. Ronny Verhoeven
(**Chairman**, FTW, Universiteit Gent, BELGIE)
Prof. Dr. Ir. Patrick Segers
(**Secretary**, FTW, Universiteit Gent, BELGIE)
Prof. Dr. Ir. Pascal Verdonck
(FTW, Universiteit Gent, BELGIE)
Dr. Ir. Xiao Yun Xu
(Department of Chemical Engineering
& Chemical Technology, Imperial College London, UK)
Prof. Dr. Alun Hughes
(Clinical Pharmacology and Therapeutics, Imperial College London, UK)
Prof. Dr. Ir. Ignace Lemahieu
(FTW, Universiteit Gent, BELGIE)
Prof. Dr. Ir. David Steinman
(Robarts Research Institute, University of Western Ontario, CANADA)
Dr Simon A McG Thom
(National Heart and Lung Institute, Imperial College London, UK)
Prof. Dr . Luc Van Bortel
(Farmacologie, Universiteit Gent, BELGIE)
Prof. Dr. Ir. Jan Vierendeels
(FTW, Universiteit Gent, BELGIE)

Contents

List of Figures

List of Tables

NEDERLANDSE SAMENVATTING

Alleen dode vissen

zwemmen altijd met de stroom mee.

– M. Muggeridge

Indeling van het proefschrift

Dit proefschrift handelt over een nieuwe techniek om de stroming in de halsslagader te visualiseren en te berekenen. In een *eerste* hoofdstuk wordt dieper ingegaan op de anatomie van de halsslagader en de ziektes die in die halsslagader voorkomen. Het *tweede* hoofdstuk concentreert zich op de techniek. In eerste instantie dient de geometrie van de halsslagader van een patiënt in beeld gebracht te worden. Vervolgens wordt de stroming in die halsslagader numeriek berekend. Tenslotte wordt een beeld gegeven van de nauwkeurigheid van de verschillende facetten van de techniek, zoals de gebruikte beeldvormende techniek en de verschillende manieren om een berekening door te voeren. In het *derde* hoofdstuk wordt de nieuwe techniek succesvol ingezet voor de realisatie van twee klinische studies. De eerste studie handelt over de impact van het draaien van het hoofd op bloedstroming in de halsslagaders. De tweede studie onderzoekt gevolgen van bloeddrukverlagende geneesmiddelen. Het *vierde* en laatste hoofdstuk vat de belangrijkste bevindingen samen.

I. Inleiding

I.1. Anatomie

Hart- en vaatziekten vormen de belangrijkste doodsoorzaak in Westerse culturen. Figuur I.1 toont aan dat cardiovasculaire aandoeningen in Europa verantwoordelijk zijn voor 33.5% van de sterfgevallen op 45 tot 54-jarige leeftijd en voor 64% van de sterfgevallen bij mensen ouder dan 85.[371] In de Verenigde Staten zijn cardiovasculaire aandoeningen in 39.4% de doods-oorzaak.[7]

Het cardiovasculair systeem bestaat uit het hart, dat het bloed door het lichaam pompt, de slagaders (arteries), die het bloed naar alle weefsels van het lichaam leiden en de aders (venen), die het bloed van de weefsels terugbrengen naar het hart.
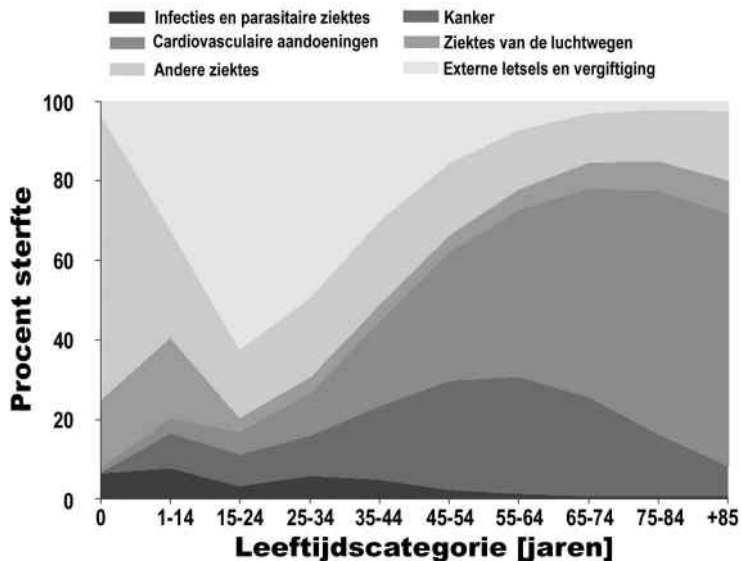
Figuur I.1.: Doodsoorzaken per leeftijdscategorie in Europa volgens de wereld gezondheids-organisatie (WHO).[371]

(a) Rechter-carotisbifurcatie[107]

(b) Posities van de aftakkingen van de aortaboog[327]
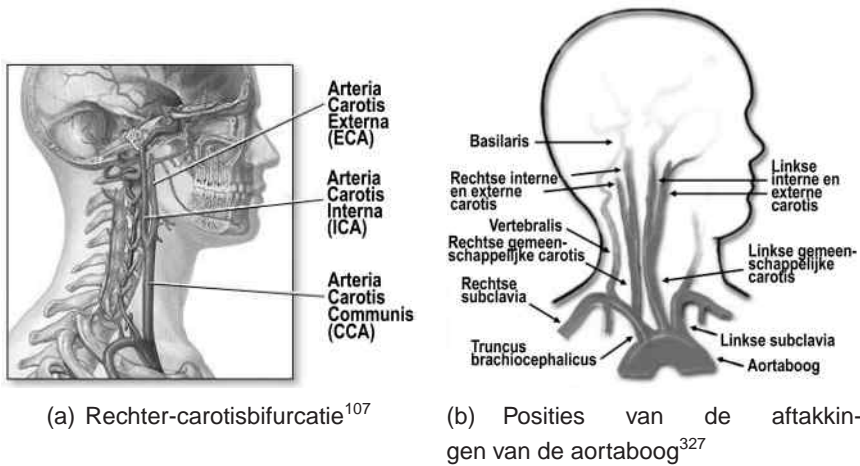
Figuur I.2.: De positie van de halsslagaders in het menselijk lichaam.

De halsslagader (arteria carotis of kortweg carotis, Figuur I.2) heeft in dit verband om een viertal redenen een bijzonder belang. (1) Vooreerst is het een arterie die zich opsplitst in 2 takken: de gemeenschappelijke halsslagader (common carotid of CCA) splitst zich in de interne (ICA) en externe halsslagader (ECA). Dergelijke *bifurcaties* behoren tot de geometrieën waarin typisch de meeste cardiovasculaire ziektes voorkomen. Zowel slagaderverkalking (atherosclerosis), aneurysmata (verslapping van de vaatwand waardoor een uitstulping van de slagader optreedt) als dissecties (afscheuren van de binnenste laag van de slagader) komen voor. (2) De halsslagader brengt het bloed naar het hoofd en meer in het bijzonder is het één van de slagaders die instaan voor de doorbloeding van de hersenen. Hierdoor heeft een pathologie van de halsslagader meteen ernstige gevolgen, bijvoorbeeld een herseninfarct. (3) Daarenboven is de halsslagader een rechtstreekse aftakking van de aorta, waardoor het opmeten van de toestand in de halsslagader een barometer kan zijn voor de hemodynamische toestand van het hart. (4) Het voordeel van de halsslagader is dat het een zeer oppervlakkig bloedvat is, dat zich gemakkelijk door niet-invasieve technieken laat opmeten. Om deze redenen is het dan ook van groot belang om te beschikken over een degelijk meetinstrument voor de visualisatie en kwantificering van de bloedstroming in de halsslagader.

I.2. Doel van het proefschrift

Hart- en vaatziekten omvatten een breed gamma aandoeningen waarvan aangeboren afwijkingen van het hart, lekkende hartkleppen, pathologiën van de hartwand, atherosclerosis en hypertensie de meest voorkomende zijn. In dit proefschrift wordt dieper ingegaan op atherosclerosis en zijn oorzaken. Atherosclerosis wordt geïnitieerd door een nefaste biomechanische situatie. De normale situatie staat geïllustreerd in Figuur I.3. Hier ziet men hoe een bloedstroming een tangentiële kracht τ uitoefent op de cellen van vaatwand, het endothelium. Deze schuifspanning τ is het product van de viscositeit van het bloed μ en de afgeleide van de snelheid u naar de normale afstand tot de wand y:

$$\tau = \mu \, \frac{du}{dy} \tag{I.1}$$

Indien de stromingsrichting definieerbaar is, zullen de cellen van de vaatwand die in contact staan met het bloed zich alingeren met de bloedstroming, zoals weergegeven door Malek[208] in Figuur I.4 (a). Vanaf schuifspanningen in de buurt van 1.5 N/m^2 vinden de endotheelcellen probleemloos
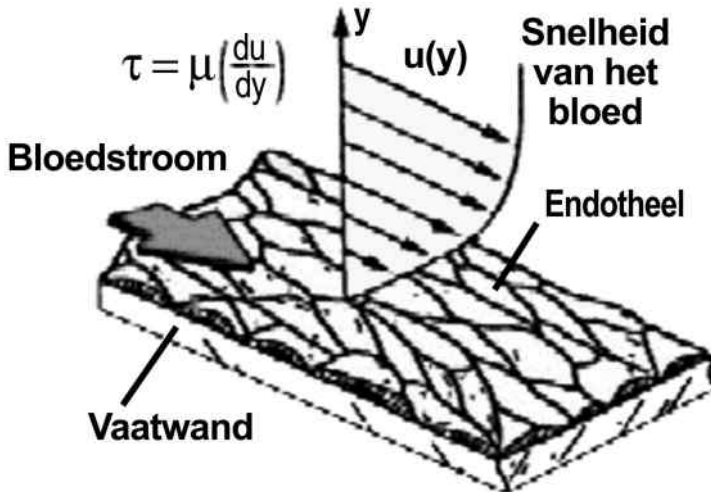
Figuur I.3.: Schuifspanning τ in gezonde slagaders.[208] De schuifspanning is de tangentiële kracht uitgeoefend op de vaatwand door het stromende bloed. Ze is gelijk aan het product van de de dynamische viscositeit van het bloed μ en de afgeleide van de snelheid u naar de normale afstand y.
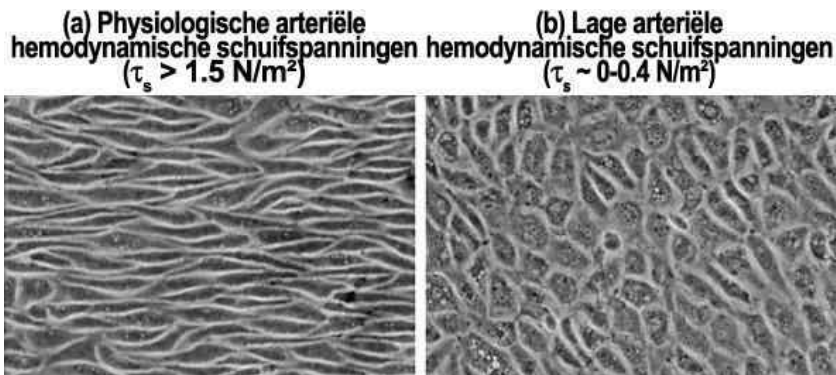
Figuur I.4.: De cellen van het endothelium in twee stromingssituaties. a: De cellen van het endothelium aligneren zich in de richting van de stroom. b: Wanneer er geen duidelijkheid bestaat i.v.m. de zin van de stroom, bv. wanneer de stroming zwak is en oscilleert, is er geen alignering van het endothelium.[208]

de juiste richting. Wanneer de bloedstroming echter zwak is en oscilleert, is de zin van de stroming niet meer duidelijk en valt er bij de endotheelcellen geen alignering te bespeuren (Figuur I.4 (b)). Malek[208] spreekt van een waarde van 0.4 N/m^2 als drempel voor lage schuifspanningen. Wanneer het endotheel zich niet alingeert, is de vaatwand vatbaar voor verkalking.

Ook bij hoge schuifspanningen treden biologische verschijnselen op die atherosclerosis in de hand werken. Zo zullen de rode bloedlichaampjes scheuren en kunnen de endotheelcellen rechtstreekse schade ondervinden door de hoge krachten die de stroming hen oplegt. Deze nefaste situaties doen zich voor[155] vanaf schuifspanningen tussen 10-15 N/m^2, maar worden pas klinisch relevant vanaf 25-45 N/m^2.

In de halsslagader treden vooral lage schuifspanningen op, maar er komen ook hoge schuifspanningen voor. Dit is voorgesteld in Figuur I.5. Kalkafzetting in de halsslagader gebeurt het meest in de zone van lage schuifspanning, in de buitenkant van de ICA.[324]

Gezien het belang van de halsslagaders en de potentiële nefaste gevolgen van wandschuifspanningen, is het bepalen van schuifspanningen in de halsslagader sinds de jaren 60 ononderbroken een technische uitdaging van maatschappelijk belang.[45, 47, 180, 380] Men kan echter de schuifspanning *in vivo* niet rechtstreeks meten, zodat men al vrij snel op zoek is gegaan naar onrechtstreekse methodes. De eerste niet-invasieve technieken die erin slaagden de schuifspanningen te begroten, kregen vorm op het eind van de vorige eeuw. Dan werd voor het eerst de halsslagader van een levend individu in beeld gebracht met MRA (magnetische resonantie angiografie)
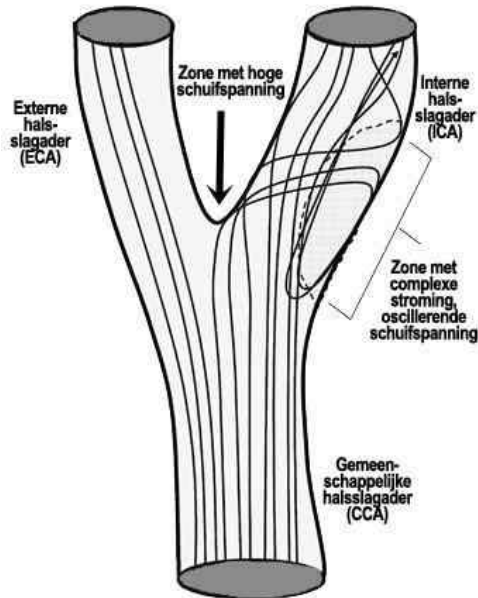
Figuur I.5.: Vooral lage maar ook hoge schuifspanningen komen voor in de halsslagader.

en gereconstrueerd in drie dimensies om dan de stroming in die halsslagader numeriek te berekenen. Het resultaat van deze berekening was het schuifspanningsveld: voor het eerst leek het mogelijk om de krachten die een vloeistof uitoefent op de vaatwand volledig niet-invasief te begroten.

Wanneer aan het huidige onderzoek begonnen werd, ebde de euforie van de eerste successen reeds weg. Gedreven door het grote maatschappelijk belang, begon men zich af te vragen hoe nauwkeurig deze techniek eigenlijk wel is, en hoe toepasbaar ze zou blijken. Het is in dát kader dat dit onderzoek past.

Het doel van dit proefschrift bestond er dan ook in een techniek operationeel te maken die de halsslagaderdoorstroming *in vivo* berekent. Hierbij werd gebruik gemaakt van medische beeldvormende technieken die in staat zijn de 3D geometrie van de slagader te reconstrueren en daarnaast ook een minimum aan informatie over de bloedstroming te rapporteren. Met behulp van een computermodel wordt de stroming in de halsslagader voor een individu gereconstrueerd door het oplossen van de Navier-Stokes vergelijkingen, i.e. de mathematische representatie van fysische wetten waaraan een fluïdum (dus ook bloed) steeds moet voldoen. Zo wordt het beeld van de stroming bekomen op een patiëntspecifieke basis, enkel met behulp van

niet-invasieve technieken. Op basis van dit beeld van de stroming kunnen schuifspanningen op de slagaderwand bepaald worden.

Behalve het 'operationeel maken' van de techniek, was één van de belangrijkste doelen van dit proefschrift het bepalen van de nauwkeurigheid van de schuifspanning *in vivo*. Als de techniek inzetbaar is voor klinische toepassingen, moet de nauwkeurigheid ervan natuurlijk exact begroot worden. Pas dan kan pre-operatief onderzoek geschieden op basis van deze combinatie van een beeldvormende techniek en numerieke stromingsmechanica. Vandaar dat een belangrijk deel van dit proefschrift handelt over de sensitiviteit van de ontwikkelde technologie.

I.3. De belangrijke parameters

Behalve de schuifspanningen, zijn er een aantal andere diagnostische parameters die in dit proefschrift aan bod komen. Deze lijst is niet begrenzend en is enkel bedoeld om de lezer voeling te geven met de parameters die verderop voorkomen.

- De **IMT** of intima-media dikte is de dikte van de binnenste twee lagen van een slagader. Het is algemeen aangenomen[236] dat een hoge IMT een marker is van een verzwakte vasculaire gezondheid.

- De **3D geometrie** van de halsslagader wordt dikwijls herleid tot een aantal **parameters**. Hieronder valt o.a. A_R, wat staat voor de verhouding van de som van de doorstroomoppervlakte van de ICA en ECA, ten opzichte van de doorstroomoppervlakte van de CCA. T_{art} is verder de kromheid van de arterie art (art = CCA, ICA of ECA).

$$T_{art} = 1 - \frac{kortste\ afstand\ inlaat - uitlaat}{lengte\ van\ arterie} \tag{I.2}$$

  De bifurcatiehoek α_{BIF} is de hoek tussen ICA en ECA. $SF_i art$ is een parameter die de vorm van de contouren begroot. Deze parameter is 1 voor een cirkel, en minder dan 1 voor alle andere vormen. Verder werden de non-planariteitsparameter NP en lineariteitsparameter L_{art} gedefinieerd door King.[157] NP wordt als volgt berekend. Eerst dienen de middellijnen van de arteries berekend te worden zoals dat gedaan wordt door Barratt.[20] De coördinaten van de middellijnen worden opgeslagen in een matrix. De singulierwaarde factorisatie van

deze matrix levert dan 3 singuliere waarden op. De - na schaling - kleinste singuliere waarde is dan de non-planariteitsparameter. Wanneer alle punten in een vlak liggen, is NP = 0, wanneer alle punten uniform verdeeld zijn in de ruimte, is NP = 33%. De lineariteitsparameter L is de grootste singuliere waarde en wordt op analoge wijze berekend. Deze parameters zijn interessant omdat die gelinkt kunnen worden aan geometrische eigenschappen die gepaard gaan met kalkafzettingen.

- Het **Reynolds-getal** wordt als volgt berekend:

$$Re \;\; = \;\; \frac{V_{gem}\, D\, \rho}{\mu} \tag{I.3}$$

$$= \;\; \frac{Q/(\pi D^2/4)\, D\, \rho}{\mu} \tag{I.4}$$

hier is V_{gem} de gemiddelde snelheid, D de diameter van het vat, ρ de bloed densiteit en μ de dynamische viscositeit. Het Reynolds getal drukt voor een stroming uit hoe de inertiekrachten zich verhouden t.o.v. de visceuze krachten. Het stromingsprofiel bij hoge Reynolds-getallen wordt bepaald door inertiewetten, terwijl bij lage Reynolds-getallen de viscositeit van het fluïdum het aanblik van de stroming bepaald. In het eerste geval spreekt men van turbulente stroming, in het tweede geval over laminaire stroming. In een rechte stijve cilindrische buis ligt de grens tussen beide stromingsprofielen in de buurt van een Reynolds-getal van 2300.

- De schuifspanning in een bepaald punt op de vaatwand kan verschillende waarden en richtingen aannemen tijdens een hartcyclus. De **OSI** ('Oscillatory Shear Index') is de fractie van de hartslag waarin de schuifspanning (WSS) niet gericht is volgens de gemiddelde richting. Ze wordt als volgt berekend:

$$OSI = \frac{1}{2}\,\left(1 - \frac{|\int_0^T \vec{\tau}\,\mathrm{d}t|}{\int_0^T |\vec{\tau}|\,\mathrm{d}t}\right) \tag{I.5}$$

waarbij T de tijd tussen twee opeenvolgende hartslagen is, t de tijdsparameter en $\vec{\tau}$ de schuifspanning. Wanneer de WSS altijd in dezelfde richting acteert is de OSI gelijk aan 0, wanneer echter de schuifspanning oscilleert rond het nulpunt zal de OSI toenemen, met 0.5 als theoretisch maximum. De cellen aan de binnenkant van de slagader,

de endotheelcellen, wensen zich altijd te oriënteren in de richting van de stroom. Wanneer echter de richting van de stroom niet duidelijk gedefinieerd is, zal de endotheelfunctie verstoord zijn hetgeen aanleiding kan geven tot verdikking van de vaatwand en slagaderverkalking.[42] De OSI helpt bij het opsporen van dergelijke zones.

- De **schuifspanningsgradiënt** wordt traditioneel gelinkt aan de permeabiliteit van de vaatwand.[173] Grote gradiënten zullen de vaatwand aantasten en zo de kans geven aan relatief grote cellen, zoals macrofagen, om in de vaatwand te diffunderen. Deze situatie bevordert het verkalkingsproces. De schuifspanning kan zowel naar de tijd als naar de plaats afgeleid worden. In het eerste geval spreekt men van de temporele schuifspanningsgradiënt of **WSSGt**, in het tweede geval van de spatiale schuifspanningsgradiënt of **WSSGs**:

$$WSSGt = \frac{1}{T} \int_0^T \left| \frac{\partial \vec{\tau}}{\partial t} \right| \, \mathrm{d}t \tag{I.6}$$

$$WSSGs = \frac{1}{T} \int_0^T \sqrt{\left(\frac{\partial \tau_m}{\partial m} \right)^2 + \left(\frac{\partial \tau_n}{\partial n} \right)^2} \, \mathrm{d}t \tag{I.7}$$

τ_m en τ_n zijn de tijdsafhankelijke componenten van de schuifspanningen in het mnl carthesisch assenstelsel. Hierbij is m de richting van de gemiddelde schuifspanning en n de tangentiële richting aan het oppervlak van de wand en loodrecht op m. Merk op dat de schuifspanning gerefereerd dient te worden in het mnl assenstelsel om berekend te worden. Dit assenstelsel in anders voor elk punt van de vaatwand.

- De hoek die gemaakt wordt tussen de schuifspanningen in twee aanpalende punten van de vaatwand is een maat voor de kans dat bloedpartikels zich afzetten op die plek.[142] Partikeldepositie bevordert kalkafzettingen. Afhankelijk van de manier waarop deze parameter wordt becijferd, refereert men naar deze parameter als de schuifspanningsdeviatie (**WSSAD**) of angulaire schuifspanningsgradiënt (**WSSAG**). De WSSAD is een gemiddelde hoek tussen de gemiddelde schuifspanning in een bepaald punt en de omliggende punten (in radialen), terwijl de WSSAG de afgeleide van deze hoek is naar de ruimte (radialen per meter).

De WSSAD wordt als volgt berekend:

$$WSSAD = C \, arccos\left(\frac{\overline{\vec{\tau_i}} \cdot \overline{\vec{\tau_j}}}{|\overline{\vec{\tau_i}}| \, |\overline{\vec{\tau_j}}|} \right) \tag{I.8}$$

waarbij

$$C = 1 \;\; als \;\; \overrightarrow{\overline{v_{l,i}}} \cdot \overrightarrow{l_i} \geq 0$$
$$C = 0 \;\; als \;\; \overrightarrow{\overline{v_{l,i}}} \cdot \overrightarrow{l_i} < 0 \tag{I.9}$$

en

$$\overrightarrow{\overline{\tau_i}} = \frac{1}{T} \int_0^T \overrightarrow{\tau_i} \, dt$$
$$\overrightarrow{\overline{v_{l,i}}} = \frac{1}{T} \int_0^T \overrightarrow{v_{l,i}} \, dt \tag{I.10}$$

Hier is $\overrightarrow{\overline{\tau_i}}$ de gemiddelde schuifspanning in punt i, $\overrightarrow{\overline{v_{l,i}}}$ de gemiddelde normale snelheid in de directe nabijheid van het punt i, $\overrightarrow{l}$ is de normaal, subscript i duidt het huidige punt aan terwijl j de index is voor de naburige punten. De factor C benadrukt de potentiële impact van stroming die de wand nadert. In de meest ernstige situatie is WSSAD gelijk aan π.

De WSSAG wordt als volgt berekend:

$$WSSAG = \frac{1}{T} \int_0^T \left| \frac{1}{A_i} \int_S \frac{\partial \phi}{\partial x} dA_i \, \vec{i} + \frac{1}{A_i} \int_S \frac{\partial \phi}{\partial y} dA_i \, \vec{j} + \frac{1}{A_i} \int_S \frac{\partial \phi}{\partial z} dA_i \, \vec{k} \right| \, \mathrm{d}t \tag{I.11}$$

met S is het volledige oppervlak van de halsslagaderwand en A_i de oppervlakte van het deel van de wand gerelateerd aan punt i. Deze parameter kan berekend worden in eender welk assenstelsel ijk of xyz. Het scalair veld angulaire verschillen ϕ is als volgt gedefinieerd:

$$\phi = arccos\left(\frac{\vec{\tau_i} \cdot \vec{\tau_j}}{|\vec{\tau_i}| \, |\vec{\tau_j}|} \right) \tag{I.12}$$

I.4. De techniek en zijn toepassingen

Het proefschrift bestaat uit twee delen. In een eerste deel wordt de techniek die medische beeldvorming combineert met numerieke stromingsmechanica (computational fluid dynamics, CFD) bestudeerd. Daarbij gaat veel aandacht naar het kwantificeren en opdrijven van de betrouwbaarheid van de

techniek. Twee beeldvormende technieken worden van dichterbij bekeken: magnetische resonantie angiografie (MRA of vasculaire kernspintomografie) in al zijn verschillende vormen en het meer toegankelijke en goedkopere ultrageluid (US) of echografie.

In een tweede deel van het proefschrift wordt de techniek in twee klinische studies succesvol toegepast. Een eerste studie bestudeerde de impact van het draaien van het hoofd op de doorstroming van de halsslagader. Een tweede studie gaat na wat de gevolgen van bloeddrukverlagende geneesmiddelen zijn op de schuifspanningen in de halsslagader.

II. Numerieke stromingsmechanica op basis van medische beelden

II.1. Overzicht

Om tot een diagnose te komen, doet men beroep op een waaier meetapparatuur en een breed gamma ingenieurstechnieken. Het bepalen van de schuifspanningen in de halsslagader van een patiënt bestaat uit de volgende stappen, geïllustreerd in Figuur II.1.

1. **Niet-invasieve beeldvorming**: Met MRA of US worden de doorsneden van de slagader gevormd. In de eerste plaats dienen ze voor de 3D reconstructie van de halsslagader. In de tweede plaats is de beeldvorming ook bedoeld voor het meten van de snelheid aan het begin en einde van het 3D model of het meten van de in- en uitlaatvoorwaarden.

2. **Segmentatie**: Op de originele beelden wordt de wand van de slagaders afgelijnd. Dit kan automatisch of manueel. Het resultaat van deze stap is een reeks contouren, i.e. dwarse secties van de slagader.

3. **Reconstructie**: De contouren worden in een gemeenschappelijk referentiestelsel geplaatst. Hierdoor wordt de 3D geometrie van de slagader zichtbaar gemaakt. Door het glad maken van de 3D reconstructie kan een realistisch computermodel van de halsslagader geconstrueerd worden.

4. **3D Discretisatie**: In deze stap wordt de binnenkant van het model, daar waar het bloed stroomt, gediscretiseerd. Dit houdt in dat het deel van de 3D ruimte, ingenomen door de bloedstroming, in kleine celletjes wordt onderverdeeld. De stromingsvergelijkingen worden later iteratief in deze celletjes opgelost. Deze stap noemt men ook het 'meshen'.

5. **Opleggen van randvoorwaarden en parameters van het model**: Vooraleer het oplossen van de stromingsvergelijkingen kan beginnen,
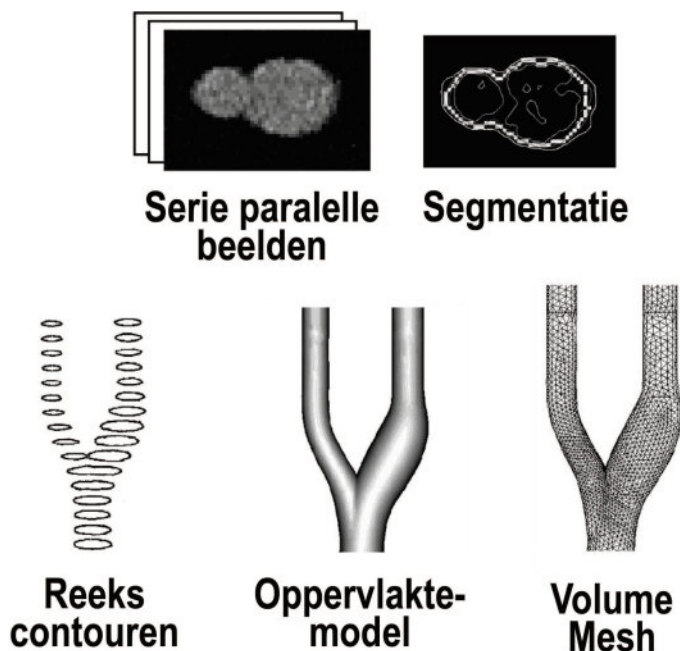
Figuur II.1.: Illustratie van enkele typische stappen die ondernomen dienen te worden voor het combineren van een beeldvormende techniek met numerieke stromingsmechanica. Na de beeldacquisitie wordt op de beelden manueel of automatisch de interface tussen lumen en vaatwand afgelijnd. Deze lijnen of contouren worden in een 3D referentiesysteem geplaatst en bewerkt om een gladde geometrie te bekomen. De 3D geometrie wordt dan gediscretiseerd of 'gemesht'. Deze 'mesh', samen met de stromingsvoorwaarden aan de in- en uitgang van het model, bevat genoeg informatie om de stroming in het model numeriek door te rekenen m.b.v. een (veelal commercieel) numerieke stromingsmechanica pakket.[306]

moeten de in- en uitlaatvoorwaarden gekozen worden. Deze zijn gebaseerd op debiet- en/of snelheidsmetingen uitgevoerd tijdens stap 1. Verder moeten nog enkele vloeistofeigenschappen bemeten worden, zoals de viscositeit en dichtheid van bloed.

6. **Numerieke Stromingsmechanica** (Computational Fluid Dynamics of CFD): nu een gediscretiseerd model bestaat en de nodige randvoorwaarden werden opgelegd, kan de volledige tijdsafhankelijke stroming van het bloed door de halsslagader berekend worden. Hiertoe lost men de gelineariseerde **Navier-Stokes** vergelijkingen op in de celletjes van de mesh:

$$\sum_{i=1}^{3} \frac{\partial u_i}{\partial x_i} = 0 \qquad\qquad\text{(II.1)}$$

$$\frac{\partial u_i}{\partial t} + \sum_{j=1}^{3} \frac{\partial}{\partial x_i}(u_i u_j) = F_i + \sum_{j=1}^{3} \frac{1}{\rho} \frac{\partial \sigma_{ij}}{\partial x_j} \qquad i = 1,2,3 \quad \text{(II.2)}$$

De onafhankelijke variabelen in een cartesiaans assenstelsel zijn de plaatsvector $\overrightarrow{x} = (x_1, x_2, x_3)$ en de tijd t. Onder de afhankelijke variabelen vallen de snelheidsvector $\overrightarrow{u} = (u_1, u_2, u_3)$ en de druk p. De krachtenvector $\overrightarrow{F} = (F_1, F_2, F_3)$ is uitgedrukt in N/kg en $\vec{\sigma} = (\sigma_{ij})$ is de spanningstensor uitgedrukt in N/m^2, bestaande uit een drukcomponent en de viscositeit. ρ is de dichtheid van de vloeistof, hier het bloed.

Voor het oplossen van de Navier-Stokes vergelijkingen kan men gebruik maken van verschillende numerieke modellen en verschillende softwarepakketten.

7. **Diagnose**: Eenmaal het stromingspatroon is gekend, kunnen diagnostisch parameters berekend worden. Bij de diagnostische parameters behoren onder andere de schuifspanningen, de krachtenbalans tussen stroming en arteriële wand, en de omvang en lokalisatie van recirculatiezones, i.e. zones waar het bloed gedurende een periode van de hartcyclus terugstroomt.

In dit hoofdstuk, dat zich vooral over de technische kant van het proefschrift buigt, worden knelpunten in bovenstaande stappen aangepakt. Deel II.2, *magnetische resonantie* (MR), gaat na hoe de 3D reconstructie het best aangepakt worden wanneer men over een MR-scanner beschikt. Analoog wordt in deel II.3, *ultrageluid* (US), de te ondernemen stappen bij het gebruik van US uit de doeken gedaan. In beide delen gaat er veel aandacht naar het kwantificeren van de nauwkeurigheid van de schuifspanning berekend met deze techniek. Deel II.5 vergelijkt de twee beeldvormende technieken, MR en US. Tussenin (deel II.4) worden keuzes gemaakt voor de parameters van het numeriek model. Hierbij wordt vooral gedacht aan de randvoorwaarden, maar ook aan de viscositeit en de invloed van de hartslag.

II.2. Magnetische Resonantie

II.2.1. Inleiding

Magnetische resonantie beeldvorming (MRI) maakt gebruik van het feit dat waterstofatomen in een groot magneetveld fungeren als magneetjes. Door in een patiënt de beweging van die magneetjes na een externe excitatie te registreren, kan men doorsneden van het menselijk lichaam in beeld brengen. Wanneer MRI gebruikt wordt voor het visualiseren van bloed, spreekt men ook van MR angiografie of MRA.

Er bestaan onder meer 3 soorten MRA: 'Black Blood' (BB), waar het bloed
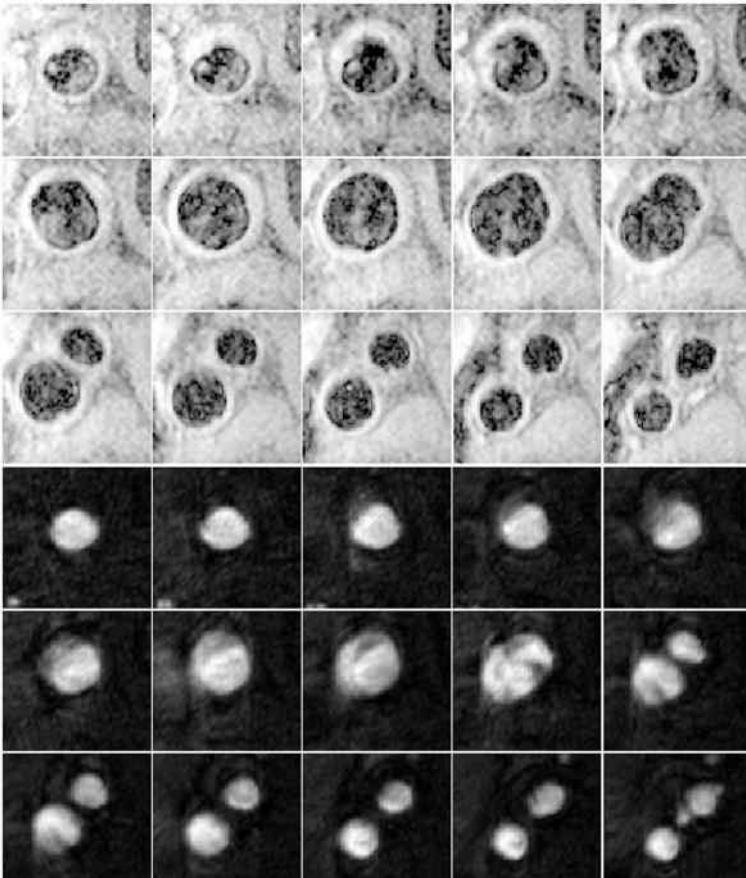
Figuur II.2.: MRA beelden van een halsslagader van een jonge hypertensieve zonder vaatvernauwing. De bovenste helft zijn BB MRI beelden, de onderste zijn TOF beelden in dezelfde locaties.

als zwart wordt afgebeeld in een beeld, 'Time-Of-Flight' (TOF), waar het bloed als witte zones wordt afgebeeld, en 'Cine Phase contrast' (PC), waar de grijswaarde van het beeld overeenstemt met de snelheid van het bloed. Omwille van hun verschillende toepassingsgebieden werden de drie soorten MRA technieken in afzonderlijke studies onderzocht en vergeleken. Figuur II.2 (bovenste helft) geeft een voorbeeld van een set BB MRI beelden genomen in een jonge, hypertensieve persoon zonder halsslagaderverkalking. In diezelfde persoon werden ook TOF MRI beelden gemaakt: deze zijn te vinden in de tweede helft van Figuur II.2.
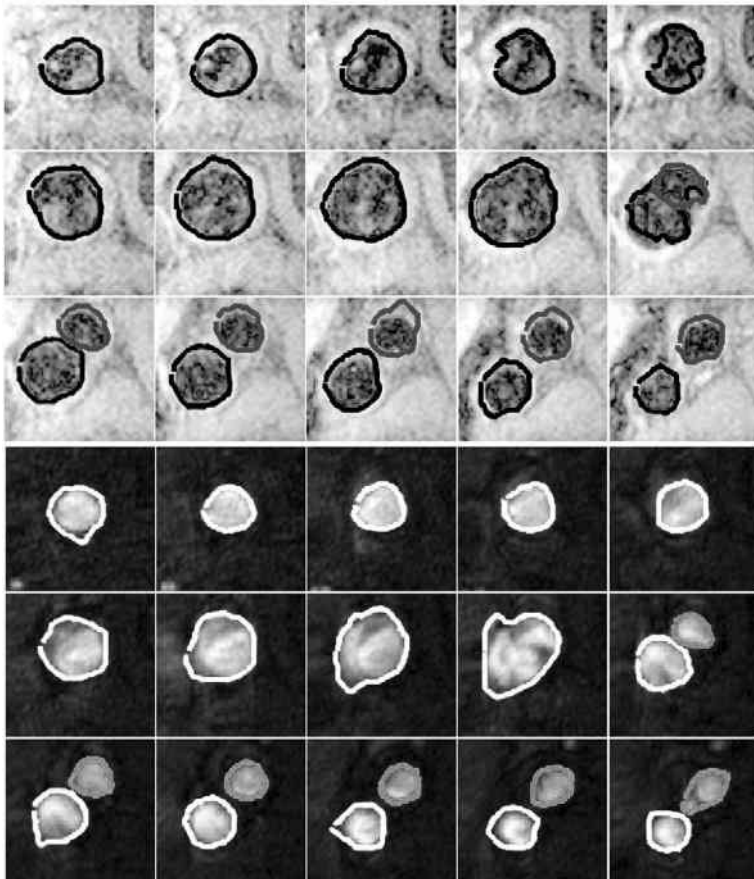
Figuur II.3.: Automatische segmentatie van de MRI beelden uit Figuur II.2. De witte of zwarte contouren zijn de resultaten van de automatische segmentatie van de CCA of ICA, terwijl de grijze contouren de ECA aflijnen.

II.2.2. Segmenteren en Reconstrueren

Het segmenteren van MRI beelden maakt gebruik van de 'region growing' methode, waarbij een operator op een beeld een punt moet aanduiden dat zich in het bloedvat bevindt. Op basis van dat punt en de omliggende grijswaarden wordt de contour automatisch teruggevonden. Na afloop gebruikt men de 'Snake' methode.[260] Dit is een segmenteringtechniek die de punten van een contour beschouwd als massa's die met veren aan elkaar verbonden zijn. Door de punten te verschuiven en hun 'energie' te minimaliseren, bekomt men de ideale gladde contour. Deze energie is opgesteld uit factoren die afhangen van de grijswaarden en van de vorm van de contour. Figuur II.3 toont het resultaat van de opeenvolging van de region growing methode en de snake methode voor de originele beelden uit Figuur II.2. Na afloop krijgt een operator de kans aanpassingen door te voeren op de afgebeelde contouren.

De contouren die na de segmentatie bekomen werden, worden nu in 3D afgebeeld in een gemeenschappelijk referentiestelsel. Om de effecten van ruis uit te schakelen, wordt de 3D reconstructie glad gemaakt. Hierbij worden de individuele punten $\overrightarrow{P_{oud}}$ van een afzonderlijke contour verschoven naar een punt op de as die $\overrightarrow{P_{oud}}$ verbindt met hun zwaartepunt $\overrightarrow{C_{oud}}$. Daarenboven worden de zwaartepunten van de contouren $\overrightarrow{C_{oud}}$ verschoven naar $\overrightarrow{C_{nieuw}}$ die op een 3D gladde lijn liggen:

$$\overrightarrow{P_{nieuw}} \quad = \quad \left(\overrightarrow{P_{oud}} - \overrightarrow{C_{oud}} \right) \times \sqrt{a_{ratio}} + \overrightarrow{C_{nieuw}} \tag{II.3}$$

Hierbij werd a_{ratio} begroot door de eis dat de oppervlaktes van de contouren niet te veel mogen fluctueren. Deze operaties verwijderen 'hoekjes en kantjes' van de 3D reconstructie hetgeen resulteert in een meer realistische 3D voorstelling van de halsslagader. Figuur II.4 toont de distributie van de OSI in een halsslagader die met verschillende graden van gladheid werd gereconstrueerd. Deze distributies tonen aan dat, behalve het wegwerken van onrealistische scherpte in de geometrie, het glad maken weinig invloed heeft op de belangrijkste kenmerken van de OSI distributie.
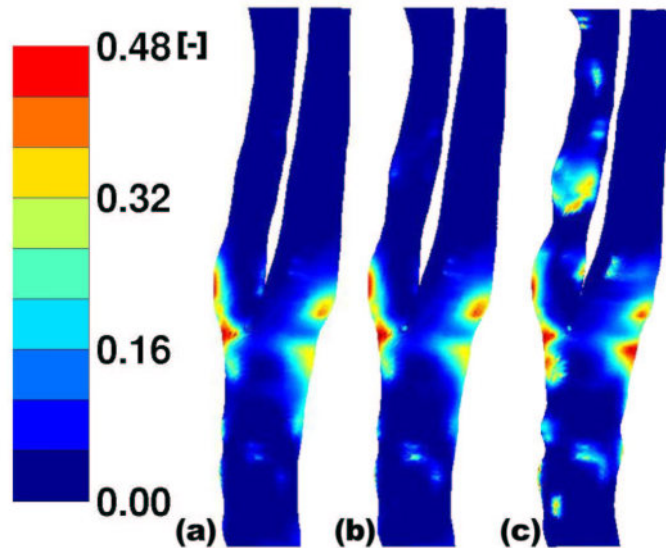
Figuur II.4.: OSI distributie in een halsslagader die met verschillende graden van gladheid werd gereconstrueerd. a: uitermate glad; b: glad; c: ruw.

II.2.3. De nauwkeurigheid van MRI gecombineerd met CFD

II.2.3.1. *In vitro* studie

In een eerste studie werd TOF MRI op de korrel genomen. Vooreerst werd een glad fantoom van de halsslagader gescand en gereconstrueerd. Deze studie liet toe de nauwkeurigheid van de techniek te bepalen. Enkele resultaten zijn geïllustreerd in Figuur II.5, waar de ware oppervlaktes van de doorsnede van de drie delen van het halsslagadermodel vergeleken worden met hetgeen werd bemeten op de 3D reconstructie met TOF MRI. De data punten zijn de doorsneden van de individuele contouren, de volle grijze lijn is de oppervlakte bemeten bij de gladde reconstructie. Voor de volledigheid werd ook een BB MRI scan uitgevoerd. De resultaten daarvan zijn mee in de figuur opgenomen. De studie toonde aan dat MRI-gebaseerde CFD klaar was voor *in vivo* toepassingen.

II.2.3.2. *In vivo* studie

Nadat de performantie van TOF MRI *in vitro* was vastgesteld, werd vervolgens een TOF reproduceerbaarheidsstudie uitgevoerd. Hierbij werden 8 gezonde personen twee keer gescand, met minstens twee weken tussen

(a) CCA

(b) ICA

(c) ECA
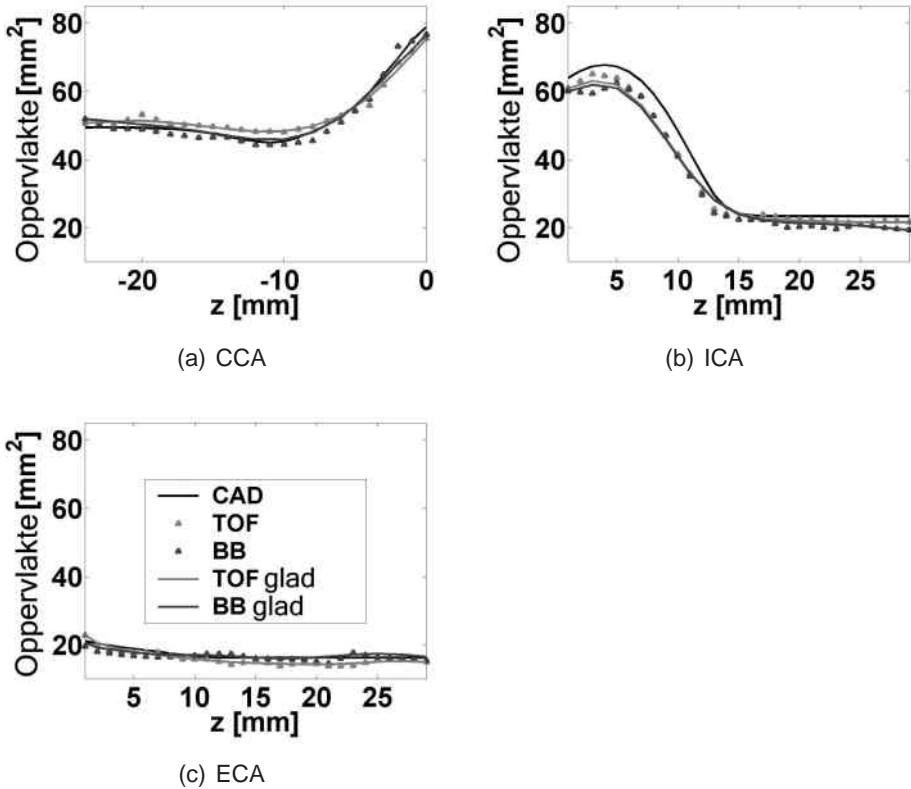
Figuur II.5.: Nauwkeurigheid van MRI in het bepalen van de doorsnede van een *in vitro* carotis. De oppervlakte van de doorsnede is voorgesteld als een functie van de verticale as z. De zwarte lijn (CAD) stelt de werkelijke data voor. De data punten zijn opgemeten oppervlaktes, en de grijze lijnen zijn de oppervlaktes in het gladde model.

de twee opnames. Het verschil tussen de twee scans is een maat voor de reproduceerbaarheid. In de simulaties die de hemodynamische parameters berekenen werd in deze studie telkens dezelfde randvoorwaarde gebruikt, dit opdat de opgemeten verschillen enkel te wijten zouden zijn aan het verschil in geometrie. Een aparte randvoorwaardestudie volgt in deel II.4. Één van de interessantste resultaten van deze studie staat vervat in Tabel II.1: ze toont de te verwachten fout voor de WSS, OSI, WSSGt, WSSGs, WSSAD en WSSAG. Deze fout werd berekend door de individuele waarde van de parameter te begroten op individuele segmenten van de halsslagader. Voor elk segment berekent men het absolute verschil tussen de te verwachten waarde (het gemiddelde van de waarde in de twee scans) en de opgemeten waarde (in één van de scans). De 'fout' of RMSE is hier gedefinieerd als het gemiddelde van deze absolute verschillen.

	arterie	WSS [N/m^2]	OSI [-]	WSSGs [N/m^3]	WSSGt [$\frac{N}{m^2.s}$]	WSSAD [-]	WSSAG [rad/m]
RMSE	CCA	0.175	0.0129	114	0.817	0.0969	22.1
	ICA	0.543	0.0325	234	2.97	0.120	67.8
	ECA	0.563	0.0296	213	3.27	0.0972	77.3
	SAMEN	0.427	0.0250	214	2.35	0.105	68.1
%	CCA	35.0	89.9	67.1	20.4	79.5	64.5
	ICA	24.9	107	68.9	19.5	121	97.5
	ECA	39.6	129	56.1	35.0	106	72.0
	SAMEN	37.9	123	65.7	30.2	102	79.8

Tabel II.1.: Fout voor de hemodynamische parameters begroot met de MRI reproduceerbaarheidsstudie (n=8). De 'fout' of RMSE is het gemiddelde absolute verschil tussen de waarde van een segment in de eerste scan en de gemiddelde waarde van het overeenkomstige segment in de twee scans. Het percentage is de fout gedeeld door de gemiddelde waarde.

Door deze studie werd voor het eerst de reproduceerbaarheid van de combinatie van MRI en CFD gekwantificeerd *in vivo*. Omdat elke meettechniek zijn eigen meetfout met zich meebrengt, valt de werkelijke geometrie en halsslagaderdoorstroming *in vivo* niet ondubbelzinnig te bepalen. Vandaar dat de 'nauwkeurigheid', wat gedefinieerd wordt als het verschil tussen de gemeten waarde en de *werkelijke* waarde, niet bemeten kan worden. Dit wordt opgevangen door het begroten van de reproduceerbaarheid, die dankzij deze studie voortaan gekend is en in het verdere verloop van het proefschrift als referentiewaarde zal worden gebruikt.

Merk op dat deze studie geen eenduidig antwoord kan geven op de vraag of de techniek nu al dan niet reproduceerbaar is. De reproduceerbaarheid is immers afhankelijk van de vereiste nauwkeurigheid in een bepaalde toepassing. Indien toepassing "A" een nauwkeurigheid van 0.5 N/m^2 voor de WSS vereist, dan is de techniek zoals die er hier voorligt reproduceerbaar aangezien de gemiddelde RMSE in Tabel II.1 0.427 N/m^2 bedraagt. Indien toepassing "B" echter een strenge nauwkeurigheid van 0.1 N/m^2 vereist, is de techniek niet reproduceerbaar genoeg.

II.2.4. De vergelijking van TOF en BB

In een volgende studie werd de nauwkeurigheid van BB MRI onderzocht *in vivo*. Hiertoe werden 8 personen elk zes keer gescand: 3 keer met TOF MRI, en 3 keer met BB MRI. BB MRI heeft enkele inherente voordelen t.o.v. TOF MRI:

(a) ICA en ECA   (b) Distal CCA
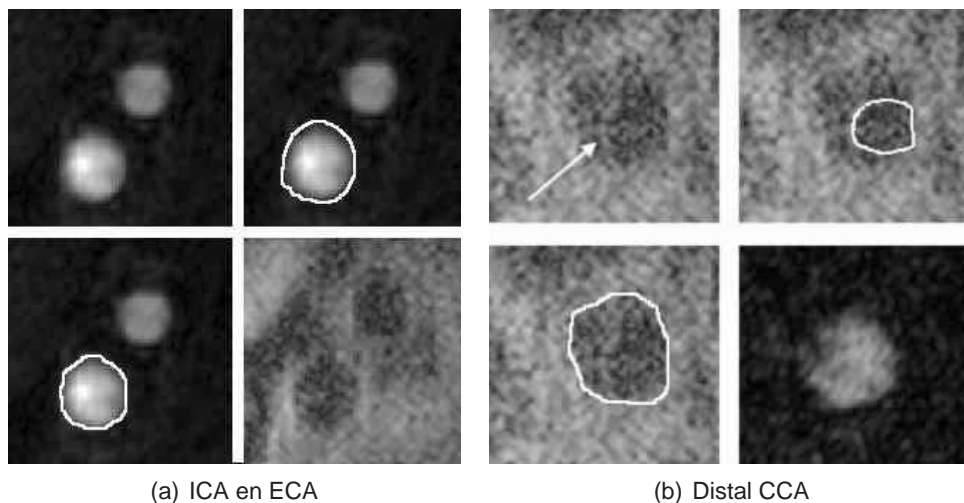
Figuur II.6.: Artefacten bij BB en TOF MRI. a: Proximale CCA coupes: het beeld links-boven is het TOF beeld, er rechts van en eronder staan twee manieren om te segmenteren. Het beeld rechtsonder is het corresponderende BB beeld. b: Distale CCA coupes: het beeld linksboven is het BB beeld, er rechts van en eronder staan twee manieren om te segmenteren. Het beeld rechtsonder is het corresponderende TOF beeld.

- Zoals Figuur II.2 (pagina NL - 20) duidelijk aantoont, heeft BB MRI de capaciteit om de dikte van de vaatwand te begroten.

- De beeldacquisitie bij BB MRI kan gesynchroniseerd worden zonder dat de acquisitietijd de grenzen van een voor de patiënt aanvaardbare tijdspanne overschrijdt.

  Samen met het eerste punt wordt het duidelijk dat BB MRI in staat is de *cyclische vervorming* van de wand te registreren.

- BB MRI vertoont minder artefacten in het bijzijn van eventuele metalen implantaten.[313]

- Figuur II.6 (a) (linksboven) is een TOF beeld van de proximale ICA. Deze kan op verschillende manieren gesegmenteerd worden, zoals wordt aangeduid rechts van en onder het originele beeld. De BB MRI tegenhanger van hetzelfde TOF beeld (rechtsonder) is van vergelijk-bare kwaliteit, maar dankzij het feit dat ondanks de grote ruis de vaat-wand goed in beeld werd gebracht, is het segmenteren van het BB beeld eenvoudiger. BB MRI is dan ook nauwkeuriger in de grotere vaten.

Maar ook TOF heeft een aantal belangrijke voordelen:

- TOF is veruit eenvoudiger om automatisch te segmenteren. Dit vertaalt zich in tijdwinst daar de operator die de automatische segmentaties dient te verwerken, veel minder werk heeft met het manueel corrigeren van de contouren.

- Voor de kleinere vaten, zoals de distale ICA en ECA, maar ook voor zones waar de bloedstroming erg complex is, zoals in de distale CCA, bereikt TOF een veel hogere nauwkeurigheid. Getuige hiervan is Figuur II.6 (b), waar linksboven een BB MRI beeld is getoond. De witte pijl duidt maanvormige ruis aan. Deze zou kunnen verward worden met de vaatwand zodat er twee verschillende segmentaties mogelijk zijn, weergegeven rechts van en onder het originele beeld. Enkel m.b.v. de TOF tegenhanger van dit beeld, dat ook niet van uitmuntende kwaliteit is, kan men zekerheid verschaffen over de grootte van de distale CCA bij deze persoon.

  Het gevolg van dit laatste punt is verregaand. Zo stelde men vast dat in deze studie de distale ICA of ECA soms volledig verdween bij de BB MRI scan, maar nog altijd aflijnbaar was bij de TOF MRI scan.

Ondanks het feit dat er in de verwerking van de beelden duidelijke verschillen tussen BB en TOF naar boven traden, bleken de kwantitatieve verschillen in de schuifspanning en andere hemodynamische parameters nog altijd van dezelfde grootteorde als die teruggevonden bij de TOF reproduceerbaarheidsstudie in paragraaf II.2.3.2 op pagina NL - 23. Omdat TOF veel snellere en in de distale delen van het model meer betrouwbare reconstructies toelaat, wordt voor de toekomst de voorkeur gegeven aan TOF MRI.

Wanneer de kennis van de dikte van de vaatwand van primordiaal belang is, kan de arts terugvallen op een BB MRI scan. Wanneer men echter zowel nauwkeurige reconstructies van de distale ICA en ECA wilt, gecombineerd met kennis van de vaatwanddikte, dient men de twee beeldvormende technieken combineren.

II.3. Ultrageluid

II.3.1. Inleiding

Ultrageluid (US) of echografie is een beeldvormende techniek waarbij golven worden uitgezonden door een probe die men op de huid plaatst. Deze trillingen zullen weerkaatsen wanneer die het scheidingsoppervlak tussen twee stoffen met verschillende impedantie[a] bereiken. Door gebruik te maken van de teruggekaatste golven, kan men een beeld vormen van de oppervlakken waarop de trillingen werden teruggekaatst. Figuur II.7 is een voorbeeld van een 'B-mode' beeld van de halsslagader. Het zwarte gebied, in de vorm van een ∞-symbool, omvat het lumen.

Wanneer de golf terugkaatst van een bewegend element, zoals bloed partikels, kan tevens de bewegingssnelheid van dat element bepaald worden. Deze techniek heet 'Doppler Ultrageluid'. Hier is het verschil in frequentie van de uitgestuurde en teruggekaatste golf evenredig met de snelheid van het element.

---

[a]impedantie = product van dichtheid en geluidssnelheid
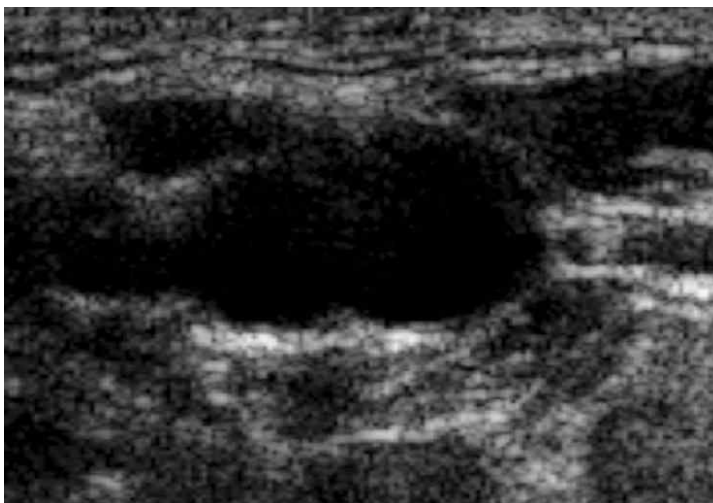
Figuur II.7.: B-mode beeld van de carotis van een gezonde 25 jarige man. De huid bevindt zich bovenaan het beeld, de bifurcatie is de zwarte zone in het midden van het beeld in de vorm van een ∞-symbool.

II.3.2. Meetprotocol

Het meetprotocol heeft als doel genoeg informatie te vergaren om de stroming in de halsslagader te reconstrueren. Zoals beschreven in het overzicht (deel II.1), zijn hiervoor zowel de geometrie als de randvoorwaarden nodig.

Om de geometrie op te meten werd gebruikt gemaakt van een 3D ultrageluid (3DUS) scanner gebouwd in het kader van een ander proefschrift.[20] Deze is gebaseerd op een commercieel beschikbare ultrasound scanner (HDI 5000, ATL-Philips Medical Systems, WA, USA) die routinematig gebruikt wordt voor vasculaire diagnoses. Een probe met linear kop (5 tot 12 MHz) wordt ingeschakeld om 2D doorsneden van de halsslagaderbifurcatie op te meten. Deze meting wordt gesynchroniseerd met de hartslag: typisch werden de beelden in late diastole opgemeten. Er kunnen tot 140 beelden opgeslagen worden, één per hartslag. De beelden worden in één beweging opgenomen, Hierbij verplaatst de arts de probe over de hals van de patiënt. Dit is geïllustreerd in Figuur II.8 door de dikke zwarte pijl van links naar rechts.
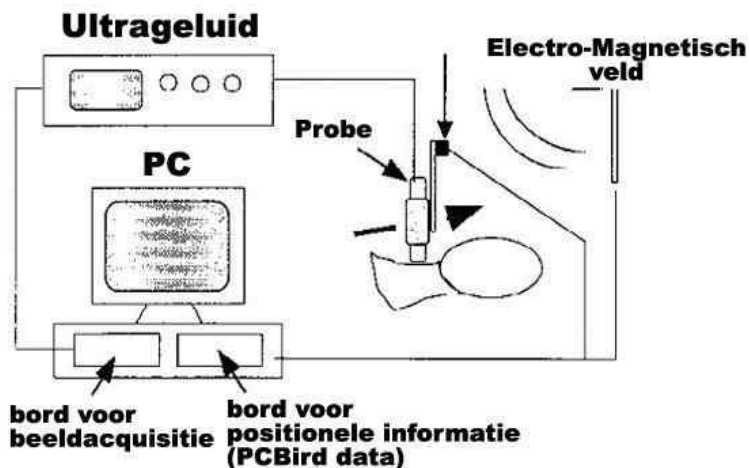
Figuur II.8.: 3DUS opstelling. De probe (verbonden aan het ultrageluid toestel) visualiseert gesynchroniseerde 2D B-mode coupes waarmee in een volgend stadium de 3D geometrie van de slagader gereconstrueerd wordt. Tegelijkertijd zendt een elektromagnetisch zendertje een signaal uit dat gebruikt wordt om de positie en oriëntatie van de probe op te meten (zwarte verticale pijl). De dikke zwarte pijl van links naar rechts illustreert de verplaatsing van de probe. Bedoeling van deze beweging is de ganse halsslagader in beeld te brengen. De B-mode beelden en de positionele informatie (PCbird data) worden samen opgeslagen in een gemeenschappelijke computer.

Tegelijkertijd registreert een elektromagnetisch positionerings- en oriënteringstoestel of EPOM (Ascension Technology Inc, Vermont, USA) de positie van de probe. Dit laat toe de positie van het beeld in 3D te berekenen.

Voor de randvoorwaarden dient de arts met Doppler ultrageluid, ter hoogte van de in- en uitlaat van het bestudeerde segment van de halsslagader, de snelheid op te meten in het centrum van het bloedvat. Aldus bekomt men een tijdsafhankelijke snelheidsmeting, typisch aan 200 Hz, voor zowel de CCA, ICA en ECA. Kennis van die snelheid samen met de kennis van de oppervlakte van de doorsnede van de slagader ter hoogte van het meetpunt laat toe, mits het veronderstellen van een rigide vaatwand en een ontwikkeld stromingsprofiel, het debiet of het tijdsafhankelijk snelheidsprofiel te berekenen.[140, 368] Aldus heeft men aan snelheidsmetingen in het centrum van het in- of uitlaatvlak genoeg om alle randvoorwaarden af te leiden.

II.3.3. Segmenteren en reconstrueren

Voor de segmentatie en de reconstructie werden in een vorig proefschrift[20] een aantal programma's geschreven. Het segmenteren van de echobeelden van de halsslagader wordt manueel gedaan, daar de beelden slecht contrast geven ter hoogte van de vaatwand. Figuur II.9 toont in het rood hoe het plaatje van Figuur II.7 manueel gesegmenteerd zou kunnen worden. Wanneer alle beelden gesegmenteerd zijn, kan men de rode contouren in de 3D ruimte op elkaar plaatsen. Hierbij wordt gebruik gemaakt van de positionele informatie vergaard met de EPOM. Nadat de geometrie is glad gemaakt, bekomt men een 3D voorstelling van en patiënt-specifieke halsslagaderbifurcatie die bruikbaar is voor numerieke stromingssimulaties.

In het kader van het huidig proefschrift werd de output van de bestaande programma's gebruikt om automatisch 3D discretisaties ('meshes') te creëren gebruik makend van programma's die geschreven werden voor de reconstructie van de halsslagader op basis van MR-beelden.

II.3.4. De nauwkeurigheid van US gecombineerd met CFD

Toen dit proefschrift in aanraking kwam met US-gebaseerde numerieke simulaties, was de nauwkeurigheid van de techniek al bepaald door Dr. A. D. Augst op een fantoom van een halsslagader. Desalniettemin werden hier, naar analogie met de studies die de nauwkeurigheid van MRI bepaalden,
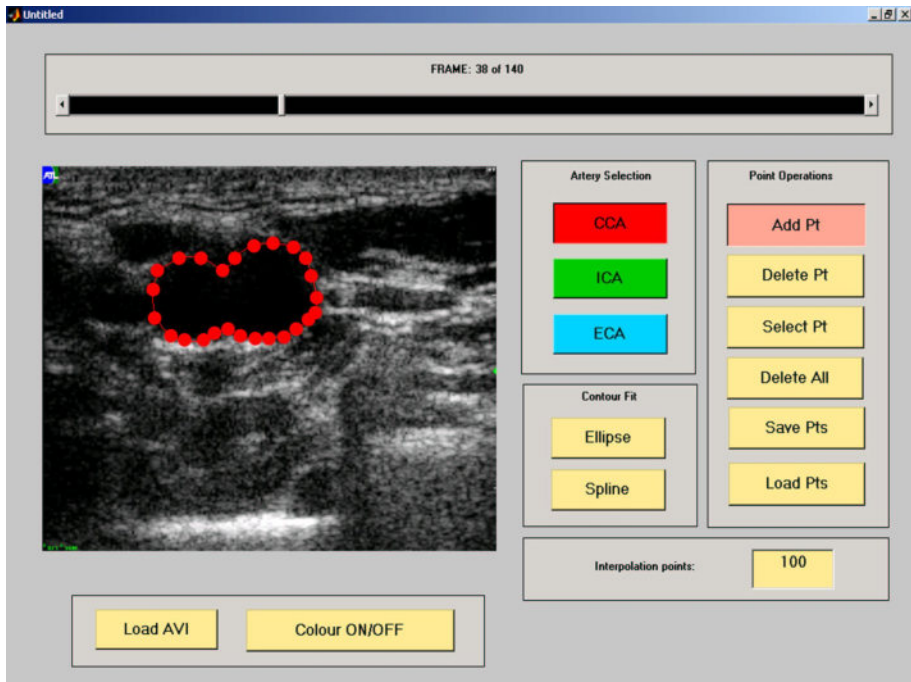
Figuur II.9.: Segmentatie van B-mode ultrageluid doorsnede van de halsslagader van Figuur II.7. Een operator plaatst de rode punten op het B-mode beeld en fit de rode lijn door te klikken op de 'spline' knop. Deze rode lijn is dan de segmentatie of de contour van dit beeld. Bovenaan het beeld kan men zien dat dit het 38ste beeld is van 140 opgeslagen beelden. Elk van die beelden is een doorsnede van dezelfde halsslagader.

weer fantoomscans uitgevoerd (deel II.3.4.1). Verder werd de *in vivo* nauwkeurigheid gedimensioneerd in een reproduceerbaarheidsstudie (deel II.3.4.2). Omdat er bij 3DUS een veel hogere graad van subjectiviteit aanwezig is dan bij MRI, waar de beelden automatisch gesegmenteerd worden, werd op het eind van dit hoofdstuk een variabiliteitsstudie uitgevoerd (deel II.3.4.3). Deze heeft als doel na te gaan wat de effecten zijn van die subjectiviteit bij het segmenteren en bij de beeldacquisitie.

II.3.4.1. *In vitro* studie

Hetzelfde fatoom dat in deel II.2.3.1 (*In vitro* studie bij MRI) was gebruikt, werd opnieuw aangewend. Het werd gescand en gesegmenteerd door twee personen. De eerste persoon (DB) was een 3DUS technieker, de tweede (BA) was een arts zonder ervaring in 3DUS. BA werd niet speciaal opgeleid vooraleer hij de scans uitvoerde.

Parameter (eenheid)	CAD Fantoom Data	DB (n=3) RMSE$\pm\sigma_{intra-op}$	BA (n=3) RMSE$\pm\sigma_{intra-op}$	$\sigma_{inter-op}$ (n=2)	σ_{al} (n=6)
A_{CCA} [mm^2]	53.214	+1.427 ± 1.915 (2.68±3.60%)	+11.172 ± 4.102 (20.99±7.71%)	7.051 (13.25%)	6.299 (11.84%)
A_{ICA} [mm^2]	37.891	+1.324 ± 0.176 (3.50±0.46%)	+9.010 ± 1.052 (23.78±2.78%)	5.434 (14.34%)	5.167 (13.64%)
A_{ECA} [mm^2]	17.309	+0.815 ± 0.173 (4.71±1.00%)	+5.027 ± 0.929 (29.04±5.37%)	2.978 (17.21%)	2.921 (16.88%)
A_R [-]	1.056	+0.103 ± 0.014 (9.77±1.30%)	+0.035 ± 0.028 (3.28±2.66%)	0.048 (4.58%)	0.069 (6.53%)
T_{CCA} [%]	0.450	+0.185 ± 0.227 (41.07±50.54%)	+0.234 ± 0.270 (52.10±60.04%)	0.059 (13.04%)	0.210 (46.59%)
T_{ICA} [%]	1.606	-0.276 ± 0.305 (17.19±18.99%)	-0.373 ± 0.155 (23.23±9.68%)	0.127 (7.92%)	0.325 (20.21%)
T_{ECA} [%]	1.974	-0.179 ± 0.136 (9.05±6.91%)	-0.248 ± 0.261 (12.57±13.23%)	0.031 (1.55%)	0.213 (10.81%)
α_{BIF} [°]	149.885	+3.777 ± 0.787 (2.52±0.52%)	+1.634 ± 0.746 (1.09±0.50%)	1.515 (1.01%)	2.706 (1.81%)
SF_{iCCA} [-]	0.964	+0.011 ± 0.005 (1.13±0.53%)	+0.007 ± 0.001 (0.77±0.07%)	0.002 (0.26%)	0.009 (0.95%)
SF_{iICA} [-]	0.993	-0.003 ± 0.004 (0.25±0.35%)	+0.002 ± 0.001 (0.22±0.13%)	0.002 (0.18%)	0.002 (0.24%)
SF_{iECA} [-]	0.993	+0.003 ± 0.000 (0.29±0.03%)	+0.002 ± 0.002 (0.21±0.17%)	0.001 (0.06%)	0.003 (0.25%)
WSS [N/m^2]	0.858	**-0.064 ± 0.060** (7.43±7.04%)	-0.167 ± 0.060 (19.42±7.04%)	0.080 (9.35%)	0.115 (13.43%)
WSS iCCA	0.416	+0.016 ± 0.021 (3.87±5.09%)	-0.021 ± 0.033 (5.17±7.94%)	0.019 (4.64%)	0.019 (4.52%)
WSS eCCA	0.491	+0.290 ± 0.103 (58.93±20.93%)	+0.081 ± 0.037 (16.47±7.52%)	0.148 (30.02%)	0.185 (37.70%)
WSS buiten ICA	1.026	+0.508 ± 0.062 (49.53±6.08%)	+0.479 ± 0.207 (46.70±20.14%)	0.021 (2.00%)	0.494 (48.12%)
WSS binnen ICA	1.512	+1.157 ± 0.072 (76.50±4.75%)	+0.891 ± 0.063 (58.89±4.16%)	0.188 (12.45%)	1.024 (67.69%)
WSS buiten ECA	0.679	+0.297 ± 0.032 (43.72±4.67%)	+0.156 ± 0.044 (22.94±6.52%)	0.100 (14.69%)	0.226 (33.33%)
WSS binnen ECA	1.131	+0.629 ± 0.051 (55.62±4.52%)	+0.387 ± 0.078 (34.22±6.89%)	0.171 (15.13%)	0.508 (44.92%)
OSI [-]	0.040	**+0.008 ± 0.003** (18.94±7.53%)	+0.007 ± 0.009 (17.66±22.21%)	0.002 (5.32%)	0.007 (18.30%)
OSI iCCA	0.075	+0.009 ± 0.009 (11.40±12.47%)	+0.022 ± 0.028 (29.58±37.21%)	0.001 (1.43%)	0.015 (20.49%)
OSI eCCA	0.040	-0.067 ± 0.002 (167.12±4.79%)	-0.043 ± 0.009 (107.31±22.97%)	0.017 (42.29%)	0.055 (137.22%)
OSI buiten ICA	0.064	+0.025 ± 0.007 (38.17±11.54%)	-0.031 ± 0.032 (47.48±49.74%)	0.030 (47.24%)	0.028 (42.83%)
OSI binnen ICA	0.001	-0.073 ± 0.000 (5319.63±13.42%)	-0.068 ± 0.005 (4953.10±331.48%)	0.004 (259.17%)	0.071 (5136.37%)
OSI buiten ECA	0.016	-0.056 ± 0.006 (350.62±39.48%)	-0.051 ± 0.017 (320.70±106.17%)	0.003 (21.15%)	0.054 (335.66%)
OSI binnen ECA	0.002	-0.072 ± 0.001 (3066.02±55.63%)	-0.070 ± 0.001 (2980.37±54.31%)	0.001 (60.56%)	0.071 (3023.20%)

Tabel II.2.: Statistiek voor de geometrische en stromingsparameters bemeten met 3DUS in combinatie met CFD op een fantoom. A_{art} staat voor de gemiddelde oppervlakte van de doorsnede van de arterie art (art = CCA, ICA of ECA), A_R staat voor de verhouding van de som van de doorstroomoppervlakte van de ICA en ECA, en CCA. T_{art} is de kromheid van de arterie art (T_{art} = 1-$\frac{kortste\ afstand\ inlaat-uitlaat}{lengte\ van\ arterie}$), α_{BIF} de hoek tussen ICA en ECA en SF_iart is een parameter die de vorm van de contouren begroot. De WSS en OSI werden uitgemiddeld over de ganse halsslagader, het deel van de CCA waar de ICA van aftak ('iCCA'), het deel van de CCA waar de ICA van aftak ('eCCA'), de binnenbocht en de buitenbocht van de ICA en ECA ('binnen' en 'buiten' ICA of ECA). Waarden zijn voorgesteld als het gemiddelde *absolute* verschil tussen de werkelijke fantoomdata en de gemeten waarde ± de standaard deviatie van de verschillen. Het teken geeft aan of de waarden gemiddeld gezien groter (+) dan wel kleiner (-) waren dan de werkelijke waarden. De percenten werden verkregen door te delen door de werkelijke waarde. CAD: werkelijke fantoomdata; DB: waarden opgemeten door DB; BA: waarden opgemeten door BA; zie tekst voor de definitie van $\sigma_{inter-op}$ en σ_{al}.

Tabel II.2 bevat de meeste resultaten van deze *in vitro* studie. De resultaten zijn voorgesteld als het gemiddelde absolute verschil tussen de gemeten waarde en de werkelijke waarde $\pm$ de standaard deviatie van het echte verschil (RMSE $\pm$ $\sigma_{intra-op}$). De 'werkelijke' waarde is weergegeven in kolom 'CAD'. Het teken geeft aan of de opgemeten waarde gemiddeld gezien groter (+) dan wel kleiner (-) was dan de werkelijke waarde. De percentages worden verkregen door te delen door de werkelijke waarde. $\sigma_{inter-op}$ is de standaard deviatie van de gemiddelden voor elke operator, en is een maat voor de variatie tussen operatoren onderling. σ_{al} is de te verwachten fout wanneer er één enkele meting wordt uitgevoerd door een onervaren operator.

Deze studie maakte volgende vaststellingen:

- σ_{al} is over het algemeen klein en vergelijkbaar met de waarden voor de gemiddelde RMSE in deel II.2.3.1, hetgeen laat vermoeden dat 3DUS klaar is voor *in vivo* toepassingen.

- De ervaren operator (DB) werkt veel nauwkeuriger dan BA. De absolute fout is immers doorgaans kleiner bij DB. Dit geeft aan dat er toch een minimum aan training vereist is vooraleer iemand het scannen met 3DUS en/of het segmenteren van US beelden goed onder de knie heeft.

- $\sigma_{intra-op}$ is vaak een grootte-orde groter dan de RMSE. Dit geeft aan dat de waarden verkregen uit twee verschillende scans door eenzelfde operator eigenlijk niet veel verschillen.

Merk op dat sommige percentages in Tabel II.2 astronomische waarden aannemen. Dit is het gevolg van het feit dat de werkelijke waarde, weergegeven in de kolom 'CAD', bijzonder klein is. In deze gevallen heeft het percentage natuurlijk weinig waarde, maar de standard deviaties blijven een maat voor de foutmarge van de techniek.

Het concept van deze studie, waar de beelden gesegmenteerd werden door de persoon die de acquisitie deed, liet niet toe na te gaan welk deel van de variantie te wijten is aan fouten in de beeldacquisitie dan wel aan segmenteringsfouten. De *in vivo* variabiliteitsstudie van deel II.3.4.3 geeft hier antwoord op.

II.3.4.2. *In vivo* studie

Opnieuw naar analogie met de MRI reproduceerbaarheidsstudie, werd hier een 3DUS reproduceerbaarheidsstudie uitgevoerd. Negen gezonde proefpersonen werden 2 keer gescand met 3DUS. De halsslagaderdoorstroming werd berekend met CFD. In alle simulaties werden dezelfde inlaatvoorwaarden gebruikt, zodat een verschil in snelheidsprofiel enkel te wijten kon zijn aan een verschil in 3D geometrie. Een aparte randvoorwaardestudie volgt in deel II.4.

Figuur II.10 toont resultaten voor proefpersoon nr. 1. Figuur (a) vergelijkt de arteriële oppervlakte van een doorsnede in de twee scans. Hierbij is de I/S as (Inferior/Superior) de as van voeten naar hoofd. Het nulpunt ligt ter hoogte van de apex van de beschouwde carotis. Figuur (b) vergelijkt dezelfde oppervlakte, maar uitgemiddeld over de I/S as. Figuur (c) tekent de centerlijn van scan 1 in het zwart en van scan 2 in het grijs. Om een 3D gevoel te krijgen van de centerlijnen, werden ze over elkaar getekend en vanuit twee standpunten weergegeven, 90° t.o.v. elkaar gedraaid. Figuren (d) tot (g) vergelijken de WSS en OSI distributie in beide scans.

(a) Verschil in oppervlakte van arteriële secties

(b) Gemiddelde oppervlakte van arteriële secties

(c) Centerlijnen

(d) WSS 1 (N/m^2)

(e) WSS 2 (N/m^2)

(f) OSI 1 (-)

(g) OSI 2 (-)
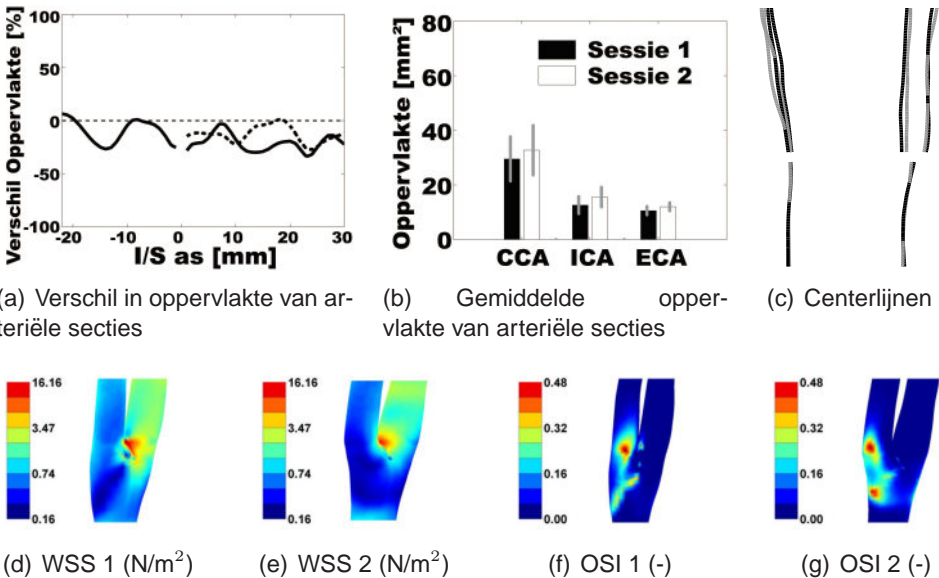
Figuur II.10.: De 3DUS reproduceerbaarheidsstudie voor een vrijwilliger. a: Verschil in oppervlakte van de arteriële doorsnede tussen de twee sessies voorgesteld als functie van de I/S as. b: Oppervlaktes uitgemiddeld over de I/S as in beide sessies. c: Centerlijn voor sessie 1 (zwart) en 2 (grijs) over elkaar getekend en 90° gedraaid. d-e: schuifspanningsverdeling in sessie 1 (d) en 2 (e). f-g: OSI verdeling in sessie 1 (f) en 2 (g).

Over alle patiënten heen werd, vergeleken met MRI, nagenoeg dezelfde graad van nauwkeurigheid behaald, al bleek 3DUS minder robuust. Vooreerst zijn er bij de positionering van de patiënt meer vrijheidsgraden, waardoor de nek en dus ook de halsslagader zich in verschillende posities bevonden bij eenzelfde patiënt. Ten tweede splitst de halsslagader zich soms pas ter hoogte van het kaakbeen, hetgeen niet toegankelijk is met een US probe. Het eerste was een kinderziekte die verholpen werd door een kleine wijziging van het protocol, het tweede is een voorlopig onopgelost probleem dat zal blijven bestaan zolang US niet toelaat door het bot metingen uit te voeren.

II.3.4.3. Variabiliteitsstudie

Tot slot werd de halsslagader van één gezonde vrijwilliger in totaal 11 keer gescand door 4 verschillende artsen (4 'DR's' die elk 3 of 2 keer de halsslagader opmaten). Elk van de artsen werd bijgestaan door een ervaren 3DUS gebruiker bij hun eerste scan. Elke data set werd gesegmenteerd door 3 operatoren (3 'OP's'), elk met een verschillende achtergrond en voorkennis. Aan deze OP's werd uitgelegd hoe men diende te segmenteren m.b.v. maximaal 10 voorbeeldplaatjes.

De resultaten van deze variabiliteitsstudie staan genoteerd in Tabel II.3. $\sigma_{inter-scan}$, $\sigma_{inter-DR}$ en $\sigma_{inter-OP}$ zijn respectievelijk de standaard deviatie van de gemiddeldes per scan (n=3), per DR (n=4) en per OP (n=3). Ze stellen respectievelijk een maat voor voor de reproduceerbaarheid, de variabiliteit te wijten aan de beeldacquisitie en de variabiliteit te wijten aan het segmenteren van de beelden. σ_{al} is de standaard deviatie van alle 33 metingen. Het percentage is berekend door te delen door de gemiddelde waarde, genomen over alle 33 metingen.

Uit deze variabiliteitsstudie kon men volgende conclusies trekken:

- σ_{al}, de totale variabiliteit, is vrij gering wanneer die vergeleken wordt met de waarden die in de reproduceerbaarheidsstudie voor MRI en 3DUS werden bekomen. Dit geeft aan dat de totale variabiliteit beperkt kan worden door een minimale training van de operatoren

- Doorgaans is $\sigma_{inter-DR}$ groter dan $\sigma_{inter-OP}$, hetgeen wilt zeggen dat de resterende, kleine, variabiliteit, voor het grootste deel te wijten is aan de subjectiviteit tijdens het scannen, eerder dan aan de subjectiviteit tijdens het segmenteren.

Parameter (eenheid)	$\sigma_{inter-scan}$ (n=3)	$\sigma_{inter-DR}$ (n=4)	$\sigma_{inter-OP}$ (n=3)	σ_{al} (n=33)
A_{CCA} [mm^2]	2.2676 (4.59%)	2.4655 (4.97%)	0.5860 (1.18%)	4.0486 (8.17%)
A_{ICA} [mm^2]	0.9320 (2.24%)	2.1353 (5.10%)	1.7138 (4.11%)	3.0903 (7.41%)
A_{ECA} [mm^2]	0.3505 (1.77%)	0.9377 (4.70%)	1.9510 (9.83%)	2.5980 (13.09%)
A_R [-]	0.0325 (3.53%)	0.0086 (0.94%)	0.0285 (3.10%)	0.0525 (5.71%)
NP [%]	0.8603 (15.32%)	1.1497 (20.64%)	0.0852 (1.53%)	1.6383 (29.34%)
NP_{CCA} [%]	0.2583 (17.58%)	0.2102 (14.52%)	0.0363 (2.52%)	0.5775 (40.07%)
NP_{ICA} [%]	0.8700 (42.19%)	0.9332 (43.54%)	0.1429 (6.88%)	1.4475 (69.75%)
NP_{ECA} [%]	0.0345 (8.03%)	0.0485 (11.15%)	0.0568 (13.14%)	0.1764 (40.83%)
L_{CCA} [%]	0.8142 (0.96%)	3.4926 (4.12%)	0.1218 (0.14%)	3.4995 (4.14%)
L_{ICA} [%]	1.3685 (1.73%)	3.7256 (4.69%)	0.3509 (0.44%)	3.4717 (4.39%)
L_{ECA} [%]	0.3844 (0.47%)	1.5485 (1.89%)	0.0519 (0.06%)	1.4426 (1.76%)
T_{CCA} [%]	0.2196 (15.35%)	0.2743 (19.82%)	0.0803 (5.70%)	0.3801 (26.99%)
T_{ICA} [%]	0.9291 (52.79%)	1.0038 (54.79%)	0.2358 (13.31%)	1.6469 (92.94%)
T_{ECA} [%]	0.0573 (8.35%)	0.2734 (38.47%)	0.1110 (16.17%)	0.7280 (105.99%)
α_{BIF} [°]	5.5711 (5.54%)	7.5465 (7.53%)	2.7725 (2.76%)	23.7628 (23.67%)
SF_{iCCA} [-]	0.0080 (0.83%)	0.0082 (0.85%)	0.0021 (0.22%)	0.0139 (1.45%)
SF_{iICA} [-]	0.0037 (0.38%)	0.0081 (0.82%)	0.0044 (0.45%)	0.0123 (1.26%)
SF_{iECA} [-]	0.0062 (0.64%)	0.0035 (0.35%)	0.0095 (0.97%)	0.0133 (1.35%)
Gem. $V_{MAX,CCA}$ [m/s]	0.0080 (3.65%)	0.0083 (3.78%)	0.0047 (2.14%)	0.0151 (6.89%)
Gem. $V_{MAX,ICA}$ [m/s]	0.0008 (0.46%)	0.0192 (10.86%)	0.0084 (4.69%)	0.0211 (11.84%)
Gem. $V_{MAX,ECA}$ [m/s]	0.0042 (2.78%)	0.0134 (8.86%)	0.0109 (7.17%)	0.0184 (12.11%)
Gem. WSS [N/m^2]	0.0087 (1.51%)	0.1155 (20.15%)	0.0467 (8.15%)	**0.1204 (20.99%)**
WSS iCCA [N/m^2]	0.0267 (5.66%)	0.0528 (11.26%)	0.0113 (2.40%)	0.0816 (17.42%)
WSS eCCA	0.0235 (5.04%)	0.0794 (16.64%)	0.0160 (3.42%)	0.0853 (18.24%)
WSS buiten ICA	0.0267 (4.08%)	0.1760 (26.84%)	0.0850 (12.97%)	0.1934 (29.51%)
WSS binnen ICA	0.0193 (2.32%)	0.1350 (16.45%)	0.0927 (11.14%)	0.1789 (21.50%)
WSS buiten ECA	0.0095 (1.54%)	0.1722 (28.35%)	0.1246 (20.31%)	0.2139 (34.85%)
WSS binnen ECA	0.0084 (1.17%)	0.1557 (21.76%)	0.1263 (17.49%)	0.2036 (28.21%)
Gem. OSI [-]	0.0062 (4.71%)	0.0272 (20.96%)	0.0048 (3.68%)	**0.0292 (22.19%)**
OSI iCCA [-]	0.0162 (10.95%)	0.0134 (8.99%)	0.0016 (1.07%)	0.0313 (20.94%)
OSI eCCA	0.0080 (4.46%)	0.0481 (27.78%)	0.0087 (4.88%)	0.0511 (28.54%)
OSI buiten ICA	0.0102 (11.19%)	0.0380 (43.20%)	0.0107 (11.87%)	0.0391 (43.45%)
OSI binnen ICA	0.0031 (6.16%)	0.0094 (18.05%)	0.0039 (7.70%)	0.0179 (35.31%)
OSI buiten ECA	0.0028 (1.95%)	0.0438 (30.12%)	0.0143 (9.82%)	0.0470 (32.27%)
OSI binnen ECA	0.0139 (15.64%)	0.0213 (23.71%)	0.0176 (19.63%)	0.0352 (39.34%)
Gem. WSSGs [N/m^3]	4.3955 (1.64%)	48.1821 (18.10%)	19.7994 (7.41%)	**50.6818 (18.97%)**
WSSGs iCCA [N/m^3]	4.8100 (2.27%)	14.0448 (6.65%)	3.7906 (1.80%)	20.1137 (9.53%)
WSSGs eCCA	6.1174 (2.81%)	14.4297 (6.62%)	5.6318 (2.59%)	20.1121 (9.25%)
WSSGs buiten ICA	16.0475 (5.87%)	79.8826 (29.21%)	39.1111 (14.30%)	88.8939 (32.49%)
WSSGs binnen ICA	9.7339 (2.34%)	50.9174 (12.39%)	40.5765 (9.79%)	74.6253 (18.00%)
WSSGs buiten ECA	7.8773 (2.60%)	74.5676 (24.81%)	58.1145 (19.19%)	96.4197 (31.83%)
WSSGs binnen ECA	2.8716 (0.77%)	51.9867 (13.93%)	54.0293 (14.41%)	85.3588 (22.77%)
Gem. WSSGt [N/(m^{2}s)]	0.1571 (1.61%)	1.4153 (14.55%)	0.6312 (6.49%)	**1.5368 (15.80%)**
WSSGt iCCA	0.2613 (2.80%)	0.6503 (6.96%)	0.2043 (2.20%)	0.9581 (10.30%)
WSSGt eCCA	0.3154 (3.40%)	0.8216 (8.81%)	0.3109 (3.36%)	1.0624 (11.47%)
WSSGt buiten ICA	0.4646 (4.71%)	2.1151 (21.50%)	1.0631 (10.79%)	2.3750 (24.10%)
WSSGt binnen ICA	0.3785 (3.33%)	2.2206 (19.69%)	1.1720 (10.33%)	2.5295 (22.28%)
WSSGt buiten ECA	0.3488 (3.70%)	2.2715 (24.33%)	1.6686 (17.72%)	2.8211 (29.96%)
WSSGt binnen ECA	0.1352 (1.38%)	2.3906 (24.55%)	1.6771 (17.09%)	2.8547 (29.09%)
Gem. WSSAG [rad/s]	6.0431 (4.36%)	16.8219 (12.14%)	1.1458 (0.82%)	**20.2853 (14.56%)**
WSSAG iCCA [rad/s]	12.7436 (10.76%)	11.9033 (9.97%)	2.5023 (2.09%)	19.2646 (16.10%)
WSSAG eCCA	1.6659 (1.08%)	27.1428 (17.96%)	4.6647 (3.03%)	30.3898 (19.74%)
WSSAG buiten ICA	5.1178 (5.01%)	10.2561 (10.04%)	9.3581 (9.12%)	21.7525 (21.20%)
WSSAG binnen ICA	9.2099 (6.07%)	23.2511 (15.14%)	19.0729 (12.50%)	36.9629 (24.22%)
WSSAG buiten ECA	4.6484 (2.48%)	32.7465 (17.47%)	1.2163 (0.65%)	40.5739 (21.65%)
WSSAG binnen ECA	14.0399 (7.46%)	48.0816 (25.45%)	6.8383 (3.62%)	54.4477 (28.79%)

Tabel II.3.: Variantieanalyse voor geometrische en hemodynamische parameters in de *in vivo* 3DUS variabiliteitsstudie, voorgesteld als standaard deviaties (percentage is de standaard deviatie gedeeld door de gemiddelde waarde (n=33)). Parameters zijn gedefinieerd in Tabel II.2 en deel I.3: 'De belangrijke parameters' (pagina NL - 12).

Deze variabiliteitsstudie gaf dus aan dat operatoren, zowel de persoon die de beelden maakt als de persoon die de beelden segmenteert, een training van slechts enkele uren vereisen vooraleer ze dezelfde nauwkeurigheid als bij MRI halen. De grootste variabiliteit zit vervat in de beeldvormingtechniek, en niet in de segmentatie.

Tabel II.3 is een interessant eindpunt van deze studie. Het toont aan, voor een resem parameters, wat de haalbare *in vivo* nauwkeurigheid is met numerieke stromingsmechanica gebaseerd op 3DUS.

II.4. De parameters van het model

II.4.1. Randvoorwaarden

II.4.1.1. MRI

'Phase Contrast' (PC) MRI, de MRI techniek die toelaat bloedsnelheden op te meten, werd onderzocht met het oog op het bepalen van de randvoorwaarde voor het computermodel. Doel van deze studie was de nauwkeurigheid van PC MRI na te gaan, en bovendien te verifiëren of het gebruik van PC MRI als randvoorwaarde de nauwkeurigheid van de simulatie kon opdrijven.

Opstelling De opstelling is voorgesteld in Figuur II.11. De pomp is de MRI versie van een 'UHDC[b] Flow Pump' (Numatics 225-3728 24VDC 6.0 Watt, Shelly Limited, London Ontario, Canada), die in staat is om een breed gamma aan debietprofielen op te leggen. De pomp bleef buiten de scanruimte om te ontsnappen aan het magnetisch veld van de scanner. Lange, versterkte - maar nog steeds flexibele - buizen verbonden de pomp met een U-bocht uit plexiglas. Een ultrasone debietmeter (HT207 Transonic Flowmeters, Transonic, Ithaca, New York, USA) was geplaatst op de buis die de U-bocht verlaat.

De nauwkeurigheid van PC MRI In een eerste proef werd een constant debiet water door het model gepompt (Reynolds getal: 404). Met behulp

---

[b]**UHDC**: University Hospital Development Canada

(a) U-tube   (b) Opstelling
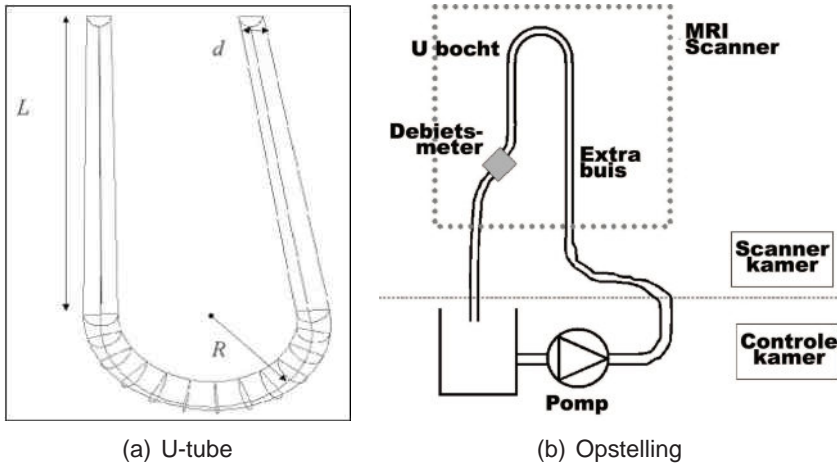
Figuur II.11.: Opstelling gebruikt bij de studie van PC MRI.

van PC MRI werden de snelheden opgemeten in de buis en vergeleken met de werkelijk optredende snelheden. Deze 'ware' snelheden in de ganse U-bocht werden bekomen door een numerieke simulatie die het gekende debiet (ingesteld op de pomp en ook opgemeten door de flow probe) oplegt op de gekende geometrie van de buis. Deze numerieke simulatie werd herhaald met twee soorten randvoorwaarden: een eerste keer met een uniform instroomprofiel ('uniform' model), en een tweede keer met een parabolisch instroomprofiel ('Poiseuille' model). Dankzij het respecteren van een instroomlengte van 8cm bij het uniform model, was er geen verschil tussen deze twee simulaties en konden snelheidsvelden bekomen uit elk van beide simulaties gebruikt worden voor de vergelijking met snelheidsvelden bemeten met MRI. Deze studie toonde aan dat de snelheidsmetingen in de axiale richting nauwkeurig zijn tot op 10% van de sensitiviteit, ingesteld door de MRI operator.

Het gebruik van PC MRI als randvoorwaarde   Figuur II.12 illustreert in de twee linkse plaatjes de uniforme en parabolische randvoorwaarde. Behalve deze twee simulaties waarin het gekende debiet opgelegd werd, werden de snelheden in het inlaatvlak (opgemeten met PC MRI) ook gebruikt als randvoorwaarde (Figuur II.12, rechts). Ook hier werden twee simulaties uitgevoerd: een eerste met de opgemeten snelheden in het inlaatvlak zelf ('MRI' model), en een tweede met snelheden uitgemiddeld over drie metin-
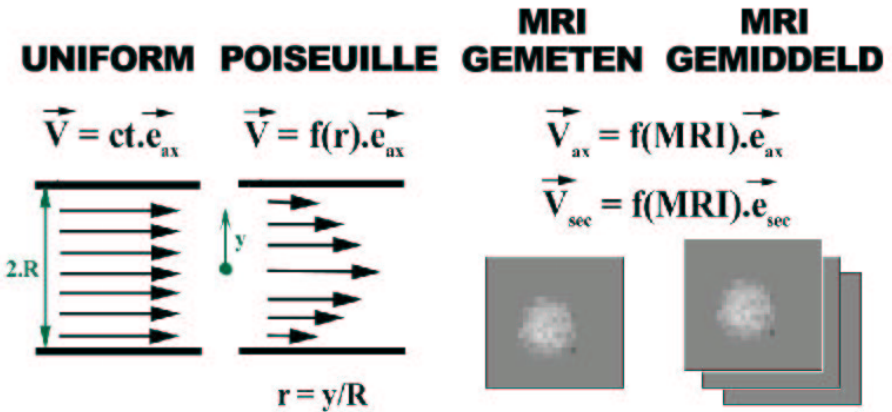
Figuur II.12.: De bestudeerde randvoorwaarden. $\overrightarrow{V}$ is de snelheid opgelegd aan de inlaat; ct is een constante gelijk aan het debiet gedeeld door de doorstroomoppervlakte; $\overrightarrow{e_{ax}}$ is de axiale eenheidsvector; $\overrightarrow{e_{sec}}$ stelt de eenheidsvector voor van beide richtingen in het vlak van het beeld; y varieert lineair tussen 0 in het centrum van de buis en R aan de omtrek; f(r) betekent dat de inlaatsnelheden afhangen van de relatieve afstand van het beschouwde punt tot het centrum van de buis; f(MRI) betekent dat de inlaatsnelheden afhangen van de PC MRI metingen, zij het van de metingen in één vlak (MRI gemeten) of opeenvolgende vlakken (MRI gemiddeld).

gen in de buurt van[c] het inlaatvlak ('MRI gemiddeld' model), gebaseerd op een idee van Weston.[362]

De verschillen in snelheidsprofielen tussen de vier numerieke simulaties - uniform, Poiseuille, MRI of MRI-gemiddeld - waren te wijten aan het feit dat het debiet bij de MR-gebaseerde randvoorwaarden niet altijd correct was opgemeten (fout van 10%). Dit onderstreept het belang van een juiste debietmeting. De 'MRI-gemiddeld' simulatie bood geen extra voordelen in vergelijking met het 'MRI' model. Verder stelde men een verschil in numerieke stabiliteit vast: ruis in de PC MRI snelheidsmeting, zoals weergegeven door cirkels A en B in Figuur II.13, ondermijnt de stabiliteit van de simulatie. Deze studie maakte duidelijk dat de inlaatsnelheden (i) gefilterd moeten worden om destabiliserende ruis weg te halen en (ii) herschaald moeten worden om in overeenstemming te zijn met een aparte, correcte debietmeting. Onder die voorwaarden kunnen de voordelen van directe snelheidsmetingen met PC MRI aangewend worden om meer realistische randvoorwaarden te genereren.

---

[c]De drie metingen omvatten een meting in een vlak 5mm proximaal van het inlaatvlak, een meting in het inlaatvlak zelf, en een derde meting 5 mm distaal van het inlaatvlak.
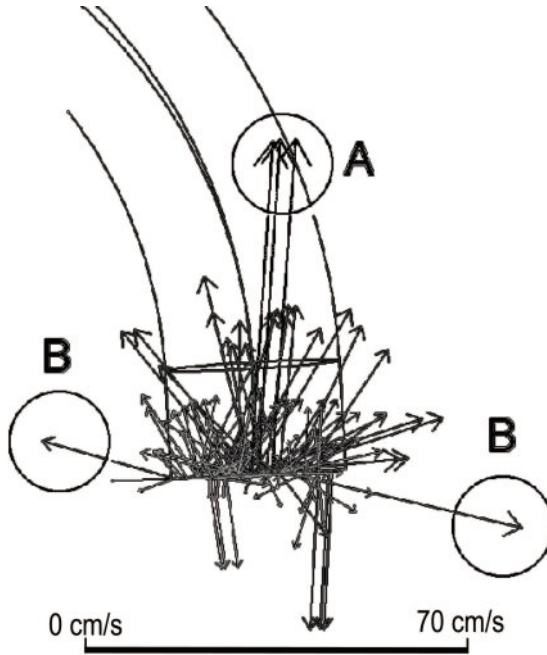
Figuur II.13.: Snelheden opgemeten in het inlaatvlak en bij wijze van voorbeeld geïmplementeerd zonder voorafgaande filtering. De grote axiale (A) en secundaire (B) snelheden zullen de numerieke simulatie destabiliseren en dienen dus gefilterd te worden.

Na deze initiële proef werden nog 6 proeven gedaan: 3 stationaire en 3 pulsatiele proeven, elk met een 40:60 verhouding glyceryne:water. Het voordeel t.o.v. water is dat dit mengsel fysische eigenschappen heeft die vergelijkbaar zijn met bloed. Opnieuw werden verschillende inlaatvoorwaarden gebruikt. De resultaten van deze proeven bevestigden wat in de initiële proef werd gesuggereerd: wanneer men de opgemeten snelheden filtert en herschaald naar een gekend debiet, dan biedt PC MRI de beste randvoorwaarden: (i) er worden immers geen veronderstellingen gedaan met betrekking tot het snelheidsprofiel, hetgeen resulteert in correctere voorspellingen van de proximale snelheidsprofielen en (ii) men kan de te simuleren 3D ruimte klein (dus snel berekenbaar) houden door de snelheidsmeting uit te voeren in de directe nabijheid van het te diagnoseren stromingsgebied.

II.4.1.2. 3DUS

Tenslotte werd ook bij US een studie uitgevoerd naar de meest nauwkeurige manier om snelheidsmetingen te implementeren als inlaatvoorwaarde.

Er wordt telkens uitgegaan van een Doppler snelheidsmeting in het centrum van de halsslagader ter hoogte van het begin (of einde) van het 3D model. Deze snelheidsmeting, gecombineerd met het oppervlak van de doorsnede, laat toe het bloeddebiet te berekenen.

Hierbij wordt een veronderstelling gemaakt over het snelheidsprofiel ter hoogte van de snelheidsmeting, i.e. ter hoogte van het in- of uitlaatvlak. Twee snelheidsprofielen werden uitgetest: een eerste waarbij een in de tijd variërend parabolisch snelheidsprofiel gebruikt werd, en een tweede waarbij een 'Womersley' profiel geprogrammeerd werd, waar het snelheidsprofiel ontstaat uit een combinatie van Besselse functies.[368, 375] De veronderstelling van een parabolisch of Womersley snelheidsprofiel laat toe aan de inlaat de snelheden te berekenen op basis van de snelheid opgemeten in het centrum van het bloedvat. Analoog kan men de fractie van het debiet berekenen dat naar elke tak van de halsslagader stroomt. Doel van de studie was na te gaan welke veronderstelling, de parabolische of de Womersley, de meest realistische is.

Beide onderstellingen werden uitgetest op één gezonde proefpersoon en vergeleken met een PC MRI meting. De studie begrootte het verlies aan nauwkeurigheid dat het gebruik van Doppler-metingen als randvoorwaarde met zich meebracht. Uit de studie kan afgeleid worden dat het beter is de parabolische veronderstelling uit te voeren, eerder dan de meer gangbare Womersley veronderstellingen. De studie toonde aan dat het de moeite loont meer proefpersonen te gaan opmeten vooraleer men verregaande conclusies trekt.

II.4.2. Viscositeit

Nadat de in- en uitlaatvoorwaarden bestudeerd waren, werden andere numerieke parameters onder de loep genomen. Bloed is geen homogene vloeistof: het bestaat uit een gele substantie, het plasma, waarin talrijke eiwitten en andere molecules in opgeloste vorm aanwezig zijn. Daarnaast bevat het bloed de bloedlichaampjes die door het bloed getransporteerd worden. Door deze samenstelling is de viscositeit van het bloed niet constant, maar hangt ze - bij eenzelfde temperatuur - af van de diameter van het bloedvat, de afschuifsnelheid en de concentratie cellen in het bloed (of het hematocriet). Dit gedrag van het bloed werd bestudeerd door talrijke onderzoekers en gebundeld in een publicatie door Zhang.[382] In het kader van dit proefschrift werd de impact nagegaan van het gebruik van een dergelijk
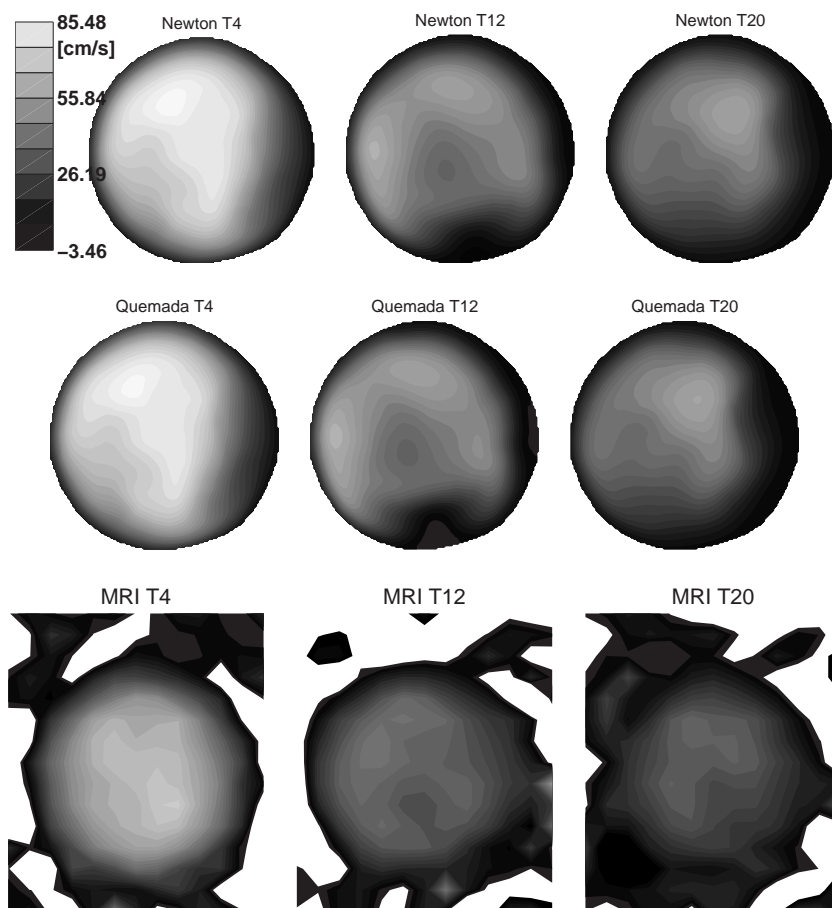
Figuur II.14.: Snelheidsprofielen bekomen met verschillende viscositeitsmodellen. T4: systole; T12: vroege diastole; T20: late diastole. 'Newton': Constante viscositeit, laminaire stroming; 'Quemada': Quemada viscositeit, laminaire stroming; 'MRI': cine PC MRI meting.

numeriek model. Hiertoe werden twee simulaties uitgevoerd: één mèt viscositeitsmodel, en één zonder. Het gekozen viscositeitsmodel was dat van Quemada, beschreven door Buchanan en Kleinstreuer.[42]

Enkele resultaten zijn vervat in Figuur II.14. Er werd vastgesteld dat de impact van het gebruik van de viscositeitsmodellen bijzonder gering was.De studie besluit dan ook dat een model zonder viscositeitswet de snelste oplossing is die slechts een kleine toegifte doet naar nauwkeurigheid. Desalniettemin, om het realisme van de simulatie op te drijven, werden nagenoeg alle berekeningen die in het kader van dit proefschrift uitgevoerd werden, met een Quemada viscositeitsmodel uitgevoerd.

II.5. Ultrageluid of Magnetische Resonantie?

In paragrafen II.2 en II.3 werd telkens gefocust op één beeldvormende tech-
niek, MRI of US. Traditioneel gebruikt men MRI bij het in kaart brengen van
de 3D geometrie van de halsslagader. Nochtans heeft MRI enkele inhe-
rente nadelen. Het is niet toegankelijk voor zwaar zieken, claustrofoben of
weerspannige kinderen. De beeldacquisitie neemt veel tijd in beslag (30
tot 45 min) en het is vooral duur. Een nieuw toestel kost gemiddeld tus-
sen de 0.8 en 1.5 miljoen euro, zonder installatiekosten of bijhorende soft-
ware. Vooral dat laatste kan de prijs opdrijven tot 2 miljoen euro (bron:
costumer services Philips Medical Belgium). In dit opzicht heeft ultrageluid
(US) duidelijke voordelen: het kan tot naast het bed van de patiënt gerold
worden, de beeldacquisitie is uiterst snel (5 tot 10 min) en het toestel kost
slechts een fractie van een MR scanner: tussen de 50000 en 150000 euro
(bron: costumer services Philips Medical Belgium). Natuurlijk kan men
alleen maar overschakelen naar US als dezelfde graad van nauwkeurigheid
behaald wordt. Om die graad van nauwkeurigheid te kennen, werden beide
beeldvormende technieken getest op een groep vrijwilligers.

Om de twee technieken met elkaar te vergelijken, werden er 9 gezonde vrij-
willigers elk twee maal gescand: één keer met BB MRI en een andere keer
met 3DUS. Zowel geometrische als hemodynamische parameters werden
vergeleken. Figuur II.15 toont de verdeling van de schuifspanning en OSI in
een vrijwilliger op basis van MRI enerzijds en 3DUS anderzijds.

Bij de geometrische parameters behoort de oppervlakte van een gemid-
delde doorsnede van de slagader. Tabel II.4 vergelijkt voor die parameter
de verschillen gemeten in deze studie met verschillen gemeten in andere
studies die de nauwkeurigheid van MRI of 3DUS bestudeerden. Er wordt
vastgesteld dat de verschillen opgemeten in deze studie groter zijn dan de
onzekerheid die gerapporteerd werd voor elk van de technieken afzonder-
lijk in hun reproduceerbaarheidsstudies,[118, 332] maar lager zijn dan de vari-

(a) WSS MRI   (b) WSS 3DUS   (c) OSI MRI   (d) OSI 3DUS
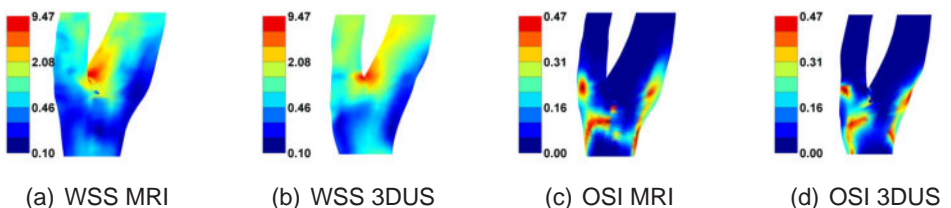
Figuur II.15.: WSS [N/m^2] en OSI [-] distributie in een vrijwilliger opgemeten met zowel MRI
als 3DUS.

Techniek	CCA	ICA	ECA
BB MRI validatie (fantoom)[225]	4.77 (7.50%)	2.12 (7.49%)	2.45 (12.5%)
BB MRI *in vivo* reprod.[332] *(n=3)*	6.36 (10.0%)	2.83 (10.0%)	1.96 (10.0%)
MRI (fantoom, vergeleken met US)[98]	9.33 (14.7%)	6.22 (22.0%)	5.18 (26.4%)
3DUS validatie op fantoom[20]	4.99 (7.85%)	2.22 (7.84%)	1.54 (7.86%)
3DUS *in vivo* reprod.[118] *(n=9)*	6.36 (10.0%)	2.83 (10.0%)	2.94 (15.0%)
US (fantoom, vergeleken met MRI)[98]	15.54 (24.43%)	10.36 (36.6%)	8.64 (44.1%)
Huidige studie: BB MRI - 3DUS	3.60±7.39	5.18±6.23	2.46±3.62
	5.66±11.6%	18.3±22.1%	12.6±18.5%

Tabel II.4.: Fout op de meting van de oppervlakte van een arteriële sectie gerapporteerd in de literatuur.[22,98,118,225,332] reprod.: reproduceerbaarheidsstudie. Wanneer de publicatie een fout op de diameter rapporteert i.p.v. een oppervlakte, werden grote diameters van 9 mm (CCA), 6 mm (ICA) en 5 mm (ECA) gekozen als referentie. Alle waarden in mm^2, behalve de percentages.

abiliteit teruggevonden in een vroegere vergelijkende studie tussen MRI en ultrageluid.[98] Dit wil zeggen dat er voor het bepalen van de oppervlakte van de dwarse doorsnede van een halsslagader een systematisch verschil bestaat tussen een meting met MRI en een meting met ultrageluid, een verschil dat overigens wel kleiner is dat de verschillen die een decennium geleden nog opgemeten werden door Frayne.[98] Merk op dat dit systematisch verschil niet significant bleek.

Voor de hemodynamische parameters is de situatie anders. De verschillen zijn weergegeven in Tabel II.5. Hier was het verschil opgemeten tussen beide technieken meestal van dezelfde grootte-orde als de reproduceerbaarheid die gekwantificeerd werd in bovenstaande studies, hetgeen aangeeft dat MRI en 3DUS uitgewisseld kunnen worden zonder dat er een klinisch belangrijk verschil in nauwkeurigheid optreedt.

Wil dat zeggen dat MR afgeschreven is om als beeldvormende techniek te dienen voor de visualisatie van de bloedstroming? Neen, US heeft immers ook een drietal nadelen. (1) Zo kan met US niet door het kaakbeen gekeken worden, hetgeen een probleem is wanneer de halsslagader zich pas op die hoogte opsplitst. (2) Bovendien kan US geen kwaliteitsvolle beelden maken wanneer de plaque calciumrijk is. (3) Tenslotte werkt US alleen bij oppervlakkige arteries zoals de halsslagader, zodat men voor het berekenen van de stroming in alle delen van de aorta a priori aangewezen is op MRI. Het tekort aan penetratie bij ultrageluid is dan ook een probleem dat het toepassingsgebied ervan beperkt. Wat deze studie wel aantoont, is dat in eerste instantie niet MRI, maar US zou moeten gebruikt worden wanneer men de schuifspanningen in de halsslagader wil meten. Deze vaststelling vermijdt het routinematig gebruik van de dure MRI scan.

arterie	WSS [N/m^2]	OSI [-]	WSSGs [N/m^3]	WSSGt [N/(s.m^2)]	WSSAG [rad/m]
CCA	0.314 (45.9%)	0.0658 (104%)	56.1 (35.3%)	1.80 (24.8%)	96.2 (78.0%)
ICA	0.534 (44.0%)	0.0416 (123%)	164 (54.5%)	3.34 (36.6%)	74.5 (91.6%)
ECA	0.397 (40.0%)	0.0420 (193%)	149 (52.8%)	2.11 (28.1%)	90.4 (88.4%)
SAMEN	0.411 (42.7%)	0.0481 (166%)	150 (55.4%)	2.29 (29.1%)	87.6 (86.3%)
Thomas[332]	0.44 (32%)	0.021 (109%)	38 (55%)	-	61 (73%)
Glor[121]	0.43 (37.9%)	0.025 (123%)	214 (65.7%)	2.35 (30.2%)	68.1 (79.8%)

Tabel II.5.: De onzekerheid (RMSE) opgemeten voor de hemodynamische parameters bij de vergelijking van MRI en 3DUS. Tabel II.1 legt uit hoe deze waarden begroot worden. Het percentage tussen haken is de RMSE gedeeld door de gemiddelde waarde (n=8 en niet n=9 omdat 1 vrijwilliger verkeerd gescand werd met 3DUS). Ter vergelijking staan de resultaten van twee MRI reproduceerbaarheidsstudies aangegeven.[121,332]

III. *In vivo* Toepassingen

III.1. Inleiding

Het eerste deel van dit proefschrift heeft zich gefocust op de techniek zelf. Het opdrijven en het kwantificeren van de nauwkeurigheid stonden daarbij centraal. Nu de nauwkeurigheid gekend is, kan de techniek ingezet worden voor verschillende klinische doeleinden.

Één van de toepassingen waar het meest van verwacht wordt, is pre-operatief onderzoek. Hier wordt bijvoorbeeld een patiënt die een aneurysma ter hoogte van de halsslagader heeft, naar de scanner gebracht. Een aneurysma is een verzwakking van de vaatwand, waardoor het onder de druk van het bloed gaat uitstulpen. In een verregaand stadium zal dit aneurysma openbarsten hetgeen doorgaans leidt tot de dood. Tegenwoordig zal men op basis van de grootte van het aneurysma beslissen over te gaan tot een operatie. Dit is echter een gevaarlijk criterium: sommige aneurysmata gaan barsten terwijl ze klein zijn, andere zijn nog stevig genoeg bij een belangrijke omvang. In het eerste geval moet men sneller ingrijpen, in het tweede geval is het niet verantwoord om de (zwakke) patiënt een gevaarlijke en dure operatie te doen ondergaan. Actueel opereert men bij een alarmerende omvang van het aneurysma, maar in feite zou de sterkte van de vaatwand een beter criterium zijn op basis waarvan men zou moeten beslissen om te opereren. Het combineren van een beeldvormende techniek met CFD (computational fluid dynamics of numerieke stromingsmechanica) laat toe de schuifspanningen aan de wand te berekenen. De beslissing om over te gaan tot een operatie laten afhangen van waarde van de spanningen in plaats van de omvang van een aneurysma zou een aanzienlijke maatschappelijke last verlichten en bovendien een geldbesparing met zich meebrengen.

Behalve voor aneurysmata heeft deze techniek een belangrijke rol te vervullen bij patiënten met stenosen of vernauwingen ter hoogte van de halsslagader. De plaque die in deze zone geconstateerd wordt, kan door een chirurgische ingreep verwijderd worden (endarterectomie). Deze operatie

is echter zeer duur waardoor de verzekeringsmaatschappijen dergelijke ingrepen enkel toestaan wanneer het duidelijk is geworden dat de patiënt last ondervindt van die plaque. Dat wil zeggen dat de operatie pas geschiedt nadat de patiënt een zogenaamde TIA overleeft (Transient Ischeamic Attack). Een TIA is een herseninfarct van voorbijgaande aard. De bloedtoevoer naar een deel van de hersenen wordt dan afgesloten totdat de obstruerende bloedklonter terug is opgelost. TIA's kenmerken zich door duizeligheid, moeite om te spreken, verlamming van gezicht of ledematen of tijdelijk verlies van de zintuigen. Bij het optreden van een TIA wordt een ingreep zeer acuut en nogal vaak komt de ingreep te laat, i.e. na verlies van een deel van de hersenactiviteit of sterfte. De bestudeerde techniek kan nietinvasief de krachten begroten die op de plaque inwerken. Kennis van die krachten en kennis van de morfologie van de plaque laten toe een gefundeerde uitspraak te maken over de kans dat een stukje kalk zou afbreken. Als de nauwkeurigheid van de techniek gekend is, kunnen prospectieve studies ondernomen worden om na te gaan of het veiliger is op basis van een verdeling van de krachten over te gaan tot een operatie eerder dan te wachten tot de eerste TIA zich voordoet.

Hoewel de techniek in dit proefschrift zich enkel op de halsslagader heeft gefocust, is haar toepassingsgebied niet beperkt tot de slagaders in de hals, maar kan ze net zo goed gebruikt worden bij aneurysmata van de aorta, bypasses van de femoralis (beenslagader), of bij problemen met de nierdoorbloeding. Het combineren van medische beeldvorming en CFD heeft dan ook een zeer breed toepassingsgebied met hoge maatschappelijke relevantie en is een groeipool binnen het biomedisch ingenieursonderzoek.

Binnen het kader van dit proefschrift werd de techniek ingezet bij twee klinische studies. Een eerste studie ging na wat de impact is van het draaien van het hoofd op de doorstroming in de halsslagader (deel III.2). Een ander project bestudeerde de veranderingen in geometrie en doorstroming van de halsslagader na orale inname van verschillende anti-hypertensiva (deel III.3).

III.2. Het draaien van het hoofd

III.2.1. Inleiding en proefopstelling

In de literatuur werd er vastgesteld dat de halsslagaders zich anders positioneren wanneer men het hoofd draait.[314] Dat de geometrie van de halsslagader een beweging ondergaat bij het draaien van het hoofd was geweten, de impact ervan was echter ongekend. Studies[241] suggereerden dat herseninfarcten te wijten kunnen zijn aan een langdurige slechte doorstroming van de halsslagader tengevolge van een langdurige slechte positionering van het hoofd vb. bij het telefoneren. Het testen van deze suggestie was één van de doelstellingen van deze studie.

Doel van deze klinische studie was de impact van het draaien van het hoofd op de doorstroming van de halsslagader te bestuderen. Hiertoe werden 9 gezonde vrijwilligers gescand met US in twee posities: éénmaal met het gezicht recht voor zich uit, en een andere maal met het hoofd 90 graden gedraaid naar links. Het belang van de studie ligt hem in het feit dat voor het eerst de veranderingen in geometrie, waarvan men wist dat ze voorkwamen, gekwantificeerd werden. Bovendien werd de impact van deze veranderingen op de doorstroming van de halsslagader mee begroot.

III.2.2. Resultaten

Figuur III.1 toont aan hoe de doorstroomoppervlakte van de carotis communis, de planariteit, het bloeddebiet en de gemiddelde schuifspanning wijzigde bij het draaien van het hoofd. Men stelde vast (Figuur III.1 (a)) dat de doorstroomoppervlakte niet wijzigde. De positie van de takken van de halsslagader t.o.v. elkaar (Figuur III.1 (b)), het debiet bloed (Figuur III.1 (c)), de schuifspanningverdeling (Figuur III.1 (d)) en de OSI wijzigden op individuele basis significant nadat het hoofd gedraaid werd. Samen met de wijzigingen in geometrie werd dus duidelijk dat ook de doorbloeding van de halsslagader (en dus de hersenen) ernstige veranderingen ondergaat.

(a)

(b)

(c)

(d)
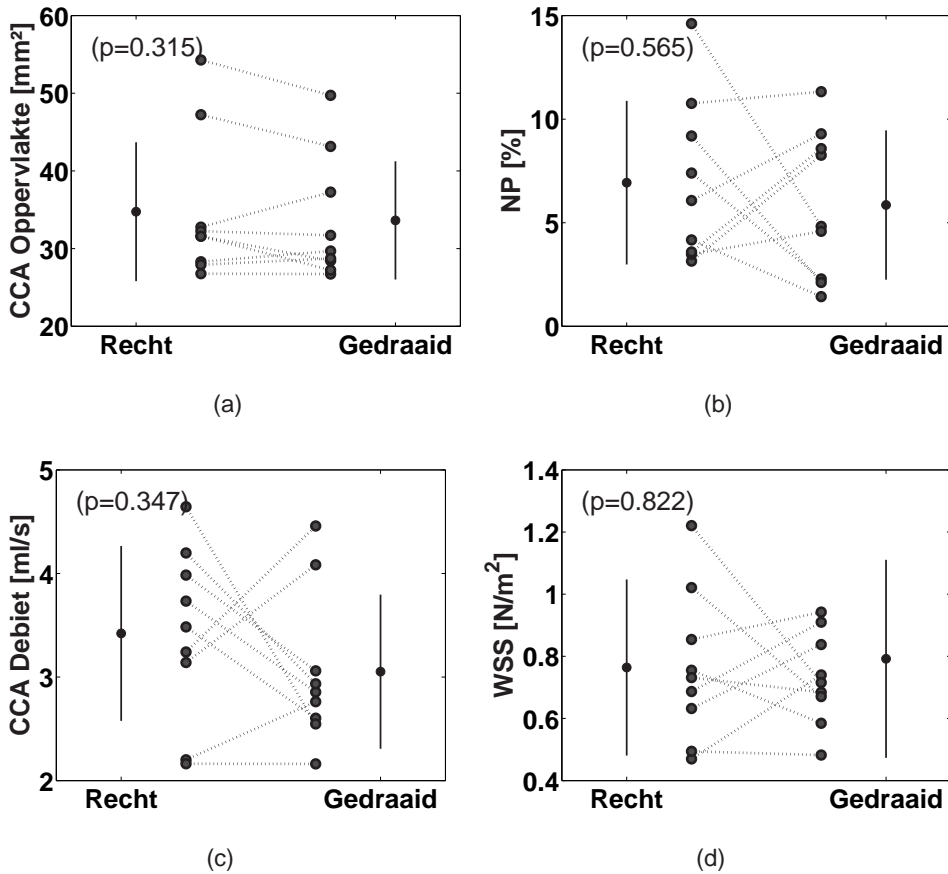
Figuur III.1.: Verandering in arteriële oppervlakte (a), planariteit NP (b), debiet (c) en WSS (d) bij het draaien van het hoofd. Het zwarte punt met de verticale lijn is het gemiddelde $\pm$ standaard deviatie over alle proefpersonen (n=9) in een bepaalde positie ('Recht': hoofd recht; 'Gedraaid': hoofd 90° gedraaid). De grijze punten zijn individuele metingen, 1 per vrijwilliger. Metingen die eenzelfde vrijwilliger toebehoren zijn met een streepjeslijn verbonden. De p-waarde test de hypothese dat de gemiddeldes per positie (i.e. de zwarte punten) gelijk zouden zijn.

III.2.3. Impact van de studie

Met deze studie werd gesuggereerd dat plaque in de halsslagader zich in een veilige situatie kan bevinden in de ene positie, maar ten gevolge van de gewijzigde krachtenverdeling zou kunnen afbreken en een herseninfarct veroorzaken in de andere positie. Gelijkaardige lessen worden getrokken door fabrikanten van implantaten voor de halsslagader. 'Stents' zijn spiralen uit metaal of kunststof. Deze worden in de halsslagader ingeplant met de bedoeling een vernauwd vat terug open te duwen. Stents zijn zeer gevoelig aan revascularisatie: een situatie waarbij de stent overgroeid wordt door het

vaatwandweefsel, wat leidt tot een nieuwe vernauwing van het vat. Om dit uit te sluiten, wordt de stroming over de stent bestudeerd: bepaalde stromingssituaties zijn behulpzaam bij het vermijden van revascularisatie. De huidige studie toont echter aan dat een stromingssituatie goed kan zijn bij een normale houding van het hoofd, terwijl revascularisatie net in de hand kan gewerkt worden in een andere houding. Producenten van stents dienen dan ook hun implantaten in verschillende houdingen uit te testen. Dezelfde redenering is geldig voor plaque-omleggingen. Een plaque-omlegging is net als de stent een implantaat voor de halsslagader, zij het met een ander doel. Een stent verwijdt de arterie, terwijl een plaque-omlegging afgebroken plaque omleidt naar weefsels in het hoofd anders dan de hersenen. Aldus wordt de patiënt gespaard van herseninfarcten. Ook dergelijke implantaten worden onderzocht naar revascularisatie en ook hier moet men rekening houden met de gewijzigde stromingssituatie bij het draaien van het hoofd.

III.3. Impact van bloeddrukverlagende geneesmiddelen

III.3.1. Inleiding

In de literatuur werd door Stanton[302] melding gemaakt van twee bloeddrukverlagende geneesmiddelen, amlodipine en lisinopril, die elk met vrucht erin slagen de bloeddruk op lange termijn te verlagen. Deze bloeddrukverlaging ging echter gepaard met verschillende veranderingen in de morfologie van de halsslagader: bij lisinopril verkleint de vaatdiameter en de wanddikte, hetgeen te verwachten is na een bloeddrukdaling. De amlodipine behandeling zal ondanks die bloeddrukdaling toch de diameter handhaven en de wanddikte nog meer doen dalen. Er moet dus een mechanisme zijn dat de diameter verwijdt om de vernauwing tengevolge van de bloeddrukdaling teniet te doen. Figuur III.2 herneemt de resultaten van Stanton. Amlodipine is een calcium kanaal blocker, en verlaagt de druk door een perifere relaxatie van de gladde spiercellen hetgeen leidt tot een vasodilatatie en een verminderde perifere weerstand. Lisinopril is een ACE[a]-inhibitor, i.e. een stof die de aanmaak van angiotensine II, een vasoconstrictor, vermijdt.

---

[a] ACE: angiotensin converting enzyme
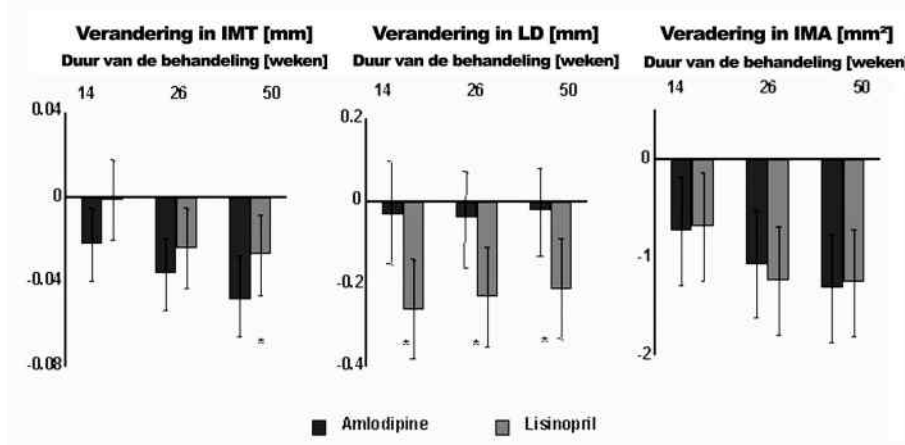
Figuur III.2.: De resultaten van Stanton[302] samengevat. De opgemeten verschillen zijn een gevolg van een behandeling van 52 weken met amlodipine (Calcium-kanaal blocker) of lisinopril (ACE inhibitor). IMT: intima-media dikte, LD: interne diameter van het bloedvat; IMA: wandmassa. '*' is significant (p=0.05).

III.3.2. Proefopstelling en Resultaten

De hypothese in onze studie was dat de veranderingen op lange termijn gerelateerd zouden zijn aan acute veranderingen in schuifspanning. Hiertoe werden 10 vrijwilligers met een hoge bloeddruk onderworpen aan achtereenvolgens drie behandelingen die elk 1 week duurden: een amlodipine, een lisinopril en een placebo behandeling. De meeste (8) werden gescand met TOF MRI en 2 claustrofoben met US.

Figuur III.3 toont de schuifspanningen voor 3 van de 10 bestudeerde hypertensieven. Merk op hoe de geometrie van de halsslagader nauwelijks wijzigt na elke behandeling. De schuifspanning nam hogere waarden aan bij een amlodipine behandeling. Hoge schuifspanningen initiëren in de vaatwand een reflex die het bloedvat zullen doen verwijden, een reflex die tot doel heeft de schuifspanning te normaliseren. Deze adaptieve verwijding van de halsslagader zal de doorstroomoppervlakte vergroten en de vaatwand uitrekken, hetgeen overeen komt met de vaststellingen op lange termijn en dus de resultaten van Stanton[302] verklaard.

III.3.3. Besluit

Aldus heeft de techniek gebaseerd op de integratie van medische beeldvorming en biomechanische modellering, bewerkstelligd in dit proefschrift,
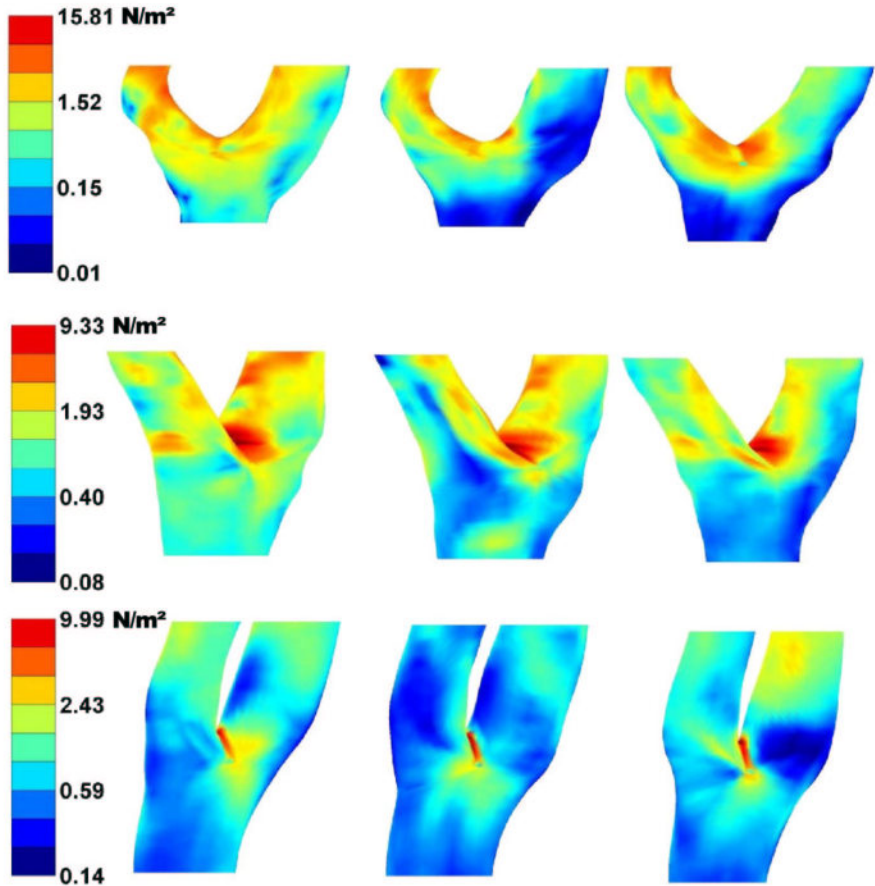
Figuur III.3.: De WSS distributie voor 3 patiënten (rijen) na inname van amlodipine (Calcium blocker, links), placebo (midden) en lisinopril (ACE-inhibitor, rechts).

bijgedragen tot het begrip van de werking van cardiovasculaire genees-middelen. Een dergelijke studie, die een antwoord bood op een vraag uit de industrie, was enkel mogelijk dankzij de beschikbaarheid van een vol-doende nauwkeurige techniek voor het begroten van de schuifspanningen in de halsslagader.

IV. Samenvatting en Besluit

Op het eind van vorige eeuw werd duidelijk dat het combineren van beeldvormende technieken met numerieke stromingsmechanica een middel was dat in staat zou moeten zijn om niet-invasief schuifspanningen te bepalen in bloedvaten. Ondanks dit besef en vroege bescheiden succesjes bestond er veel scepsis over de nauwkeurigheid van deze techniek. Dat die techniek het waard was om verder onderzocht te worden, wordt bewezen door de vele ziektes die beter begrepen of gediagnosticeerd zouden worden indien de schuifspanning met een voldoende nauwkeurigheid bepaald kon worden. Daarom werd in een eerste deel van het proefschrift de nadruk gelegd op het kwantificeren en het opdrijven van de nauwkeurigheid voor toepassing op de bloedstroming door de halsslagader. Dit proefschrift toont verder aan dat ultrageluid (echografie) net als magnetische resonantie angiografie (MRA) in staat is om dienst te doen als initiële beeldvormende techniek, hetgeen, gezien de grotere kost van deze laatste, een grote besparing betekent. Bovendien wordt de techniek toegankelijk voor vele hospitalen, dus ook voor hospitalen die over beperkte middelen beschikken.

Eens de nauwkeurigheid gekend was, lieten de toepassingen niet op zich wachten. In een tweede deel van het proefschrift werden dan ook twee studies in zeer uiteenlopende domeinen uitgevoerd. De eerste studie onderzocht de impact van bewegingen van het hoofd op de doorstroming van de halsslagader. Een tweede studie ging - op vraag van de farmaceutische industrie - na of er een verschil in stromingssituatie bestaat wanneer twee even efficiënte bloeddrukverlagende geneesmiddelen ingenomen worden. Deze twee studies toonden aan dat het toepassen van de techniek geen verre droom meer is, maar reeds binnen het kader van dit proefschrift werd gerealiseerd.

ENGLISH
TEXT

Statistics is like a Bikini:

what is revealed is suggestive,

but what is concealed is vital.

Preface

The manuscript describes and uses a technique for calculating the flow profiles in human carotid arteries. The technique is based on medical imaging and numerical modelling: it is called image-based computational fluid dynamics (CFD). In the introductional part (part **A**), the anatomy of the carotid arteries is explained, as well as its main pathologies. After an explanation on the numerical tools used in this thesis, the history of the technique is presented. Subsequently, part **B** investigates the technique from a technical point of view. The result of this part is a detailed description of the technique, together with figures on its accuracy, reproducibility and operator dependence. Once the technique was established, it was successfully used in two clinical studies described in part **C**. A first study investigated the effect of head turns on carotid geometry and flow. In a second study, a group of patients were administered two anti-hypertensive drugs. Aim was to analyse the effects on carotid geometry and flow. The final part contains a summary and technical notes aimed at improving the current protocols.

Part A.

INTRODUCTION

I. Anatomy and Physiology

Calculation of blood flow in the carotid bifurcation is the major topic of interest for this thesis. In the introductory section, the location and anatomical features of the carotid arteries are described (section I.1). In the following section, the values for blood pressure and flow in healthy humans are given. The composition of arterial wall is described in section I.3 and finally, the two last sections discuss specific functions of the carotid bifurcation other than blood supply.

I.1. Location of the Carotid Bifurcation in the Blood Supply chain

All tissues in the human body require a blood supply for their survival. Blood is pumped through the body by the contraction of the heart muscle, which is in fact a cavity which is filled during its relaxation phase (diastole) and contracts in systole. The contraction of the cavity causes blood to leave the heart at high velocities and pressures. The pressure has to be high since the blood needs to travel through the blood vessels and tissues, using the energy acquired in the heart. The tissues in the upper extremities of the body, the face and brain, set the target for heart: the blood pressure generated in the heart, needs to be high enough to reach the upper extremities. There are a number of blood vessels that transfer blood through the neck towards the head. The carotid arteries are two of them.

There are 3 carotid arteries on either side of the neck: the Common Carotid Artery (CCA) bifurcates into the Internal (ICA) and the External Carotid Artery (ECA). Arteries in general are vessels that carry blood away from the heart and to the tissues. The role of an artery in the vascular tree can be deduced from its cross-sectional size (see Table I.1).[73] The common carotid arteries are 2 of several arteries that supply blood to the head. See Figure I.1 (a)[107] for a schematic diagram showing the position of the right carotid bifurcation. Figure I.1 (b)[327] shows the relative positions of all the

Vessel Type	Diameter (mm)	Function
Aorta & Very Large Arteries	4.0 - 25	Pulse dampening and distribution
Large Arteries	1.0 - 4.0	Distribution
Small Arteries	0.5 - 1.0	Distribution and resistance
Arterioles	0.01 - 0.50	Resistance (pressure/flow regulation)
Capillaries	0.006 - 0.010	Exchange
Venules	0.01 - 0.50	Exchange, collection, and capacitance
Veins	0.5 - 5.0	Capacitance function (blood volume)
Large Veins and Vena Cava	5.0 - 35	Collection

Table I.1.: The function of the arteries and veins is linked to their cross-sectional size. The CCA and ICA are both damping and distributing arteries, the ECA is usually smaller and thus just a distributing artery.

(a) Right Carotid Bifurcation[107]

(b) Relative positions of arteries originating in the aortic arch[327]
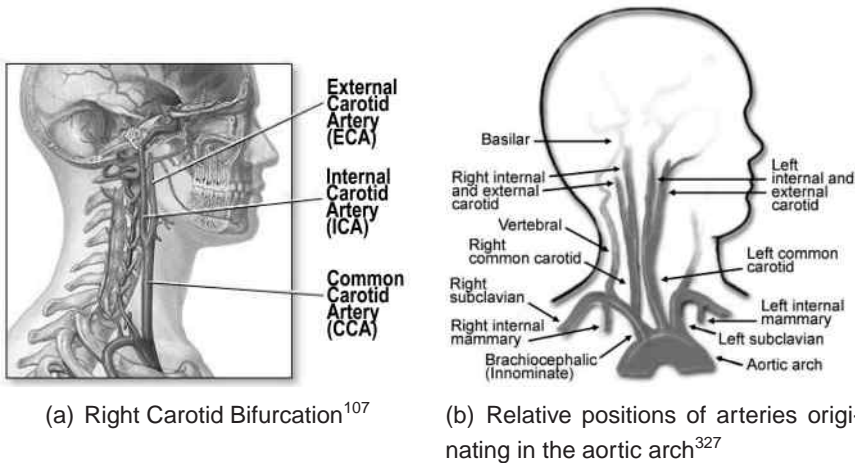
Figure I.1.: The position of the carotid arteries in the human body.

arteries originating from the aortic arch. The *right* common carotid artery branches from the brachiocephalic artery and extends up the right side of the neck. The *left* common carotid artery branches immediately from the aorta and extends up the left side of the neck. Each carotid artery branches into internal and external vessels approximately near the top of the thyroid[2] (i.e. the small butterfly-shaped gland, located in the neck, wrapped around the windpipe, behind and below the Adam's Apple area).

The ICA is the primary blood supply to the brain and the eyes. It anastomoses with the vertebral arteries and the contralateral internal carotid artery in the cerebral arterial circle (of Willis) as shown in Figure I.2.[227] Note that the ICA's are not *the only* arteries feeding the brain. At the point where the ICA emerges from the common carotid, i.e. immediately after branching, the internal carotid widens a little. This small widening is know as the **carotid**

The Arterial Circle of Willis

Inferior view of the Brain

Arteries of the Circle of Willis

1. Anterior Communicating
2. Anterior Cerebral
3. Internal Carotid
4. Posterior Communicating
5. Posterior Cerebral
6. Basilar
7. Vertebral
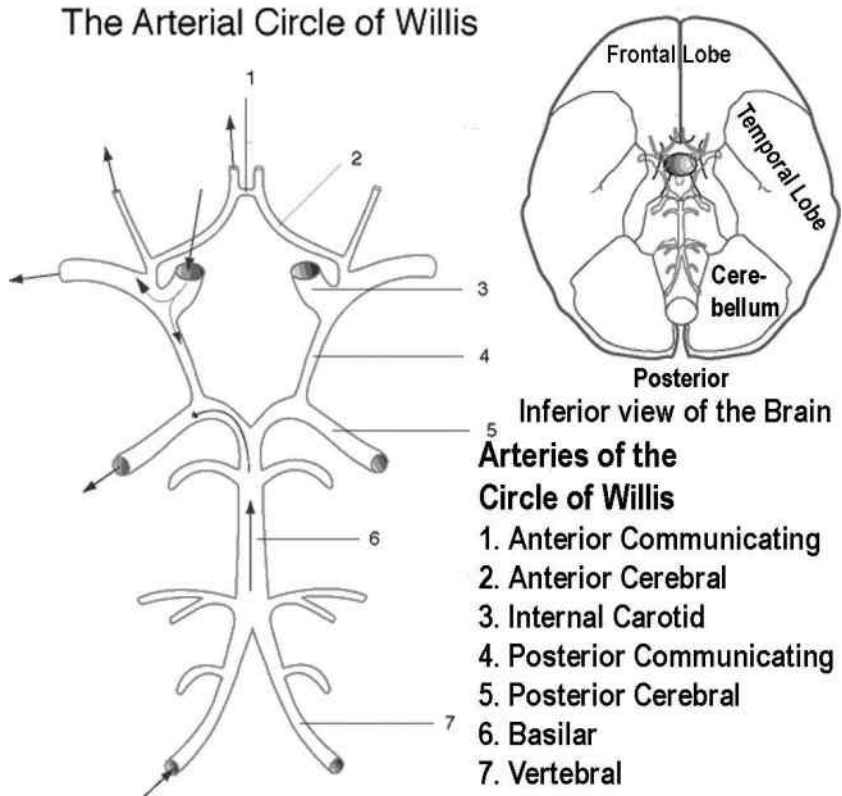
Figure I.2.: The circle of Willis is the blood supply of the brain.[227]

sinus or **carotid bulb**. Its shape, length and width can be very different from one subject to the other. The ECA branches off to supply oxygenated blood to the throat, neck, glands, tongue, face, mouth, ear, scalp and dura mater of the meninges (i.e. the ensemble of layers covering the brain, separating it from the skull).

Due to the carotid bifurcation being a complex 3D structure on one hand and the large inter-subject variations on the other hand, there is no clear definition of a 'typical' carotid geometry. Nevertheless, Figure I.3 illustrates the general features observed in a carotid bifurcation: the CCA widens and bifurcates into the ICA (right) and ECA (left). The carotid bulb marks the origin of the ICA while the ECA is smaller than the ICA. In the past, attempts to quantify carotid geometry have failed to reach an agreement. Gnasso[123] reported 5.9 mm as typical CCA lumen diameter (LD) (n = 42, mean age 49.0 years). Geigy Scientific Tables[174] showed 6.1 mm (n = 20, 'young adults'), Boutouyrie[37] found 5.21 mm (n = 15 females, 43±16 years), Ferrara[95] reported 6.0±0.8 mm (n = 20, 47.0±7 years) and Liang[182] 5.47±0.08 mm
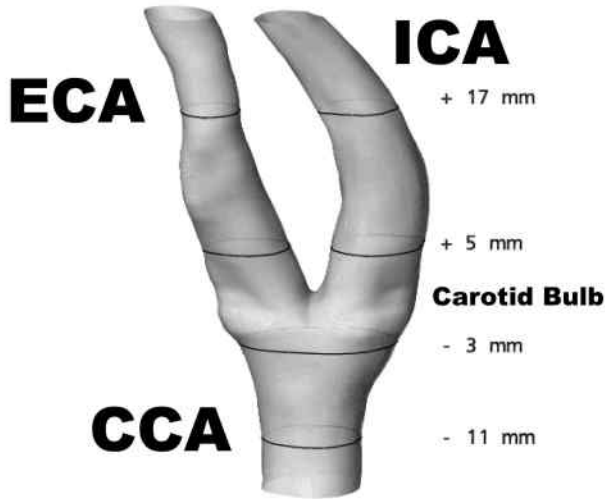
Figure I.3.: Typical carotid geometry;[15] z=0mm is located at the bifurcation apex.

(n = 237) for non-smokers respectively as opposed to 6.09±0.11 mm (n = 185, 63.1±6.6 years) for smokers. Sass[273] derived the change in CCA LD as a function of age and gender (n = 369). Table I.2 summarises Sass's findings. Females between 41 and 45 years have an average LD of 5.17 ± 0.57 mm (n = 37) which agrees with Boutouyrie's reports.[37] Scheel performed a similar study a few years later,[275] and found CCA LD's of 6.0±0.7 mm (n = 24, ages 20-39), 6.1±0.8 mm (n = 24, ages 40-59) and 6.2±0.9 mm (n = 30, ages 60-85). It is clear from Sass's and Scheel's results that a typical carotid bifurcation geometry is impossible to define. Note that the LD in the discussed studies[37, 95, 123, 174, 182, 273, 275] was measured by B-mode ultrasound (see section II.17 on page 49) in the proximal CCA, i.e. the CCA before it starts widening. Studies that include the region of the flow divider in the definition of the CCA will find a larger CCA LD. Bladin[29] found that the distal end of the CCA is on average 4% larger than the proximal CCA (n = 125). The bifurcation zone, the most distal part of the CCA, is obviously larger.

The subject-variability is even greater for ICA geometry than for CCA LD. Diameter of the ICA bulb has been reported to be 27±20% greater than that of the proximal CCA.[29] A different study conducted by Schulz[279] found a smaller disproportion between the proximal CCA LD and the bulb diameter: 13±18%. Moving up in the ICA, Schulz[278] reported that LD in the proximal ICA (after the bulb) is 36±11% smaller than the LD in the distal CCA (before bulb). The ICA LD, but not the bulb diameter, is larger for women by 13%.[279]

age	10-12	13-14	15-16	17-18	19-24	35-40	41-45	46-53
	M=23	M=13	M=20	M=17	M=12	M=19	M=34	M=31
	F=23	F=24	F=23	F=17	F=21	F=33	F=37	F=22
Male	4.99	4.99	5.14	5.39	5.36	6.01	6.07	5.97
	±0.41	±0.39	±0.44	±0.50	±0.60	±0.46	±0.62	±0.57
Female	4.92	4.88	4.87	5.01	4.92	5.09	5.17	5.29
	±0.54	±0.45	±0.36	±0.49	±0.44	±0.46	±0.57	±0.51

Table I.2.: Common carotid LD as measured by Sass.[273] M=number of participating males. F=number of participating females. All values in mm, reported as mean value ± standard deviation.

From a study conducted by Long[194] using time-of-flight magnetic resonance imaging (see VI.1), it can be seen that the ICA LD drops from very high values (up to 8 mm) in the bulb to below 5 mm. Scheel[275] measured ICA diameters in 78 subject '1.5 to 2 cm' above the carotid bulb. He reported 4.8±0.5 (ages 20-39), 4.7±0.6 (ages 40-59) and 4.9±0.8 mm (ages 60-79).

The ECA is not as complex as the ICA: it has no explicit widening of the lumen at the start, making it more comparable to a cylindric tube than the ICA. Nevertheless, there are a number of side branches (such as the thyroid artery) branching off the proximal ECA.[308, 386] Schulz[278] measured that the LD in the proximal ECA (before any branching) is 44±12% smaller than the LD in the distal CCA (before bulb). Scheel[275] measured ECA diameters as well: 4.0±0.4 (ages 20-39), 4.1±0.7 (ages 40-59) and 4.3±0.7 mm (ages 60-79). From Long's study,[194] ECA LD is found to be very subject-dependent, varying from 2.5 to 5 mm. Note that errors were found to be large in ECA due to its relatively small size and the presence of side branches.

With knowledge of the LD's of the separate arteries, their function becomes clear. The CCA and ICA LD are greater than 4.0 mm, belonging to the 'very large arteries' whose main functions are to damp the pressure pulse (see section I.2) and to contribute to blood distribution. The ECA can be classified as a distribution artery.

I.2. Pressure and Flow

Pressures in the arteries, veins and heart chambers are the result of the pumping action of the heart. Figure I.4 illustrates the pressure variation in the heart and the aorta during a cardiac cycle in a healthy human. When the ventricles of the heart contract, left ventricular (LV) pressure rises until the

Pressure	Systolic	Diastolic	Pulse	Mean
Aorta	100-130	60-90	30-50	70-105
Left Ventricle	100-130	4-12	-	-
Left Atrium	15	4	-	4-12
Pulmonary Artery	15-30	6-12	-	9-18
Right Ventricle	25-30	0-8	-	-
CCA Pressures				
Mitchell[221] (n = 30, aged 59±10)	119.1±11	n/a	n/a	n/a
Mitchell[222] (n = 40, aged 57±10)	124±24	n/a	n/a	94±12
Boutouyrie[37] (n = 15, aged 43±16)	n/a	n/a	47±16	n/a
Liang[182] (n = 237, aged 62.6±6.8)	n/a	n/a	36±10	n/a
Waddell[344] (n = 57, aged 59±9)	116±2	n/a	38±1	n/a

Table I.3.: Normal pressures [mmHg].[72] The pulse pressure is the difference between systolic and diastolic pressure.

LV pressure exceeds the aortic pressure. The blood flows from the ventricle to the aorta through the opened aortic valve, the valve separating the aorta from the LV. As blood enters the aorta, the aortic pressure begins to rise and forms the systolic pulse. When the heart starts relaxing, the pressure drops to a certain point where the LV pressure is lower than the aortic pressure. At this point, the aortic valve closes again. Closure of the aortic valve produces a disturbance or a notch in the aortic pressure called the **dicrotic notch**. Thanks to the elastic recoil, the aorta now functions as a blood reserve under pressure. It slowly empties into the vascular tree, feeding all body tissues with blood. Normal blood pressures are shown in Table I.3 as published by Darovic.[72]

The aortic blood flow resulting from this pressure curve is illustrated in Figure I.4. In a resting state, for a normal adult, the blood flow ranges between 4 and 8 litres per minute.[72] Velocities in the aorta go up to 2m/s. Further down the branches, blood velocity declines and the pressure and flow rate curves change significantly in shape. Figure I.5 shows how pressure, mean velocity and the total perfused cross-sectional area change throughout the vascular tree. Note how pressure can be higher in large arteries distal from the aorta. This is due to pressure wave propagation and reflection within the arterial tree. These pressure wave reflections originate from pressure waves bouncing off both distal and proximal bifurcations and the geometric and elastic tapering of the arterial network. In the capillaries, the tiny vessels at the extremities of the arteries, the mean velocity is brought down to 1 mm/s, and the pressure is constant.

Where is the carotid artery situated in this framework? In the common carotid artery, closer to the aorta, velocities can be as high as 1.5 m/s. The
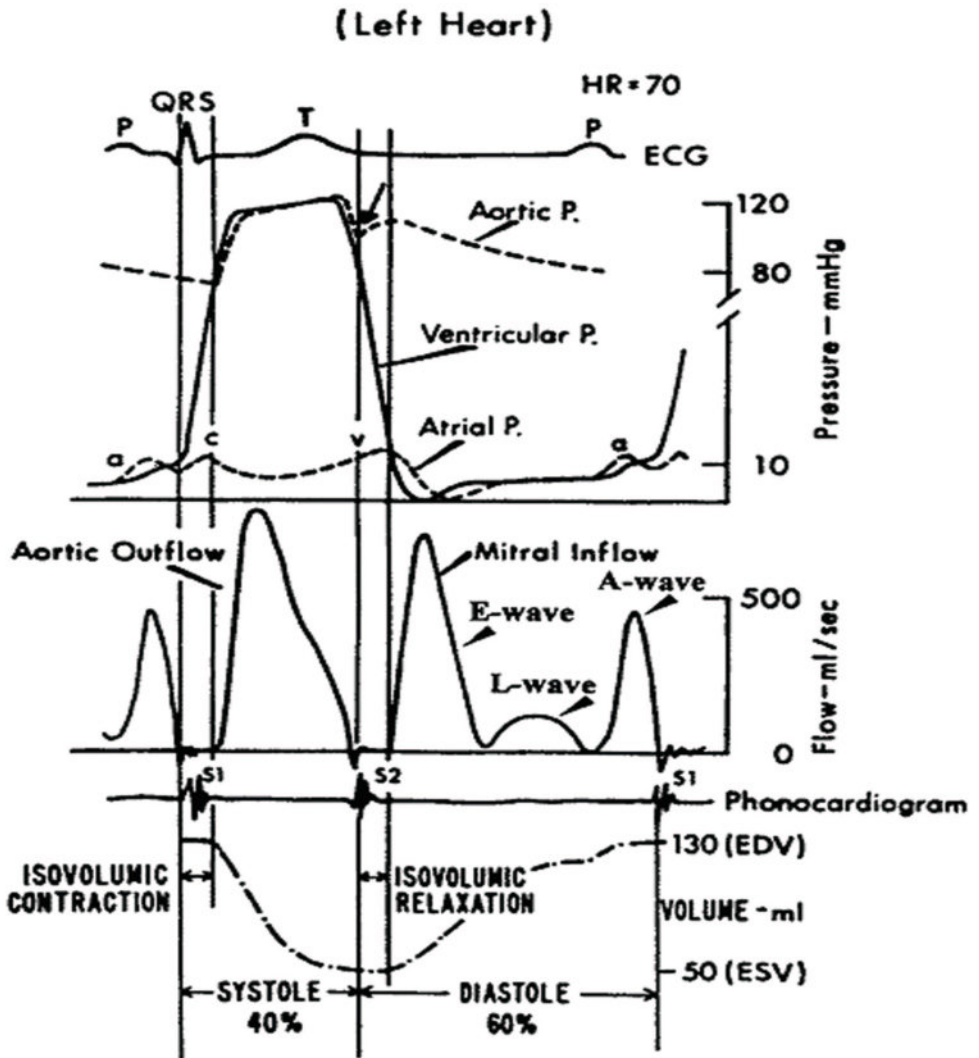
Figure I.4.: Pressure and flow during one cardiac cycle.[377]

carotid artery is one of the arteries where, due to wave reflections, pressures can be higher than in the aorta. Both pressure and flow are very pulsatile. Figure I.6 (a) shows a typical pressure wave form,[222] see Table I.4 for the definition of the feature points. Table I.3 gives an overview of measured values for carotid pressures, from which we can see that carotid pressures roughly range from 75-85 (diastole) to 110-130 (systole) in resting state. Note that here, 'systole' and 'diastole' refer to the maximum and minimum carotid pressure as opposed to the state of the heart muscle.
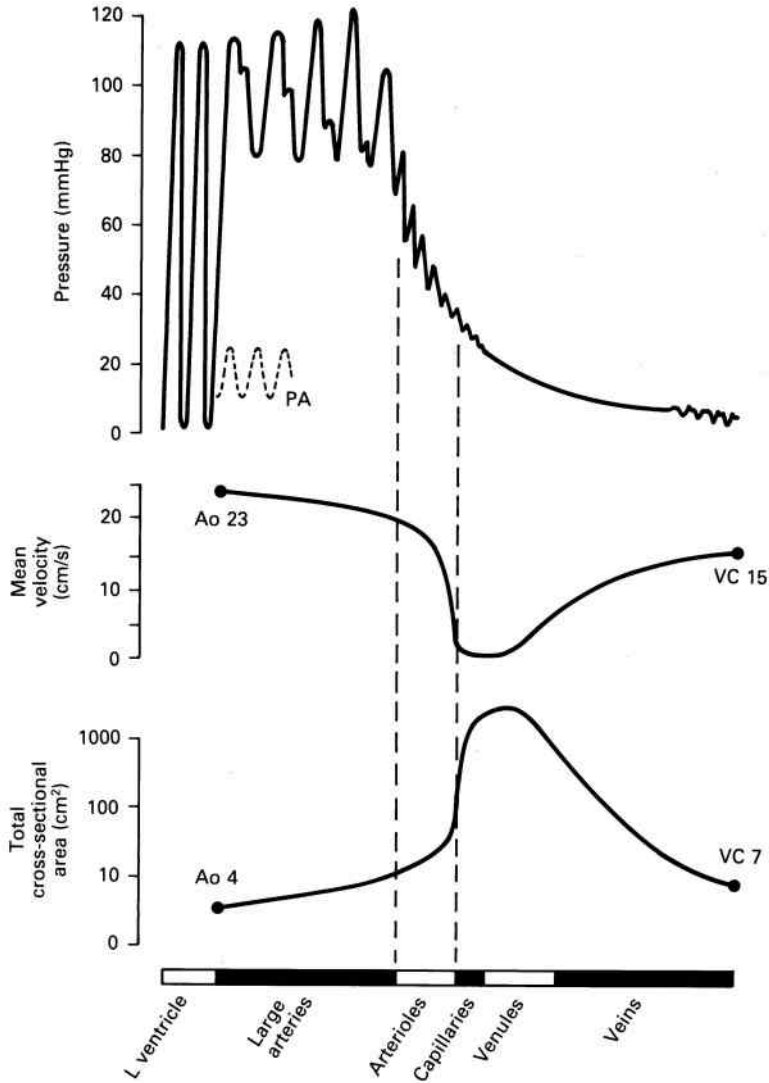
Figure I.5.: The profile of blood pressure and velocity in the systemic circulation of a resting man. The abscissa is distance along the vessels. The greatest fall in pressure occurs across arterioles and the tiniest arteries. This is in agreement with Table I.1 where the smaller arteries have been described as resistances regulating the blood flow to particular organs. Mean velocity is the cardiac output divided by total cross-sectional area of the vascular bed at that point. Pressure in the pulmonary artery (PA) is shown as a dotted line. Ao: human aorta; VC, human vena cava.

(a) Carotid Pressure (b) Centreline velocity
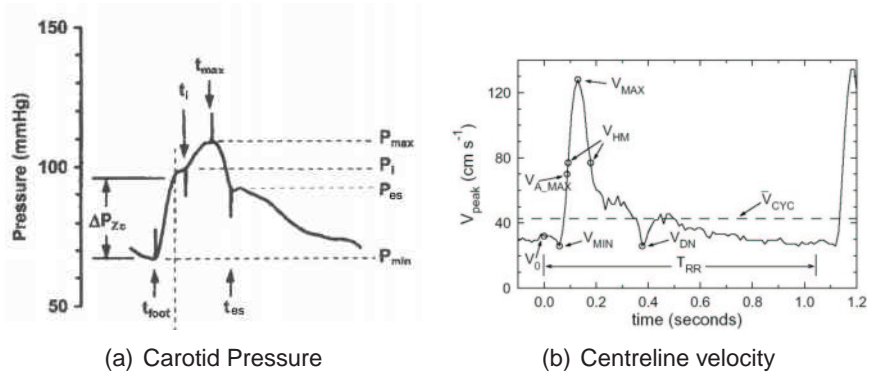
Figure I.6.: a: Typical carotid pressure in one cardiac cycle.[222] b: Vessel spatial peak blood velocity (V_{peak}) in the common carotid artery measured with a vector Doppler-ultrasound system in a normal human subject.[140] For a definition of other feature points, see Table I.4.

Parameter	Definition
t_{foot}	Time of rise of pressure
t_i	Inflection point, signaling return of reflected wave
t_{max}	Time of peak pressure ($\neq T_{MAX}$)
t_{es}	End-systolic time
P_{min}	Minimum pressure
P_i	Pressure at inflection point
P_{max}	Maximum pressure
P_{es}	End-systolic pressure
ΔP_{Zc}	Pressure in common carotid when flow rate in aorta valve reaches 95% of its maximum - P_{min}
T_{RR}	Cardiac interbeat interval
V_{CYC}	Vessel spatial peak velocity, averaged over one cardiac cycle
V_{MIN}	Minimum diastolic velocity
T_{MIN}	Time of diastolic minimum velocity
A_{MAX}	Maximum acceleration
T_{A_MAX}	Time of maximum acceleration
V_{A_MAX}	Velocity at point of maximum acceleration
V_{MAX}	Maximum systolic velocity
T_{MAX}	Time of maximum systolic peak-velocity ($\neq t_{max}$)
V_{HM}	$V_{HM} = \frac{V_{MAX}-V_{MIN}}{2} + V_{MIN}$
T_{LHM}	Time during early systole at which $V_{peak} = V_{HM}$
T_{FWHM}	Time period during which $V_{peak} \geq V_{HM}$
V_0	Velocity at cardiac systole
V_{DN}	Minimum velocity in dicrotic notch
T_{DN}	Time of minimum velocity in dicrotic notch

Table I.4.: Definitions of pressure and peak-velocity wave form feature points.[140]

15

Figure I.6 (b) shows a typical velocity measurement in a healthy human subject.[140] See Table I.4 for the definition of the feature points. At systole (t=0), the flow ejected by the heart into the aorta has not entered the carotids yet: the flow takes a time T_{MIN} to reach the common carotid. After T_{MIN}, the velocities rise steeply until they reach a maximum V_{MAX}, and fall again. The dicrotic notch, caused by the aortic valve closure, is still noticeable in the carotid velocity profile. Table I.5 quantifies the average timing and velocity parameters for 17 normal volunteers (24 to 34 years).[140] The velocity profiles were measured 2 cm proximal from the bifurcation apex. Table I.5 also shows, for comparison, the same parameters as quantified in other studies.[123, 170, 229, 275] Velocities are higher in men than in women. This, together with the larger CCA radius for men (Table I.2), shows that the blood flow through the carotid arteries is higher for men.

The velocity wave forms in the ICA and ECA are similar to that in the CCA shown in Figure I.6 (b). Due to the damping effect of the compliant vessel wall, peaks are weakened and the dicrotic notch becomes hard to distinguish, especially in the ICA. Typical values for ICA and ECA V_{MAX} and V_{CYC} are given in Table I.6 based on studies by Ferrara,[95] Nagai,[229] Lee[170] and Scheel.[275] Note the important differences in V_{MAX} between Nagai's and Scheel's study. For example, the V_{MAX} is 72±18 cm/s in Scheel's study whereas Nagai measures 82 cm/s in men and 93 cm/s in women of the same age groups. This is partly due to the large inter-subject variability (see column 4 in Table I.6), but especially due to the fact that the velocities were measured at different locations: '1.0 to 1.5 cm distal from the tip of flow divider' in Nagai's study[229] and '1 to 2 cm above the carotid bulb' in Scheel's study.[275] Lee[170] measured the velocities at three sites in the ICA: 'one location in the bulb, and two locations in the ICA'. Their results illustrate the large range of velocities occurring in the ICA.

As mentioned above, the blood flow for a normal adult ranges between 4 and 8 litres per minute or approximately 65 to 130 ml/s,[72] of which 13% goes to the brain (approximately 7 to 14 ml/s). As stated in section I.1 and Figure I.2, an important part of the blood supply to the brain happens through the internal carotid arteries. Figure I.7 shows measurements of the blood flow in the CCA, ECA and ICA of a healthy subject, measured with MRI (see section VI.1). Note how the CCA flow wave form is substantially different from the aortic flow wave form (Figure I.4), but very similar to the velocity wave form (Figure I.4(b)): there is a steep rise in flow rate, a maximum, a fast decrease in flow rate, a dicrotic notch and further slow decrease in flow rate towards the end of the cardiac cycle. Maximum flow rate in this subject was around 25 ml/s, average flow around 7 ml/s. Table I.7 summarises

Parameter	Unit	Mean	Standard Deviation	Max	Min
T_{RR}	s	0.917	0.119	1.414	0.601
V_{CYC}	cm/s	38.8	7.3	58.7	19.4
V_{MIN}	cm/s	20.9	4.8	36.2	7.0
T_{MIN}	s	0.055	0.014	0.118	0.011
A_{MAX}	cm/s^2	2441	456	8048	1233
T_{A_MAX}	s	0.110	0.010	0.154	0.035
V_{A_MAX}	cm/s	47.7	7.2	114.2	6.4
V_{MAX}	cm/s	108.2	17.8	171.2	68.2
T_{MAX}	s	0.153	0.011	0.189	0.118
V_{HM}	cm/s	64.6	10.2	100.24	39.7
T_{LHM}	s	0.116	0.010	0.151	0.088
T_{FWHM}	s	0.103	0.024	0.257	0.06
V_{DN}	cm/s	19.4	6.6	45.6	5.6
T_{DN}	s	0.398	0.016	0.448	0.342
V_{MAX}	n	Mean	Standard Deviation	Age	
Gnasso[123]	42	79.8	16.0	49.0±12.4	
Lee[170]	85	75.2	22.1	59±12	
Scheel[275]	24	101	22	20-39	
	24	89	17	40-59	
	30	81	21	60-85	
Nagai[229]	17 men	115	n/a	20-39	
	24 men	97	n/a	40-49	
	22 men	97	n/a	50-59	
	22 men	89	n/a	60-69	
	27 men	81	n/a	70-79	
	25 women	105	n/a	20-39	
	46 women	92	n/a	40-49	
	38 women	87	n/a	50-59	
	26 women	77	n/a	60-69	
	11 women	76	n/a	70-79	
V_{CYC}	n	Mean	Standard Deviation	Age	
Ferrara[95]	20	34.2	4.8	47.0±7.0	
Gnasso[123]	42	36.2	5.4	49.0±12.4	
Scheel[275]	24	40	6	20-39	
	24	42	7	40-59	
	30	36	10	60-85	

Table I.5.: Average timing and velocity parameters for human CCA wave forms as measured by Holdsworth in 17 subjects (24 to 34 years)[140] and the comparison with other studies.[123,170,229,275] See Table I.4 for a definition of the feature points.

n	Age	Mean	Variability
V_{MAX}	ICA	**Nagai**[229]	
17 men	20-39	82	(50-112)
24 men	40-49	76	(60-101)
22 men	50-59	80	(59-96)
23 men	60-69	79	(62-109)
27 men	70-79	71	(40-97)
25 women	20-39	93	(52-124)
46 women	40-49	87	(58-116)
38 women	50-59	87	(60-115)
26 women	60-69	86	(60-113)
11 women	70-79	75	(43-100)
V_{MAX}	ICA	**Lee**[170]	
85 (bulb)	59	64.6	$\pm$ 23.6
(proximal ICA)		59.5	$\pm$ 17.3
(distal ICA)		65.2	$\pm$ 17.1
V_{MAX}	ICA	**Scheel**[275]	
24	20-39	72	$\pm$ 18
24	40-59	65	$\pm$ 10
30	60-79	58	$\pm$ 11
V_{MAX}	ECA	**Scheel**[275]	
24	20-39	86	$\pm$ 14
24	40-59	85	$\pm$ 18
30	60-79	81	$\pm$ 30
V_{CYC}	ICA	**Ferrara**[95]	
20	47.0$\pm$7.0	32.7	$\pm$ 3.0
V_{CYC}	ICA	**Scheel**[275]	
24	20-39	39	$\pm$ 7
24	40-59	38	$\pm$ 6
30	60-79	33	$\pm$ 8
V_{CYC}	ECA	**Scheel**[275]	
24	20-39	30	$\pm$ 5
24	40-59	35	$\pm$ 7
30	60-79	33	$\pm$ 11

Table I.6.: Velocities in the carotid branches. V_{MAX}: maximum velocity, V_{CYC}: cycle-averaged peak velocity. All values in cm/s and based on studies by Ferrara,[95] Nagai,[229] Lee[170] and Scheel.[275] The fourth column represents a measure of variability, shown either as '$\pm$ standard deviation 'or' (5-percentile 95-percentile) '.
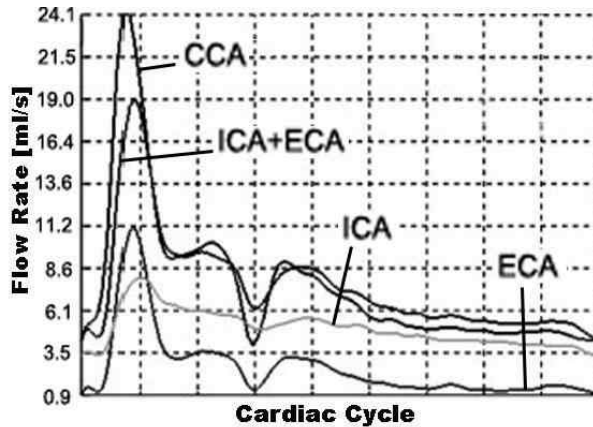
Figure I.7.: The flow rate was measured at two locations: (1) the common carotid artery (CCA) and (2) the internal (ICA) and external carotid arteries (ECA). Note that the sum of instantaneous flow in the internal and external branches differs substantially from the flow in the common carotid, due to the wall compliance and to MRI acquisition errors (see section VI.1).[49]

values for the flow rate in each of the carotid arteries. There is no significant difference between the left and right carotid arteries, measured with a variety of techniques. Blood flow decreases with ageing in the CCA and ICA, but increases in the ECA. Common values for cycle-averaged blood flow are 4.5 to 10 ml/s for the CCA, 3 to 6 ml/s for the ICA and finally 1.5 to 4.5 ml/s for the ECA. On average, this means that the flow division ICA:ECA is approximately 60:40.

I.3. Arterial Wall Structure[26]

In its journey from the heart to the tissues, the blood passes through channels of six principal types: elastic arteries, muscular arteries, arterioles, capillaries, venules and veins. In this system, the arteries show a progressive decrease in diameter as they recede from the heart, from about 25 mm in the aorta to 0.3 mm in some arterioles (**geometrical tapering**, Figure I.5). The reverse is true for the veins; the diameter is small in the venules and progressively increases as the veins approach the heart. All arteries are composed of three distinct layers, *intima, media and adventitia* (Figure I.8), but the proportion and structure of each varies with the size and function of the particular artery (**elastic tapering**). A large artery, such as the aorta, is comprised of the following layers, going from the lumen to the most external layers:

STUDY	N	AGE	MEAN	STANDARD DEVIATION
CCA				
Keller[154]	22	23-45	5-8	
Fitzgerald[96]	25	42	8.93	± 1.73
Uematsu[338]	16	21-40	7.98	± 1.50
Uematsu[338]	14	41-60	7.22	± 1.15
Donis[80]	66	16-19	6.67	± 0.45
Donis[80]	50	70-78	5.37	± 1.90
Hamada[132]	28	71±7	9.57	n/a
Schöning[277]	46	20-63	7.83	± 2.00
Weskott[359]	174	20-87	6.92	± 1.45
Holdsworth[140]	17	24-34	6.0	(min-max: 0.4-12.3)
Scheel[275]	24	20-39	7.10	± 1.65
Scheel[275]	24	40-59	7.23	± 1.85
Scheel[275]	30	60-85	6.22	± 1.33
ICA				
Leopold[175]	20	32	4.23	± 0.93
Fortune[97]	20	33	5.50	± 0.32
Schöning[277]	46	20-63	4.42	± 0.43
Scheel[275]	24	20-39	4.62	± 0.82
Scheel[275]	24	40-59	4.23	± 0.95
Scheel[275]	30	60-85	3.73	± 0.72
ECA				
Schöning[277]	46	20-63	2.67	± 1.1
Scheel[275]	24	20-39	2.42	± 0.53
Scheel[275]	24	40-59	2.92	± 1.22
Scheel[275]	30	60-85	2.83	± 0.87

Table I.7.: CCA, ICA and ECA time-averaged blood flow according to literature.[80,96,97,132,140,154,175,275,277,338] Values in ml/s.

1. the **lamina intima**, or innermost layer, consists of a monolayer of endothelial cells separated from the inner layer by a narrow layer of connective tissues which anchors the cells to the arterial wall.

2. A large layer of elastic fibres forming the **lamina elastica interna**.

3. Below this layer are concentric waves of *smooth muscle cells* intermixed with *elastic fibres*. Elastic lamellae and smooth muscle cells are imbedded in a ground substance rich in proteoglycans. Proteoglycans are formed of disaccharides bound to protein and serve as binding or 'cement' material in the interstitial spaces.

4. Between the smooth muscle layer and the adventitia (cfr. 5.), there is again another layer of elastic fibres, the **lamina elastica externa**. Layers 2, 3 and 4 form the **lamina media**. The width of layers 1 to 4 is known as the 'intima-media thickness' or **IMT**.
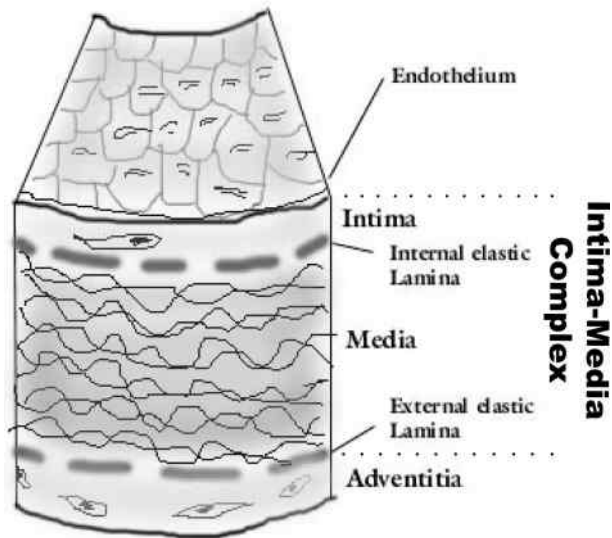
Figure I.8.: The layers of an arterial wall.[379]

5. The outer layer or **lamina adventitia** is formed of irregularly arranged collagen bundles, scattered fibroblasts, a few elastic fibres and blood vessels which, because of their location, are called **vasa vasorum** or vessels of the vessels.

This *structure of the aorta and large arteries* (such as the common carotid) corresponds well to their function which serves as a blood reservoir and to stretch or recoil with the pumping action of the heart. This is the so-called **windkessel effect**.[342]

The wall of the arterioles contains less elastic fibres but more smooth muscle cells than that of the aorta. The arterioles represent the major site of the resistance to blood flow and small changes in their caliber cause large changes in total peripheral resistance.

I.4. Pressure Regulation: baroreceptors

Apart from supplying oxygenated blood, the carotid bifurcations play an important role in the blood pressure regulation. As in the aorta and in the right heart, the carotid sinus contains **baroreceptors**. When pressure rises in

the blood circulation, the carotid wall will stretch. Via a cranial nerve (nerve number 'IX') the brain is informed of this pressure rise. At that point, the brain will incite a series of reactions, aiming to reduce the blood-pressure. The reaction can include decreased heart rate or widening of the arteries ('vasodilatation'). Thus, when blood pressure rises, this **carotid sinus reflex** makes pressure fall.

I.5. Oxygen Regulation: chemoreceptors

The level of carbondioxide (CO_2), oxygen (O_2) and acidity (H^+) in the blood are closely monitored. The carotid sinus (and the aortic arch) contains in its wall **chemoreceptors**, bodies that detect changes in blood level of CO_2, O_2 and H^+. If oxygen levels go down or carbon dioxide and hydrogen ion levels go up, a signal is sent to the brain, which triggers a rise in blood pressure and influences the breathing. The general purpose is to bring the levels of CO_2, O_2 and H^+ back to their original values.

II. Pathology and Diagnosis

II.1. Carotid Pathology

The carotid artery is susceptible to a number of vascular diseases. Carotid dissection, the pathological condition where blood intrudes the intima media, is defined and discussed in section II.1.1. The most common form of carotid disease, atherosclerosis, is discussed in section II.1.2. Less frequent but more severe are carotid aneurysms, a widening of the carotid lumen, which are explained in section II.1.3.

II.1.1. Carotid Dissection[8, 90]

Arterial dissection is a condition in which blood penetrates through a tear in the intima, separating and dissecting it from the media. The dissection may be focal but more commonly it extends for several centimeters. The most common sites of arterial dissection are the internal carotid artery (both intracranially and extracranially, with the former being more rare and severe), and the vertebral artery in its distal extracranial portion where it penetrates the dura to become intracranial (Figure I.1 (c)). Dissection of intracranial arteries, basilar artery and middle cerebral artery, are also possible but much less common.

See Figure II.1 for an illustration of a carotid dissection. Two streams are visible in the carotid lumen: a normal stream (red), and a stream underneath the intima (more colours than just red).[106]

Cervical artery dissection is a significant cause of stroke in patients younger than 40 years. Carotid artery dissections have nonspecific presenting symptoms such as neurologic deficits and headache and occur at a relatively young age. They often happen in previously healthy individuals and develop either spontaneously or following various degrees of trauma.
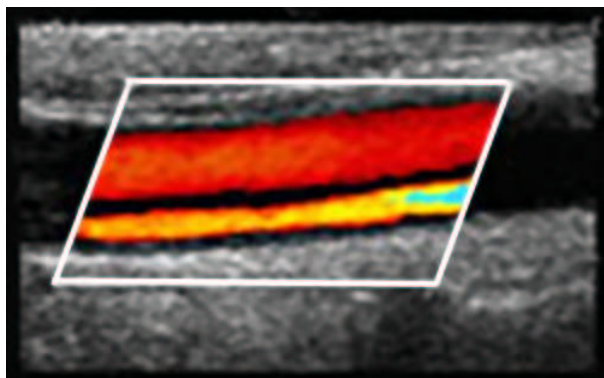
Figure II.1.: A 'Duplex' image of common carotid dissection. The black and white image is acquired using B-mode Ultrasonography. The black void in the center of the image represents the CCA lumen. The colours represent blood velocities acquired with Doppler ultrasound (see section VII.1.3). The visualisation of colour Doppler velocities on a B-mode image is called a **Duplex** image. Flow is from left to right. There are two streams visible: a 'red' and a 'coloured' stream. The red stream is the normal blood flow, the coloured stream goes under the vessel wall and resurfaces further distal.[106]

While the pathophysiology of carotid artery dissection remains largely unclear, mechanical factors and other underlying vascular diseases may be the cause. Dissections usually are subadventitial (between the media and adventitia or within the media), creating a false lumen that can cause stenosis (LD decrease), occlusion, or pseudoaneurysm of the vessel. Simultaneously, the dissection may cause the formation of a thrombus (blood clot) from which fragments embolise. Strokes resulting from carotid dissection thus may have a haemodynamic or embolic origin.

The annual incidence of symptomatic carotid artery dissection is 2.6 per 100000.[7] The actual incidence may be higher, since many episodes may be asymptomatic or cause only minor transient symptoms and remain undiagnosed.

Morbidity from carotid artery dissection varies in severity from transient neurologic deficit to permanent deficit and death. Intracranial internal carotid artery dissection is associated with a 75% mortality rate. Male-to-female ratio is 1.5:1.[8]

Carotid artery dissections are most common in young adults. While the mean age for extracranial internal carotid artery dissection is 40 years, intracranial dissections are more common in those aged 20-30, with half occurring in the first 2 decades. Approximately 20% of strokes in the young

are caused by carotid artery and vertebral artery dissections in the neck, compared to 2.5% in older patients.

II.1.2. Atherosclerosis

II.1.2.1. Definition, Prevalence and Localisation

Arteriosclerosis can be described as: 'A chronic disease in which thickening, hardening, and loss of elasticity of the arterial walls result in impaired blood circulation. It develops with ageing, and is correlated with hypertension, diabetes, hyperlipidemia[a], and other conditions.'[250]

Atheroslerosis: 'A form of arteriosclerosis characterised by the deposition of atheromatous plaques containing cholesterol and lipids on the innermost layer of the walls of large and medium-sized arteries.'[250]

Cardiovascular disease (CVD) is responsible for the majority of deaths in both Europe (33.5% of deaths at 45-54 years of age, 64% of deaths at ages above 85)[371] and the US (39.4% of all deaths in 2000).[7] The majority of CVD is attributable to atherosclerosis. The most common form of carotid artery disease is atherosclerosis. This means that the carotid arteries develop a build-up of plaque caused by hardening of the arteries. The narrowing of the vessel lumen caused by plaque is called a stenosis. When the buildup becomes very severe, it can cause a stroke.

Other vessels prone to atherosclerosis are the coronary arteries, the visceral branches of the abdominal aorta, and the infra-renal abdominal aorta and its femoral branches (Figure II.2).[75]

II.1.2.2. Pathophysiology[131, 287]

Before elabourating the link with haemodynamics, arteriosclerosis must be well understood. Figure II.3 shows what happens in the arterial wall. It usually starts with a subtle damage of the **glycocalyx**, the layer lining the endothelium. Damage to the glycocalyx leads to damage to the endothelial cells. This lesion will attempt to heal itself by inducing an inflammatory reaction: white blood cells will be called to the lesion by chemicals released

---

[a]increased level of lipids in blood serum
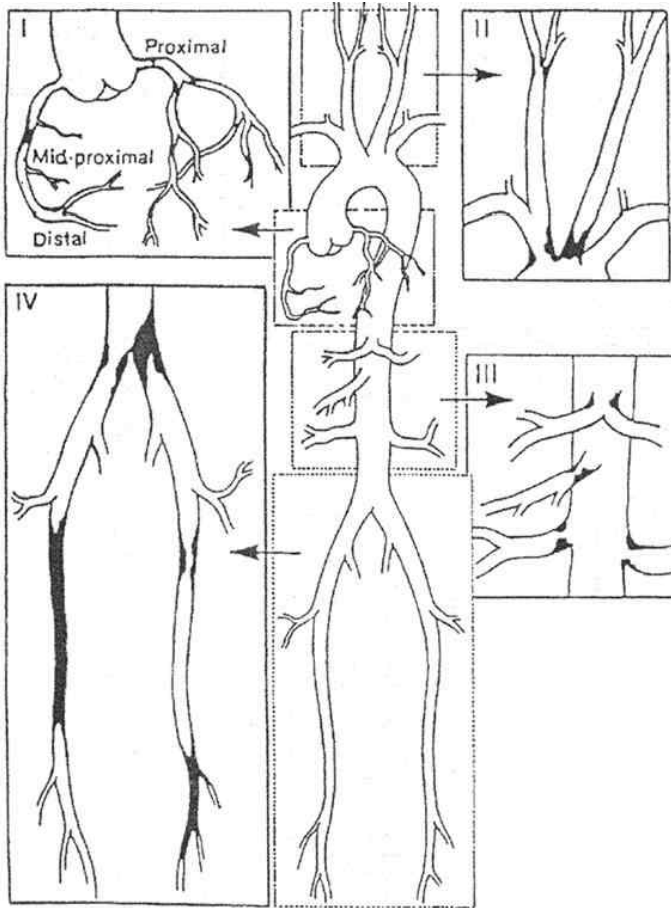
Figure II.2.: Atherosclerotic plaques tend to form in specific areas of the vascular tree, including (I) the coronary circulation, (II) the carotid vessels, (III) the visceral branches of the abdominal aorta, and (IV) the infra-renal abdominal aorta and its femoral branches.[75]

at the lesion site. White blood cells will ingest fatty particles and stay in the lesion zone as so called **foam cells**. Thus, **fatty streaks** appear: these are very common at an early age and some may go away if there are no other damaging influences.

Various factors from platelets, white blood cells and the blood plasma make the muscle cells in the arterial wall increase in number.[131] Cholesterol accumulates in these cells causing more damage and further narrowing of the artery. Some of the muscle cells die forming a collection of cholesterol and dead cells (this is the **atheromatous plaque**). Calcium may be deposited in the arterial wall at areas of damage and these areas become scarred forming **atherosclerotic plaques**. Atherosclerotic plaques are characterised by
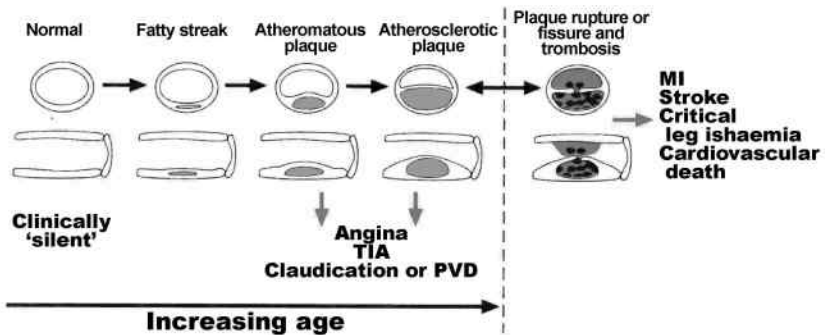
Figure II.3.: The atherosclerotic process. TIA: transient ischaemic attack; Angina: chest pain; Claudication: predictable pattern of lower leg pain caused by inadequate blood flow to exercising muscle; PVD: peripheral vascular disease; MI: myocardial infarction.[131]

the accumulation of cholesterol, macrophages, smooth muscle cells and extracellular matrix proteins in the intimal layer of the vessel wall. The tissues beyond the narrowing are deprived of a full blood flow and become so-called **ischaemic** tissues.

At a critical moment, plaque can rupture and blood platelets will clot the lesion, forming a 'thrombus', which may occlude totally the artery (**infarction**) or may be ripped off, obstructing narrower arteries further downstream the blood-circulation (**embolus**). Several factors incite arteriosclerosis, among them elevated cholesterol levels, hypertension,[315] smoking,[31] diabetes mellitus,[66] stress[150] and obesity.[19] A detailed review of arteriosclerosis was given by Simons.[287]

The body may be able to dissolve the clot and the situation may revert to an atherosclerotic plaque - usually with more narrowing of the artery.

Instead of narrowing the artery, the above processes may cause the artery to become weakened so that it balloons out - this is called an aneurysm (See section II.1.3).

II.1.2.3. Treatment

Once a patient has been diagnosed with carotid plaque, several treatments can be considered. Anti-hypertensive drugs can be administered, reducing the blood pressure and thus the chances for endothelial or plaque damage. Patients are asked to refrain from smoking and from excessive alcohol-
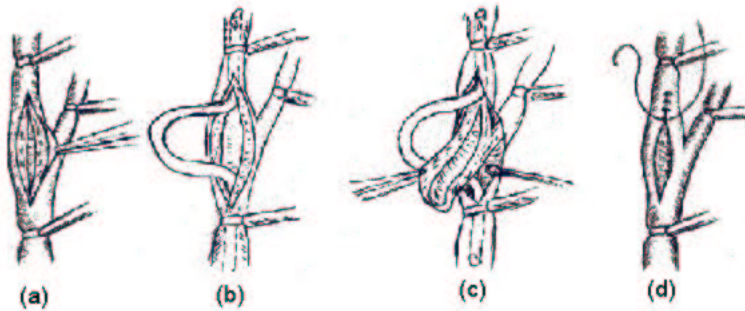
Figure II.4.: Carotid Endarterectomy. a: Carotid bifurcation clamped and opened. b: CCA-ICA bypass introduced. c: Plaque removal. d: Carotid sewed up.[378]

consumption. Another medical strategy is the use of platelet anti-aggregants, reducing the chance for blood clotting.

If an artificial widening of the vessel lumen is needed, two treatments are commonly performed:

1. **Carotid Endarterectomy** (Figure II.4). Carotid endarterectomy is a surgical procedure where the plaque is removed from the carotid inner wall. This ultimately removes the source of material which can potentially travel from the artery up to the brain causing a stroke. In a first step (Figure II.4 (a)[378]), the carotid bifurcation is clamped to prevent any blood flow through the bifurcation while an incision is made in the carotid. A piece of flexible tubing is introduced into the carotid, connecting the CCA with the ICA while bypassing the stenosed region (Figure II.4 (b)). The plaque can now be removed (Figure II.4 (c)). After plaque removal, the carotid is clamped again, the bypass removed, and the vessel wall sewed (Figure II.4 (d)).

2. **Carotid Stenting** (Figure II.5).[300] Carotid stenting is a percutaneous technique, i.e. a technique that does not require surgery in the form of an incision, but requires entry into a peripheral artery i.e. the femoral artery in the groin via a small tube which subsequent catheters and wires are passed through up to the neck where the carotid artery is located. Once it reaches its destination, the catheter will inflate to open up the blockage. In some cases, the catheter will leave a 'stent' at the diseased site: a metal or polymer construction that provides a scaffold to keep blockages from recoiling. Percutaneous techniques have the potential for being safer, less traumatic, more cost effective,
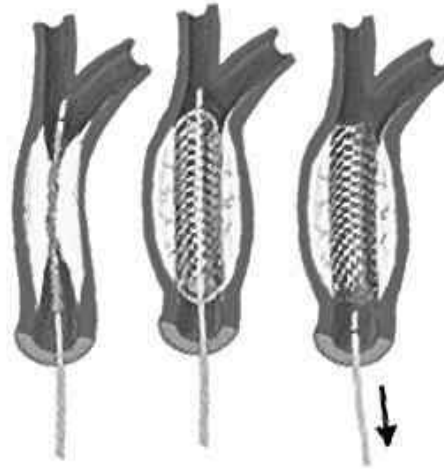
Figure II.5.: Carotid stenting: A mechanical device called a 'balloon' catheter is inserted into the narrowed carotid to widen it. The stent, a tiny wire-mesh scaffolding, is then placed in the newly expanded artery to keep it from narrowing again.[300]

and feasible in patients at high surgical risk. The procedure needs to be performed by individuals skilled in using various catheters that have balloons to open up blockages and/or stents.

Endarterectomy or Stenting? Stenting is less demanding for the patient. The stent is inserted via a catheter, threaded through a small incision in the groin, up to the neck. Patients typically stay in the hospital overnight. In contrast, carotid endarterectomy requires general anaesthesia and a two- to three-day hospital stay. It is performed through an incision in the neck area. However, endarterectomy has been performed since 1954, whereas the first carotid stent was placed in 1980. Due to the 26 years of extra experience and research, carotid endarterectomy is still often regarded as the more reliable technique and thus as the surgical procedure of choice.[84, 189, 267]

When is surgery required?

Asymptomatic Carotid Artery Stenosis
Asymptomatic carotid artery atherosclerosis is highly prevalent in the general population, particularly the elderly. However, severe (more than 70

percent area reduction) carotid artery stenosis is rare, especially in asymptomatic persons. Compared with symptomatic stenosis, asymptomatic carotid artery stenosis is associated with a relatively low risk of ipsilateral[b] cerebral infarction. About 4 percent of adults have asymptomatic neck bruits[c], but a carotid bruit is a poor predictor of extracranial carotid artery disease or high-grade stenosis.[274]

By actuarial analysis, patients with asymptomatic carotid bruits have an estimated annual risk of stroke of 1.5 percent at one year and 7.5 percent at five years.[366] Asymptomatic carotid artery stenosis of 75 percent or less carries a stroke risk of 1.3 percent annually.[233] When stenosis is more than 75 percent, the combined rate for TIA (transient ischaemic attacque) and stroke is 10.5 percent per year, with most events occurring ipsilateral to the stenosed carotid artery.[233]

Because of the low risk of stroke in asymptomatic patients, some experts recommend surgery only when the degree of stenosis is more than 80 percent.[28]

Symptomatic[d] Carotid Artery Stenosis
For symptomatic patients with carotid artery stenosis, the story is very different. Stroke is often caused by atherosclerotic lesions of the carotid artery bifurcation. The degree of internal carotid artery stenosis is the most important predictor of cerebral infarction among patients with extracranial carotid artery disease.[325] The severity of carotid artery bifurcation stenosis is directly related to the risk of stroke.

Through the removal of atherosclerotic plaques, carotid endarterectomy restores cerebral blood flow and reduces the risk of cerebral ischemia. Results from three major prospective studies provide compelling evidence for the benefit of carotid endarterectomy, when performed by experienced surgeons, in improving the chance of stroke-free survival in high-risk symptomatic patients.[213, 325, 351]

---

[b]Ipsilateral: Located on or affecting the same side of the body.[250]

[c]A carotid bruit is an abnormal sound, heard when using a stethoscope to listen to blood flow in the carotid artery. A bruit indicates a fatty buildup.

[d]typical symptoms: weakness or total inability to move a body part numbness, loss of sensation (tingling), decreased or lost vision (may be partial or temporary), language difficulties (aphasia), inability to recognise or identify sensory stimuli (agnosia), loss of memory, loss of coordination, swallowing difficulties, personality changes, mood and emotion changes, urinary incontinence (lack of control over bladder), lack of control over the bowels, consciousness changes[6]

II.1.3. Aneurysms[138]

An aneurysm is a bulging out of part of the wall of a blood vessel. It forms where the wall has weakened, often due to the build-up of plaque. Aneurysms can therefore be, just as stenoses, a consequence of atherosclerosis. It may also be an inherited condition or a complication of high blood pressure (hypertension). Left untreated, aneurysms may tear or burst. Ruptures are very painful events that cause massive internal bleeding. The patient must be treated within minutes in order to have a chance of survival. If an aneurysm bursts in the brain, it could cause a **haemorrhagic stroke**. If an aneurysm bursts in the chest, there is only a 20 percent chance of survival. Therefore, early diagnosis and treatment are critical. Because aneurysms often produce either no symptoms or mild symptoms (e.g., back pain), routine physical examinations are strongly encouraged so that a physician can regularly test for warning signs.

There are a number of different types of aneurysms, which include the following:[138]

- *Aortic aneurysm*: A general condition characterised by the distention, or ballooning out, of part of the wall of the aorta. Typically, the widened part of the aorta is considered to be an aneurysm when it is more than 1.5 times its normal size. If accompanied by an aortic dissection, it is
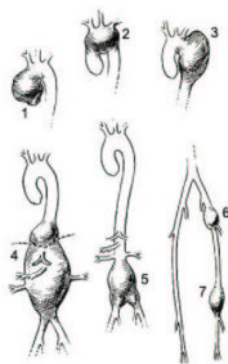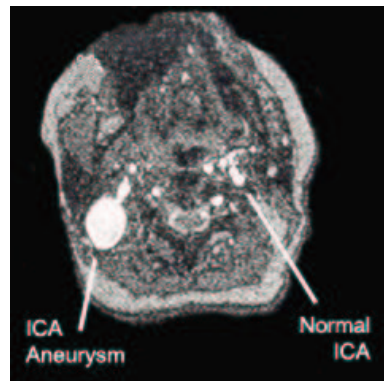
(a) Aortic[188] (b) Carotid[243]

Figure II.6.: Aneurysms. a: Different types of aneurysms found in the aorta and its branches: (1) ascending aorta; (2) aortic arch involving the brachiocephalic, carotid, and subclavian arteries; (3) descending portion of the aortic arch; (4) thoracoabdominal aneurysm involving the celiac, superior mesenteric, and renal arteries; (5) abdominal aorta and iliac arteries; (6) femoral artery; (7) popliteal artery.[188] b: Time-of-flight MR image of a subject with a normal ICA on one side and an ICA aneurysm on the other side of the neck.[243]

classified as a dissecting aortic aneurysm. Typical aortic aneurysms are depicted in Figure II.6 (a).[188]

- *Cerebral aneurysm*: Also known as a **berry aneurysm**, this is a bulge in the wall of a blood vessel in the brain (one of the cerebral arteries). A cerebral aneurysm is typically found where the arteries branch at the base of the brain. The cause is unknown, but smoking increases a person's risk of developing this condition.

- *Ventricular aneurysm*: A bulging or ballooning out of part of the wall of one of the heart's lower chambers (ventricles), usually the left. If the aneurysm is present in the wall between the ventricles (the ventricular septum), it is also known as a ventricular septal aneurysm, an inter-ventricular aneurysm or simply a septal aneurysm. It may be present since birth (congenital) or may be a complication of a heart attack or other trauma.

- *Carotid aneurysm*: In Figure II.6 (b),[243] a cross-section of a neck of a patient has been imaged using time-of-flight magnetic resonance imaging (TOF MRI). The ICA on one side of the neck is normal, but the ICA on the other side contains an aneurysm.

- *Atrial aneurysm*: A bulging or ballooning out of part of the wall of one of the heart's upper chambers (atria). If the aneurysm is present in the wall between the atria (the atrial septum), it is also known as an atrial septal aneurysm (ASA). An ASA has been associated with an increased risk of stroke and is often accompanied by the presence of a patent foramen ovale, an opening between the upper chambers (atria) of the heart. Normally, this opening is present in the developing foetus, and closes shortly after birth. It is often present since birth (congenital).

- *Cirsoid aneurysm*: The enlargement of a network of blood vessels that commonly occurs on the scalp and may result in the formation of a tumour.

Strategies for preventing an aneurysm include managing high blood pressure and preventing the build-up of plaque.

II.2. Pressure, Geometry and Flow features

Now that the carotid diseases are described, the search for potential causes of these diseases can start. Based on its high prevalence and high death rate, the focus will be on atherosclerosis. It has already been stated (see section II.1.2) that several factors incite arteriosclerosis, among them elevated cholesterol levels, arterial hypertension,[315] cigarette smoking,[31] diabetes mellitus,[66] stress[150] and obesity.[19] Other factors include older age, male gender, African-American ethnicity, family history, dyslipidemia[e], heart disease, excessive alcohol intake, abnormal body mass index and low socioeconomic status.[28] The development of atherosclerotic disease occurs in a localised fashion that spares certain segments of the vascular tree while affecting others (see Figure II.2). Cited risk factors for vascular disease are systemic in nature, and do not explain the specific location of plaques to particular segments of the vascular system. However, there is a strong correlation of atherosclerosis with regions of disturbed blood flow, which suggests that changes in local haemodynamic forces may affect its development.

In what follows, certain risk factors are studied more closely: pressure, geometry and flow-related features with a clinical significance are defined and discussed. In section II.3, these features are translated into physically measurable parameters, 'markers' of atherosclerosis.

II.2.1. Pressure

A clear relationship between pressure and the presence of atherosclerosis has been established:[216] patients undergoing sustained increased blood pressures have a higher incidence of atherosclerosis. The reason for this relationship is not entirely clear. Two theories have been put forward.

1. Atherosclerosis is a hardening of the arterial system. The loss of arterial compliance increases the pumping power required for maintaining the blood circulation. This is achieved by increasing the arterial blood pressure. In this theory, atherosclerosis is the cause of hypertension.

2. Pressure in the surrounding tissue of an artery is the reference pressure, 0 mmHg. Blood pressure is therefore entirely dissipated in the arterial wall. This pressure dissipation gives rise to a wall tension which

---

[e]changed level of lipids in blood serum
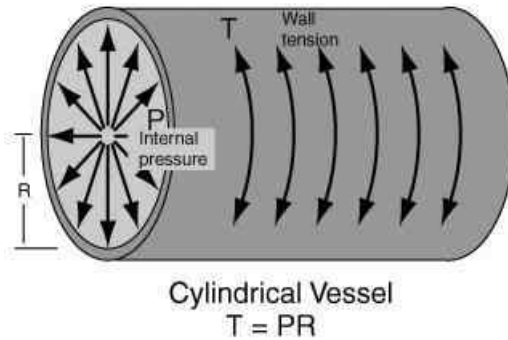
Figure II.7.: Laplace's Law. P: pressure in the tube; T: Wall Tension; R: radius. Laplace's law can be used to estimate the wall tension in an artery.[108] Note that Laplace's law assumes thin walls, circular tubes and uniform pressures, which is why it can only be used as an approximation.

can be calculated using Laplace's law (see Figure II.7): assuming a cylindrical shape for the vessel, the tension T is given by

$$T = P \times radius \tag{II.1}$$

here, P is the blood pressure and the considered radius is the lumen radius. The arterial circumferential wall stress can be derived from the wall tension

$$\sigma_{wall} = \frac{T}{IMT} = \frac{P \times radius}{IMT} \tag{II.2}$$

assuming that the pressure is dissipated in the intima and the media. An increased pressure will increase the wall tension. The vessel wall will remodel until it reaches the circumferential wall stress in the normotensive situation. This is achieved by proliferating the IMT. This proliferation enhances the progression of plaque formation.

Apart from its indirect effect on the vessel wall thickness, the pressure has a direct damaging consequence on the endothelium in the lamina intima. The induced damage could be the onset of the atherosclerotic process.

In this second theory, hypertension is the cause of atherosclerosis.

The two theories are probably both happening to a certain extent. In any case, blood pressure is a clear marker of atherosclerosis.[216] It is the most important modifiable risk factor for stroke.[28]

In a series of publications, Boutouyrie[36,37,109,147] and Mitchell[221,222] argued that not the systolic blood pressure (SBP) or mean arterial pressure (MAP) was the pressure parameter with the highest diagnostic value for atherosclerotic pathology, but the pulse pressure (PP). They described how blood pressure increased with age in all Western countries, but above the age of 60 the increase of systolic pressure with age was accompanied by a stabilisation or a decrease in diastolic blood pressure. Since the PP is the difference between systolic and diastolic pressure, there will be a progressive increase in PP despite a stable MAP. This trend results in a growing population with **isolated** or **disproportional** hypertension: SBP > 160 mmHg and DBP <90 mmHg.[146] It appears that the PP is an important independent marker of carotid intimal thickening in both healthy people and persons with essential hypertension[f]. This is because cyclic stretching (i.e. increased PP) has a more important influence on the expression and growth of smooth muscle cells than a static load (i.e. increased blood pressure).[36] In conclusion, pulse pressure is, in comparison with systolic or diastolic pressure, a better marker for vascular pathology.

II.2.2. Arterial Geometry

II.2.2.1. Basic parameters

Initima-Media Thickness and Lumen Diameter As stated on page 21, the arterial wall consists of three layers: tunica intima, media en externa (Figure I.8). The cumulative thickness of intima and media of large arteries, such as the carotid, is called the intima-media thickness (IMT). The IMT has been widely used as a marker of vascular disease, since it can be a direct evidence of the atherosclerotic process. A thickened IMT is either a consequence of sustained high blood pressures or evidence of an inflammatory reaction initiating atherosclerosis as explained on page 25.

A growth in IMT is associated with an increasing chance for stroke or cardiac infarction.[34] Moreover, growth in IMT is correlated with a vast spectrum of other cardiovascular risk factors such as age, male gender, ethnicity, hyperlipidemia, smoking, diabetes mellitus, left ventricle hypertrophy and hypertension.[34] Simon[285] acquired the IMT in a population of 788 healthy subjects (326 men) of all ages, as shown in Figure II.8. Overall, it can be stated that the IMT increases with age, from values around 390 to 480 μm

---

[f]essential hypertension is hypertension with no clearly definable reason
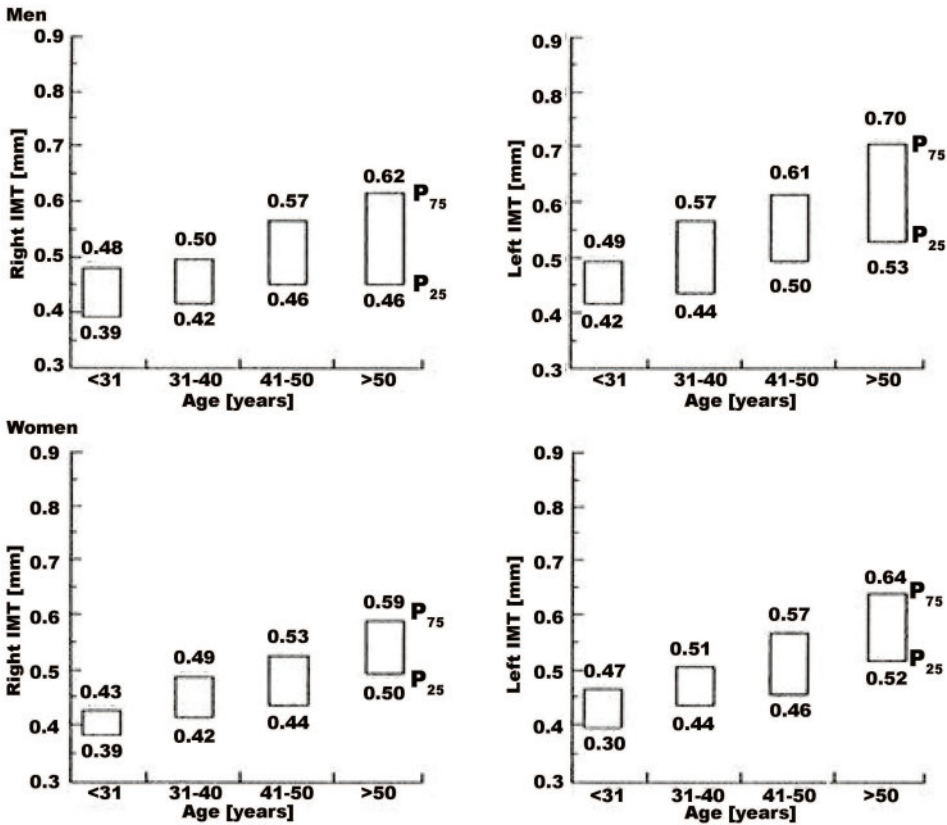
Figure II.8.: Distribution of 'normal' values of common carotid artery far wall IMT in a population of healthy men and women by age range. Upper and lower limits of bars are 75th upper (P_{75}) and 25th lower percentiles (P_{25}) of IMT distribution within the age range indicated in the x-axis. Abnormal IMT's are values above the 75th upper percentile in each category of age. (n=788 (326 men))[285]

for young men to 460 to 620 μm for men older than 50. Two more features emerge from Figure II.8: (1) women have IMT values significantly lower than men and (2) the IMT in the right CCA is larger than that in the left CCA. The first feature can be explained by the fact that men have larger carotid arteries (see Table I.2), the second one has also been reported in other studies[77, 316] but, as stated by Sun,[316] *"The mechanism for this asymmetry cannot be elucidated from present data and remains unclear"*.

The IMT is not constant along the carotid bifurcation.[48, 76, 110, 271, 316, 384] For healthy people, Gianaros found that the IMT was 11.1% thicker in the bulb, but 11.1% thinner in the ICA after the bulb than in the CCA, based on 82 subjects.[110] Similarly, Casiglia found that for hypertensives, the IMT was 6.5% *thinner* in the bulb, and 19.5% thinner in the ICA after the bulb than in

the CCA, based on 97 subjects.[48] A separate study suggested that IMT in the ECA was approximately 87.5% of that in the ICA (post-bulb).[384]

Derived Parameters   Note that the carotid IMT needs to be considered relative to the lumen diameter (LD):[34] the intima-media layer is subjected to the pressure difference between the blood in the vessel and the surrounding tissue, according to equation II.2. It shows that the tension in the IMT will be smaller if LD is smaller. If LD is large, IMT will be adaptively increased, owing to the complex wall remodelling process. Imagine the following four hypothetical subjects, each with the same blood pressure and carotid blood flow rate. *Subject A* has a small LD and a small IMT. Although his IMT may appear to be low, his IMT/LD will be normal. *Subject B* has a small LD and an average IMT. This subject could be classified as normal if only the IMT was taken into account. However, his IMT/LD ratio will show that he has signs of an abnormally thick IMT. *Subject C* has a large LD and an average IMT: the tensile stress in his vessel wall could be relatively high. *Subject D* has a large LD and a large IMT. Considering the IMT alone, he would be classified as a pathological case. Considering both IMT and LD, it becomes clear that his IMT needs to be larger in order to alleviate the normal blood pressure occurring in the vessel. These four examples show that although IMT is a very valuable marker of atherosclerosis, it should always be considered relative to the local LD.

Another way of taking account of the LD when using the IMT for diagnostic purposes, is to calculate the cumulative area of intima and media in an arterial cross-section. This area is called the **intima-media area** or IMA. A change in LD could change the IMT passively because of the reduced or increased tension in the wall. In this case, the vessel wall mass does not change, it just gets redistributed around the lumen, and the IMA remains constant. Taking advantage of the incompressibility of the vessel wall, the IMA (as opposed to the IMT) is therefore a better marker for vascular hypertrophy since it is independent of variations in blood pressure or LD.

Carotid compliance[167]   Arterial compliance is defined as the change in arterial volume induced by a pressure change:

$$C = \frac{\partial V}{\partial p} \qquad\qquad \text{(II.3)}$$

with V the arterial volume and p the blood pressure.

Arterial compliance is an important measure of the health status of an artery. The elastic behaviour of conduit arteries has a major influence on the left ventricular function and aortic flow.[89, 111, 152, 317, 353] A loss in arterial compliance will increase the pulse pressure, an index of the pulsatile haemodynamic load. An increased pulsatile load is a risk factor for the development of congestive heart failure[58, 60g]. Therefore, impaired arterial elasticity is particularly deleterious in patients with congestive heart failure. Elasticity of conduit arteries is determined by both structural and functional factors. Both sets of factors are governed by the tunica media, which constitutes a large part of the arterial wall and is the principal determinant of the vessel's mechanical properties. Structural factors that passively alter arterial elastic properties include degeneration of elastic fibres, increased collagen content, and calcium deposition (e.g. in the formation of atherosclerotic plaque). Functional factors actively reduce distensibility of arteries by constricting vascular smooth muscle. These factors, which include vasoconstrictive substances related to increased activity of sympathetic nervous and renin-angiotensin systems, may be particularly relevant to abnormal elasticity in patients with heart failure.

It has been recognised that arterial compliance reduces with age, as demonstrated by Laogun in a study conducted on 600 'normal' volunteers.[168] He found the following relationships between arterial compliance and pressure, age as well as sex:

- Pressure: acute changes in MAP do not significantly affect compliance for normotensives and hypertensive adults, however, hypertensive young (< 20 years) subjects show a markedly reduced compliance.

- Age: compliance increases from birth and shows a maximum around the first decade of life after which there is progressive decrease with age.

- Sex (Figure II.9): both sexes have approximately the same compliance at birth, and it increases at the same rate to the peak value between 8-10 years of age. Whilst the male compliance decreases steadily, the rate of fall of the female compliance decreases and begins to diverge

---

[g]**congestive heart failure**: disorder in which the heart loses its ability to pump blood efficiently. The term 'heart failure' should not be confused with 'cardiac arrest', a situation in which the heart stops beating.
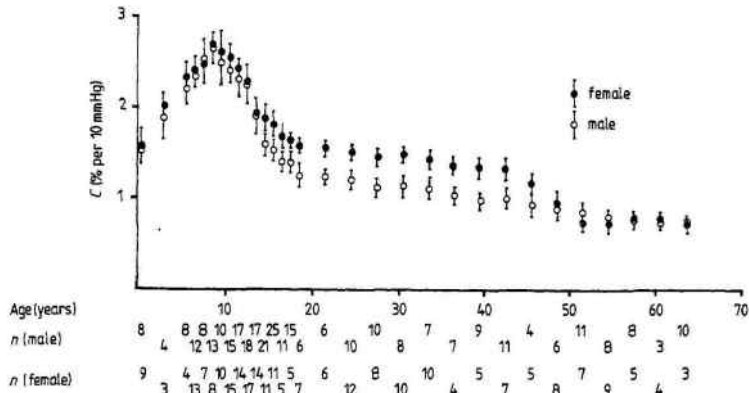
Figure II.9.: Variation of aortic compliance in females compared with males from birth to 65 years.[168] n denotes number of subjects in each age range for which the compliance is given as mean $\pm$ standard deviation. The compliance is expressed as a percent volume change per change in pressure of 10 mmHg.

from male at around 14-15 years of life. There is a marked change in the rate of decay in the compliance value for males and females at around 18 years. Female compliance is now larger than male compliance, until the marked fall in female compliance at 45 - 50 years, attributed to the menopause. After the fifth decade, there is no observable difference between the male and the female compliance.

II.2.2.2. Geometric risk factors

As illustrated in Figure II.2, atherosclerosis tends to form at particular sites in the vascular tree. Especially bifurcations and bends are concerned. In the past, researchers have attempted to find which geometric features would be more atherogenic than others.[45, 100, 157, 223, 289, 293, 331, 334, 389] For a bifurcation, the planarity, i.e. degree to which the arteries all lie in a plane, have been postulated as risk factors for atherogenesis.[45, 100, 157, 281, 389] Other researchers[331, 334] state that it is not the planarity, but rather the curvature, linearity and tortuosity of an artery that is responsible for the predisposition to atherosclerotic plaque. Bifurcation angles are usually thought to be atherogenic when very large. The definition of a 'bifurcation angle' remains obscure although many suggestions have been made in the literature.[289, 293] Finally, the bifurcation area ratio, i.e. the ratio of the cross-sectional area distal to and proximal from the apex, has been investigated for its relationship with atherogenic sites.[223]

It is important to note that it is in fact not geometry per se, but the effect of geometry on the local blood flow that renders specific geometric features interesting in the context of atherogenesis.

II.2.3. Flow

II.2.3.1. What is Wall Shear Stress?

As blood flows through a vessel, it exerts a physical force on the vessel wall. This force can be resolved into two principal vectors.[342] Shear stress, being tangential to the vessel wall, represents the frictional force exerted by the flowing blood at the endothelial surface of the vessel wall. Normal stress, or pressure, is perpendicular to the vessel wall. It represents the dilating force of blood pressure on the vessel wall. The whole vessel wall, including the endothelium, smooth muscle cells and the extracellular matrix, is exposed to it. In contrast, only the inner surface of the vessel wall, the endothelial cells, are exposed to the frictional force of shear stress. There is some slow transmural flow around smooth muscle cells in arterial walls, but this force is considered insignificant when compared with the normal wall stress to which these cells are exposed.[19] These haemodynamic forces are affected by fluid viscosity and by vessel diameter, thickness, and distensibility (Figure II.10). Mathematically, instantaneous shear stress in laminar flow is defined as

$$\vec{\tau} = \mu \frac{\partial \vec{v}}{\partial y} \tag{II.4}$$
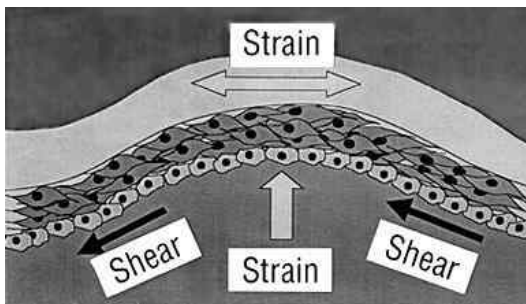
Figure II.10.: Schematic of an artery and the haemodynamic forces generated during a systolic pulsation. The shear stress force vector is parallel to the flow of blood and unidirectional. However, the cyclic strain force exerted on the vessel is multi-dimensional and stretches the vascular cells along multiple planes.[11]

here, $\overrightarrow{v}$ is the velocity vector, y is the normal distance from the vessel wall, and μ is the dynamic viscosity. For laminar flow (flow rate Q) in circular tubes (radius r), the shear stress at the wall can be written as

$$\overrightarrow{WSS} = \overrightarrow{\tau_w} = 4\frac{\mu}{\pi}\frac{Q}{r^3}\overrightarrow{e_{ax}} \tag{II.5}$$

with $\overrightarrow{e_{ax}}$ the axial unit vector.

II.2.3.2. The effect of Wall Shear Stress

Shear stress and tensile stress are the predominant haemodynamic forces produced by the pulsatile blood flow. These forces affect the function, morphology, and proliferation of vascular cells, and the local development and progression of atherosclerotic disease.

In a *normal* situation, wall shear stress is used to regulate the cross-sectional area of the vessel. Endothelial cells 'sense' the shear stress using their outer layer, the glycocalyx, which is approximately 0.5 μm thick and consists of substances combining sugar and protein elements. The layer contains minute hairs. It is thought to signal to the endothelial cells when more blood flows through an artery, so that the endothelial cells release nitric oxide (NO). Nitric oxide is one of the pivotal molecules coordinating vascular function.[343] Figure II.11 (by Powell[252]) shows the consequences of a NO release by the vascular endothelium, one of which being vasodilatation. The high WSS, which caused the NO release, will decrease with increased cross-sectional area at a constant flow rate (see equation II.5). The endothelium releases NO to protect itself from the damaging influences of high WSS.

The importance of wall shear stress and flow separation regions with regard to *atherosclerosis* and endothelial lesion has been investigated in a large number of studies;[11, 47, 156, 187] what follows is a short overview of why vessel wall shear stress became an important research topic.

Several factors contribute to the clinical importance of wall shear stress. Regions with *low* (0.5 $\frac{N}{m^2}$) wall shear stress show an increased endothelial cell loss and even desquamation[h] as the results of apoptotic cell death.[63] Subsequently, the subendothelium gets exposed to the blood flow, promoting

---

[h]**Desquamation**: endothelial peeling
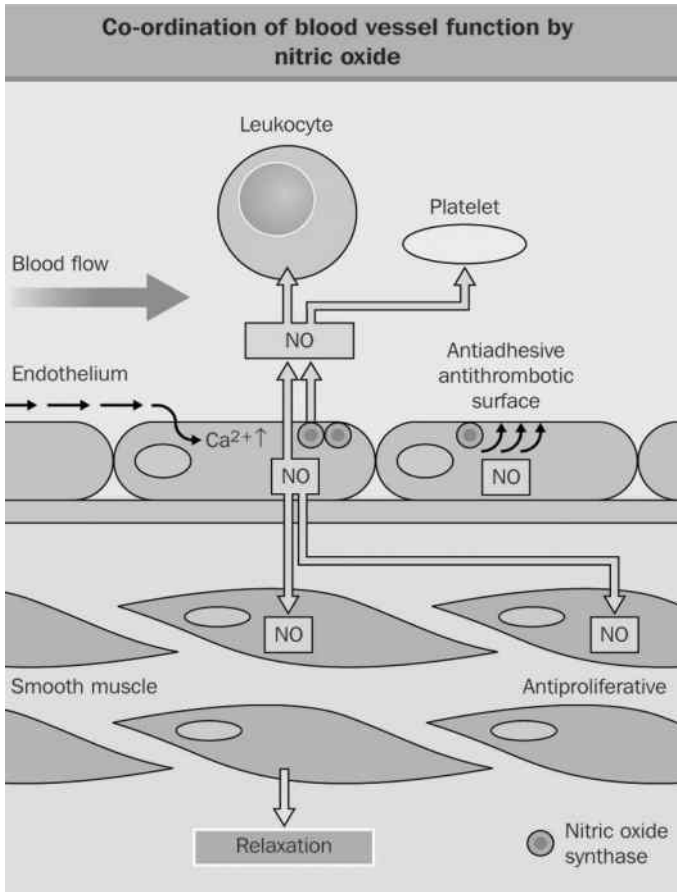
Figure II.11.: Coordinating and protective roles of nitric oxide (NO) released by vascular endothelium.[252] NO is very chemically reactive. Increased blood flow and many agonists that bind to endothelial cell receptors lead to an influx of calcium into the endothelium, which results in increased production of NO. Secretion of NO into the vessel lumen results in reduction of the adhesive properties of platelets and leukocytes. Increased levels of NO within endothelial cells dampens metabolic pathways leading to endothelial cell activation. Secretion of NO into the smooth muscle cells of the media causes vasorelaxation (via the interaction of NO with the enzyme guanylate cyclase).

platelet aggregation and consequently thrombosis. Furthermore, a low wall shear stress increases the production of chemicals attracting monocytes and proliferation of resident macrophages and smooth muscle cells.[18] On the other hand, non-pulsatile *high* (2.5 $\frac{N}{m^2}$) wall shear stress induces the release of factors from the endothelial cells that inhibit coagulation, migration of leukocytes and vascular smooth muscle cell proliferation, while simultanuously promoting endothelial cell survival. Higher WSS ($>$10-15 N/m^2, problematic from 25-45 N/m^2)[155] causes endothelial trauma and haemolysis. In
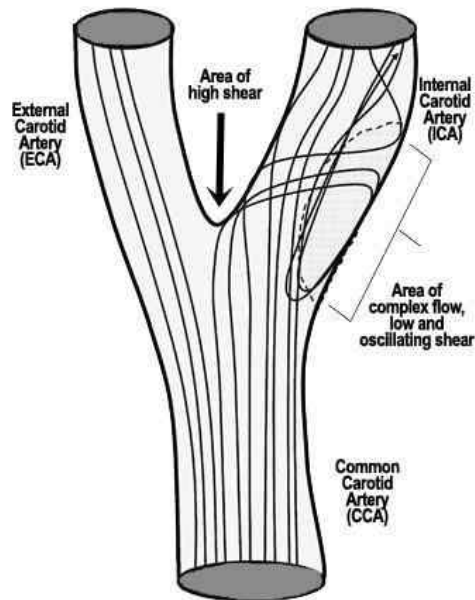
Figure II.12.: In the carotid artery, low but also high wall shear stress values are common.
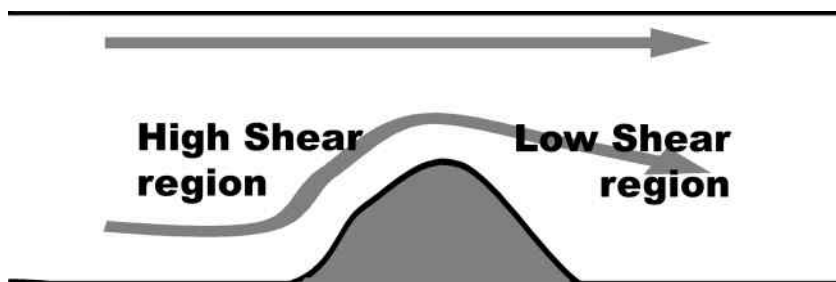
Figure II.13.: Schematic representation of the wall shear stress distribution in a stenosed vessel. The grey arrows represent blood flow, the black solid lines are the vessel wall, the grey surface is the stenosis.

the carotid artery, low but also high wall shear stress values are common (Figure II.12).

Knowledge of the wall shear stress is thus important to identify areas prone to plaque formation, but *once plaque has formed, knowledge of the wall shear stress remains important*, as illustrated in Figure II.13. The area proximal from the plaque will show high wall shear stress. Clowes[67] showed that the high wall shear stress reduced the stability of the formed plaque. This may lead to rupture, blood clotting and finally infarction or embolism.

This hypothesis was supported by Lovett's recent results which showed that plaque rupture sites tend to localise to the proximal part of the plaque where shear stress is highest.[202] Tricot[336] disagreed and showed that it was *not* the area upstream the plaque that would rupture. The distal area, where low shear stress is usually found, is more susceptible to disruption and subsequent thrombosis.

II.2.3.3. Oscillating Shear Stress

In the previous section, the consequence of static low or high shear stresses was described. Oscillating shear stress induces a biological mechanism on its own. It has been shown that endothelial cells tend to align in the direction of the flow.[180] Figure II.14, published by Malek,[208] illustrates on the left the alignment of endothelial cells. In the absence of a clearly defined flow direction, the endothelial cells do not align and the pattern in Figure II.14 (right) is seen. The lack of alignment in endothelial cells might preferentially activate circulating monocytes and encourage local adhesion and diapedesis[i]. Moreover, the endothelial cells are encouraged to produce certain mediators and growth-factors that perpetuate underlying smooth muscle and fibroblast proliferation. In addition, the endothelial cells will show a reduced production of clot-resolving enzymes, which may foster focal platelet aggregation and fibrin deposition, accelerating plaque formation and increasing the risk of thromboembolic events.

---

[i]Diapedesis: The movement or passage of blood cells, especially white blood cells, through intact walls into surrounding body tissue.
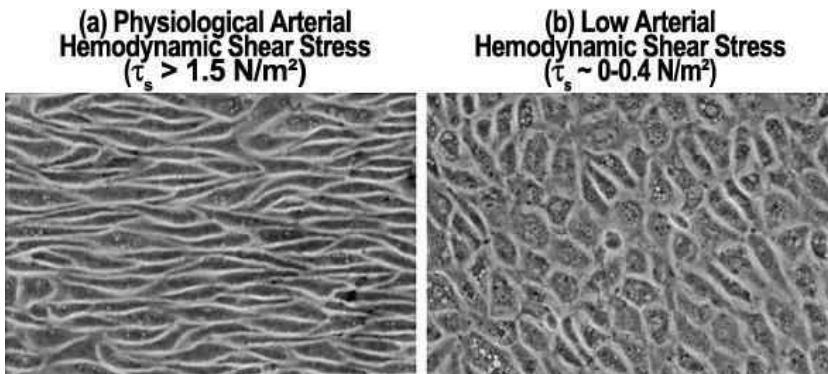
Figure II.14.: Endothelial alignment. a: Endothelial cells tend to align in the direction of the flow. b: When there is a lack of a clearly defined WSS direction, e.g. in zones of low and oscillating WSS, the endothelial cells will be aligned randomly.[208]

The absence of a clearly defined flow direction in physiological circumstances is due to the presence of both pulsatile flow and complex geometry: flow separation and flow reversal are features typical of stenoses and bifurcations.

II.2.3.4. Shear Stress Gradients

Apart from the shear stress and its oscillations, Kleinstrueur's group argued that not so much the WSS, but its gradients (both in time and in space) show a closer relation to the atherogenic behaviour seen in carotid bifurcations or femoral grafts.[42, 43, 142, 159, 160, 171, 172, 173, 200, 354] The authors[42] found that areas of high gradients of WSS were related to lesion growth intimal hyperplasia[j]. It is argued[173] that for an intact endothelium, the cross-wall mass transfer is mainly via an active transport mechanism, i.e., it is controlled by the endothelium depending on the need of the arterial wall for different substances. However, when the endothelium is locally injured, possibly due to high WSS, it causes, among other things, the intracellular space to widen substantially. This allows intimal hyperplasia enhancing molecules (such as low-density lipoprotein (LDL) and even cells (monocytes)) to simply diffuse in the intercellular space. The endothelial cell response aims to keep the integrity of intercellular junctions and prevent endothelial cells from hydrodynamic injury. However, significant and sustained WSSG values will handicap the cell response, initiating the process of atherosclerosis.

II.2.3.5. Shear Stress Angles

In zones where the endothelial's defensive function is weakened, flow moving towards the wall is problematic since atherogenic particles and cells such as monocytes could adhere to the endothelium and migrate into the wall at sites of increased permeability. Examining the shear stress angles is a technique that offers a view on the direction of flow.

---

[j]**Intimal Hyperplasia**: overexpression of the intima, i.e. pathological growth of the endothelial layer.

II.2.3.6. Haemodynamically induced Plaque Formation

Overall, the haemodynamic abnormalities observed in a vessel of complex geometry can facilitate plaque formation by multiple mechanisms:

- *Flow separation* and **stasis** (blood stagnation) allow for prolonged blood-vessel wall interaction with atherogenic particles, which may increase their local deposition.[11]

- Flow stasis, thus, *low shear stress*, is associated with decreased secretion of atheroprotective substances by endothelial cells.

- *Flow oscillations* are characterised by reversals in the direction of blood flow during the cardiac cycle, and can disrupt endothelial cells that are normally aligned in the direction of blood flow. Disruption of the cell alignment can *alter the barrier function of the cells* and can also *facilitate the deposition of atherogenic substance* in the vessel wall.

- High *WSS gradients* may widen intracellular space impeding the protective mechanism of the vessel wall.

- The atherosclerotic process can be sped up when blood flow is directed towards already injured endothelial wall.

Knowledge of the haemodynamics and the quantification of wall shear stress (WSS) in particular is therefore absolutely required in atherogenic research. Note that although the importance of the WSS is widely acknowledged, most of the mechanisms explained above are still hypotheses that have not thoroughly been proven.

II.3. Measurement of Designated Markers

The pernicious features discussed in the previous section can be quantified using a variety of parameters. In this section, the parameters are defined and discussed in a first step. In a second step, the techniques available for measruing these parameters are presented.

II.3.1. Pressure

II.3.1.1. Sphygmomanometry

Blood pressures are routinely measured using a sphygmomanometer (a blood pressure cuff). The cuff was previously attached to either an enumerated dial or stand. In the models with stands, bars of mercury will line up with the numbers. the model with dials have an arrow that will point to numbers as the pressure changes. Nowadays, the pressure is read on a digital display. Also attached to the cuff is a source for creating pressure. The more modern versions are inflated automatically by a purpose-built compressor, although usually the pressure source is a hand-held balloon that the examiner squeezes to inflate the cuff. In this 'manual' model, the balloon has a valve to release air from the cuff. When this valve is closed and the balloon is squeezed, the cuff will inflate and increase its pressure. To lower the pressure, turning the valve releases air. Figure II.15 shows how the pressure measurement works in practice.[14]

The cuff is placed over bare skin above the elbow. The arm is passively raised to the level of the heart. Moreover, the patient should be as relaxed as possible throughout the exam. This means both physical and emotional relaxation. At this point the cuff is inflated to a pressure at which the radial
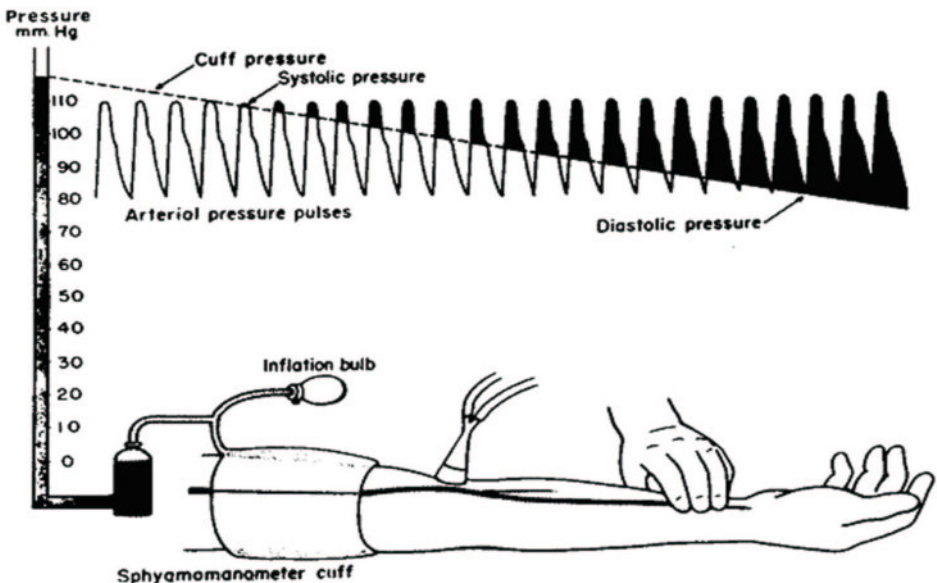
Figure II.15.: Sphygmomanometry in clinical practice.[181]

pulse cannot be palpated in the wrist. This means that the superficial arteries of the upper arm are now occluded by the inflated cuff. The examiner then listens to the radial artery with a stethoscope as the pressure is slowly lowered in the cuff. The point at which the heart exerts enough pressure to overcome the pressure applied via the cuff is the systolic blood pressure. The reason for hearing the blood flow is the fact that a partially occluded artery will cause the flow to 'spurt' and create turbulence. This pulse will still be heard as the pressure is slowly lowered. At a lower pressure the heart easily overcomes the pressure of the cuff and no pulse can be heard, this is the diastolic blood pressure.

II.3.1.2. Tonometry[68]

Arterial tonometry is a non-invasive technique that offers the clinician a beat-to-beat blood pressure waveform along with numerical values for systolic, mean and diastolic pressures, as well as pulse rate. It consists of using a sensor placed on the wrist over the superficial artery, for example the radial artery (Figure II.16 (a)). This sensor contains piezoelectric pressure transducers. A pneumatic pump presses the transducer array against the skin and tissue above the artery (Figure II.16 (b)). This pressure is known as the 'hold down pressure' (HDP). To determine optimal HDP, the monitor searches through a range of pressure values until it measures a signal indicating that the artery is of the form in Figure II.16 (b), i.e. the form giving the highest signal as in Figure II.16 (c). When the artery is partially flattened, a graph can be plotted to show sensor pulse amplitude versus time.
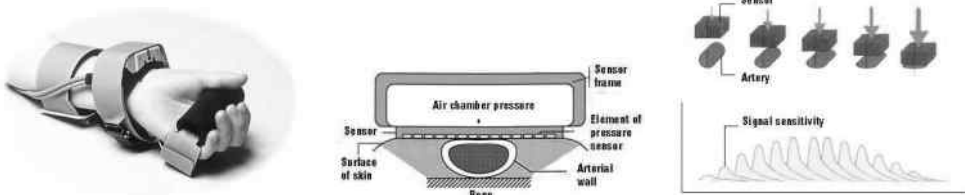
(a) Tonometer placed on radial artery

(b) cross-section through the artery

(c) determining HDP

Figure II.16.: The principle of tonometry. a: Photograph of a tonometer placed on a radial artery. b: The tonometer presses the artery against the underlying bone and senses the pressure pulses in the artery. c: Application of different hold down pressures (HDP's), different signals are measured due to the different shapes of the artery.[68]

For the carotid artery, the graph is of the form measured by Mitchell[222] in Figure I.6 (a) on page 15. At this stage, the waveform is not calibrated yet. For that purpose, the maximum and minimum in the acquired pressure waveform can be set equal to the systolic and diastolic pressure measured using a cuff as in Figure II.15. To complete the calibration, all values between the maximum and minimum pressure are found by linearly interpolating between the systolic and diastolic pressure.

II.3.2. Arterial Geometry

II.3.2.1. Basic Parameters

IMT and LD   Measuring the IMT is clinically performed using an ultrasound machine. An ultrasound image is formed by transmitting a high-frequency (1-12 MHz) beam into the body, and collecting and analysing the returned echoes to produce an image whose intensity is related to the echogenicity of the tissue and tissue interfaces. Modern 'B-mode' ultrasound readily allows the visualisation of the intima-media layer of superficial large arteries such as the common carotid. Figure II.17 shows a B-mode image representing a longitudinal cross-section of the common carotid artery and an amplification of that same image (Figure II.17 (b)). The black region on top of the image corresponds to the carotid lumen. Figure II.17 shows how the LD and IMT are measured on the image.

The principles and validity of B-mode ultrasound measurements of IMT were

(a) longitudinal cross-section of CCA   (b) close-up
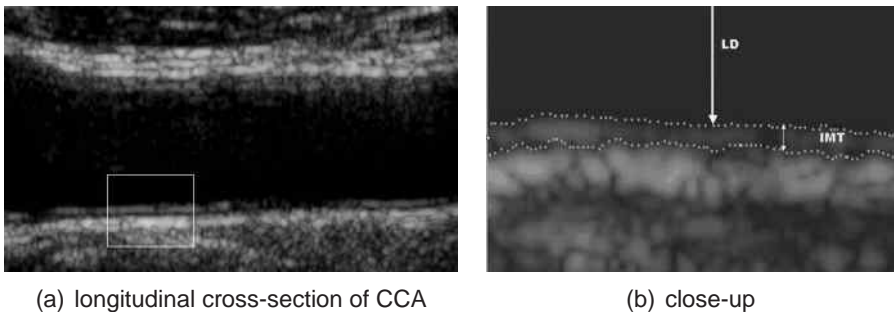
Figure II.17.: A longitudinal image of the distal carotid artery using B-mode ultrasound. A region of the intima media complex is magnified and highlighted for reference. Flow is from right to left. Note that the distal end of the white box in the upper image corresponds to the start of the distal end of the common carotid artery

Study	Mean Difference ($\pm$ SD)
Mayet[214]	0.01 $\pm$ 0.045 mm
Bots[35]	0.03 $\pm$ 0.12 mm
Selzer[280]	0.04 $\pm$ 0.05 mm
Gariepy[104]	0.02 $\pm$ 0.02 mm
Riley[265]	0.01 $\pm$ 0.13 mm
Salonen[269]	0.03 $\pm$ 0.09 mm

Table II.1.: A summary of the reproducibility of IMT measurement from a number of groups.[35, 104, 214, 265, 269, 280]

first described by Pignoli.[251] This group showed that ultrasound of the normal carotid artery demonstrated a 'double-line' pattern: the first 'echogenic' line on the far wall corresponding to the lumen-intima interface, and the second line to the media-adventitia interface (Figure II.17 (b)). Comparison with measurements of wall thickness in histological arterial wall specimens confirmed that this distance between the two echogenic lines correlated well with the far wall IMT, albeit often being an overestimate.[249, 369] Conversely, the near wall IMT is often an underestimate of the corresponding histological IMT measurement, proving less reliable than measurement of the far wall, and in part being affected by the gain setting of the ultrasound scanner[355, 369k].

Further comparisons with histological samples have also confirmed that the distance of the leading edge of the intima-lumen interface of the near wall to the leading edge of the lumen-intima interface of the far wall reflected the lumen diameter.

A common methodology for IMT analysis has been to restrict the IMT measurement to the distal end of the common carotid artery.[105, 214] On B-mode ultrasound, the distal end of the common carotid is defined as the beginning of the dilatation of the carotid bulb, with loss of the parallel configuration of the near and far walls of the common carotid artery (Figure II.17). This has certain advantages: this region of the carotid artery is often a superficial, straight segment demonstrating the IMT as two parallel echogenic interfaces (Figure II.17), making it a section that may be analysed with high precision and reproducibility (Table II.1).

IMT/LD and IMA   B-mode ultrasound thus allows the measurement of IMT and LD with high reproducibility (Table II.1). Follow-up parameters include

---

[k]This discrepancy may be due to post mortem tissue shrinkage and the tissue contraction that occurs with fixation.

the IMT/LD ratio and the intima-media area (IMA), estimated as the difference in area between two concentric circles: one with radius LD/2 and another with LD/2 + IMT:

$$
\begin{aligned}
IMA &= \pi \times \left(\frac{LD}{2} + IMT \right)^2 - \pi \times \left(\frac{LD}{2} \right)^2 \\
&= \pi \times IMT \times (LD + IMT)
\end{aligned}
\tag{II.6}
$$

Compliance   Many different techniques for calculating the compliance have been suggested in literature,[36, 167, 222] some involving the measurement of the pulse wave velocity (PWV), i.e. the speed with which a pressure wave travels through the arterial tree. In this manuscript, the vessel compliance C_o will be defined as follows:

$$
C_o = \frac{\Delta V}{\Delta P} = L \, \frac{\frac{LD_s^2 \, \pi}{4} - \frac{LD_d^2 \, \pi}{4}}{PP}
\tag{II.7}
$$

with L the axial vessel length, PP the pulse pressure, LD_s and LD_d the systolic and diastolic LD respectively. The compliance per unit length will be:

$$
C = \frac{C_o}{L} = \frac{\pi}{4} \, \frac{LD_s^2 - LD_d^2}{PP}
\tag{II.8}
$$

Note that the pulse pressure used here, is the local pulse pressure, i.e. the one occurring at the site where compliance is to be quantified. When the PP originating from a cuff measurement is used, there will be an error in the estimation of C.

Young's modulus and distensibility coefficient   Using a method described by Brands,[40] the Young's modulus is defined as:

$$
E = \frac{LD_d}{IMT_d \times DC}
\tag{II.9}
$$

where IMT_d is measured in diastole, LD_d is the lumen diameter in diastole and DC is the distensibility coefficient. The distensibility coefficient is defined as:

$$DC = \frac{1}{PP} \frac{2 \times \Delta LD}{LD_d} \tag{II.10}$$

where ΔLD is the change in lumen diameter from systole to diastole, and PP the pulse pressure within the common carotid artery measured by arterial tonometry.

Wall Tension and Tensile Stress   Using Laplace's law (section II.2.1), an approximation of the peak (T_p) and mean (T_m) circumferential carotid arterial wall tension can be calculated as:

$$T_p[Pa\ m] \;=\; SBP \times \frac{LD_s}{2} \tag{II.11}$$

$$T_m[Pa\ m] \;=\; MAP \times \frac{LD_d}{2} \tag{II.12}$$

where SBP is the systolic pressure and MAP the mean arterial pressure. LD_s and LD_d are the lumen diameters measured in systole and diastole respectively.

Furthermore, peak (σ_p) and mean (σ_m) tensile stress can be obtained by dividing the wall tension by the time-dependent IMT:

$$\sigma_p[Pa] \;=\; \frac{T_p}{IMT_s} \tag{II.13}$$

$$\sigma_m[Pa] \;=\; \frac{T_m}{IMT_d} \tag{II.14}$$

Similar to the definitions of LD_d and LD_s, IMT_d and IMT_s are measured in diastole and systole.

II.3.2.2. Vascular imaging

As described in section II.2.2.2, complex arterial geometry may induce adverse haemodynamic situations. A number of parameters have been suggested to describe haemodynamic conditions that are prone to atherosclerosis. In order to calculate most of these parameters, a 3D model of the carotid bifurcation needs to be reconstructed. Several imaging modalities can be used to reconstruct the realistic carotid geometries: X-ray, magnetic resonance imaging (MRI) and both intravascular and extravascular ultrasound. A short description of each of these techniques, with their advantages and disadvantages, is provided in what follows. The paragraphs on X-ray angiography, MRI and ultrasound are based on publications by Steinman,[304, 305] with permission.

X-ray angiography[304, 305]   The electromagnetic (EM) spectrum offers two windows through which one can explore the human body: the *high-energy X-ray range* and the *low energy radio wave range* (Figure II.18). In X-ray imaging, a high-energy 'X-ray' beam is sent through the body. These rays are captured by a device behind the body. The attenuation of the beam is a measure of body density and can therefore be used to differentiate particular zones in heterogeneous bodies. Note that X-ray imaging produces projection images as opposed to cross-sections of a body.
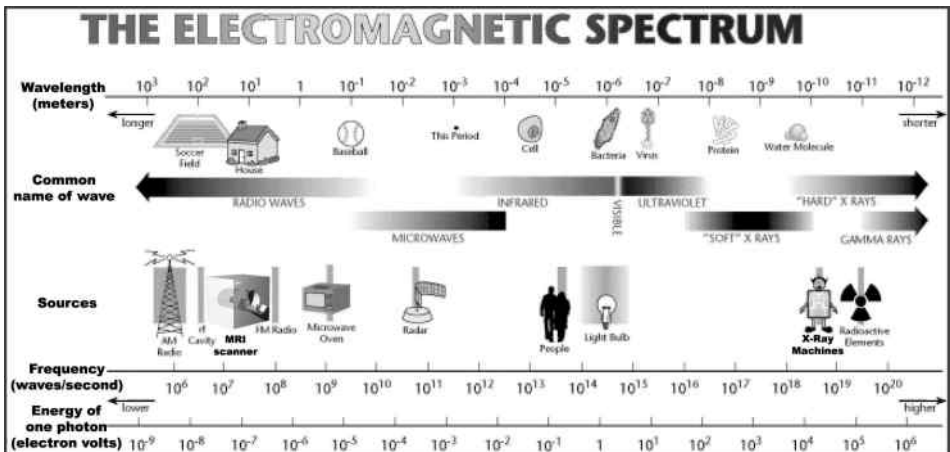
Figure II.18.: The electromagnetic spectrum and its applications. X-ray has a high energy and high frequencies, whereas MRI has the exact opposite: low energies and low frequencies.[86] A new tool for medical imaging, **TeraHertz Imaging**, uses intermediate energies and intermediate frequencies, i.e. frequencies in the *TeraHertz* range.

The first image-based computational fluid dynamics (CFD) studies of anatomically realistic arterial geometries were derived from clinical X-ray angiograms.[112] One of the first attempts to reconstruct a carotid bifurcation from medical images was published by Gibson.[112] In this study, patients were followed for three years via the so-called cine angiography of their coronary arteries as part of the Harvard Atherosclerosis Reversibility Project (HARP) to assess the rate of change in coronary artery diameter due to dietary versus drug therapy. Vessel centrelines and boundaries were identified from X-ray angiographic projection images and used to track the change in lumen diameter. Assuming circular cross-sections, this data was used to reconstruct two-dimensional axisymmetric models of the coronary segments at baseline. This particular study illustrates both the advantages and disadvantages of using projection angiography for image-based studies. The most obvious advantage is that X-ray angiography remains the gold-standard for quantifying atherosclerotic disease, owing to the high resolution and unambiguous delineation of the lumen made possible via the intra-arterial injection of contrast agent. This makes it relatively straightforward to derive the models from what is often readily available clinical data. In the absence of multiple projections and/or computed tomography (CT) reconstructions (available in other studies[306]), however, assumptions must be made about the cross-sectional shape of the lumen in order the reconstruct a three-dimensional model. Tascyian[322] used a slightly different technique to reconstruct 2D *in vivo* carotid models: single projections were acquired, from which corresponding images were digitally subtracted to remove background bone and tissue, further highlighting the vessel lumen. These were then used to reconstruct a 2D-model of a carotid bifurcation, shown in Figure II.19 (a). This technique is called **digital subtraction angiography** or DSA.

Later on, 3D models of the carotid have been reconstructed using X-ray. Reconstruction of 3D models requires at least two (ideally orthogonal) projections, and some assumptions about the shape of the lumen cross-sections. Ene-Iordache et al[91] successfully reconstructed the geometry of *in vivo* arteriovenous fistulas for haemodialysis using DSA in 2 orthogonal planes. Alternatively, recent advances in X-ray imaging technology make possible the rapid (4-6 s) acquisition of multiple (200) projection images,[92] from which the 3D lumen geometry can be reconstructed at high (200-400 μm) spatial resolution without the need for a priori assumptions about lumen shape. The last evolution of this technique has been illustrated by Cademartiri[44] on a 65-year old symptomatic man. Cademartiri showed that the use of multislice (MS) CT scanners offer a spatial resolution high enough to allow not only carotid bifurcation reconstruction (Figure II.19 (b)), but also visualisation of carotid artery atherosclerosis. The advantage of X-ray angiogra-

(a) 2D[322]   (b) 3D[44]
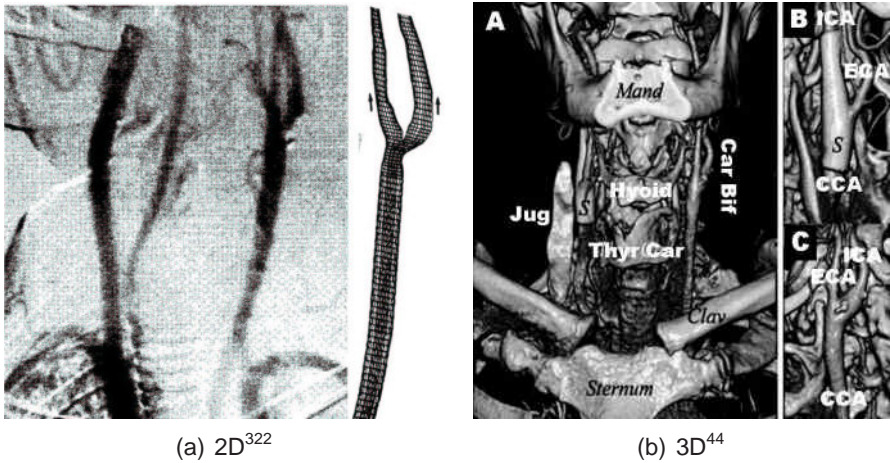
Figure II.19.: 2D and 3D Carotid geometries reconstructed from X-ray imaging. a: *Left*, X-ray depiction of a minimally stenosed carotid bifurcation; *Right*, mesh representation of the minimally stenosed carotid bifurcation. b: Direct 3-dimensional volume rendering (A, B, and C) using multislice CT shows the anatomy of the arteries of the neck at the level of the carotid bifurcation (Car Bif). Clav indicates clavicle; Hyoid, hyoid bone; Jug, jugular vein; Mand, mandible; and Thyr Car, thyroid cartilage. A magnified view of the right (B) and left (C) carotid bifurcations permits recognition of the common carotid artery (CCA), the internal and external carotid arteries (ICA and ECA), and a wall stent (S) at the right side. The left carotid bifurcation (C) is patent but is slightly dilated at the origin of ICA. A few calcified spots also are present. Note the backflow of iodinated contrast material into the right jugular vein (Jug in A).[44]

phy over other medical imaging modalities is the superior contrast-to-noise ratio, combined with high temporal and spatial resolution. The price paid for this quality is the finite risk associated with catheterisation, which is in fact greater than the risk associated with the radiation dose itself.[25] A less invasive alternative is to inject contrast intravenously (as opposed to intra-arterially), and rapidly acquire the 3D volume using single or multiple ring helical CT scanners. This approach typically produces poorer contrast images of the lumen. As a result, it is difficult to carry out human studies of early atherosclerosis and local haemodynamics using X-ray angiography, since it is typically performed only for patients with known or suspected vascular disease.

Intravascular Ultrasound (IVUS)[305]   In the context of the reconstruction of *in vivo* carotid geometries, the above-noted disadvantages of projection angiography can largely be overcome through the incorporation of intravascular ultrasound (IVUS), in which case X-ray angiography is used to guide an ultrasound probe-tipped catheter and landmark its position for subsequent
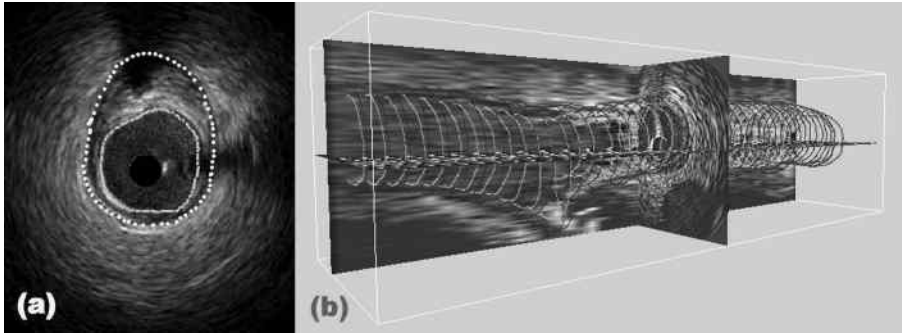
Figure II.20.: Using IVUS for the reconstruction of coronary geometry. a: A single IVUS image. The image is segmented, delineating the lumen (inner line) and the intima (outer line). b: A number of images are aligned, representing the 3D geometry of the coronary artery.[176]

reconstruction of the three-dimensional lumen and wall from the cross-sectional ultrasound images. The power of this approach was first demonstrated by Krams,[162] who used biplane angiography and IVUS data obtained at end-diastole to construct a three-dimensional model of a segment of a patient's atherosclerotic right coronary artery. This technique has proved its success in other arteries than the coronary. It was also used to reconstruct the 3D geometry of a stented coronary artery.[275, 291, 335, 357, 358] Owing to its ability to resolve the vascular wall *in vivo*, IVUS is becoming an increasingly popular approach for vessel reconstruction studies in which invasiveness is not an issue, such as animal studies or studies on patients already referred for cardiac catheterisation. Figure II.20 illustrates how 3D geometries are extracted from IVUS images.[176]

Magnetic Resonance Imaging (MRI)[305] MRI has emerged in the last decade as one of the most powerful and flexible imaging techniques, by virtue of the fact that contrast between tissues can be achieved by exploiting differences in the magnetic spin relaxation properties of the various bodily tissues and fluids. In the context of image-based CFD studies of atherosclerosis, MRI is particularly attractive since, unlike X-ray angiography, blood itself can be used as a contrast agent. This can take the form of 'bright blood' or 'time-of-flight' (TOF) techniques, which, just as conventional angiography, enhance the signal from flowing blood at the expense of signal from surrounding tissue. When it is necessary to resolve the vessel wall itself, 'black blood' techniques can be used to suppress the lumen signal. Several MRI protocols have been used in order to reconstruct a carotid geometry (Table VIII.1 on page 196). The detailed description of how *in vivo* carotid bifurca-

tions are reconstructed in this manuscript is explained in sections VI.2 and VI.3.

Three-dimensional Ultrasound (3DUS)[305] Three-dimensional ultrasound (3DUS) is a relatively recent development that makes it possible to acquire three-dimensional images of superficial vessels such as the carotid bifurcation using relatively fast and inexpensive ultrasound imaging techniques. Owing to its novelty, however, applications using 3DUS are comparatively still in their infancy. The first attempts to reconstruct carotid geometries from ultrasound images were not very successful,[114, 210] especially in comparison with the accuracy obtained by MRI at the time. Recently, two approaches have been able to overcome the early difficulties encountered.

- In a first approach,[20] conventional (two-dimensional) B-mode ultrasound images are acquired in a long sweep of the ultrasound probe over the subject's neck. Simultaneously, the probe is tracked in space. The images, together with the knowledge of their positions, are used to provide geometric parameters for three-dimensional carotid bifurcation models. For more details about the practical implementation of this approach, see sections VII.2 and VII.3.

- In a second approach, the probe is not swept over the subject's neck, but the probe's transducers can make a fan-like movement[376] (Figure II.21). After some off-line data processing, which primarily consists of 3D interpolation, a 3D data set is extracted.

Note that extravascular ultrasound is limited to superficial vessels such as the carotid bifurcation. Moreover, when not obscured altogether by the jaw, access to the carotid bifurcation often requires a twisting of the head and neck that may distort the 'natural' orientation of the vessel. Furthermore, the need to sweep the ultrasound probe, often manually, over the length of the carotid bifurcation renders ultrasound more operator-dependent than other imaging techniques. Nevertheless, compared to all other imaging modalities ultrasound is the least expensive, least invasive, and most widely available, which from a practical and economic perspective alone renders it an extremely promising tool for large-scale, prospective investigations of haemodynamics and vascular disease.

Geometrical Features   Regardless which of the above imaging techniques is used, a set of images will be obtained which enable the reconstruction of the carotid bifurcation. The following geometrical features can then be calculated.

- The **average cross-sectional area** in CCA, ICA and ECA (A_{CCA}, A_{ICA}, A_{ECA}).

- Here, the **area ratio** A_R is defined using the area of the most proximal ICA and ECA cross-section (a_{ICA} and a_{ECA}) and the area of the CCA cross-section 2 mm proximal from the considered ICA and ECA area (a_{CCA}):

$$A_R = \frac{a_{ICA} + a_{ECA}}{a_{CCA}} \tag{II.15}$$

- The **non-planarity** parameter NP as defined by King.[157]   In short, this non-planarity parameter is obtained as follows. First, the centre-lines are calculated as shown below,[20] and the coordinates of the centrelines are gathered in a matrix. The singular value decomposition (SVD) of this matrix will result in three singular values. The smallest singular value is a measure of non-planarity. For points on a plane, NP is zero, for points on a sphere, NP is $\frac{1}{3}$ or 33%. Figure II.22 gives a feel for the non-planarity parameter. The non-planarity can be calculated for each of the three vessels, NP_{CCA}, NP_{ICA} and NP_{ECA}.

Data Processing

Data Acquisition

3-Dimensional Data Set
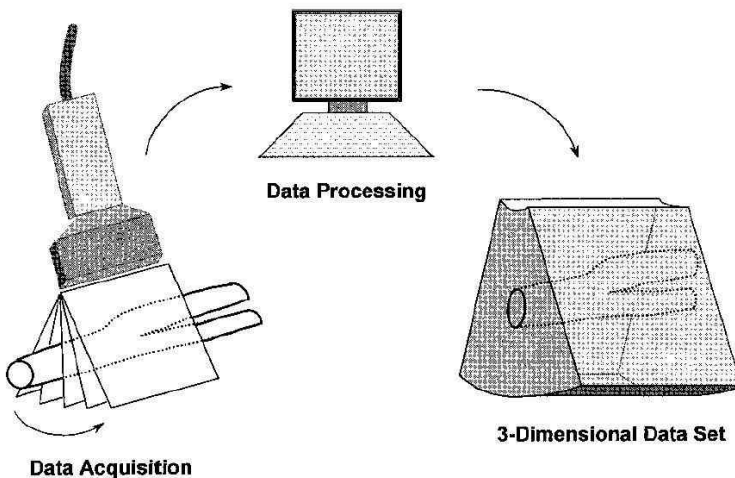
Figure II.21.: Schematics showing the principle of 3-D ultrasound data acquisition and production of a volumetric data set of the carotid artery.[376]

The centreline itself consists of the centroids (center of mass) of the cross-sections of the carotid arteries. The centroids of axial cross-sections are calculated by the expression

$$
\begin{aligned}
c_x &= \frac{\int \int x \mathrm{d}A}{A} \\
c_y &= \frac{\int \int y \mathrm{d}A}{A}
\end{aligned}
\tag{II.16}
$$

Here, c_x and c_y are the coordinates of the centroid in an (x, y)-orthogonal reference system and A is the surface of the cross-section for which the centroid is sought. Equation II.16 reduces to the following for an arbitrary polygon with nodes (x_i, y_i) (i=1,2,...,n):

$$
\begin{aligned}
c_x &= \frac{1}{6\,A} \sum_{i=0}^{n-1} \left((x_i + x_{i+1})(x_i\,y_{i+1}) - x_{i+1}\,y_i \right) \\
c_y &= \frac{1}{6\,A} \sum_{i=0}^{n-1} \left((y_i + y_{i+1})(x_i\,y_{i+1}) - x_{i+1}\,y_i \right)
\end{aligned}
\tag{II.17}
$$

Note that x_n is assumed to be x_0, in other words the polygon is closed. In order to obtain this formula, the polygon was divided in triangles, for which is straightforward to find centroids. The centroid of the polygon is an area-weighted average of the centroids of the triangles.

- A different centreline agreement measure, z_{DIST}, based on a definition by Long et al,[194] is defined as the average distance between the two centrelines. Because two different sets of centrelines can be totally different yet have the same NP, z_{DIST} is a more robust quantification of centreline difference.

- Similarly, the largest singular value is a measure of the **linearity** of the centrelines, L_{CCA}, L_{ICA} and L_{ECA}. The theoretical minimum is 33%. Figure II.22 gives a feel for the linearity parameter.

- Apart from the SVD method, the vessel linearity is also reflected by a *tortuosity* parameter defined as

$$
T_{vessel} = 100 \times \left(1 - \frac{D}{D_s} \right) [\%]
\tag{II.18}
$$

Non-P=0%   **Non-P=0%**   **Non-P>0%**
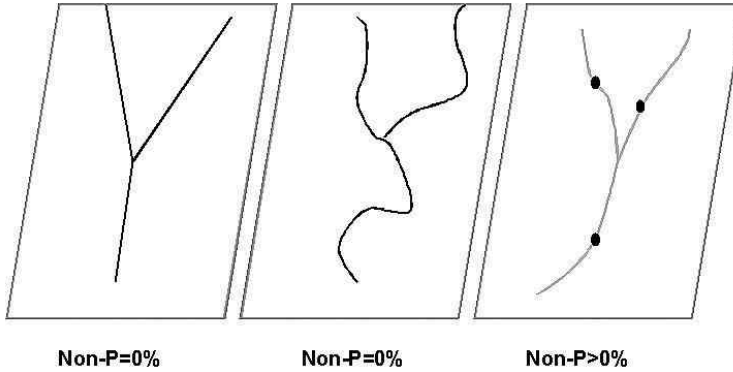
Figure II.22.: The Non-Planarity parameter NP as introduced by King.[157] The quadrangle represents a plane, whereas the lines in the quadrangle are centrelines of the carotid bifurcation. The centreline starting at the bottom of each figure represents the CCA, which splits into two other centrelines: the ICA and ECA. In the first case, the centrelines are straight segments: NP is 0% and L is 100% for each of the arteries. In the second case, the centrelines are planar, but not straight: NP is still 0% but L will have taken a value between 33% and 100%. Only in the third case, where the centrelines come in and out of the 'best-fit'[157] plane (at the black dots), NP will differ from 0%.

here, D is the shortest distance between the end-points of the considered vessel whereas D_s is the actual distance along the centreline between the end-points.

- Different ways to define a bifurcation angle have been suggested in the past. Here, the *bifurcation angle* α_{BIF} is defined as the angle between two vectors, $\overrightarrow{C_{CCA}, C_{ICA}}$ and $\overrightarrow{C_{CCA}, C_{ECA}}$. C_{CCA} was the CCA centroid of the most distal CCA slice. Similarly, C_{ICA} and C_{ECA} were the centroids of the ICA and ECA in the most proximal ICA and ECA slice.

- It is clear that cross-sectional areas and centrelines alone cannot describe a carotid geometry. In order to 'quantify' cross-sectional shapes, the **individual shape factor** (SF_i) has been introduced. It can be defined as by Barratt,[21] i.e. as the fraction of $4\pi\times$area and the square of the circumference. The SF_i is 1 for a circle, and smaller than 1 for anything else.

- **The comparative shape factor** (SF_c) is used when the shape of two cross-sections need to be compared. It can be defined based on a publication by Long.[194] It was evaluated here as follows (Figure II.23): (1) the two cross-sections to be compared were scaled to a cross-sectional area of 1, (2) the center points were aligned, (3) the area lying inside both cross-sections was denoted as A, whereas the area
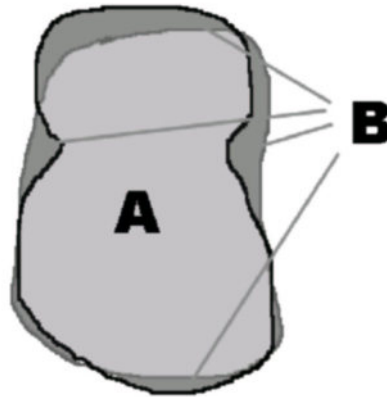
Figure II.23.: Definition of the area's A and B for comparative shape factor SF_c based on a publication by Long.[194]

outside the overlapping area was B, (4) the ratio B/(A+B) was defined here as the shape factor. It should be 0% for a perfect match between two shapes. For a hypothetical case where the shape is a circle in one cross-section, and a square in the other, the shape factor is 27%.

II.3.3. Flow

In the previous two sections, pressure and geometric parameters of interest have been defined. The last group of 'designated markers' are the flow parameters. The flow parameters have been divided into 3 sections. A first set of parameters (section II.3.3.1) concentrates on what can be measured without the need for 3D carotid geometry reconstruction. The calculation of entire flow fields is described in section II.3.3.2, whereas haemodynamic vessel wall parameters are defined in section II.3.3.3.

II.3.3.1. Heart and Flow Rate

Heart Rate The heart rate (HR) is usually expressed as the number of beats the heart performs per minute. It is often monitored by an electrocardiogram, i.e. a test that records the electrical activity of the heart.

Flow Rate Measuring flow rates *in vivo* is not always straightforward. The two techniques used in this study are described here.

Phase Contrast MRI

Axial velocities in a particular cross-section of an artery can be measured using an MRI technique called **cine phase contrast MRI** or cine PC MRI (see section VI.1). The flow rate can be calculated by the following two steps. (1) On the cine PC image, the pixels in the arterial lumen are separated from the other pixels. (2) Let V_p be the velocity measured by MRI in a particular pixel and A_p the area of a single pixel. The blood flow rate Q will be:

$$Q = \sum_{p=pixels\ in\ lumen} (V_p \cdot A_p) \tag{II.19}$$

In section VIII.1.1, the reliability of this technique is investigated.

Pulse Doppler Ultrasound

Carotid flow rate is often[39, 115, 140, 367, 384] calculated using **pulsed Doppler ultrasound** (see section VII.1.3). Pulsed Doppler outputs the blood velocity in a control volume with a high temporal resolution ($\pm$ 200 Hz). For carotid flow rate measurements, the control volume is positioned in the center of a CCA cross-section. This will measure the 'centreline velocity', and it is often assumed that this centreline velocity represents the peak velocity V_{peak}. It is well known that, for fully developed, laminar, steady flow of a Newtonian fluid in a straight rigid tube of circular cross-section (i.e. parabolic flow profile), $V_{mean}=V_{peak}/2$, and hence it is straightforward to estimate the volume flow rate given only the peak velocity and vessel cross-sectional area. Under fully developed pulsatile flow conditions, however, V_{peak}/V_{mean} is time varying and depends strongly on the dynamics of the flow field. Assuming that V_{peak} lies on the lumen central axis at all times (a good assumption for the CCA wave forms), it is possible to compute this time-dependent ratio by invoking Womersley's analytic solution for velocity profiles under pulsatile flow conditions.[39, 367, 368]

The mathematical solution is elabourated here as by Holdsworth.[140] Consider the Fourier-decomposed, peak-velocity wave form:

$$V_{peak}(t) \;=\; \sum_{k=0}^{\infty} V_{peak,k}\, cos(k\omega t - \phi_k)$$

$$=\; \sum_{k=0}^{\infty} Real\left[V_{peak,k}\, e^{i(k\omega t - \phi_k)} \right] \tag{II.20}$$

We wish to derive the Fourier-decomposed, mean-velocity wave form, i.e.:

$$V_{mean}(t) \;=\; \sum_{k=0}^{\infty} V_{mean,k}\, cos(k\omega t - \psi_k)$$

$$=\; \sum_{k=0}^{\infty} Real\left[V_{mean,k}\, e^{i(k\omega t - \psi_k)} \right] \tag{II.21}$$

For k = 0 (i.e. the steady flow component), the velocity profile is parabolic, in which case $V_{mean,0} = V_{peak,0}/2$. For the k > 0 terms, Womersley's analytic solution of sinusoidal flow in a straight, rigid tube (expressed here as a function of the mean velocity) is invoked:

$$v(y,t) = Real\left\{ V_{mean,k} \left[\frac{J_0(\tau_k) - J_0(\tau_k\, y)}{J_0(\tau_k) - 2J_1(\tau_k)/\tau_k} \right] e^{i(k\omega t - \psi_k)} \right\} \tag{II.22}$$

where J_0 and J_1 are the zeroth and first Bessel functions of the first kind, i = $\sqrt{-1}$, Real{.} denotes the real part of a complex quantity, y is the radial position normalised to the vessel radius (R) and:

$$\tau_k = \alpha_k\, i^{-3/2} \tag{II.23}$$

where α_k is the Womersley number of the kth harmonic, i.e.:

$$\alpha_k = R\, \sqrt{\frac{k\omega}{\nu}} \tag{II.24}$$

and ν is the blood kinematic viscosity. On the centreline (i.e. y=0), equation II.22 reduces to:

$$v(0,t) = Real \left\{ V_{mean,k} \left[\frac{J_0(\tau_k) - 1}{J_0(\tau_k) - 2J_1(\tau_k)/\tau_k} \right] e^{i(k\omega t - \psi_k)} \right\} \qquad \text{(II.25)}$$

Recognizing that $v(0,t)$ is simply the kth term of $V_{peak,t}$, equating the arguments to Re in equations II.25 and II.20 leads to the following relationship between the Fourier coefficients for $V_{peak,t}$ and $V_{mean,t}$:

$$V_{mean,k}\ e^{-i\psi_k} = V_{peak,k}\ e^{-i\phi_k} \left[\frac{J_0(\tau_k) - 2J_1(\tau_k)/\tau_k}{J_0(\tau_k) - 1} \right] \qquad \text{(II.26)}$$

Thus, given $V_{peak,k}$ and ϕ_k from the Fourier-decomposed, peak-velocity wave form, and α_1, the mean-velocity wave form can be reconstructed from the computed $V_{mean,k}$ and ψ_k using equation II.21. Finally, the flow wave form is calculated by multiplying V_{mean} by the CCA cross-sectional area in the section where the control volume was positioned. In this manner, it is possible to calculate the pulsatile blood-flow wave form that is consistent with the observed peak blood-velocity wave form, assuming Womersley flow. This means assuming pulsatile laminar flow conditions in a straight, long and rigid tube.

Derived Parameters With the knowledge of the heart rate (HR), flow rate (Q) and geometry, following flow-related characteristic dimensionless numbers can be calculated. The **Reynolds number** Re is defined as:

$$Re\ =\ \frac{V_{mean}\ D\ \rho}{\mu} \qquad \text{(II.27)}$$

$$=\ \frac{Q/(\pi D^2/4)\ D\ \rho}{\mu} \qquad \text{(II.28)}$$

here, V_{mean} is the area and time-averaged blood velocity, D is the vessel diameter, ρ is the blood density whilst μ is the dynamic viscosity of blood. The Reynolds number expresses the relative importance of the inertial and viscous forces. High Re indicates flow dominated by inertial forces, while flow with low Re is mainly influenced by viscous forces. For steady flow in

a straight, rigid tube, a Reynolds number less than 2300 indicates laminar flow. Using the values in Tables I.2 and I.7 for D (5 to 9 mm) and Q (4.5 to 10 ml/s), and assuming a blood density of 1100 kg/m^3 and viscosity of 4 mPa.s, a typical Reynolds number for a carotid varies between 175 and 750, which is well within the laminar flow regime. Similarly, Reynolds number vary between 100 and 600 for the ICA and 100 and 800 for the ECA.

Another dimensionless flow parameter is the **Womersley number**, introduced by Womersley,[368] defined as:

$$\alpha = R\sqrt{\frac{\omega\rho}{\mu}} \tag{II.29}$$

$$= \frac{D}{2}\sqrt{\frac{(2\pi HR/60)\rho}{\mu}} \tag{II.30}$$

with HR the heart rate expressed in beats per minute (bpm).

The Womersley number represents the ratio of the inertial force to the viscous force in pulsatile flow. Small values mean small inertial forces and will result in quasi-steady flow with parabolic velocity profiles. However, large values indicate highly oscillating flow and will lead to near-wall velocity overshoots, where the maximum velocity no longer occurs at the centreline. Assuming heart rates between 50 and 100 bpm in 'resting' state, the Womersley number varies between 3 and 8 (CCA), 2 and 9 (ICA) and 1 and 3.5 (ECA).

II.3.3.2. Velocity

If velocities at a particular position are required, performing a Pulse Doppler measurement or a cine PC MRI scan as explained in II.3.3.1 (page 61) can be sufficient. However, if an entire flow field is required, this type of imaging will take too long and is often of dubious quality.[161]

Image-based computational fluid dynamics (CFD) offers a solution to this problem. In short, image-based CFD consists of the following steps:

1. An imaging modality is used to reconstruct the 3D carotid geometry

2. Information on the flow situation at the model inlet (the CCA) and out-lets (ICA and ECA) is acquired. These data are called **boundary conditions** (BC's).

3. The 3D geometry and the flow information allow the reconstruction of the entire flow field between in- and outlets, using CFD. On the rationale of CFD, see chapter III.

For the first step, the reconstruction of 3D geometry of the carotid bifurcation, X-ray (CT), IVUS, MRI and 3DUS can be used (see section II.3.2.2). Once the 3D models of the carotids have been reconstructed, the geometry can be discretised for numerical purposes. By imposing the correct BC's (step 2), CFD will calculate the entire flow field (step 3).

Similar to the variety of techniques available for 3D reconstruction, there are again a number of techniques capable of offering a reliable tool for boundary condition acquisition.

X-ray imaging is extremely reliable for geometry extraction, and it can also be used to measure blood flow rates *in vivo*. But flow rate measurements using X-ray remain largely experimental, and thus not yet practical for image-based CFD studies.[304] Carotid bifurcations reconstructed using IVUS or 3DUS can be linked to a Pulsed Doppler flow rate measurement in both the in- and outlet plane. Using equations II.20 to II.26, the velocities in all points on the in- and outlet planes can be measured. Augst[16] was among the first to try this purely US-based technique for carotid velocity predictions. He used a 3DUS-technique of the type introduced by Barratt,[20] i.e. the technique where the operator needs to sweep the tracked probe over the subject's neck as opposed to the technique where the probe does a fan-like movement. The most widely used technique for BC acquisition is MRI. Steinman stated:[305] *"While not capable of detailed velocity measurements in regions of complex flow,[161] techniques such as phase contrast MRI can nevertheless be used to measure the time-varying blood flow rates from the more uniform flows found proximal and distal to these regions.[56] This ability to derive, from a single non-invasive imaging study, all of the necessary CFD boundary conditions made MRI a popular choice for image-based CFD studies to characterise the haemodynamic environment of asymptomatic or ostensibly normal vessels."*

Obviously, hybrid approaches, where one imaging technique is used for 3D reconstruction whereas another is used for the measuremnt of BC's, are feasible: Zhao[387] used the combination of contrast enhanced time-of-flight

MR angiography for 3D geometry reconstruction and Doppler ultrasound for BC acquisition in order to compute the velocities in the carotid bifurcations of five normal subjects.

A velocity parameter often used in this thesis, is calculated as follows. In a first step, the maximum velocity at each time-step in each cross-section is stored. Consequently, this stored value is averaged along the cardiac cycle. This operation yields for every cross-sectional position z along the I/S[1] axis a single value V_{max}(z). Finally, V_{max}(z) can be averaged along the considered artery (CCA, ICA, ECA) to obtain a single value for V_{max}. The higher this parameter is for a constant flow rate and cross-sectional area, the more peaked the velocity profile is. Conversely, the lower this parameter is for a constant flow rate and cross-sectional area, the blunter the velocity profile is. The theoretical minimum occurs with plug flow and is equal to the average flow rate divided by the luminal cross-sectional area.

II.3.3.3. Vessel Wall Parameters

All vessel wall parameters are derived from the 3D geometry and the near-wall velocities. If wall parameters in a particular position are required as an output, performing a pulse Doppler measurement or a cine PC MRI scan can be sufficient. Usually, an entire WSS distribution is required. If all velocities need to be acquired using Doppler or MRI, imaging will take too long and has been shown to deliver dubious quality in a study by Köhler.[161]

Any of the techniques applied for the acquisition of the entire velocity field can give the WSS distribution as calculated by equation II.5 (page 41) in a carotid bifurcation. Apart from the WSS, other wall parameters can be derived:

- The **oscillatory shear index** (OSI) can be defined as follows:[42]

$$OSI = \frac{1}{2} \left(1 - \frac{|\int_0^T \vec{\tau} \mathrm{d}t|}{\int_0^T |\vec{\tau}| \, \mathrm{d}t} \right) \tag{II.31}$$

  here, t is the time-parameter, T is the cardiac period and $\vec{\tau}$ is the instantaneous wall shear stress.

  The OSI is 0 when flow is unidirectional. For oscillating flow, the OSI will be greater than 0 with a maximum of 0.5. Imagine a point on the

---

[1]The I/S axis is the axis from foot to head.

(a) WSS always in same direction

(b) $|\int_0^T \vec{\tau}\mathrm{d}t|$

(c) $\int_0^T |\vec{\tau}|\,\mathrm{d}t$
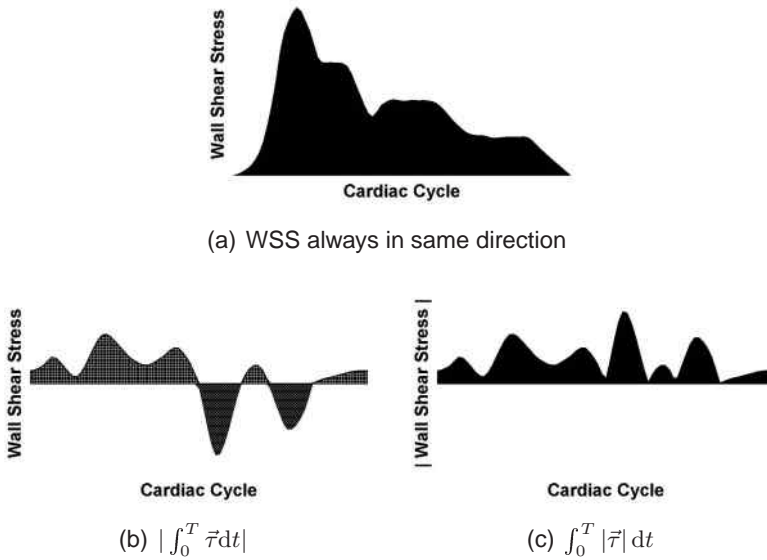
Figure II.24.: Mathematical definition of OSI and its effectiveness in highlighting oscillating wall shear stress. a: There is no oscillating WSS in this point, thus OSI will be 0. b: The oscillating flow in this point will make the value of $|\int_0^T \vec{\tau}\mathrm{d}t|$ smaller than $\int_0^T |\vec{\tau}|\,\mathrm{d}t$ (shown in image (c)), thus resulting in an OSI between 0 and 0.5.

vessel wall where the WSS always has the same direction. During the cardiac cycle, the WSS in that point will vary between two positive values as illustrated by Figure II.24 (a). The numerator of the fraction in the definition of OSI ($|\int_0^T \vec{\tau}\mathrm{d}t|$) will have the same value as the denominator in the definition of OSI ($\int_0^T |\vec{\tau}|\,\mathrm{d}t$). Thus, the OSI will be $0.5 \times (1-1) = 0$. Now imagine that in this point, the WSS varies between a negative and a positive value as in Figure II.24 (b). Here, the value of the numerator, which is the area filled with vertical and horizontal lines minus the area filled with white minus signs in Figure II.24 (b), will have a value inferior to the denominator, which is the black area in Figure II.24 (c).

Therefore, the OSI can be physically regarded as a weighted fraction of a cardiac cycle during which the instantaneous wall shear stress is 'ill-directioned'. The weighing is done using the value of the instantaneous wall shear stress. For the purpose of illustration, the WSS was only allowed to change in 1 direction in Figure II.24. In that example, the 'good' direction is the most common one, i.e. the positive direction in Figure II.24. In the event that the positive direction occurs less frequently than the negative direction, the 'good' direction would be the negative direction. In other words: the 'good' direction for a particular point is by definition the direction of the mean WSS. As

a consequence, the OSI can never take values beyond 0.5 since that would imply that the ill direction would be more frequent than the mean direction, which contradicts the definition of the ill direction. In practice, the WSS changes along two dimensions. The 'good' direction is still defined as the direction of the mean WSS.

• The gradients of WSS can be defined in two ways. The first is the **spatial WSS gradient** (WSSGs) which consists of the WSS components derived in space in their own direction, averaged over a cardiac cycle:

$$WSSGs = \frac{1}{T} \int_0^T \sqrt{\left(\frac{\partial \tau_m}{\partial m}\right)^2 + \left(\frac{\partial \tau_n}{\partial n}\right)^2} \, \mathrm{d}t \qquad (\text{II.32})$$

τ_m and τ_n are the time-dependent components of the wall shear stress in the mnl coordinate system, where m is the temporal mean wall shear stress direction and n is the tangential to the surface and perpendicular to m. Note that in order to calculate the WSSGs, the WSS has to be referred to in the mnl reference system. This reference system is different for every point on the vessel wall. In this manuscript, the WSSGs is defined as above (equation II.32) and never in any different way suggested in literature.

Lei, Kleinstrueur and Truskey[173] tried to set up a mathematical relationship between the WSSGs and the permeability[m] of the wall. They calculated the WSSGs in a rabbit aorto-celic junction and related that to sites of high permeability in order to establishing a relationship between WSSG and permeability. They found that

$$
\begin{aligned}
P(s) &= 4.38 \; 10^{-10} \frac{m}{s} \left[\frac{1}{T} \int_0^T |WSSGs|_{nd} \, dt \right]^{0.24} \\
&= 4.38 \; 10^{-10} \; (|\overline{WSSGs}|_{nd})^{0.24} \qquad (\text{II.33})
\end{aligned}
$$

with P(s) the increase in permeability in a point s on the vessel wall. Note that here, the dimensionless WSSGs ($|WSSGs|_{nd}$) was used as opposed to the regular WSSGs:

$$|WSSG|_{nd} = \frac{|WSSGs|}{\tau_0/d_0} \qquad (\text{II.34})$$

---

[m]**Permeability** is a parameter describing the behaviour of the wall towards migration of elements through it.

where the WSSGs is defined as in equation II.32 and τ_0 and d_0 are a reference WSS and lumen diameter.

Apart from the spatial WSSG, a **temporal WSSG** (WSSGt) can be defined:

$$WSSGt = \frac{1}{T} \int_0^T \left| \frac{\partial \vec{\tau}}{\partial t} \right| dt \tag{II.35}$$

The WSSGt is nothing more than the cycle-averaged magnitude of the time-derived instantaneous WSS.

- The **wall shear stress angle deviation** (WSSAD) is defined as:[142]

$$WSSAD = C \ arccos \left(\frac{\overrightarrow{\tau_i} \cdot \overrightarrow{\tau_j}}{|\overrightarrow{\tau_i}| \ |\overrightarrow{\tau_j}|} \right) \tag{II.36}$$

where

$$C = 1 \ if \ \overrightarrow{v_{l,i}} \cdot \overrightarrow{l_i} \geq 0$$
$$C = 0 \ if \ \overrightarrow{v_{l,i}} \cdot \overrightarrow{l_i} < 0 \tag{II.37}$$

and

$$\overrightarrow{\tau_i} = \frac{1}{T} \int_0^T \overrightarrow{\tau_i} \, dt$$
$$\overrightarrow{v_{l,i}} = \frac{1}{T} \int_0^T \overrightarrow{v_{l,i}} \, dt \tag{II.38}$$

Here, $\overrightarrow{\tau_i}$ is the time-averaged wall shear stress vector at surface point i, $\overrightarrow{v_{l,i}}$ is the time-averaged, near-wall velocity component normal to the surface i, $\overrightarrow{l}$ is the normal vector of the wall, subscript i is for the current node and j is an index for neighbouring cells. With a number of neighbouring cells, typically 4, a mean WSSAD is computed for each location i. The factor C emphasises the potential impact of approaching flow. In the most severe conditions, WSSAD will be close to π.

The WSSAD has been linked to sites of particle deposition.[142]

- The final parameter is the **wall shear stress angle gradient** (WSSAG):[199]

$$WSSAG = \frac{1}{T} \int_0^T \left| \frac{1}{A_i} \int_S \frac{\partial \phi}{\partial x} dA_i \, \vec{i} + \frac{1}{A_i} \int_S \frac{\partial \phi}{\partial y} dA_i \, \vec{j} + \frac{1}{A_i} \int_S \frac{\partial \phi}{\partial z} dA_i \, \vec{k} \right| dt \qquad \text{(II.39)}$$

S is the complete surface of the carotid wall and A_i is the surface of a cell face i. The $WSSAG$ is calculated in an arbitrary coordinate system ijk or xyz. The scalar field of angular differences ϕ is defined as follows:

$$\phi = arccos \left(\frac{\vec{\tau_i} \cdot \vec{\tau_j}}{|\vec{\tau_i}| \, |\vec{\tau_j}|} \right) \qquad \text{(II.40)}$$

here, $\vec{\tau_i}$ refers to the stress vector at the location of interest and $\vec{\tau_j}$ represents the surrounding stress vectors: shear stress and normal stress. The WSSAG was adopted to replace the wall shear stress angle deviation (WSSAD) as a marker for sites of dysfunctional endothelial cells. The WSSAG has the advantage of being a mesh independent parameter.[199] In this thesis, both markers are still used.

In summary, the WSSAG represents the magnitude of the shear stress angle deviation. Large WSSAG tends to occur in regions of dysfunctional cells, and hence sites of intimal thickening.[199]

III. Computational Fluid Dynamics

The importance of Computational Fluid Dynamics (CFD) has increased rapidly in the past decades. After initially (and still) proving its value for military purposes,[203] CFD has made major contributions to aviation, the automobile industry, machinery and chemical engineering. In biomedical environments, the use of CFD is widely explored. The simulation of biofluid flow such as air flow in the bronchial tubes,[139] blood flow in the cardiovascular system or in anastomoses,[281] the investigation of cerebrospinal fluids[149] and the study of the ion transfer over membranes in artificial lungs[103] and kidneys[88] are only a few of the biomedical research topics where CFD is used. For a review of the applicability of CFD in biomedical research, see issue 26 (vol. 7) of Artificial Organs (July 2002). The goal of CFD studies in the cardiovascular system is always similar: calculating variables such as the fluid velocity components and deriving from them parameters such as pressure[83] and wall shear stress.[253] The latter parameters cannot be measured directly, or involve the use of invasive techniques.

This chapter aims at explaining the principles of CFD, without discussing issues of stability or convergence. In short, CFD calculates the velocities in a domain by solving the Navier-Stokes equations (section III.1) in a mesh (section III.2) under appropriate boundary conditions (section III.3). Although the same governing equations are considered, the numerical techniques for solving the equations are diverse. Two techniques, implemented in PAM-FLOW™ and CFX4™, are presented in section III.4. The final section in this chapter addresses the potential pitfalls when using CFD.

III.1. Governing Equations

The Navier-Stokes equations are the equations derived from Newton's laws, describing mathematically the laws any fluid has to physically obey. The first law describes mass conservation, i.e. a fluid can expand, move or evaporate, but its total mass always remains constant. Similarly, the second law

expresses conservation of momentum. For incompressible, isothermal flow, the physical laws reduce to equations III.1 (mass conservation) and III.2 (momentum) in an arbitrary fluid volume:[238]

$$\sum_{i=1}^{3} \frac{\partial u_i}{\partial x_i} = 0 \tag{III.1}$$

$$\frac{\partial u_i}{\partial t} + \sum_{j=1}^{3} \frac{\partial}{\partial x_i}(u_i u_j) = F_i + \sum_{j=1}^{3} \frac{1}{\rho} \frac{\partial \sigma_{ij}}{\partial x_j} \qquad i = 1, 2, 3 \tag{III.2}$$

The independent variables in a Cartesian coordinate system are the position vector $\vec{x} = (x_1, x_2, x_3)$ and the time t. The dependent variables are the fluid velocity vector $\vec{u} = (u_1, u_2, u_3)$ and the pressure p. The force vector $\vec{F} = (F_1, F_2, F_3)$ is expressed in N/kg and $\vec{\sigma} = (\sigma_{ij})$ is the stress tensor, consisting of a pressure component and a viscous force:

$$\sigma_{ij} = -p\,\delta_{ij} + \tau_{ij} \qquad i, j = 1, 2, 3 \tag{III.3}$$

Here, δ_{ij} is the Kronecker delta, and $\vec{\vec{\tau}}$ represents the viscous stress tensor. For a Newtonian fluid, this tensor can be calculated as:

$$\tau_{ij} = 2\,\mu \left[\frac{1}{2}\left(\frac{\partial u_i}{\partial x_j} + \frac{\partial u_j}{\partial x_i}\right) - \frac{1}{3}\sum_{k=1}^{3}\frac{\partial u_k}{\partial x_k}\,\delta_{ij} \right] \qquad i, j = 1, 2, 3 \tag{III.4}$$

with μ the dynamic viscosity.

In the Navier-Stokes equations (III.2), the first term embodies the inertial forces, the second convective features, and last one models the viscous forces and the impact of the static pressure.

These equations form a system of coupled non-linear partial differential equations (PDEs). Because of the non-linear terms in these PDEs, analytical methods can yield very few solutions. In general, closed form analytical solutions are possible only if these PDEs can be made linear. This is achieved in some cases because non-linear terms naturally drop out, e.g. fully developed flows in ducts and flows that are inviscid and irrotational everywhere. In other cases, non-linear terms are small compared to other

terms so that they can be neglected, e.g. creeping flows, small amplitude sloshing of liquid, etc. If the non-linearities in the governing PDEs cannot be neglected, which is the situation for most engineering flows, then numerical methods are needed to obtain solutions.[1]

CFD is the art of replacing the differential equations governing the fluid flow, with a set of algebraic equations (the process is called discretisation), which in turn can be solved with the aid of a computer to obtain an approximate solution. The best known discretisation methods used in CFD are Finite Difference Method (FDM), Finite Volume Method (FVM) and Finite Element Method (FEM).[1] A thorough explanation of these techniques falls beyond the scope of this work. In short, FDM replaces the derivatives in the equations by differences. FEM splits the fluid domain into a finite number of subdomains (elements). It then assumes a simple variation of the dependent variables over each computational element. For FVM, the equations are integrated over an element's volume.

III.2. Meshing

CFD requires the fluid domain, i.e. the vessel lumen, to be subdivided into small cells. The discretised Navier-Stokes equations will be solved in these cells separately. The meshing techniques utilised here, the advancing front technique and a home-built method, are discussed below.

Meshes can be structured or *un*structured. In a structured mesh, the domain is usually divided into a number of topologically similar blocks which are then subdivided into smaller cells in a structured manner. In contrast to the structured mesh, the mesh points in an unstructured grid system are not organised in an orderly manner. Structured grids are most frequently built using hexahedral cells, whereas the tetrahedron is the most common element shape of an unstructured grid. Structured grids are usually solved using FVM whereas unstructured grids are used with FEM. It has to be noted that this distinction in solver strategy is getting increasingly outdated. The main advantage of an unstructured mesh over the structured mesh is in the handling of extremely complex geometries. In this work, two commercially available CFD software packages were used. In the first one, PAM-FLOW™ (ESI Group, Krimpen aan den IJssel, The Netherlands), the Navier-Stokes equations are solved using the finite element technique in unstructured grids. The second software package, CFX4™ (AEA Technology, Didcot, Oxfordshire UK), uses the FVM in structured meshes.

III.2.1. The advancing front technique

The advancing front technique generates an unstructured mesh, using PAM-GEN3D™, a commercially available CFD software. A **front** is a triangulated surface. In the *first step*, this technique triangulates all the bounding surfaces of the domain, i.e. inlet, outlet and walls. The triangulation is performed by taking into account spatial variation of the size, stretching, and stretching direction of the elements to be generated. This yields the initial front of faces such as the one shown in Figure VIII.3 (b) on page 202. The *second step* consists of creating a tetrahedron using a triangle on the front and a new point, computed by taking into account spatial size variation, stretching, and stretching direction of the elements. The three points of the triangle and the new point constitute a tetrahedron. A tetrahedron has four surfaces, at least one of which is already known: the triangle part of the front. This triangle, along with other subsequently known surfaces, is deleted from the front and replaced with the new surfaces. This second step is *repeated* until there are no faces left in the front. This means that the whole domain has been filled by tetrahedrons and the mesh is complete. Details of the mesh generation technique can be found in the PAM-GEN3D™ manual.[239]

III.2.2. The in-house carotid mesh builder

This meshing strategy was based on previous work presented by Long,[197] who treated the arteries as three separate distorted cylinders, the CCA, ICA and ECA. Each of the branches was subdivided in the same structure: 8 contiguous blocks filled the cylinder. Each block started at the inlet of the considered cylinder and ended at the outlet. In a cross-section of the artery, each of the blocks can be visualised as in Figure III.1 (a). Figure XI.2 on page 276 shows meshes generated by Dr. Long for a reproducibility study. Note that the CCA is bounded by two planes perpendicular to the I/S axis. This made it necessary to distort the mesh in the carotid branches extensively, yielding highly skewed cells in the bifurcation area.

In the enhanced method, the three arteries CCA, ICA and ECA were still regarded as three separate tubes, each subdivided using the same block-structure. However, now the CCA expanded into the bifurcation area as seen in Figure III.1 (b) and (c). Because of the reduced skewness, this method yielded better-quality grids. Details about how to define the three sectioning planes which divided the carotid bifurcation in three arteries are explained in section VI.3.3.
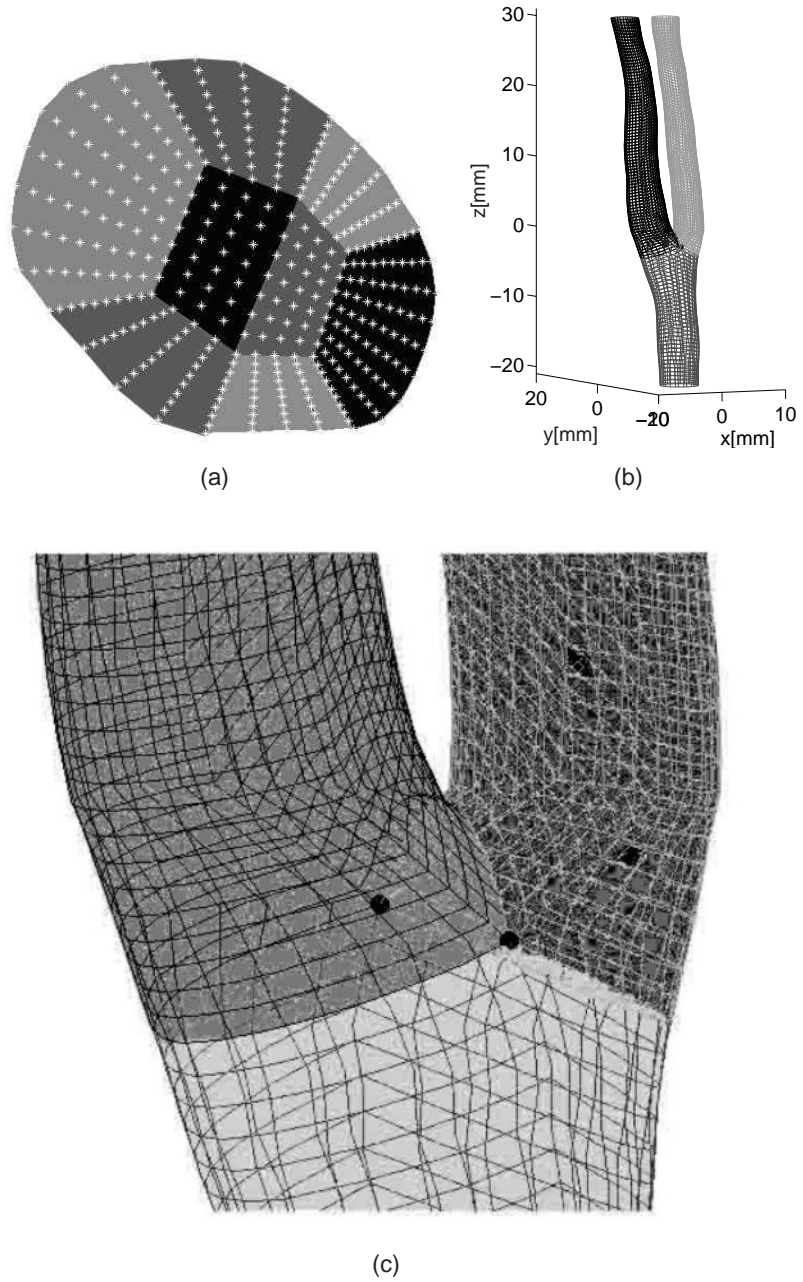
Figure III.1.: a: Block structure of the mesh in a cross-section of CCA. b-c: Surface mesh for a healthy subject. The two black dots represent the points where three set of blocks belonging to different arteries come together.

Mesh generation thus consisted of three steps:

1. Define the longitudinal splines bordering the vessel lumen. Note that 'longitudinal' refers to splines originating in the proximal CCA and ending in the distal ICA or ECA.

2. Separate the arteries in the neighbourhood of the bifurcation apex.

3. Use the separated splines to fill the vessel lumen (or the computational domain) with structured cells.

The third step consists of 5 steps itself. *First*, the splines are subdivided in the longitudinal direction into a certain number of cells, subject to mesh independence tests. If there are K cells along a spline, there will consequently be $K + 1$ nodes on each longitudinal spline. In Figure III.2, the kth nodes on all splines are called M_i (i=1,2) and S_i (i=1,2,...,2×4n, with n equal to 1/8th of the number of cells along the circumference). The points at one side of the line $M_1 M_2$ belong to splines that all start on one particular plane and end on a different plane. For example, the nodes named S_1 till S_{4n-1} could all belong to splines of the CCA, starting in the proximal CCA plane and all ending at the CCA/ICA planar interface. If all splines were subdivided into K cells using the same rules, S_i on one side of the line $M_1 M_2$ will be planar for a given k ($1 < k < K$). If points S_i on either side of the line $M_1 M_2$ are not equidistance, they will be redistributed. In the *second* step, point M is defined as the center of the line $M_1 M_2$, and points D_i (i=1,2,3,4) are calculated by placing them at a certain fraction f away from M along the radius MM_1 for D_1, MS_n for D_2, etc. So

$$f = \frac{|MD_1|}{|MM_1|} = \frac{|MD_2|}{|MS_n|} = \frac{|MD_3|}{|MS_{3n}|} = \frac{|MD_4|}{|MM_2|} \tag{III.5}$$

where the operator |...| denotes the distance between the two points mentioned in the argument. In the *following step*, lines $D_1 D_2$ and $D_3 D_4$ are subdivided into n parts (illustrated by the grey points between D_1 and D_2 in Figure III.2) and simultaneously the line $D_2 D_3$ is divided into $2 \times n$ parts, just as the line $D_1 D_4$. In *fourth* step, the points on the 'D'-lines, i.e. on $D_1 D_2$, $D_2 D_3$, etc., are connected to the S_i points in the only way in which the connecting straight lines do not cross each other. Similarly, the central block $D_1 D_2 D_3 D_4$ can be divided into quadrangles by connecting the points defined in the previous step with straight lines. In the *final* step, the radial lines connecting the D-lines to the vessel wall are subdivided into m parts
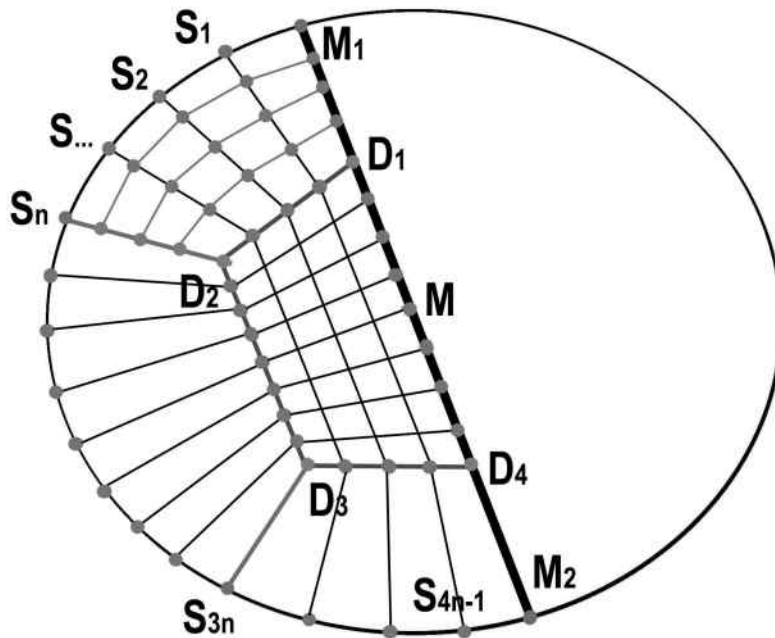
Figure III.2.: Building a structured mesh starting from longitudinal splines.

as illustrated in Figure III.2 in the block $M_1D_1D_2S_n$ with $m = 4$. Repeating this procedure for every k ($1 < k < K$), for both sides of the M_1M_2 line and for each of the three arteries, gives all the necessary nodes for defining a structured mesh as illustrated in Figure III.1.

In this thesis, meshes have been generated using in most cases the following values for $n/f/m$: $4/0.5/9$. This yields meshes with high density cells near the wall for increased accuracy for the predicted WSS.

III.3. Boundary Conditions

Equations III.1 and III.2 need to be solved under appropriate boundary conditions (BC). The boundaries concerned here are inlets, outlets and walls. An overview of all possible boundary conditions is given in CFD software manuals.[3, 238]

On the vessel wall, the so-called **no-slip** condition is specified, i.e. all velocity components are zero. For the inlet and outlets, several BC's can be imposed:[3]

- An **inlet** in the mathematical definition is a boundary where the values of variables are specified. This is known as a **Dirichlet** boundary condition. The most common Dirichlet BC, is a prescribed velocity profile. An example is a uniform velocity profile, i.e. all the fluid elements on the inlet plane have equal velocities.

- **Mass flow** boundaries are used to model inflow and more commonly outflow boundaries where the total mass flow rate into or out of the domain is known, but the detailed velocity profile is not. In this case, **Neumann** boundary conditions are imposed on all transported variables (such as velocity or, in thermodynamic simulations, temperature). This means that their normal gradients along the boundary is specified, rather than their values. This is equivalent to an assumption of fully developed flow at the outlet. It is most accurate when the outlet is placed far downstream, and the width of the flow domain is constant at the outlet. Pressure is extrapolated from upstream.

- **Pressure** boundaries are used to model inflow and outflow boundaries where the surface pressure is known, but the detailed velocity distribution is not. This is in fact a combined Dirichlet/Neumann boundary condition: Dirichlet boundary conditions are imposed on pressure, i.e. it is specified by the user. Neumann boundary conditions, i.e. zero normal gradients, are imposed on velocity as well as other transported variables, temperature, user scalars, volume fractions, etc.

In this thesis, the boundary conditions issues are dealt with in section VIII.1.1 by investigating all possible boundary condition types used in literature for image-based CFD (see table VIII.1).

III.4. Solvers

As mentioned in section III.1, the governing equations are not analytically solvable, except for the simplest cases. They are solved numerically, i.e. by meshing the domain first, and then solving the equations in an iterative manner. A variety of numerical algorithms exist and those adopted in this thesis are described below.

III.4.1. Spatial Discretisation

The Navier-Stokes equations (eq. III.2) contain both time and spatial deriva-
tive terms. The first step in CFD is to perform a spatial discretisation. In this
step, the Navier-Stokes equations are rewritten in each point in the form:

$$\frac{\partial u}{\partial t} + f(u_1^{I,t}, u_1^{In,t}, u_1^{I,t+1}, u_1^{In,t+1}, p_1^{I,t}, p_1^{In,t}, p_1^{I,t+1}, p_1^{In,t+1}, \mu) = 0 \qquad \text{(III.6)}$$

where we have taken the direction $i = 1$ as an example, the viscosity as
constant and neglected the external forces F_1. Here, $f(...)$ is a function ob-
tained by spatial discretisation of the Navier-Stokes equation. The index I
refers to a particular point in the mesh and the index In refers to its neigh-
bouring points. The index t stands for the value of the indexed parameter at
the current time-step, whereas $t + 1$ is the unknown value of the parameter
at the next time-step. The spatial discretisation consists of finding a good
function f in order to replace the spatial derivatives by solvable equations.
If the function $f(...)$ does not contain any values at $t + 1$, the solver is called
explicit. Otherwise, the solver is **implicit**. Any spatial discretisation tech-
nique can be implicit or explicit, depending on whether or not the $t+1$ values
have been used to estimate the spatial derivatives.

III.4.1.1. CFX4™

As an example, the spatial discretisation used in this work in all the sim-
ulations performed using CFX4™ is explained. The differencing scheme
used to derive the function $f(...)$ is called the **Quadratic Upwind Interpo-
lation Convective Kinematics** (QUICK) scheme. In short, QUICK works
as follows. Consider a one-dimensional control volume as shown in Figure
III.3. The point P is the node of interest. However, neighbouring nodes W, E
and WW must also be considered. The dashed lines (denoted by lower case
symbols, w and e) denote cell face boundaries and the symbol ϕ denotes the
value of the property of the variable being calculated (e.g. u_1). The QUICK
scheme uses three points with a quadratic interpolation for calculating cell
face values. The face value of the variable ϕ is found by the application of a
quadratic function passing through two bracketing nodes (one each side of
the face) and a node on the upstream side as shown in Figure III.3. When
both u_w (velocity in point w) and u_e are positive, a quadratic fit through WW,
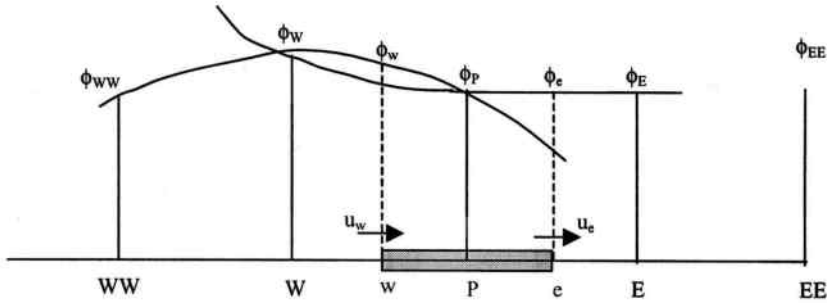
Figure III.3.: QUICK: The Quadratic Upwind Interpolation Convective Kinematics.

W and P is used to evaluate ϕ_w, and a further quadratic fit through W, P and E used to calculate ϕ_e.

For the situation shown in Figure III.3 and for a positive value of u_w, the bracketing nodes for the west face, w, are W and P, and the upstream node WW and

$$\phi_w = \frac{6}{8}\phi_W + \frac{3}{8}\phi_P - \frac{1}{8}\phi_{WW} \qquad (III.7)$$

Similarly, for positive u_e, the bracketing nodes for the east face, e, are P and E, and the upstream node is W and

$$\phi_e = \frac{6}{8}\phi_P + \frac{3}{8}\phi_E - \frac{1}{8}\phi_W \qquad (III.8)$$

Thus, in the QUICK-scheme, the variation of ϕ is assumed to be described as a quadratic function. This assumption leads to estimates of ϕ at the cell faces. The estimates are third order accurate. The estimates are required if the function f(...) from equation III.6 is to be solved using the FVM.

III.4.1.2. PAM-FLOW™

The spatial discretisation in PAM-FLOW™ is computed explicitly using the so-called **Roe flux-splitting scheme** with **fourth order diffusion**. The mathematical explanation of the Roe flux-splitting scheme falls beyond the scope of this work. Details can be found in the PAM-FLOW™ solver theory manual.[238]

III.4.2. Temporal Discretisation and Solution

III.4.2.1. CFX4™

The Navier-Stokes equations (equation III.2) can also be written as (vectorial notation):

$$\frac{u^{t+1} - u^t}{\Delta t} + u^t \cdot \nabla u^t + \frac{1}{\rho} \nabla p^{t+1} = \nabla \mu \nabla u^t \qquad \text{(III.9)}$$

In this representation, the term with the time derivation ($\frac{\partial u}{\partial t}$) has been discretised with Δt the time-step duration (temporal discretisation). The other terms need to be spatially discretised as illustrated in the previous section (QUICK, ROE flux-splitting scheme, etc.). Note that, apart from the first term, there are no velocities with indices $t + 1$ in equation III.9. This means that the discretisation as presented here is explicit for the velocity, but implicit for the pressures (semi-implicit).

To solve this equation, use the pressure value at the previous time step (t). This will yield

$$\frac{u^{t+1,*} - u^t}{\Delta t} + u^t \cdot \nabla u^t + \frac{1}{\rho} \nabla p^{t+1,*} = \nabla \mu \nabla u^t \qquad \text{(III.10)}$$

Here, $u^{t+1,*}$ is a guess of u^{t+1} using $p^{t+1,*}$, a guess of the pressure at step $t + 1$. In the first iteration, $p^{t+1,*}$ is p^t, the pressure value in step t. Substraction of equations III.9 and III.10 yields:

$$\frac{u_{corr}}{\Delta t} + \frac{1}{\rho} \nabla p_{corr} = 0 \qquad \text{(III.11)}$$

with

$$u_{corr} = u^{t+1} - u^{t+1,*} \qquad \text{(III.12)}$$

$$p_{corr} = p^{t+1} - p^{t+1,*} \qquad \text{(III.13)}$$

This is the point where the condition of mass conservation is used, i.e. equation III.1 or (vectorial):

$$\nabla u^{n+1} = 0 \qquad \text{(III.14)}$$

By taking the gradient of equation III.11, bearing in mind that $\nabla u^{n+1} = 0$, the following is obtained:

$$\frac{\nabla u^{t+1,*}}{\Delta t} = \frac{1}{\rho} \nabla^2 p_{corr} \qquad \text{(III.15)}$$

Now, with the knowledge of $u^{t+1,*}$ from equation III.10, p_{corr} can be calculated using equation III.15 and thus p^{t+1} (eq. III.13). This p^{t+1} is not the correct p^{t+1}, but a new guess of p^{t+1}, i.e. $p^{t+1,*}$. $p^{t+1,*}$ can now be used to recalculate $u^{t+1,*}$ using eq. III.10. The second iteration has now started. This iterative process continues until the changes in $p^{t+1,*}$ (or $u^{t+1,*}$, depending on user's settings) between two consecutive iterations are within preset tolerances. That is how the Navier-Stokes equations are solved numerically.

The algorithm presented here is the basis of SIMPLE, implemented in CFX4™ and used in all CFX™-related simulation in this work. The acronym SIMPLE stands for Semi-implicit Method for Pressure-Linked Equations. The algorithm is semi-implicit and not purely explicit because equation III.9 contains an index $t + 1$ in the *pressure* term.

III.4.2.2. PAM-FLOW™

In PAM-FLOW™, an implicit solver is used:

$$\frac{u^{t+1} - u^t}{\Delta t} + u^t \cdot \nabla u^t + \frac{1}{\rho} \nabla p^{t+1} = \nabla \mu \nabla \left[u^t + \theta (v^{t+1} - v^t) \right] \qquad \text{(III.16)}$$

with θ the amount of implicitness. Note that when $\theta = 0$, equation III.16 becomes equation III.9. Consider the case where $\theta = 1$, equation III.10 becomes:

$$\frac{u^{t+1,*} - u^t}{\Delta t} + u^t \cdot \nabla u^t + \frac{1}{\rho} \nabla p^{t+1,*} = \nabla \mu \nabla u^{t+1,*} \qquad \text{(III.17)}$$

from where $u^{t+1,*}$ can be deduced in a different manner when compared to the explicit method. When it is assumed that

$$\nabla \mu \nabla u^{t+1,*} = \nabla \mu \nabla u^t \qquad \text{(III.18)}$$

substraction of equations III.16 and III.17 yields again equation III.11. The rest of the sequence is similar to the semi-implicit method.

III.4.3. Validation

CFX4™ has been extensively validated for internal flows, i.e. flows in tubes or arteries, in a preceding PhD thesis.[193] However, PAM-FLOW™ has never been used for internal flows by any of the research groups involved, nor by the code vendor. Therefore, for this work, code validation is necessary.

For validation of the PAM-FLOW™ CFD code, the Hagen-Poiseuille flow in a rigid circular tube was studied. The diameter of the tube was 8 mm, the tube length 50 cm. The fluid used in the computation was water at 20 °C, i.e. with a dynamic viscosity of 1mPa.s and a density of 998 kg/m^3. At the inlet, a uniform velocity profile of 3.35 cm/s was set, this yields a tubular Reynolds number of 268 (see equation VIII.1 on page 199). Because the Reynolds number is below 2300, the flow is laminar and a Hagen-Poiseuille velocity profile is expected within a reasonable length downstream the entry plane.[276] For a uniform entry profile, this length *l* is calculated as follows:[362]

$$\frac{l}{d} = 0.065 \, Re_t \qquad \text{(III.19)}$$

Which in this case would be 14 cm, well within tube length. Note that several formulae for l can be found in literature,[276, 362] the one used here tends to overestimate the entrance length.
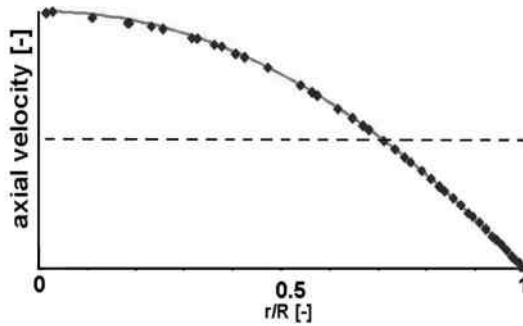
(a) Poiseuille Flow
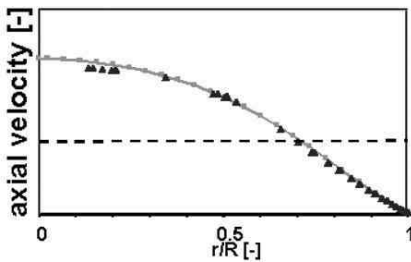
(b) 0.2×T
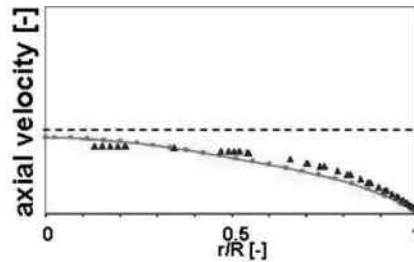
(c) 0.7×T

Figure III.4.: (a) Steady and (b-c) Unsteady validation. *Squares* or *Triangles*: calculated velocities; *line*: Poiseuille/Womersley theory. T: period, 0.833 s. The maximum flow occurs at a time 0 or T. The dotted line represents the time and area averaged velocity. r is the distance from the tube centreline and R is the vessel radius. Axial velocity is normalised using the mean velocity. (b) Velocity profile at time = 0.2 T. (c) Time = 0.7 T.

Figure III.4 (a) shows a comparison between the theoretical parabolic profile (Hagen-Poiseuille) and the CFD prediction using PAM-FLOW™ at 25 cm down the tube. The quantitative agreement is very good, the average error being within 0.75 %.

PAM-FLOW™ was further validated for *unsteady* flow using the Womersley velocity profiles in a rigid circular tube. The diameter of the tube was again 8 mm, the tube length 20 cm. A 40/60-glycerine/water mixture with a dynamic viscosity of 4.38 mPa.s and a density of 1112.7 kg/m^3 was computed. At the inlet, a uniform velocity was imposed. The flow rate varied sinusoidally from 1 ml/s to 5ml/s with a frequency of 1.2 Hz (72 bpm). This yields a time-averaged tubular Reynolds number of 125 and a Womersley parame-

ter (equation II.29 on page 65) of 5.53. Because of the unsteadiness, the entrance length must be increased by l_p:[362]

$$\frac{l_p}{r} \approx \frac{Re_a}{\alpha^2} \qquad \text{(III.20)}$$

Here Re_a stands for the **radial Reynolds number**, which is half of the tubular Reynolds number. In this case, l would be 64 mm and l_p around 8 mm, thus the computed tube was long enough (200 mm) to obtain a developed velocity profile. For the values of Reynolds number and Womersley parameter in this case, the Womersley theory is applicable.[368] This theory solves the Navier-Stokes equations analytically, which provides us with a time-varying developed velocity profile.

In Figure III.4 (b-c), the solid lines correspond to the Womersley velocity profiles at two time points, while CFD predictions are drawn denoted by symbols. The agreement is generally satisfactory, however, it is less impressive than in the steady case (maximum errors up to 7%).

III.5. Potential Pitfalls

Results obtained using CFD are subject to a number of errors. Therefore, it is necessary that results are validated to ensure their reliability. A few steps of primary importance need to be taken.

- Where possible, the solver should be validated. This means that a known geometry (with known, measurable, flow parameters as velocity and pressure) is calculated. When the computational solver gives the same results as in the measured case, the solver is validated. Obviously, the solver should be validated under flow conditions similar to those in which the solver is intended to be used.

- Grid-independence (or 'mesh sensitivity') tests should be performed. This means that the mesh, used for the computational calculation, should be refined until a mesh with a finer density gives results within an acceptable tolerance when compared with results from a coarser mesh. The coarser mesh would then be used in order to save CPU-time. The 'results' and the 'tolerance' are kept vague on purpose, since these differ depending on the aim of the study.

- For periodic time-varying problems, calculation should be performed for as many cycles as required until cycle n gives results within an acceptable tolerance when compared with results from cycle $n - 1$.

- For time-dependent calculations, the time-step is to be considered with great scrutiny. Especially when time-steps are 'chosen' by the operator, these time-steps should be refined (shortened) until the refined time-step yields same results as the coarser time-step. When time-steps are calculated during the simulation, special care must be taken regarding the choice of the Courant-number (CFL-factor):

$$CFL = \frac{\Delta t \, V}{\Delta x} \tag{III.21}$$

  here, Δt is the time-step, V the velocity, Δx the mesh size. A high CFL-number will increase the time-step and decreases the CPU-time, but when the CFL-number is too high, numerical stability is lost.

- Even if all of the above steps were performed satisfactory, it is always good to regard the results obtained from CFD with a healthy portion of scepticism.

IV. Carotid Haemodynamics and image-based CFD

'Hey, shear stress is something funny!' It was in the late 1960s and early 1970s that researchers found for the first time that atherosclerosis and local haemodynamics had something to do with each other.[306] Fry[102] suggested that high shear rates had a direct damaging influence on the intima, i.e. on the endothelial cells. Caro[45] was categorical in his disagreement, stating that *"Several workers have proposed a relationship between arterial blood mechanics and the development of atheroma. However, as we subsequently show, their appreciation of the mechanics has been erroneous."* Caro showed *subsequently* that it was not high shear rates, yet cites of low shear rates that were associated with atherogenic zones. The link between atherosclerosis was clearly not fully understood, but the presence of a link was acknowledged. This motivated researchers to develop techniques capable of measuring the shear stress. It was only later that effects on (i) smooth muscle cell migration, proliferation and metabolism, (ii) expression of extracellular matrix, (iii) lipoprotein kinetics and binding, (iv) monocyte chemotaxis and conversion to macrophage, and (v) foam cell formation were investigated and modelled in a shear-dependent manner.[99]

Early CFD and other research techniques CFD made an early introduction in this research field. Friedman[101] published one of the first articles using CFD for shear stress prediction, admittedly in a bifurcation of the aorta. The computational models at that time were restricted to 2D idealised models: 3D computations were too expensive and *in vivo* imaging was slowly emerging. Together with CFD, numerous other *in vitro* techniques have been established, all aiming at giving insights into the shear stress distributions in arterial bifurcations. These techniques include fabricating glass[185] or elastic phantoms[186] and using a variety of measurement techniques, e.g. Laser Doppler Anaemometry[184] (LDA). Considering the cost involved in CFD calculations, it was not surprising that it had taken another decade before CFD became a feasible alternative to building *in vitro* models.

CFD is taking over An important advantage of CFD lies in the fact that it can quantify shear stresses in the entire model, whereas a large number of time-consuming individual measurements need to be done if physical casts are to be used. Moreover, CFD has the advantage of not having to repeat the laboratory test in case a different parameter is to be measured. Finally, CFD is not sensitive to features such as drift and jitter, typical of measurement equipment. This renders CFD a preferred choice to time-consuming laboratory measurements. Slowly, CFD became a common tool for haemodynamic research. At first, CFD simulations were performed on 3D models present at the laboratory.[27,244] This gave the researcher a way to validate the CFD calculations using high-quality laboratory measurements. In further steps, computational models were built without necessarily having an actual physical phantom.[246,247] This was often done in order to investigate a particular feature, such as a new and improved numerical code[247] or the effect of bifurcation angles on shear stresses.[246] In an attempt to build more realistic *in vitro* models, Goubergrits and Affeld produced 3D vessel casts of human carotid arteries based on post mortem excised arteries.[4,125,127] In a later stage, the internal structure and morphology of the vessel wall were linked to haemodynamic parameters acquired with CFD.[126]

While CFD was getting more and more accepted as the main tool for research on the carotid blood flow, it was simultaneously ameliorated at different levels. Perktold[248] was among the first[113,382] to examine the effect of shear-dependent behaviour of blood on flow patterns and created a code to be used in case blood viscosity had to be shear-dependent. The same group[178,245,249] was again among the first[49,50,56,384,386,387] to incorporate moving vessel walls into computational simulations.

Subject-specific images as a basis The previously mentioned studies had shown that the carotid geometry (e.g area ratios A_R and vessel tortuosity) had an important influence on the distribution of WSS. It was becoming increasingly clear that the dynamics of blood flow *in vivo* are more complex and variable than suggested by idealised models such as the ones used thus far. This aspect combined with the notion of the fact that human carotid arteries show a large inter-subject geometry variability prompted researchers to extract *in vivo* subject-specific carotid geometries using medical images. As explained in section II, a variety of imaging techniques can be used as a basis for image-based CFD. This technique was at first tested on simple[224,362] and realistic[16] phantoms, both rigid[16] and elastic.[33] The combination of imaging and CFD has only recently been implemented *in vivo*.[56,178,198,219,324,370] *"When coupled with ongoing improvements in*

computing and image processing, it becomes possible to consider CFD as a viable tool for studying, for the first time at the level of an individual patient, the complex and dynamic relationship between haemodynamic forces and atherosclerosis.[305]"

Direct Methods   Recently, several studies have investigated *direct* WSS measurement *in vivo*. Although *in vivo* techniques would still not provide the WSS distribution in an entire carotid bifurcation, these techniques are very interesting from a cost-effective point of view bearing in mind that they bypass the use of CFD. To date, both ultrasound[270] and cine PC MRI[61,161] have been used for direct WSS estimation, but the techniques seem thus far only reliable in phantoms.[61,161]

What shall we do ... ?   In conclusion, although the use of CFD is demanding on computational resources, it is a promising tool for investigating arterial haemodynamics: it can be made subject-specific, does not require post-mortem data, is reproducible (to be demonstrated later), not affected by drift, and more reliable in comparison to direct methods.

The major objective of this work therefore consists of smoothing away the technical difficulties impeding the use of image-based CFD for large-scale studies. As part of that, one of the aims of this thesis is to define the 'best' imaging protocols. In this context, 'best' means a mix between reliable and feasible (or fast). Another main objective is to define the 'best' way to *build and solve* the computational model. What is the difference between the results in a steady simulation and those in a pulsatile simulation? Are the assumptions of newtonian flow and rigid walls justifiable? Once the technique is built, the goal is to put error-bars on haemodynamic parameters such as WSS and OSI. The final objective is to use this technique in clinical studies.

Part B.

ESTABLISHING THE TECHNIQUE

V. Overview

Subject-specific image-based CFD makes use of a number of techniques. The following tasks are to be performed and optimised in order to obtain a reliable subject-specific simulation of the carotid flow.

1. The first step obviously consists of *imaging* the carotid bifurcation. Numerous questions pop up. Which imaging modality should be used as a basis for carotid CFD? This can be chosen from CT, MRI and 3DUS. In this work, we will focus on the two least invasive: MRI and 3DUS. When the imaging modality is chosen, a good scan protocol needs to be defined. A 'good' scan protocol is fast, easy, robust, accurate, and provides all the information necessary for reliable CFD simulations.

   Another issue, is the output format of images. This is important if the images are to be processed in further steps. The aspect of data transmission has been thoroughly studied by the **Digital Imaging and Communications in Medicine** (DICOM) **Standards Committee**.[78] It exists to create and maintain international standards for communication of biomedical diagnostic and therapeutic information in disciplines that use digital images and associated data. The goals of DICOM are to achieve compatibility and to improve workflow efficiency between imaging systems and other information systems in healthcare environments worldwide. Every major diagnostic medical imaging vendor in the world has now incorporated the standard into their product design and most are actively participating in the enhancement of the standard. Most of the professional societies throughout the world have supported and are participating in the enhancement of the standard as well. In short, a DICOM-file always consists of 2 parts: a header and the image. The image can be a matrix of greyscales represented by values ranging from 0 to 100. The header contains information about the scan, e.g. name of the patient, age, date of imaging, name of operator, position of the imaging plane, resolution, etc.

2. Carotid images are usually acquired to show 2D cross-sections of a subject's neck. For the reconstruction of the lumen, the edge of the
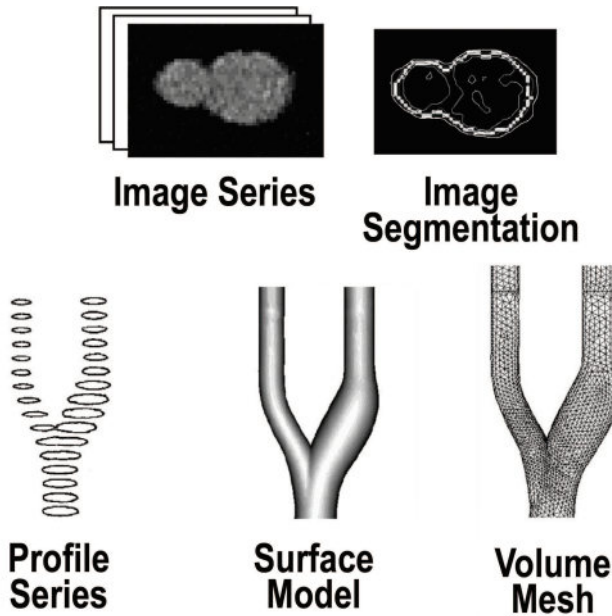
Figure V.1.: Illustration of the typical steps involved in constructing an image-based CFD model of the carotid bifurcation. Following acquisition of the data, manual or computer-assisted techniques are used to outline the lumen boundary from each slice. This series of profiles forms the scaffold upon which a continuous surface and, subsequently, the volumetric finite element mesh are generated. This mesh, plus the assumed or measured inlet and outlet flow rates or velocities, provides the necessary input for the CFD modelling software, which solves for the time-varying velocity field data from which desired haemodynamic indicators can be calculated.[306]

vessel wall needs to be delineated from the image. This delineation is called *segmentation*. It can be done either manually or automatically.

3. After the segmentation step, a series of 2D contours of the carotid are produced. By stacking the contours in 3D space, a first approximation of the *3D carotid geometry is reconstructed*. After this, the geometry is smoothed in order to eliminate image artefacts[a].

4. In the fourth step, the 3D volume obtained from reconstruction must be descretised into small computational cells, i.e. to generate the *mesh*. In order to be compatible with the next step, the mesh needs to be validated as explained in section III.5 on page 87.

5. The previous steps yield a computational mesh of the carotid bifurcation, usable in a CFD software package. Before starting the sim-

---

[a]In some cases, segmentation and 3D reconstruction is done at the same time. See publication by Ladak[164] for MRI and Gill[114] for US.

ulations, certain *model parameters* need to be set, among them the boundary conditions. Apart from the boundary conditions, fluid parameters such as viscosity and density should be specified.

6. When the geometry and model parameters are well defined, the *simulation* can start. After the simulation, the software outputs results such as velocities, pressures and shear rates, depending on the user's instructions.

7. In the final step, computational results are visualised in various ways using *postprocessors*, i.e. visualisation software.

See Figure V.1 for a schematic representation of steps 1 to 4.[306] In what follows, many of the steps above are optimised and discussed. Chapters VI and VII explain how subject-specific 3D carotid geometries can be reconstructed from respectively MRI and 3DUS images. Chapter VIII will discuss (1) the boundary conditions to be used in computational carotid haemodynamics, (2) the effect of parameters such as heart rate and viscosity and (3) the use of viscosity laws. In the last chapter, MRI and 3DUS-based CFD are compared in a cross-comparison study. All technical improvements suggested in the following chapters are performed bearing in mind that the total processing time, from image acquisition to final analysis, should be minimised.

VI. MRI-based carotid reconstructions

VI.1. The I in MRI

VI.1.1. Brief History[230]

Felix Bloch and Edward Purcell, both of whom were awarded the Nobel Prize in 1952, discovered the magnetic resonance phenomenon independently in 1946. In the period between 1950 and 1970, Nuclear Magnetic Resonance (NMR) was developed and mainly used for chemical and physical molecular analysis. In 1971, Raymond Damadian showed that the nuclear magnetic relaxation times of tissues and tumours differed, thus motivating scientists to consider magnetic resonance for the detection of disease. In 1973, Magnetic Resonance Imaging (MRI) was first demonstrated on small test tube samples by Paul Lauterbur. In 1975, Richard Ernst proposed magnetic resonance imaging using phase and frequency encoding, and the Fourier Transform. This technique is the basis of current MRI techniques. In 1977, Raymond Damadian demonstrated MRI of the whole body. Edelstein and coworkers demonstrated imaging of the body using Ernst's technique in 1980. A single image could be acquired in approximately five minutes by this technique. By 1986, the imaging time was reduced to about five seconds, without sacrificing too much image quality. In 1987, Charles Dumoulin was perfecting Magnetic Resonance Angiography (MRA), which allowed imaging of flowing blood without the use of contrast agents. In 1991, Richard Ernst was rewarded for his achievements in pulsed Fourier Transform MRI with the Nobel Prize (in Chemistry). In 1993, functional MRI (fMRI) was developed. This technique allows the mapping of the function of the various regions of the human brain. In 2002, Kurt Wüthrich was awarded the Nobel Prize (in Chemistry) for his development of nuclear magnetic resonance spectroscopy for the determination of the three-dimensional structure of biological macromolecules in solution.[145] One year later, in 2003, the Nobel Prize (in Medicine) was again awarded to researchers in MRI,

Paul Lauterbur and Peter Mansfield, 'for their discoveries concerning MRI'. Paul Lauterbur discovered that the introduction of gradients in the magnetic field made it possible to differentiate structures that could not be visualised by other techniques.[145] Peter Mansfield showed how the detected signals could be analysed rapidly and effectively and transformed to an image. This was an essential step in order to obtain a practical method. Leuterbur's and Mansfield's discoveries were done in the seventies, the implementation of their techniques became useful in clinical practice a decade later.

In this introduction to MRI, focus will be on the blood visualising methods, i.e. on MRA: **Magnetic Resonance Angiography**. First, the basis of the technique is explained (section VI.1.2). The description of the MRA techniques time-of-flight, black blood and cine PC are explained in the following sections.

VI.1.2. Principles of MRI

The principles of MRI are described here as by Mackiewich.[206] At the basis, there is the directional magnetic field, or moment, associated with charged particles in motion. Nuclei containing an odd number of protons and/or neutrons have a characteristic motion or precession. Because nuclei are charged particles, this precession produces a small magnetic moment.

When a human body is placed in a large magnetic field, many of the free hydrogen nuclei align themselves with the direction of the magnetic field. The nuclei precess about the magnetic field direction like gyroscopes. This behaviour is termed **Larmor precession**.

The frequency of Larmor precession is proportional to the applied magnetic field strength as defined by the Larmor frequency, ω_o:

$$\omega_o = \gamma B_o \qquad \qquad (VI.1)$$

where γ is the **gyromagnetic ratio** and B_o is the strength of the applied magnetic field. The gyromagnetic ratio is a nucleus-specific constant. For hydrogen, γ=42.6 MHz/Tesla.

To obtain an MR image of an object, the object is placed in a uniform magnetic field, B_o, normally between 0.5 to 1.5 Tesla, although 3.0 Tesla is becoming increasingly common. As a result, the object's hydrogen nuclei align
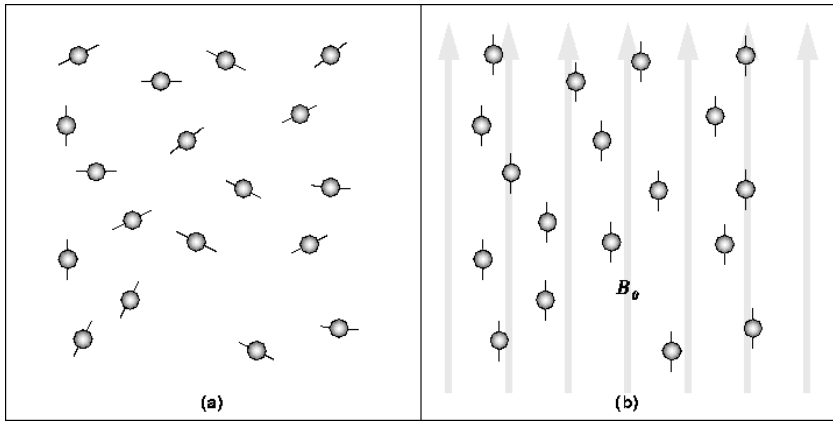
Figure VI.1.: Alignment of nuclei by a strong magnetic field. In the absence of a strong magnetic field, hydrogen nuclei are randomly aligned as in (a). When the strong magnetic field, B_o, is applied, the hydrogen nuclei precess about the direction of the field as in (b).
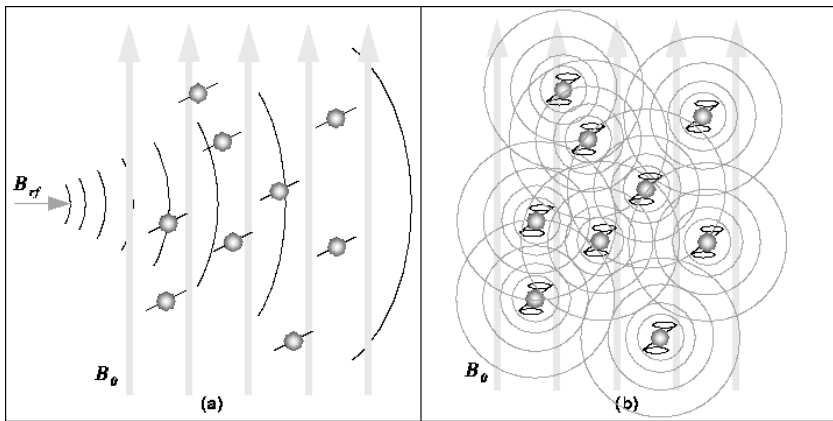
Figure VI.2.: Excitation of nuclei by radio-frequency pulses. a: The RF pulse, B_{rf}, causes the nett magnetic moment of the nuclei, M, to tilt away from B_o. The flip angle (FA) in this sketch is around 60°. b: When the RF pulse stops, the nuclei return to equilibrium such that M is again parallel to B_o. During realignment, the nuclei lose energy and a send out a measurable RF signal.

with the magnetic field and create a nett magnetic moment, M, parallel to B_o. This behaviour is illustrated in Figure VI.1.

Next, a radio-frequency (RF) pulse, B_{rf}, is applied perpendicular to B_o. This pulse, with a frequency equal to the Larmor frequency, causes M to tilt away from B_o as in Figure VI.2 (a).

Once the RF signal is removed, the nuclei realign themselves such that

their nett magnetic moment, M, is again parallel with B_o. This return to equilibrium is referred to as **relaxation**. During relaxation, the nuclei lose energy by emitting their own RF signal (see Figure VI.2 (b)). This signal is referred to as the **free-induction decay** (FID) response signal. The FID response signal is measured by a conductive field coil placed around the object being imaged. This measurement is processed or reconstructed to obtain 3D grey-scale MR images.

To produce a 3D image, the FID resonance signal must be encoded for each dimension. The encoding in the axial direction, the direction of z, is accomplished by adding a gradient magnetic field to B_o. This gradient causes the Larmor frequency to change linearly in the axial direction. Thus, an axial slice can be selected by choosing the frequency of B_{rf} to correspond to the Larmor frequency of that slice. The 2D spatial reconstruction in each axial slice is accomplished using frequency and phase encoding. A 'preparation' gradient, G_y, is applied causing the resonant frequencies of the nuclei to vary according to their position in the y-direction. G_y is then removed and another gradient, G_x, is applied perpendicular to y. As a result, the resonant frequencies of the nuclei vary in the x-direction due to G_x and have a phase variation in the y-direction due to the previously applied G_y. Thus, x-direction samples are encoded by frequency and y-direction samples are encoded by phase. A 2D Fourier Transform is then used to transform the encoded image to the spatial domain.

In MRI, the imaging protocols are described using a number of parameters. T_1 **and** T_2 are relaxation times, linked to the time it takes for M, the nett magnetic moment of the nuclei in the core of the magnet, to realign with B_o. T_1 is related to the relaxation time of the projection of M on the axis of B_o, whereas T_2 is related to the relaxation time of the projection of M on the plane perpendicular to B_o. T_R, the **repetition time**, is the time between two consecutive RF pulses. T_E, the **echo time**, is related to the time in which images are acquired. The NEX or **number of excitations** is the number of times the imaging sequence was repeated. Increasing this number will increase signal to noise ratio (SNR), but will also increase imaging time. The FOV or **Field-Of-View** is expressed as a length and a width, delineating the imaged plane. The **flip angle** (FA) is the direction of the RF pulse with respect to the B_o direction, which is also the angle between M and B_o after the RF pulse. In Figure VI.2 (a), the FA is approximately 60°. The **echo train length** or ETL denotes the number of 'echoes' used in image acquisition. An 'echo' occurs when a large number of spins are aligned again after RF excitation followed by an initial dephasing.

VI.1.3. Time-Of-Flight

The TOF method refers to the motion of blood into and out of the plane of the section as shown in Figure VI.3. The stationary tissues remain in the section and are affected repeatedly by a section-selective repetitive RF pulse. If the repetition time of this RF pulse (T_R) is shorter than the relaxation time of the tissues, then the magnetisation of the tissues is saturated. Saturated tissue does not emit an acute measurable relaxation, and is therefore 'suppressed' and appears dark.[198] On the other hand, blood coming from outside the section is unaffected by the section-selective RF and is thus fully magnetised. The technique is therefore often referred to as 'flow related enhancement'. As more unsaturated spins flow into the slice during each T_R, overall signal strength rises and is maximised when all the partially saturated flowing spins in the slice are replaced during each T_R. As seen in Figure VI.3, the image will be black where the stationary tissue is, and white where the flowing blood is found. This is why TOF is sometimes called 'bright blood imaging'. Figure VI.4 gives an example of TOF images acquired in the right carotid bifurcation of a young hypertensive subject, free of any stenosis. The bright white zones contain flowing blood. The image at the top left is the most proximal cross-section in the CCA. The image right next to it is a cross-section located 2 mm above the previous image, i.e. inter-slice distance is 2 mm.
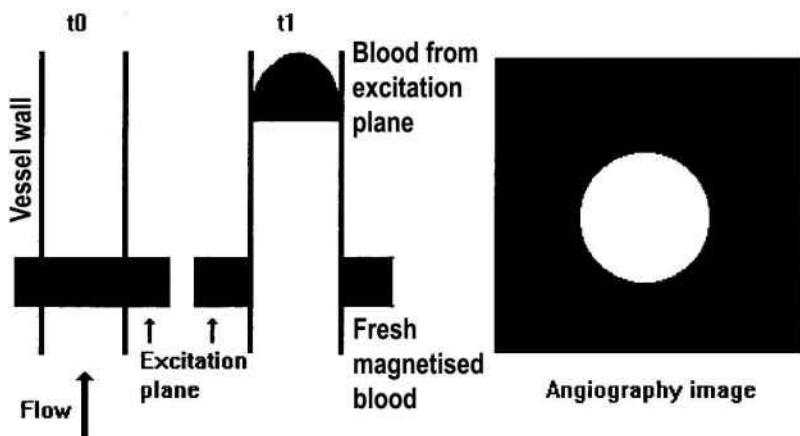
Figure VI.3.: Schematic illustration of the time-of-flight method. The imaging slice is magetised repetitively until it is saturated (repetition time T_R shorter than the relaxation time of the tissues). Fresh blood replaces the saturated blood and yields a white region in the image.[198]
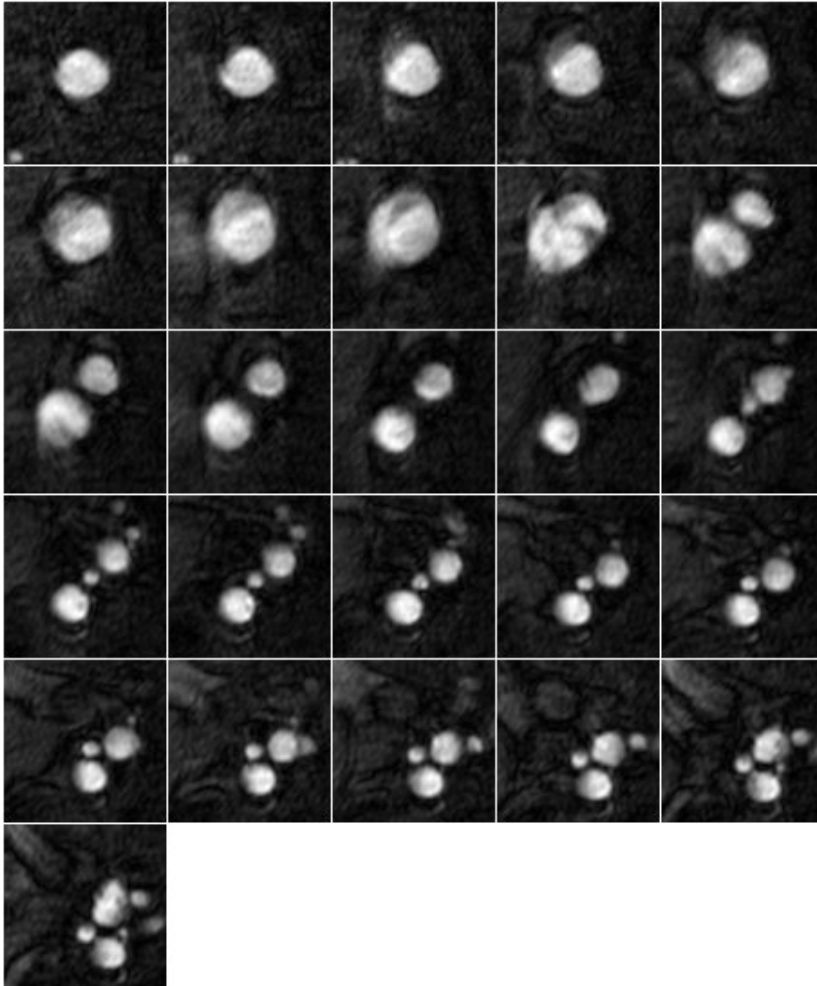
Figure VI.4.: MR images of a carotid bifurcation of a young, non-stenosed hypertensive using TOF. The bright white zones contain flowing blood. The image at the top left is the most proximal cross-section in the CCA. The image right next to it is a cross-section located 2 mm above the previous image, i.e. inter-slice distance is 2 mm.

VI.1.4. Black Blood

The 'black blood' MRI technique is explained schematically in Figure VI.5. The method has been described by Song[299] and consists of a preparation period that contains two spin inversion pulses. The first pulse is *nonselective*, i.e. it inverts all the spins within the sensitive volume of the RF coil. The second pulse, immediately following the first pulse, is slice-selective. It is the 90° pulse in Figure VI.5. This pulse restores the magnetisation of the
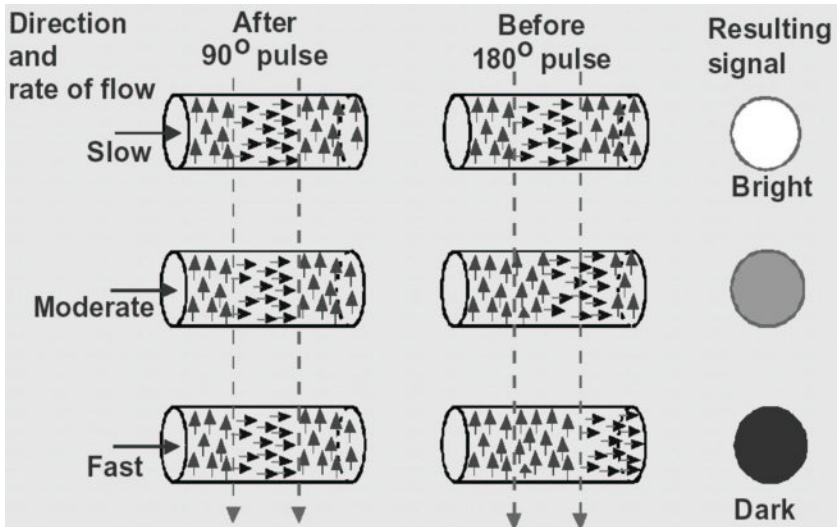
Figure VI.5.: Black blood MRI. Two pulses, a nonselective and a slice-selective one, will magnetise the entire coil volume except for the imaged slice. At the time of image acquisition, the blood in the vessel will appear white if it has not yet been replaced by inflowing magnetised blood.

spins that lie within the slice of interest to the positive z axis. The nett effect of the two pulses is the inversion of the spins outside the desired slice, while those in the slice are unaffected. This is called **presaturation**. 'Inverted' blood then flows into the imaging slice, replacing unaffected blood. When an image is made (by a 180° pulse as shown in Figure VI.5) at the moment where the unaffected blood has flown into the slice, the blood will appear black (hence 'black blood') and the vessel wall white. Figure VI.6 gives an example of BB images acquired in the right carotid bifurcation of a young hypertensive subject, free of any stenosis. The black ellipse-shaped zones contain flowing blood. The image at the top left is the most proximal cross-section in the CCA. The image right next to it is a cross-section located 2 mm above the previous image, i.e. inter-slice distance is 2 mm. These BB images are the counterparts of the TOF images shown in Figure VI.4.

VI.1.5. Cine PC MRI

Phase Contrast (PC) imaging refers to a family of MR imaging methods that exploit the fact that spins that move through magnetic field gradients obtain a different phase than static spins, enabling the production of images with controlled sensitivity to flow.[198] Protons move along the gradients and go out of phase. The Larmour frequency will change depending on the gradient and
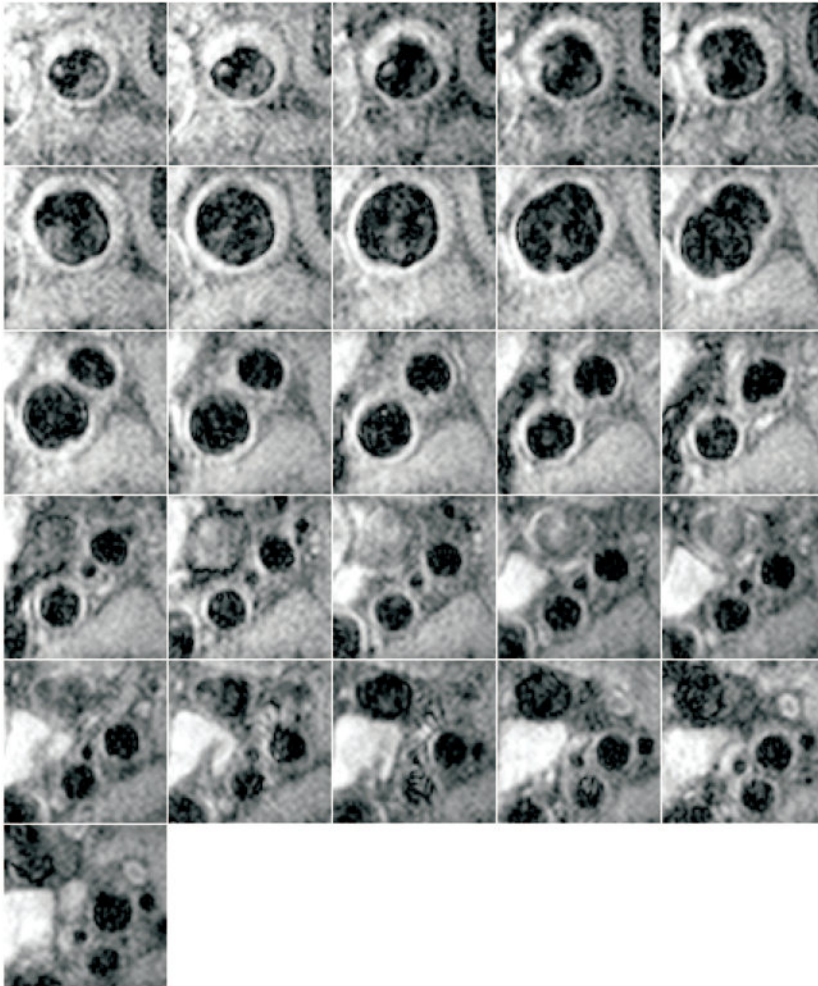
Figure VI.6.: MR images of a carotid bifurcation of a young, non-stenosed hypertensive using BB. These images are the BB counterparts of the TOF images shown in Figure VI.4

the spin-position. In PC imaging, a positive gradient is applied first, then a negative one. Spins in stationaire tissue, such as the vessel wall, now have the same phase. The phase in moving spins, such as spins in blood, will change due to the gradient switch. The phase shift caused by the positive gradient will not have been corrected by the negative gradient, due to the spin movement.[226] When the phase of the signal is measured, the vessel wall can be clearly delineated.

PC MRI is also used for VENC or velocity encoding techniques to determine the flow velocity of the blood. Thus, MR scanners can be used for acquiring

blood velocities in voxels[a] in an entire cross-section of the artery. The V_{enc}, or velocity encoding, is a value set by the operator, denoting the range of velocities measurable: $[-V_{enc}, V_{enc}]$. Velocities can be measured in all 3 orthogonal directions.

The term 'cine' refers to the fact that it is possible to acquire a number of images during one cardiac cycle. When the images are sequentially displayed, they give the impression of a moving fluid using the same principles of cinema, hence 'cine' PC MRI.

---

[a]**voxel**: 3D pixel

VI.2. Segmentation

Segmenting the raw images is necessary for separating the vessel lumen from the surrounding tissue. The delineated contours in 3D space form the basis of the 3D reconstruction. The method used in this work consists of the **region growing method** (RGM) followed by the **snake algorithm**. In the end, the operator is allowed to refine the automatically segmented contour. The technique presented here is based on the segmenting technique used in Dr. Long's PhD thesis[193] and personal communications with Dr. P-L. Cheong. The user-interface was based on work performed by Dr. D.C. Barratt for his PhD thesis.[20]

VI.2.1. Region Growing Method

The region growing method as used in this study consists of 3 steps:

1. An initial guess of the vessel cross-sectional area (A_g) must be made. This initial guess will be used as a threshold to terminate the region growing method. In this work, the initial guess had to be made in the proximal CCA. For each arterial cross-section, another initial guess should be made since the CCA dilates before the bifurcation. Experience showed that the best results were reached if the initial guess was $1.5 \times A_g$ in the distal CCA. In the most distal CCA, this was increased to $2.5 \times A_g$. For the proximal ICA, usually the position of the bulb, the value of the area in the most distal CCA slice was used as the initial guess. Towards the distal ICA, this value was reduced quadratically to half of the mean value of the cross-sectional area in the CCA. In the ECA, the initial guess was half of A_g. With this algorithm, a single initial guess and the notion of the position of each slice provided the values for all the slices on the carotid bifurcation.

2. In the second step, the operator needs to initiate the region growing process. In practice, this is done by a click of the mouse in the vessel lumen. This click denotes the position of the **seed point**. The seed point does not need to be in the exact center of the lumen, its position is in fact of no importance as long as it lies within the lumen.

3. The seed point is in a first approximation the only point in the 'region'. Neighbouring points of the seed point are added to the region if the

grey-scale values of that point fulfil a particular condition. This condition can be any of the following:

- **Grey-scale thresholding**: if a grey-scale value of a neighbouring point is smaller than a preset value, the point is added to the region.

- **Gradient condition**: if the difference between the grey scale value of a neighbouring point and the point in the region is smaller than a preset value, the point is added to the region.

In both conditions a 'preset value' is required. It is initially very small. This initial value or threshold will create a region with a certain area A_{RGM}. If A_{RGM} lies within $A_g \pm A_{ref}$, the region is stored as a potential output of the RGM. A_{ref} is 10% of A_g in the proximal CCA, it increases quadratically to 30% in the bifurcation and drops back to 15% in the distal end of the carotid branches. As long as A_{RGM} is smaller than $A_g + A_{ref}$, the threshold will be increased by a certain increment and the region is grown again using the new threshold. The output of the RGM is the region found with the largest threshold yielding an area smaller than $A_g + A_{ref}$.

From experience, it was clear that RGM was more successful with TOF when a gradient condition was used, whereas the grey-scale thresholding was preferable in BB images.

In order to increase the effectiveness of the RGM, the images were *interpolated* and *filtered* beforehand. This was intended to increase contrast and/or reduce image noise. Interpolation was bilinear, increasing image size from an $m \times n$ matrix to $(2m-1) \times (2n-1)$, thus also increasing the computational requirements. In this context, 'filtering' meant replacing the grey-scale value in a certain pixel either by (i) using the values of the neighbouring pixels (local filtering) or by (ii) calculating a new value for the grey-scale using only the initial grey-scale value and a mathematical formula (global filtering). **Median filtering** is an example of local filtering: the grey-scale value is replaced by the median value of the neighbouring grey-scales. The 'neighbourhood' can be defined differently depending on the application, in this work a 3×3 neighbourhood gave good results for both TOF as BB images. **Gamma filtering** is an example of global filtering: the grey-scale value is increased ($\gamma < 1$) or decreased ($\gamma > 1$) by a percentage depending on the individual grey-scale value and the value of γ. For details on bilinear interpolation, median and gamma filtering, see the MATLAB imaging toolbox manual.[329]

In the end, the RGM yields a 'region' for each image. The circumference of this region, a 'contour', will be saved for further use. This contour is not necessarily smooth, therefore the snake method is implemented in order to adjust the contours.

VI.2.2. Snake Method

The Snake Method attributes an energy to a closed contour or snake. It was originally introduced by Kass.[153] It considers contour nodes (points) as masses connected by springs. The nodes of the contour are then moved around in the image until the energy of the contour is minimised. The energy is the consequence of both internal and external forces:[373]

1. The internal forces are the snake's tension and rigidity. Tension is related to the first derivative of the contour, while rigidity is related to the second derivative.

2. The external forces relate to the grey-scale value of the nodes. Several functions can be used to model the external force, such as the grey-scale values themselves or their gradient, possibly blurred using a Gaussian function.[372]

For a detailed description of the Snake Method as used in this study, see Dr. P-L. Cheong's PhD dissertation.[62] Figure VI.7 gives an example of the automatic segmentation of TOF images acquired in the right carotid bifurcation of a young hypertensive subject, free of any stenosis. The white contours surrounding white zones are automatically segmented luminal cross-sections of the CCA or ICA, while the grey contours delineate the ECA. The image at the top left is the most proximal cross-section in the CCA. The image right next to it is a cross-section located 2 mm above the previous image, i.e. inter-slice distance is 2 mm. Figure VI.7 is analogous with Figure VI.4, where the raw images were given. Similarly, Figure VI.8 is the segmented Figure VI.6.

VI.2.3. Manual Corrections

As seen in Figures VI.7 and VI.8, the segmentation does not always work for various reasons. The most frequent reason is poor image quality, very
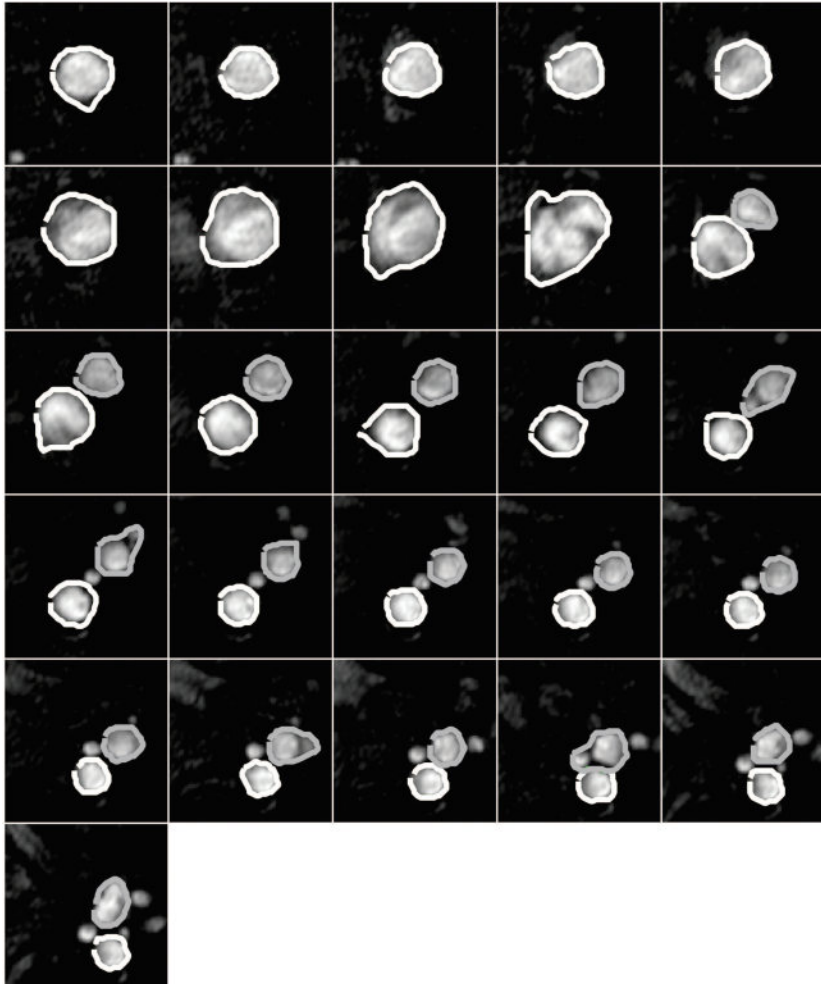
Figure VI.7.: MR images of a carotid bifurcation of a young, non-stenosed hypertensive using TOF as shown in Figure VI.4. The white contours surrounding white zones are automatically segmented luminal cross-sections of the CCA or ICA, while the grey contours delineate the ECA.

common around the bifurcation apex. Another reason for poor automatic segmentation is an inadequate initial value for the cross-sectional area A_g. In Figure VI.8, the side branches of the ECA are included in the ECA contour because of this. An operator always needs to confirm and possibly change the automatically segmented contours. This is done by running a program on a MATLAB platform (The Mathworks Inc., Cambridge, UK).[328] The visual interface is shown in Figure VI.9. It shows every contour superimposed on the matching image to the operator who is allowed to add, delete or move around points on the automatically segmented contour. Because editing
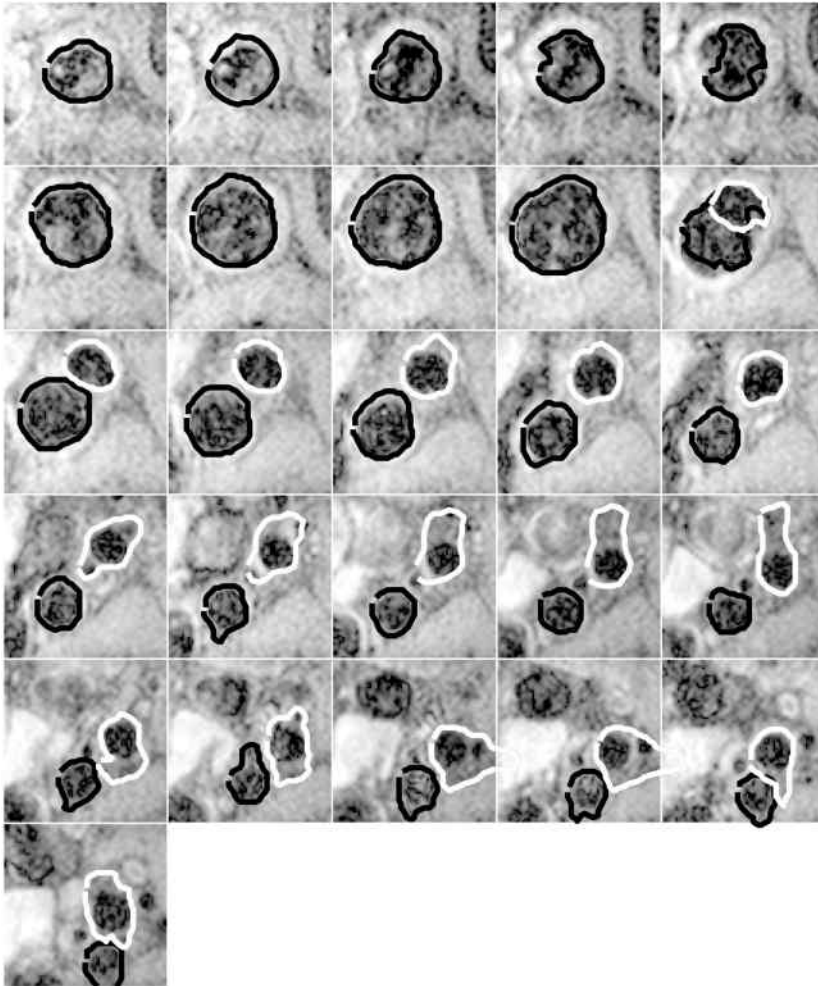
Figure VI.8.: MR images of a carotid bifurcation of a young, non-stenosed hypertensive using BB as shown in Figure VI.6. The black contours surrounding black zones are automatically segmented luminal cross-sections of the CCA or ICA, while the white contours delineate the ECA.

single points can be time-consuming, the program also allows the operator to move around, shrink or expand a contour if necessary.

As an example, Figure VI.10 (a) shows the raw BB MR image acquired in the right CCA of a healthy subject. By using the region growing method together with the snake model, a contour is obtained as is shown in Figure VI.10 (b). Figure VI.10 (c) illustrates an example where the semi-automatic segmentation technique failed. This was due to the presence of the white signal at the bottom left corner of the image, caused by slow, recirculating
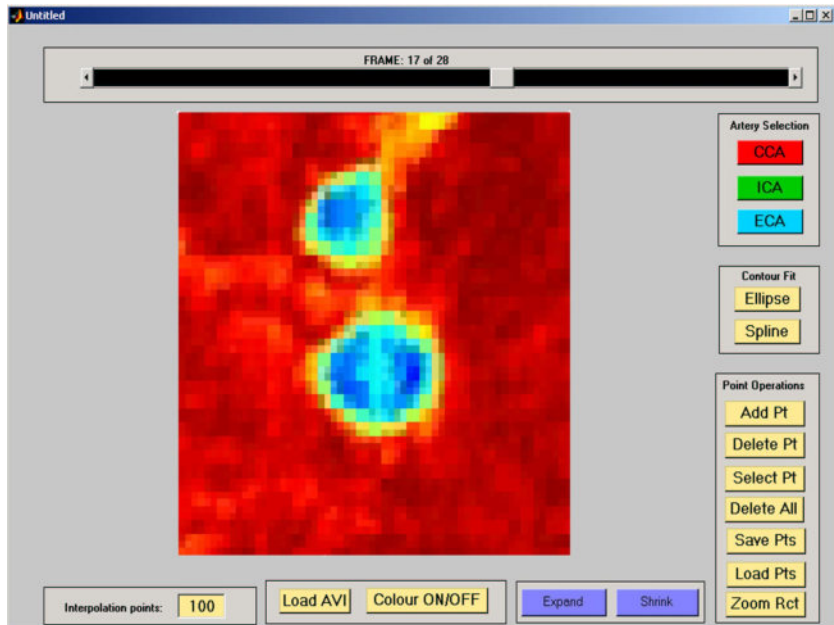
Figure VI.9.: Manual segmentation interface, called in MATLAB. The slider at the top is used to choose the image to be viewed, from the most proximal image (image 1, proximal CCA) to the most distal one. The image viewed here is a TOF image shown in Figure VI.4.
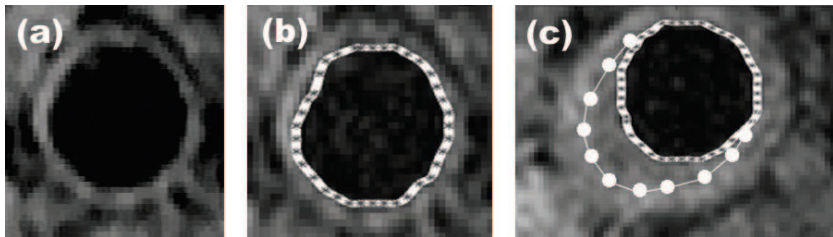
Figure VI.10.: BB MRI segmentation of the right carotid arteries for a healthy subject. a: Raw image. b: Segmentation of image (a). c: Unsuccessful image segmentation. The white signal at the lower left corner consists of both the vessel wall and blood. The dotted white line is a manual correction. Images (a) and (c) were taken from the same subject, but at different slice locations.

blood particles. The segmentation program treated the white signal as the lumen border, hence giving the contour shown in Figure VI.10 (c). An operator would then have to replace part of this contour, as shown in Figure VI.10 (c) by the dotted line. For this purpose, the generated contour is drawn on the original image and shown to the operator. By keeping the correct parts of the contour and replacing the spurious parts by operator-fitted splines, the final contour was obtained.

VI.3. Reconstruction

VI.3.1. 3D Smoothing

At the end of the segmentation procedure, a series of parallel lumen contours can be lined up in 3D space. Due to potential errors in segmentation, it is necessary to adjust the contours in order to obtain a smooth 3D reconstruction.[224] In this work, based on methods suggested by Moore,[224] the smoothing consisted of 2 parts which were conducted at the same time.

- **Area smoothing**. Cross-sectional areas were calculated for each lumen contour. For the example of a CCA, this results in a plot such as the one shown by the black dots in Figure VI.11 (a). A cubic smoothing spline is fitted using these points, as shown by the grey line in Figure VI.11 (a). This is performed for each of the arteries (CCA, ICA and ECA) separately. The cross-sectional areas of the most proximal and most distal contours cannot be altered to avoid a potential mismatch between the preceding or following artery.

- **Centreline smoothing**. For each of the contours, a centroid can be defined as explained by Barratt.[20] These centroids, or 'centers' of the lumens, form a line in 3D space: the centreline. This centreline is also smoothed using a cubic smoothing spline. Figure VI.11 (b) shows the centroids as black dots and the smoothing spline as a grey line.

With the knowledge of the new position of the centroid, $\overrightarrow{C_{new}}$, and the required enlargement of the cross-sectional area, a_{ratio}, the new points on a contour $\overrightarrow{P_{new}}$ can be calculated as

$$\overrightarrow{P_{new}} \;=\; \left(\overrightarrow{P_{old}} - \overrightarrow{C_{old}}\right) \times \sqrt{a_{ratio}} + \overrightarrow{C_{new}} \qquad\qquad \text{(VI.2)}$$

using $\overrightarrow{P_{old}}$ and $\overrightarrow{C_{old}}$, which are the original corresponding points on the contour and the old centroid respectively. Note that the square root of the area ratio is used as a scaling factor, in contrast to using the area ratio as such. This is because the value being changed with a shift to $\overrightarrow{P_{new}}$ and $\overrightarrow{C_{new}}$, is in fact the local cross-sectional radius ratio, which is equal to the squared area ratio.

(a) CCA Cross-sectional Area   (b)
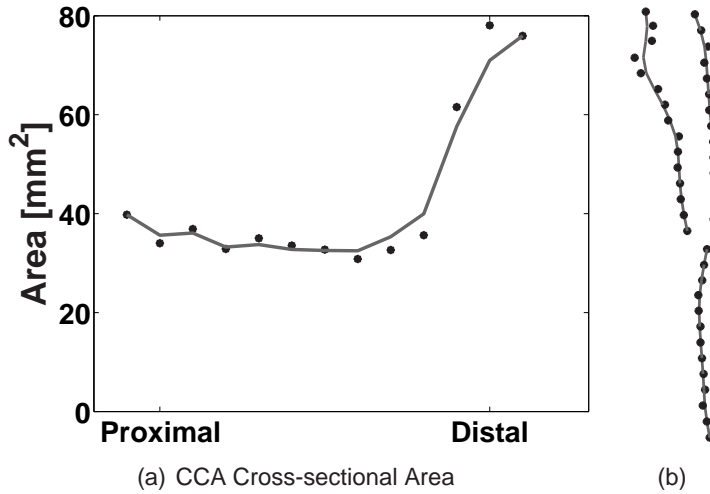
Figure VI.11.: Three-Dimensional smoothing. a: Smoothing cross-sectional areas: the black dots represent cross-sectional areas of the 2D equidistance contours acquired after manually correcting the automatically segmented images. The grey line is the new cross-sectional area of the contours. b: Smoothing centrelines. The black dots represent the position of the centroids of the 2D equidistance contours acquired after manually correcting the automatically segmented images. The grey line is the 3D smoothed centreline. Note how there were important shifts in the distal end of one of the branches.

Cubic smoothing splines are calculated using the original points in need of smoothing, weighting factors and a smoothing parameter p. The weighting factors can be used to prevent the points at the extremities from moving. The smoothing parameter determines the relative weight placed on the contradictory demands of having a smooth cubic spline vs a spline close to the data. For $p = 0$, the spline is the least-squares straight line fit to the data, while, at the other extreme, i.e. for $p = 1$, the spline is the variational, or 'natural' cubic spline interpolant. As p varies from 0 to 1, the smoothing spline changes from one extreme to another.

In order to determine the optimal smoothing parameters, 9 carotid bifurcations were reconstructed using the same basic set of data acquired from a healthy 28-year old male. For the smoothing parameters, values of 0.1, 0.5 and 0.9 were chosen for both the area and the centreline smoothing, thus resulting in 9 different carotid bifurcations. The predicted OSI distribution in each of these bifurcations is shown in Figure VI.12. It is important to note that the difference in smoothing parameters was the only difference in image treatment between the results shown in Figure VI.12. The smoothest reconstruction (p values of 0.1) is illustrated in Figure VI.12 (a). Each row of images has the same area smoothing parameter and each column has the same centreline smoothing parameter. Clearly, the main features of the OSI

distribution, namely the two peaks of high OSI on both sides of the bifurcation area, are preserved throughout the images. High-frequency changes in the OSI distribution of Figure VI.12 (i), i.e. the roughest reconstruction, are filtered by both the area as well as the centreline smoothing. This can be illustrated by two examples. In a first example, consider the scattered peaks of high OSI in the CCA of Figure VI.12 (i). Bearing in mind that healthy CCA's are generally smooth, such scattered and high peaks should not exist. The smoothing implemented here managed to eliminate the scattered OSI peaks without influencing the OSI distribution. Consider, for the second example, the high OSI region found in the ECA of Figure VI.12 (i). This is very probably due to segmentation complications with ECA side branches. The ECA cross-section proximal from the side branch may widen similarly to what happens in the distal CCA. Since the side branches of the ECA are neglected when simulating carotid blood flow, the operator may have chosen to draw a smaller contour at the location of the widening or at the location of the branch itself. This operator-dependent guess of the contour could have been too small or slightly shifted in comparison with the distal ECA, giving rise to zones of recirculation after the considered contour. This effect has been compensated for by smoothing.

In conclusion, smoothing is necessary and does not result in loss of important information. It is therefore recommended to set the smoothing parameters to 0.1. This is how the most 'physiologically realistic' geometries are obtained, based on this subject. Note that this smoothing study has been performed on a healthy subject, thus the results retrieved from this study are only applicable to healthy subjects. It is very likely that these smoothing parameters may not be appropriate for the reconstruction of stenosed carotid bifurcations, where both the centrelines and lumen areas can change more dramatically.

VI.3.2. Spline Fitting

After segmentation and 3D smoothing, the available data consists of 2D contours, smoothed and readjusted in 3D space, which allow the reconstruction of a smooth 3D surface. In order to fit a volume to the surface, longitudinal splines are fitted through the contours. This is performed by taking N equally spaced points on two consecutive contours. There are $2 \times N$ possible ways to connect the points from each contour with a counterpart on the other contour: point i on the first contour can be connected to point i on the second contour, point i+1 to point i+1, etc. But point i can also be connected
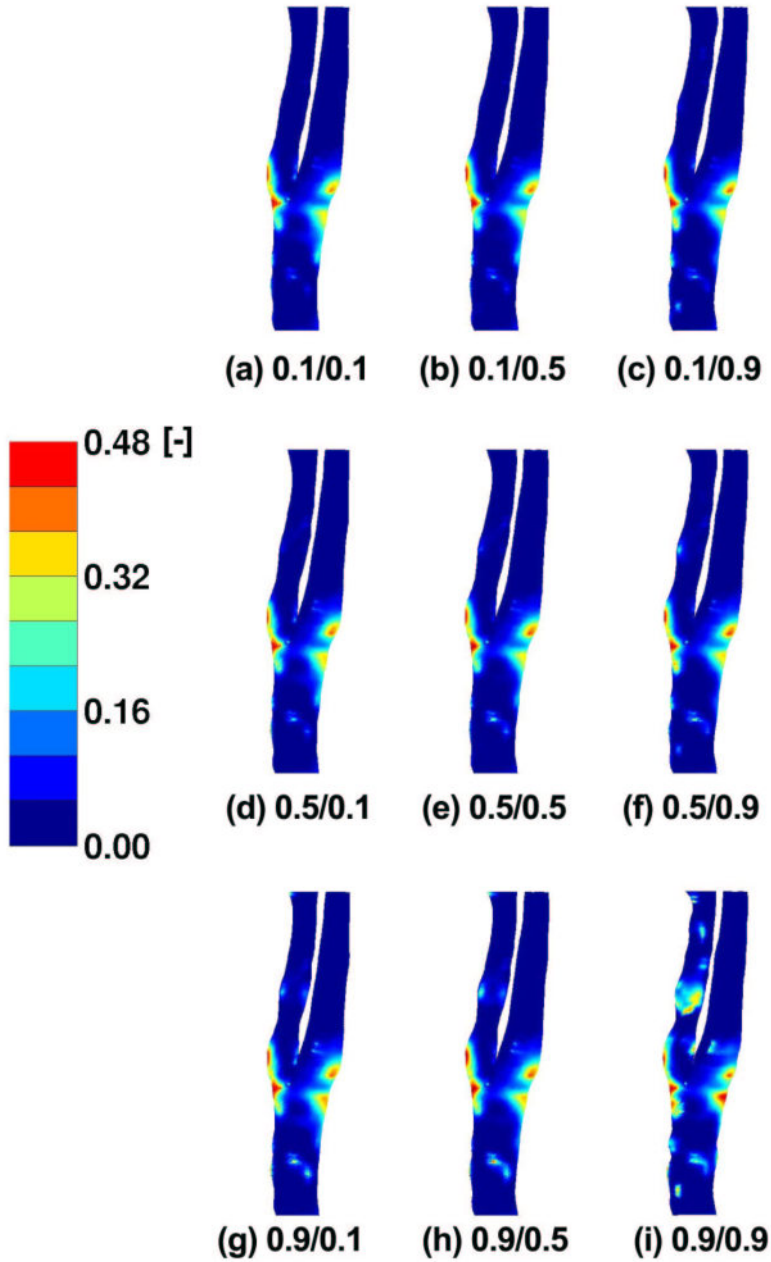
Figure VI.12.: OSI distributions for one particular subject, using different smoothing parameters in the 3D reconstruction. The area smoothing parameter (p_1) and centreline smoothing parameter (p_2) are reported as (p_1)/(p_2).

to point i+1, i+1 to i+2, etc. Finally, point i can be connected to point i just as in the first case, but point i+1 could be connected to point i-1, etc. The best way to connect two consecutive contours is the one where the cumulative distance between the connected points from two different contours is minimal. The lines connecting the points from different contours are considered boundaries between vessel wall and lumen.

The above operation decides on how two consecutive contours can be connected. This procedure is initiated in the distal ICA and repeated until all ICA contours have been connected. At that point, the most proximal ICA contour is connected to the most distal CCA contour. Similarly, the ECA can be connected to the CCA. Thus, the carotid bifurcation is now represented as the integration of two parts: one connecting the CCA to the ICA (disregarding the ECA), the other connecting CCA to ECA (Figure VI.13 (a)).

Note that the splines connecting the contours are in fact piecewise linear segments. This ensures that no neighbouring splines will overlap with each other, without compromising smoothness owing to the 3D smoothing performed in the previous step.

VI.3.3. Artery Splitting

In order to split the two parts shown in Figure VI.13, the following procedure was performed. *First*, a point M was defined as the center of the shortest straight line that connects the first distinguishable ICA and ECA contours distal from the apex (See Figure VI.13 (a)). This plane is located at z=1 mm in an orthogonal reference system where the z-axis coincides with the inferior/superior axis (or I/S-axis). In *second* step, all 360 lines (uniformly radiated from M with a 1° interval) that are perpendicular to the Inferior/Superior (I/S) axis (or z-axis) were calculated. Of all lines, only a few did not cross the ICA or ECA lumen. The average of these lines was the ICA/ECA separating line $\vec{M}$ (the thick dashed line in Figure VI.13 (b)). The *third* step was to determine the bifurcation apex. This was achieved by treating the carotid bifurcation as the integration of two parts, one connecting the CCA to the ICA (disregarding the ECA), the other connecting CCA to ECA (Figure VI.13 (a)), as explained in section VI.3.2. The two parts were separated by an intersecting plane going through M and defined by the directions $\vec{M}$ and z. In Figure VI.13 (c), the intersections of this plane with the CCA-ICA vessel are depicted as black points at -1 mm $< z <$ 1 mm (the intersections with the CCA-ECA as grey points). The intersection point closest to M was chosen

(a) Carotid bifurcation represented as two integrated parts

(b) Separating the ICA from the ECA

(c) Separating CCA, ICA and ECA
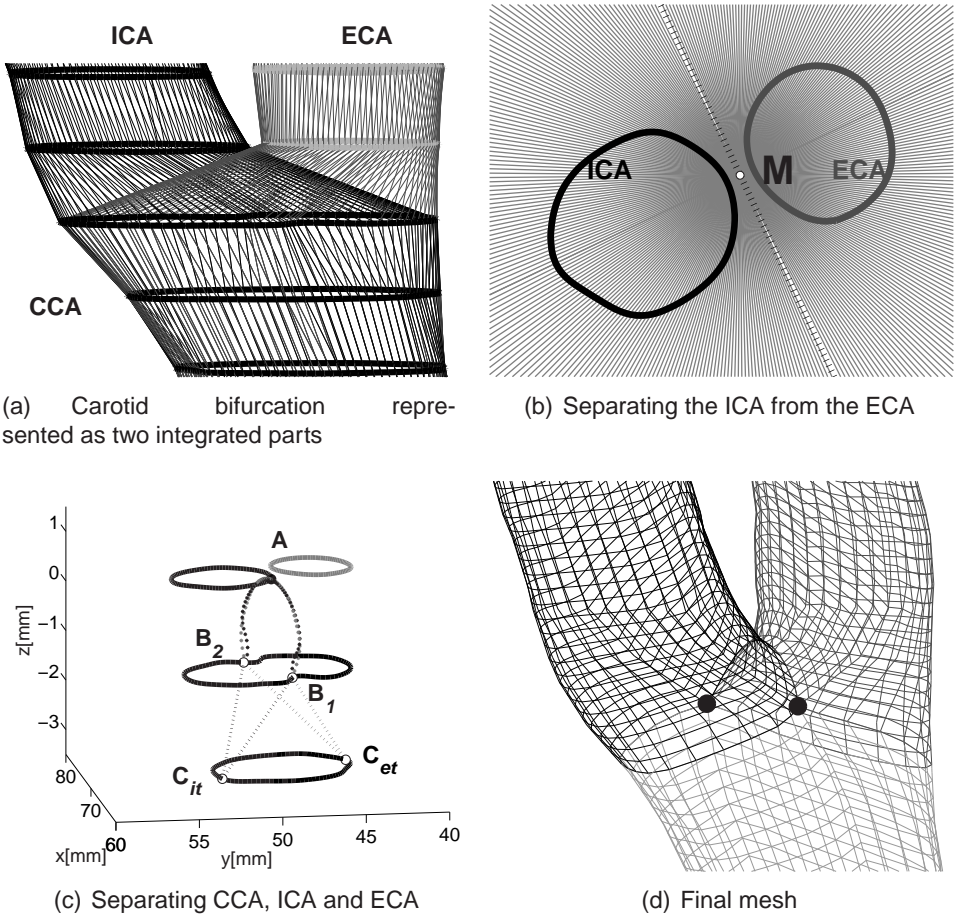
(d) Final mesh

Figure VI.13.: Generation of a computational mesh from cross-sectional contours. a: The carotid bifurcation represented as the integration of the CCA-ICA (thick black contours and thin black longitudinal splines) and CCA-ECA (thick grey contours and thin grey longitudinal splines). b: Thick black line: first ICA contour after CCA; thick grey line: first ECA contour; white point M: center of the shortest straight line connecting ICA and ECA contours; grey lines: lines through M uniformly radiated with a 1° interval; thick dotted line: line chosen to separate ICA and ECA. c: Definition of the bifurcation apex A, points B_1 and B_2, and points C_{it} and C_{et} (see text for details). d: The final surface mesh; the black dots represent the locations of points B_1 and B_2.

as the apex A. In *step four*, two additional points B_1 and B_2 were defined as the intersection of the separating plane and the most distal CCA contour (at z=-1 mm in Figure VI.13 (c), i.e. 2 mm below the ICA and ECA contour in step 1). The parabola with its maximum at the z-value of the apex A and going through points B_1 and B_2 (and thus lying in the ICA/ECA separating plane), created a part of the lumen border. Apart from the plane separating the ICA and ECA, two other planes need to be defined in the *fifth* step: a plane separating the CCA from the ICA and another separating CCA from ECA. These planes were defined by points B_1, B_2, and a third point C (C_i and C_e for resp. ICA and ECA) at approximately 4 mm below the bifurcation apex (i.e. at z=-3 mm) and on the CCA wall. Every point on the CCA contour at z=-3 mm was a candidate for points C_x, but only two of them resulted in a plane (formed by B_1, B_2 and C_x) intersecting with the CCA contour at one point only. These two points C_{it} (ICA) and C_{et} (ECA), are shown on Figure VI.13 (c), C_i (ICA) and C_e lie 0.1 mm above C_{it} (ICA) and C_{et} respectively.

VI.4. Accuracy and Reproducibility

An important part of this research has been dedicated to finding the accuracy of the WSS and its related parameters when derived using image-based CFD. **Accuracy** is traditionally determined using phantom studies: the root mean square difference between the measured value and the correct value is then regarded as the accuracy. There are, however, a number of reasons why *in vivo* image-based CFD is expected to be less accurate than in phantoms: the geometry is more complex and unknown. Furthermore, imaging is hampered by motion artefacts: both due to respiratory motion, subject movement (swallowing, sneezing, etc.) or arterial deformation. However, since the technique needs to be validated for use in human subjects, the accuracy *in vivo* should be quantified. For *in vivo* cases, however, the true values of the geometry parameters are not known, thus the accuracy cannot be evaluated. The 'reliability' of the technique is therefore expressed by its **reproducibility**.

In what follows, the accuracy of TOF-based CFD is quantified on a carotid phantom. The subsequent section (VI.4.2) deals with *in vivo* reproducibility.

VI.4.1. Accuracy in Phantoms

VI.4.1.1. Methods

An anthropomorphic carotid artery phantom (R.G. Shelly Ltd., London, Ontario, Canada) was scanned under static conditions using both BB and TOF MRI. The phantom consists of silicon tubing moulded to the shape of a carotid bifurcation and embedded in agar. The process used to fabricate the phantom vessel is based on a novel technique using the low melting point metal Cerrolow 117.[295] It had been previously shown by Smith[294, 295] that the phantom had an RMS fabrication accuracy of 0.160 mm in lumen radius, estimated by comparing the input CAD dimensions with those measured from a radiograph at 100 locations.[295] Details of the phantom geometry have been described elsewhere.[294, 295] In short, the phantom is planar, has a CCA lumen diameter (LD) of 8 mm which enlarges distally and splits into an ICA and ECA. The bulb has an LD of 9 mm which decreases gradually to 5.5 mm in the distal ICA. The ECA LD is 4.5 mm.

The phantom was filled with tap water, which remained stationary during the scan. This involved some changes to the TOF imaging protocol. Two imaging sequences, both for which a 2-element phased array carotid surface RF coil was applied, were performed on this setup. Each scan produced images at 28 slices of 2 mm. The TOF MRI sequence had T_E / T_R / FOV / FA / NEX set to 6.9 ms / 100 ms / 134 $\times$ 100 / 50° / 1 yielding an in-plane resolution of 0.52 mm. The BB MRI sequence had T_E / T_R / FOV / FA / NEX / ETL set to 11 ms / 655 ms / 120 $\times$ 24 / 180° / 1 / 11 yielding an in-plane resolution of 0.47 mm. Both sets of images were segmented and reconstructed using the techniques explained in sections VI.2 and VI.3. The smoothing parameters used in this study were 0.5 for both area and centreline.

VI.4.1.2. Results

The results of this study are summarised in Table VI.1. The column labelled CAD contains the true values for mean cross-sectional areas (A_{art}), area ratio (A_R), individual shape factor (SF_{iart}), tortuosity (T_{art}), bifurcation angle (α_{BIF}) and centreline distance (z_{DIST}). See section II.3.2.2 for definitions of these parameters. Next to the true values, the measured values are presented. In order to appreciate the influence of the 3D smoothing performed during reconstruction, the results of the unsmoothed data are presented as well.

The accuracy of cross-sectional areas is further detailed in Figure VI.14,

Parameter [unit]	CAD	TOF	BB	TOF smooth	BB smooth
A_{CCA} [mm^2] =	52.72	53.60 (1.7)	51.98 (-1.4)	53.61 (1.7)	52.93 (0.4)
A_{ICA} [mm^2] =	38.17	35.42 (-7.2)	33.91 (-11.2)	35.10 (-8.1)	34.32 (-10.1)
A_{ECA} [mm^2] =	17.04	15.88 (-6.8)	16.47 (-3.4)	15.90 (-6.7)	17.07 (0.2)
A_R [-] =	0.80	0.72 (-9.9)	0.67 (-16.6)	0.72 (-9.9)	0.69 (-14.0)
SF_{iCCA} [-] =	0.9557	0.9702 (1.5)	0.9661 (1.1)	0.9702 (1.5)	0.9661 (1.1)
SF_{iICA} [-] =	0.9884	0.9928 (0.4)	0.9976 (0.9)	0.9927 (0.4)	0.9980 (1.0)
SF_{iECA} [-] =	0.9881	0.9944 (0.6)	0.9967 (0.9)	0.9944 (0.6)	0.9975 (0.9)
T_{CCA} [%] =	0.53	0.72 (35.8)	0.56 (5.7)	0.22 (-58.1)	0.36 (-31.3)
T_{ICA} [%] =	1.68	2.00 (19.2)	1.67 (-0.3)	1.24 (-26.3)	1.36 (-18.9)
T_{ECA} [%] =	2.03	2.63 (29.5)	2.19 (7.7)	2.00 (-1.4)	1.99 (-2.1)
α_{BIF} [°] =	149.67	151.43 (1.2)	151.40 (1.2)	151.63 (1.3)	151.39 (1.1)
z_{DIST} [mm] =	0.00000	0.01486	0.01359	0.01450	0.01371

Table VI.1.: Accuracy of MRI using a carotid phantom. CAD: true values; TOF: Time-of-flight; BB: Black blood; smooth: smoothed geometry. The values in brackets are the percentage difference with respect to the true (CAD) value. The column z_{DIST} was defined as the average distance between the measured centreline and the true centreline. See section II.3.2.2 for definitions of the used parameters.
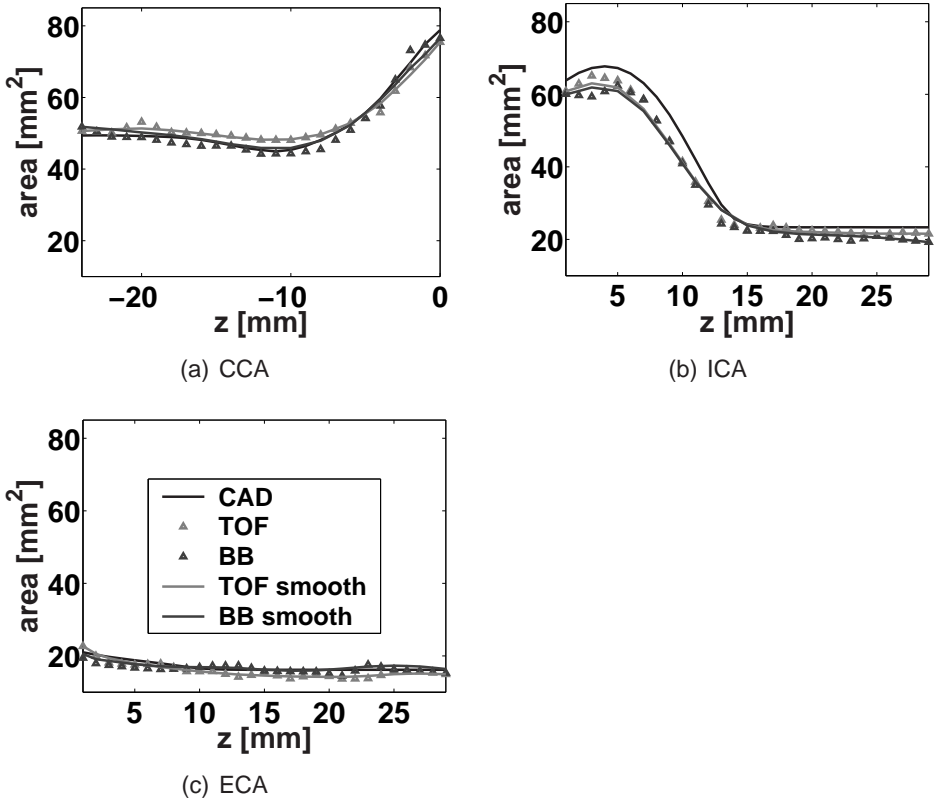
Figure VI.14.: Accuracy of cross-sectional areas reconstructed by MRI using a carotid phantom. The cross-sectional area is presented as a function of the I/S axis z. The black line represents the true CAD data. The symbols are measured cross-sectional areas and the grey lines are smoothing splines through the measurements.

where the cross-sectional area is presented as a function of the I/S axis z. The black line represents the true CAD data. The data points are measured cross-sectional areas and the grey lines are smoothing splines through the data points obtained by setting the smoothing parameters to 0.5. Figure VI.15 shows the centrelines of the phantom overlaid by the centrelines found from the TOF-scan (dark grey) and the BB MRI-scan (light grey).

VI.4.1.3. Discussion

In this study, an anthropomorphic carotid artery phantom was scanned under static conditions using both BB and TOF MRI. The serial 2D MR images were segmented and reconstructed using techniques developed in this thesis as discussed in sections VI.2 and VI.3. Table VI.1 shows that the ac-

Figure VI.15.: Centrelines in MR phantom study deduced from true phantom geometry (black), TOF scan (dark grey) and BB MRI (light grey).

curacy in reconstruction for all geometric parameters was very high. The good area agreement gave rise to low percentage errors when compared to a study performed by Frayne,[98] who found errors in area measurements of $\pm 15\%$ (see also Table IX.8 on page 261). It can be noted from Figure VI.14 (b) that the areas were systematically underestimated in the ICA, both with TOF and BB. Smoothing was not responsible for this slight discrepancy, since the percentage area error was hardly influenced by smoothing (-11.2% before and -10.1% after smoothing, BB ICA mean area error, Table VI.1). The reason for this error probably lay in the fact that the imaging planes in the bulb were not perpendicular to the vessel axis, yielding MRI artefacts. Centreline agreement was almost perfect (Figure VI.15), implying that the values for centreline agreement parameters, reflected in the tortuosity, bifurcation angle and z_{DIST}, are good standards for further centreline comparison studies. Finally, there was little error in the individual shape factor, partly due to the simple geometry used in this setup. Note that both the TOF and BB scan gave adequate results, which in addition compared very well to each other.

It is clear that the accuracy found here is only valid for the phantom, and cannot be regarded as the *in vivo* accuracy. Nevertheless, this phantom study provides reference values for the accuracy of a number of parameters. Moreover, the good agreement between the true data and the 3D reconstructions encourages the use of MRI-based CFD for *in vivo* applications. Therefore, the next section will take the technique to the next step, i.e.

to study the *in vivo* reproducibility by scanning a number of healthy subjects twice and comparing the 3D reconstructions of both scans to each other.

VI.4.2. *In Vivo* Reproducibility

This study aims to evaluate the reproducibility of the MRI-based CFD approach for the prediction of flow and wall shear stress related parameters when applied to *in vivo* situations. For this purpose, the carotid bifurcations of 8 healthy subjects were scanned two times. The reproducibility of the approach for geometry reconstruction has previously been studied.[194] This work investigates the reproducibility of the predicted flow field.

VI.4.2.1. Methods

Volunteers and Scanning Protocol Eight healthy volunteers, 5 males and 3 females aged between 22 and 36, were scanned on two separate occasions between 2 to 4 weeks apart. On each occasion the subject lay flat within the MRI scanner with his/her head kept in a straight position by means of a saddle-shaped cushion under the neck. Since changes in neck angles might influence the carotid haemodynamics, it was necessary to keep the subject's neck in the same position in both scans. Cross-sectional images of the right carotid bifurcation were acquired using a GE MR scanner (1.5T, Signa) with a 2D TOF 'SPGR'[b] sequence. For further reference, the first scan will be referred to as scan A and the second scan as scan B, subjects will be numbered from 1 to 8. Slice thickness was 1.5 mm, 64 parallel images were obtained covering the bifurcation over a region about 100 mm in length. Other scan parameters were T_R=45ms, T_E=8.7ms, FA=60 degrees, NEX=2.0, FOV=16x12cm and matrix size 256x192, which gave an in-plane resolution of 0.625 mm. A 5 inch surface RF coil was used for data acquisition. The research protocol was approved by the local institutional review board and the local research ethics committee.

Geometry The image segmentation and 3D reconstruction were performed using the methods described previously.[197] These methods are an earlier version of the techniques found in sections VI.2 and VI.3. For the recollection of the reader, the reconstruction method is explained here in short.

---

[b]**SPGR**: SPoiled Gradient Recalled
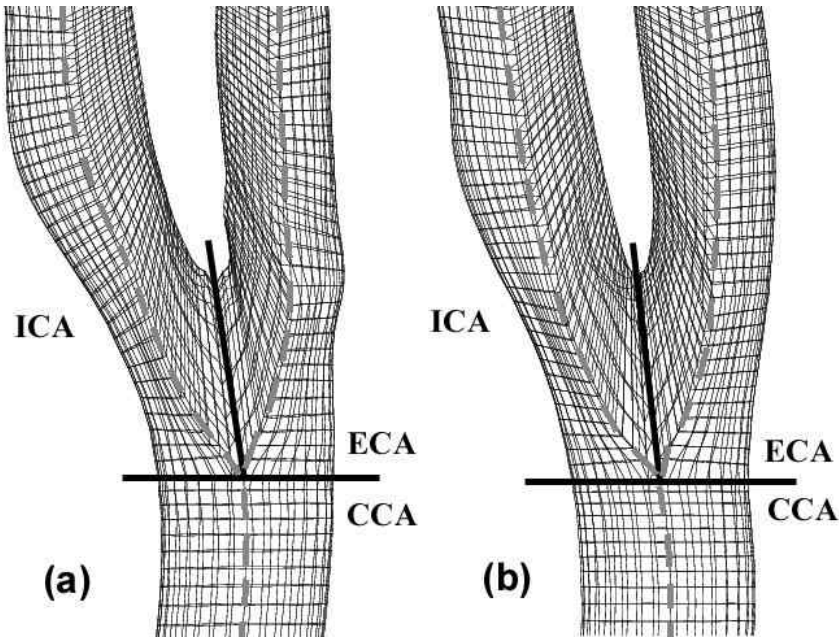
Figure VI.16.: Structured hexahedral meshes for subject 5. The geometry in scan A (a) differs from the geometry in scan B (b). The solid black lines show how the mesh is divided into a CCA, ICA and ECA block. The grey dashed line shows where the seperate arteries are 'cut open' in order to patch the haemodynamic wall parameter data. (See page 130.)

Once the images were acquired, high quality contours were extracted from the 2D images using a region growing method for initial contour definition, and the snake method for final contour extraction. These serial 2D contours were then aligned to produce a 3D vessel surface geometry. Smoothing was done in two steps: centreline smoothing and area smoothing. The mesh was generated using an in-house purpose-built mesh generator described by Long.[197] For mesh independence tests, 4 different meshes were generated, the coarsest one having 29640 cells, the finest one 54600 cells for the same vessel volume of approximately 120 ml. A mesh was considered sufficiently dense when, as suggested by Prakash,[253] the values of the wall shear stress were within acceptable tolerance in two simulations using meshes of different densities. The coarser mesh would then be used for time-saving reasons. In this study, multi-block, structured meshes containing 41600 hexahedral cells were adopted. The resulting wall shear stress differences between the finest mesh and the used mesh were within 1.0%. Figure VI.16 shows the computational meshes for subject 5 (scan A in Figure VI.16 (a) and scan B in Figure VI.16 (b)). Clear geometric differences between the two scans can be noticed.

Computational Details The governing equations were solved numerically using the 'QUICK' differencing scheme available with CFX4™,.[3] The computations were performed for two cycles, since the third cycle resulted in instantaneous WSS differences below 0.01% compared to the second cycle. Each cycle was divided into 80 equally spaced time-steps of 0.0125s. This time resolution was considered sufficient since the resulting wall shear stress differed by only 0.1% when a greater time resolution (160 time-steps per cycle) was used. The dynamic viscosity was set to 4 mPa.s (Newtonian flow) and the density 1176 kg/m^3. Flow simulations were carried out on a SUN Blade 1000 Workstation (Ultrasparc III processor, 512Mb RAM, 750 MHz). At the wall, 'no-slip' boundary conditions were imposed, i.e. the blood velocity on the wall was set to be the wall velocity itself, which for rigid walls is zero. The rigid wall assumption has been questioned in several studies.[178, 387] Zhao[387] showed that the effect of moving walls was a general reduction in the magnitude of WSS, but the global characteristics of the flow and the stress patterns remained unchanged. In this study, the influence of geometric uncertainties on the flow was studied. It is clear that, as shown by Zhao,[387] flow in a rigid model will certainly be different from that in a deformable model. However, since it is very difficult to acquire time-resolved carotid images that are of sufficient temporal and spatial resolution for the reconstruction of a deformable CFD model, the rigid wall assumption was made.

Several authors have studied the effect of inlet boundary conditions on the CFD predictions of pulsatile flow (See also section VIII.1.1, where different in- and outflow conditions for MRI-based CFD are discussed and tested). Redaelli[261] found that a uniform profile developed faster than a parabolic one. Cebral showed that using MRI measurements as boundary conditions, different results were obtained when measured velocities were imposed on inlet or outlets.[49] Shipkowitz[282] emphasised the importance of the effect of the secondary velocities at the inlet subsection. We have analysed MRI measurements (later in the thesis), demonstrating a high reliability of 3D cine MRI measurements: the measured velocity profiles were not fully developed, but physiologically correct, resulting in correct WSS distribution with minimal entrance effects.

It is therefore important to emphasise that boundary conditions can influence the flow pattern significantly. By using the same inlet boundary conditions for both scans and for each subject, it was ensured that flow pattern differences in this study would only be due to geometrical differences between two scans, and would be completely independent of MR velocity acquisition errors. A typical flow wave form (Figure VI.17), obtained from the common
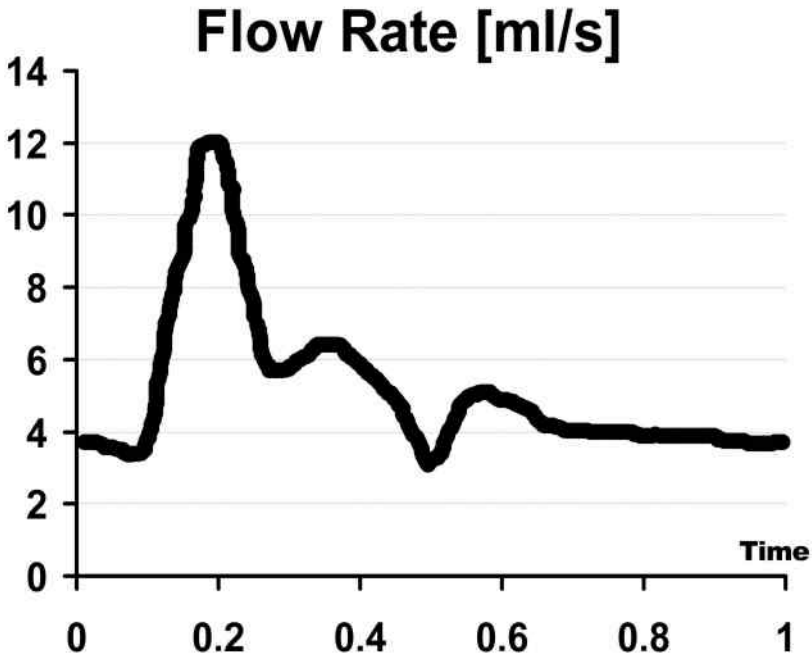
Flow Rate [ml/s]

Figure VI.17.: Flow Rate Data. This flow wave form was obtained from the common carotid of a normal subject using pulsed Doppler (see section II.3.3.1 on page 61). It was used to calculate time-varying Womersley profiles,[368] which were imposed at the inlet of the numerical model.

carotid of a normal subject using pulsed Doppler (see section II.3.3.1 on page 61), was used to calculate Womersley profiles.[368] These time-varying velocity profiles were imposed at the inlet. Since the same flow wave form was used in all simulations, the inlet velocities derived from the Womersley theory could be different depending on the inlet area. When analysing the results, one has to be aware that this solution is an oversimplification, however, the downstream effects of using idealised boundary conditions but true flow rates have been shown to be minimal after a short redeveloping distance (less than 1.5 diameters).[122]

At the outlet, a constant flow ratio of 70:30 was adopted between the internal carotid artery (ICA) and external carotid artery (ECA) throughout the whole cardiac cycle.

Derived Parameters   Time-averaged wall shear stress (WSS), and several other WSS derived parameters were evaluated. These included the oscillatory shear index (OSI, equation II.31), time-averaged spatial wall shear

stress gradient (WSSGs, equation II.32), temporal WSSG (WSSGt, equation II.35), wall shear stress angle deviation (WSSAD, equation II.36) and wall shear stress angle gradient (WSSAG, equation II.39). Apart from the WSS, OSI, WSSAD, WSSAG and WSSG, other haemodynamic parameters (such as the maximum WSSGt in a cardiac cycle[283]) have been introduced and validated in literature. For practical reasons, the flow analysis has been restricted to the aforementioned haemodynamic parameters.

Quantitative Analysis of Reproducibility   Flow patterns cannot be compared in a direct manner. The velocity profile is three-dimensional and time-dependent. The wall shear stress and derived parameters are even less comparable: the geometry of the vessel wall in scan A differs (slightly) from scan B, and it is exactly on the vessel wall that the shear parameters are of high clinical importance. The results on the walls from 2 different scans need to be compared while making abstraction of the wall itself. The following ways of analysing these complex patterns were introduced here.

Area of overflow/underflow

Areas of low ($< 0.5\ N/m^2$) and high ($> 2.5\ N/m^2$) time-averaged WSS were identified.[208] Thresholds like those for the time-averaged WSS were also defined for OSI (> 0.2), WSSGs ($> 4\ kN/m^3$),[173] WSSGt ($> 50\ \frac{N}{s\ m^2}$) and WSSAD ($> \frac{\pi}{3}$).[143] For each case, the area trespassing these thresholds was calculated and presented as a percentage of the bifurcation area. The difference in area percentage between results corresponding to two scans of every subject indicates the error. Dividing this error by the scan-averaged value yields a relative error.

Maximum Velocity and I/S Correlation

The V_{max} (see section II.3.3.2 on page 67) can be represented as a function of the I/S axis. Note that the origin of the I/S axis was at the bifurcation point for each scan, allowing alignment of the data for comparison between scans. This way of representing the results provides information concerning the 'equality' of the velocity pattern in both scans.

A similar approach was used for the wall shear stress parameters. For each cross-section, a mean was calculated, allowing the differences between scans to be evaluated at each location. In addition to quantifying the difference along this axis by a Root Mean Square method, a correlation coefficient R was computed, comparing the curves obtained from the two

scans on each of the subjects. The correlation coefficient is a normalised measure of linear relationship between two sets of data, with R=1 indicating straight line relationship and R=0 uncorrelated.

Statistical Analysis

Differences between the reconstructed geometries of the two scans for each individual lead to differences in the associated meshes. Consequently, a mesh point in mesh A will not coincide with a mesh point in mesh B, making a point-by-point comparison impossible. Thomas[333] described a method to overcome this difficulty by displaying the wall thickness and the WSS related parameters as patched data. In short, 'patching' the data in this study consisted of four steps. First, the three arteries were disconnected from each other. Second, the vessel was 'cut open' and 'unwrapped' until a flat irregular shape was obtained. The line along which the individual arteries were cut depended on the mesh structure (see Figure VI.16). Third, this irregular shape was transformed into a rectangle. Finally, the vessel wall was divided into small rectangular *patches*, and each patch was colour-coded by the average value of the shear stress parameters in that patch. Patching allowed a paired student test to be performed (p<0.05).

The number of patches differed between every artery and subject. Selecting too few patches could smooth out important features in a distribution. However, too many patches would cause the patched values to be overde-pendent on local geometry features, allowing small geometrical differences to introduce large errors. The number of patches in the circumferential and longitudinal direction of the vessel was therefore chosen based on their abil-ity to minimise the variance of (e.g. WSS) values of the cells lying in a patch and maximise the number of normal error-value distributions. Typically, a high number of patches were required along the circumference (up to 12 patches, i.e. 1 patch every 30 degrees). There was, however, no preferen-tial number of patches along the longitudinal direction.

For each artery, parameter and subject, two sets of patched data were ac-quired: one for each scan. The 'resemblance' between those two scans was assessed using a linear regression analysis. This would result in a 2D linear correlation factor *2DR*, which was close to 1 if the 'resemblance' was high. As opposed to the vertical axis analysis, the correlation performed here was two-dimensional. It should be emphasised that correlation param-eters provide little information about accuracy. For example, if the values of the WSSG in scan A were exactly twice those of scan B, *2DR* would be maximal, i.e. 1. The accuracy of measurement, however, would be low. This

does not imply that the *2DR* should be discarded: the correlation parameters are very useful in assessing the qualitative agreement between two scans: if one scan delivers low values in a particular part of the vessel wall but high values in the subsequent scan, then the correlation parameter will be very small (i.e. near zero).

VI.4.2.2. Results

Correlation between measurements   Three of the comparative tools used to quantify reproducibility between scan A and scan B, provided a feel for the *qualitative* agreement. The 'I/S Correlation' and 2D Correlation expressed respectively how good the resemblance was between two scans when travelling through a vessel or when unwrapping the vessel wall. Finally, the overflow/underflow analysis showed whether or not the surface of zones undergoing 'pathologic' WSS related parameters can be determined.

Figure VI.18 provides an example of the vertical (or I/S) correlation analysis. Table VI.2 shows the averaged R-values for every artery and parameter. With the exception of spatial WSSG, all correlations were greater than 0.70, indicating that the qualitative agreement was high when evaluated by travelling through a vessel. Predicting locations prone to particle deposition (embodied in WSSAD) seemed to be less reproducible in the CCA. Taking all the derived parameters into account, as shown in Table VI.2, there appeared to be no difference in the reproducibility between arteries.

Figure VI.19 shows the patched WSSAD distribution for the ICA for scan A (left) and scan B (right) for subject 3. The corresponding 2D correlation was 0.80. Table VI.3 gives the averaged $2DR$ values for every artery and parameter. The results suggest that combined MRI and CFD achieve an acceptable qualitative reproducibility, as the mean values for every parameter

Artery	V_{max}	WSS	OSI	WSSGs	WSSGt	WSSAD	mean
CCA	0.76	0.71	0.74	0.75	0.78	0.57	0.72
ICA	0.83	0.72	0.79	0.54	0.77	0.83	0.75
ECA	0.76	0.71	0.83	0.53	0.74	0.83	0.73
mean	0.78	0.71	0.79	0.61	0.76	0.74	0.73
S_d	0.04	0.01	0.04	0.13	0.02	0.15	-

Table VI.2.: Mean I/S correlation R for all subjects (n=8). Values closer to 1 have more important resemblance. See Figure VI.18 for an example. S_d is the standard deviation of the mean correlation coefficients for different arteries. Small values of S_d indicate less variations of reproducibility among vessels (CCA, ICA and ECA).
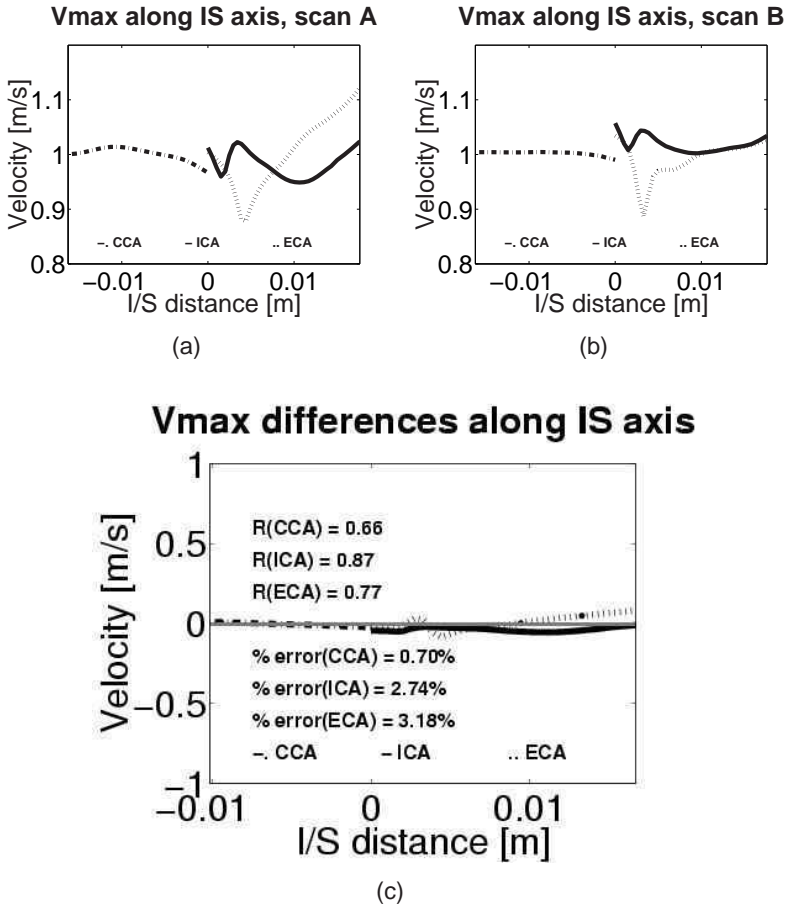
Figure VI.18.: An example of maximum velocity V_{MAX} [m/s] analysis along I/S axis [m]: scan A (a), scan B (b) and the difference (c). I/S: inferior-superior axis. The factors R are linear correlation parameters. The errors given are root mean square errors.

were greater than 0.70. However, all parameters, except WSS and WSSGs, were not reliably reproducible in the CCA. The relatively low $2DR$ values were due to the fact that the haemodynamic parameters in the CCA were either fairly uniformly distributed, or close to zero. The OSI, for instance, is fairly constant in the healthy CCA, and does not differ substantially from zero. This resulted in a low 2DR value even for a rather small deviation.

Overflow/Underflow analysis Results showed that areas of low WSS (maximum error 9%), high OSI (2%), high WSSAD (1%), high WSSGs (0.15%) and high WSSGt (1.5%) were better reproduced than areas of high WSS (20%).

WSS Angle Deviation for ICA

WSS Angle Deviation for ICA

0.00　　　　　0.50　　　　　1.01　　0.00　　　　　0.50　　　　　1.01

(a)　　　　　　　　　　　　　　(b)
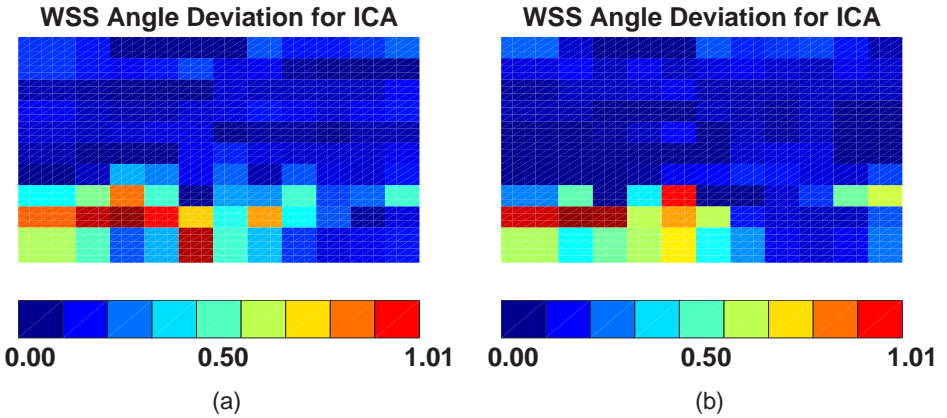
Figure VI.19.: Patched WSSAD in ICA for subject 3, scan A (a) and scan B (b). The bottom end of the picture represents the bifurcation, the top end is the ICA outflow. Thus, blood flow direction is upwards in this representation of the vessel wall. Patching the data allows statistical evaluation. Here, the $2DR$ is 0.80 and the paired t-test yielded a value of 1.548.

Artery	WSS	OSI	WSSGs	WSSGt	WSSAD	mean
CCA	0.70	0.58	0.75	0.59	0.63	0.65
ICA	0.84	0.75	0.90	0.82	0.78	0.82
ECA	0.81	0.82	0.88	0.80	0.83	0.83
mean	0.79	0.71	0.84	0.74	0.75	0.76
S_d	0.07	0.12	0.08	0.12	0.10	0.05

Table VI.3.: Mean 2D correlation of the patches for all subjects (n=8). Values closer to 1 have more important resemblance. See Figure VI.19 for an example. S_d defined in Table VI.2.

Differences between measurements　The Root Mean Square of the velocity errors along the I/S axis (as defined on page 129) was 2.5% for the CCA, 4% for the ICA and 4.5% for the ECA.

The mean differences (mean of values in scan A minus values in scan B) for all the WSS derived parameters are shown in Table VI.4 with associated RMSE. The error used to calculate the RMSE is the difference between the value of a patch in scan A and scan B *and the most likely value*, i.e. the mean of the value in scan A and B. All errors are at least one order of magnitude smaller than the range in which the considered haemodynamic parameter is considered clinically important *(see Area of overflow/underflow)* and the RMSE is greater than the mean error in all cases. These findings show that the haemodynamic error between the two scans is clinically acceptable.

The paired t-test yielded for Figure VI.19 a t-value of 1.548, and thus considered reproducible (p<0.05). The paired T-test is a useful tool as it can

	artery	WSS [N/m^2]	OSI [-]	WSSGs [N/m^3]	WSSGt [$\frac{N}{m^2.s}$]	WSSAD [-]	WSSAG [rad/m]
Mean	CCA	0.0196	3.13e-04	10.3	-0.177	8.21e-04	0.65
error	ICA	0.0280	-6.23e-04	50.1	0.277	-4.01e-03	1.23
	ECA	-0.112	1.74e-03	74.6	-0.867	6.81e-04	5.54
	mean	-0.0216	4.77e-04	45.0	-0.256	-8.35e-04	2.04
RMSE	CCA	0.175	0.0129	114	0.817	0.0969	22.1
	ICA	0.543	0.0325	234	2.97	0.120	67.8
	ECA	0.563	0.0296	213	3.27	0.0972	77.3
	mean	0.427	0.0250	214	2.35	0.105	68.1
%	CCA	35.0	89.9	67.1	20.4	79.5	64.5
	ICA	24.9	107	68.9	19.5	121	97.5
	ECA	39.6	129	56.1	35.0	106	72.0
	mean	37.9	123	65.7	30.2	102	79.8

Table VI.4.: Mean error and RMSE, (n=8). The 'error' is the difference between the value in a patch from scan A and that from scan B. The error used to calculate the RMSE is the difference between the value of a patch in scan A and scan B and the mean of the value in scan A and B. The percentage is the RMSE divided by the average value.

Artery	WSS	OSI	WSSGs	WSSGt	WSSAD	Total
CCA	4/7	8/8	3/4	4/4	7/8	26/31
ICA	4/6	5/5	5/6	4/6	7/7	25/30
ECA	3/6	5/7	6/7	2/5	6/6	22/31
Total	11/19	18/20	14/17	10/15	20/21	73/92

Table VI.5.: Reproducibility summary for all 8 subjects. The first number is the number of times the T-test gave a reproducible result. The second number is the number of times the error-value distribution was considered normal (for details, see Bland and Altman[30]). The maximum normal distributions per artery and parameter is equal to the number of subjects.

be applied to different carotid geometries, different meshes and to all possible wall related parameters. However, it does assume the error is normally distributed. The normality of the data distribution was tested using the 95% rule.[30] Cases that did not show a normal distribution for the error, were examined for a relationship between the error and the scan-averaged value.

The results of the paired T-test are tabulated in Table VI.5. Overall, a reproducibility rate of 79% (73/92) was found. Considering each individual parameter, the WSSAD (95%) and the OSI (90%) did remarkably well when compared with the WSS (58%) and both WSSGs (82%) and WSSGt (75%). The results also suggested that the parameters were less reproducible in the ECA than in the other arteries.

Whenever the errors were not normally distributed, the presence of a systematic error was suspected. In the case of the OSI, a linear correlation

between errors and values was always found, whereas this was only sporadically the case for the other parameters.

VI.4.2.3. Discussion

Moore[224] has found that the peak error in WSS in a straight tube can be up to 60%, due to limited spatial resolution, image segmentation and model reconstruction. Even after geometric smoothing, they reported an uncertainty of 16%. They noted that this value could in no circumstances be regarded as the worst case, because of the simple geometry used in their experiments. Considerable efforts have been made to reduce the processing time from image acquisition to simulation, and, more importantly, maximising the reliability and amount of information obtainable with the combined MRI and CFD approach. This may be achieved by shortening the acquisition time,[262] automating the contour-extraction[164, 197, 262] or the mesh generation,[55] speeding up the numerical solver[203] or writing a user-friendly software that integrates all the actions from contour-extraction to CFD data processing.[324] The quality of simulation can be improved by using a measurement technique with little artefacts.[59, 93] Other ways to improve the quality of a simulation are: minimising errors in segmentation of geometry,[54] generating higher quality grids,[54, 192] and setting more reliable boundary conditions.[49, 122, 261]

In this study, the overall reproducibility of the combined MRI/CFD approach has been assessed. The three arteries in the carotid bifurcation are anatomically very different. The CCA has a significantly larger cross-section than the ECA, and the ICA starts with a very individually shaped bulb. These features can influence the haemodynamics greatly, and imply that the reproducibility in the three arteries might be different. Moreover, it has been demonstrated in the past that the geometric accuracy of the reconstruction is related to the artery diameter.[194] Our results showed that qualitatively, there was no suggestion that the reproducibility of any of the arteries differed. Quantitatively however, Tables VI.4 and VI.5 suggest the ECA is less reproducible, albeit slightly. This may be due to relatively smaller dimensions of the ECA, making the effect of uncertainties in MR acquisition more important.

Overall, the qualitative agreement between the two scans was very good, demonstrating that the combined MRI/CFD approach is capable of producing highly reproducible patterns of various WSS related parameters. Quantitatively, the reproducibility varied depending on which parameter was of
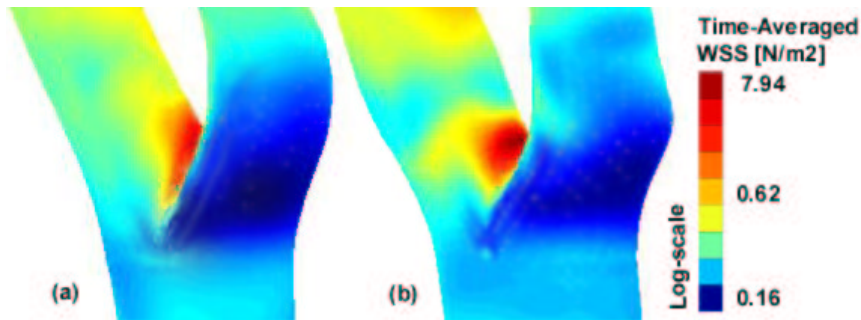
Figure VI.20.: Time-Averaged WSS distribution for subject 4 in scan A (a) and scan B (b). Differences in wall areas having high WSS (in red) are much more pronounced than those having low WSS (in dark blue).

particular interest. However, it should be borne in mind that a number of assumptions were made in this study, including Newtonian blood viscosity, rigid wall and idealised inflow velocity profiles. These assumptions will influence the predicted WSS magnitude, and therefore the flow patterns obtained here will differ slightly from the physiological ones. Nevertheless, for relative flow comparisons between two serial scans, these assumptions are considered justifiable.

Time Averaged Wall Shear Stress   The time-averaged WSS was not adequately reproducible (reproducibility rate of 58%). It appears that predicting areas of high time-averaged WSS - occurring near the bifurcation point - is difficult, making these estimations unreliable. This does not appear to be the case when quantifying areas of low WSS as illustrated in Figure VI.20. It means that at the bifurcation point, the predicted values of WSS could be unreliable. Modelling and meshing the bifurcation area has proven to be a difficult task in the past, which is why, as suggested by Cebral,[55] sophisticated meshing programs and detailed geometry reconstruction tools should be applied when high WSS are of particular interest.

Oscillatory Shear Index   Areas where the direction of the WSS vector changes frequently will have high OSI values which have been related to intimal thickening. The OSI proved to be highly reproducible (reproducibility rate of 90%). Systematic errors tended to occur only with the OSI, as illustrated in Figure VI.21 by the red arrow. Errors in geometric reconstruction can lead to exaggerations in the areas of flow separation predicted by CFD, increasing the OSI. This phenomenon does not appear to involve er-
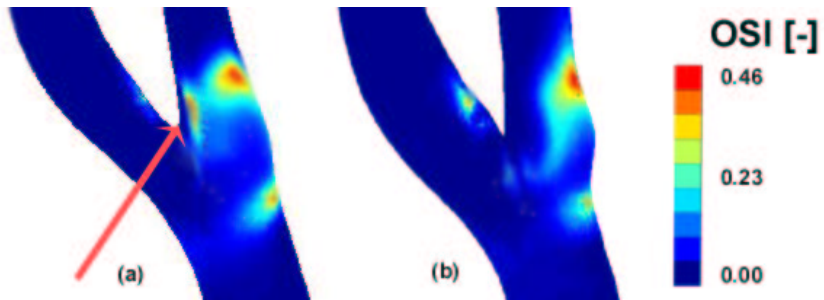
Figure VI.21.: OSI distribution for subject 7 in scan A (a) and scan B (b). Relatively small deviations in the geometry can cause OSI peaks to occur in different locations. In scan A (a), an OSI peak is found in the bifurcation region (in the ECA, indicated by the red arrow), whereas this peak is not there in scan B (b). This effect will become clear numerically in a Bland-Altman plot. However, this geometrically induced flow difference does not influence the reproducibility significantly.

rors large enough to significantly affect the reproducibility as assessed by the paired T-test, or make the error in the area trespassing an OSI value of 0.20 significant.

Wall Shear Stress Angle Deviation & Gradient   WSSAD was highly reproducible both when assessed qualitatively and quantitatively, suggesting that MR image-based CFD predictions have a good potential for predicting areas prone to particle deposition and prolonged particle residence time. The RMSE's for the WSSAG, summarised in Table VI.4, are comparable with values found in a similar reproducibility study using BB MRI as a basis.[332]

Wall Shear Stress Gradients   The WSSG proved to be a more difficult parameter to reproduce, and the spatial WSSG more than the temporal one. As was the case for the time-averaged WSS, high WSSG values occurred at the bifurcation point. WSSGs is, because of its derivative nature, very grid dependent and therefore sensitive to geometry changes. Whilst quantifying the WSSG is difficult, the high $2DR$ values showed that the WSSG distribution can be done reliably, a finding consistent with those of Siauw,[283] who showed that the WSSG was very sensitive to changes in computational rheological parameters, whereas the WSSG distribution remained the same. Our findings showed that the WSSG *distribution* is reliable, although WSSG *values* were not. If WSSG values are to be used for further analysis of wall permeability - as suggested by Lei[171] - imaging and meshing quality will have to be improved, especially for the area near the bifurcation point. This

finding sheds a new light on mesh convergence tests. When CFD was first introduced, mesh dependence meant making sure the calculated velocities on a coarser and a finer mesh were the same. Later,[253] the WSS field superseded the velocity field as the determinant for mesh density; WSS requiring a denser mesh for grid convergence. Our data now suggests that WSSG should be used to determine the mesh density if WSSG values are of great importance.

Relation of Flow Errors to Geometrical Errors The area agreement and parameters z_{DIST} and SF_c were quantified in a study by Long.[194] Since the same boundary conditions were used in all the simulations, differences in predicted haemodynamic parameters were only due to geometric variations. Further study will aim to relate mathematically the haemodynamic errors to geometric variations. Among the geometrical factors already investigated, were relationships between the error in velocity and cross-sectional area, since the flow rate was constant. Classical fluid mechanics theory also dictates that for a fully developed flow in a circular tube, WSS is inversely related to the third power of the tube radius. For more complex geometries, Thomas[334] found that vessel out-of-plane curvature could influence the WSS distribution greatly, whereas non-planarity of the bifurcation did not, implying that geometric errors would have a more pronounced effect on WSS predictions when vessel out-of-plane curvature is high. Other factors, such as difference in cross-sectional shape, may also contribute to differences in WSS and its derived parameters.

Preliminary results showed that there were no simple relationships between haemodynamic errors and single geometric error. For complex geometries such as the carotid artery bifurcation, all geometric parameters including vessel tortuosity, cross-sectional area or cross-sectional shape may act together to influence the total haemodynamics, making it very difficult to point out which geometric error is to blame for the occurring haemodynamic differences.

VI.4.3. Conclusion on Accuracy and Reproducibility of MRI-based CFD

In section VI.4.1, it was shown that the combination of MRI and CFD was ready for *in vivo* application: a carotid phantom was scanned using both TOF and BB MR imaging protocols, and the reconstructions showed good

accuracy when compared with the exact geometry (see Table VI.1). In parallel, it was shown that 3D smoothing, apart from filtering high-frequency changes in the vessel wall distribution as discussed in section VI.3.1, did not influence the important geometric features of a 3D carotid reconstruction. Furthermore, it was found that the BB and TOF scans compared very well to each other.

In the reproducibility study (section VI.4.2), the carotid arteries of 8 healthy subjects were scanned twice. For each scan, the flow patterns were reconstructed using a combination of MRI and CFD. The resemblance between flow patterns was assessed by comparing the clinically important haemodynamic parameters both qualitatively and quantitatively.

All differences in flow patterns are due to geometric uncertainties since the effect of boundary conditions was excluded. The geometric uncertainties influenced the flow patterns in different ways. Overall, the flow was reproduced very well. Velocities were reproduced with an accuracy of over 95%, OSI and WSSAD had reproducibility rates above 90%. Poor reproducibility was found in the region around the bifurcation apex where WSS is usually high. Hence, special care should be taken to model the bifurcation apex area and sophisticated mesh generators should be used if high WSS is of main interest. These steps should also be followed if the focus of interest is the WSSG. In addition, grid convergence criteria should be refined until the error in WSSG is below a certain threshold, rather than using the error in WSS or the velocity. Finally, this study has shown that haemodynamic differences may not be attributed to a specific geometric factor, but rather result from the interaction of the entire set of geometric differences taken as a whole.

VI.5. Black Blood MRI vs Time-Of-Flight

VI.5.1. Introduction

Time-of-flight (TOF), phase-contrast (PC) and black blood (BB) methods are among the most common magnetic resonance angiography (MRA) techniques. *TOF* images rely on short repetition times 'T_R' (in the order of tens of milliseconds) to saturate all stationary tissue. This distinguishes flowing blood from the vessel wall, producing an image with white ('bright') blood. Its use is common for cerebral,[235] carotid,[121] liver,[318] pelvic[197] and renal angiography.[211] However, signal loss occurs when flow is in-plane and short 'T_1' tissues (such as fat and thrombus) can appear the same as flow. Consequently, TOF may not be the optimum imaging method for angiography. *PC* images contrast the spin phase stability of stationary protons against the phase accumulation of flowing protons as they move through an MR gradient field. Thus, PC MRA allows velocity measurement. The major drawback of PC MRA is the longer imaging time. Furthermore, PC MRA requires larger voxel sizes which makes it susceptible to artefacts in zones of complex flow such as the carotid bulb. Thanks to the ability to visualise slowly moving fluids, PC tends to be used for intracranial arteries,[52] venous occlusive disease,[183] renal arteries[211] and arteriovenous malformations.[57] Furthermore, PC MRA is used for blood velocity,[122, 240, 361] shear stress[161] and strain rate[81] measurements. *BB* imaging saturates the magnetic signal from flowing blood, rendering the lumen dark while retaining the magnetic signal from surrounding tissue. As with TOF, BB MRA is relatively insensitive to slow flow, but it has the ability to visualise blood vessel wall characteristics. BB is used for imaging intracranial arteries,[190] carotid vessels,[71, 308] liver perfusion,[318] aorta[309] and coronary arteries.[93]

PC MRA has to our knowledge never been used for carotid bifurcation reconstruction, probably because of the extended duration of the scan protocol. When the flow through the reconstructed carotid arteries is to be calculated with CFD, PC MRA is very common and reliable as a velocity acquisition technique.[56] Traditionally, TOF images have been used for carotid bifurcation reconstruction, contrast enhanced at first,[50, 55, 195] but bolus^c-free scans have proved efficient as well.[121, 194, 225, 262, 384, 387] BB MRA gives the advantage of allowing wall thickness and wall volume measurements,[71] two early markers of atherosclerosis.[13, 272] Steinman and co-workers have been pio-

---

^{c}**bolus**: A concentrated mass of a substance administered intravenously for diagnostic or therapeutic purposes

neers in the use of BB MRA-based carotid haemodynamics,[219, 307, 308, 332, 333, 334] and their example has been followed by others.[119, 120]

The purpose of this study is to determine *which of the TOF or BB MR imaging modality is preferable for carotid geometry and flow reconstruction*. Therefore, the right carotid bifurcations of 8 young hypertensive subjects were scanned 6 times: thrice with BB MRA and thrice with TOF on 3 separate occasions.

VI.5.2. Methods

VI.5.2.1. Subjects and Scan Timing

Eight subjects were scanned. These subjects were young patients (mean 42 (35-52) years) with hypertension (systolic blood pressure >150 mmHg and/or diastolic > 90 mmHg) and were taking part in a randomised, placebo controlled, double blind cross over study examining the effects of two antihypertensive drugs on carotid blood flow. See chapter XII for a detailed decription of the study protocol. For future reference, the subjects will be numbered 1 to 8. Scans were performed on three separate occasions, each scan following a week of treatment with either a placebo or one of the studied anti-hypertensive compounds. On each of these three occasions, the right carotid artery was scanned twice, once with BB MRA and once with TOF MRA. Thus, data sets comprised 24 TOF scans and 24 matching BB MRA scans. The scans between sessions were not compared for reproducibility as both compounds have been shown to have effects on carotid artery remodelling, albeit at 14 weeks of treatment.[302] For reproducibility studies for the TOF technique see Glor[121] and for BB MRA see Thomas.[332]

VI.5.2.2. MRA protocol

All MR scans involved were carried out on a Siemens Magnetom Sonata 1.5T scanner. The images were acquired using a purpose-built 2-element phased-array coil.

Black Blood MRA protocol   For each subject, two sets of images were acquired at different phases of the cardiac cycle, typically at mid-to-late di-

astole and end-systole. In this study, 'systole' refers to the moment in the cardiac cycle where the carotid cross-section is maximal. For these *volume selective Turbo Spin Echo (TSE)* images, a true (non-interpolated) pixel size of 0.47 x 0.47 mm in-plane (zero-filled on reconstruction) and a field-of-view (FOV) of 120 x 24 mm were typical with 28 slices (2 mm thick). An echo train length of 11 was used to fit the scan within the desired acquisition window (65 ms). For a T_1 weighted image, T_E was 11ms and gating was every cardiac cycle (T_R=RR, the interval between consecutive R-waves). Each 3D image acquisition took 3 to 5 minutes, depending on the subject's heart rate. Further details on the scan protocol have been described by Crowe.[71]

Time Of Flight MRA Protocol   The TOF scan parameters were 28 contiguous slices 2mm thick, FOV 130 x 100mm, 0.52 x 0.52 mm pixel size, T_R 28 ms, T_E 7ms. The TOF images were acquired in the exact same planes as the BB scan.

3D Phase Contrast   The BB and TOF series were required for geometry reconstruction. Complementary, PC flow measurements were carried out in the CCA at a slice position in line with geometry scans as close to the most proximal slice as signal to noise ratio (SNR) would allow. A second scan was taken in the CCA for a slice relatively close to the bifurcation but far enough to ensure undisturbed flow. ECA and ICA flow were measured as far distal as possible but before any ECA branching occurred. The in-plane resolution was 1.1 x 0.75mm with a slice thickness of 6mm. The first scan, close to the first slice, will be referred to as the 'inlet' scan, the other two scans as 'midpoint' and 'outlet' scan. For the outlet and midpoint scan, temporal resolution was 29ms (1 reference and 1 velocity encoded image). The inlet flow was measured in 3 orthogonal directions (1 reference and 3 velocity encoded images) thereby reducing the temporal resolution by a factor of 2. This reduction in temporal resolution is the price paid for acquisition of velocities in the three orthogonal planes. The assessment of the blood flow rate, performed using the 'midpoint' scan, is not affected by this loss of temporal resolution in the 'inlet' plane.

VI.5.2.3. 3D Reconstruction

The segmentation and reconstruction procedure has been thoroughly explained in sections VI.2-VI.3. Carotid reconstructions were performed using

the region growing method and snake method, in some cases preceded by a bilinear interpolation, median filter or gamma filter. An operator was allowed to make manual corrections. This segmentation protocol only worked if blood was darker than its surroundings, therefore the TOF images were inverted before segmentation. This was the only difference in image treatment between the TOF and BB images.

MRA yielded serial contours in equidistance planes. With the knowledge of the position of the contours in 3D space, they can be positioned accordingly to produce a 3D vessel surface geometry. Smoothing was performed in two steps[224] using smoothing parameters calculated in a separate study.[120]

VI.5.2.4. Meshing

The mesh was generated using an enhanced in-house purpose-built mesh generator described in section III.2.2 (page 76). Figure VI.22 (a) shows a mesh reconstructed from BB MRA for subject 5, scan 2, whereas the mesh for the matching TOF scan is given in Figure VI.22 (b).
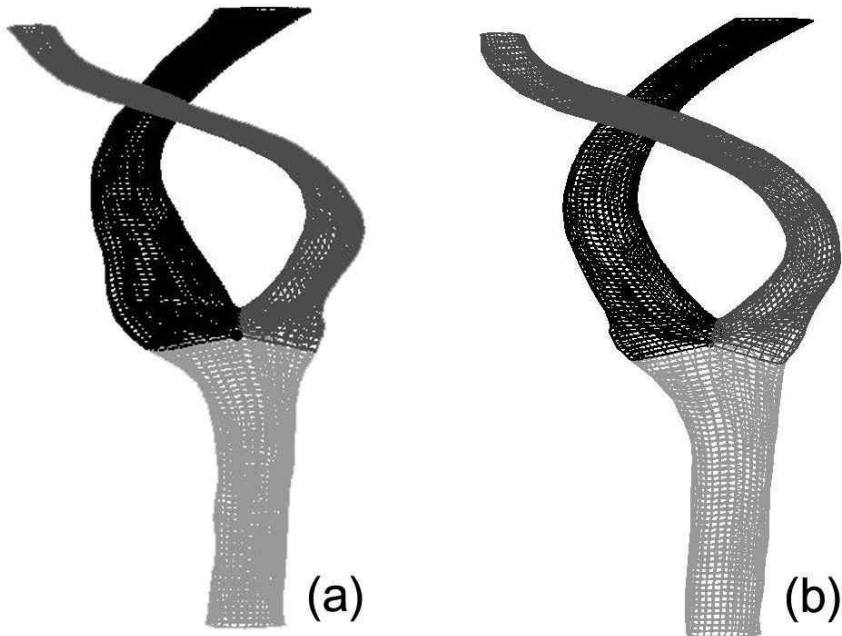
Figure VI.22.: 3D Meshes for subject 5, scan 2. a: BB MRA; b: TOF MRA. Note the very high tortuosity of the ECA (dark grey) and the good agreement between the BB and TOF scan.

VI.5.2.5. Computational details

The Navier-Stokes equations for laminar flow were discretised using the 'QUICK'-scheme explained in section III.4.1.1. Two cardiac cycles of 80 equally spaced time-steps were simulated. The size of the time-step varied according to the measured heart rate. Blood density was 1176 kg/m^3, and the Quemada-model was used for modelling the non-Newtonian viscosity of blood.[42] The wall was modelled as a rigid, no-slip surface. Because of the important influence of secondary velocities on carotid blood flow,[282] the velocities were measured in 3 dimensions at the inlet of the CCA. The axial velocities were filtered for partial volume effects by discarding the velocities at the vessel wall if they were higher than 20% of the V_{enc}. In each voxel, secondary velocities larger than 30% of the axial velocity were also discarded. The discarded velocities were replaced by interpolated values. Hence, for each voxel, a time-dependent velocity profile was reconstructed. As explained further down the manuscript (section VIII.1.1), the velocities were scaled to match a reliable measurement of the flow rate. Flow rate was evaluated from the 'midpoint' cine images. At this location, the velocities were only measured in the axial direction as opposed to the 3 directions in the inlet plane. As a consequence, a higher time-resolution was achieved ($\pm$ 28 images as opposed to $\pm$14 images per cycle). Thus, the flow rate deduced from the 'midpoint' scan was more reliable than the 'inlet' scan. Flow rate measurements were performed using CMRTools (Imperial College London, London, UK). In short, the flow rate was found by drawing a contour (representing the lumen border) on the cine image. The velocities inside the lumen were integrated in space in each image. Per image, this technique yields an instantaneous flow rate. The time-dependent flow rate was found by piecewise cubic interpolation. The 'outflow' cine series were used to compute the time-varying ICA and ECA flow rates. From the calculated outflow rates, time-dependent mass outflow ratios were deduced and set as boundary conditions on the model outlets.

VI.5.2.6. Comparative Parameters

The aim of this study was to assess the two MR imaging methods for carotid geometry and flow reconstruction when combined with CFD. For the purpose of quantitative analysis, a number of geometry and flow parameters were computed and compared. The geometry parameters, summarised in Table VI.6, include the average cross-sectional areas in the CCA, ICA and ECA (A_{CCA}, A_{ICA}, A_{ECA}), the area ratio A_R, the non-planarity parameter

NP and linearity parameter L as defined by King[157] (NP, NP_{CCA}, NP_{ICA} and NP_{ECA}, L_{CCA}, L_{ICA} and L_{ECA}), the tortuosity of the vessel (T_{CCA}, T_{ICA} and T_{ECA}), the bifurcation angle α_{BIF} and the individual shape factor (SF_i). See section II.3.2.2 for a definition of these parameters.

Flow parameters included the 3D distribution of the time-averaged wall shear stress (WSS), the oscillatory shear index (OSI), the time-averaged wall shear stress gradient (both spatial (WSSGs) and temporal (WSSGt)) and the wall shear stress angle gradient (WSSAG). These parameters have been extensively defined and described in literature[42, 119, 199] and in section II.3.2.2.

VI.5.2.7. Statistical Analysis

An RMSE (root-mean-square error) was calculated as the mean absolute difference between the parameter calculated in each imaging technique and the mean value of the parameter averaged over the two imaging techniques. Finally, the differences were presented as mean $\pm$ standard deviation and using the methods advocated by Bland and Altman for method comparisons.[30]

Comparing haemodynamic wall data is often done by evaluating patches of averaged data.[121, 332] The patching was performed here using other techniques than those described in the TOF MRI reproducibility study (section VI.4.2). Briefly, *patching* involves separating the three arteries (CCA, ICA and ECA), unwrapping the artery surface and subdividing it into small patches. The definition of the 'end' of CCA and 'beginning' of its branches is given by the mesh structure as illustrated by the three colours in Figure VI.22.

Figure VI.23 explains how the number of patches per artery was defined. In Figure VI.23 (a), the OSI distribution in subject 1, obtained using BB MR images, is shown. After separating the arteries and unwrapping the vessel wall, the OSI distribution in the ICA can be displayed as shown in Figure VI.23 (b). Note that the vessel wall was mapped onto a rectangle coordinate system for statistical analyses. The mapping was performed using the mesh-structure as a basis. In order to avoid any Gibbs-ringing in the following Fourier decomposition, a two-dimensional Hamming window was used to filter the OSI distribution.[329] The two-dimensional Fourier power spectrum was then computed as shown in Figure VI.23 (c). The power-spectrum was used to define the number of patches along the longitudinal and the circumferential dimension: for each dimension, the number of patches was equal
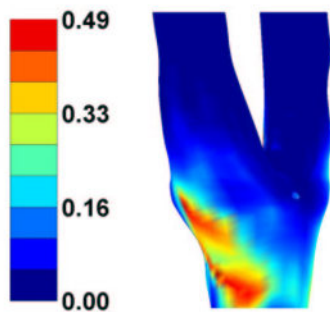
(a) OSI distribution
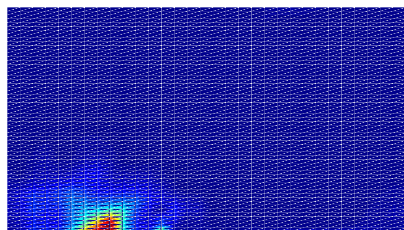
(b) 2D representation of the ICA vessel wall with color-coded OSI (dimensionless)
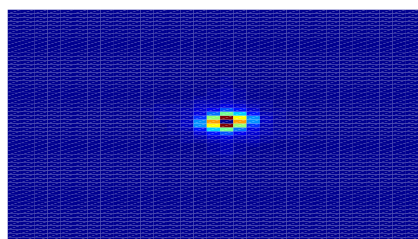
(c) 2D Fourier power spectrum of Figure VI.23 (b) (unit is fraction of total power spectrum)
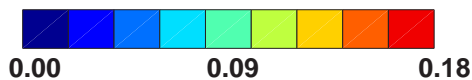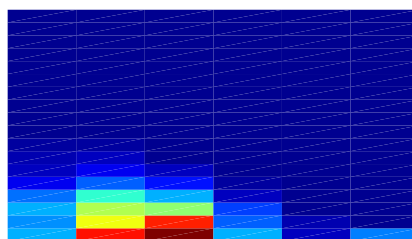
(d) patched representation of the vessel wall with color-coded OSI (dimensionless)

Figure VI.23.: Determining the optimal number of patches

to the number of rows (columns), counting from the middle row (column), needed to include 99% of the power spectrum. The number of patches is limited to one third of the number of elements along each dimension, in order to have a minimum of 9 faces per patch. This way, in two corresponding sets of data (e.g. OSI in ICA for subject 1 from BB and from TOF MRI), 2 sets of patch sizes are suggested: one set for each imaging technique. The largest one would be used to patch both sets of data, because this set would contain at least 99% of the power of both data sets. Once the number of patches was defined, the rotational misalignment was compensated by allowing the artery in one of the scans to rotate over its centreline between -30 and 30 degrees. The optimal alignment was obtained when the two-dimensional linear correlation (function corr2 in Matlab Statistics Toolbox[330]) was max-

imised. Figure VI.23 (d) shows the final patched representation of the OSI in the ICA of subject 1, reconstructed from BB MRI. Here, 19 patches in the longitudinal and 7 in the circumferential direction were needed.

The main advantage of patching is that it allows parameters corresponding to slightly different points in 3D space to be compared using statistical tools. The two-dimensional correlation between two sets of patched data is a measure of parameter *distribution* agreement, whereas the Wilcoxon rank-sum test, the average difference and RMSE are measures of parameter *value* agreement. The error used to calculate the RMSE is the difference between the value of a patch in the TOF scan and the BB scan and the mean of the value in both scans.

VI.5.3. Results

VI.5.3.1. Reconstruction

Figure VI.24 shows MR angiographies at two locations in subject 5: Figures VI.24 (a) and (b) are cross-sections of the CCA, whereas Figures VI.24 (c) and (d) cross-sections of the carotid branches. Figures VI.24 (a) and (c) are performed with the black blood sequence, conversely, Figures VI.24 (b) and (d) were acquired using the time-of-flight procedure. Note how the image quality is poor in the branches using BB MRA.

The hypothesis that TOF MRA yields better image quality is confirmed when looking at the operator intervention rate (OIR). As explained in section VI.2, image segmentation was performed by a manual intervention after an automatic segmentation process, using the region growing method and the snake model. Images of good quality did not require operator intervention. The operator intervention rate was roughly defined as the ratio of the number of contours requiring operator intervention and the total number of contours. For TOF MRA images, the OIR varied between 7% and 41% (mean 28%). For BB MRA images, the OIR varied between 15% and 70% (mean 39%). The image quality was poorest in the end of the CCA for both imaging techniques. As illustrated by Figure VI.24, the higher OIR for BB MRA was due to the lower image quality for the ECA.

The automatic segmentation program searches for the best possible image filter before running the region growing procedure. In practice, TOF images worked best after median filtering (either once or twice). BB MRA images, in
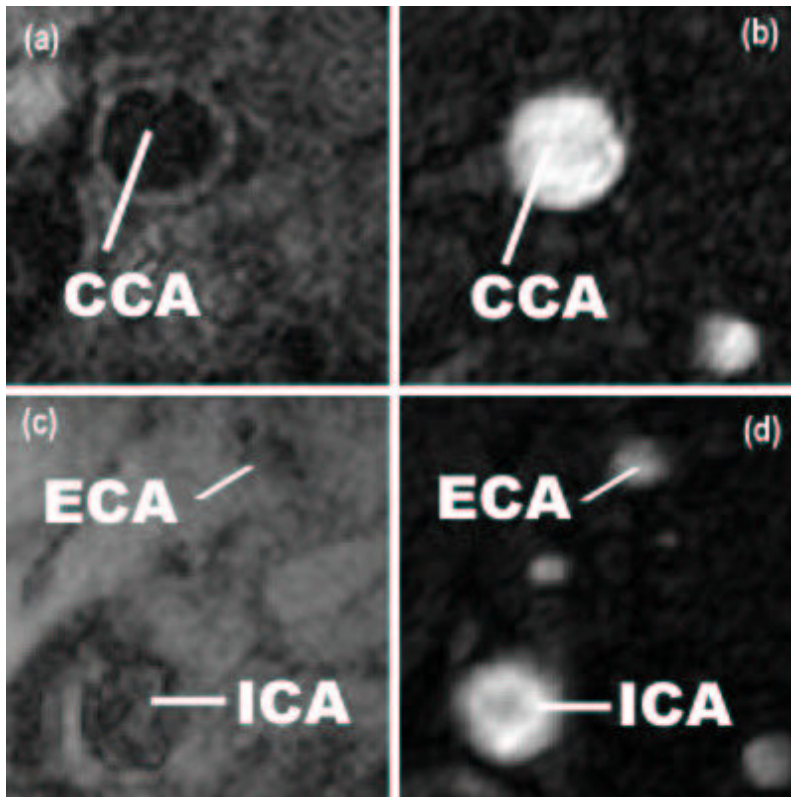
Figure VI.24.: MR images of subject 5. a: BB MRA in CCA; b: TOF MRA in CCA at same location as (a); c: BB MRA in branches; d: TOF MRA in branches at same location as (c).

general, required sequentially 2-dimensional interpolation, median filtering, and a 0.9 gamma filter.

VI.5.3.2. Geometry comparison

Table VI.6 summarises the results for the geometry parameters. The table contains the mean $\pm$ standard deviation of the considered parameter in each imaging technique and the mean $\pm$ standard deviation of the difference between the techniques. Furthermore, a paired Student test was performed, yielding a p-value related to the hypothesis that the considered parameter is equal in both imaging techniques. Finally, the last column of Table VI.6 shows the RMSE (as absolute value and as percentage) of the considered parameter, defined as half the mean absolute difference.

	BB	TOF	TOF-BB	p	RMSE
A_{CCA} [mm^2]	47.68 ± 11.37	49.07 ± 12.42	1.39 ± 2.39	0.0106	1.17 (2.42%)
A_{ICA} [mm^2]	25.55 ± 6.33	24.82 ± 6.51	-0.73 ± 3.10	0.2688	1.36 (5.41%)
A_{ECA} [mm^2]	18.45 ± 5.20	16.63 ± 3.99	-1.82 ± 4.07	0.0435	1.58 (9.00%)
A_R [-]	0.89 ± 0.11	0.81 ± 0.12	-0.09 ± 0.15	0.0104	0.07 (7.95%)
NP [%]	4.76 ± 1.80	3.92 ± 1.62	-0.84 ± 0.88	0.0001	0.53 (12.21%)
NP_{CCA} [%]	0.52 ± 0.32	0.45 ± 0.29	-0.07 ± 0.26	0.2037	0.10 (21.19%)
NP_{ICA} [%]	1.13 ± 0.83	1.08 ± 0.91	-0.05 ± 0.32	0.4909	0.13 (11.45%)
NP_{ECA} [%]	1.07 ± 0.70	0.93 ± 0.78	-0.14 ± 0.48	0.1817	0.20 (19.56%)
L_{CCA} [%]	90.05 ± 2.55	92.26 ± 2.17	2.21 ± 0.71	0.0000	1.11 (1.21%)
L_{ICA} [%]	89.02 ± 1.55	91.30 ± 1.59	2.28 ± 0.88	0.0000	1.14 (1.26%)
L_{ECA} [%]	88.49 ± 2.15	90.63 ± 2.68	2.14 ± 1.32	0.0000	1.14 (1.28%)
T_{CCA} [%]	1.30 ± 0.80	1.40 ± 1.06	0.10 ± 1.00	0.6400	0.34 (25.02%)
T_{ICA} [%]	4.28 ± 4.22	5.24 ± 5.55	0.96 ± 2.47	0.0742	0.81 (16.93%)
T_{ECA} [%]	5.05 ± 5.09	5.44 ± 4.96	0.39 ± 2.64	0.4864	0.96 (18.37%)
α_{BIF} [°]	148.47 ± 7.44	149.00 ± 6.99	0.53 ± 4.15	0.5469	1.47 (0.99%)
SF_{iCCA} [-]	0.96 ± 0.03	0.97 ± 0.01	0.01 ± 0.02	0.1254	0.01 (0.72%)
SF_{iICA} [-]	0.97 ± 0.02	0.97 ± 0.02	0.00 ± 0.02	0.7578	0.01 (0.59%)
SF_{iECA} [-]	0.96 ± 0.03	0.96 ± 0.04	0.00 ± 0.02	0.5855	0.01 (0.68%)

Table VI.6.: Comparison of geometric parameters. BB: Black blood; TOF: Time-of-flight; p: p-value testing the hypothesis that the considered parameter was the same in BB as in TOF; RMSE: root-mean-square error calculated as the mean absolute difference between the parameter calculated in each imaging technique and the mean value of the parameter averaged over the two imaging techniques.

VI.5.3.3. Flow comparison

Figure VI.25 shows the WSS, OSI, WSSGs, WSSGt and WSSAG distribution in subject 5, second visit. In Table VI.7, the first 4 lines represent the patched RMSE found here, whereas the bottom 5 lines show the RMSE found in a TOF MRA reproducibility study[121] and a BB MRA reproducibility study.[332]

Artery	WSS N/m^2	OSI -	WSSGs N/m^3	WSSGt N/(m^2.t)	WSSAG 1/m
CCA	0.372 (38.1%)	0.0465 (70%)	99.1 (37.8%)	1.74 (23.7%)	84 (43.9%)
ICA	0.767 (31.8%)	0.0223 (164%)	197 (39.8%)	3.02 (25%)	64.7 (71%)
ECA	1.03 (45%)	0.0233 (179%)	362 (60.6%)	6.33 (38.6%)	86.4 (77.1%)
Mean	0.722 (38.3%)	0.0307 (138%)	219 (46.1%)	3.7 (29.1%)	78.4 (64%)
Mean BB[332]	0.44 (32%)	0.021 (109%)	38 (55%)	-	61 (73%)
CCA[121]	0.175	0.0129	114	0.82	-
ICA[121]	0.543	0.0325	234	2.97	-
ECA[121]	0.563	0.0296	213	3.27	-
Mean TOF[121]	0.43 (37.9%)	0.025 (123%)	214 (65.7%)	2.35 (30.2%)	-

Table VI.7.: Root Mean Square Error for all cases (n=24). Between brackets, the percent RMSE, i.e. 100 x RMSE/(average value). For comparison, the result of two MR reproducibility studies[121,332] have been added.
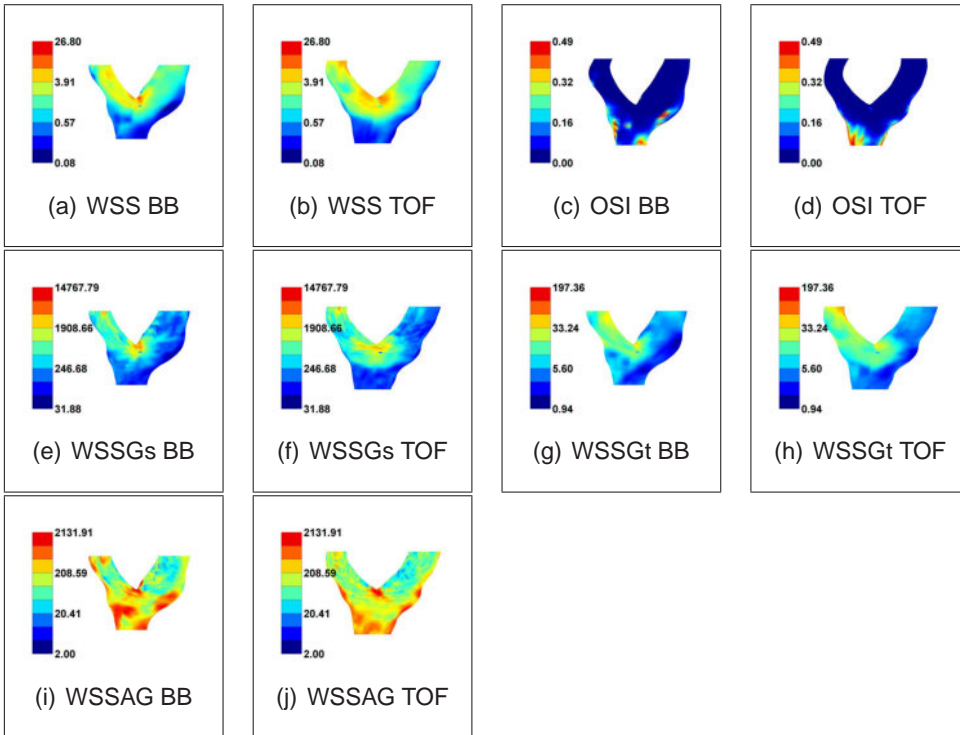
Figure VI.25.: Distribution of the haemodynamic parameters in Subject 5, visit 2 using BB (a,c,e,g,i) and TOF (b,d,f,h,j). a-b: WSS [N/m^2]; c-d: OSI [-]; e-f: WSSGs [N/m^3]; g-h: WSSGt [N/(s m^2)]; i-j: WSSAG [rad/m].

VI.5.4. Discussion

In this study, the carotid geometry was measured using two different MRA-based techniques: TOF and BB MRA. Cine PC MRA was used to quantify flow at boundaries. For the comparison between TOF and BB MRA, 24 scans were performed on 8 different subjects using each imaging technique. The scans were used to reconstruct the 3D geometry of the carotid bifurcation. In addition, cine PC MRA (with 3 orthogonal directions) provided boundary conditions for the numerical simulation of the blood flow.

VI.5.4.1. Chosen Imaging Parameters

The present BB MRA protocol was aimed at increasing the spatial resolution, without a loss of SNR. Precision was increased by zero-filling until an in-plane resolution of 0.47 mm was reached, which is comparable to the in-plane resolution in the TOF protocol (0.52 mm). This agreement in

in-plane resolution favours comparability of the two techniques. BB MRA-based carotid reconstructions have been successfully performed using a higher in-plane resolution (approximately 0.20 mm) by Thomas,[332] but this resolution could not be achieved in every subject without a prohibitively long scan time or loss of SNR. On the other hand, the TOF protocol was performed using a finer in-plane resolution than earlier protocols: previously 0.625 mm,[121,194] now 0.52 mm.

Although a maximum of imaging parameters agreement was aimed for, is was not possible to gate both sequences and to have the same imaging time. Here, the BB MRA protocol was ECG gated, whereas the TOF protocol was not. This way both scans took approximately the same length of time. BB has an inversion time before imaging which impedes the use of the whole cardiac cycle for image acquisition. Moreover, a previous study[71] has shown significant motion of the CCA vessel wall using BB MRI, therefore motion blurring, occurring in an ungated sequence, was suppressed here. In order to be in accordance with the BB scans, the TOF scan should also be gated, but this resulted in unacceptably long imaging times. The use of cycle-averaged (ungated) instead of gated TOF induced a motion blurring at the vessel wall resulting in an averaged geometry, but as a result of a high contrast, TOF images were of high quality despite the motion blurring. In the hypothetical case that BB were ungated, the motion blurring would have had a more severe effect since the narrow wall did not have the same level of contrast as the TOF. Motion blurring would have made wall or lumen boundary difficult to distinguish.

VI.5.4.2. Segmentation and reconstruction

It is clear from Figure VI.24, which represents an average quality image in both the CCA and the branches using each of the two imaging techniques, that the BB image quality gave rise to problems in the segmentation of the ECA. The high OIR and dependence on image filters reinforced the statement that TOF-based reconstructions were more reliable than the BB MRA counterparts.

Since BB MRA results in a slightly better in-plane resolution than TOF (0.47 mm vs 0.52 mm), it was expected that BB MRA would have been more reliable for carotid reconstructions than TOF. The present results suggest that BB MRA was hampered by noise in the branches to such an extent that

the TOF images, with better contrast, yielded better segmentation reliability, despite a coarser resolution.

VI.5.4.3. Geometry Comparison

Areas   The BB images were gated in diastole, whereas the TOF images were not gated at all: each image represents a time-averaged situation. Since diastole lasts longer than systole, TOF images are expected to measure cross-sectional areas only slightly smaller than with BB MRA. This is not reflected in the results for the CCA cross-sectional area (first line in Table VI.6), but the RMSE for the CCA (2.42%) was much lower than the 10% found in BB MRA[332] and TOF[121] reproducibility studies. This means that the differences between TOF areas and BB areas were smaller than the expected variability of each of the techniques. This was also the case for the RMSE in the ICA (5.41%) and ECA (9.00%). However, Table VI.6 showed that the ECA cross-sectional area was almost 2 mm^2 smaller when measured with TOF ($p<0.05$). Following reasons have been postulated for these small differences.

- TOF images may suffer signal loss in areas of slow flow or at stenoses. Similarly, residual blood signal may be seen on BB MRA, but is often distinguishable from the surrounding tissue. Figure VI.26 (a) shows in the top left corner a TOF image taken in the branches of subject 4. The ICA and ECA are well localised, but the slow flow at the lumen border decreases the contrast. Two possible ways of segmenting such an image are presented in Figure VI.26 (a): (i) the image in the top right includes all white signal in the lumen, regarding it as 'slow flow' thus part of the lumen. (ii) The image in the bottom left corner regards some of the white signal as an artefact related to the cyclic motion of the artery. The first contour will be greater than the second contour. Figure VI.26 (a) shows the corresponding BB MRA image in the bottom right. Here, despite the higher noise, the vessel wall is well defined thus giving clarity on the position of the lumen border. In summary, for images free of obvious artefacts and complex flows, TOF tended to focus on the main flow, whereas BB MRA achieves better contrast at the vessel lumen.

- Both imaging techniques have their flaws in regions of complex flow. Figure VI.26 (b) shows in the top left corner a BB image in the distal CCA of subject 4. The distal CCA is marked as a region of complex

(a) Carotid branches   (b) Distal CCA
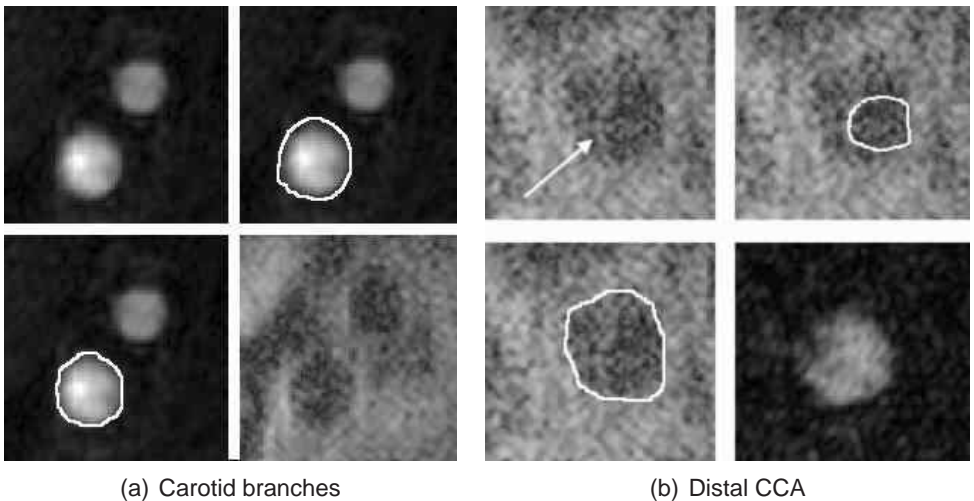
Figure VI.26.: MR images of subject 4. a: Proximal CCA slices: the image at the top left is the TOF image, segmented in two different ways in the images right of and under it. The final image is the corresponding BB image. b: Distal CCA slices: the image at the top left if the BB image, segmented in two different ways in the images right of and under it. The final image is the corresponding TOF image.

flow due to the proximity of the flow divider. Two ways to segment this image are presented in Figure VI.26 (b): (i) in the top right, the operator interpreted the white signal marked by the arrow as vessel wall. (ii) in the bottom left, the operator considered all black signal as blood, despite the lack of a clear definition of a vessel wall. The TOF image in the bottom right, taken at the same position, discarded the first solution, but based on the BB images alone, the distinction could not have been made. In summary, for the bifurcation area, where blood flow is slow and multidirectional, the shortcomings of the TOF images seemed easier to adjust for than for the equivalent BB MRA images, see Figure VI.26 (b). Currently, work is being done on adding a phase sensitive velocity encoding pulse to the BB sequence. With no important change to the acquisition protocol, a magnitude and phase reconstruction could be done and used as a threshold to remove slow flow artefact from the lumen. This should increase BB contrast by reducing residual blood signal.

- Images in the carotid branches seemed to be more reliable using TOF than BB MRA. Apparently, the effect of the low contrast in ECA lumen pushes the automatic program/operator to overestimate the ECA lumen area.

The area ratio A_R, linked to the development of atheroma,[151,278] was apparently difficult to predict judging by the standard deviation of the difference (0.15), an important fraction of the inter-individual variability of 0.25.[278] This low A_R reliability is due to the fact that the areas used for the calculation of these parameters have low accuracy in both imaging techniques, caused by the complex flow occurring at these sites.

Centrelines   When performing the centreline comparison, the importance of the reduced quality of the BB MR images becomes clear: in none of the 24 cases, the centreline was misregistered for the CCA (0%). However, for the ICA and ECA, this went up to respectively 8.3% and 12.5%. Main reason for this centreline mismatch, is the fact that the ECA was not always distinguishable from its branches. As a consequence, the operator regarded one of the ECA branches as the ECA itself. Judging by the very good correspondence in α_{BIF} (see Table VI.6), the centrelines were in good agreement around the bifurcation apex and potential centreline misregistration only occurred at the distal extremities of the carotid branches.

Overall, the RMSE in NP did not exceed 1%, i.e. the reproducibility found in a previous study using TOF MRA.[157] However, there were some statistically very significant observations: the centrelines were in general more planar and more linear in TOF than with BB MRA (see lines 5 and 9-11 in Table VI.6). The present findings is not restricted to the cases with centreline registration errors, but occurs in almost all subjects. The change in overall planarity could not be contributed to any of the arteries in particular, since the arterial non-planarities were similar (lines 6-8 in Table VI.6). These observations are probably due to the lower image quality in the daughter branches using BB MRA: the lower reliability will introduce noise on centreline registration. Noise favours non-planarity and decreases the linearity. Surprisingly, this finding was not illustrated using tortuosity (T_{vessel}) as a marker for linearity, suggesting that the parameter L_{vessel} using the singular value decomposition was a better measure of linearity than T_{vessel}.

Shapes   Judging by Table VI.6, where shape factors (SF_i) show an RMSE of 0.01 for each artery, one could conclude that the SF_i was the same in each imaging modality. When investigating the SF_i in more detail using Figure VI.27, two features were encountered.
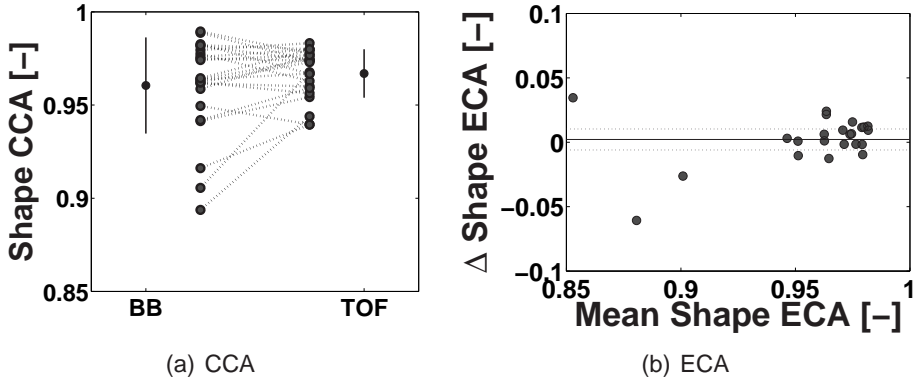
Figure VI.27.: Shape factor (SF_i). a: CCA SF_i for every case studied. The black dot with the black lines represent the mean±standard deviation. The dotted lines connect the individual values found for the CCA SF_i. b: ECA SF_i: the difference between the two values from 2 scans is plotted vs the mean value of the two scans as done by Bland and Altman.[30] The solid line is the mean error and the dashed line is the confidence interval (p=0.05, paired Student Test).

- Figure VI.27 (a) represents the CCA SF_i for every case studied. The black dot with the black lines represents the mean±standard deviation. The dotted lines connect the individual values found for the CCA SF_i. Overall, it can be seen that the SF_i variability was much smaller using TOF images. Three data points in BB MRA (with values around 0.9) seemed to be responsible for this increased variability. When going back to the original images, it was noticed that these 3 cases with large differences belonged to 3 different subjects, suggesting that this difference is independent of the considered subject. They were data sets with poor BB MRA quality. This finding has 3 consequences: (i) TOF MRA is more reliable than BB MRA for estimating CCA cross-sectional shape. (ii) The CCA SF_i for untreated hypertensive subjects is in fact very close to 1. A study by Thomas[331] found that 'mildly diseased' subjects underwent geometrical remodelling of the carotid bifurcation. This statement was underlined by the relatively high tortuosity found in this study. The SF_i in the CCA, however, remains high. (iii) Assuming a circular CCA cross-section, as done in many ultrasound systems for flow[140] or WSS[270] estimation, is a plausible assumption.

- Figure VI.27 (b) shows a Bland and Altman plot for the ECA SF_i. Again, 3 data points fell out of range in comparison with the others (3 points around 0.9 and lower). In this case, the 3 data points all belong to subject 5, suggesting that error in SF_i is related to that particular subject. Some 3D geometries for subject 5 (visit 2) were given in Figure VI.22. The very high tortuosity of the carotid branches is

the most remarkable feature of this bifurcation (T_{CCA}=1.77%, T_{ICA}=17.78% and T_{ECA}=19.56%, values averaged over the TOF and the BB second visit). When examining the images (Figure VI.24), it was again clear that the TOF images were of superior quality in comparison to the BB counterparts regarding ECA contrast. In this particular subject, the ECA was misregistered in two of the 3 sets due to this reduced ECA contrast.

In conclusion, TOF was more reliable for artery shape acquisition.

VI.5.4.4. Flow Comparison

Computational Details   Subject-specific boundary conditions have been used in this study. Within every matching set of TOF and BB data, i.e. in one particular visit, the same (subject-specific) boundary conditions were used. Thus, differences in flow pattern were not attributable to different boundary conditions but were all a direct consequence of the geometry differences. For one particular subject, different boundary conditions were acquired in different visits. Together with the correction for flow rate (using the midpoint scan), the most realistic boundary conditions are used: flow rate accuracy with cine PC MRA is around 10%.[122] Furthermore, no assumptions were made concerning the outflow division ratio: the cine PC MRA measurements in the 'outflow' plane yielded subject-specific outflow conditions.

The only limitation of the current model, was the lack of fluid-structure interaction and the fact that turbulent flow was neglected. The very low Reynolds numbers observed in the carotid bifurcations render turbulence obsolete except for stenosed regions,[341] but the subjects selected for this study were free of carotid stenosis. The first restriction was introduced due to significant complexity of fluid-structure interaction. There are several approaches to accommodate fluid-structure interaction, described by Leuprecht,[178] Cebral[56] and Zhao.[384] Since the effect of wall compliance on carotid haemodynamics was found to be quantitative[387] rather than qualitative, this study was restricted to the rigid wall model.

Comparison with Flow Reproducibility studies   It can be seen from Figure VI.25 that the agreement between TOF and BB-based carotid haemodynamics is very high. Table VI.7 shows how this study relates to separate

TOF and BB reproducibility studies. Note that in the mentioned reproducibility studies, the subjects were scanned twice on different occasions. Here, the compared geometries were acquired at the same visit. This means that the agreement between the TOF and BB MRA geometries can be expected to be better than the one found in the reproducibility studies, since physiological changes in geometry can be excluded. On the other hand, small yet systematic differences in carotid geometry as found in Table VI.6 could induce important haemodynamic differences.

The OSI in the CCA was very high for the hypertensive subjects in this study (mean 0.0465/70% = 0.0664). This result is endorsed by the fact that carotid bifurcations tend to be more tortuous in 'mildly diseased' subjects.[331] As a result of this discrepancy in mean CCA OSI in this study relative to reproducibility studies, the comparison of OSI values between the studies was slightly impeded.

Although the WSS *distribution* showed very good agreement between the two imaging methods (see Figure VI.25), the RMSE was a poor 0.372 N/m^2 (0.175 N/m^2 in the TOF reproducibility study, Table VI.7). This effect is attributed to the smaller cross-sectional area (A_{CCA}) measured with BB MRA (line 1 in Table VI.6): the theoretical WSS in a long concentric tube with laminar flow decreases with the third power of the cross-sectional area.[232] As a result, the WSS measured with the gated BB sequence was different from the WSS derived from the ungated TOF. The constatation that the percent WSSGt RMSE was better in the present study (29.1%) than in the TOF reproducibility study (43.2%) underlines the statement that the high RMSE for the WSS is due to the different gating protocols rather than to be consequences of the differences in image contrast.

Finally, the percent RMSE for WSSGs and WSSAG was similar to the RMSE found in a reproducibility study (Table VI.7), suggesting that these haemodynamic parameters can be well reproduced using either imaging protocol.

VI.5.5. Summary and Conclusion

MRA is the gold standard for image-based numerical blood flow simulation. Accurate geometry acquisition is crucial for the reliability of the blood flow simulation. For studying carotid blood flow, both BB MRA and TOF MRA have been used in the past. In this study, the carotid bifurcations of 8 subjects were scanned 6 times on 3 occasions: on each of the occasions, there was one TOF and one BB scan. The black blood protocol had a 10% bet-

ter in-plane resolution, and any image artefacts in the CCA and proximal ICA were easier to correct for than signal losses in TOF images (see Figure VI.24 (a)). BB MRA has 3 other inherent advantages over TOF: (i) BB MRA allows wall thickness and wall volume measurements. (ii) BB MRA allows gating within reasonable acquisition time. Currently it is believed that carotid distensibility is an important marker for atherosclerotic disease.[109] If BB images are acquired at peak systole and diastole, distensibility becomes measurable.[71] An advantage of acquiring images at 2 key instances during the cardiac cycle, is the possibility to model a non-rigid vessel wall by imposing vessel wall motion as done by Leuprecht.[178] (iii) BB TSE is not as sensitive to artefacts due to metallic implants as TOF.[313]

Nevertheless, TOF showed superior contrast, in particular at the flow divider (see Figure VI.26 (b)) and at the distal end of the ICA and ECA. As a result, automatic segmentation was much more successful on TOF images. Although cross-sectional areas in the larger vessels seemed easier to delineate on BB images, the upper extremities of the carotid branches had better contrast using TOF. The reduced contrast using BB induced misregistrations in the carotid branches, especially when tortuosity was high. Furthermore, the shapes seemed more reliable using TOF.

Differences in haemodynamic parameters such as the WSS, OSI, WSSG and WSSAG compared well with the expected variability within each imaging modality.

In conclusion, considering the agreement in TOF and BB-based results and the relative ease in reconstructing carotid bifurcations from TOF images, it is concluded that the 3D reconstruction of the carotid bifurcation should be done using TOF images. In case the wall thickness measurements or the distensibility are required, two solutions can be suggested: (i) either perform a BB scan, bearing in mind the possible loss of information in the distal carotid bifurcation, (ii) or, if the image quality in the bifurcation region and distal ICA/ECA should not be compromised, use a hybrid approach where both a TOF and a BB scan are performed.

VII. Three-Dimensional Ultrasound

MRI is often regarded as the gold standard 3D-imaging modality for CFD, as it has been introduced as a tool in image-based CFD earlier than 3DUS. The first US-based computational models only started to emerge in the late 1990s,[114,210] by then, MRI-based CFD was common.[198] Moreover, MRI has been recently successfully validated in reproducibility studies.[332] MRI is non-invasive and can provide quantitative information about the arterial wall and carotid geometry, but it remains expensive, time consuming and is often limited in availability and patient tolerability.

Ultrasound provides an alternative non-invasive method for visualising the arterial tree and its haemodynamics. Widespread availability, relatively low cost, high temporal resolution and ability to provide simultaneous, real-time acquisition of both flow and vessel wall data have allowed ultrasound to become a first line vascular imaging technique. With the development of 3DUS techniques, ultrasound can provide an alternative to MRI for acquiring the 3D geometry of large superficial arteries such as the carotid.

VII.1. The I in 3DUS

VII.1.1. Brief History[41,301]

As it often happens with technical innovations, clinical ultrasound finds its roots in a technique developed for military purposes during a war. At the end of World War I, Paul Langevin, a French professor of physics, developed a tool to locate German submarines.[87] Ultimately, he developed the SONAR (Sound Navigation and Ranging), but too late to be operationally useful. The technique consists of sending out sound waves and using their reflections to reconstruct the image of the body on which they are reflected. Bearing in mind the tragedy with the Titanic in 1912, one of the first applications of SONAR was to use icebergs as reflecting bodies, allowing ships to navigate

safely through the arctic. SONAR subsequently inspired early ultrasound investigators, who explored ways to apply the concept to medical diagnosis.

The use of ultrasound in medicine began during and shortly after the second World War in various centres around the world. The work of Dr. Karl Theodore Dussik in Austria in 1942 on transmission ultrasound investigation of the brain provides the first published work on medical ultrasonics.[82] Shortly after the end of World War II, researchers in Japan began to explore medical diagnostic capabilities of ultrasound, building the first model of ultrasonic equipment with A-mode presentation which was followed by work in B-mode presentation of two-dimensional, grey scale images (see section VII.1.2). The work on ultrasound in Japan was relatively unknown in the United States and Europe until the 1950s. Then, researchers presented their findings on the use of ultrasound to detect gallstones, breast masses, and tumours to the international medical community. Japan was also the first country to apply Doppler ultrasound (section VII.1.3), an application of ultrasound that detects internal moving objects for cardiovascular investigation.

From the mid sixties onwards, the advent of commercially available systems allowed the wider dissemination of the art. Ultrasound pioneers working in the United States contributed to many innovations and important discoveries to the field during the following decades. Researchers learned to use ultrasound to detect potential cancer and to visualise tumours in living subjects and in excised tissue. Real-time imaging, another significant diagnostic tool for physicians, enabled the display of ultrasound images directly on the system's screen at the time of scanning. The introduction of spectral Doppler and later colour Doppler depicted blood flow in various colours to indicate speed of flow and direction of motion.

VII.1.2. B-mode Ultrasound

As mentioned in the previous section, an ultrasound image is formed by transmitting a high-frequency (1-12 MHz) beam into the body, and collecting and analysing the returned echoes. Figure VII.1 (a) shows the first application of ultrasound: A-mode ultrasound, now obsolete in medical imaging. The 'image' is formed by a single beam, and is nothing more than the intensity of the reflected beam. The received signal may show wave spikes which reveal the presence of an echogenic surface. An 'echogenic' surface

(a) A-mode

(b) M-mode[215]
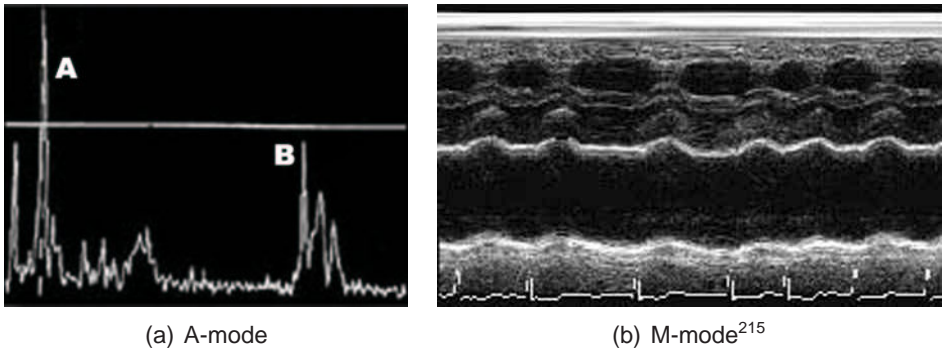
Figure VII.1.: a: A-mode Ultrasound. Wave spikes are represented when a single beam passes through objects of different consistency and hardness. The distance between these spikes (for example A and B) can be measured. b: M-mode ultrasound.[215] Each vertical line represents a single A-mode image. The horizontal line represents the time. At the bottom, the ECG is displayed.

is a surface which separates two tissues with a different impedance Z, defined as

$$Z = \rho \times c \qquad \qquad (VII.1)$$

with ρ the density of the considered tissue and c the speed of sound in it. When multiple spikes are measured in an A-mode image (for example A and B in Figure VII.1 (a)), it means that the beam passes through objects of different consistency and hardness. The distance between those surfaces can be estimated accurately by multiplying the speed of sound in tissue (1540 m/sec) by half the travel time of the sound.

B-mode imaging, already illustrated in Figures II.1 (page 24) and II.17 (page 49) and here again in Figure VII.2, is obtained when a number of beams are used together, each generating an A-mode signal. The beams all lie in a single plane, and when in this plane the brightness changes corresponding to the amplitude of reflected sound, a B-mode image is acquired.

M-mode imaging uses again only 1 beam. Similar to B-mode imaging, the brightness of the corresponds to the amplitude of reflected sound. When this is repeated at high frequencies, images as in Figure VII.1 (b)[215] are obtained. Here, each vertical line represents the signal acquired at the beam. The horizontal axis represents the time of acquisition. Because of its high sampling frequency (up to 1000 pulses per second), M-mode is useful in
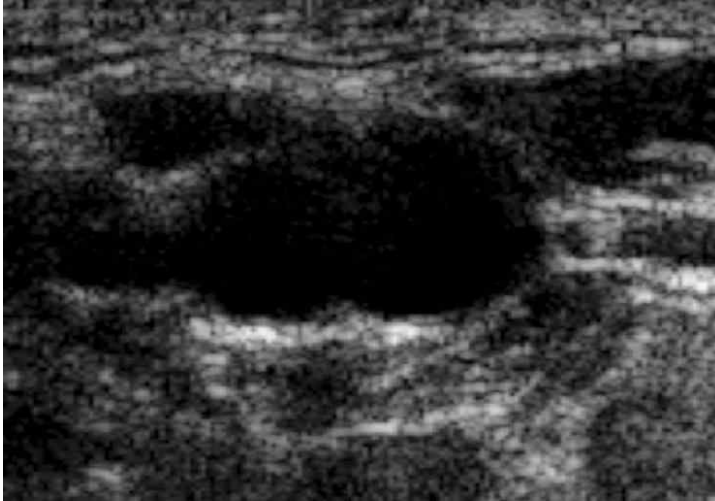
Figure VII.2.: Carotid B-mode of a healthy 25-year old male. Skin lies at the top of the image, the carotid bifurcation is the hourglass-shaped black region in the center of the image. For a duplex image of this carotid cross-section, see Figure VII.3 (b). For a segmentation of this image, see Figure VII.5.

assessing rates and motion. M-mode imaging is used for tracking rapid (e.g. intra-heart cycle) changes of the CCA LD.

VII.1.3. Doppler Ultrasound

When a sound wave with a certain frequency and amplitude hits an object, it will be reflected. This is the basis of ultrasound imaging. When this object is moving, the frequency of the reflected sound wave will change. This is the **Doppler Effect**. This effect can be used for measuring the velocity of blood particles.

Pulsed Doppler ultrasound[10]   Pulsed Doppler ultrasound is a Doppler ultrasound technique for measurement of blood-flow velocity using the pulse echo method. This method transmits short pulses of ultrasound with a certain frequency, the pulse repetition frequency. Between pulse transmissions, echoes are continuously returning to the transducer, but most of them are not analysed. A receiver gate opens only once between each pulse transmission to allow estimation of the Doppler frequency shift from only one predetermined range along the ultrasound beam, the sample volume. This Doppler frequency shift is related to the velocity of the element on which the

(a) Carotid Doppler

(b) Carotid colour Doppler
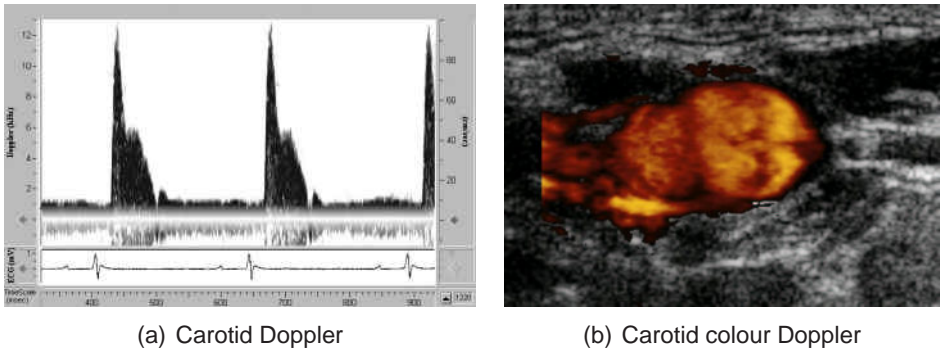
Figure VII.3.: a: Carotid Arterial Flow Velocity in a mouse using pulsed Doppler Ultrasound.[144] The frequency shift (left vertical axis) is directly related to the velocity in the sample volume (right vertical axis). b: Colour Doppler Ultrasound in right CCA of a healthy 25 year old male. The colour velocity information is superposed on the B-mode image from Figure VII.2.

beam was reflected. If the sample volume is in the middle of the CCA, as in Figure VII.3 (a), flow rate can be estimated using Womersley's assumption (see page 61).

The Doppler technique is based on measurement of small changes in ultrasound frequency from transmission of the pulse to reception of the echo, it is therefore important that the transmitted pulse contains a uniform, narrow bandwidth frequency (i.e. small frequency range). The longer the pulse, the narrower the bandwidth, and the spatial pulse length is therefore usually longer than the one used in B-mode imaging (usually 525 cycles per pulse).

Colour Doppler ultrasound[9]   Colour Doppler ultrasound is an ultrasound technique producing grey-scale B-mode images with superimposed colours indicating blood-flow velocity. Unlike pulsed Doppler ultrasound techniques, which acquire Doppler signals at restricted predetermined depths only, colour Doppler sonography acquires Doppler information at multiple locations along each scan line, i.e. along each scan line and at each position of the ultrasound beam. A commonly used method for measuring blood-flow velocity in colour Doppler sonography is autocorrelation, which involves repeating the pulse - echo-sequence several times (typically 48) along the same scan line, and comparing the phase of the echo signal at each depth from one pulse - echo sequence to the next. For stationary reflectors, the phase is the same from one echo to the next. For moving reflectors, like red blood cells, the phase of the signal will vary from echo to echo according to the flow velocity and direction. The autocorrelation technique estimates the mean velocity

and variance at each depth location and places this information in a colour image memory, a process which provides data for a single scan line. The ultrasound beam is then moved to the next scan line position, and the procedure repeated. In the final image, each pixel containing flow information is colour-coded according to blood flow direction and mean velocity. To improve time resolution, the colour-coded field may be restricted to only a part of the entire image (rectangle in Figure II.1). **Duplex** ultrasound is obtained when the colour-coded velocities are superposed on a B-mode image as done in Figure VII.3 (b).

VII.1.4. Imaging Protocol

The imaging protocol, the segmentation and reconstruction has been developed by Dr. D. C. Barratt and described in his PhD Thesis.[20] In short, imaging the carotid arteries was performed as follows. The 3DUS scanner was based on a commercial ultrasound scanner (HDI 5000, ATL-Philips Medical Systems, WA, USA) which is routinely used for vascular investigations. A 5 to 12 MHz broadband, linear array transducer (L12-5) was used to acquire ECG-gated, 2D transverse cross-sections of the carotid bifurcation following a subject-specific delay relative to the R-wave. B-mode and colour Doppler images were acquired simultaneously in order to obtain DUPLEX images which could help during segmentation. Up to 140 images can be acquired, one per cardiac cycle. Images are acquired in one sweep of the probe over the subject's neck. So if the heart rate was 60 bpm and 120 images were acquired, the acquisition would take 2 minutes. An electromagnetic position and orientation measurement (EPOM) device (Ascension Technology Inc, Vermont, USA) was mounted on the ultrasound transducer and enabled the transducer, and hence the captured ultrasound images, to be located in 3D space. The imaging protocol as suggested by Barratt[20] was not changed in this work. See Figure VII.4 for a schematic representation of the 3DUS imaging setup. The error in 3D distance measurements by the EPOM device was found to be -0.45$\pm$1.30 mm in a previous study.[22]
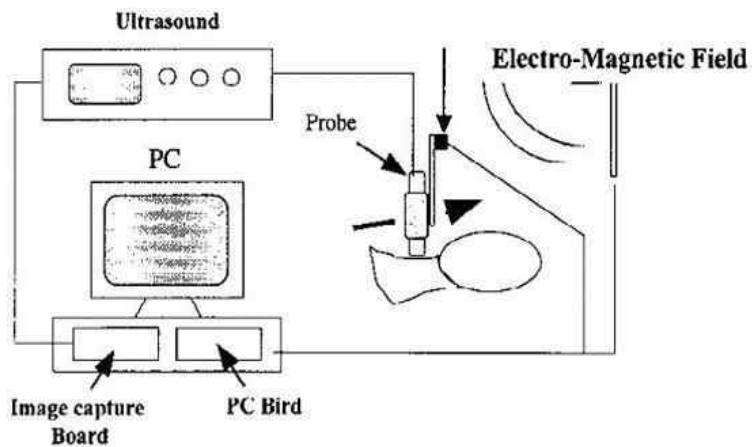
Figure VII.4.: 3DUS imaging setup. The probe, attached to the US machine, captures ECG-gated B-mode images. Simultaneously, a transmitter emits an electro-magnetic field which tracks the positioning and orientation device on the probe (see black vertical arrow). The thick black arrow from left to right shows the manual displacement of the probe, aimed at covering the entire carotid bifurcation including its branches. The B-mode images and the information of the position of the probe (PC Bird data) are stored off-line in the same PC.

VII.2. Segmentation

Acquired images were segmented using purpose-built software, also introduced by Barratt.[20] It runs in a MATLAB environment. The software is used to manually select points on the vessel wall to which a smooth cubic spline or ellipse was fitted. Figure VII.5 shows the visual interface of this program. The image loaded is the B-mode image shown in Figures VII.2 and VII.3. The red dots on the B-mode image are placed by the operator, the red line, a cubic interpolating spline, was fitted by clicking on the 'spline' button. Alternatively, the user could have fitted an ellipse by clicking on the 'ellipse' button. The red line is the segmentation of this image. Pressing 'Colour ON/OFF' toggles the colour Doppler information, which can be useful during segmentation. Its use should be discouraged since it is an averaged rather than an ECG gated image. Note how on top one can see that this is image 38 of a total of 140 stored B-mode images, each a cross-section of the carotid bifurcation of this particular subject. As mentioned in section VII.1.4,
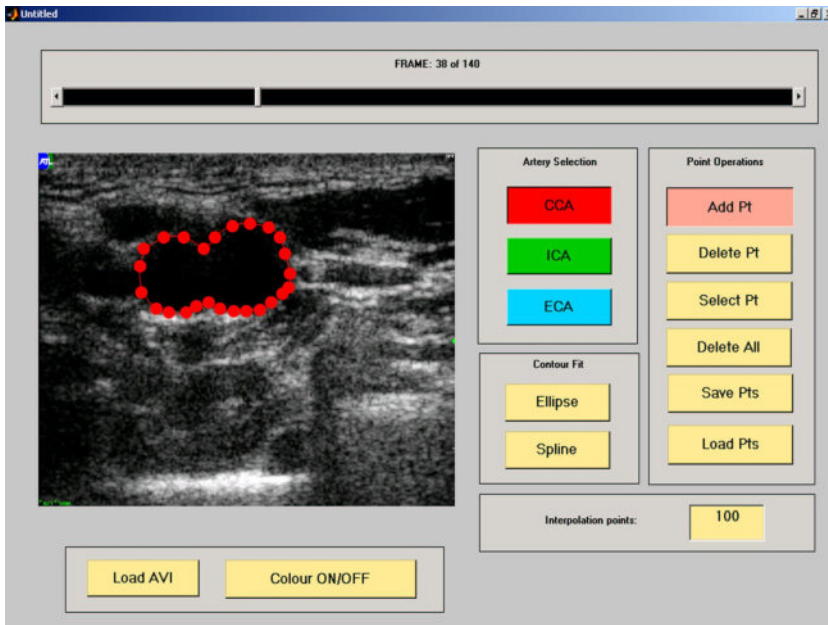
Figure VII.5.: Segmenting the B-mode ultrasound cross-sectional carotid image shown in Figures VII.2 and VII.3. The operator places the red dots on the B-mode image and fits the red spline by clicking on the 'spline' button. This red line is the segmentation of this image. Note how on top one can see that this is image 38 of a total of 140 stored B-mode images, each a cross-section of the carotid bifurcation of this particular subject.

there was one image per cardiac cycle and all images were acquired in a single sweep.

The delineated contour represented the intima-media interface rather than the lumen, and hence it needs to be readjusted by subtracting the IMT from it (assumed to be uniform around the vessel). Measurements of the IMT for each subject were made approximately 1 cm proximal from the carotid bulb, using a validated semi-automated program (see Figure II.17 on page 49 and Table II.1 on page 50) which allows IMT measurements with a reproducibility of $10\pm45\mu$m. Three ways of using the estimate of the IMT to adjust the vessel contours were evaluated. The *first* and easiest way was to move every point on the contour towards the contour centroid by a constant radial distance, corresponding to the measured IMT. In the *second* approach, all contour points were moved towards the centroid by a specified fraction of their local radii. This fraction was estimated from the measured IMT obtained approximately 1 cm proximal to the carotid bulb, as well as the local cross-sectional area, and was assumed to be constant for the entire bifurcation. In the *third* and most realistic approach, the IMT in the ICA and ECA were estimated based on the knowledge of the 'normal' variability of the IMT within a carotid bifurcation. As stated in section II.2.2.1, for healthy people, the IMT is 11.1% thicker in the bulb than the reference value in the proximal CCA, but 11.1% thinner in the ICA after the bulb than the reference value. Furthermore, the IMT in the ECA is approximately 87.5% of that in the distal ICA. Two sixth-degree polynomial functions were fitted into these data, ensuring a first derivative smooth IMT variation along the carotid bifurcation: one for the IMT in CCA and ICA and another for the ECA. This approach was implemented here and the bulb dilatation was selected to serve as a landmark for indicating the border between the distal CCA and the carotid bulb. Note that these parametrical polynomials are not valid for hypertensive or atheromatous subjects. The IMT evolution is illustrated with an example in Figure VII.6.

VII.3. Reconstruction

The lumen contours, combined with the positioning information from the EPOM device, allowed the 3D geometry of the carotid bifurcation to be reconstructed following alignment and smoothing. The reconstruction program, provided by Dr. Barratt, used the lumen contours and their positional information to output resliced lumen contours in equidistance planes (at 1
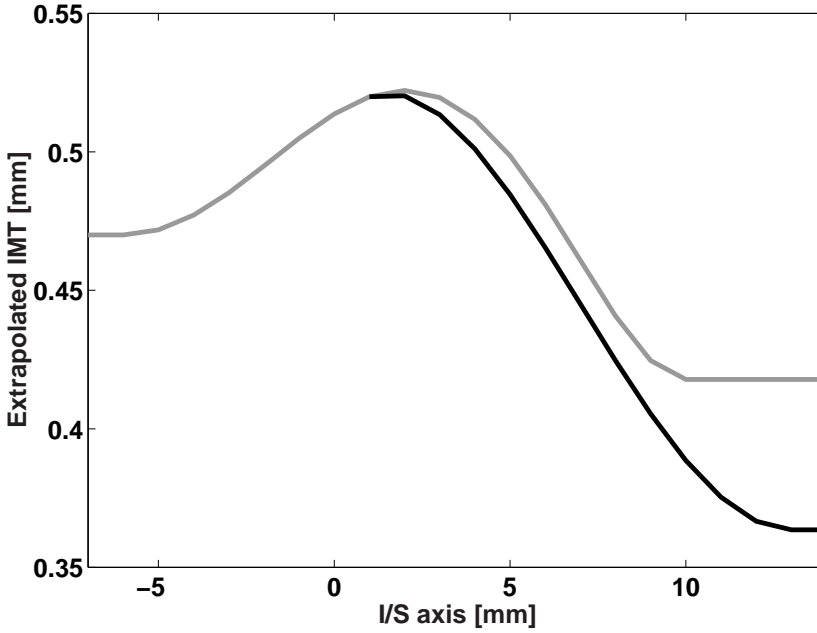
Figure VII.6.: IMT extrapolation in the carotid artery for a healthy 24-year old male. Horizontal axis is the position z along the I/S axis. Grey line represents the IMT in the CCA and ICA, black line represents IMT in ECA. The IMT (0.47mm) was measured 1cm proximal from the bulb, i.e. z=-16 mm in this graph (position not shown in graph). The bulb starts and ends at z=-6 mm and z=10 mm respectively. It is assumed that the ECA IMT already reaches its most distal value at z=10+3 mm. The IMT is maximal (1.111*0.47 mm) at the middle of the bulb, at z=2 mm. Assuming the IMT is constant in the CCA (0.47 mm) and ICA (0.889*0.47 mm) and that within the bulb IMT changes according to a first order smooth sixth degree polynomial, the above parameters are necessary and sufficient to reconstruct the IMT in the CCA and ICA (grey line). Similarly, the IMT along the bulb towards the ECA can be approximated using a first order smooth sixth degree polynomial to fit the extrapolated downstream IMT in the ECA (0.889*0.875*0.47 mm), the position of the apex (z=1 mm), the assumption of first-order smoothness and the presence of an inflection point exactly in the middle between z=1 mm and z=10+3 mm. Note that the values for z and IMT can be very different for another subject, but the rules to reconstruct the IMT-evolution remain the same.

mm). Details of the 3D reconstruction have been published by Barratt.[20, 21] Note that centreline smoothing was performed in a slightly different way from the procedure applied to MRI data. There was no area smoothing, however, the longitudinal splines were smoothed using modified cubic smoothing splines. This was equivalent to the area smoothing in MRI.

In this thesis, a number of functions in the reconstruction program was modified. In the previous version, the points on the segmented contours had to be defined in order and counter-clockwise. This is no longer required. In the old version of the segmentation program, reslicing of the longitudi-

nal splines at equidistance planes was performed using a cubic smoothing spline interpolation. This introduced in some cases 'border effects', which are undesired high-frequency changes in the longitudinal spline, originating from the condition that forced the spline to go through a given set of points. By increasing the number of points through which the interpolating spline needed to pass, this undesired effect was filtered. The increase of points was achieved using *linear* interpolation.

In order to generate a mesh through the resliced contours, the same techniques as explained in sections VI.3.2, VI.3.3 and III.2.2 for MRI were used.

VII.4. Accuracy, Reproducibility and Variability

The reader is reminded that an important part of this research has been dedicated to determining the accuracy of the WSS and its related parameters when derived using image-based CFD. Accuracy, traditionally determined using phantom studies, has been quantified by Dr. Augst, the pioneer of 3DUS-based CFD.[16]

In what follows, the 'reliability' of 3DUS-based CFD is estimated in three studies. First, the accuracy, reproducibility and operator dependence are tested on a phantom (section VII.4.1). The second study, in section VII.4.2, examines 'reliability' using a reproducibility study based on a number of healthy subjects. The subsequent section (VII.4.3), is concerned with operator dependence. It involved 4 ultrasound-trained physicians and 3 image processing operators with various experiences using 3DUS. Each of the physicians scanned the same carotid bifurcation a number of times, and each of the scans was reconstructed by each of the image processing operators.

VII.4.1. 3DUS Phantom Study

Although the accuracy of carotid 3DUS-based CFD had been assessed in a previous study,[16] a phantom study has been performed in order to obtain baseline data on the accuracy and reproducibility of carotid geometry and flow reconstruction. In this study, the anthropomorphic carotid artery phantom (R.G. Shelly Ltd., London, Ontario, Canada) used for the accuracy study in MRI (section VI.4.1) was scanned under static conditions using 3DUS by 2 operators.

VII.4.1.1. Methods

Phantom and Operators The details of the phantom are explained in section VI.4.1. In short, the phantom was made from polyester tubing moulded into the shape of a carotid bifurcation with dimensions derived by averaging angiographic measurements. The phantom was embedded in an agar-based tissue mimicking material to facilitate ultrasound imaging. Connectors at the proximal and distal ends of the phantom enable fluid to be pumped through the phantom, although in the experiments carried out for this study,

the phantoms were filled with a static water-glycerol solution with a speed of sound comparable to that of blood.

The phantom was scanned using 3DUS 3 times by 2 operators, i.e. a total of 6 scans. The first operator was a 3DUS expert (DB), and the second operator was a physician experienced in conventional ultrasound but not in 3DUS (BA). He was not especially instructed before starting the scans. The scans were performed using the imaging protocol described in section VII.1.4, using the HDI 5000 for B-mode image acquisition and an EPOM device to track the probe in 3D space.

Reconstruction and Computation   The scans were segmented and reconstructed in MATLAB by the operator who scanned the phantom using the methods described in sections VII.2 and VII.3, except that IMT measurement for contour adjustment was not necessary. Two operators scanned and processed the data three times yielding 6 sets of contours which were reconstructed and meshed using the methods described in section VII.3.

Computational details were the same as those for the 3DUS reproducibility study (see the next section, VII.4.2), except for the viscosity for which a Quemada (non-Newtonian) model was used (see section VIII.1.1).

In addition to the 6 scans, a CFD model was also built using the exact geometry of the phantom. The subsequent simulation returned the 'true' WSS and OSI distributions.

Statistics   Using the data from the reconstructed models and those from the exact phantom, the following statistical values were computed for the concerned parameters.

- RMSE, the mean absolute difference between the values found by the operators and the true values from the known geometry. This provides a measure of the *accuracy* of the technique.

- $\sigma_{intra-op}$, the standard deviation on the values obtained by 1 operator. This is a measure of the *reproducibility* of the technique.

- For each operator, each parameter was averaged over the scans. $\sigma_{inter-op}$, found by taking the standard deviation of these averages, is a measure of *operator dependence*.

- Finally, σ_{all} was computed as the standard deviation of all absolute differences between the values found by the operators and the true values from the known geometry set. It can be regarded as the error-bar when a single measurement is made.

VII.4.1.2. Results

Figure VII.7 shows the OSI distribution in the phantom (Figure VII.7 (a)), in the three scans by operator DB (Figure VII.7 (b-d)) and operator BA (Figure VII.7 (e-g)).

(a) True Geometry

(b) DB1

(c) DB2

(d) DB3

(e) BA1

(f) BA2

(g) BA3
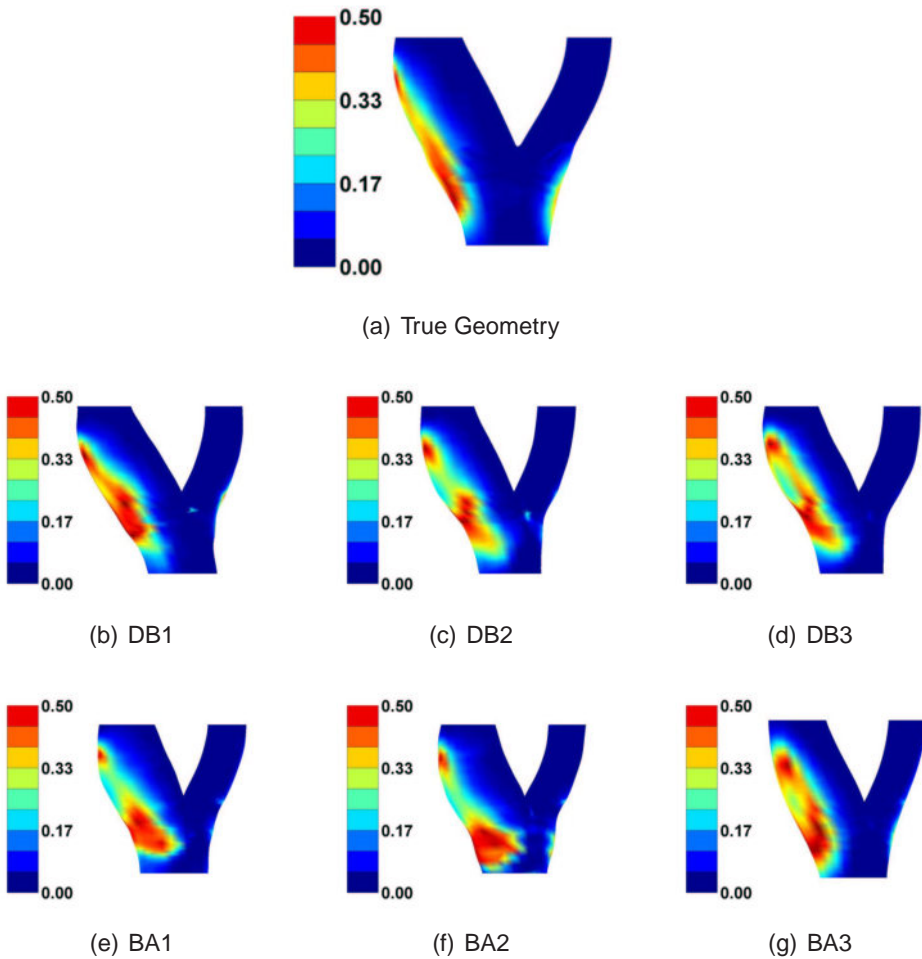
Figure VII.7.: Oscillatory Shear Index (OSI) distribution in true geometry (a), in the three scans performed by DB (b-d) and BA (e-g) (dimensionless).
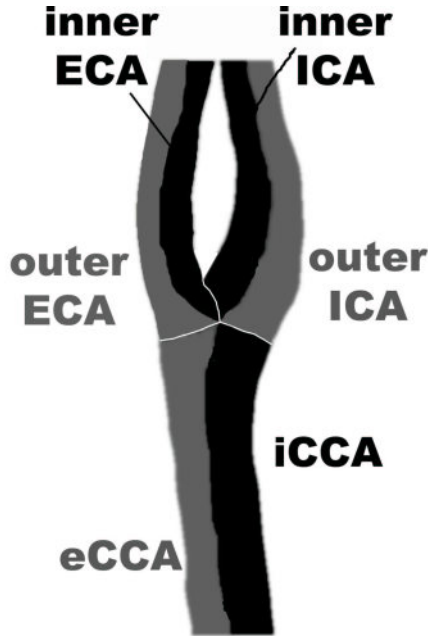
Figure VII.8.: Definition of the regions over which the haemodynamic parameters are averaged.

Table VII.1 summarises the statistics performed on parameters describing area, centreline, shape, WSS and OSI agreement. The parameters WSS and OSI are area-averaged over the entire bifurcation, the part of the CCA from which the ICA emerges (marked as 'iCCA'), the part of the CCA from which the ECA emerges ('eCCA'), the inner and outer ICA and ECA, 'inner' referring to the part containing the apical region. See Figure VII.8 for a definition of the regions over which the parameters were averaged. The other parameters described here are defined in section II.3.2.2. In the columns labelled 'DB' and 'BA', values are presented as the mean absolute difference between the true phantom value and the measured value averaged over three scans $\pm$ standard deviation (of the true difference). The reported sign denotes whether the values were on average over- (+) or underestimated (-) by the operator. The mean value is a measure of accuracy (RMSE) whereas the standard deviation is a measure of reproducibility ($\sigma_{intra-op}$). Note that the 'true phantom value' of the WSS and OSI were obtained from the CFD model of the true phantom using the same boundary conditions as in the reconstructed models. The values in percentage were obtained by dividing the considered statistical measure by the true value, found in the column labelled 'CAD'.

Parameter [Unit]	CAD Phantom Data	DB RMSE±$\sigma_{intra-op}$ (n=3)	BA RMSE±$\sigma_{intra-op}$ (n=3)	$\sigma_{inter-op}$ (n=2)	σ_{all} (n=6)
A_{CCA} [mm^2]	53.214	+1.427 ± 1.915 (2.68±3.60%)	+11.172 ± 4.102 (20.99±7.71%)	7.051 (13.25%)	6.299 (11.84%)
A_{ICA} [mm^2]	37.891	+1.324 ± 0.176 (3.50±0.46%)	+9.010 ± 1.052 (23.78±2.78%)	5.434 (14.34%)	5.167 (13.64%)
A_{ECA} [mm^2]	17.309	+0.815 ± 0.173 (4.71±1.00%)	+5.027 ± 0.929 (29.04±5.37%)	2.978 (17.21%)	2.921 (16.88%)
A_R [-]	1.056	+0.103 ± 0.014 (9.77±1.30%)	+0.035 ± 0.028 (3.28±2.66%)	0.048 (4.58%)	0.069 (6.53%)
T_{CCA} [%]	0.450	+0.185 ± 0.227 (41.07±50.54%)	+0.234 ± 0.270 (52.10±60.04%)	0.059 (13.04%)	0.210 (46.59%)
T_{ICA} [%]	1.606	-0.276 ± 0.305 (17.19±18.99%)	-0.373 ± 0.155 (23.23±9.68%)	0.127 (7.92%)	0.325 (20.21%)
T_{ECA} [%]	1.974	-0.179 ± 0.136 (9.05±6.91%)	-0.248 ± 0.261 (12.57±13.23%)	0.031 (1.55%)	0.213 (10.81%)
α_{BIF} [°]	149.885	+3.777 ± 0.787 (2.52±0.52%)	+1.634 ± 0.746 (1.09±0.50%)	1.515 (1.01%)	2.706 (1.81%)
SF_{iCCA} [-]	0.964	+0.011 ± 0.005 (1.13±0.53%)	+0.007 ± 0.001 (0.77±0.07%)	0.002 (0.26%)	0.009 (0.95%)
SF_{iICA} [-]	0.993	-0.003 ± 0.004 (0.25±0.35%)	+0.002 ± 0.001 (0.22±0.13%)	0.002 (0.18%)	0.002 (0.24%)
SF_{iECA} [-]	0.993	+0.003 ± 0.000 (0.29±0.03%)	+0.002 ± 0.002 (0.21±0.17%)	0.001 (0.06%)	0.003 (0.25%)
$V_{MAX,CCA}$ [m/s]	0.292	+0.004 ± 0.006 (1.44±2.20%)	-0.003 ± 0.002 (1.16±0.64%)	0.005 (1.69%)	0.004 (1.30%)
$V_{MAX,ICA}$ [m/s]	0.291	-0.009 ± 0.010 (2.98±3.56%)	-0.015 ± 0.019 (5.07±6.62%)	0.005 (1.81%)	0.012 (4.03%)
$V_{MAX,ECA}$ [m/s]	0.235	+0.006 ± 0.010 (2.65±4.09%)	-0.016 ± 0.008 (7.00±3.29%)	0.014 (5.97%)	0.011 (4.82%)
WSS [N/m^2]	0.858	**-0.064 ± 0.060** (7.43±7.04%)	-0.167 ± 0.060 (19.42±7.04%)	0.080 (9.35%)	0.115 (13.43%)
WSS in iCCA [N/m^2]	0.416	+0.016 ± 0.021 (3.87±5.09%)	-0.021 ± 0.033 (5.17±7.94%)	0.019 (4.64%)	0.019 (4.52%)
WSS in eCCA [N/m^2]	0.491	+0.290 ± 0.103 (58.93±20.93%)	+0.081 ± 0.037 (16.47±7.52%)	0.148 (30.02%)	0.185 (37.70%)
WSS in outer ICA [N/m^2]	1.026	+0.508 ± 0.062 (49.53±6.08%)	+0.479 ± 0.207 (46.70±20.14%)	0.021 (2.00%)	0.494 (48.12%)
WSS in inner ICA [N/m^2]	1.512	+1.157 ± 0.072 (76.50±4.75%)	+0.891 ± 0.063 (58.89±4.16%)	0.188 (12.45%)	1.024 (67.69%)
WSS in outer ECA [N/m^2]	0.679	+0.297 ± 0.032 (43.72±4.67%)	+0.156 ± 0.044 (22.94±6.52%)	0.100 (14.69%)	0.226 (33.33%)
WSS in inner ECA [N/m^2]	1.131	+0.629 ± 0.051 (55.62±4.52%)	+0.387 ± 0.078 (34.22±6.89%)	0.171 (15.13%)	0.508 (44.92%)
OSI [-]	0.040	**+0.008 ± 0.003** (18.94±7.53%)	+0.007 ± 0.009 (17.66±22.21%)	0.002 (5.32%)	0.007 (18.30%)
OSI in iCCA [-]	0.075	+0.009 ± 0.009 (11.40±12.47%)	+0.022 ± 0.028 (29.58±37.21%)	0.001 (1.43%)	0.015 (20.49%)
OSI in eCCA [-]	0.040	-0.067 ± 0.002 (167.12±4.79%)	-0.043 ± 0.009 (107.31±22.97%)	0.017 (42.29%)	0.055 (137.22%)
OSI in outer ICA [-]	0.064	+0.025 ± 0.007 (38.17±11.54%)	-0.031 ± 0.032 (47.48±49.74%)	0.030 (47.24%)	0.028 (42.83%)
OSI in inner ICA [-]	0.001	-0.073 ± 0.000 (5319.63±13.42%)	-0.068 ± 0.005 (4953.10±331.48%)	0.004 (259.17%)	0.071 (5136.37%)
OSI in outer ECA [-]	0.016	-0.056 ± 0.006 (350.62±39.48%)	-0.051 ± 0.017 (320.70±106.17%)	0.003 (21.15%)	0.054 (335.66%)
OSI in inner ECA [-]	0.002	-0.072 ± 0.001 (3066.02±55.63%)	-0.070 ± 0.001 (2980.37±54.31%)	0.001 (60.56%)	0.071 (3023.20%)

Table VII.1.: Statistics for parameters describing area, centreline, shape, WSS and OSI agreement in the phantom study. The parameters WSS and OSI are area-averaged over the entire bifurcation, the part of the CCA from which the ICA emerges (marked as 'iCCA'), the part of the CCA from which the ECA emerges ('eCCA'), the inner and outer ICA and ECA, 'inner' referring to the part containing the apex. See section II.3.2.2 for a definition of the other parameters. Values are presented as the mean absolute difference between the true phantom value and the measured value averaged over three scans ± standard deviation of the true difference. The reported sign denotes whether the values were on average over- (+) or underestimated (-) by the operator. The values in percentages are obtained by dividing the error-measure by the true value. CAD: true phantom data; DB: values found by DB; BA: values found by BA; see the text for definitions of $\sigma_{inter-op}$ and σ_{all}.

VII.4.1.3. Discussion

Study setup   In this study, an anthropomorphic carotid phantom was used to assess accuracy, reproducibility and operator dependence of *in vitro* 3DUS-based CFD. Two operators each scanned the phantom 3 times, yielding 6 data sets. These data sets were compared to the true values provided by the manufacturer of the phantom. The first operator (DB) was a skilled 3DUS technician whereas the second (BA) was a skilled US physician who had never used 3DUS before and was not trained for it before using the 3DUS protocol. This choice of operators allowed the 3DUS researchers to assess how robust the technique was, and whether or not operators should be specifically trained before they can perform a 3DUS scan. The setup of this study, where each person segmented his own scan, did not reveal whether the inter-operator differences were due to differences in imaging or segmentation.

Accuracy and Error-bars   The accuracy of the technique can be found in Table VII.1 in the columns labelled 'DB' and 'BA'. It is the scan-averaged absolute difference between the true and the measured values and thus the RMSE. For example, the accuracy in the average CCA cross-sectional area (A_{CCA}) is 2.68% and 20.99% for operators DB and BA, respectively.

It is immediately clear that, especially for the geometry parameters, the accuracy was higher for the trained 3DUS technician (DB) than for the US physician (BA). This highlighted the impact of experience and training with the use of 3DUS. The accuracy achieved with operator DB is the expectable accuracy by a trained operator, whereas the error registered for operator BA can be considered as the typical error for an inexperienced operator. This also means that the values found for DB rather than σ_{all} should be regarded as the error-bar of the technique, unless untrained operators are to be performing and segmenting 3DUS-scans.

In a study performed by Augst,[16] the WSS in selected cross-sections was used to identify WSS accuracy and reproducibility. He found an accuracy of 0.29 N/m^2 in the considered sections, which represented the worse case scenario. Here, the accuracy for region-averaged WSS and OSI has been presented, showing a smaller RMSE for the WSS in the CCA (σ_{all}=0.019 and 0.185 N/m^2 < 0.29 N/m^2), but higher values in the ICA and inner ECA. The apex region, part of inner ECA and inner ICA, had the largest errors.

Reproducibility   The intra-observer variability, measured by $\sigma_{intra-op}$ in Table VII.1, is generally low. This meant that the variability in the results was small in comparison to the exhibited error. For example, the error in A_{ICA} (3.50%) was an order of magnitude larger than the reproducibility (0.46%) (DB).

Operator Dependence   The values found by each operator change very little between the different scans, but differ from one operator to the other. For example, $\sigma_{inter-op}$ for the A_{CCA} (13.25%), a measure of operator dependence, is much greater than $\sigma_{intra-op}$ found for each operator independently (3.60 and 7.71%). It is clear that the trained operator gave the best accuracy, showing that there is a need for at least a minimum of training before 3DUS-based CFD can be used by an US physician with no experience in 3DUS. Since the current study setup has one trained and one untrained operator, the uncertainty when an untrained physician performs the scans and the segmentations is given by the $\sigma_{inter-op}$ column in Table VII.1. The setup of the phantom study, where each person segmented his own scan data, did not reveal whether the inter-operator differences were due to differences in imaging or segmenting habits.

VII.4.1.4. 3DUS Phantom study: the conclusion

In conclusion, the present phantom study quantified the accuracy of *in vitro* 3DUS-based CFD. Operator dependence was rather high, probably due to the lack of training of one of the operators. The reproducibility of the technique was very high, implying that there is no real need for different scans to be performed by the same operator. The phantom study showed that 3DUS-based CFD was ready for *in vivo* applications. Therefore, in the following section, the *in vivo* reproducibility (section VII.4.2) and variability (section VII.4.3) of the technique will be assessed.

VII.4.2. *in Vivo* Reproducibility

It is important to realise that the accuracy and reproducibility of 3D ultrasound-based CFD have been defined for *in vitro* phantom studies[16] and that the technique has been successfully applied to *in vivo* studies of carotid bifurcations.[17] However, the reproducibility of this approach in the latter case is

yet to be assessed. This study was therefore designed to investigate the reproducibility of 3D carotid bifurcation reconstruction using ultrasound, and its effects on predicted blood flow using CFD.

VII.4.2.1. Materials and Methods

Data Acquisition   Nine healthy volunteers were scanned by a single observer on two separate occasions, at least two weeks (max four weeks) apart using the 3DUS system described previously in this chapter.

Geometry Reconstruction and Mesh Generation   Acquired images were segmented using the custom written software illustrated in section VII.2. In short, the software was used to manually define points on the vessel wall to which a smooth cubic spline or ellipse was fitted, as appropriate. This manual segmentation was performed on every B-mode image obtained. On transverse B-mode images, the lumen-intima border is rather obscure, therefore the points were chosen to delineate the media-adventitia border. Since the flow needs to be calculated within the lumen volume, the fitted splines were then adjusted to allow for the thickness of the intima-media complex. IMT was measured using B-mode ultrasound as described in Figure II.17 on page 49. Thus, a series of readjusted cross-sectional contours, defining the lumen geometry of the carotid bifurcation, were produced. The centreline formed by the centroids of each of these contours was smoothed and used to realign the cross-sectional contours. Finally, the vessel inner surface was reconstructed by fitting smoothing splines to successive contour points.[20] A detailed description of the reconstruction protocol, including the smoothing algorithms, has been presented by Barratt.[21]

The mesh was generated using the in-house purpose-built mesh generator described in section III.2.2. The meshes in Figure III.1 (page 77) belong to subject 1 (session 2) in this study. For mesh sensitivity tests, six meshes of different axial, radial and circumferential mesh densities were generated and their time-dependent wall shear stress distributions were compared. The resulting wall shear stress[253] differences between the finest mesh and the chosen mesh were within 0.15 N/m^2 (RMSE: 3.94%). This mesh had 32 cells along the circumference, and 26 or 27 across a diameter. The axial distance between two cells was an average of 0.42 mm (maximum 0.55 mm).

Computational Fluid Dynamics The Navier-Stokes equations for laminar flow were discretised using the QUICK differencing scheme and then solved using the SIMPLEC algorithm implemented in CFX4™.[3] The computations were carried out for two cycles, since the third cycle resulted in instantaneous wall shear stress differences below 0.01% compared to the second cycle. Each cycle was divided into 80 equally spaced time-steps of 12.5ms, based on previous experience. The dynamic viscosity of blood was set to be 4 mPa.s (Newtonian fluid), the density was 1176 kg/m^3 and the walls were assumed to be rigid. With pulsed wave Doppler, time-dependent velocities at the center of the CCA of a representative subject were recorded. The flow wave form was computed from the centreline velocities based on the Womersley theory.[368] Finally, the Womersley velocity profiles were derived and imposed at the inlet. Since the same flow wave form was used in all simulations, the inlet velocities derived from the Womersley theory could be different depending on the inlet area. At the outlet, a constant flow ratio of 70:30 was adopted between the ICA and ECA throughout the cardiac cycle. Flow simulations were carried out on a SUN Blade 1000 Workstation (Ultrasparc III processor, 512Mb RAM, 750 MHz).

VII.4.2.2. Results

Geometrical Reproducibility Cross-sectional areas were averaged along the considered artery i and presented in Figure VII.9 for all subjects as A_i $\pm$ the standard deviation. The Bland-Altman plots[30] for each carotid segment are shown in Figure VII.10. Figure VII.11 shows the percentage area difference along the Inferior/Superior (I/S) axis:

$$percent \; difference \; at \; z \;\; = \;\; \frac{A_{z,1} - A_{z,2}}{\frac{1}{2} \left(A_{local,1} + A_{local,2} \right)} \qquad \text{(VII.2)}$$

here, $A_{z,1}$ was the cross-sectional area at position z along the I/S axis in the first scan, with z=0 mm being at the apex, z$<$0 mm in the CCA and z$>$0 mm in the carotid daughter branches. Similarly, $A_{z,2}$ is the cross-sectional area at position z along the I/S axis in the second scan, $A_{local,1}$ is the mean area measured in the first scan (averaged over 1.5 mm) and again, $A_{local,2}$ is the mean area measured in the second scan (averaged over 1.5 mm).

Subject-averaged difference in the CCA is 5.75 $\pm$ 6.17 mm^2, in the ICA 3.54 $\pm$ 3.64 mm^2 and in the ECA 2.02 $\pm$ 1.28 mm^2 (mean error$\pm$ 95% confidence intervals at n=9 (number of subjects)). It can be seen from Figure VII.9 and
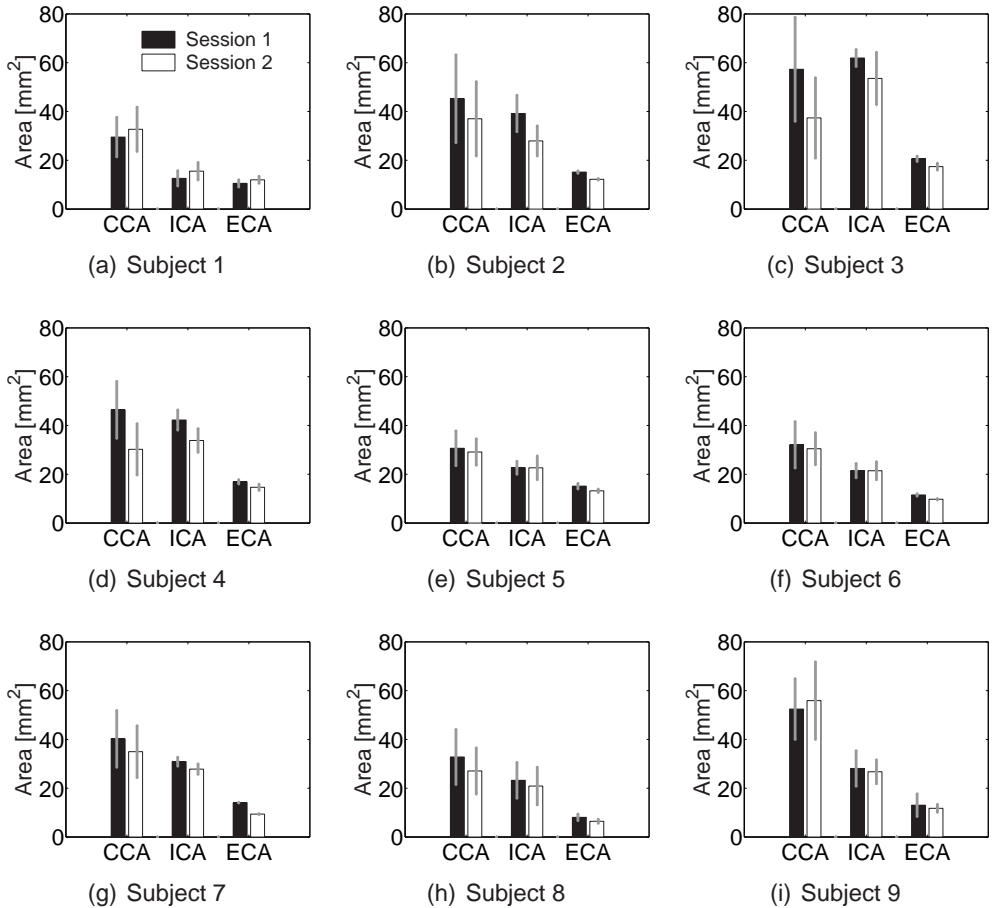
Figure VII.9.: Average area in CCA, ICA and ECA for all subjects in both sessions. The error-bar on the blocks represent the standard deviation on the measured area.

Figure VII.11 that the large area difference in subjects 3 and 4 accounted for most of this area discrepancy.

The centrelines are shown in Figure VII.12. Table VII.2 uses the singular value decomposition (SVD) approach described in section II.3.2.2 as a measure of centreline agreement.[157]

Flow Reproducibility   Figure VII.13 shows the WSS distribution for all subjects, whereas the OSI distribution is given in Figure VII.14. Each of these figures contains 18 3D views of WSS or OSI distributions: 1 view per scan and per subject.

(a) CCA (b) ICA (c) ECA
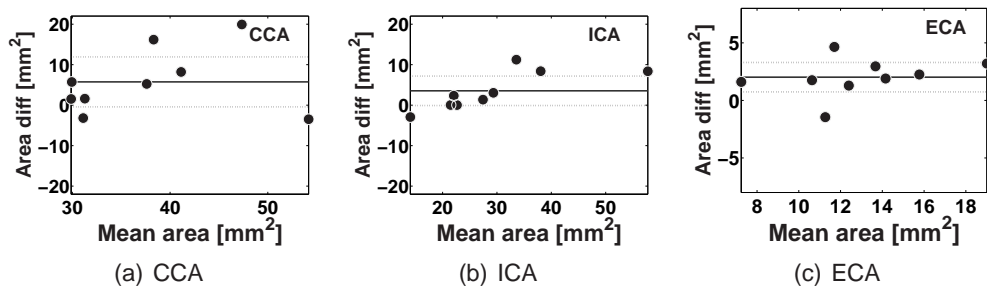
Figure VII.10.: Bland-Altman plot of mean area difference vs. mean area in CCA (a), ICA (b) and ECA (c). 'Area diff' stands for the difference in measured mean arterial area between the first and the second scan. The solid line is the mean difference, the dashed lines are the 95% confidence limits (n=9 subjects).

Subject	Session 1 [%]	Session 2 [%]	difference [%]
1	5.45	6.80	1.35
2	2.51	3.24	0.74
3	2.90	2.67	0.24
4	1.40	2.53	1.13
5	5.32	4.09	1.23
6	2.47	2.15	0.32
7	2.14	3.41	1.26
8	4.87	3.89	0.98
9	9.71	4.03	5.69
Mean±Standard Deviation	4.10±2.61	3.65±1.37	1.44±1.66

Table VII.2.: Comparison of bifurcation non-planarity NP between two sessions.

VII.4.2.3. Discussion

Areas Figure VII.9 shows that the mean areas (averaged along an artery) are generally well reproduced. With the exception of the CCA area in subjects 3 and 4, differences in mean area are fairly small ($<$10% of the mean in CCA and ICA, $<$15% in the ECA, although they can be higher around the bifurcation apex, see Figure VII.11). Barratt[22] used a phantom and found that the error in 3D distance estimation was -0.53±3.39%, corresponding to a projected uncertainty of 8% (=2.(0.53+3.39)%) in area. The implementation of 3DUS *in vivo* in terms of the error in cross-sectional area measurement is therefore only marginally inferior to its performance *in vitro*. 3DUS compares well to black blood MRI (the more standardised technique for obtaining vascular geometry): Thomas[332] showed an average *in vivo* reproducibility of 5% for vessel radius, thus of 10% for vessel area. The Bland-Altman plots (Figure VII.10) show that zero is within the mean error±95% confidence margins for the CCA and ICA, suggesting there is no evident bias for area measure-
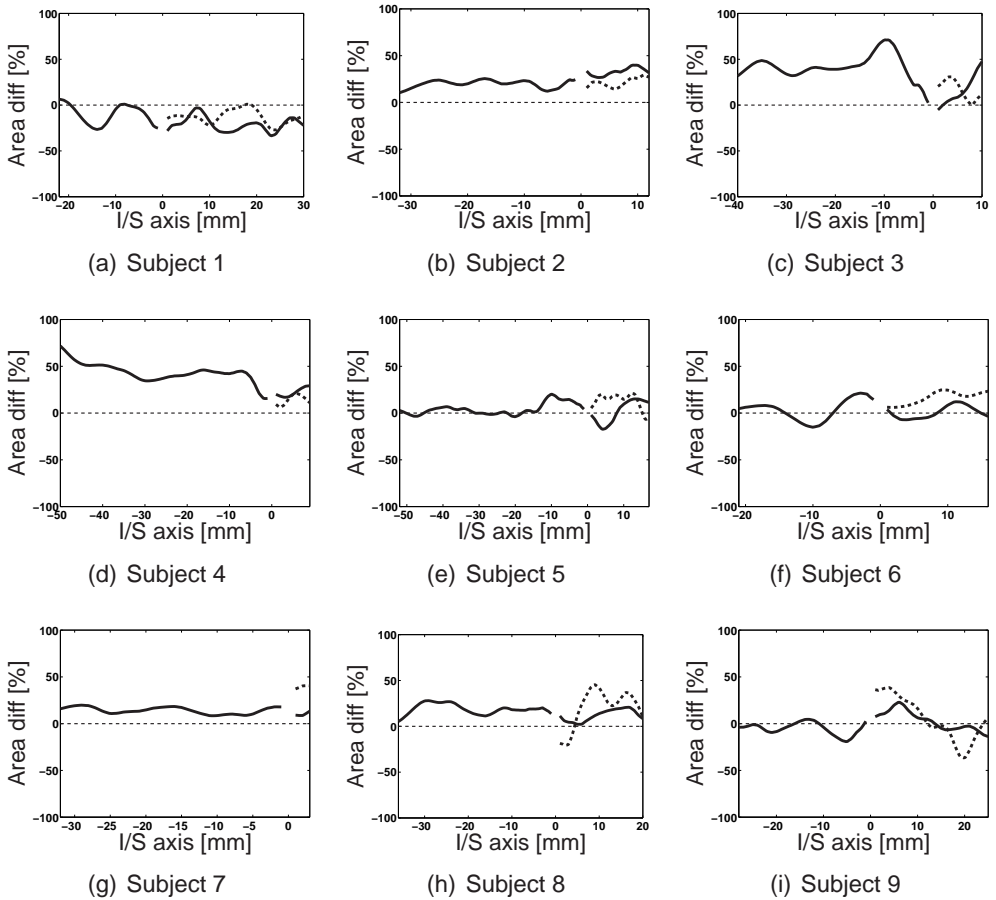
Figure VII.11.: Area differences between the two sessions in the three arteries (CCA, ICA and ECA), along the Inferior/Superior (I/S) axis in each of the 9 subjects. The CCA and ICA are represented by the solid lines, respectively at I/S positions $<$ and $>$ zero, the ECA is represented by the dashed line. The percent difference is defined by equation VII.2.

ments. For the ECA, the 95% confidence margins just exclude zero, but the absolute error is very small (maximal error of 4.65 mm^2).

The following possible causes for errors have been suggested:

1. Although the two scan sessions were performed under standardised conditions, physiological differences may contribute. Influences such as recent medication, salt loading, exercise and mental activity may have had important haemodynamic effects on cardiac output, blood pressure and cerebral blood flow. Blood pressure was measured on both occasions and while no significant difference was found, it has to be noted that the variability of repeated blood pressure measure-
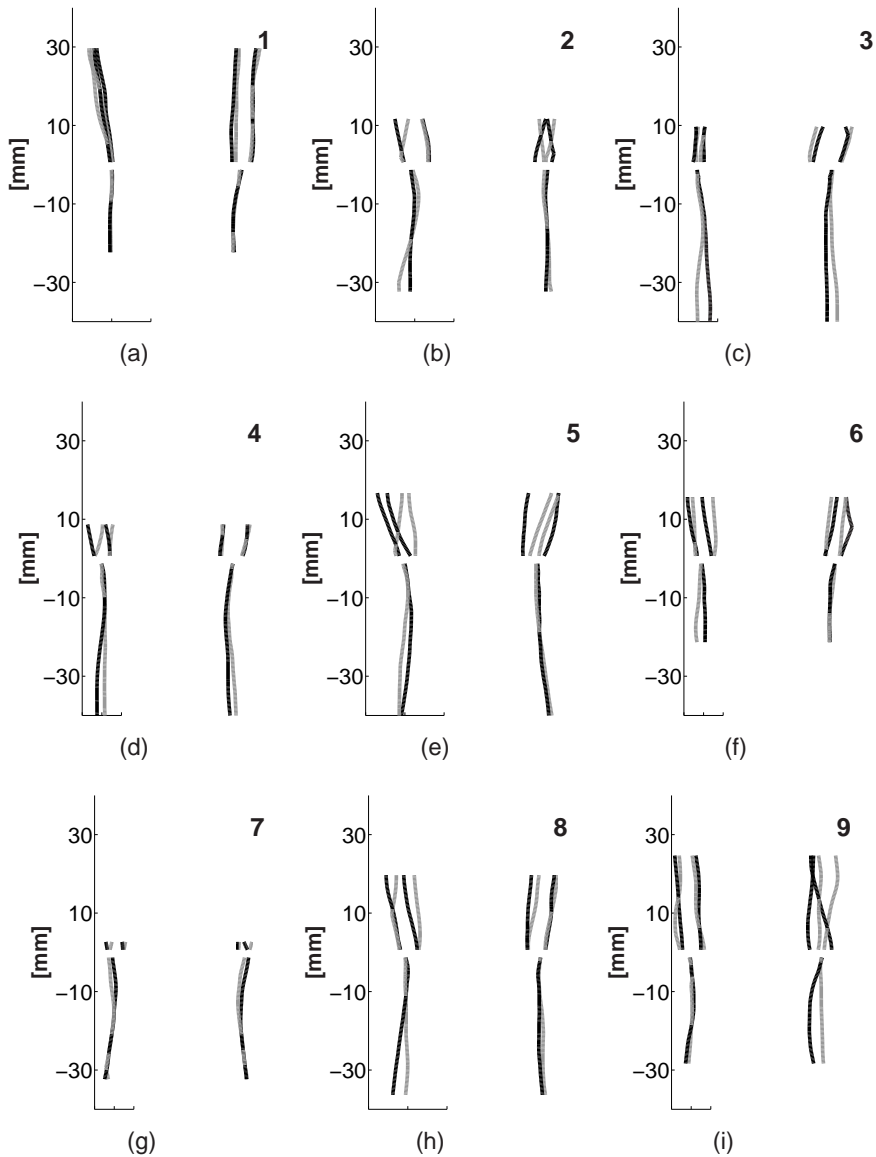
Figure VII.12.: Centrelines for all subjects in both sessions in two views. Session 1 is in black, session 2 in grey. Subject number at the top right-hand corner.
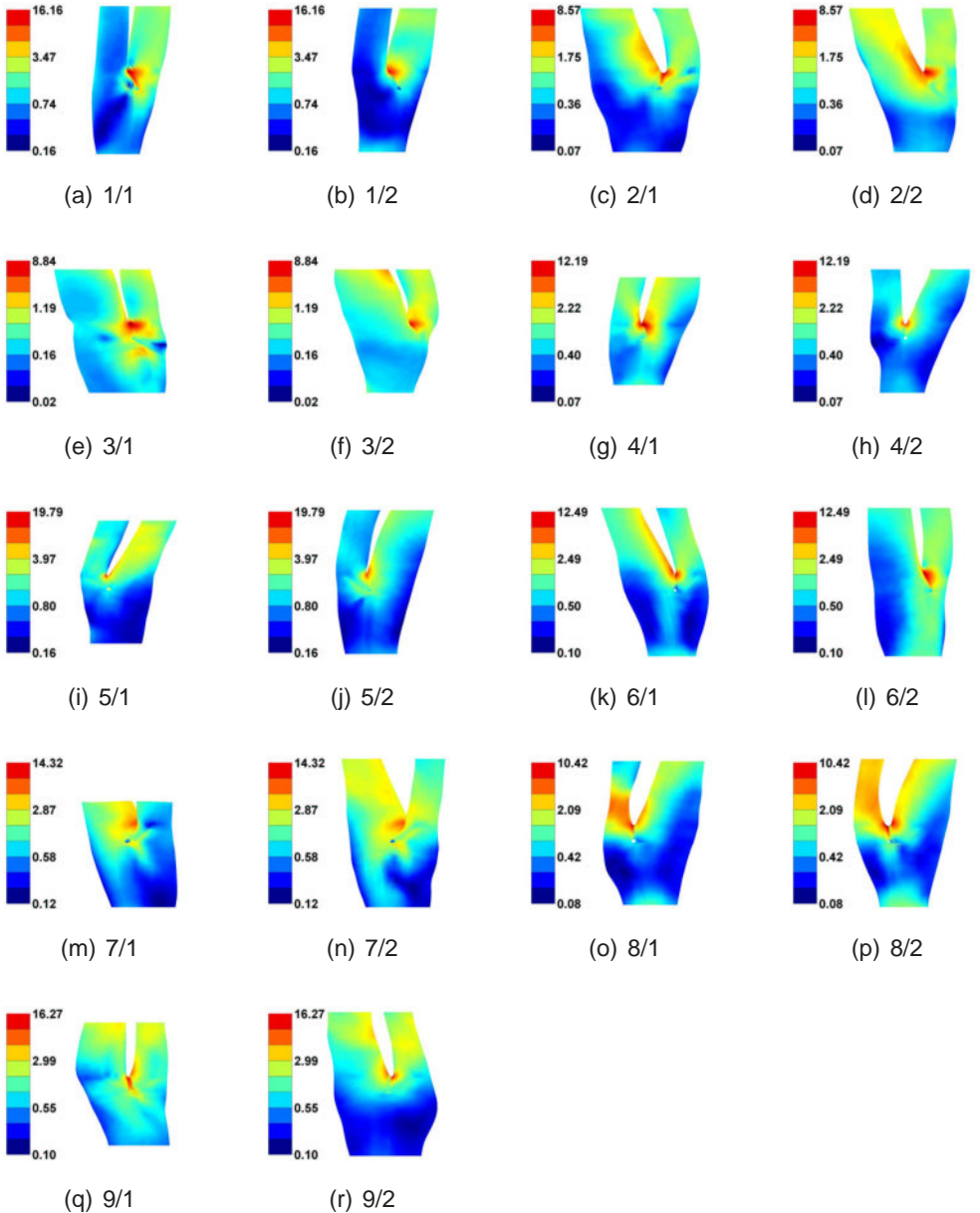
Figure VII.13.: Time-averaged wall shear stress (WSS) distribution in all sessions (subjects 1-9). Subcaptions encoded as subject/session. (N/m^2, logarithmic scale)

(a) 1/1   (b) 1/2   (c) 2/1   (d) 2/2

(e) 3/1   (f) 3/2   (g) 4/1   (h) 4/2

(i) 5/1   (j) 5/2   (k) 6/1   (l) 6/2

(m) 7/1   (n) 7/2   (o) 8/1   (p) 8/2

(q) 9/1   (r) 9/2
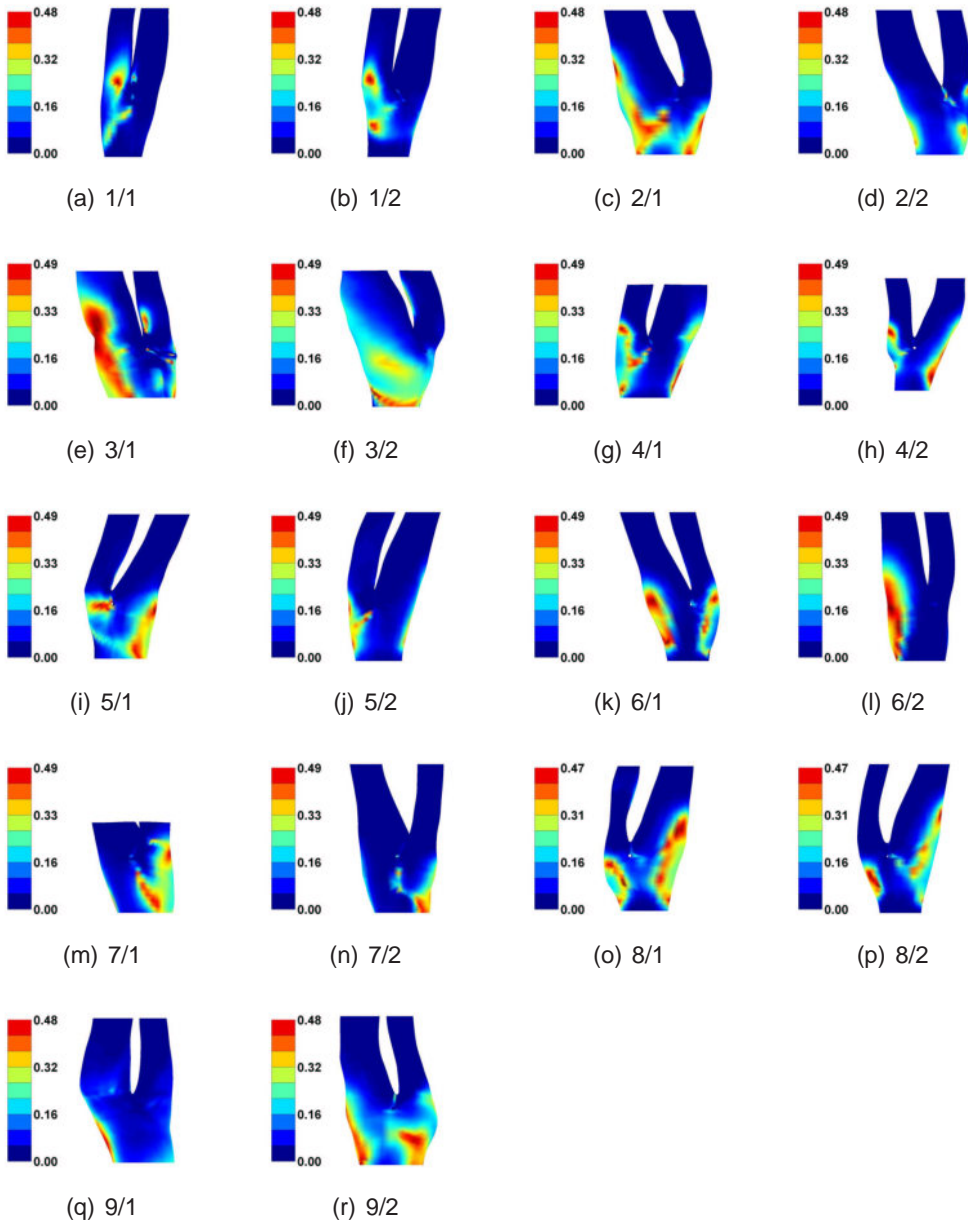
Figure VII.14.: Oscillatory Shear Index (OSI) distribution in all sessions (subjects 1-9). Sub-captions encoded as subject/session (dimensionless).

ments is in the range of 10%.[124] Variation in blood pressure is likely to contribute to variability of carotid cross-sectional area.

2. The diversity of the techniques involved is considerable. Ultrasound is used for IMT measurements and 3D carotid geometry acquisition. An EPOM device provides the 3D coordinates of the ultrasound probe during the scan. The contours are smoothed and discretised before area assessment. Each of the techniques introduces errors due to inherent uncertainties.

3. Ultrasound scan quality increases when the imaging slices are perpendicular to the vessel centreline. Because the ultrasound probe has to follow neck skin curvature rather than carotid centreline curvature, orthogonality could not be maintained throughout.

4. Due to the semi-automatic nature of the reconstruction technique, reconstruction will be, to some extent, operator dependent and subject to intra-observer variability. Inter-observer variability in reconstruction is not relevant as all scans were analysed by a single operator. The effect of operator variability is studied in the next section.

5. IMT measurements were made at a single location approximately 1 cm proximal to the carotid bulb, and with that measurement, the IMT values in the carotid tree were estimated using subject-specific polynomial functions. Although this mathematical approximation is likely to be a realistic way of estimating the IMT in the carotid tree, subject-variability is known to be high and errors are certainly introduced by these assumptions.

For subjects 3 and 4, the rather large differences are probably a combination of several influences. For subjects 1, 2, 7, 8 and 9, where areas in session 1 seem to be proportional to those in session 2, it can be speculated that the area difference in those subjects is either due to operator-dependence or physiological changes.

Centrelines   Figure VII.12 shows that the reproducibility of the reconstructed vessel centrelines is rather poor. Although only subject 9 has a difference in non-planarity parameter (NP) of more than 1.5% (see Table VII.2), subjects 2, 3, 5 and 6 show noticeable centreline differences. The fact that these differences do not show in the non-planarity parameter NP, is because this parameter represents the deviation of the centreline from the best fit plane.

That particular plane or the way the centreline deviates can be different in the two sessions, while the non-planarity parameter may change very little. The errors induced by the pcBird positioning system reported by Barratt[22] may play a role but cannot be the sole cause of it. A likely explanation for the rather poor centreline reproducibility is the variation in subject's head and neck positioning between scans. Although a standard scanning position was adopted by each subject, no fixed constraint was imposed on them, hence modest variations in neck angles between scans could have occurred. Another factor that may influence the centrelines, is the alignment technique used. Here, the apices have been overlaid in order to perform the numerical comparison. It is clear that an error in apex registration will induce an error in centreline agreement quantification. Since for the subjects with poor centreline agreement in Figure VII.12 the centrelines around the bifurcation apices seem to correspond well but diverge rather randomly after the bifurcation zone, it is thought that the effect of misalignment is negligible.

Time-averaged Wall Shear Stress and Oscillatory Shear Index distribution. It is worth noting that the same boundary conditions were used for all simulations. The 'typical wave form' was acquired in one subject and used in all simulations. It is clear that patient-specific flow wave forms would have been clinically more realistic. However, it would have been impossible to ascertain whether flow differences were due to flow measurement uncertainties rather than geometrical differences. The aim of this study was to assess the effect of geometric uncertainties on the flow, therefore, the flow boundary conditions were constrained.

The effect on the flow of the described geometrical differences can be evaluated in Figure VII.13 for the WSS and Figure VII.14 for the OSI. Although absolute average WSS differences are often greater than the 0.29 N/m^2 reported by Augst[16] on a carotid phantom, the agreement in WSS patterns is generally satisfactory. Noticeable differences can be observed in regions where area error is large (see subjects 3 and 4). Centreline variations seem to have a less important effect on WSS, although the WSS patterns in subjects 6 and 9 are clearly influenced by the change in centreline. On the other hand, subjects with obvious centreline differences (subjects 2, 3, 5, 6 and 9) all show an altered OSI distribution. Moreover, subjects with poor area agreement but good centreline agreement, show similar OSI distributions. High OSI values correspond to areas of flow recirculation. Although lumen area is an important factor in determining the presence or absence, location and size of recirculation, changes in curvature and non-planarity of vessel centrelines appear to have a more significant influence on OSI. Overall, the

WSS and OSI distributions were reproduced well, but the absolute values of WSS and OSI were influenced by respectively the area and centreline differences.

Limitations and Further work   In this study, inlet velocities were calculated theoretically, based on the same carotid flow wave form. Flow data is, however, very subject dependent, and individual flow rate measurements should ideally be used. The reproducibility of incorporating subject-specific pulsed wave Doppler measurements into carotid flow simulations will be investigated in the future.

Although 3DUS of the carotid bifurcation is possible, its applicability can be significantly impaired if there is insufficient visualisation of the bulb, internal and external carotid arteries. This is particularly the case when the bifurcation point is high in the neck and the carotid bulb is large. In such cases, the angle of the jaw physically impedes the access of the ultrasound probe to the vessels of interest. Unfortunately, these are not uncommon anatomical features,[16] suggesting that this restriction may be an important drawback of this technique.

Given the current degree of reproducibility and the promise of further improvements in both ultrasound imaging techniques and carotid reconstruction programs, ultrasound can be a useful and relatively inexpensive alternative to MRI for geometry acquisition of the carotid artery.

VII.4.2.4. 3DUS *in vivo* reproducibility: summary

In this study, the carotid bifurcations of 9 healthy volunteers were scanned twice with 3D ultrasound at least two weeks apart. From the ECG gated transverse 2D images, their 3D geometries were reconstructed and blood flow was calculated numerically.

Geometric reproducibility was assessed by examining area differences, area changes, centreline differences and non-planarity. Areas proved to be very reproducible, whereas centrelines appeared to be more sensitive. Very probably, variations in subjects' neck and head positions between the two scans were responsible for this finding. In future, the 3DUS protocol will be improved to reduce neck- and head position effects as much as possible.

Flow reproducibility was judged by evaluating velocities and the clinically more relevant parameters, namely WSS and OSI. WSS and to a lesser extent OSI distributions showed satisfactory reproducibility, although WSS had a low tolerance for area errors and OSI distributions were more sensitive to centreline variations. With standardisation of the ultrasound scan protocol, 3DUS has a great potential to become a useful and inexpensive alternative to MRI for geometry acquisition of superficial vessels.

VII.4.3. Operator Dependence

The previous section (VII.4.2) focussed on how reproducible the 3DUS technique is. The study showed, among other things, that the operator dependence could be a potential reason for the measured error. The phantom study had shown that operator dependence could indeed be an important source of error. Operator dependence can be subdivided into two parts: the variability due to the use of different scan operators ('SO') and the variability due to the use of different image processing operators ('IO'). The phantom study did not allow differentiation between variability caused by imaging and variability caused by segmentation since the images were segmented by the same person who performed the scans. In the current *in vivo* study, the operator dependence was therefore evaluated using 4 physicians and 3 IO's. Aim of the present study is to quantify the expected variability on a 3DUS measurement.

VII.4.3.1. Methods

Volunteer, Physicians and Operators   The right carotid bifurcation of a healthy 25 year old male sexy football phenomenon was scanned in total 11 times by 4 different physicians using the imaging protocol described in section VII.1.4. The subject's head was kept in the same position throughout the examination in order to avoid potential changes in the carotid geometry due to changes in head- or neck angles.

The SO with the largest experience using 3DUS (BA) scanned the subject twice, whereas the other physicians (AZ, SB and MJ) scanned the subject three times, assisted by BA at their first scan. AZ, SB and MJ had a large experience with cardiovascular US, but not with 3DUS. In order to eliminate potential physiological changes in the carotid bifurcation, all scans were performed in one afternoon.

Reconstruction and Computation The 11 right carotid bifurcations were segmented and reconstructed by 3 operators using the methods described in sections VII.2 and VII.3. In short, acquired images were segmented using purpose-built software in a MATLAB environment. A single IMT measurement was used for contour adjustment. Operator FG, a 3DUS technician, had the largest experience with segmentation. Operator MB was a physiotherapy student with limited experience in dealing with US images. Operator MA was a technician with no experience interpreting US images. IO's MB and MA were assisted by FG for their first segmentations (max. 10 images). Each of the operators segmented each of the 11 scans, yielding 33 sets of contours which were reconstructed and meshed using the methods described in section VII.3.

Computational details were the same as those for the 3DUS reproducibility study (section VII.4.2), except for the viscosity for which a Quemada (non-Newtonian) model was used (see section VIII.2).

Statistical Analysis Parameters describing area, centreline, shape and haemodynamic wall parameter agreement were computed for each simulation, which resulted in 33 values for each of the parameters. Using these values, the following standard deviations were computed:

- For each parameter examined, SO- and IO-mean values were calculated for each of the 3 scans, resulting in 3 values per parameter: one for each scan. $\sigma_{inter-scan}$ is the standard deviation of these means, n=3. The value of $\sigma_{inter-scan}$ is related to the level of repeatability achieved by a scan and image processing operator.

- $\sigma_{inter-SO}$, the standard deviation of the means for each physician, i.e. n=4. To acquire the 4 values for a particular parameter, the parameter was averaged over the operators and scans. $\sigma_{inter-SO}$ is related to the amount of the aforementioned variability that can be attributed to the fact that different physicians acquired the images.

- Averaging all values obtained by a particular image processing operator yielded 3 values for each parameter: 1 for each IO. $\sigma_{inter-IO}$ is the standard deviation of these 3 values, and it measures the inter-IO variability.

- σ_{all}, the standard deviation of the entire set of data, i.e. n=33. It gives an impression of the potential error if an untrained operator segmented the scan of an untrained physician.

VII.4.3.2. Results

Table VII.3 gives the standard deviations for the average arterial cross-sectional area, the area ratio, the overall and arterial non-planarity, the arterial linearity and tortuosity, the arterial shape and the bifurcation angle. For definitions of these parameters, see section II.3.2.2. Similar to Table VII.1, haemodynamic parameters have been presented as area-averaged means. Together with the WSS and OSI, WSSGs, WSSGt and WSSAG have been calculated. See section II.3.3.3 for a definition of these haemodynamic parameters. The bracketed values in Table VII.3 next to the considered σ are σ as a percentage of the mean (n=33).

VII.4.3.3. Discussion

Study setup   In this study, 3 image processing operators ('IO') reconstructed the right carotid bifurcation of a 25 year old male with no history of cardiovascular disease, using the scans of 4 different scanning operators ('SO') who each imaged the subject several times. All scans were performed in a single session in order to avoid important physiological changes in the carotid artery geometry and flow. Although only 1 subject was used in this study, the amount of data acquired on this subject was sufficient to get a representative value for the 3DUS operator dependence, especially bearing in mind that carotid B-mode ultrasound image quality has a small variability from one subject to the other.[289]

Prompted by the results of the *in vitro* study, operators were granted a minimum training: physicians were assisted by a trained 3DUS operator for their first scan, and IO's were taught how to segment using a maximum of 10 didactic B-mode images.

Statistics   The statistical analysis was performed here by reporting standard deviations rather than performing an ANOVA-test for each considered parameter. The goal of this study was to quantify the uncertainty of the parameters estimated using a combination of 3DUS and CFD. An ANOVA test informs on whether or not means of different groups (scans, physicians or operators) are *significantly* different, but the applicable significance level is very hard to determine, and depends on the application. The experienced standard deviation gives a measure of the expectable uncertainty, which is of greater clinical value.

Parameter [Unit]	$\sigma_{inter-scan}$ (n=3)	$\sigma_{inter-SO}$ (n=4)	$\sigma_{inter-IO}$ (n=3)	σ_{all} (n=33)
A_{CCA} [mm^2]	2.2676 (4.59%)	2.4655 (4.97%)	0.5860 (1.18%)	4.0486 (8.17%)
A_{ICA} [mm^2]	0.9320 (2.24%)	2.1353 (5.10%)	1.7138 (4.11%)	3.0903 (7.41%)
A_{ECA} [mm^2]	0.3505 (1.77%)	0.9377 (4.70%)	1.9510 (9.83%)	2.5980 (13.09%)
A_R [-]	0.0325 (3.53%)	0.0086 (0.94%)	0.0285 (3.10%)	0.0525 (5.71%)
NP [%]	0.8603 (15.32%)	1.1497 (20.64%)	0.0852 (1.53%)	1.6383 (29.34%)
NP_{CCA} [%]	0.2583 (17.58%)	0.2102 (14.52%)	0.0363 (2.52%)	0.5775 (40.07%)
NP_{ICA} [%]	0.8700 (42.19%)	0.9332 (43.54%)	0.1429 (6.88%)	1.4475 (69.75%)
NP_{ECA} [%]	0.0345 (8.03%)	0.0485 (11.15%)	0.0568 (13.14%)	0.1764 (40.83%)
L_{CCA} [%]	0.8142 (0.96%)	3.4926 (4.12%)	0.1218 (0.14%)	3.4995 (4.14%)
L_{ICA} [%]	1.3685 (1.73%)	3.7256 (4.69%)	0.3509 (0.44%)	3.4717 (4.39%)
L_{ECA} [%]	0.3844 (0.47%)	1.5485 (1.89%)	0.0519 (0.06%)	1.4426 (1.76%)
T_{CCA} [%]	0.2196 (15.35%)	0.2743 (19.82%)	0.0803 (5.70%)	0.3801 (26.99%)
T_{ICA} [%]	0.9291 (52.79%)	1.0038 (54.79%)	0.2358 (13.31%)	1.6469 (92.94%)
T_{ECA} [%]	0.0573 (8.35%)	0.2734 (38.47%)	0.1110 (16.17%)	0.7280 (105.99%)
α_{BIF} [°]	5.5711 (5.54%)	7.5465 (7.53%)	2.7725 (2.76%)	23.7628 (23.67%)
SF_{iCCA} [-]	0.0080 (0.83%)	0.0082 (0.85%)	0.0021 (0.22%)	0.0139 (1.45%)
SF_{iICA} [-]	0.0037 (0.38%)	0.0081 (0.82%)	0.0044 (0.45%)	0.0123 (1.26%)
SF_{iECA} [-]	0.0062 (0.64%)	0.0035 (0.35%)	0.0095 (0.97%)	0.0133 (1.35%)
Mean $V_{MAX,CCA}$ [m/s]	0.0080 (3.65%)	0.0083 (3.78%)	0.0047 (2.14%)	0.0151 (6.89%)
Mean $V_{MAX,ICA}$ [m/s]	0.0008 (0.46%)	0.0192 (10.86%)	0.0084 (4.69%)	0.0211 (11.84%)
Mean $V_{MAX,ECA}$ [m/s]	0.0042 (2.78%)	0.0134 (8.86%)	0.0109 (7.17%)	0.0184 (12.11%)
Mean WSS [N/m^2]	**0.0087 (1.51%)**	**0.1155 (20.15%)**	**0.0467 (8.15%)**	**0.1204 (20.99%)**
WSS in iCCA [N/m^2]	0.0267 (5.66%)	0.0528 (11.26%)	0.0113 (2.40%)	0.0816 (17.42%)
WSS in eCCA [N/m^2]	0.0235 (5.04%)	0.0794 (16.64%)	0.0160 (3.42%)	0.0853 (18.24%)
WSS in outer ICA [N/m^2]	0.0267 (4.08%)	0.1760 (26.84%)	0.0850 (12.97%)	0.1934 (29.51%)
WSS in inner ICA [N/m^2]	0.0193 (2.32%)	0.1350 (16.45%)	0.0927 (11.14%)	0.1789 (21.50%)
WSS in outer ECA [N/m^2]	0.0095 (1.54%)	0.1722 (28.35%)	0.1246 (20.31%)	0.2139 (34.85%)
WSS in inner ECA [N/m^2]	0.0084 (1.17%)	0.1557 (21.76%)	0.1263 (17.49%)	0.2036 (28.21%)
Mean OSI [-]	**0.0062 (4.71%)**	**0.0272 (20.96%)**	**0.0048 (3.68%)**	**0.0292 (22.19%)**
OSI in iCCA [-]	0.0162 (10.95%)	0.0134 (8.99%)	0.0016 (1.07%)	0.0313 (20.94%)
OSI in eCCA [-]	0.0080 (4.46%)	0.0481 (27.78%)	0.0087 (4.88%)	0.0511 (28.54%)
OSI in outer ICA [-]	0.0102 (11.19%)	0.0380 (43.20%)	0.0107 (11.87%)	0.0391 (43.45%)
OSI in inner ICA [-]	0.0031 (6.16%)	0.0094 (18.05%)	0.0039 (7.70%)	0.0179 (35.31%)
OSI in outer ECA [-]	0.0028 (1.95%)	0.0438 (30.12%)	0.0143 (9.82%)	0.0470 (32.27%)
OSI in inner ECA [-]	0.0139 (15.64%)	0.0213 (23.71%)	0.0176 (19.63%)	0.0352 (39.34%)
Mean WSSGs [N/m^3]	**4.3955 (1.64%)**	**48.1821 (18.10%)**	**19.7994 (7.41%)**	**50.6818 (18.97%)**
WSSGs in iCCA [N/m^3]	4.8100 (2.27%)	14.0448 (6.65%)	3.7906 (1.80%)	20.1137 (9.53%)
WSSGs in eCCA [N/m^3]	6.1174 (2.81%)	14.4297 (6.62%)	5.6318 (2.59%)	20.1121 (9.25%)
WSSGs in outer ICA [N/m^3]	16.0475 (5.87%)	79.8826 (29.21%)	39.1111 (14.30%)	88.8939 (32.49%)
WSSGs in inner ICA [N/m^3]	9.7339 (2.34%)	50.9174 (12.39%)	40.5765 (9.79%)	74.6253 (18.00%)
WSSGs in outer ECA [N/m^3]	7.8773 (2.60%)	74.5676 (24.81%)	58.1145 (19.19%)	96.4197 (31.83%)
WSSGs in inner ECA [N/m^3]	2.8716 (0.77%)	51.9867 (13.93%)	54.0293 (14.41%)	85.3588 (22.77%)
Mean WSSGt [N/(m^{2}s)]	**0.1571 (1.61%)**	**1.4153 (14.55%)**	**0.6312 (6.49%)**	**1.5368 (15.80%)**
WSSGt in iCCA [N/(m^2 t)]	0.2613 (2.80%)	0.6503 (6.96%)	0.2043 (2.20%)	0.9581 (10.30%)
WSSGt in eCCA [N/(m^2 t)]	0.3154 (3.40%)	0.8216 (8.81%)	0.3109 (3.36%)	1.0624 (11.47%)
WSSGt in outer ICA [N/(m^2 t)]	0.4646 (4.71%)	2.1151 (21.50%)	1.0631 (10.79%)	2.3750 (24.10%)
WSSGt in inner ICA [N/(m^2 t)]	0.3785 (3.33%)	2.2206 (19.69%)	1.1720 (10.33%)	2.5295 (22.28%)
WSSGt in outer ECA [N/(m^2 t)]	0.3488 (3.70%)	2.2715 (24.33%)	1.6686 (17.72%)	2.8211 (29.96%)
WSSGt in inner ECA [N/(m^2 t)]	0.1352 (1.38%)	2.3906 (24.55%)	1.6771 (17.09%)	2.8547 (29.09%)
Mean WSSAG [rad/s]	**6.0431 (4.36%)**	**16.8219 (12.14%)**	**1.1458 (0.82%)**	**20.2853 (14.56%)**
WSSAG in iCCA [rad/s]	12.7436 (10.76%)	11.9033 (9.97%)	2.5023 (2.09%)	19.2646 (16.10%)
WSSAG in eCCA [rad/s]	1.6659 (1.08%)	27.1428 (17.96%)	4.6647 (3.03%)	30.3898 (19.74%)
WSSAG in outer ICA [rad/s]	5.1178 (5.01%)	10.2561 (10.04%)	9.3581 (9.12%)	21.7525 (21.20%)
WSSAG in inner ICA [rad/s]	9.2099 (6.07%)	23.2511 (15.14%)	19.0729 (12.50%)	36.9629 (24.22%)
WSSAG in outer ECA [rad/s]	4.6484 (2.48%)	32.7465 (17.47%)	1.2163 (0.65%)	40.5739 (21.65%)
WSSAG in inner ECA [rad/s]	14.0399 (7.46%)	48.0816 (25.45%)	6.8383 (3.62%)	54.4477 (28.79%)

Table VII.3.: Analysis of Variance for all Parameters in *in vivo* study represented as standard deviation (percentage is standard deviation divided by the overall mean (n=33))

Geometry Table VII.3 summarises the statistical analysis for the *in vivo* study. σ_{all}, a measure of the uncertainty on a single measurement performed by an inexperienced physician and segmented by an inexperienced operator, is very low for the considered parameters (e.g. 8.17% for A_{CCA}). For the geometry parameters, this uncertainty is mainly due to the fact that images were acquired by different physicians, more than the fact that images were segmented by different operators ($\sigma_{inter-IO}$ in general smaller than $\sigma_{inter-SO}$). The inter-scan differences show similar variability to the inter-physician variability. For the velocity and WSS-related parameters, variability is mainly caused by $\sigma_{inter-SO}$, suggesting that different physicians give different results, albeit slightly.

Flow For the flow parameters, $\sigma_{inter-scan}$ has dropped in importance in comparison to the $\sigma_{inter-scan}$ for geometry parameters, which means that the learning curve reaches its maximum level using the minimal amount of training to which the physicians and operators were subjected in this study. Furthermore, the same features are observed as for the geometry parameters: $\sigma_{inter-SO}$ makes in general the largest contribution to σ_{all}. The subject reported differences in probe pressure between physicians: these small differences in scan techniques could be the reason for the relative importance of $\sigma_{inter-SO}$ for flow parameters. Moreover, the operators reported differences in image quality related to the physicians: some physicians made easily segmentable images in comparison to others. One would expect the physician with the largest 3DUS experience to be the one generating the best quality images, but in fact it was the physician with the largest experience in regular 2D US who created the images with the best contrast. This should not surprise since 3DUS makes use of conventional 2D B-mode imaging. Thus, our results suggest that the imaging rather than the segmentation caused the main part of the total uncertainty.

VII.4.3.4. 3DUS *in vivo* variability: summary

In this study, 4 physicians (of which 3 were inexperienced) scanned the right carotid bifurcation of a healthy volunteer a total of 33 times. These scans were segmented by 1 experienced and 2 inexperienced operators. It was shown that 3DUS-based CFD is a robust, reproducible and operator-independent technique for assessing carotid haemodynamics. The residual uncertainty was mainly due to the uncertainty in B-mode imaging rather than to the 3D reconstruction.

Table VII.3 is an interesting end-point of this study. It gives the expected uncertainty on a single scan, but also the cause of this uncertainty. If, in future, a study was to be performed by a single operator, the minimal detectable change in a parameter's value can be found in Table VII.3 in the columns labelled $\sigma_{inter-scan}$ or $\sigma_{inter-IO}$. For example, the minimal detectable change in overall NP is of the order of 0.9%, consistent with values found for NP reproducibility using MRI for carotid reconstructions.[157]

VII.4.4. 3DUS reliability: summary

In this section, the 'reliability' of 3DUS-based CFD was assessed in a number of ways. In a first study, the accuracy, reproducibility and operator dependence were judged on a phantom study. Table VII.1 shows the results of these quantifications for both the geometry and flow parameters. The study showed that 3DUS-based CFD can be very accurate provided that operators receive at least a minimum of training. It was clear that 3DUS-based CFD was ready for the next step: the assessment of *in vivo* reproducibility. In this study, 9 healthy subjects were scanned twice and the agreement between the two scans was quantified. It was found that cross-sectional area agreement was good, but centreline agreement was less so. The reproducibility of the haemodynamic parameters WSS and OSI seemed linked to respectively the reproducibility of cross-sectional areas and centrelines.

Because there was a need for a clear definition of the reliability of *in vivo* 3DUS-based CFD, a large operator dependence study was set up. Here, the operator dependence was divided into imaging and segmenting dependence, using 4 physicians for the image acquisition and 3 operators for the segmentation. The physicians were assisted at their first scan by an experienced 3DUS physician. The operators with no segmenting experience were given a minimum of training as suggested by the phantom study. Admittedly, only 1 subject was used in this variability study and the values for the variability could be subject-dependent. Nevertheless, a total of 33 simulations were performed using this subject's right carotid bifurcation, which is a vast data set enabling the user to acquire good insights on operator dependence. It was found that with a minimum of training, operator dependence can be minimised. Table VII.3 is an interesting end-point. It quantifies, for a large number of geometry and flow parameters, the answers on questions such as:

- 'How accurate is 3DUS-based CFD?'

- 'How reproducible is 3DUS-based CFD?'

- 'What is the minimum detectable change in 3DUS-based CFD?'

VIII. Choice of model parameters

In this chapter, computational details of image-based modelling are discussed. These include issues related to the boundary conditions (section VIII.1), non-Newtonian models (section VIII.2) and heart rate (section VIII.3).

VIII.1. Boundary Conditions

Image-based CFD requires all of the following: (1) the reconstruction of arterial geometries based on medical images, (2) boundary conditions at the inlet and outlet of the model and (3) a computational solver for obtaining the solutions to the governing equations. This section will be focussed on the boundary conditions.

VIII.1.1. In- and Outflow Conditions for MRI-based models

VIII.1.1.1. Study Motivation

The question on the choice of boundary conditions has been examined in a number of studies. Wood[370] was one of the first to raise the question in their study describing the haemodynamics in the descending aorta. Others, such as Ladak,[164] Milner,[219] Thomas,[334] Cebral,[50] Zhao[387] and Long[195] investigated this in the carotid arteries. In other studies,[196,197,198,374] Long and Xu concentrated on the abdominal bifurcation. Saber[268] used *in vivo* MRI measurements of a left ventricle to investigate the possibilities of CFD in capturing the three-dimensional contraction and expansion phases of endocardial motion in the left ventricle.

Although most of the studied vessels have similar sizes and flow conditions, it is striking to realise that a wide range of different boundary conditions have been used: a summary is given in Table VIII.1. It indicates that *in vivo* MRI

WORK	TARGET	GEOMETRY RE-CONSTRUCTION	INFLOW	OUTFLOW
Milner[219]	Carotid bif.	Manually	MR-developed	mass (ICA),
Moore[223]	Abdominal bif.	Prewitt	developed	mass
Moore[225]	Carotid bif.	Prewitt	developed	Uniform pressure (ICA), mass (ECA)
Ladak[164]	Carotid bif.	3D Snake	MR-developed	MR-developed (ECA), mass (ICA)
Thomas[334]				MR-developed (ECA)
Steinman[308]	Carotid bif.	Snake	MR-developed	Uniform pressure (ICA), MR-developed (ECA)
Thomas[332]	Carotid bif.	Snake	MR-developed	MR-developed (ICA), mass (ECA)
Weston[362]	U-tube	Prescribed	MR (steady) Plug (puls.)	MR+mass,
Wood[370]	Descending aorta	CFD software	MR	Uniform pressure
Saber[268]	Left ventricule	By hand	Mass	Mass
Long[197,198]	Abdominal bif.	RGM & Snake	Mass	MR
Xu[374]	Abdominal bif.	RGM & Snake	MR+mass	MR
Long[195]	Carotid bif.	RGM & Snake	MR+mass	MR
Long[196]	Abdominal bif.	RGM & Snake	MR+mass	MR
Zhao[387]	Carotid bif.	RGM & Snake	Uniform pressure	mass-dev. (Dop)
Köhler[161]	Carotid bif. model	RGM & Snake	MR	mass
Zhao[384]	Carotid bif.	RGM & Snake	mass-dev. (Dop)	mass-dev. (Dop) (ICA), Uniform pressure (ECA)
Zhao[385]	Carotid bif.	RGM & Snake	MR	mass
Botnar[33]	Carotid bif.	WLS	MR	n.a
Leuprecht[177,178]	Descending aorta	n.a.	MR	Uniform pressure
Cebral[50]	Carotid bif. model	TDF	MR-parabolic	uniform pressure (ICA), MR-parabolic (ECA)
Cebral[54]	Circle of Willis	RGM & DT	Chosen	Uniform pressure
Cebral[56]	Carotid bif.	TDF	Uniform pressure	MR
Cebral[53]	Circle of Willis	RGM & DT	MR-developed	MR-developed or Uniform pressure
Redaelli[262]	Carotid bif.	RGM	n.a. (steady)	mass
Stroud[311]	*Ex vivo* Carotid stenosis	n.a.	Plug	Uniform pressure
Walker[346,347]	Carotid bif.	Manual	MR	n.a.

Table VIII.1.: Reconstruction of geometry and choice of inflow and outflow boundary condition type in different studies combining MRI and CFD. Key to geometry reconstruction models: Snake: snake model; RGM: region growing method; Prewitt: Prewitt edge detection algorithm; DT: direct tesselation; TDF: tubular deformable model; Balloon: virtual inflated balloon model; WLS: surface modelling using weighted least-squares splines. Key to boundary conditions: MR: MRI velocity measurements; MR+mass: MRI velocity measurements scaled to match the flow rate; mass: mass conservation; developed: a developed velocity profile was set, based on the knowledge of the flow rate; Plug: plug flow or uniform velocity flow; MR-developed: here, MRI velocity measurements provided the flow rate, this was used to calculate an pulsatile developed flow profile and then set as boundary condition; mass-dev. (Dop): same as 'MR-developed' but with flow rate acquired from pulsed Doppler; Uniform pressure: a uniform pressure distribution is set on the boundary; MR-parabolic: a parabolic velocity profile is set, resulting of a flow rate measured by MRI. n.a.: not available

measured velocities can be used as inflow boundary conditions in a number of ways. However, little is known about the effect of different inflow and outflow boundary conditions on predicted flow parameters. Some of these effects are examined in detail in this section.

VIII.1.1.2. Study Setup

Because it was believed that a U-tube could be used as a simplified model of the human aorta, both steady and pulsatile flows in a U-tube have been studied extensively by a number of research groups since the early seventies.[5, 38, 64, 65, 133, 134, 141, 205, 228, 237, 288, 292, 296, 297, 298, 319, 320] A U-tube phantom was chosen in this study to investigate the effects of in- and outflow boundary conditions. Collins and Dennis published fully developed steady axial velocity profiles[69] for Dean numbers 66.1, 77.1, 190.9 and 369.5. The fully developed profiles in the bend are shown in Figure VIII.1. Soh and Berger[296] did a similar study for Dean numbers 108.2 and 182.9. Here, these velocity profiles were compared with those obtained from MRI-based simulations using different boundary conditions.

(a) 66.1

(b) 77.1

(c) 190.9
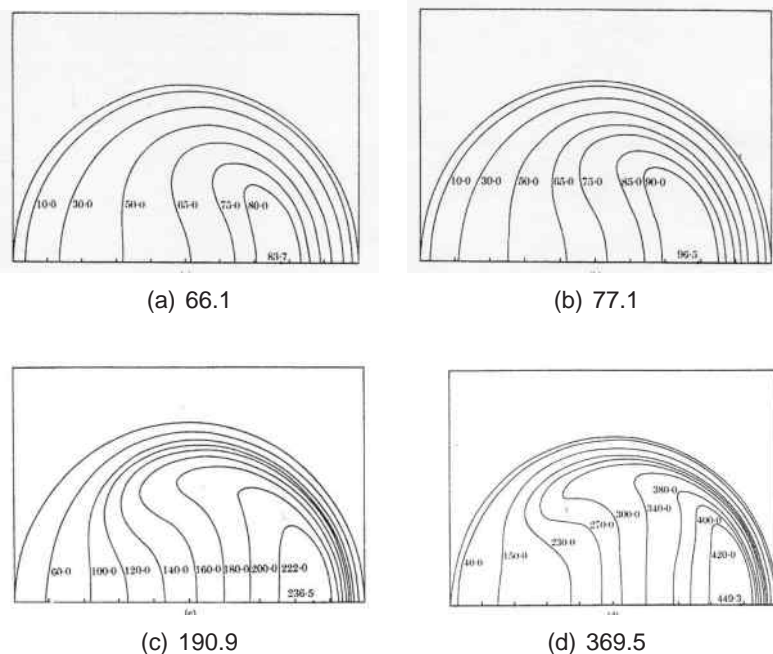
(d) 369.5

Figure VIII.1.: Fully developed profiles in the bend at Dean numbers $\kappa = 66.1$ (a), 77.1 (b), 190.9 (c) and 369.5 (d) as published by Collins.[69] The pilot study was performed at $\kappa = 163$, the steady tests at $\kappa = 66.1$, 77.1 and 191 (see Table VIII.2).

Phantom   All the tests were performed on the same U-bend, made of agar gel, which gives very good MRI-contrast. Its internal diameter D is 8 mm (D=2 r). The bend radius R is 25 mm, yielding a curvature ratio δ of 0.16, defined as the ratio of the internal radius to the bend radius ($\delta = r/R$).

Setup   The pump used in this setup (Figure VIII.2) is the MRI version of a UHDC[a] Flow Pump (Numatics 225-3728 24VDC 6.0 Watts, Shelly Limited, London Ontario, Canada), capable of generating a range of time-varying flow profiles. The pump was placed outside the scanner chamber in order to stay away from the magnetic field of the scanner during flow measurements. Reinforced (but still flexible) tubes, passing through a hole in the wall, connected the phantom to the pump. To extend the entrance length, a straight rigid 8 mm tube with a length of 40 cm was connected to the U-bend, bringing the total rigid entrance length L over 50 cm. This was necessary for the flow to become fully developed.[276]

---

[a]**UHDC**: University Hospital Development Canada
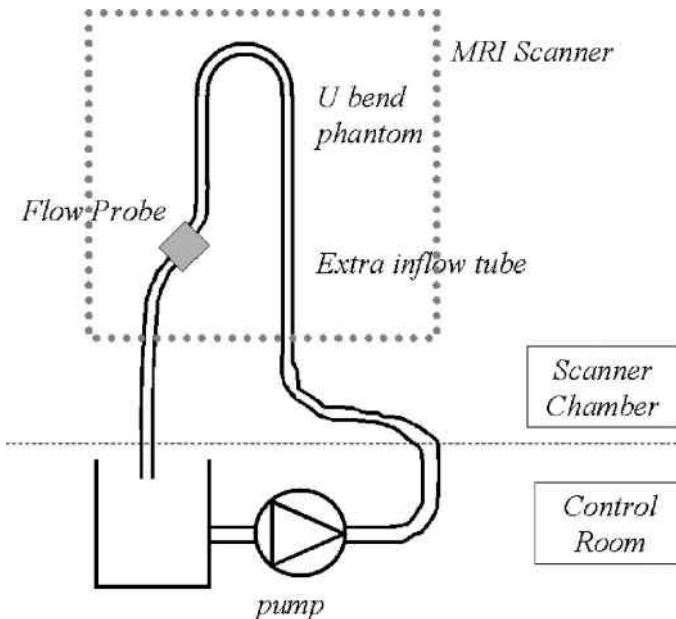
Figure VIII.2.: Setup

Imposed Flow Conditions   The **tubular Reynolds** number is defined as:

$$Re_t = \frac{V_{mean} \, D \, \rho}{\mu} \qquad\qquad \text{(VIII.1)}$$

Here V_{mean} is the cross-sectional average velocity. The **Dean number**, used to classify flows in rigid curved tubes, is defined as follows:

$$\kappa = \frac{2 \, V_{mean} \, r \, \rho}{\mu} \sqrt{\frac{r}{R}} \qquad\qquad \text{(VIII.2)}$$

In a pilot study, performed before all other experiments, the steady flow rate was 10 ml/s, the Reynolds number was 404 and the Dean number 163. An ultrasonic flow probe (HT207 Transonic Flowmeters, Transonic, Ithaca, New York, USA), was connected to the tube leaving the U-bend. A fluid- and tube-specific calibration of the flow probe was performed. The flow was measured continuously at a sampling rate of 200 Hz (computer A/D card, National Instruments, Austin, Texas, USA). The flow was also measured by timed collection (volumetrically) during the tests.

First, the pilot study was performed for a steady flow as described in Table VIII.2. The results were used to establish guidelines for filtering the MRI velocity profiles before they can be used as inflow boundary condition in the CFD model. *Next*, three steady and three pulsatile flows were performed as presented in Tables VIII.2 and VIII.3. The Tables also contain the V_{enc} settings for the cine PC MRI measurements.

Name	Fluid	κ	Re	Flow [ml/s]	L [cm]	$V_{enc}X$ [cm/s]	$V_{enc}Y$ [cm/s]	$V_{enc}Z$ [cm/s]
Pilot study	40/60 Gly/Water	163	404	10	21	70	70	70
Steady 1	Tap water	66.1	220	1.39	12	2	2	9
Steady 2	Tap water	77.1	267	1.67	14	2	3	11
Steady 3	Tap water	191	882	5.55	46	10	5	35

Table VIII.2.: Flow parameters for the steady tests. κ, the Dean number, and Re, the tubular Reynolds number, are dimensionless parameters defined in the text. L, the 'entrance length', is the theoretical length required for a uniform inflow profile to become fully developed (parabolic). V_{enc} is a parameter set by the MRI operator, restricting the acquirable velocities to [-V_{enc},+V_{enc}]. The directions are the horizontal in-plane direction (x), the vertical in-plane direction (y) and the horizontal out-of-plane direction (z). Flow is through-plane.

Name	Re	κ	α	Q_m [ml/s]	Q_p [ml/s]	f [bpm]	V_{enc}X [cm/s]	V_{enc}Y [cm/s]	V_{enc}Z [cm/s]
Pulsatile 1	101	40.5	11	1.22	4	72	4	4	15
Pulsatile 2	177	70.8	11	2.14	7	72	7	4	25
Pulsatile 3	253	101	11	3.055	10	72	10	6	35

Table VIII.3.: Flow parameters for the pulsatile tests. Here, the dimensionless parameter α, known as the Womersley parameter, reflects the influence of the periodicity; Q_m: mean flow; Q_p: peak flow; f: frequency in beats per minute. See Table VIII.2 for the definition of other parameters.

The pilot study was intended to assess the reliability of velocity measurements with MRI. It was performed with a 40/60 glycerine/water mixture. The dynamic viscosity, measured with a capillary viscosimeter, was 4.38 mPa.s. The density of 1112.7 kg/m^3 was read from a densimeter (Avensis, Namur, Belgium). Both values for viscosity and density were measured at 22 °C. The other steady flow tests were performed with water at 22 °C, yielding a density of 998 kg/m and a viscosity of 0.9596 mPa.s.

MRI measurements Velocities were measured using the cine 3D Phase Contrast technique. A 1.5 T MRI Scanner (Philips Medical Systems, Best, The Netherlands) was used, the principal scanner settings for the gradient-echo velocity acquisition sequences were: T_E = 9.39 ms (shortest), T_R = 18.72 ms (shortest), flip angle (FA) = 10 degrees, Number of Excitations (NEX) = 2, matrix size = 256x256, Field of View = 160 mm and slice thickness = 5 mm. This sequence was used to measure the axial and secondary velocities in cross-sectional planes. For the pulsatile scans, 16 equally distributed time frames were imaged.

Meshes & Solver The true geometry of the tube was meshed using the advancing front technique implemented in PAM-GEN3D™.[239] Table VIII.4 shows the specifications of the used meshes. The meshes A, B, E, F, H, J, K and L are for half of the tube, taking advantage of the symmetry. These were used in simulations where symmetric boundary conditions were implemented. The meshes described in Table VIII.4 were obtained after grid convergence tests as described in section III. For instance, in the case of mesh E, two other grids were tested, one with 45957 elements (mesh E') and another with 127939 elements (mesh E"). The results of mesh E (58814 elements) compared very well with those in the fine mesh but differed from the results of the coarse mesh. In order to restrict CPU time, mesh E was chosen above mesh E", the only two meshes yielding a correct

Mesh	Nelem	CV [cm^3]	BEZ [mm]	Th [mm]	PL	PR [-]	N	Refining in ...	REZ [mm]
A	92547	12.03	0.8	3	Log	1.2	7	Bend	0.6
B	51056	5.74	1.8	3	Power	1.2	7	Bend	0.6
C	152261	13.50	1	-	-	-	-	Bend	0.33
								Outflow leg	0.33
D	112387	10.99	0.6	-	-	-	-	Bend	0.33
								Outflow leg	0.33
E	58814	7.00	0.8	2	Log	1.25	10	Bend	0.4
F	45305	4.24	0.8	2	Log	1.25	10	Bend	0.4
G	42053	3.48	0.7	-	-	-	-	Bend	0.4
H	96581	14.79	0.8	2	Log	1.25	10	Bend	0.65
J	60548	5.87	0.8	2	Log	1.25	10	Bend	0.4
K	67781	7.83	0.8	2	Log	1.25	10	Bend	0.4
L	79559	9.52	0.8	2	Log	1.25	10	Bend	0.4

Table VIII.4.: Parameters for the mesh generation using the advanced front technique. CV: computing volume; PAMFLOW™ parameters: Nelem: number of elements; BEZ: Basic element size; Th: boundary layer thickness; PL: progression law: a mathematical rule describing how the element size changes from the wall inwards; PR: progression rate: a parameter required by the progression law; Refining in ...: the region where the mesh was refined;REZ: refined element size: the minimum element size required. See PAM-GEN3D™ manual[239] for details.

flow profile. The definition of the parameters of the boundary layer meshes (thickness Th, number of elements N and progression rate PR) is shown on Figure VIII.3 (b). Figure VIII.3 (d) gives an overview of the surface mesh G, whereas Figure VIII.3 (c) is a close-up of the part where the coarse mesh is refined before entering the bend.

In this work, PAMFLOW™ was used to solve the Navier-Stokes equations and the numerical algorithm employed are well documented.[238]

Boundary Conditions　On the tube wall, no-slip boundary conditions were imposed. The outflow boundary condition was set at a constant pressure. Four types of inlet boundary conditions were used (see Figure VIII.4) :

- **Uniform**: When using the *uniform* boundary condition, the mean velocity V_{mean} was set in all points of the inlet plane. In the pulsatile case, *uniform* meant that a time-varying flow rate with a uniform velocity profile at each time point was set. The uniform profile was preferable in comparison with a parabolic profile because it reaches a developed profile more quickly, as found by Redaelli.[261]
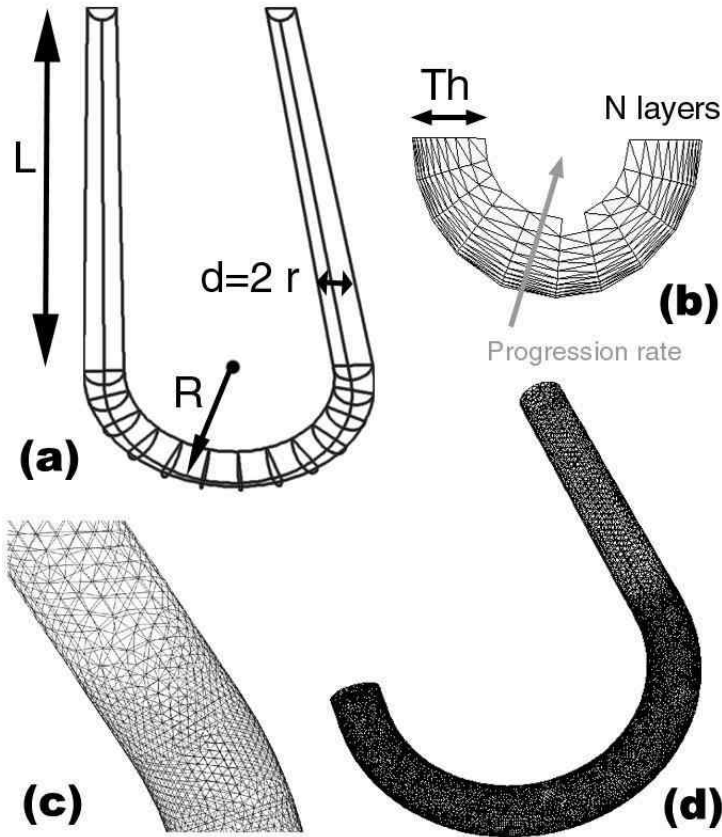
Figure VIII.3.: a: Geometry of the U-bend. Inflow and outflow length L 135 mm, diameter D 8 mm, bend radius R 25 mm. The picture shows only half of the U-tube, due to symmetry. b: Boundary layer mesh at inflow plane using a logarithmic progression rate. Th, the boundary layer thickness, shows how far the boundary layer extends. N is the number of layers. The thickness of every layer can be calculated from the thickness of the preceding layer following a mathematical rule, called the progression rate.[238] Examples of progression rates are: uniform, logarithmic, exponential or no progression rate. c: Detail of surface mesh G. This mesh is used for coupling with MRI velocity measurements (inlet is left on the image). d: Overview of the same surface mesh G. See PAM-GEN3D™ manual[239] for details.

- **Parabolic**: A parabolic inlet boundary condition is a Poiseuille velocity profile:

$$v(r) = 2\,V_{mean}\left(1 - \frac{4r^2}{D^2}\right) \tag{VIII.3}$$

where v is the velocity and r is the radial distance to the centre of the (circular) tube.
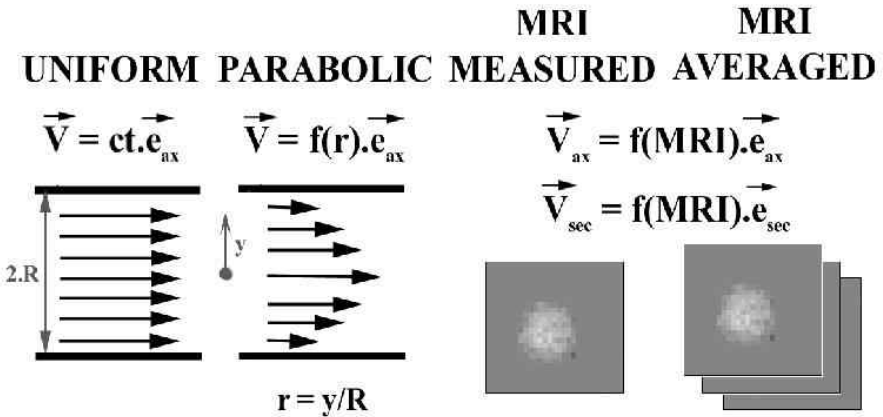
Figure VIII.4.: The used boundary conditions. $\vec{V}$ is the velocity set at the inlet; ct is a constant equal to the flow rate divided by the lumen area; $\overrightarrow{e_{ax}}$ is the axial unit vector (the unit vector in the I/S axis); $\overrightarrow{e_{sec}}$ represents both in-plane unit vectors; y varies linearly between 0 in the centre of the tube and the tube radius R at the circumference; f(r) means that the set velocities depend on the relative distance from the considered point to the tube centre; f(MRI) means that the set velocities depend on the velocities measured in MRI, either in a single plane (MRI measured) or consecutive planes (MRI averaged).

- **MR measured**: velocity measurements were made with MRI at exactly 5 mm proximal from the bend/straight tube interface. The velocity values were extracted and implemented as inlet boundary condition. When using MRI velocity measurements as boundary condition, not only the axial velocities but also the secondary velocities were used, since they have important haemodynamic influences.[282] Note that although the velocities were measured at the end of the straight tube, there could be secondary velocities due to the upstream influence of the bend.[38] In the pilot study, the measured velocities were used 'as such', i.e. without any smoothing or filtering. In the other studies, the velocities were filtered and scaled to match the flow rate as explained subsequently.

- **MR averaged**: Weston[362] observed in their velocity measurements with MRI unexpected flow profiles showing random asymmetries. The authors therefore suggested that a more reliable velocity profile for the inflow boundary condition should be derived by averaging the velocity measurements made at two or more upstream planes. The *MR averaged* boundary condition used the velocity profile resulting from averaging the profiles measured at three sections: the inlet, the section 5 mm distal from the inlet, and the section 5 mm proximal from

the inlet. Velocities were averaged for each of the three components. Similar to the 'MR' boundary condition, the measured velocities were used 'as such' in the pilot study, whereas in the other simulations, the velocities were filtered and scaled to match the flow rate as explained subsequently.

Hence, the only difference in inlet boundary conditions between the simulations was the shape of velocity profiles (*uniform, parabolic, MRI or MRI averaged*). Note that the *position* of the inlet relative to the bend differed between the cases: e.g. when using a uniform velocity profile, the inflow plane was chosen far enough from the bend to allow for full development of the flow. In simulations that used MRI data as inlet boundary conditions, the model started at the acquisition plane (5mm proximal from the straight tube/bend interface). In Figure VIII.3 (d), the MRI acquisition plane was very close to the bend, resulting in a truncated inflow leg. Note that this reduces the computational domain drastically. Another implication of the use of MR measured boundary conditions, was the loss of *symmetry*. For the simulations with assumed inflow velocity profiles, the U-tube could be split into two symmetrical parts and simulated for half only, as mentioned above. However, when using MRI measured velocities as boundary condition, the whole domain had to be used and simulated since these velocities are not necessarily symmetric.

The MR velocity Filter   Figure VIII.5 shows the measured profile at the entry to the bend before filtering. The directions of the arrows on the picture correspond to the velocity directions and the length of the arrows corresponds to the velocity magnitude. Clearly, the three arrows encircled by circle A, which occur at the border, are unrealistically large. Other velocities, encircled by circle B, have secondary velocities higher than the primary velocities. Filtering the velocity measurements is required.

Nevertheless, the 'MR' boundary conditions described above were implemented without smoothing or filtering in the pilot study. Comparison of the pilot study with the studies under steady flow conditions allows the effect of filtering to be examined. The consequences can be seen clearly when evaluating the **CFL**-numbers (Courant number)[b] required in the different simulations[238] (Table VIII.5). A high CFL-number will increase the time step and thus reduce the CPU time. However, stability is weakened with increasing CFL-numbers. Measurement errors, such as those illustrated in Figure

---

[b]For a definition of the CFL number, see equation III.21 on page 88.
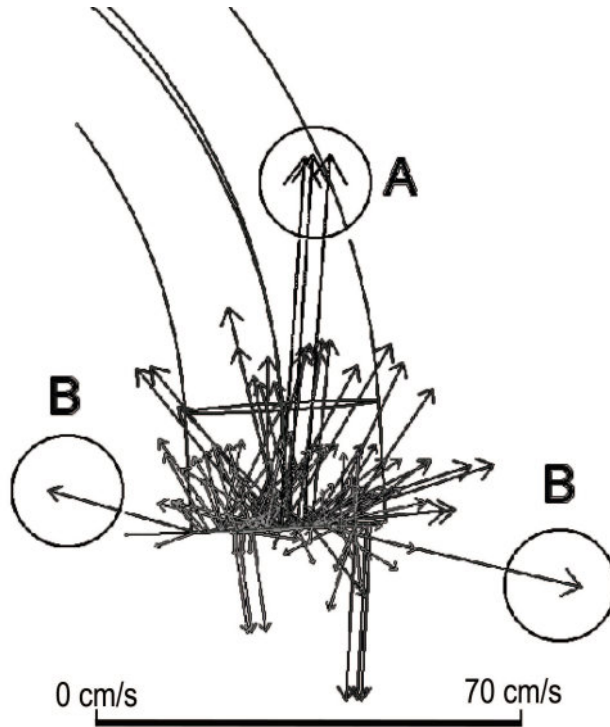
Figure VIII.5.: Inflow velocities without filtering.

VIII.5, favour instability. Therefore, in order to establish a stable simulation in the situations where no velocity filters were used, a sufficiently low CFL-number had to be set: 0.1 and 0.15 in the non-filtered cases, versus 0.3 in filtered cases.

The filtering consisted of two criteria.

CFL-factor	Uniform	Parabolic	MR	MR averaged
Pilot Study	0.3	0.3	0.15	0.1
Steady 1	0.3	0.3	0.3	0.3
Steady 2	0.3	0.3	0.3	0.3
Steady 3	0.3	0.3	0.3	0.3
Pulsatile 1	0.1	-	0.3	0.3
Pulsatile 2	0.1	-	0.3	0.3
Pulsatile 3	0.1	-	0.3	0.3

Table VIII.5.: Summary of the CFL-factors used for each simulation.

1. When MRI velocity measurements were used as the inflow boundary condition, the location of the measurement plane was chosen proximal to the bend so that secondary velocities were very small in comparison to the axial velocities.[5, 320] Therefore, secondary velocities greater than 10% of the axial velocity were set to 0 cm/s.

2. Near the wall, large errors in the MRI measured velocities may occur due to the partial volume effect (PVE). The PVE is an undesired effect which occurs in pixels consisting of partly moving fluids and partly stationary tissue. Therefore, near-wall axial velocities larger than 20% of the maximum absolute value defined for the acquisition (V_{enc}) were set to 0 cm/s.

VIII.1.1.3. Results

Figure VIII.6 (a) shows a comparison of the axial velocity profiles for simulations using different inflow boundary conditions in the pilot study (see Table VIII.2 for flow parameters). The velocities are shown in the plane separating the bend and the outflow leg of the U-tube, marked 'exit bend' in Figure VIII.7. The measured axial velocity profile in this plane is shown in Figure VIII.6 (b). Figure VIII.8 (a-d) shows the secondary velocity profiles for simulations using different inflow boundary conditions in the second steady case. Table VIII.2 shows the flow parameters for these steady cases. Figure VIII.8 (e) gives for comparison the secondary velocity profile measured with MRI. Finally, Figure VIII.9 compares MRI axial velocity measurements (upper row) with predictions done by CFD using different types of inflow boundary conditions for the third pulsatile test case (see Table VIII.3 for flow parameters). The velocities in Figures VIII.8 and VIII.9 are shown in the section 120 degrees downstream the inflow of the bend, as defined in Figure VIII.7.

VIII.1.1.4. Discussion

Filtering   The CFL-factor for the Pilot Study was significantly lower than in the studies where the MRI velocities were filtered (Table VIII.5). Lowering the CFL-factor was necessary in order to obtain a stable numerical simulation. At the lumen border, unrealistically high blood velocities (for large part due to the partial volume effect) could induce a strong swirling motion in the tube. Similarly, errors in in-plane velocity measurements could cause

(a) Calculated   (b) Measured
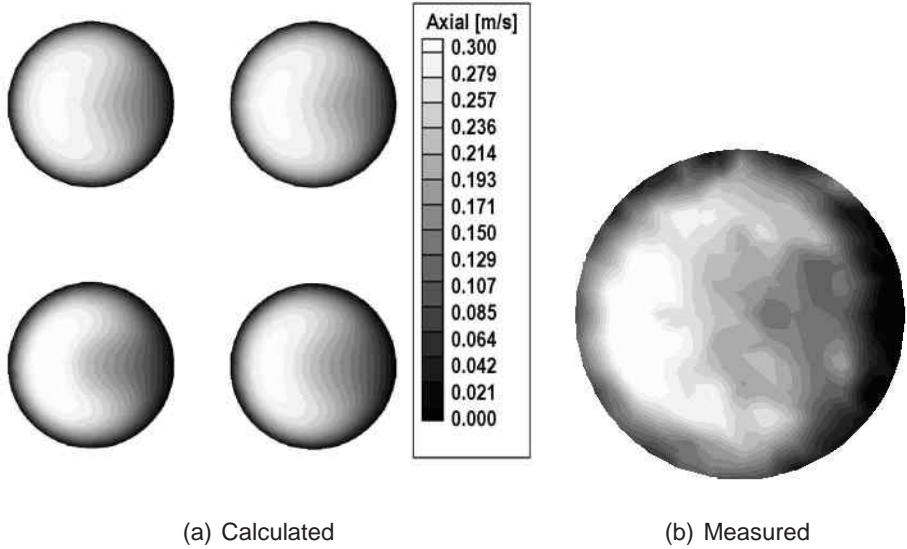
Figure VIII.6.: Axial velocities at the exit of the bend in PILOT study. a: Calculated velocities for the uniform inflow boundary condition (**upper left**); for the parabolic boundary condition (**upper right**); for the boundary condition extracted from the measured velocities *without* averaging (**lower left**); for the boundary condition extracted from the measured velocities *with* averaging (**lower right**). b: Measured axial velocities
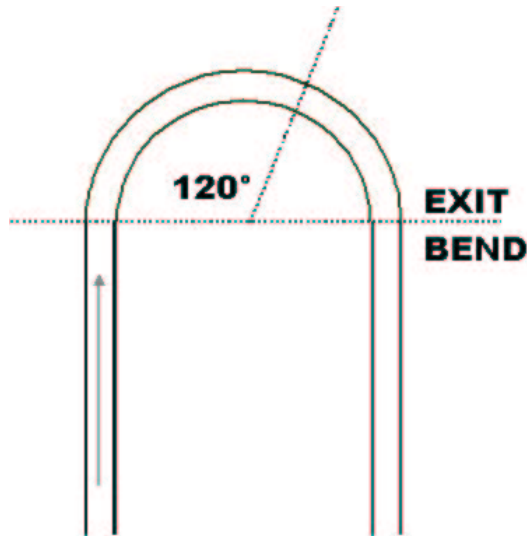
Figure VIII.7.: Location of planes for velocity comparison: Figures VIII.8 and VIII.9 show velocities at 120° through the bend, whereas Figure VIII.6 compares velocities at the exit plane.
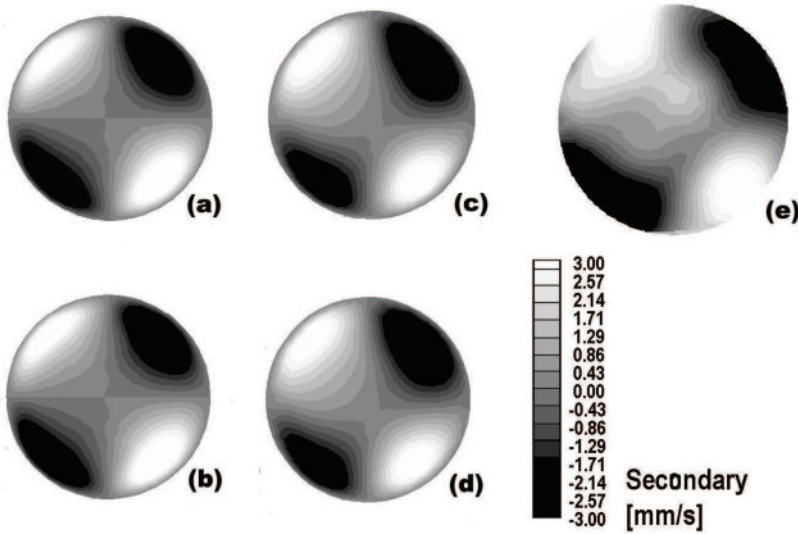
Figure VIII.8.: Vertical velocity profiles in the tube at 120 degrees through the bend, using different inflow boundary conditions: white is upwards and black is downwards velocities. Note that the secondary velocity is composed of the horizontal in-plane velocity V_x and the vertical in-plane velocity V_y (see Table VIII.2). a: Uniform inflow; b: Parabolic inlet; c: cine PC MRI measurements as inlet boundary condition; d: averaged cine PC MRI measurements as inlet boundary condition. e: Velocity profile at 120° as measured by cine PC MRI.

spurious swirl. This swirling motion impeded simulation stability, therefore filtering erroneous velocities was imperative. In the case of a simple U-bend, setting filters for 'realistic' and 'unrealistic' velocities are fairly easy. Based on literature concerning U-tube flows,[69,296] a threshold of 20% of the V_{enc} was chosen for the axial velocities at the tube wall, and secondary velocities larger than 10% of the axial velocities were set to 0 as well. When velocities are measured *in vivo*, velocities will still need to be filtered, but two changes need to be made in comparison with the present filtering protocol:

- The used filtering thresholds need to be evaluated. If the velocities were acquired in a section showing skewed flow, velocities at the lumen border could be higher than 10% of the V_{enc}.

- Instead of replacing the rejected velocities by 0, the velocities should be calculated by interpolating velocity values either from neighbouring points or neighbouring time steps or a combination of both.

Pilot Study - κ **= 163**   *First,* Figure VIII.6 (a) (upper left, uniform inflow) and Figure VIII.6 (a) (upper right, parabolic inflow) are compared with the
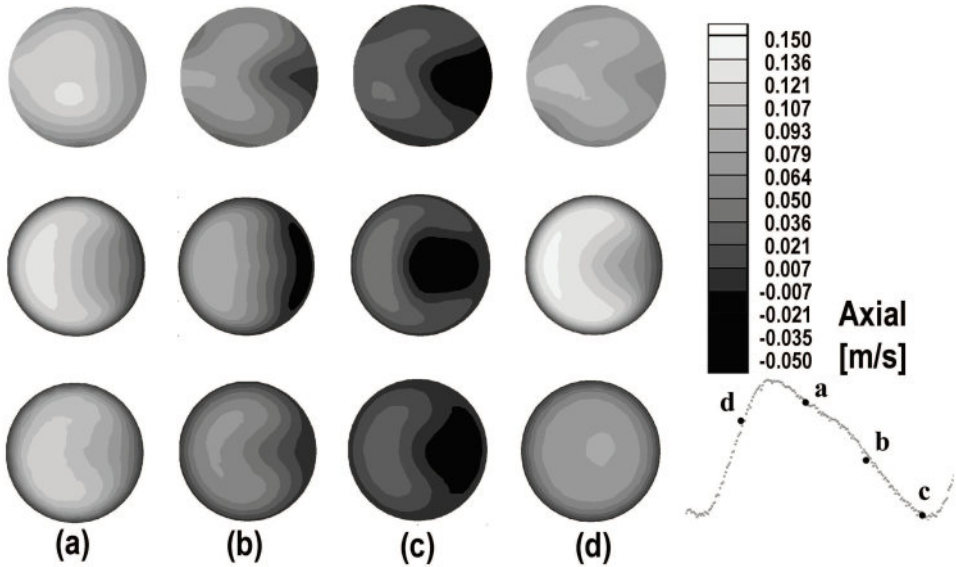
Figure VIII.9.: The upper row are MRI measurements at 120 degrees through the bend at time-points a, b, c and d as shown at the lower right corner, which shows the measured flow wave form at the exit of the bend. This differs from the imposed flow rate because of the length and compliance of the tubes connecting the pump outside the MRI scanner room to the phantom in the centre of the magnet. The second row are the results of the simulation using a uniform velocity profile as inflow. The third row represents the results of the simulation with 'MRI' boundary condition.

theoretical results of Collins and Dennis[69] (Figure VIII.1). The two Figures show favourable qualitative and quantitative agreement with the theoretical velocity profiles, however there are two main differences:

1. the predicted velocity profile is less shifted towards the outer bend;

2. the moon- or mushroom-shape in an iso-velocity plot, a typical feature in curved tubes, is more pronounced in the theoretical cases than in the calculated upper cases of Figures VIII.6. The mushroom-shape is a consequence of the tendency of the velocity profile to evolve to a thin layer of high velocities near the outer bend. This will be more pronounced for larger Dean numbers, as illustrated by Collins[69] (Figure VIII.1).

The main reason for the observed differences is the fact that the theoretical profiles are for fully developed flow, whereas at the exit plane, imaged in Figure VIII.6, the flow is not fully developed. This is because of the upstream influence of the straight part after the bend which is changing the

velocity profile back to the parabolic shape.[38] The documented profiles[69] are only valid in the developed case, far enough from the bend inlet but also far enough from the bend outlet.[133] This is confirmed by Chung[65] who made the same comments when comparing his results to the ones calculated by Olson and Snyder.[237]

Second, when comparing Figure VIII.6 (a) (upper row) with the MRI velocities measured at the exit of the bend (Figure VIII.6 (b)), the same observations 1 and 2 are made as when comparing upper Figures VIII.6 (a) to the theory.[69] This also means that the MRI velocity profile is qualitatively very close to the theoretical one. Quantitatively, the agreement between theory and MRI is less satisfactory, showing errors in velocities up to 25%. Nevertheless, the correct velocity profile is a smoothed version of the measured data, as found by Weston.[362] The comparison between MRI velocity measurements and CFD predicted flow patterns was made at 15 sections which were 5 mm apart, all showed very good qualitative and reasonable quantitative agreement.

Third, the lower part of Figure VIII.6 (a) is considered. The contour plot on the left corresponds to results obtained using direct MRI velocity measurements at the inlet, whereas for the case shown on the right, velocities averaged over three slices near the inlet were used. These results compare better with the theoretical solutions than those with assumed profiles. There are noticeable differences between the two results. Figure VIII.6 (a) (lower right) contains less curvature, a smaller maximum velocity and less significant moon-shape. The reason for these differences becomes clear when comparing the computed mass-flow in Table VIII.6, which can be obtained only after the simulation has been performed. For the simulation using the 'MR' boundary condition, the flow rate is underestimated by approximately 5%. For the MR averaged case, this becomes 10%. The incorrect flow rate is directly linked to the differences observed between the lower plots in Figure VIII.6. This indicates that averaging the MRI velocity data between three planes, as suggested by Weston,[362] does not improve the results. Instead, the comparison between the lower figures in Figure VIII.6 (a) clearly shows the importance of the correct flow rate.

Steady Test Cases   When comparing MRI measurements with CFD-predictions using several inflow boundary conditions, very high qualitative agreement is found. Because of a different velocity acquisition range (V_{enc}) for secondary velocities, the quantitative agreement is impressive in comparison to the pilot study (maximal errors around 10%), even for secondary ve-

Case	Inflow [ml/s]	outflow [ml/s]	Averaged error [%]
Uniform	9.89	10.05	0.32
Parabolic	10.07	9.89	0.14
MR measured	9.54	9.39	5.36
MR averaged	9.01	9.04	9.72

Table VIII.6.: Computed mass-flow in the different cases for the pilot study. The prescribed in- and outflow is 10 ml/s. This flow rate is used to calculate the (flow rate) error.

locity components (17% for horizontal, in-plane velocities; up to 55% for vertical, in-plane velocities). These seem to be high, however large relative errors occur where velocities are very low, therefore absolute errors are rather insignificant. The results compare very well with those of Collins[69] (Figure VIII.1). The different simulations for the same steady case predict the same velocity profile, allowing for typical visualisation errors as described by Long.[198] The secondary velocities for the second steady case shown in Figure VIII.8 are in good agreement with each other. It even seems that the simulations done using MRI velocities as boundary condition compare *better* with the MRI measurements. The explanation for this observation can be found in the fact that (i) the computational model uses the accurate *geometry* specifications provided. Furthermore, (ii) we must take into account that the phantom is included in a flow circuit applying a *theoretically specified flow*. In reality, the geometry and (more probably) the flow profile is not perfect, changing the flow in a way detectable by MRI. This means that setting a disturbed flow as boundary condition (measured by MRI), will result in a different flow profile, which is closer to the true profile. This observation denotes clearly the advantage of using scaled MRI velocity data as inflow boundary condition. In this context, 'scaled' means scaling up the velocities acquired from cine 3D PC MRI in order to obtain the correct flow rate.

Pulsatile Cases   It is clear from Figure VIII.9 that the quantitative agreement is less satisfactory than in the steady cases, however very good qualitative agreement is reached almost throughout the cycle. Comparison of the results between the different simulations in all available planes and time steps yields the same conclusion as for the steady case: when scaled for mass flow rate, using the MRI velocity data as inflow boundary condition provides more reliable results than in the case where a uniform inflow was set far from the region of interest.

CPU time   It is important to emphasise that the use of different inflow boundary conditions - uniform, parabolic, filtered MRI measurements or averaged MRI measurements - all produce nearly the same, correct flow field for flow in a U-bend. CPU time should also be considered when deciding on the type of boundary condition. Because all the geometries show comparable mesh densities, a large computing volume will have more elements and thus demands more CPU time. Evaluating the boundary conditions in terms of CPU costs, the following descending order is obtained: *uniform, parabolic, MRI averaged, MRI*. This sequence is logical when related to the computing volume. Using the uniform inflow boundary condition requires a (long) entrance length before realistic flow can be computed. Using the developed flow, a certain distance from the region of interest is required because of upstream influences of the geometry (e.g. a bend) on the flow.[38] The 'MRI' and 'MRI averaged' boundary condition can be obtained in the immediate vicinity of the region of interest, yielding a small computing volume (see mesh G in Figure VIII.3) and a shorter CPU time. When evaluating the boundary conditions in terms of CPU time, the CPU time required in the simulations in half geometries was doubled, since the entire arterial geometry will have to be simulated in *in vivo* cases. Thus, the most interesting boundary condition is the MRI velocity measurement. The extra computations due to spatial and temporal interpolations required in the 'MRI' boundary condition, did not increase the CPU time significantly.

Summary   Three types of inflow boundary conditions were tested: a uniform profile, a fully developed profile, and MR measured velocities. The first one is simple, but requires a long inflow tube, and is not physiological. The second one reduces CPU time significantly, but assumes a developed flow, which is an assumption that cannot be made for most of the arteries.[342] The third one has to be filtered and scaled, but can save CPU time even more if the acquisition plane is chosen near the region of interest. Note that the gain in CPU time is more important than the extra time needed for velocity acquisition. The choice of the filtering thresholds is operator dependent and therefore subjective. However, different thresholds have shown to generate comparable results on the general flow field. This option is preferred especially for *in vivo* applications, but requires reliable cine PC MRI measurements. This reliability of velocity measurements is discussed in two parts: the velocity profile, and the mass flow.

The *velocity profile* generated using 3D Phase Contrast velocity encoded MRI is accurate to 10% of the used V_{enc}, as illustrated in Figures VIII.6, VIII.8 and VIII.9. The *flow rate*, however, is subject to large errors (see Table

VIII.6). Therefore, it is concluded that additional flow measurement is required. The challenge now is how to perform reliable flow rate measurement. Chatzimavroudis[59] state that MRI can produce extremely reproducible flow rate measurements *in vivo*. Their conclusions hold for the cycle-averaged flow rate. But for use as boundary condition in a CFD simulation, the flow rate has to be correct for every time step. Furthermore, their results show that significant errors can occur when mass flow is low. Unfortunately, the regions of interest (bifurcations, aorta, left ventricle) usually show complex flow patterns, where MRI velocity measurements are less reliable.

Comparison with Literature   To our knowledge, no previous study has used the mass scaled MRI velocities as boundary condition (Table VIII.1) using a separate mass flow rate measurement. An important number of authors[33, 195, 197, 198, 362, 370, 374] set velocities as measured by MRI on all the inlets and outlets except for one. For the last boundary condition, there are several options: a scaled MRI-velocity profile,[195, 196, 362, 374] a uniform velocity profile,[362] a mass-flow boundary[197, 198] or a uniform pressure distribution on an inflow or outflow plane.[370] A *second* group of authors set developed profiles - or calculate the developed flow-profiles using a long entrance length - on all inflow and outflow boundaries but one. These profiles are calculated in advance using time-varying flow rates assessed either by MRI[50, 164, 219, 334] or Doppler.[387]

The lack of reliability in the flow measurements will inevitably introduce errors in the simulation, an aspect which will play an important role in the aforementioned studies for the first group of authors, who use MR measurements as boundary conditions. With MRI, Weston[362] measured a flow rate for a steady case which was 16% higher than the flow rate measured volumetrically. For a pulsatile case, the mean flow rate obtained with MRI was also 15% higher than measured with timed collection. The observation that to our knowledge no authors have successfully set MRI velocity data on all the boundaries is related to the accuracy in measuring the flow rate. In order to be able to set velocities on all boundary conditions, the accuracy on the flow rate should be higher than the machine accuracy of the platform on which the CFD simulations are solved.[3] As a consequence, MRI-velocities can be set on all the boundaries, but the last one has to be scaled in order to satisfy mass conservation required for a stable simulation. In a simulation with MRI measurements as boundary condition, the simulated flow rate is deduced from the velocity measurements used as boundary condition; unfortunately, this flow rate is not necessarily correct. This uncertain flow rate might explain the relatively large discrepancies found between measured MRI data

and calculated flow profiles during the flow deceleration in Long.[195] In their work on a human descending aorta, Wood[370] observed differences in the time-mean flows: 5.0 litres/minute at inlet, and 3.5 litres/minute at outlet (30% less). These discrepancies are attributed to measurement uncertainties, outflow to small branches and the neglect of compliance effects. An uncertainty on the flow rate of $\pm$ 28% was defended. The authors conclude that the discrepancy between inlet and outlet flows falls broadly within uncertainty limits. Although this is a justified statement, it exposes the vulnerability of *in vivo* MRI flow measurement.

The importance of Mass Flow Rate   The present study underlines the importance of making use of the correct flow rate. There is a need for a good understanding and treatment of the parameters that lead to the current uncertainty in flow rate measurement.

One of these uncertainties is due to the neglect of *arterial distensibility*. During a cardiac cycle, the diameter of the common carotid artery can change up to 17%.[264] Flow rate is obtained by multiplying the mean velocity with a cross-sectional area, so uncertainties on the lumen diameter (LD) measurement (due to compliance) will induce uncertainties in flow rate measurements. Because of this, the cycle-averaged LD is usually used, however, the closer the arteries are to the heart, the more important the diameter changes will become and the less correct the use of an average artery LD will be. Note that the neglect of compliance also contributes to the error in the flow rate in a different way. The blood entering the carotid bifurcation, does not necessarily need to leave the carotid bifurcation instantaneously, since the vessel walls can expand. Therefore, the measured instantaneous inlet flow rate would not be the same at the outlets. In the present study, MRI-velocity measurements result in significant flow rate errors although no compliance is present, so the error in the flow rate cannot be explained with compliance alone, and has to be due to velocity measurement errors. Note that compliance can be successfully implemented in the flow simulation as showed by Zhao[387] for the carotid bifurcation. Their results reveal velocity profiles that are different from those found with idealised models, such as stronger secondary flows, lower wall shear stress and larger backflows. The computational cost of the coupling between MRI, CFD and solid mechanics (**fluid-structure interaction**) is currently the main drawback of this modelling approach.

What about outflow boundary conditions? This study has concentrated on inflow boundary conditions by performing simulations which differed only in their implementation of the conditions at the inlet. Nevertheless, the same considerations are valid at the outflow as well. This study recommends measuring velocities at the outflow plane, and using the 'filtered' and 'scaled' velocities as boundary conditions. Note that it is not recommended to set velocities on all boundaries, unless the flow rate can be set as accurate as machine accuracy. In some cases it is not even possible to acquire enough velocity information at the outlets, usually due to time restrictions. Several solutions can be put forward. Admittedly, all the suggestions cited below do not give any information on secondary flow in the outlet planes, which is against Shipkowits's recommendations.[282] Nevertheless, they provide physiological boundary conditions suitable for coupling with CFD.

- Instead of performing velocity measurements in three directions, only the axial velocity could be measured. This shortens the acquisition time considerably, and it also yields a mass flow rate measurement using the most reliable *in vivo* technique.

- Recently, other techniques for setting outflow boundary conditions have been investigated by Cebral[53] for MRI-based CFD in the circle of Willis. Under normal conditions, four feeding vessels supply the circle of Willis: two internal carotids and two vertebral arteries (see Figure I.1 (b)). The flow rates in these vessels can be measured by PC MRI techniques and used to impose inflow boundary conditions during the solution of the flow equations. Furthermore, in many cases all these flows can be measured with only one PC-MRI sequence. However, in general it is difficult to measure flow rates in all the efferent vessels of the circle of Willis. This would require MRI exams that are too long and the flow measurements in some of the smaller vessels may not be very reliable. Therefore, in such cases the outflow boundary conditions must be derived using models of the distal vascular bed. This means that the distal parts of the vessels, beyond the outlet of the model, are replaced by a mathematical representation and implemented in the model. This mathematical representation can be based on an analogy between the distal vascular bed and series of resistors in parallel, structured fractal trees or porous media. However, Cebral[53] clearly denotes that these techniques are still in their infancy and that further research is necessary before they can replace cine PC MRI measurements.

VIII.1.1.5. Conclusion

For *in vivo* haemodynamic studies combining CFD to MRI velocity measurements, the boundary conditions need to be handled with special care. A study of the effect of different inflow boundary conditions on flow simulations in a rigid U-bend phantom has been presented. A pilot study revealed the key role played by a correct flow rate. Comparing MRI velocity measurements with CFD predictions showed that both axial and secondary velocities can be measured reliably with cine PC MRI (maximum error 10% for axial velocities in a rigid tube under laboratory conditions). This study has demonstrated that MRI velocities could be used as boundary conditions in a CFD-simulation. The raw velocity data needs to be

1. filtered for partial volume effects: axial velocities at the lumen border have poor accuracy and should be replaced by interpolation if their values exceed a certain threshold (here: 20% of the V_{enc}).

2. filtered for errors in secondary flow: secondary velocities greater than a certain percentage (here: 10%) of the axial velocities can often be blamed on measurement uncertainty and can thus be replaced by interpolation.

3. rescaled to match a reliable flow rate measurement.

These procedures can help to obtain a reliable and cost-effective CFD simulation. Our study suggests not to use a uniform or developed boundary condition unless no other information is available about the inlet velocity profile.

VIII.1.2. In- and Outflow Conditions for 3DUS-based models

VIII.1.2.1. Introduction

The problem with Doppler Preferably, velocities should be acquired at the entire inlet plane. Cine PC MRI is ideally suited for this purpose: it generates velocities in all three orthogonal directions with a reasonable spatial resolution ($\pm 1mm \times 1mm$) at a sampling rate up to 25 acquisitions per cycle.[347] In Doppler ultrasound, there are 2 methods for velocity acquisition (see section VII.1.3).

- *Pulsed wave Doppler* outputs velocities at a very high sampling rate, typically 200 Hz: much better than the 25 images per cycle in cine PC MRI. However, Doppler velocities originate from a single sample volume of 1.5 mm^2, whereas in MRI an entire transverse section can be imaged. The technique can be altered to scan velocities along a line as opposed to a single point,[270] only with some marginal loss of temporal resolution. Nevertheless, pulsed wave Doppler still stands far from the spatial resolution achievable with MRI.

- *Colour Doppler* generates a high spatial resolution, theoretically equal to the inverse of the used wavelength, but is by definition cycle-averaged.

Clearly, the use of Doppler Ultrasound to acquire velocities for boundary conditions has its limitations in comparison with cine PC MRI. Nevertheless, in the absence of MRI velocity data, Doppler velocity can be analysed and processed to give time-varying velocity profiles by making a few assumptions.

Making use of Doppler   Doppler measurements can be made in the centre of a proximal CCA cross-section. This yields images such as Figure VII.3 (a) on page 163. Since Doppler ultrasound can only measure the flow velocity in a small sample volume, two methods were devised to calculate the actual volumetric flow rate.

The *first* method, henceforth known as the 'Simple' method, applied the assumption of a parabolic flow profile at every instant and that the measured Doppler velocity was its peak. Hence, the volumetric flow rate could be calculated by

$$Q = \frac{V_{PEAK}}{2} \times A \qquad \text{(VIII.4)}$$

where Q is the volumetric flow rate, V_{PEAK} is the centre stream velocity and A is the cross-sectional area of the vessel. The measurement site for the CCA should be at a location proximal to the bifurcation point where the vessel is relatively straight and flow could be considered undisturbed. Note that a fully developed profile in pulsatile flow would be the Womersley profile, which can be very different from the parabolic profile suggested in this method. This simplification is the reason for the name 'Simple' method.

The *second* method was based on the Womersley solution for pulsatile flow, assuming again the measured velocity to be the centre stream velocity. A MATLAB-based program was developed to perform this calculation, which required the input of time varying velocities V_{PEAK} as well as the radius of the vessel. For details of this method, see section II.3.3.1.

Both methods, the 'Simple' and 'Womersley' method, use the centreline velocity in the proximal CCA to extrapolate a flow rate and a velocity profile in the entire inlet section. But in both cases, an assumption was made concerning the velocity profile: a pulsatile parabolic profile was imposed in the Simple case, and a Womersley profile in the second method.

VIII.1.2.2. Study setup

In a first attempt to validate the solutions proposed in the previous section, the two calculation methods, namely the Simple and the Womersley method, based on Doppler ultrasound, were compared to cine PC MRI for obtaining the inlet mass flow boundary conditions in the CCA. For this purpose, a healthy male subject was scanned using Doppler ultrasound and Phase Contrast (PC) MRI. Moreover, the carotid geometry was assessed using Time of Flight (TOF) MRI. The study had 3 goals:

- Goal 1: Assess how the Simple and Womersley methods compare with the PC MRI data.

- Goal 2: Assess which boundary conditions to set at the flow outlet.

- Goal 3: Study the effect of using MR or US-based boundary conditions.

The study has been performed in a collaboration with Augst.[15]

Doppler Ultrasound   CCA centreline velocities were obtained using a standard 2D ultrasound scanner (HDI 5000 with a L12-5 (5-12MHz) linear array transducer, ATL-Phillips Ltd., Bothell, MA, USA). This returned velocities in the proximal CCA at a sampling rate of 200 Hz. The procedure was repeated to measure the centreline velocities in the daughter vessels. ECA and ICA flow measurements were influenced by the position of the bifurcation point

relative to the jaw bone. Since these were taken as far distal as possible, this position is approximately 1.5 CCA diameters distal to the bifurcation point.

From the raw flow data acquired, the following parameters were calculated and compared. Firstly, the volumetric flow rates in the CCA were computed. Secondly, the flow rates in the ICA and ECA were computed. Thirdly, to test for conservation of mass and to determine what to set as outlet boundary condition, the sums of ICA and ECA flow were set against the CCA. Lastly, outflow ratios were computed using two different schemes. Scheme 1 computed the ratio of the ICA and ECA flow from measurements made in the respective vessels, whereas Scheme 2 estimated flow in the ECA by subtracting the ICA flow from the CCA.

MRI protocol   For comparison, the velocities were also measured with cine PC MRI. The MRI scan was carried out using a Siemens Magnetom Sonata Scanner 1.5T. The phase encoding resolution was 1.1mm, the frequency encoding resolution was 0.75 mm with a slice thickness of 6 mm. Temporal resolution was 29 ms. PC flow measurements were carried out in the CCA in a region relatively close to the bifurcation but far enough to ensure undisturbed flow while ECA/ICA were measured as far distal as possible but before any branching occurred. Magnitude and phase images were processed with phase image intensities related to velocity. To determine the volumetric flow rate, the vessel cross-section was drawn manually on the magnitude image and copied to the corresponding phase image. The regions on images at different time points were adjusted to fit the vessel outline, determined from the initial magnitude image where the lumen boundary is clearly defined. The through-plane flow was calculated using the analysis package on the scanner.

3D reconstruction and computational details   The lumen geometry of the subject was reconstructed from TOF MRI images and a computational mesh was generated. Details of the imaging protocol can be found in section XII.3. The mesh had 60544 hexahedral cells in a fully structured multi-block arrangement suitable for the designated CFD solver, i.e. the commercially available finite volume package CFX4™. Simulations were carried out using MRI and the Simple ultrasound CCA boundary conditions and a fixed 60:40 outlet mass flow ratio. The MRI velocities were filtered as explained in section VIII.1.1, and scaled using an extra cine PC MR image series for flow rate measurement. The 'MR measured' boundary condition contained

velocity information for all three vector components while the ultrasound de-
rived ones assumed parabolic profiles with zero secondary velocities. The
Quemada model as presented by Buchanan[42] was used to model the non-
Newtonian behaviour of blood and its density was set to 1176 kg/m^3. Time-
averaged wall shear stress (WSS) and oscillatory shear index (OSI) were
computed and compared.

VIII.1.2.3. Results

Figure VIII.10 (a) shows the computed volumetric flow rates for both imag-
ing modalities, using the Womersley and Simple calculation methods for
ultrasound. Figure VIII.10 (b) shows the flow wave in the daughter vessels.
These Figures allow comparison of the Simple and Womersley method to
the cine PC MRI method for flow rate measurement (Goal 1). Note that the
waves were truncated at the last measured value from ultrasound. Figure
VIII.11 (a) shows the sum of the flow leaving ECA and ICA compared to the
measured CCA rates. Figure VIII.11 (b) shows the outflow ratios as mea-
sured (solid) and as computed from measured CCA and ICA alone (dashed)
for ultrasound (black), and MRI (grey) (Goal 2). Figure VIII.12 shows cir-
cumferential plots of WSS and OSI at selected locations defined by z, their
position along the I/S axis. Note that in Figure VIII.12, TAWSS stands for
Time-Averaged WSS.

(a) CCA   (b) Branches
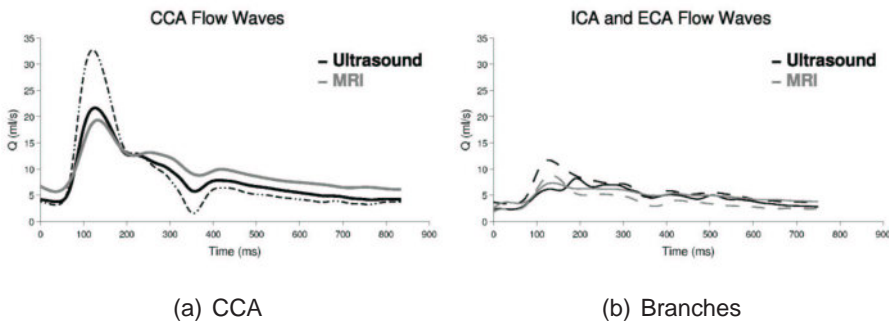
Figure VIII.10.: 'Simple' and Womersley method for deriving flow rates from Doppler Ultra-
sound compared to MRI. a: Volumetric flow waves in the CCA computed from MRI (grey)
and ultrasound (black). With ultrasound, flow waves have been derived using the Simple
method (solid) and Womersley's solution (dashed). b: Volumetric flow waves in the ICA
(solid) and ECA (dashed) computed from MRI (grey) and from ultrasound (black) using the
Simple method.

(a) CCA vs ICA+ECA   (b) ICA/ECA
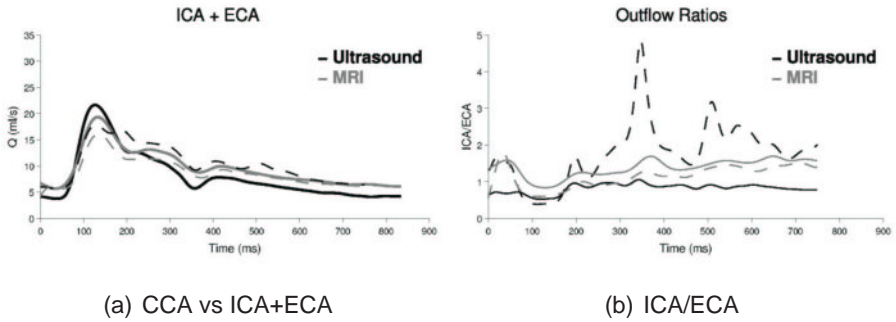
Figure VIII.11.: Testing the flow rates acquired by Doppler ultrasound for mass conservation. a: Volumetric flow waves in the CCA as measured (solid) and as sum of the ICA and ECA flow rates (dashed) computed from ultrasound (black) using the Simple method and MRI (grey). b: Outflow ratios as measured (solid) and as computed from measured CCA and ICA alone (dashed) for ultrasound (black), and MRI (grey).

VIII.1.2.4. Discussion

In this study, the CCA centreline velocity, acquired using pulsed wave Doppler, was used to derive carotid flow rate and velocities for the inlet boundary condition. Two methods for this derivation have been proposed (Simple and Womersley) and compared to cine PC MRI measurements. The aim of the study was to (i) assess whether the Simple or Womersley methods compares better with the PC MRI scan, (ii) assess which boundary conditions to set at the flow outlet and (iii) study the effect of using MR or US-based boundary conditions.

Since the cross-sectional area was kept the same for all the methods, the derived volumetric flow rates depended entirely on the velocity data and the calculation method employed. Even though the results of only one sample subject were presented, some generally relevant observations could be made. From Figure VIII.10 (a), it can be seen that the ultrasound derived flow rate calculated by the Simple method agrees much better with the MRI measured flow rate, than the commonly used Womersley solution. This shows that the assumptions made on the shape of velocity profiles in the Womersley method may not be physiologically realistic. However, implementing the flow rate calculated from the Simple method on a straight tube will lead to a considerable underestimation of centreline velocity at peak systole, hence leading to a mismatch with the measured Doppler velocity wave. This shows that it is difficult to obtain an accurate simultaneous representation of both flow rate and profile from Doppler ultrasound. The site of
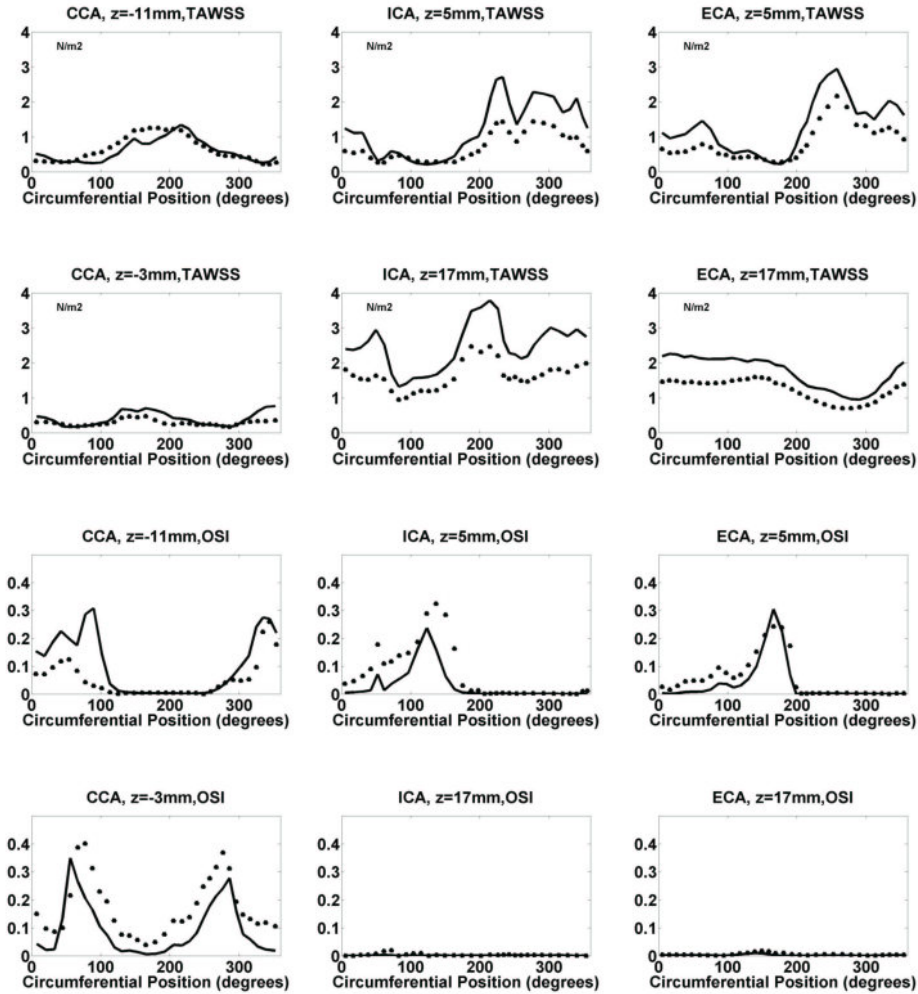
Figure VIII.12.: WSS [N/m^2] and OSI [-] at cross-sections using MRI (solid) and ultrasound (dots) for boundary condition acquisition. The position of the cross-section is determined by the parameter z, denoting the position along the I/S axis ($z < 0$ is in CCA, $z > 0$ in ECA/ICA).

velocity measurement is unlikely to have had an influence on the data due to the relatively straight vessel geometry and undisturbed flow in the region.

Similar issues can be addressed considering the results in Figure VIII.10 (b). Here, another factor affecting flow wave forms may be present, namely the downstream location of measurement. As mentioned earlier, the thyroid artery and possibly a number of smaller branches can affect flow velocity and flow rate in the ECA. It can be seen that the ultrasound measured wave displays a much higher flow rate than its MRI counterpart with similar wave

form. This may indicate a source of varying resistance nearby, i.e. the presence of a vessel side branch and/or a measurement error due to a strongly skewed velocity profile. Since both effects were ignored in the CFD parts of the present study, this must be considered an undesired error. It must be kept in mind, though, that there may be an error also in the MRI measurement for similar reasons.

The ICA measurements show good agreement in terms of total flow while the wave forms differ in shape. This is interesting, since the scan location can also be influential for the ICA velocity measurements, due to the acceleration of fluid out of the bulb. It seems however, that this undesired effect has been largely avoided here. More importantly, the velocity profiles may be relatively complex in this region, which can be picked up by MRI but not by Doppler, hence possibly introducing an error in the ultrasound measurements.

The suspicions about a possible underestimation in MRI measurements in the ECA were confirmed in Figure VIII.11 (a, grey lines). There is a constant, relatively small underestimation of flow out of the daughter vessels compared to the inflow, most likely due to the loss from branching vessels and possible induced flow disturbances. In case of Doppler measurements, the overestimation of the ECA flow suspected from Figure VIII.10 (b) was confirmed (black dashed line higher than black solid line in Figure VIII.10 (a)). The underestimation of total outflow during systole was mostly due to the ICA wave form. This has strong implications on the calculations of outflow ratios shown in Figure VIII.11 (b). It can be seen that the two outflow calculation methods show good agreement for MRI, confirming the relatively high accuracy of measurement in this case. But this is not the case for ultrasound, where Scheme 2 (estimating ECA flow from measured CCA and ICA flows) yields a much higher ICA to ECA flow ratio with strong temporal variations, while Scheme 1 (using measured ICA and ECA flows) shows a good agreement with the MRI data. At this stage, another problem with Doppler ultrasound is worth pointing out, which is not present with MRI. While flow measurements in both vessels were made simultaneously during the MRI scan, this was not possible for Doppler ultrasound. Hence, beat-to-beat differences are inevitable, possibly accounting for some of the errors in Figure VIII.11. The problems with Scheme 2 for Doppler ultrasound may be specific for this case, as the large discrepancy to Scheme 1 between 300 and 400 ms is induced by the closeness of ICA and CCA flow rates. Hence, the usefulness of Scheme 2 to alleviate the problems of ECA measurement may be questionable.

The plots of WSS and OSI shown in Figure VIII.12 exhibit great similarity between MRI and Doppler. As expected from the flow waves in Figure VIII.10 (a), the WSS for MRI is generally higher due to the higher average inflow velocity. This effect increases downstream due to higher momentum and a stronger skewed velocity profile. The OSI overall is higher for the Doppler set, most probably due to the more pronounced peak and dicrotic notch. Overall, the differences can be regarded as small considering the range of values present in this data set.

VIII.1.2.5. Conclusion

Two techniques for extrapolating inlet boundary conditions from a centreline velocity measurement acquired from Doppler Ultrasound were presented. In the first one, 'Simple', a parabolic profile is imposed on the inlet section, whereas in the second one, 'Womersley', Womersley profiles are derived. This study, performed in one subject, showed that the flow rate derived with the Simple method agreed better with the flow rate acquired from cine PC MRI. This is surprising since it is less realistic considering that in a straight tube with pulsatile flow, the Womersley flow should develop.[232] Nevertheless, the assumption of developed flow could be fundamentally wrong, and the complex profile occurring instead of a Womersley profile may be closer to a parabolic one. More subjects are needed to see whether this finding is statistically significant.

At the boundary outlets, it was noted that both the ICA and ECA flow rate were overestimated using Doppler. When setting a (time-varying) mass division at the model outlets, it is recommended to use the mass flow ratio derived from the ICA and ECA measurements as opposed to derive it from the CCA and ICA measurement.

The WSS and OSI patterns showed high qualitative agreement. There was, however, a clear overestimation of the WSS in the study with the highest flow rate. This confirms what was seen in the previous section (section VIII.1.1 on boundary conditions in MRI-based CFD), namely that the WSS patterns are highly influenced by the flow rate. Using a suboptimal boundary conditions in combination with the correct flow rate, is therefore only important in a redeveloping zone.

VIII.1.3. The wall as model boundary

The easiest way to model the boundary wall, is to represent it as a rigid, 'no slip' surface. This means that the vessel wall remains in its position and that the fluid at the vessel wall is stationary. In reality, the vessel wall is compliant. Several groups have introduced compliance into their image-based models. Noteworthy are Leuprecht's,[177,178] Zhao's[387] and Cebral's[56] solution for computational modelling of carotid vessel walls.

Leuprecht[177,178] uses cine PC MRI to extract geometries from a descending aorta. Since this technique gives several images along a cardiac cycle, 'cine' PC MRI yields not 1 but several reconstructions of the aorta, each one corresponding to a different point in the cardiac cycle. The aorta geometries are used to impose the movement of the vessel wall. The velocity of the fluid on the vessel wall is equal to the velocity of the vessel wall, i.e. the no-slip condition is applied.

Zhao introduced vessel wall movement to the carotids.[387] Here, the solid motion equations are solved together with the Navier-Stokes equations, the technique is termed fluid-structure interaction. The subject-specific wall data, required for the solid equations (elasticity, etc.), were acquired with B-mode ultrasound. Zhao[387] found that the effect of introducing fluid-structure interaction was an overall decrease of the WSS, while keeping the WSS *distribution*. See Figures VIII.13 and VIII.14 for an extract of Zhao's results.

Cebral[56] used an assumed value for the elastic modulus and pressure values at the in- and outlets of the model. The knowledge of the pressure field and the elastic modulus combined with the velocity boundary conditions on the outlet of the model allowed reconstruction of the entire flow field and wall movement using fluid-structure interaction. The pressures at the lumen boundaries were estimated using the flow rates (measured with cine PC MRI) at inlet and outlet.

The comparison of different techniques to model vessel wall compliance fell out of the scope of this work. But the effect of wall compliance on calculated WSS can be found in Figure VIII.13.
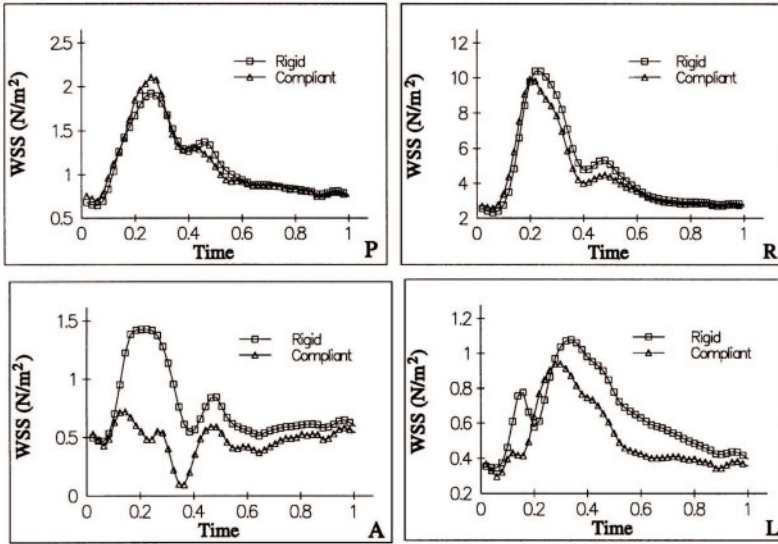
(a)
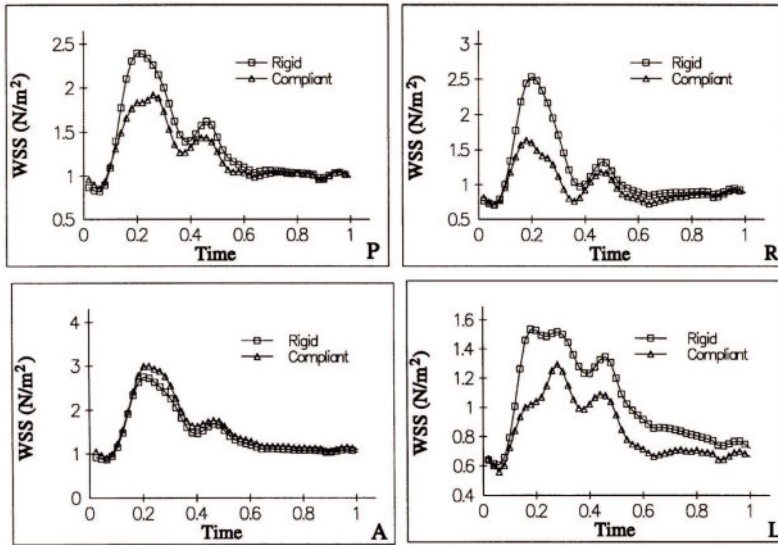
(b)

Figure VIII.13.: Comparisons of wall shear stress magnitudes at two selected locations (a and b) in the internal carotid artery between the coupled and its corresponding rigid model. a: carotid sinus; b: one-diameter downstream of (a), as shown in Figure VIII.14. At each location, results are given on the Posterior, Right, Anterior, and Left wall (from Zhao[387]).
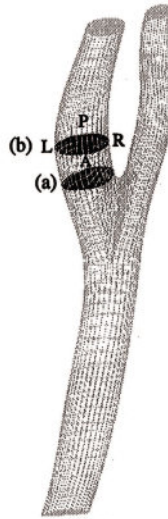
Figure VIII.14.: Measurement locations for Figure VIII.13 (from Zhao[387]).

VIII.1.4. Boundary Conditions: Summary

This summary describes which boundary conditions should be used in future studies using image-based CFD as a tool for investigating carotid haemodynamics.

For *MRI-based CFD*, the velocities in 3 directions will be measured at the inlet and outlet planes. The velocities are filtered for the partial volume effect and for noise in the secondary velocity components. An additional flow rate measurement is required, which can be performed at a location with an extra cine PC MR imaging sequence in a location with good signal. This flow rate is used to rescale the axial velocities at the inlet.

At the outlet, flow rates will be estimated from the cine PC MRI images and used to describe mass flow boundary conditions using a mass division ratio.

For an example where 3DUS-based CFD was used as a tool for investigating carotid haemodynamics using the above boundary conditions, see section XII (*The Acute Effect of Hypertensive Drugs*).

For *3DUS-based CFD*, the secondary velocities will be discarded. The axial velocities will be derived from centreline velocity measurement in the CCA using the Womersley method. The Womersley method was preferred here

to the Simple method because it is still widely used in the absence of true velocity data.

At the outlet, a mass division ratio is set just as for the MRI-based CFD studies. The problem of how the outflow ratio should be calculated remains to be dealt with. First, the flow rates are calculated in CCA, ICA and ECA using centreline measurements and the Womersley assumption. Then, out-flow ratio can be calculated from the ICA and ECA, CCA and ICA and even CCA and ECA. Although the study in section VIII.1.2 suggested to use the ICA and ECA, in practice, the ratio will be calculated using the flow rates yielding a division ratio closest to the expectable 55:45 (ICA:ECA). This al-lows to filter out major acquisition errors. In order to deal with the potential high-frequency changes seen in the black dashed line in Figure VIII.11 (b), the time-dependent outflow ratio is smoothed. Note that the presence of a stenosis will alter the flow division dramatically, which makes the expectation of a flow ratio of 55:45 unrealistic. Thus, the used technique of setting outlet boundary conditions is only plausible in non-stenosed carotid bifurcations.

For an example where 3DUS-based CFD was used as a tool for investigating carotid haemodynamics using the above boundary conditions, see chapter XI (*The Head Position Study*).

Both for MRI and 3DUS-based CFD, the wall will be modelled as a rigid wall with no slip. The reader should be aware of the fact that the calculated WSS is therefore slightly higher than the true WSS[387][c].

VIII.2. Viscosity

VIII.2.1. What's the effect of viscosity on shear?

VIII.2.1.1. Introduction

The viscous force is a force exerted by a fluid as a resistance to flow. The dynamic viscosity is the degree to which a fluid resists flow under an applied force, measured by the tangential friction force per unit area divided by the

---

[c]Note that the reason why the WSS was found to be lower in the compliant model was because the geometry used in the rigid model was taken as the geometry in diastole when pressure was the lowest. If it was taken as the systolic geometry in the compliant model, the conclusion would have been different.

velocity gradient under conditions of streamline flow. In a numerical flow simulation, the viscosity is an important fluid property and needs to be set. If we consider that the dynamic viscosity of blood is within the range of 3 to 5 mPa.s, the question of which value to set for the simulation is raised. However, before the value of the viscosity is questioned, the effect of setting different viscosities needs to be studied.

VIII.2.1.2. Study setup

In this study, the right carotid bifurcation with no stenosis acquired with BB MRI from a hypertensive 38 year old subject was imaged, segmented, reconstructed and meshed as explained in sections XII.3 (imaging protocol), VI.2 (segmentation), VI.3 (reconstruction and mesh generation).

On this mesh, three simulations were performed. Velocities measured with PC MRI at the inlet were filtered and scaled (as explained in section VI.5.2.5) for use as inlet boundary conditions. The wall was modelled as a no-slip, rigid surface. Blood density was 1176 kg/m^3. Three simulations were undertaken. Each had a different value for the viscosity: 3, 4 and 5 mPa.s. This was the only difference between the simulations. The simulation was performed using CFX4™,[3] over 2 cycles of 80 time-steps of 9.1 ms each. Validation and mesh independence tests were performed in other studies (section XII.3.5.4).

VIII.2.1.3. Results

The results are given in Table VIII.7. It shows the values of WSS, OSI, WSSG, WSSGt, WSSGs and WSSAG averaged over certain zones of the carotid for each of the three simulations. See section II.3.3.3 for a definition of these parameters, and see Figure VII.8 (page 173) for a definition of the zones in which the averaging was done.

VIII.2.1.4. Discussion and Implications

In this study, three simulations were performed. The only difference in the simulations, was the value set for the dynamic viscosity. Note that a New-

Parameter [Unit]	μ=3 mPa.s	μ=4 mPa.s	μ=5 mPa.s
WSS ALL [N/m^2]	**2.631**	3.083	**3.522**
WSS CCA [N/m^2]	1.774	2.140	2.511
WSS iCCA [N/m^2]	1.832	2.236	2.645
WSS eCCA [N/m^2]	1.697	2.015	2.335
WSS ICA [N/m^2]	3.478	4.001	4.479
WSS outer ICA [N/m^2]	2.766	3.169	3.545
WSS inner ICA [N/m^2]	4.689	5.418	6.069
WSS ECA [N/m^2]	3.939	4.573	5.182
WSS outer ECA [N/m^2]	1.887	2.238	2.615
WSS inner ECA [N/m^2]	3.939	4.573	5.182
WSS bulb [N/m^2]	2.352	2.739	3.116
OSI ALL [-]	**0.030**	0.021	**0.016**
OSI CCA [-]	0.055	0.038	0.027
OSI iCCA [-]	0.045	0.026	0.016
OSI eCCA [-]	0.067	0.053	0.042
OSI ICA [-]	0.019	0.016	0.013
OSI outer ICA [-]	0.027	0.024	0.018
OSI inner ICA [-]	0.004	0.004	0.004
OSI ECA [-]	0.005	0.003	0.002
OSI outer ECA [-]	0.012	0.007	0.004
OSI inner ECA [-]	0.005	0.003	0.002
OSI bulb [-]	0.035	0.024	0.017
WSSGs ALL [N/m^3]	**734**	817	**891**
WSSGs CCA [N/m^3]	462	532	600
WSSGs iCCA [N/m^3]	474	544	617
WSSGs eCCA [N/m^3]	446	517	578
WSSGs ICA [N/m^3]	847	937	1014
WSSGs outer ICA [N/m^3]	630	697	757
WSSGs inner ICA [N/m^3]	1216	1346	1452
WSSGs ECA [N/m^3]	1417	1558	1672
WSSGs outer ECA [N/m^3]	567	613	657
WSSGs inner ECA [N/m^3]	1417	1558	1672
WSSGs bulb [N/m^3]	531	591	647
WSSGt ALL [N/(m$^2 \times s$)]	**11.51**	13.01	**14.42**
WSSGt CCA [N/(m$^2 \times s$)]	9.24	10.77	12.25
WSSGt iCCA [N/(m$^2 \times s$)]	9.21	10.85	12.42
WSSGt eCCA [N/(m$^2 \times s$)]	9.26	10.68	12.03
WSSGt ICA [N/(m$^2 \times s$)]	14.90	16.89	18.70
WSSGt outer ICA [N/(m$^2 \times s$)]	13.65	15.55	17.33
WSSGt inner ICA [N/(m$^2 \times s$)]	17.03	19.16	21.03
WSSGt ECA [N/(m$^2 \times s$)]	13.56	14.81	15.99
WSSGt outer ECA [N/(m$^2 \times s$)]	8.47	9.09	9.66
WSSGt inner ECA [N/(m$^2 \times s$)]	13.56	14.81	15.99
WSSGt bulb [N/(m$^2 \times s$)]	11.70	13.41	15.03
WSSAG ALL [rad/m]	**171.2**	146.8	**129.8**
WSSAG CCA [rad/m]	219.9	182.9	159.8
WSSAG iCCA [rad/m]	228.9	177.2	148.2
WSSAG eCCA [rad/m]	208.3	190.3	175.0
WSSAG ICA [rad/m]	154.7	145.2	130.3
WSSAG outer ICA [rad/m]	186.2	173.7	152.3
WSSAG inner ICA [rad/m]	101.2	96.6	92.7
WSSAG ECA [rad/m]	151.8	120.6	106.0
WSSAG outer ECA [rad/m]	93.2	78.2	70.8
WSSAG inner ECA [rad/m]	151.8	120.6	106.0
WSSAG bulb [rad/m]	172.2	146.4	127.1

Table VIII.7.: Effect of different viscosities on predicted wall shear stress (WSS), oscillatory shear index (OSI), wall shear stress gradient (WSSGt: temporal; WSSGs: spatial) and wall shear stress angle gradient (WSSAG).

tonian fluid has been assumed here, for a discussion on the validity of this assumption, see section VIII.2.2 (page 232).

WSS and WSSG   Since the shear stress is calculated as the product of the dynamic viscosity and the shear rate, the shear stress could have been expected to increase linearly with the increase in viscosity. However, change in viscosity also affects the shear rate, so the expectable change is not easily predicted. Table VIII.7 shows that the values of WSS and WSSG increase with increasing viscosity, albeit not linearly.

OSI   Since viscous fluids have a higher resistance to flow, they are not expected to recirculate easily. When there is no recirculation, the WSS will refrain from oscillating. This behaviour is confirmed by Table VIII.7 where the OSI, the parameter linked to flow recirculation, decreases with increasing viscosity.

WSSAG   Bearing in mind (1) that the WSSAG embodies the difference in flow direction of two neighbouring points on the vessel wall, and (2) that viscous fluids have a higher resistance to flow, the WSSAG is expected to decrease for viscous fluids. This is confirmed in Table VIII.7.

Effect   Table VI.4 (page 134) summarises the reproducibility of an *in vivo* MRI-based carotid flow simulation. The RMSE was 0.427 N/m^2, 0.0250, 214 N/m^3, 2.35 $N/(s.m^2)$ and 68.1 rad/m for the WSS, OSI, WSSGs, WSSGt and WSSAG respectively. The differences between the simulations were approximately of 0.4 N/m^2, 0.08, 80 N/m^3, 1.5 $N/(s.m^2)$ and 20 rad/m, respectively, as illustrated in Table VIII.7. These differences are a significant fraction of the RMSE, which means that the implementation of the wrong value for the viscosity has significant effects on the calculated haemodynamic parameters.

Consequences   The knowledge that the value of the viscosity has a significant effect on the quantification of haemodynamic parameters implies that individual viscosity measurements should be made for each subject. One of the main problems with *in vivo* viscosity measurements is that they are invasive, even when a viscosity is derived from other measurements.[270] The

concept of performing invasive measurements does not rime with the goal of this research, which is to create a fully non-invasive technique for quantifying blood flow and shear stresses in the carotid arteries. However, blood samples are often taken from patients for a variety of reasons and usually, the haematocrit[d] is then measured. From this cell count, a viscosity can be deduced as explained by Samijo.[270] This way, the subject-specific viscosity can be obtained, without any additional invasive tests.

Men and women have different typical haematocrit values: 40% for women and 45% for men.[32] This induces differences in blood viscosity. It is therefore recommended to set lower values for the viscosity for women.

VIII.2.1.5. Conclusion

This study concluded that the effect of different viscosities is not minor. In order to improve reliability of the predictive tool, the individual viscosity needs to be estimated. This estimation is hampered by the lack of non-invasive techniques for the measurement of blood viscosity. For this research, the blood viscosity implemented in most of the simulations will be set to 4 mPa.s in order to avoid invasive tests. For clinical studies where blood tests are performed, it is recommended to set an individually measured viscosity.

VIII.2.2. Non-Newtonian?

VIII.2.2.1. Introduction

Blood consists of a faintly yellow fluid, the plasma or **liquor sanguinis**, in which are suspended numerous minute particles, the blood cells, the majority of which are coloured and give the blood its red tint (erythrocytes or red blood cells). Due to this composition, blood does not behave as a Newtonian fluid, i.e. a fluid with a shear-independent viscosity. Increasing the haematocrit renders the blood thicker and thus more viscous. Furthermore, blood viscosity is known to increase as flow decreases, because red blood cells adhere to each other, and to the vessel walls. When red blood cells pass

---

[d]**haematocrit**: The ratio of the volume of red cells to the volume of whole blood. Normal range for haematocrit is different between the sexes and is approximately 42 - 54% for men and 36 - 48% for women.[32]

through small vessels, they line up, reducing the blood viscosity (**Fahraeus-Lindqvist effect**).

Many researchers have tried to model the non-Newtonian behaviour of *in vivo* blood, determining the blood viscosity as a function of shear, haematocrit and/or vessel diameter. See for instance the models documented by Whitmore,[364,365] Haynes,[136] Quemada,[255,256,257,258,259] Carreau, Cross,[70] Casson, Luo-Kuang,[204] Wang,[348,349,350] Weaver,[352] Walburn[345] and Zhang.[382] The latter has written a comprehensive overview of all common viscous models. As a consequence, several authors employed viscosity models in their CFD simulations. Augst[16] implemented a Quemada-model in their numerical code for calculating *in vivo* carotid haemodynamics based on 3DUS imaging. Perktold and Rappitsch[247] used a modified Cross model when studying haemodynamics in an elastic carotid phantom. Other models have been employed for carotid haemodynamics, including the Carreau-Yasuda[113] and the Casson model.[246] Clearly, mathematical representations of the viscous behaviour of blood are complex and non-unified, but there seems to be a consensus that blood should not be presented as a New-tonian fluid in a computer simulation. On the other hand, one needs to realise that the viscosity law equations are solved together with the Navier-Stokes equations (equations III.2) in a numerical simulation, therefore, a non-Newtonian model requires more processing time.

The present study performs two simulations that differ only in the viscosity model used: the first simulation is performed with constant viscosity, whereas in the second simulation, the Quemada model was imposed.

VIII.2.2.2. Methods

For this study, a carotid bifurcation with no stenosis acquired with BB MRI from a hypertensive 38 year old subject was imaged, segmented, recon-structed and simulated. Note that the imaging protocol included among other things an inlet velocity measurement in three directions (cine PC MRI), and another velocity measurement at a location in the distal CCA, in the I/S direction only. The second measurement was made to obtain flow rate with higher time resolution than the inlet velocity measurements, thus this flow rate was more reliable than the flow rate measured from the inlet velocities directly. As explained in the previous section (*In- and Outflow Conditions for MRI-based models*, section VIII.1.1), this more reliable flow rate was used to scale the axial velocities at the inlet. Moreover, the velocities from the

second measurement were compared with the velocities obtained from the simulation. These velocities measured with cine PC MRI will therefore be referred to as the 'validation' velocities.

Two simulations were performed. For the first simulation, the computational settings were the same as for the 3DUS reproducibility study, found on page 177. This included Womersley inlet flow and a Newtonian viscosity of 4 mPa.s. The second simulation used the Quemada model as implemented by Augst[16] and documented by Buchanan.[42] The viscosity μ is given by:[42, 258, 259]

$$\mu = \left(\sqrt{\mu_x} + \frac{\sqrt{\tau_o}}{\sqrt{\lambda} + \sqrt{\dot{\gamma}}} \right)^2 \qquad (VIII.5)$$

here, $\dot{\gamma}$ is the shear rate, μ_x, τ_o and λ are constants with the dimensions of viscosity, shear stress and shear rate respectively. Buchanan[42] generated these constants using a least squares regression to match the rheologic data of Merril[217] for a typical haematocrit of 40% and found μ_x = 2.65 mPa.s, τ_o = 0.00432 N/m^2 and λ = 0.0218/s. Note that these values should be changed if individual haematocrit value is available. Equation VIII.5 yields an *apparent* viscosity: this viscosity is not the *true* velocity, but a value which, when used in the Navier-Stokes equations, allows the calculation of the correct flow field.

VIII.2.2.3. Results

Figure VIII.15 shows a comparison between velocity profiles acquired with the Newtonian model, the Quemada model and the actual cine PC MRI measurements. There were 26 images with MRI, numbered from 1 to 26. The title of each figure contains the number of the compared frame after the 'T'. Frame 3 corresponds to the accelaration phase, 5 to peak systole, 8 to deceleration phase and 21 to late diastole.

Figure VIII.16 does the same as Figure VIII.15 but for the secondary velocities. There were no MR measurements of secondary velocities in the validation plane. Note that white means high positive velocity components, and black means high negative velocity components. The positive direction is up for the vertical velocity component and right for the horizontal component.

234
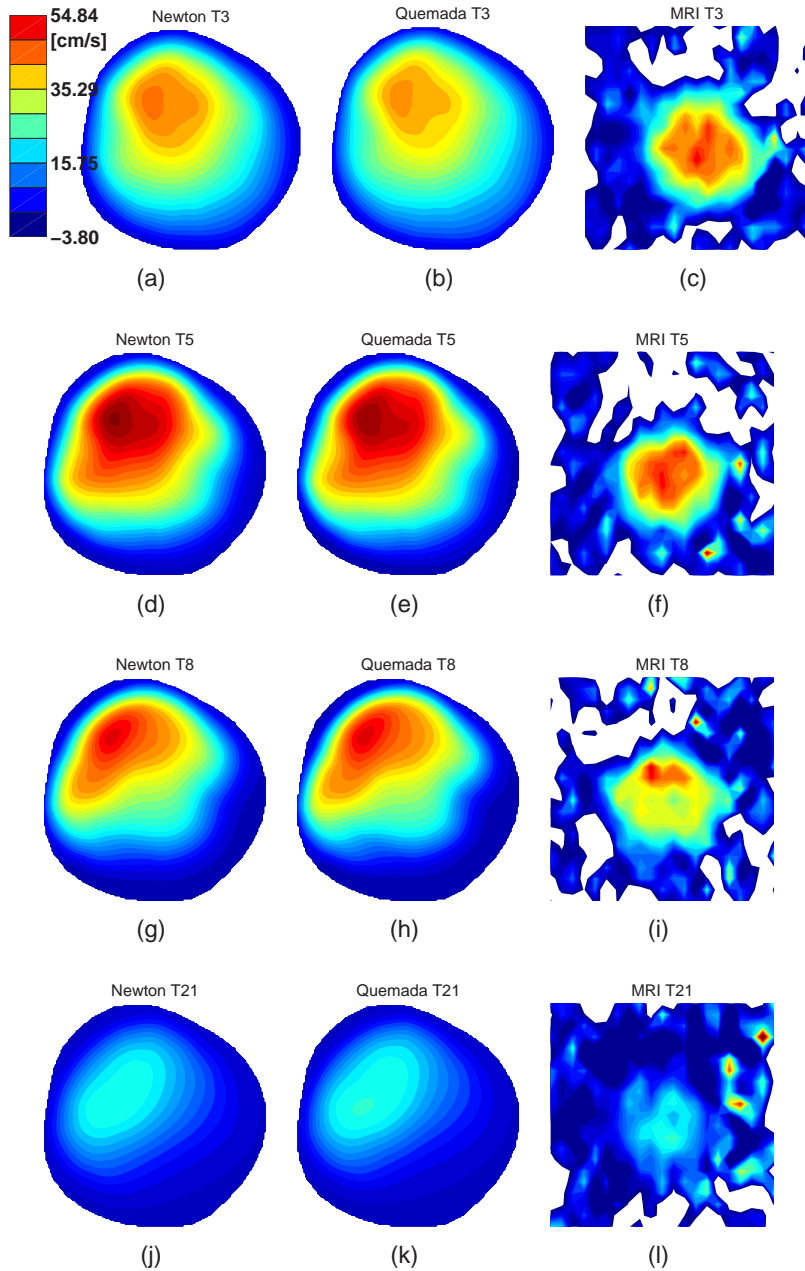
Figure VIII.15.: Comparison between axial velocity profiles acquired with the Newtonian model, the Quemada model and the actual cine PC MRI measurements. The number after 'T' denotes the time-point in the cardiac cycle, 3 corresponds to the acceleration phase, 5 to peak systole, 8 to deceleration phase and 21 to late diastole.
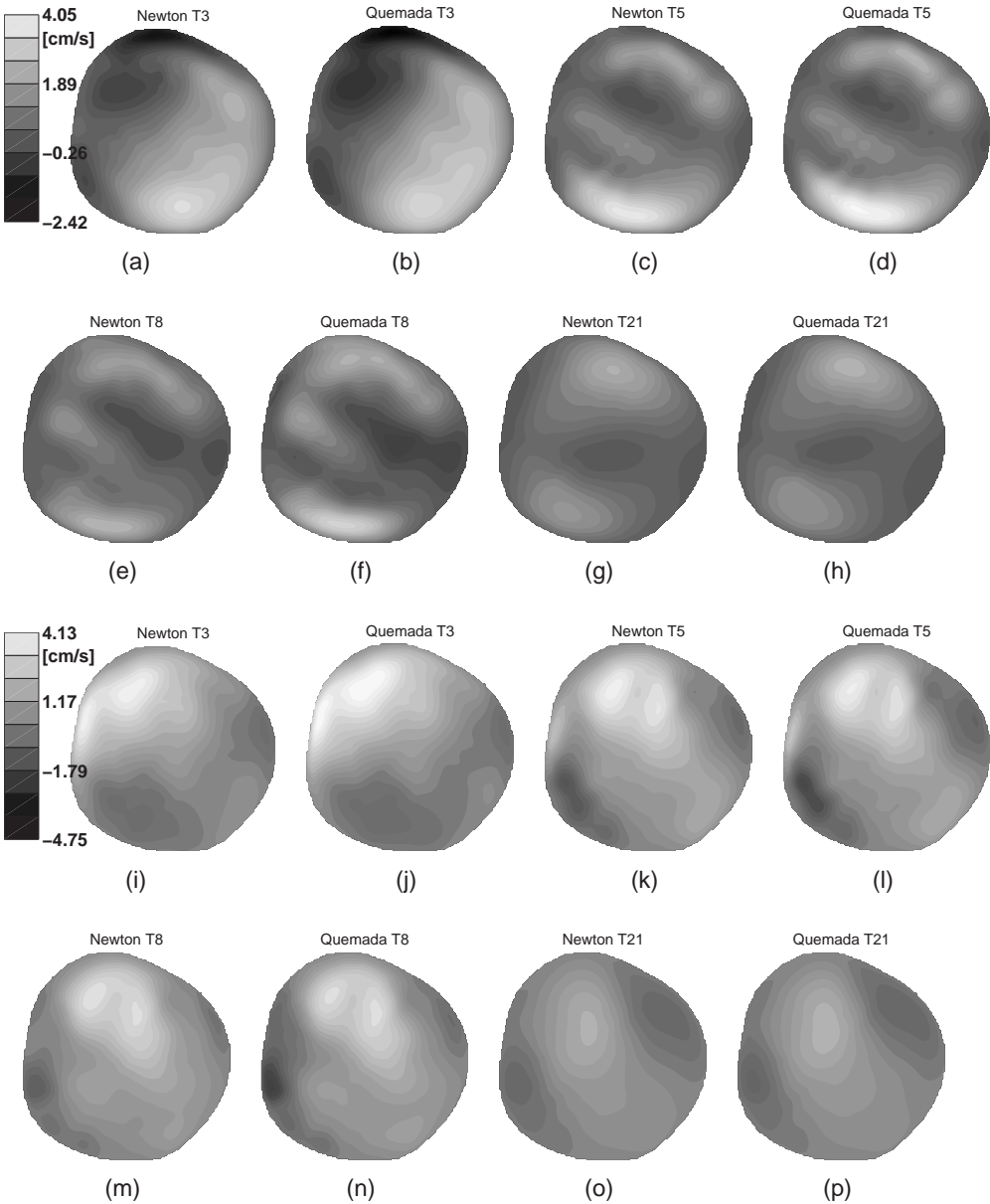
Figure VIII.16.: Comparison between secondary velocity profiles acquired with the Newtonian model and the Quemada model. a-h: horizontal component; i-p: vertical component. The number after 'T' denotes the time-point in the cardiac cycle, 3 corresponds to the acceleration phase, 5 to peak systole, 8 to deceleration phase and 21 to late diastole. Note that white means high positive velocity components, and black means high negative velocity components. The positive direction is up for the vertical velocity component and right for the horizontal component.

(a) WSS with Newtonian model   (b) WSS with Quemada model

(c) OSI with Newtonian model   (d) OSI with Quemada model
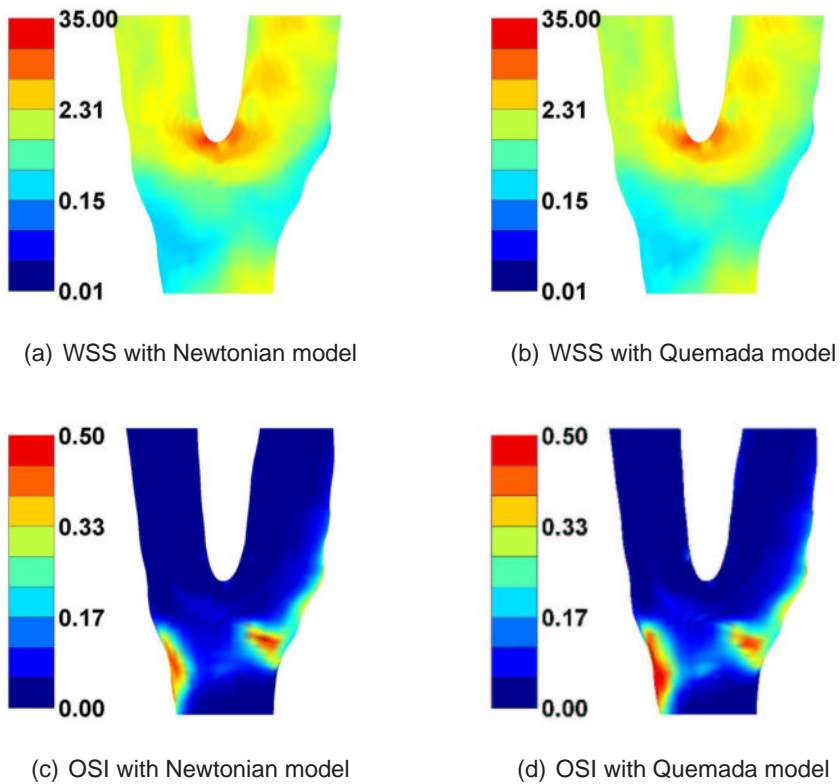
Figure VIII.17.: Wall shear stress (WSS) [N/m^2, logarithmic scale] and oscillatory shear index (OSI) [-] in Newtonian and Quemada model.

The WSS and OSI distribution in the carotid bifurcation can be found in Figure VIII.17.

VIII.2.2.4. Discussion

Figure VIII.15 compares the axial velocity profile found in the Quemada model to the one in the Newtonian model. It is clear that in general, the agreement between the models is very good. At peak systole (T5), the profiles originating from the Quemada model seem slightly blunter than the Newtonian ones. Figure VIII.15 also allows the comparison between simulated and measured velocity profiles. It is clear that the differences between measured and simulated velocities are larger than the differences caused by using different viscosity laws. This means that with the current study, it is

impossible to state whether the introduction of non-Newtonian viscosity was an improvement.

Bearing in mind that velocity measurements such as those in Figure VIII.15 are used as boundary conditions and flow rate estimation, it is clear that the uncertainty in MRI-based CFD will be mainly caused by the uncertainty of MRI velocity measurements rather than the use of a particular viscosity law. Therefore, the extra computational cost needed by the viscosity law is not necessary.

Figure VIII.17, which compares the WSS and OSI distribution found using the different models, further confirms the statement that the differences between the Newtonian and the non-Newtonian model are marginal for the purposes served in this study. Therefore, further investigations on the use of different non-Newtonian models were not pursued.

VIII.2.2.5. Conclusion

In conclusion, the differences between simulations using Newtonian vs non-Newtonian fluids are several orders of magnitude smaller than the differences seen between simulated and measured flow fields, implying that the potential error induced by the use of a Newtonian fluid is much lower than the error induced by using cine PC MRI data - the most reliable technique for non-invasive *in vivo* flow rate measurements - as inlet boundary condition. Cebral stated:[56] *"It is known that, since blood consists in a suspension of particles (red blood cells, white blood cells, platelets) in an aqueous medium, it behaves as a non-Newtonian fluid. Although typically neglected for large arteries, recent studies[23] suggest that non-Newtonian effects may be important in regions of low flow and during some portions of the cardiac cycle.[51] In addition, the use of non-Newtonian models does not increase the computing time substantially. Therefore, to be on the safe side we prefer to always include these effects."*

So for all future studies, such as the ones in part **C**, the Quemada model will be used as presented here. That puts us *on the safe side*.

VIII.3. Heart Rate

Similar to section VIII.2.1, where the effect of setting different viscosities was studied, this section examines the effect of different heart rates on predicted shear stresses.

The geometry and computational details used in section VIII.2.1 were employed here in 5 simulations. In these simulations, the viscosity was constant at 4 mPa.s and the cardiac period was set to 700, 800, 900, 1000 and 1100ms respectively (equivalent to heart rates of 86, 75, 67, 60 and 55 beats per minute, normal values for the resting state). The simulation was still performed using 80 equally spaced time-steps, but the time-steps varied from one simulation to the other, depending on heart rate. The flow profile was scaled in order to keep the carotid blood flow rate constant.

The results are given in Table VIII.8. It shows the values of WSS, OSI, WSSG, WSSGt, WSSGs and WSSAG averaged over certain zones of the carotid for each of the three simulations. See section II.3.3.3 for a definition of these parameters, and see Figure VII.8 (page 173) for a definition of the zones in which the averaging was done.

The differences here are again put into perspective by using the results of the reproducibility study. Table VI.4 (page 134) summarises the reproducibility of a single *in vivo* MRI-based carotid flow simulation. The RMSE found there was 0.427 N/m^2, 0.0250, 214 N/m^3, 2.35 N/(s.m^2) and 68.1 rad/m for the WSS, OSI, WSSGs, WSSGt and WSSAG respectively. The differences between the simulations here were approximately of 0.003 N/m^2, 0.02, 5 N/m^3, 0.4 N/(s.m^2) and 3 rad/m, respectively, as illustrated in Table VIII.8. Thus, contrary to the viscosity, the heart rate has no significant influence on the shear stresses.

Parameter [Unit] / cardiac period :	700 ms	800 ms	900 ms	1000 ms	1100 ms
WSS ALL [N/m^2]	**3.083**	3.081	3.080	3.079	**3.078**
WSS CCA [N/m^2]	2.142	2.137	2.134	2.132	2.130
WSS iCCA [N/m^2]	2.237	2.233	2.231	2.229	2.227
WSS eCCA [N/m^2]	2.017	2.012	2.008	2.005	2.003
WSS ICA [N/m^2]	4.002	3.999	3.996	3.994	3.993
WSS outer ICA [N/m^2]	3.171	3.165	3.161	3.158	3.156
WSS inner ICA [N/m^2]	5.418	5.418	5.417	5.417	5.417
WSS ECA [N/m^2]	4.572	4.576	4.579	4.582	4.584
WSS outer ECA [N/m^2]	2.238	2.239	2.240	2.241	2.241
WSS inner ECA [N/m^2]	4.572	4.576	4.579	4.582	4.584
WSS bulb [N/m^2]	2.741	2.736	2.733	2.731	2.729
OSI ALL [-]	**0.022**	0.020	0.019	0.018	**0.018**
OSI CCA [-]	0.038	0.036	0.033	0.032	0.030
OSI iCCA [-]	0.027	0.024	0.022	0.020	0.019
OSI eCCA [-]	0.054	0.051	0.049	0.047	0.046
OSI ICA [-]	0.017	0.015	0.014	0.014	0.013
OSI outer ICA [-]	0.024	0.022	0.021	0.019	0.018
OSI inner ICA [-]	0.004	0.004	0.004	0.004	0.004
OSI ECA [-]	0.003	0.003	0.003	0.003	0.003
OSI outer ECA [-]	0.007	0.007	0.007	0.007	0.006
OSI inner ECA [-]	0.003	0.003	0.003	0.003	0.003
OSI bulb [-]	0.025	0.022	0.021	0.019	0.018
WSSGs ALL [N/m^3]	**818**	814	811	809	**807**
WSSGs CCA [N/m^3]	534	528	524	520	518
WSSGs iCCA [N/m^3]	546	540	536	533	531
WSSGs eCCA [N/m^3]	519	512	508	504	501
WSSGs ICA [N/m^3]	939	934	930	928	926
WSSGs outer ICA [N/m^3]	699	692	687	684	681
WSSGs inner ICA [N/m^3]	1348	1345	1344	1343	1343
WSSGs ECA [N/m^3]	1557	1558	1557	1558	1558
WSSGs outer ECA [N/m^3]	613	612	611	610	609
WSSGs inner ECA [N/m^3]	1557	1558	1557	1558	1558
WSSGs bulb [N/m^3]	593	586	581	576	574
WSSGt ALL [N/(m$^2 \times s$)]	**13.10**	12.81	12.61	12.45	**12.34**
WSSGt CCA [N/(m$^2 \times s$)]	10.88	10.55	10.31	10.14	10.00
WSSGt iCCA [N/(m$^2 \times s$)]	10.95	10.63	10.40	10.22	10.09
WSSGt eCCA [N/(m$^2 \times s$)]	10.78	10.45	10.20	10.02	9.88
WSSGt ICA [N/(m$^2 \times s$)]	17.03	16.59	16.29	16.08	15.95
WSSGt outer ICA [N/(m$^2 \times s$)]	15.73	15.16	14.74	14.43	14.19
WSSGt inner ICA [N/(m$^2 \times s$)]	19.23	19.01	18.92	18.90	18.94
WSSGt ECA [N/(m$^2 \times s$)]	14.80	14.83	14.87	14.91	14.93
WSSGt outer ECA [N/(m$^2 \times s$)]	9.13	8.96	8.80	8.65	8.52
WSSGt inner ECA [N/(m$^2 \times s$)]	14.80	14.83	14.87	14.91	14.93
WSSGt bulb [N/(m$^2 \times s$)]	13.57	13.06	12.69	12.41	12.20
WSSAG ALL [rad/m]	**147.3**	145.5	143.9	142.4	**141.3**
WSSAG CCA [rad/m]	183.8	180.6	177.7	175.3	173.2
WSSAG iCCA [rad/m]	178.2	174.8	171.6	168.4	165.8
WSSAG eCCA [rad/m]	191.1	188.3	185.7	184.2	182.8
WSSAG ICA [rad/m]	145.5	144.2	142.9	141.6	140.9
WSSAG outer ICA [rad/m]	174.3	172.3	170.3	168.3	167.1
WSSAG inner ICA [rad/m]	96.7	96.5	96.3	96.2	96.1
WSSAG ECA [rad/m]	120.8	120.2	119.8	119.5	119.3
WSSAG outer ECA [rad/m]	78.4	78.0	77.7	77.6	77.5
WSSAG inner ECA [rad/m]	120.8	120.2	119.8	119.5	119.3
WSSAG bulb [rad/m]	147.3	144.3	141.8	139.6	138.1

Table VIII.8.: Effect of different heart rates on predicted wall shear stress (WSS), oscillatory shear index (OSI), wall shear stress gradient (WSSGt: temporal; WSSGs: spatial) and wall shear stress angle gradient (WSSAG).

IX. So, which is better?

IX.1. Motivation for investigating 3DUS

Knowing that both MRI (black blood or time-of-flight) and 3DUS can be used for image-based haemodynamics, the question of which technique is better arises. Inherently, MRI has a number of advantages over 3D ultrasound (3DUS): images are easier to segment and the technique is not restricted to superficial arteries such as the carotid bifurcation, the femoral or the radial arteries. Nevertheless, 3DUS has very interesting advantages making it an imaging technique capable to compete with MRI as imaging tool of choice for image-based haemodynamics.

- Ultrasound scanners are an order of magnitude cheaper than MRI scanners.

- The 3DUS protocol requires 20 minutes of a patient's time. The imaging part only takes 2 minutes - a big difference with the 20 to 30 minutes of immobility required from a patient in the MRI protocol.

- MRI is inaccessible to patients with pacemakers, claustrophobia or bearers of metal implants. Scanning children or hyperkinetic patients is feasible but very difficult due to the subject's inability to lay still. For these people, 3DUS is the preferred imaging modality when diagnosing flow patterns in superficial arteries.

- Data for reconstructing the carotid bifurcation consists of a number ($\pm$ 30) of contours in equidistance planes in MRI, whereas in 3DUS, the amount of contours from which the reconstruction is initiated generally lies between 80 and 140, which means that a higher spatial resolution can be achieved for 3DUS.

While the advantages of 3DUS are clear, its *in vivo* reliability needs to be quantified. In this chapter, 9 subjects were scanned using both imaging

modalities. Aim is to quantify the differences measured between imaging methods, and to investigate how these differences relate to the expected uncertainty of MRI found in *in vivo* reproducibility studies.[121,332]

IX.2. Methods

IX.2.1. Black Blood MRI protocol

Details on the scan protocol can be found in Crowe.[71] Nine healthy volunteers (8 males and 1 female), aged between 24 and 56, participated in the study.

- **Imaging Protocol:** Subjects were scanned while lying supine with their head held in a straight position. The subjects will be referred to as subjects 1 to 9. All MRI scans were carried out on a Siemens Magnetom Sonata 1.5 T scanner. The images were acquired using a purpose-built 2-element phased-array coil. For each subject, two sets of images were acquired at different phases of the cardiac cycle, typically during mid-to-late diastole when the pressure was minimal and peak-systole when the pressure was at its peak. For the volume selective Turbo Spin Echo (TSE) images, a true (non-interpolated) pixel size of 0.47 mm x 0.47 mm in-plane and a field-of-view of 120 mm x 24 mm were typical with 28 slices (2 mm thick). An echo train length of 7 was used to fit the scan within the desired acquisition window (65 ms). For a T_1 weighted image, T_E was 9 ms and gating was every cardiac cycle, thus T_R=RR, the interval between consecutive R-waves. Each 3D image acquisition took 3 to 5 minutes, depending on the subject's heart rate. For systolic TSE imaging, a modified sequence with dark blood preparation at the end of the preceding cardiac cycle was used.

- **Segmentation:** The BB MR images were segmented semi-automatically using the region growing method and a snake model as described in section VI.2. Due to acquisition artefacts inherent to BB MRI as described by Steinman,[307] it was necessary to evaluate the segmented contours and make manual adjustments where appropriate.

- **Reconstruction:** The 3D carotid geometry was reconstructed from the contour segments as described in section VI.3. In short, the 3D

geometry was obtained by stacking the 2D contours in 3D space. Smoothing was performed in two steps: *first*, the areas of consecutive cross-sections were smoothed using a cubic smoothing spline and *in a second step*, the centrelines were smoothed using cubic splines. The smoothing parameters were both set to 0.1. See Figure VI.12 on 117 for the rationale for smoothing and for details concerning the smoothing parameters.

- **Mesh Generation:** After obtaining the 3D geometry, a fully structured mesh was fitted into the geometry as described in section III.2.2.

IX.2.2. 3D Ultrasound

The same 9 subjects were scanned with 3DUS within 2 to 6 weeks. The 3DUS protocol used here is the one described in chapter VII. In short, the carotid imaging and reconstruction was performed using following steps:

- **Imaging:** The Philips ultrasound scanner (ATL-Philips Medical Systems, WA, USA), equipped with the conventional 5 to 12 MHz broadband linear array transducer (HDI 5000, ATL-Philips Medical Systems, WA, USA) was used to acquire the ECG gated 2D transverse images of the carotid bifurcation.

- **Positional information:** Meanwhile, an electromagnetic position and orientation measurement (EPOM) device (Ascension Technology Inc, Vermont, USA), mounted on the probe, recorded the position and orientation of the probe in 3D space.

- **Segmenting:** The acquired images were segmented manually using purpose-built software in a MATLAB environment (see section VII.2).

- **Contour adjustment:** The delineated contour represents the media-adventitia border rather than the lumen-intima border, hence it needs to be adjusted by subtracting the IMT from it. Measurements of the IMT were made approximately 1cm proximal to the carotid bulb, using longitudinal B-mode ultrasound images from at least three projections for each subject.[214] IMT in the ICA and external carotid artery ECA were estimated based on the IMT measured in the CCA and the method described in section VII.2.

- **Recontruction:** The resultant lumen contours were combined with the positional information from the EPOM device to allow the 3D geometry

of the carotid bifurcation to be reconstructed. In the final step, contours originating from non-parallel slices were registered in a fixed 3D space, smoothed and then resliced in order to obtain a set of parallel slices with an inter-slice distance of 1 mm. In the rest of this section, the 'first' slice will refer to the slice most proximal to the heart, whereas the 'last' slice will be the slice most distal from the heart.

- **Mesh Generation:** Similar to the mesh generation in MRI, the resliced contours were used to fit a fully structured mesh into the geometry (see section III.2.2).

IX.2.3. Aligning MRI and 3DUS geometry

For the purpose of comparison, the reconstructed carotid arteries need to be aligned. First, three points were used to define a geometrical centre of the bifurcation. The first point (C_{ICA}) was the centroid of the most proximal cross-section of the ICA. For BB MR images, C_{ICA} was the centroid of the ICA in the first image where ICA and ECA could be distinguished. Similarly for 3DUS, the C_{ICA} was the first centroid in the ICA in the resliced representation of the carotid bifurcation. C_{ECA} was found as the centroid of the first cross-section of the ECA. The third point, C_{CCA}, was found as the centroid of the CCA cross-section 2 mm below the cross-section in which C_{ICA} and C_{ECA} were defined. In BB MR images, C_{CCA} was the CCA centroid of the most distal image where the cross-section of carotid bifurcation consisted of a single artery. In 3DUS images, C_{CCA} was the centroid in the last-but-one CCA cross-section in the resliced representation of the carotid bifurcation. The *centre of the bifurcation* was defined as the centre of gravity of the triangle formed by the three points, C_{CCA}, C_{ICA} and C_{ECA}. After definition of the bifurcation centrepoints, they were translated to the centre of the cartesian reference system. Finally, the 3DUS carotid centrelines were rotated along each of the three orthogonal axes by such an angle that the summed squared distance between the centrelines of the two reconstructions was minimised.

IX.2.4. Computational Fluid Dynamics

The computational details applied here were the same for MRI- and 3DUS-based CFD. They can be found in the 3DUS reproducibility study: section VII.4.2.1 on page 177. Note that blood parameters included in the model

were dynamic viscosity 4×10^{-3}Pa.s (Newtonian flow[a]) and density 1176 kg/m^3. At the inlet, Womersley profiles were derived from a typical flow waveform measured in the common carotid. The same flow waveform was used in all simulations, therefore the inlet velocities derived from the Womersley theory could be different depending on inlet section area, but the flow rate was the same in all subjects.

IX.2.5. Compared Parameters

The compared parameters can be divided into two groups: a set of geometry related parameters, deduced from the 3D reconstructions, and a set of flow related parameters, deduced from the simulations.

- *Geometry parameters* included average cross-sectional area's (A_{CCA}, A_{ICA} and A_{ECA}), non-planarity (NP), centreline agreement (z_{DIST}) and the comparative shape factor (SF_{cCCA}, SF_{cICA} and SF_{cECA}). See section II.3.2.2 for definitions of these parameters. Moreover, diameter ratios, calculated as $\sqrt{A_{art1}}/\sqrt{A_{art2}}$, have been quantified.

- One of the aims of this study was to quantify the differences in flow patterns reconstructed by coupling two different imaging techniques (BB MRI and 3DUS) to CFD. This is traditionally done by comparing velocity profiles, however, the use of haemodynamic wall parameters, derived from predicted velocities, is more interesting for clinical-oriented studies, since they are associated with intimal thickening and thrombosis formation. Therefore, the flow was compared by evaluating both the velocity parameter V_{MAX} and the 3D distribution of the time-averaged WSS, the oscillatory shear index (OSI), the time-averaged wall shear stress gradient (both spatial (WSSGs) and temporal (WSSGt)) and the wall shear stress angle gradient (WSSAG). See sections II.3.3.2 and II.3.3.3 for the definition of these haemodynamically important parameters.

IX.2.6. Statistical approach

The statistical approach for comparing geometry parameters is rather straightforward and are therefore evident when the results are presented. The fo-

---
[a]see page 267 for a discussion on the use of the Newtonian flow assumption.

cus of this section is to explain how the comparison of the WSS-derived parameters was performed. The statistics are based on those used for the TOF-based CFD reproducibility study in section VI.4.2.

IX.2.6.1. Area of overflow/underflow

The chosen haemodynamic parameters have all been proposed to be related to atherogenic process. When the parameters trespass a certain value, the haemodynamic situation becomes potentially harmful. It is difficult to define correct thresholds for 'good' and 'bad' flow, since they need to be considered in conjunction with the time during which a cell is exposed to a certain WSS threshold.[179] In this study, areas at a WSS lower than 0.4 N/m^2 or higher than 2.5 N/m^2, an OSI higher than 0.2, a WSSGt higher than 50 N/s m^2, a WSSGs higher than 4 kN/m^3 and a WSSAG beyond 350 rad/m were considered 'undesirable'. The choice of these thresholds is based on results from several haemodynamic studies.[137, 155, 171, 179, 208, 332]

IX.2.6.2. Analysis along Inferior/Superior axis

Haemodynamic wall parameters were averaged along the circumference of a carotid cross-section, and shown in a plot with abscissa representing distance along the I/S axis. The linear correlation R and the root mean square error (RMSE) between the BB MRI and 3DUS results are measures of haemodynamic agreement. The velocity parameter V_{max} was also examined along the I/S axis.

IX.2.6.3. Patched Analysis

The patched analysis was explained in Figure VI.23 on page 146. In short, the vessel data were averaged in 'patches', small parts of the vessel wall containing a number of computational cells. The patch size was chosen such that it kept 99% of the 2D Fourier power spectrum of the unpatched representation of the vessel wall. The error used to calculate the RMSE is the difference between the value of a patch in the 3DUS scan and the value in the MRI scan and the mean of the value in both scans. A parameter $2DR$ was defined as the linear regression coefficient between patched

data. Finally, a paired rank-sum test was performed on each matching set of patched data.

IX.3. Results

IX.3.1. Geometry Results

IX.3.1.1. Areas

Comparisons of average lumen areas derived from the MR images showed that areas measured in diastole were on average 1.50 mm^2 smaller than those measured in systole. This area change was more obvious in the CCA (average vessel enlargement of 2.85 $\pm$4.93 mm^2 in systole, including the results for subject 1, where the CCA area was clearly overestimated in diastole). In the branches, the area change was not always noticeable (average shrinkage of 0.31 $\pm$3.39 mm^2 in the ICA and *expansion* of 0.40 $\pm$2.38 mm^2 in ECA).

In Figure IX.1, differences in cross-sectional area between (diastolic) 3DUS and diastolic MRI are given as a percentage along the I/S axis. Each of the points in Figure IX.1 was calculated as follows:

$$percent\ difference\ at\ z\ =\ \frac{A_{z,3DUS} - A_{z,MRI}}{\frac{1}{2}\left(A_{local,3DUS} + A_{local,MRI}\right)} \tag{IX.1}$$

This definition is similar to the percent difference defined in the 3DUS reproducibility study in equation VII.2. $A_{z,3DUS}$ is the cross-sectional area at position z along the I/S axis in 3DUS, with z=0 mm being at the apex, z<0 mm in the CCA and z>0 mm in the carotid daughter branches. Similarly, $A_{z,MRI}$ is the cross-sectional area at position z along the I/S axis in MRI, $A_{local,3DUS}$ is the mean area measured with 3DUS (averaged over 1.5 mm) and again, $A_{local,MRI}$ is the mean area measured with MRI (averaged over 1.5 mm). Note that in Figure IX.1, no data are given in the region of the bifurcation apex. This is because cross-sectional areas at the bifurcation point were not available and hence were extrapolated from the nearest cross-sections by making mathematically expressible assumptions on the geometry.
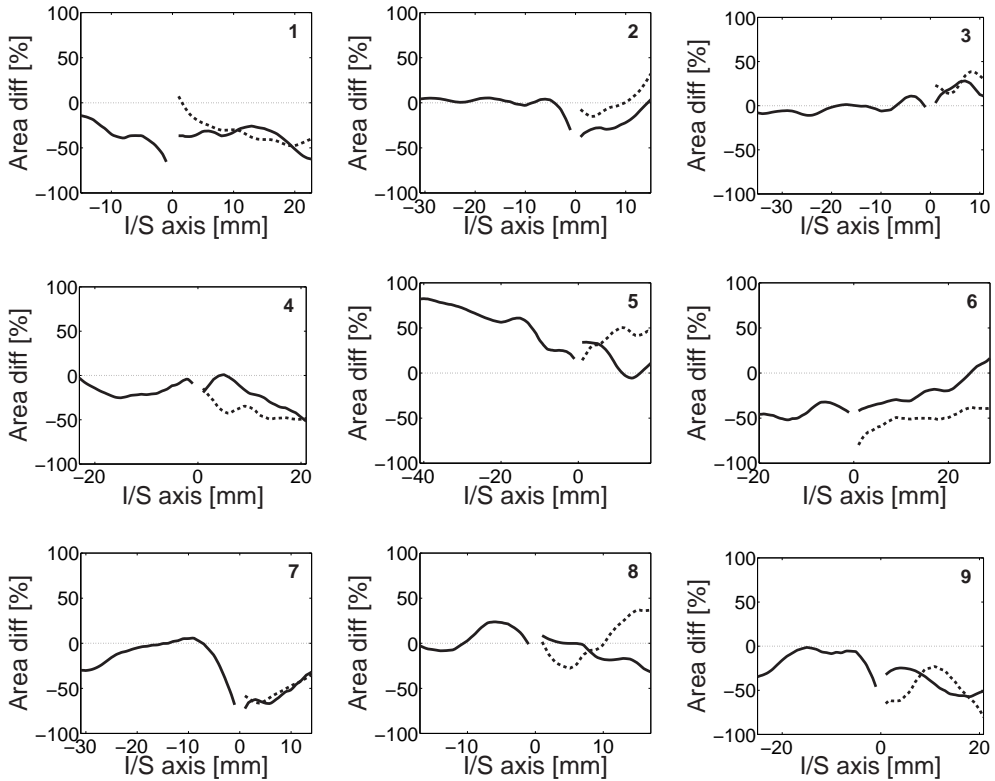
Figure IX.1.: Area differences between 3DUS and diastolic MRI in the three arteries (CCA, ICA and ECA), along the Inferior/Superior (I/S) axis in each of the 9 subjects (numbered in top right corner). The CCA and ICA are represented by the solid lines, respectively at I/S positions lower and larger than zero, the ECA is represented by the dashed line. The percentage difference is defined by equation IX.1.

The mean areas for each individual artery are shown in Figure IX.2. The error bars denote the measurement uncertainty (10% for CCA and ICA and 15% for ECA) based on separate BB MRI and 3DUS reproducibility studies.[118,332] A Bland-Altman[30] plot of the average cross-sectional area has been made: the cross-sectional area averaged over the artery and over the two modalities is plotted against the area difference (3DUS area - MRI area) in Figure IX.3 to illustrate the agreement/disagreement in mean artery area. It was found that areas estimated from MRI were larger than those from 3DUS by 3.60 ± 7.39 mm^2 in CCA, by 5.18 ± 6.23 mm^2 in ICA and by 2.46 ± 3.62 mm^2 in ECA (mean and 95% confidence interval), although in all cases the 95% confidence interval included zero.
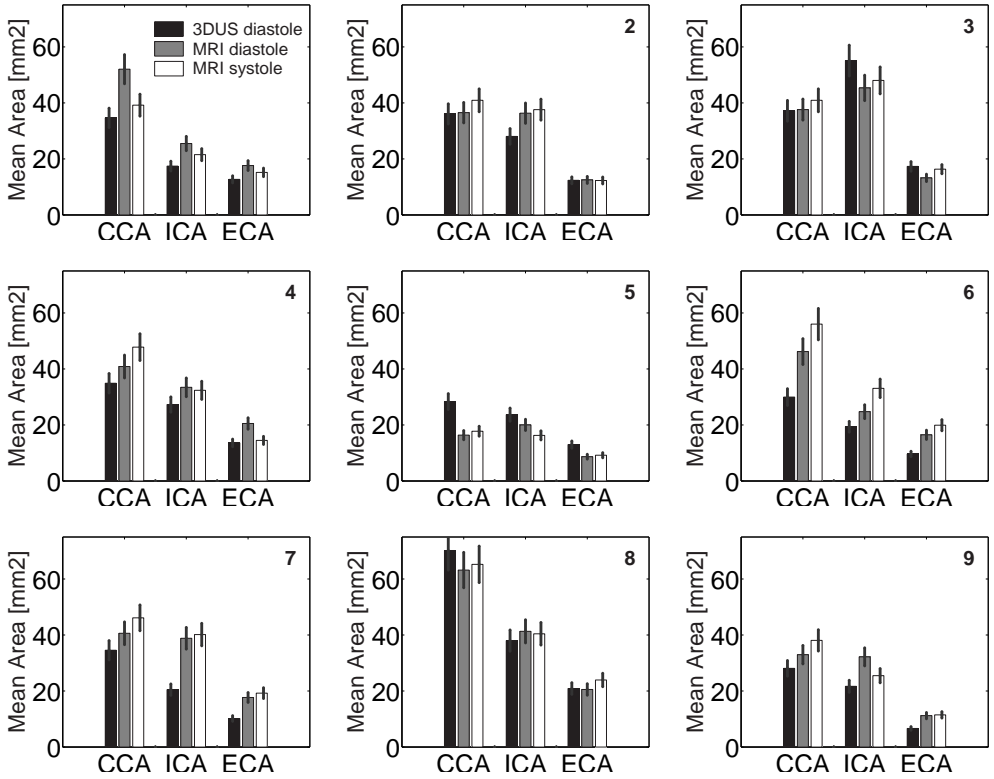
Figure IX.2.: Average lumen area in CCA, ICA and ECA derived from 3DUS, diastolic MRI and systolic MRI in each of the 9 subjects (numbered in top right corner). The error bars are expected uncertainties of 10% for CCA and ICA and 15% for ECA, a percentage based on BB MRI and 3DUS reproducibility studies.[118, 332]
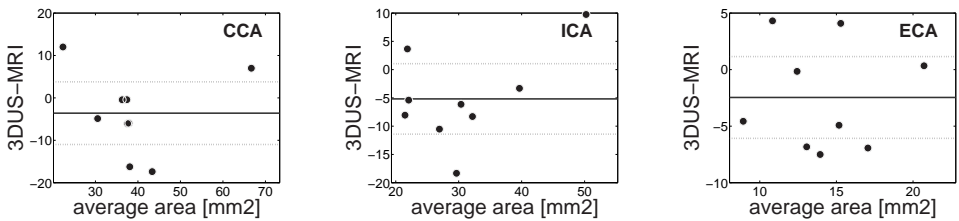
Figure IX.3.: Bland-Altman[30] plots of the CCA, ICA and ECA areas measured with 3DUS and BB MRI. The solid line is the mean difference, the dashed lines are the limits of agreement at p=0.05 and n=9.

Subject	3DUS [%]	Diastolic MRI [%]	Systolic MRI [%]	Difference
1	6.8	5.6	5.0	1.2
2	4.1	5.6	5.5	-1.5
3	3.1	4.0	3.4	-0.9
4	6.3	5.3	4.2	1.0
5	5.1	2.6	6.4	2.5
6	3.1	2.3	2.4	0.9
7	6.9	7.2	7.1	-0.4
8	7.2	1.8	3.3	5.5
9	4.4	6.8	8.3	-2.5

Table IX.1.: Comparison of non-planarity parameter NP determined for 3DUS and MRI (both diastolic and systolic) for 9 subjects. 'Difference' refers to the difference between the 3DUS and diastolic MRI non-planarity.

IX.3.1.2. Diameter Ratios

The diameter ratios are calculated as the square root of the mean area ratios. They can visually be represented as a circle with diameter 1 representing the normalised CCA, and two other circles representing the ICA and ECA. Their diameters depend on the observed diameter ratios. Figure IX.4 visualises the diameter ratios for all 9 subjects. Note that the ICA had a bigger mean cross-sectional area than the CCA in some cases. This is made possible due to the presence of the carotid bulb: when a short stretch of the ICA is used for area averaging, the ICA area can indeed exceed the CCA area.

IX.3.1.3. Centrelines

Figure IX.5 shows the centreline comparison between diastolic MRI (black) and 3DUS (dark grey) for all subjects. The value at the bottom of the centrelines is z_{DIST}, the centreline agreement parameter, in mm. Table IX.1 shows for each subject the values for NP, determined for the MRI and 3DUS scan. Differences between MRI and 3DUS were noticeable.

IX.3.1.4. Shape Factors

Figure IX.6 shows the change of comparative shape factor SF_c along the I/S axis when the diastolic MRI and 3DUS data were compared, and Table IX.2 summarises the mean SF_c for all subjects.
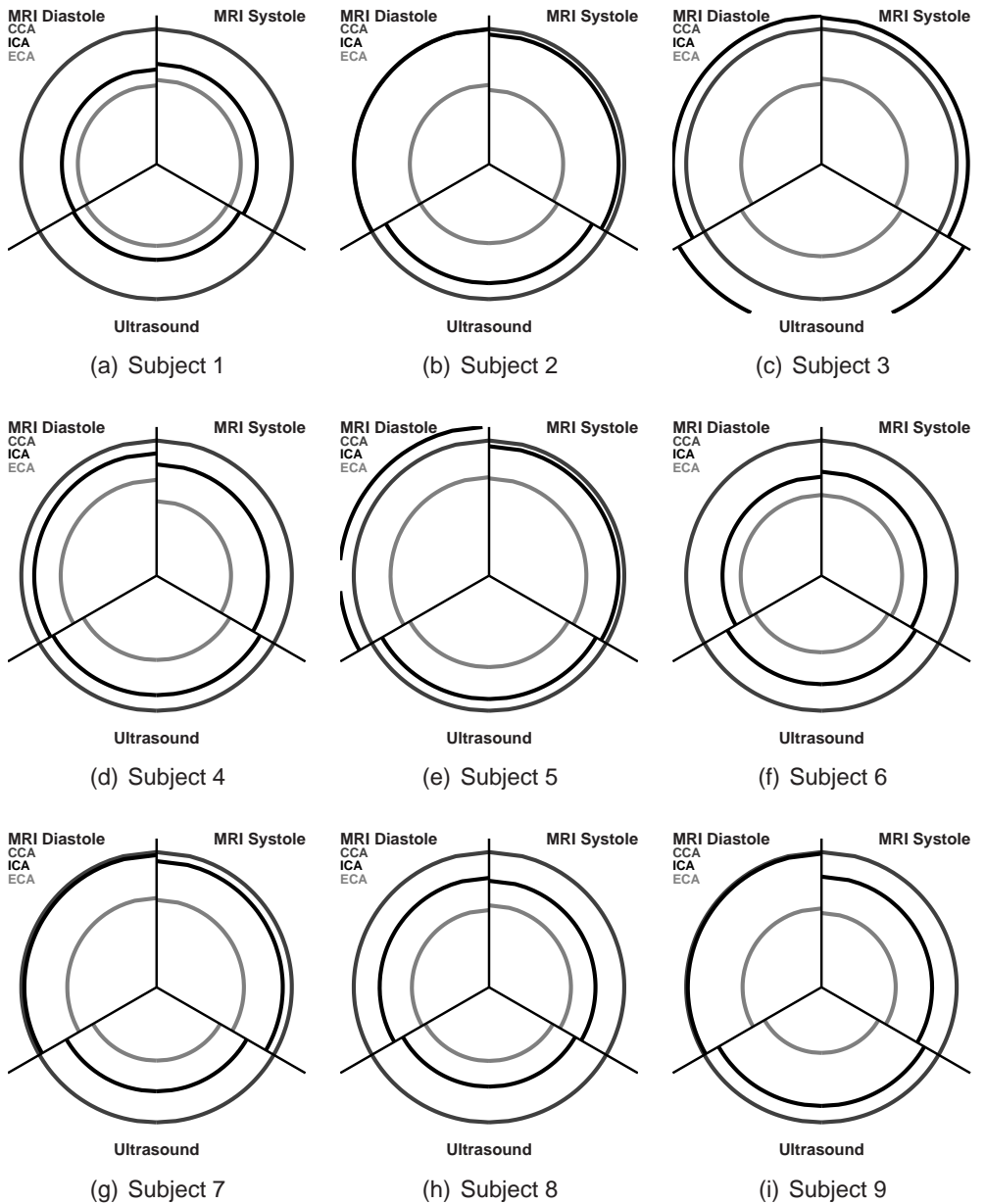
Figure IX.4.: Diameter ratios for all subjects measured with (diastolic) ultrasound, diastolic MRI and systolic MRI.
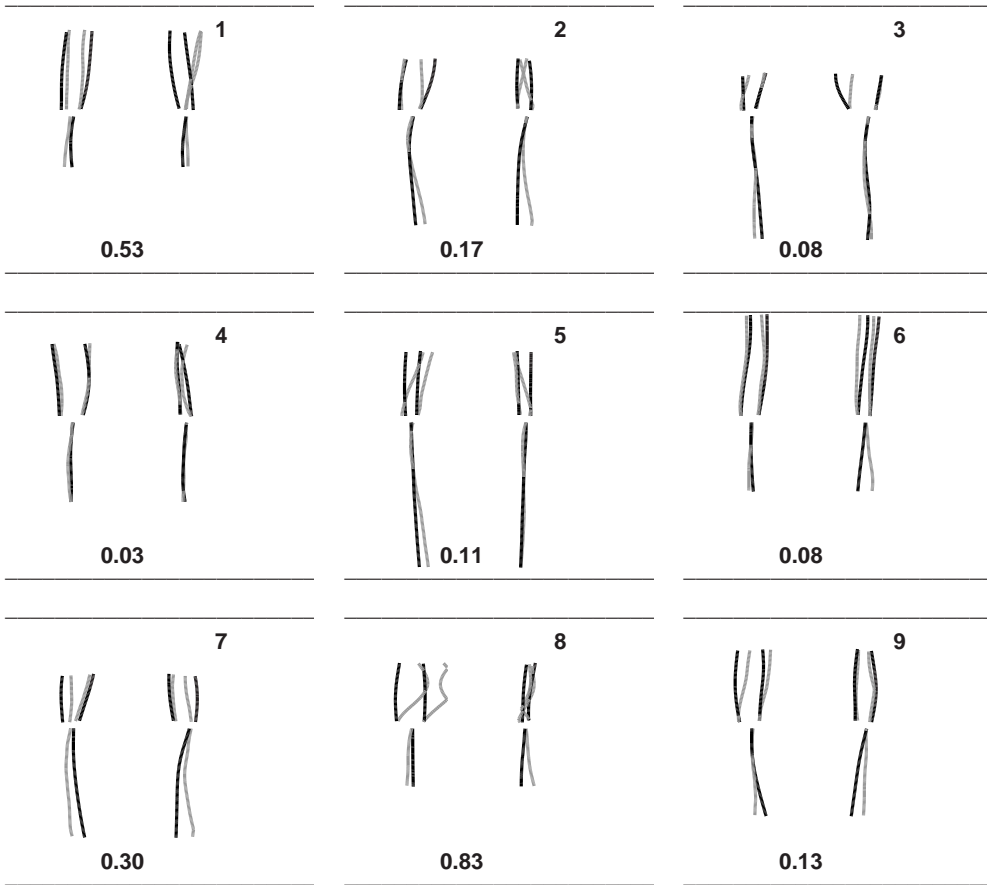
Figure IX.5.: Centreline comparison (in two different views rotated 90 degrees relative to each other) between diastolic MRI (black) and 3DUS (dark grey) in each of the 9 subjects (numbered in top right corner). The value at the bottom of the centrelines is z_{DIST}, the centreline agreement parameter, in mm.

Subject	CCA	ICA	ECA
1	4.6 ± 2.0	5.9 ± 2.2	8.8 ± 5.4
2	4.3 ± 2.2	4.5 ± 1.0	7.9 ± 4.7
3	5.2 ± 2.2	4.3 ± 1.1	12.1 ± 7.2
4	9.0 ± 5.4	6.5 ± 2.3	13.3 ± 5.7
5	8.8 ± 2.3	5.2 ± 2.1	17.3 ± 7.4
6	14.3 ± 7.3	6.1 ± 2.2	9.6 ± 4.8
7	8.4 ± 6.6	8.8 ± 4.8	7.6 ± 4.7
8	7.4 ± 2.3	4.9 ± 1.2	11.7 ± 5.2
9	7.7 ± 2.7	4.7 ± 2.1	9.1 ± 5.3
Mean	7.7 ± 3.1	5.7 ± 1.4	10.8 ± 3.1

Table IX.2.: Mean±standard deviation of comparative shape factors [%] in CCA, ICA and ECA in each of 9 subjects. These values correspond to the average of data in Figure IX.6.

IX.3.2. Flow Results

Figures IX.7 and IX.8 show respectively the WSS and OSI distribution for all subjects. The most favourable agreement between MRI and 3DUS derived WSS was found in subject 4, whereas subject 8 exhibited the largest discrepancy. The OSI distribution agreed extremely well in subject 2, but differed significantly in subject 6.
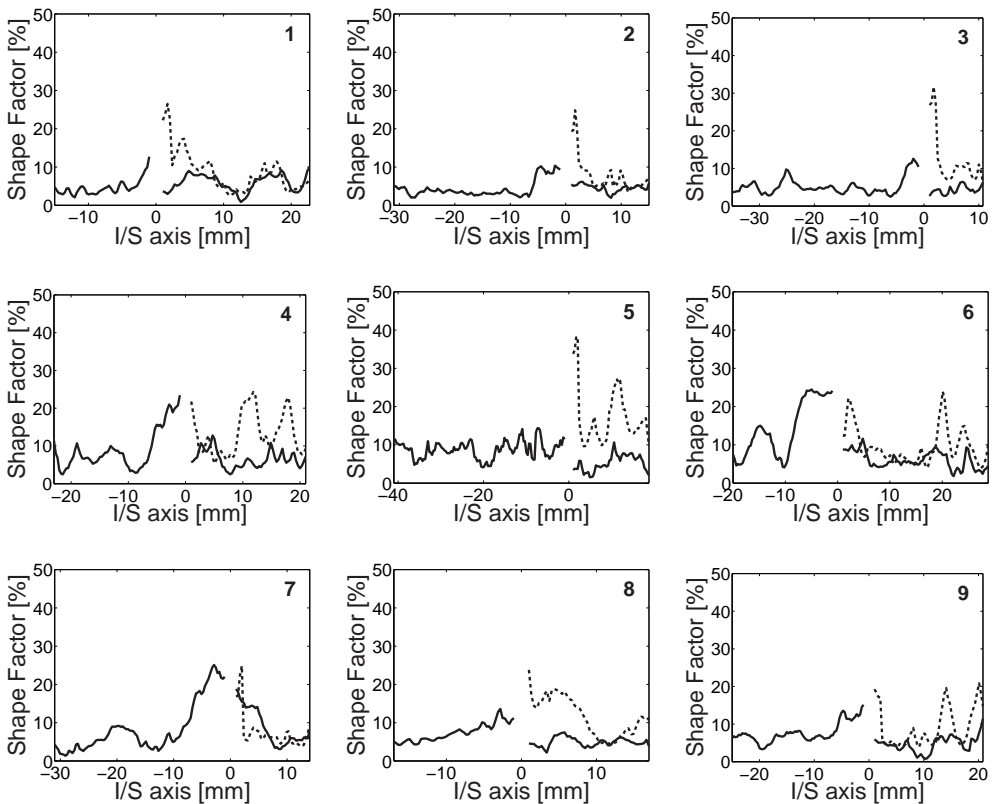
Figure IX.6.: Shape factor evolution along the I/S axis in each of 9 subjects (numbered in top right corner). The CCA and ICA are represented by the solid lines, respectively at I/S positions lower and larger than zero, the ECA is represented by the dashed line. The shape factors were derived from the matching sets of diastolic MRI and 3DUS contours. The mean $\pm$ standard deviation of the SF_c can be found in Table IX.2.

(a) MRI, 1   (b) 3DUS, 1   (c) MRI, 2   (d) 3DUS, 2

(e) MRI, 3   (f) 3DUS, 3   (g) MRI, 4   (h) 3DUS, 4

(i) MRI, 5   (j) 3DUS, 5   (k) MRI, 6   (l) 3DUS, 6

(m) MRI, 7   (n) 3DUS, 7   (o) MRI, 8   (p) 3DUS, 8

(q) MRI, 9   (r) 3DUS, 9
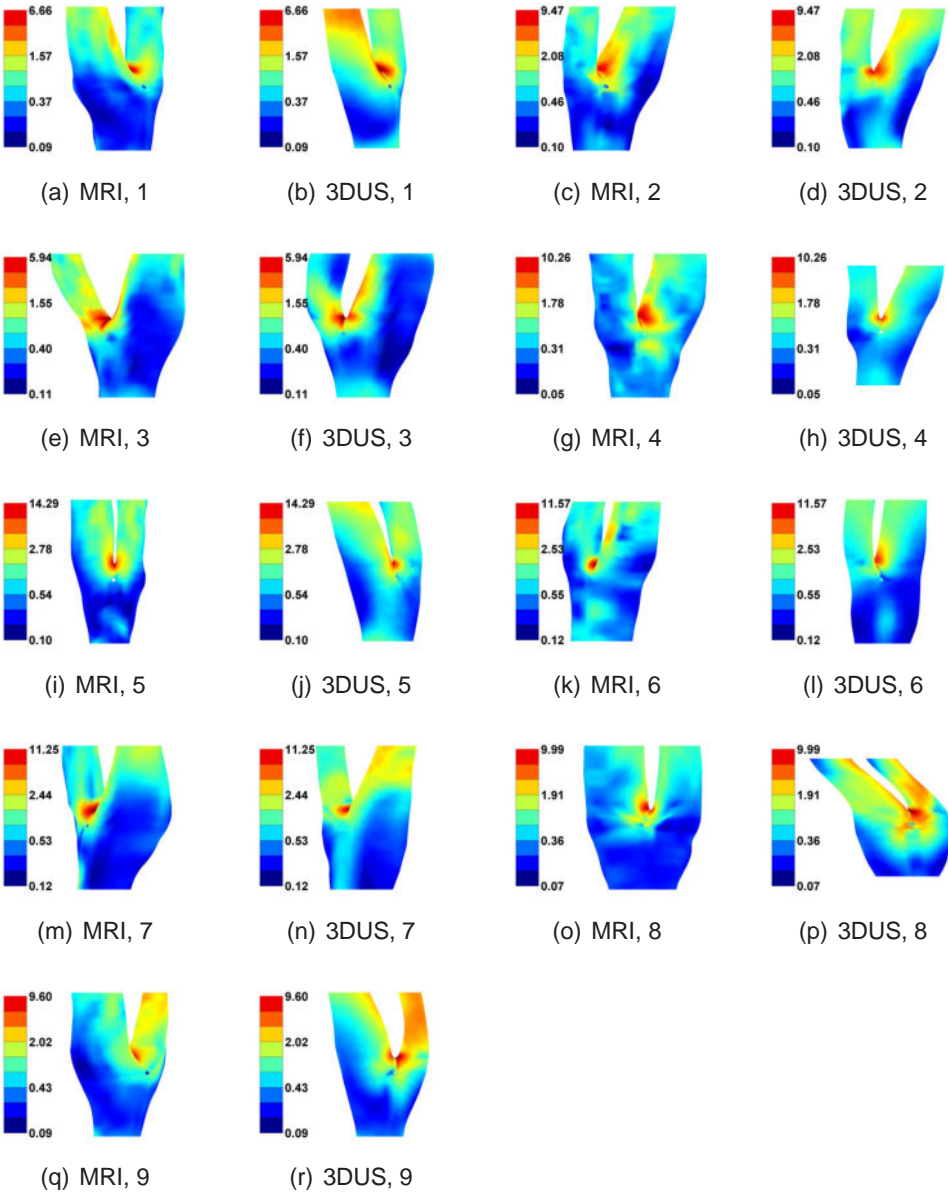
Figure IX.7.: Wall Shear Stress distribution in all subjects and all scans [N/m^2, logarithmic]. Subject number and imaging modality are mentioned in individual captions.

(a) MRI, 1   (b) 3DUS, 1   (c) MRI, 2   (d) 3DUS, 2

(e) MRI, 3   (f) 3DUS, 3   (g) MRI, 4   (h) 3DUS, 4

(i) MRI, 5   (j) 3DUS, 5   (k) MRI, 6   (l) 3DUS, 6

(m) MRI, 7   (n) 3DUS, 7   (o) MRI, 8   (p) 3DUS, 8

(q) MRI, 9   (r) 3DUS, 9
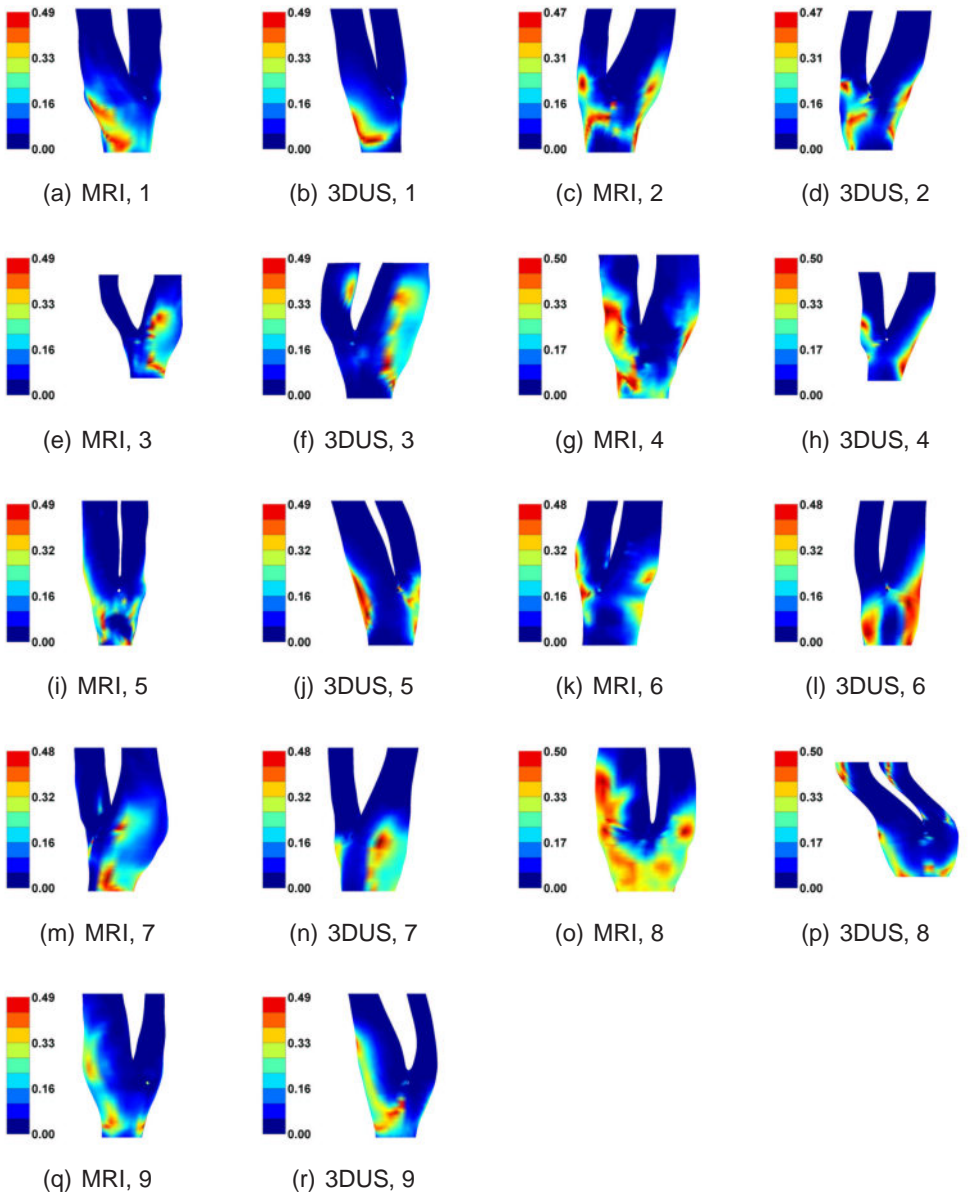
Figure IX.8.: Oscillatory Shear Index distribution in all subjects and all scans [-]. Imaging modality and subject number are mentioned in individual captions.

Parameter	Threshold	ϵ_1 [%]	ϵ_2 [%]	ϵ_1 [%] (Threshold)
WSS	$< 0.40\ N/m^2$	16.08±10.75	49.36±26.48	9% (0.5)
WSS	$> 2.50\ N/m^2$	1.85±1.23	55.48±26.96	20%
OSI	> 0.20	5.40±5.01	25.79±22.36	2%
WSSGs	$> 4000\ N/m^3$	0.22±0.11	70.55±24.73	15% (25000)
WSSGt	$> 15\ N/(s\ m^2)$	2.15±2.20	86.56±38.59	1.5% (50)
WSSAG	> 350 rad/m	6.49±6.94	42.86±18.02	-

Table IX.3.: Differences in Area of overflow/underflow. See text for a definition of ϵ_1 and ϵ_2. The result is given as mean±standard deviation (n=8 instead of n=9 because of omission of subject 8, see discussion). The last column is copied from the TOF MRI reproducibility study,[121] reported in section VI.4.2. Note that the thresholds from that study[121] are shown between brackets when different.

IX.3.2.1. Area of overflow/underflow

Table IX.3 shows the average difference±standard deviation in estimating the area of overflow/underflow. The difference considered is the following error measure:

$$\epsilon_1 = \frac{(A)_{MRI}}{Abif_{MRI}} - \frac{(A)_{3DUS}}{Abif_{3DUS}} \qquad \text{(IX.2)}$$

Here, the 'bifurcation area' $Abif$ is the vessel wall area within a vertical distance of 1.5 cm of the bifurcation apex. The area of overflow/underflow in MRI and 3DUS is respectively $(A)_{MRI}$ and $(A)_{3DUS}$. Another error measure, ϵ_2, quantifies the relative error:

$$\epsilon_2 = 2 \times \frac{(A)_{MRI} - (A)_{3DUS}}{(A)_{MRI} + (A)_{3DUS}} \qquad \text{(IX.3)}$$

IX.3.2.2. Analysis along Inferior/Superior axis

Table IX.4 gives the average RMSE of all considered haemodynamic parameters when analysed along the I/S axis. Note that the analysis along the I/S axis is equivalent to choosing an infinite number of patches in the longitudinal direction, and only 1 patch in the circumferential direction.

Parameter	CCA	ICA	ECA	mean	S_d
Vmax [m/s]	0.0323	0.0310	0.0242	0.0291	0.0044
WSS [N/m^2]	0.158	0.395	0.311	0.288	0.120
OSI [-]	0.0234	0.0235	0.0223	0.0231	0.0007
WSSGs [N/m^3]	26.6	98.6	78.7	68.0	37.2
WSSGt [N/(s m^2)]	1.02	2.53	1.97	1.84	0.765
WSSAG [rad/m]	41.1	44.2	53.9	46.4	6.68

Table IX.4.: Average Root-Mean-Square error along I/S axis (n=8 instead of n=9 because of omission subject 8, see discussion). S_d is the standard deviation of the mean of each artery. Large S_d denotes important differences between arteries.

Parameter	CCA	ICA	ECA	mean	S_d
WSS	0.45±0.14	0.68±0.10	0.78±0.09	0.59±0.18	0.15
OSI	0.46±0.15	0.63±0.29	0.50±0.28	0.55±0.22	0.08
WSSGs	0.47±0.22	0.77±0.12	0.94±0.04	0.69±0.21	0.17
WSSGt	0.67±0.16	0.61±0.17	0.65±0.12	0.65±0.14	0.02
WSSAG	0.47±0.21	0.60±0.11	0.63±0.11	0.60±0.16	0.08
mean	0.50±0.20	0.66±0.19	0.70±0.22	0.62±0.19	-

Table IX.5.: Summary of the 2D correlation coefficient (n=8 instead of n=9 because of omission subject 8, see discussion). The results is shown as mean±standard deviation. S_d defined in Table IX.4.

Artery	WSS	OSI	WSSGs	WSSGt	WSSAG	Total
CCA	4 / 8	4 / 8	3 / 8	5 / 8	2 / 8	18/ 40
ICA	3 / 8	3 / 8	2 / 8	2 / 8	1 / 8	11/ 40
ECA	2 / 8	2 / 8	2 / 8	1 / 8	1 / 8	8/ 40
Total	9 / 24	9 / 24	7 / 24	8 / 24	4 / 24	37 / 120

Table IX.6.: Summary of the paired Wilcoxon test (rank-sum test) for all subjects (n=8 instead of n=9 because of omission of subject 8, see discussion). The results are presented as 'number of positive results / maximum number of positive results' (p<0.05).

IX.3.2.3. Patched Analysis

Table IX.5 summarises the results for the 2D linear correlation coefficients between the patched data from MRI and 3DUS. In Table IX.6, the results of the paired rank-sum test, performed on every matching set of patched data, are summarised. The root-mean-square error (RMSE) in patched value is shown in Table IX.7.

Artery	WSS $[N/m^2]$	OSI $[-]$	WSSGs $[N/m^3]$	WSSGt $[N/(s\,m^2)]$	WSSAG $[rad/m]$
CCA	0.314 (45.9%)	0.0658 (104%)	56.1 (35.3%)	1.80 (24.8%)	96.2 (78.0%)
ICA	0.534 (44.0%)	0.0416 (123%)	164 (54.5%)	3.34 (36.6%)	74.5 (91.6%)
ECA	0.397 (40.0%)	0.0420 (193%)	149 (52.8%)	2.11 (28.1%)	90.4 (88.4%)
mean	0.411 (42.7%)	0.0481 (166%)	150 (55.4%)	2.29 (29.1%)	87.6 (86.3%)
Thomas[332]	0.44 (32%)	0.021 (109%)	38 (55%)	-	61 (73%)
Glor[121]	0.43 (37.9%)	0.025 (123%)	214 (65.7%)	2.35 (30.2%)	68.1 (79.8%)

Table IX.7.: Summary of the root mean square error (RMSE) in the patched analysis. Between brackets, the percent RMSE, i.e. 100 x RMSE/(average value) (n=8 instead of n=9 because of omission subject 8, see discussion). For comparison, the result of two MR reproducibility studies[121,332] have been added.

IX.4. Discussion

IX.4.1. Cross-Comparing MRI and ultrasound

This study cross-compared 3DUS with BB MRI to assess the quantitative differences between the two imaging modalities in reconstructing *in vivo* carotid bifurcation geometry. A similar study was performed by Frayne[98] on a carotid phantom. It was reported that the geometry could be successfully reconstructed using either (3DGRASS) MR, X-ray or ultrasound. Root-mean-square deviations in radius between ultrasound, MRI and projection radiography measurements on the phantom (considered to be the gold standard) were estimated to be 0.55 mm and 0.33 mm respectively. However, to our knowledge, comparative studies on *in vivo* imaging for 3D reconstruction are lacking. The two methods employed here are capable of acquiring not only geometrical data suitable for constructing CFD models of the carotid bifurcation, but also wall data such as IMT and wall compliance (when combined with systolic and diastolic blood pressures). Crowe[71] used BB MRI for *in vivo* carotid IMT and area measurements, and compared MRI data with the more commonly accepted ultrasound measurements. The results showed good agreement when the *average change* in lumen diameter over the length of the common carotid in MRI was compared to the *averaged lumen diameter* resulting from 3 planes for ultrasound. In that study, BB MRI values for wall thickness were consistently about 0.35 mm higher than ultrasound IMT measurements. The authors concluded that this difference arose because BB MRI measures total wall thickness (i.e. media-adventitia thickness plus IMT), whereas ultrasound only measures IMT. To our knowledge, no studies have so far addressed the differences between MRI and 3DUS for *in vivo* carotid geometry reconstruction.

MRI is currently regarded as the modality of choice for large artery CFD

modelling, but has the disadvantage of being expensive, time consuming and of limited availability. 3DUS offers a cost-effective way of imaging superficial vessels prone to atherosclerosis, such as the carotid artery. However, the *in vivo* applicability of 3DUS to the carotids is affected by the location of the bifurcation point in the neck. In those subjects with relatively high bifurcation points, the jaw bone often physically limits the accessibility of the ultrasound transducer to the carotid bulb, and/or the internal and external carotid arteries. This can lead to insufficient geometrical information for subject-specific flow simulations.

IX.4.2. Image Processing

It is important to note that image segmentation and the geometry reconstruction were performed in very different ways with the two types of images. In MRI, a semi-automatic contour detection algorithm was used, whereas lumen contours were defined manually in 3DUS. Ultrasound images were usually found not to be defined well enough to allow automatic segmentation. Automated segmentation of ultrasound images using a technique similar to that used for BB MRI would undoubtedly result in time gain, but contour accuracy would have been compromised. Mao[210] presented a segmentation process based on a deformable model method with only one seed point, and compared the results from the automatic segmentation to the manually segmented counterparts. Although they described manual segmentation for ultrasound as tedious, prone to variability and requiring substantial experience, they still considered the manual segmentation as more reliable than their particular segmentation algorithm. The reproducibility of the ultrasound segmentation protocol adopted in this study was investigated both on a carotid phantom[16] and on healthy volunteers,[117] for which an experienced operator performed all the manual segmentations.

Another difference between the MRI and 3DUS data was the number of transverse images along the vessel length. MRI data were available in 28 slices whereas in 3DUS anything between 80 and 140 images were acquired. With those slices and with the information from the EPOM device, the carotid geometry was resliced into about 50 slices with a constant interslice distance of 1 mm. While this may be regarded as a limitation of the comparison, we think different reconstruction techniques are inevitable because of the different configuration of the data. In this study, the most appropriate and well tested reconstruction techniques were used, although this meant using different reconstruction techniques for MRI and 3DUS.

IX.4.3. Geometry differences

IX.4.3.1. Areas

Figure IX.2 shows that for subjects 2, 3, 4, 8 and 9, areas measured with 3DUS were similar to those measured with BB MRI. In subject 1, the only subject where the mean diastolic area of CCA was larger than its systolic value, the BB MRI-based carotid reconstruction clearly overestimated the diastolic CCA. In the carotid daughter vessels, the BB MRI protocol failed to detect the expected change in cross-sectional area, partly because of the technical difficulties involved in visualising small sized vessels, and partly because the anticipated cyclic area change in the smaller daughter vessel is much smaller than in the CCA. Figure IX.3 shows that there was no statistically significant difference in areas measured by 3DUS and BB MRI, but areas measured by BB MRI tended to be greater, and the variability of differences in measured areas was rather high.

Barratt[20] found that with 3DUS, error in 3D distance measurements on a phantom was up to -0.53±3.39% (mean±standard deviation). Assuming that the diameter of the CCA is 9 mm, which is large but not uncommon, this would result in an uncertainty in area of 4.99 mm^2 (=uncertainty in radius $\times$ circumference = abs((-0.53%-3.39%) $\times$ 4.5 mm $\times$ 9 mm $\times$ π)). Values for ICA (2.22 mm^2) and ECA (1.54 mm^2) were found using estimated diameters of 6 mm and 5 mm respectively. Moore[225] reported an uncertainty of 0.15 mm on the 4 mm radius of a carotid phantom reconstructed from BB MRI, giving a relative uncertainty of 3.75% (=100 $\times$ 0.15 mm/4 mm). For the CCA radius used for comparison purposes in the present study, this would result in an error of 4.77 mm^2 (=3.75% $\times$ 4.5 mm $\times$ 9 mm $\times$ π = uncertainty in radius $\times$ circumference). Similarly, values of 2.12 mm^2 and 2.45 mm^2 have been found for ICA and ECA. Apart from being validated on phantoms in 3DUS[20] and BB MRI,[225] the reproducibility of both carotid reconstruction techniques has also been investigated. In section VII.4.2 (page 176), we demonstrated that lumen area reconstructed from 3DUS was reproduced within 10% for CCA and ICA (or $10\% \times \pi \times (4.5 \text{ mm})^2$=6.36 mm^2 for a large CCA) and 15% for the ECA. Long[194] showed that carotid bifurcations reconstructed with TOF-MRI were reproducible using 8 subjects. Similarly, Thomas[332] performed a separate reproducibility study using BB MRI and reported lumen diameter to be precise to within 5%. Referring this result to an area error, the same uncertainty of 6.36 mm^2 (=5% $\times$ 4.5 mm $\times$ 9 mm $\times$ π) was found. In the comparative study on a carotid bifurcation phantom,[98] root-mean-square errors of 0.55 mm and 0.33 mm in artery radius

Technique	CCA	ICA	ECA
BB MRI validation on phantom[225]	4.77 (7.50%)	2.12 (7.49%)	2.45 (12.5%)
BB MRI *in vivo* reproducibility[332] *(n=3)*	6.36 (10.0%)	2.83 (10.0%)	1.96 (10.0%)
MRI on phantom (for cross-comparison)[98]	9.33 (14.7%)	6.22 (22.0%)	5.18 (26.4%)
3DUS validation on phantom[20]	4.99 (7.85%)	2.22 (7.84%)	1.54 (7.86%)
3DUS *in vivo* reproducibility[118] *(n=9)*	6.36 (10.0%)	2.83 (10.0%)	2.94 (15.0%)
US on phantom (for cross-comparison)[98]	15.54 (24.43%)	10.36 (36.6%)	8.64 (44.1%)
Present study: difference between BB MRI and 3DUS	3.60±7.39	5.18±6.23	2.46±3.62
mean ± standard deviation (n=9)	5.66±11.6%	18.3±22.1%	12.6±18.5%

Table IX.8.: Uncertainties in cross-sectional area for carotid geometry reconstructions in literature.[22,98,118,225,332] When the publication mentions a cross-sectional diameter instead of an area, large carotid diameters of 9 mm (CCA), 6 mm (ICA) and 5 mm (ECA) were chosen as a reference. The percentage is calculated using these reference values. BB MRI: Black blood MRI; 3DUS: Three-dimensional Ultrasound. All values in mm^2, except those with percent sign.

were found for US and MRI respectively. Referring this to an arbitrary CCA with diameter 9 mm, this translates to a 12.22% (=0.55 mm/4.5 mm) error in radius or an uncertainty of 15.54 mm^2 (=0.55 mm × 9 mm × π = uncertainty in radius × circumference) for US. Summarising all this information in terms of area in Table IX.8, we can appreciate the level of correspondence between 3DUS and BB MRI in terms of quantifying cross-sectional areas: the present variability is higher than the uncertainty reported in the reproducibility studies of each of the techniques separately,[118,332] but lower than the variability found in the comparative study of MRI and US on a carotid phantom.[98] This variability is likely to be related to several factors inherent to *in vivo* acquisition:

- When an ultrasound image is of poor quality, the boundaries between vessel lumen and vessel wall, and between lamina adventitia and media, become blurred, which can cause the operator to make a segmentation error.

- A known artefact in BB MRI is 'residual signal',[307] which causes slowly moving or recirculating blood to appear white instead of black, making it look as if it was part of the wall or possible plaque. This effect can cause the IMT to be overestimated and the cross-sectional area to be underestimated (see Figure VI.10 (c)). Recently, a similar segmentation technique has proved reliable[165] in similar studies with healthy subjects, but in diseased vessels, with moderate or severe stenoses, BB MR image segmentation is yet to be validated.

- When an artery cross-section is not imaged perpendicular to its axis, artefacts like vessel boundary blurring can occur. These effects are more pronounced in 3DUS than MRI, since the US-probe has to follow

the patient's neck curvature which is not necessarily the same as the carotid bifurcation curvature.

In subjects 1, 6 and 9, the quantitative area agreement is not as good as in subjects 2, 3, 4 and 8, but the ratios between the branch (ICA or ECA) area and CCA area correspond remarkably well (Figure IX.4). This suggests that there might be a systematic (yet over all subjects statistically insignificant at p=0.05, Figure IX.3) area difference in these subjects. The following systematic errors might contribute to the observed differences between the BB MRI and 3DUS reconstructed carotid geometries.

- BB MR images with a lot of residual signals are likely to cause an underestimation of the lumen. Our results showed that, on the contrary, areas deduced from BB MRI tended to be greater than those from 3DUS. Possibly the 3DUS areas were in some cases underestimated even more due to the IMT deduction (see next point).

- IMT measurements were only made 1 cm proximal to the carotid bulb, and with that measurement, the IMT in the carotid tree was estimated as explained in Figure VII.6 on page 168. Although this mathematical approximation is likely to be clinically realistic, subject-variability is known to be very high and a poor estimate of the IMT will result in systematically over- or underestimated cross-sectional areas.

- Although the two scan modalities were performed under standardised conditions, physiological differences may have been involved. Influences such as recent medication, salt loading, exercise and mental activity may have important haemodynamic effects on cardiac output, blood pressure and cerebral blood flow. Blood pressure was measured on both occasions and no significant difference was found. However, it is possible that an individual's carotid cross-sectional area could be very pressure dependent. Sugawara[312] demonstrated that mild changes in blood pressure (<20 mmHg) can induce a diameter change of up to 1 mm. Their findings showed that this effect is very subject-dependent.

In subjects 5 and 7, where both diameter ratios and mean areas failed to agree, the error was likely to be due to a combination of the aforementioned reasons and to the diversity of the techniques involved. *Ultrasound* was used for IMT measurements and 3D carotid geometry acquisition. An EPOM device provided the 3D coordinates of the ultrasound probe during the scan.

The contours were smoothed before area assessment. *MR* images were acquired with a slice thickness of 2 mm, which led to a rather sparse sampling of the vessel geometry compared to 3DUS. MR image segmentation involved some degree of manual adjustment and smoothing was also performed. Each of the techniques has inherent uncertainties.

IX.4.3.2. Centrelines

Figure IX.5 shows the centreline comparison between diastolic MRI, drawn in black, and diastolic ultrasound, drawn in grey. In subjects 3, 4, 5 and 6, the agreement is satisfactory. However, major differences can be observed in some subjects. This is reflected by the poor agreement in the non-planarity parameter NP (in Table IX.1) and z_{DIST} (in Figure IX.5). The centreline mismatch in subjects 1, 2, 7 and 9 was very likely to be caused by the different scan positions in MRI and 3DUS. For MRI, the patient's head is usually held in a straight position. In contrast, it is often necessary for the ultrasonographer to reposition the subject's neck to achieve better ultrasound images or more coverage of the carotid branches. Different head- and neck angles are likely to influence the centreline and the non-planarity parameter. This point is addressed in chapter XI.

Another reason for centreline mismatch is due to practical problems during image acquisition. A subject might sneeze, move or swallow when lying in the MRI scanner or on the ultrasound couch. The error in subject 8, where the 3DUS centrelines take an unphysiological twist immediately after the bifurcation apex, is more likely to be due to this cause. In view of this, two additional points make MRI preferable: (1) the narrow MRI bore has more restrictions on the head movement as compared to the couch used for US. (2) The slice orientation information in MRI is more reliable than the EPOM device, used to track the position and orientation of the probe. When patients succeed in lying still and in the absence of head- and neck angle differences, the centrelines scanned by 3DUS were similar to those scanned by BB MRI.

IX.4.3.3. Shape Factor

Two issues can influence the shape factor negatively:

1. In MRI, the semi-automatic segmentation technique could result in irregular shapes, whereas in 3DUS, the operator was allowed to fit an ellipse when deemed appropriate.

2. The operator needed to press the probe onto the patient's skin in order to obtain an image in 3DUS. The harder the operator presses, the more the shape of the vessels might deform.

The results in Table IX.2 and Figure IX.6 show a very good agreement in contour shape in the CCA and ICA. This helps to justify the use of the simplified contour shape in 3DUS segmentation. From this result, it can also be concluded that the effect of probe pressure on vessel shape is almost negligible. However, for the ECA, the shape factor was less satisfactory. Apart from the aforementioned factors, the shape of ECA is also influenced by the way its side branches are treated. The thyroid artery originates in the ECA and does show up in both US and MRI scans as an additional branch. Because flow in the thyroid artery is of less interest and because of the non-negligible technical difficulties involved in incorporating the ECA's side branches in CFD models, the thyroid artery is usually neglected in carotid bifurcation models.[386] In the thyroid bifurcation zone, the operator would exclude the thyroid branch by drawing a small segment of a contour across the inlet of the thyroid artery. It is clear that contour shapes in this region are highly operator dependent.

IX.4.4. Effect on flow

From the WSS and OSI distributions in Figures IX.7 and IX.8, two observations can be made. (1) In subject 8, the carotid branches (ICA and ECA) derived from 3DUS are strongly skewed towards one side, a feature which is absent in the MRI-derived geometry. This is very probably due to a sudden movement of the subject deemed unimportant by the operator. For this reason, subject 8 has been eliminated from the statistical analysis. (2) Except for subject 8, the overall agreement in WSS and OSI distribution is satisfactory: two matching sets of carotid bifurcations show sufficient agreement to be recognised as a single bifurcation belonging to a single person.

IX.4.4.1. Comparison of Haemodynamic Parameters

Among the haemodynamic parameters related to the atherogenic process, the WSS and OSI are the most commonly quoted haemodynamic parameters. In the present study, the WSSG and WSSAG have also been evaluated. Sites of high WSSG are linked to intimal hyperplasia, formation of atherosclerotic lesions inside the arteries, and increased vessel wall permeability.[159] The WSSAG represents the magnitude of the shear stress angle deviation. Large WSSAG tends to occur in regions of dysfunctional cells, and hence sites of intimal thickening.[199]

Velocity Table IX.4 shows that the velocity parameter, representing the correspondence in flow profile, agrees very well in all arteries. In the region of complex flow in the ICA, which is very geometry dependent, the uncertainty in V_{max} was only 3 cm/s, corresponding to a 10.9% uncertainty.

WSS According to Table IX.6, the WSS was reproduced most closely by the two imaging techniques. The uncertainty in measuring areas of low WSS was higher in the present cross-comparison study than in the MR reproducibility study[121] (Table IX.3), but the uncertainty in quantifying areas of high WSS was lower (Table IX.3), probably due to the improved meshing technique. Overall, values for the RMSE in WSS (both circumferential (Table IX.4) and patch-wise (Table IX.7)) fall within the 0.45 N/m^2 found in MRI reproducibility studies.[121,332]

OSI In Table IX.6, the OSI - similar to the WSS - seemed to be one of the most robust haemodynamic parameters when switching between MRI and 3DUS-based CFD. Quantification of the vessel wall area overflowing an OSI of 0.2 proved to be a reliable process (Table IX.3). The high percent RMSE is due to the fact that the OSI is 0 in the majority of the vessel wall. The rather low $2DR$ value of 0.54 (Table IX.5) combined with the small RMSE in Table IX.4 showed that the OSI peaks were well localised along the I/S axis, but less reliably along the circumference. Overall, the RMSE for the OSI is below 0.07, which is larger than what has been found in reproducibility studies, but still very small considering that the OSI ranges from 0 to 0.5.

WSSG Table IX.6 shows that although the WSSG values had a less favourable agreement than the WSS or OSI values, the WSSG *distribution* was extremely robust (Table IX.5: highest $2DR$ off all parameters). This was echoed by fairly small ϵ-values when compared with other studies (Table IX.3). The spatial WSSG had a percent RMSE of 55% and the temporal WSSG an RMSE of 2.42 N/(s m^2), which compared well with values found in MRI reproducibility studies.

WSSAG Of all parameters, the WSSAG had the worst result in the rank-sum test. Measuring areas of high WSSAG seemed easier than areas of other parameters, but a comparison with MRI reproducibility studies cannot be done. The RMSE (circ: 46.4 rad/m; patch-wise: 87.0 rad/m) was 26 rad/m higher than the patch-wise RMSE found for MRI reproducibility (61 rad/m).

Summary Thomas[332] published a BB MRI-based flow reproducibility study using the same haemodynamic parameters. For most parameters, the RMSEs found in their study are comparable to those given in Table IX.7 which suggests that the differences in predicted flow between MRI and 3DUS are at a similar level to the uncertainties involved in using each of the imaging modalities alone.

IX.4.4.2. Comparison of Arteries

Table IX.6 shows that the reliability of parameter values was usually higher in the CCA than in the daughter branches. The overall low $2DR$ in CCA (Table IX.5) seems to contradict the statement that the correspondence in the CCA was high, but linear correlation can be misleading when comparing two sets of patched data with little variation. For example, the time-averaged WSS tends to be fairly constant around a value of 0.7 Pa in a CCA in typical circumstances. A significantly better reliability of the proximal CCA could have been expected because of two reasons. (1) BB MR image quality tends to be better for the proximal CCA than for the branches.[71] As a consequence, the bulb *location* can match quite well between MRI and 3DUS, but the largest differences in both cross-sectional area and cross-sectional shape occur in the bulb.[120] (2) Flow patterns are less complex proximal from the apex, resulting in better image quality.

No obvious difference between ICA and ECA reliability was found. When examining each parameter in more detail (Table IX.7), it can be seen that the WSS and WSSG agreed better in the CCA than in the daughter branches, but the opposite was true for the OSI and WSSAG, suggesting that geometry differences had different effects on different haemodynamic parameters.

IX.4.5. Limitations

A first simplification of the model, was the fact that blood was modelled as a Newtonian fluid, i.e. with a constant blood velocity. Bearing in mind that the use of a non-Newtonian model would result in similar changes in flow profiles for both the MRI- and 3DUS-based models, the *difference* found with the Newtonian model presented here should be expected to represent what would be found with a non-Newtonian model. Therefore, a Newtonian model was used in this study to save processing time. See section VIII.2 on page 228 for a discussion on the necessity of the implementation of non-Newtonian viscosity models.

Due to significant complexity of fluid-structure interaction, rigid walls have been assumed in the simulations. This is another simplification of the models. See section VIII.1.3 on page 225 for a discussion on the necessity of the implementation of fluid-structure interaction.

The subjects in this study were all healthy, normotensive volunteers. In elderly people, the potential presence of plaque will introduce difficulties in segmenting images acquired with BB MRI due to possibilities of confusing residual signal[304] in blood on one hand and plaque on the other. In 3DUS the potential presence of plaque will discourage the use of the IMT substraction model because it assumes constant IMT along a circumference. Furthermore, in the presence of calcified plaque the use of 3DUS will be impeded. Because of the possible complications in pathological cases, the flow differences found between MRI and US in this study cannot be regarded as a worst case scenario.

IX.5. Summary and Conclusion

The carotid bifurcations of nine subjects were scanned twice: once with black blood MRI, and once with 3D ultrasound. The aim of the study was

to assess the differences of two imaging modalities when applied to *in vivo* carotid geometry reconstruction. Although image artefacts such as residual signals in BB MRI and indiscernible lumen-intima borders with ultrasound hamper the reliability of both techniques, lumen cross-sectional areas estimated from the two imaging modalities showed a good agreement. Centre-line agreement is rather poor and this was very probably due to the inability to scan the subjects with the same head- and neck angles in MRI and 3DUS. Overall, 3DUS proves to be able to reconstruct 3D *in vivo* carotid geometries which are suitable for CFD simulations, and the reconstructed geometries are comparable to those obtained from MRI. The inter-technique flow differences are comparable to intra-technique flow differences, suggesting that BB MRI and 3DUS are interchangeable for carotid flow reconstruction. MRI has several advantages over 3DUS, including (1) the ability to scan vessels beyond the physical restriction of the jaw-bone and the ability to scan non superficial arteries and (2) the inherent robustness of 3D MRI for centreline registration due to the restricted freedom of movement. The advantages of 3DUS are (1) the low relative cost of a set of images, (2) the easy accessibility of the scanner couch as opposed to the MRI scanner for children, claustrophobic patients and people wearing pacemakers, (3) the widespread availability of US scanners and (4) the speed of imaging in US.

In future, the 3DUS protocol will aim for standardisation in order to avoid centreline differences due to arbitrary head- and neck angles. Two suggestions can be made: (1) patients can be scanned in an anterior position by convention, or (2) patients can be scanned in different positions and take a weighted mean. The first suggestion assumes the anterior head position to be overwhelmingly more common than any other positions, the second recommendation accounts for possibilities that patients may adopt other positions that are comfortable to them, such as subject who sleep in the prone position. Furthermore, IMT measurements will need to be made along the carotid tree instead of using a single site IMT measurement for the entire tree, and ways to extend the ICA and ECA geometry beyond the physical restriction of the jaw-bone need to be investigated. With the current level of agreement achieved between BB MRI and 3DUS, and with the promise of imaging and reconstruction improvements, 3D ultrasound has the potential to become a relatively inexpensive, fast and accurate alternative to MRI for image-based subject-specific carotid haemodynamic simulations.

Part C.

APPLICATIONS

X. So... what does it do?

In part **B**, image-based CFD has been optimised, both for 3DUS and for MRI-based simulations of carotid flow. Furthermore, the achievable reproducibility, accuracy and variability have been quantified in various studies. Now that the 'reliability' of the technique is known, it can be used to perform *in vivo* studies which investigate the carotid blood flow.

In the past, CFD has been used to explain MRI flow artefacts. Here, the voids in MR images are linked to flow features disturbing the expected magnetisation.[148, 307] These studies are performed in the conviction that a thorough understanding of MRA demands a careful analysis of flow-related effects. These early studies linking imaging and CFD do, however, not incorporate a geometry reconstruction based on MR images: their aims can be achieved by performing an MRI (phantom) experiment and a CFD simulation using data originating from pumps and phantom manufacturers. No MRI data is required for the CFD simulation, therefore the techniques of MRI and CFD are not really 'combined'.

The first applications of image-based CFD were aimed at understanding the effects of flow on the process of atherosclerosis.[91, 162, 199, 191, 324, 356] These studies have investigated the role of haemodynamic parameters (WSS, OSI, etc.) in the initiation and progression of atherosclerosis.

One of the potential applications of image-based CFD is in pre-operative planning. Taylor[323] suggested building a Simulation-Based Medical Planning Suite at Stanford University. Here, a patient's vasculature can be scanned and reconstructed in 3D. Before the operation, the effect of implanting a vascular graft or stent can be simulated and adjusted. The surgeon would gain important information from such a simulation. 'How should the incisions be made?', 'Where does the stent need to be placed', 'Which stent is suited for this patient', 'Is there a need at all for the operation, or can we wait and see how the pathology evolves?'. These and many other important questions can be answered using patient-specific image-based CFD.

A recent study[303] used 3DUS-based CFD to investigate the effects of hyperoxia[a] and hypoxic hypercapnia[b] on carotid artery local haemodynamics. Distinct changes in local haemodynamic patterns between these two physiological states were demonstrated, despite little change in the overall carotid blood flow rate.

Along those lines, Ariff[12] performed a study in which the differing effect of angiotensin- vs. β-receptor blockers is compared on carotid IMT, left ventricular mass index, and carotid haemodynamics. From their data it could be suggested that one particular drug performed better in lowering blood pressure and made a more positive effect on haemodynamic risk factors, i.e. in reducing OSI and raising WSS. The identity of the drug could not be disclosed yet.

In our labs, two studies were performed using the combination of imaging and CFD: the Head Position Study (chapter XI) and the study on the Acute Effect of Hypertensive Drugs (chapter XII). In the Head Position study, 9 subjects were scanned in two head positions: head straight, and head turned left. The geometry of their right carotid bifurcation was reconstructed and the subject-specific flow fields were simulated in order to study the effect of head rotations on the haemodynamic situation in the carotid arteries. The study has an effect on two levels. *First*, it informs the 3DUS technicians whether or not diagnoses obtained in one head position are still valid in another head position. *Second*, the study has a more clinical effect: it warns manufacturers of carotid stents or emboli diverters on potential pitfalls typical of the carotid site, it also shows the variety of forces vulnerable plaque is exposed to.

In the study on the acute effect of hypertensive drugs, the aim is to inspect acute effects of two types of anti-hypertensive drugs on the haemodynamics of the carotid artery. A second aim is to explain the results found by Stanton[302] in a long-term study comparing the same compounds. It was found that one type of drugs preserved luminal diameter (LD) and decreased IMT and IMA. Another compound reduces LD, and showed a smaller decrease in IMT with a similar decrease in IMA.

---

[a]**Hyperoxia**: An abnormal increase in the amount of oxygen in the tissues and organs.
[b]**Hypoxic Hypercapnia**: The presence of an abnormally high level of carbon dioxide in the circulating blood, induced by a lack of oxygen in the air

XI. Head Position Study

XI.1. Introduction

The effects of body posture and head positions on respiration and cerebral haemodynamics have been investigated in a number of studies.

The effects on *respiration* seem to suggest that body posture rather than head position has the greatest effects.[24] In infants, sleeping in a prone position has been shown to be associated with increases in heart and respiratory rates, decreases in oxygen saturation and marked pallor in comparison to infants sleeping in a supine position.[290] These changes, however, do not occur with changes in head positions alone.[79] In adults, changes in head position also do not seem to change oxygenation or maximum inspiratory pressure.[79] Adopting a supine position, however, increases pharyngeal resistance[337] and has been shown to worsen apnoeic episodes in those suffering from obstructive sleep apnoea.[24]

The *haemodynamic effects* of body posture and head position have also been examined. In infants, while cerebral blood flow rate remains constant during head rotations in the supine position, keeping the head straight favours cerebral venous drainage and helps to prevent an elevation of cerebral blood volume.[242] Eichler[85] showed that in infants, blood velocity profiles changed in the internal carotid artery (ICA), basilar and vertebral artery with head rotations. Kinking of the vertebral artery at the base of the skull with head rotation may explain the change in flow in the vertebral and the basilar artery.[135] The altered velocity profile in the ICA was not accompanied by a change in flow rate.

Studies in adults have shown marked changes in geometry and the relative positions of the carotid arteries and the internal jugular vein when rotating the head.[314] In addition, rotation of the head is accompanied by significant changes in blood flow patterns and blood velocity profiles in the vertebral and basilar arteries[207,266] as well as in the ICA,[263] although total cerebral blood flow is kept constant.[263] The blood flow patterns in the ICA and verte-

bral arteries also differ from left to right: e.g. the right ICA shows increased blood flow rates with rotation to the contra-lateral position, but the left ICA did not show the same trend.[263]

With the knowledge of potential changes to the carotid geometry and haemo-dynamics on one hand, and the elucidated link between blood flow patterns and atherosclerosis on the other hand,[47, 380] the question of how impor-tant the impact of the potential haemodynamic changes is on the risk for atherosclerosis is raised. Therefore, the aim of this study was to investigate the effect of the change in geometry on carotid haemodynamics as a result of head rotation. Haemodynamic wall parameters such as wall shear stress (WSS) and oscillatory shear index (OSI) were evaluated, as these have been linked to different stages of the atherosclerotic process. To our knowledge, this is the first study to examine the 3D carotid blood flow patterns in dif-ferent head positions using *in vivo*, subject-specific data. The hypothesis is that turning the head has an important effect on both the carotid geometry, as suggested by Sulek,[314] and the carotid haemodynamics. This would im-ply that the risk for atherosclerosis to develop in the carotid arteries, which is thought to be associated with low WSS and/or high OSI, may vary with head position. The altered distribution of heamodynamical forces could also be the cause of so-called 'Telephone Strokes':[241] strokes occurring at the occasion of prolonged telephone calls during which the patient holds the phone with shoulder and ear.

XI.2. Methods

XI.2.1. Subjects and Head Positions

The right carotid arteries of nine healthy subjects, 1 male and 8 female, aged 26.6±3.0 years, were investigated with ultrasound by a single operator. All of the subjects were normotensives with no history of vascular diseases. They were scanned twice serially in a supine position. In the first scan, the subject's head was positioned face up with a purpose-built cushion. In the second scan, the subject was asked to turn his/her head far to the left and to fix on a point on the wall. The two scans will be referred to as 'Straight' and 'Turned' scan, respectively. See Figure XI.1 for an illustration of the head positions. In both scans, the subject's head was tilted forward a little from the supine position because of the cushion. The head tilt was the same for every subject.

Figure XI.1.: Definition of Head Positions: Head Straight: 'Straight'; Head turned left: 'Turned'.

XI.2.2. 3D Ultrasound and CFD

The goal of this study was to evaluate the differences in geometry and haemodynamic parameters at the right carotid bifurcation between 2 head positions. For the first time, 3DUS coupled to CFD was the method of choice for visualising the flow in carotid arteries. The technique has been described in section VII. Technically, the settings for this study were the following:

- The in-house three-dimensional ultrasound (3DUS) scanner (ATL-Philips Medical Systems, WA, USA), in fact equipped with a 2D conventional 5 to 12 MHz broadband linear array transducer (HDI 5000, ATL-Philips Medical Systems, WA, USA) was used to image the ECG gated 2D transverse cross-sections of the carotid bifurcation as described in section VII. Simultaneously, the electromagnetic position and orientation measurement (EPOM) device (Ascension Technology Inc, Vermont, USA), mounted on the probe, recorded the position and orientation of the probe in 3D space. The 2D transverse cross-section and the information from the EPOM device allowed 3D reconstruction of the carotid bifurcations.

- In order to use *in vivo* acquired boundary conditions, the ultrasound machine was used to acquire CCA centreline velocities with pulsed-Doppler. These velocities were measured at the location where the first cross-section of the CCA was acquired.

- The mesh was generated as described in section III.2.2. Figure XI.2 shows the computational surface mesh for subject 1 in both head positions. Note that the z-axis was the Inferior/Superior axis, but the x
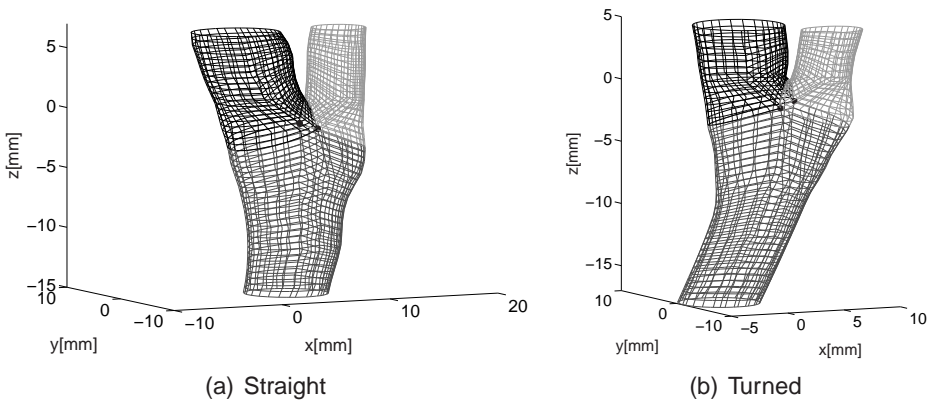
Figure XI.2.: Surface meshes for subject 1 in the two head positions: Straight (head straight) and Turned (i.e. head turned to the left).

and y-axis move with the ultrasound probe and were not the same in both scans.

- The computational settings were the following. The vessel wall was assumed to be rigid with no mass transfer and zero-velocity (no-slip) condition. At the inlet, Womersley profiles derived from the measured flow waveform in the common carotid were imposed. The flow waveform was acquired from the centreline velocity, assuming developed Womersley flow in the CCA.[368] At the outlet, a constant flow ratio of 55:45 was adopted between the internal (ICA) and external carotid artery (ECA) throughout the whole cardiac cycle. The Navier-Stokes equations were solved using the 'QUICK' differencing scheme implemented in CFX4™,[3] on a SUN Blade 1000 Workstation (Ultrasparc III processor, 512Mb RAM, 750 MHz) as mentioned in section III.3. Two cardiac cycles, each consisting of 80 equally spaced time-steps, were simulated. Refinement of time-step or increase in simulated cycles resulted in instantaneous WSS differences below 0.5% and 0.01% respectively. For the fluid properties, a blood density of 1176 kg/m^3 was set. The non-Newtonian behaviour of blood viscosity was incorporated using the Quemada-model.[42]

XI.2.3. Comparative study

The effect of change in head position was quantified by geometric and haemodynamic parameters. The first geometric parameter is the mean lumen area A_{CCA}, A_{ICA} and A_{ECA}. The bifurcation non-planarity (NP) intro-

duced by King[157] was used. Furthermore, z_{DIST},[194] defined as the average distance between the two centrelines, was computed. In addition to non-planarity (NP) and z_{DIST}, the linearity[157] L was also derived for each of the three arteries. The final geometric parameter was the cross-sectional comparative shape factor introduced by Long.[194] As a general guide, shape factor of below 10% could be considered acceptable,[194] but with 3DUS, the accuracy of the shape factor is restricted to 15% in the ECA (see section IX). See section II.3.2.2 (page 53) for a clear definition of the used geometry parameters.

The haemodynamic parameters comprise the velocity-dependent parameter V_{max}, the time-averaged wall shear stress (WSS) and the oscillatory shear index (OSI). See section II.3.3.3 (page 67) for a definition of these parameters.

The average WSS and OSI values alone are not sufficient as markers for atherogenecity. The localisation and area of the vessel wall experiencing WSS and OSI above certain limits may also be important. For statistical purposes, the average WSS and OSI on the inner and outer walls of the ICA and ECA have been calculated separately. Here, 'inner wall' stands for the half of the daughter vessel on the flow divider side, whereas 'outer' stands for the other half of the wall, i.e. the half that could be viewed as the outer bend of the vessel. Similarly, the CCA has been divided into two portions: one on the ICA side and another on the ECA side. See Figure VII.8 (page 173) for a definition of the regions over which the parameters were averaged.

XI.3. Results

XI.3.1. Geometry

Figure XI.3 (a-c) summarises the findings for the arterial cross-sectional areas: both the sample-averaged means (black dots) and the individual changes (dotted lines) are represented. Note that 'sample-averaged mean' stands for the value averaged over all subjects in one head position. The p-value in Figure XI.3 is obtained by testing the hypothesis that the sample-averaged means in the two head positions are equal (paired Student test). For clarity, a p-value close to zero rejects the hypothesis and suggests that the sample-averaged means are different, whereas a p-value close to 1 concludes that the sample-averaged means are equal. Note that the uncertainty

of 3DUS for cross-sectional area measurement is around 10% for the CCA and ICA and 15% for the ECA.[118] Table XI.1 gives the shape factor, i.e., the parameter describing the correspondence in cross-sectional shape between the Straight and Turned scans. Long's reproducibility study[194] suggested that the cross-sectional shape could be considered unchanged when the comparative shape factor was smaller than 10% for the CCA and ICA and smaller then 15% for the ECA. Figure XI.4 overlays the centrelines of the Straight and Turned scans. The quantitative analysis is done in Figure XI.3 (d) using the non-planarity parameter NP presented by King.[157] This parameter is reproducible to within 1%.[157] Furthermore, Table XI.2 shows the other measure of vessel planarity, z_{DIST}, deduced from Long's study.[194]
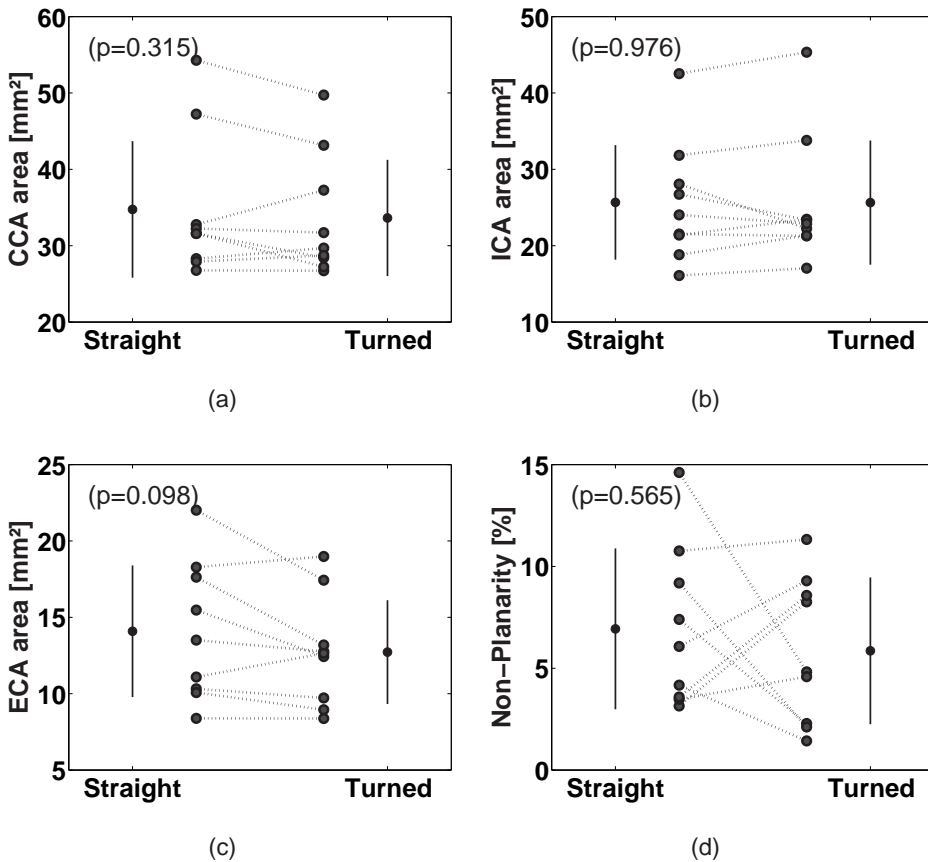
Figure XI.3.: a-c: Individual and overall change of cross-sectional area with head straight and turned. The black dot on the vertical line gives the sample-averaged mean±standard deviation. Each of the dotted lines corresponds to a single subject. d: Non-Planarity (NP). The p-value tests the hypotheses that the sample-averaged means in the two head positions are different (paired Student test).

Subject	CCA	ICA	ECA
1	2.53	6.09	5.95
2	4.08	2.02	11.02
3	6.05	6.78	5.66
4	1.54	2.90	5.80
5	1.54	6.53	10.45
6	3.25	6.88	4.93
7	2.51	4.57	3.52
8	1.39	8.04	4.80
9	3.36	6.51	5.66
Mean	2.92±1.50	5.59±2.00	6.42±2.56

Table XI.1.: Shape Factor for all subjects [%] (n=9). Subject-Mean results are given as mean ± standard deviation.

Subject	z_{DIST} [μm]
1	106.9
2	91.4
3	37.2
4	63.4
5	35.8
6	111.8
7	111.3
8	60.1
9	67.7
Mean	76.2±30.3

Table XI.2.: Centreline Distance z_{DIST} (deduced from Long's study[194]) for all subjects (n=9). Subject-Mean results are given as mean ± standard deviation.

In Table XI.3, a statistical analysis of the centreline agreement is presented. In the first column, the studied centreline-related parameter is named. The second column gives the tested hypothesis, and the last column gives the p-value for this hypothesis using a Student test. Whether the Student test was one- or two-tailed, is reported in the third column. The table compares z_{DIST} (the parameter showing overall centreline mismatch), NP (the non-planarity parameter) and L (the linearity parameter) between the two scans.

XI.3.2. Flow

Figure XI.5 (a) shows the mean flow rate in the CCA for all subjects in all scans, and Figure XI.5 (b-d) contains the velocity-dependent parameter V_{max}. Table XI.4 shows in the first three rows the V_{max} averaged over
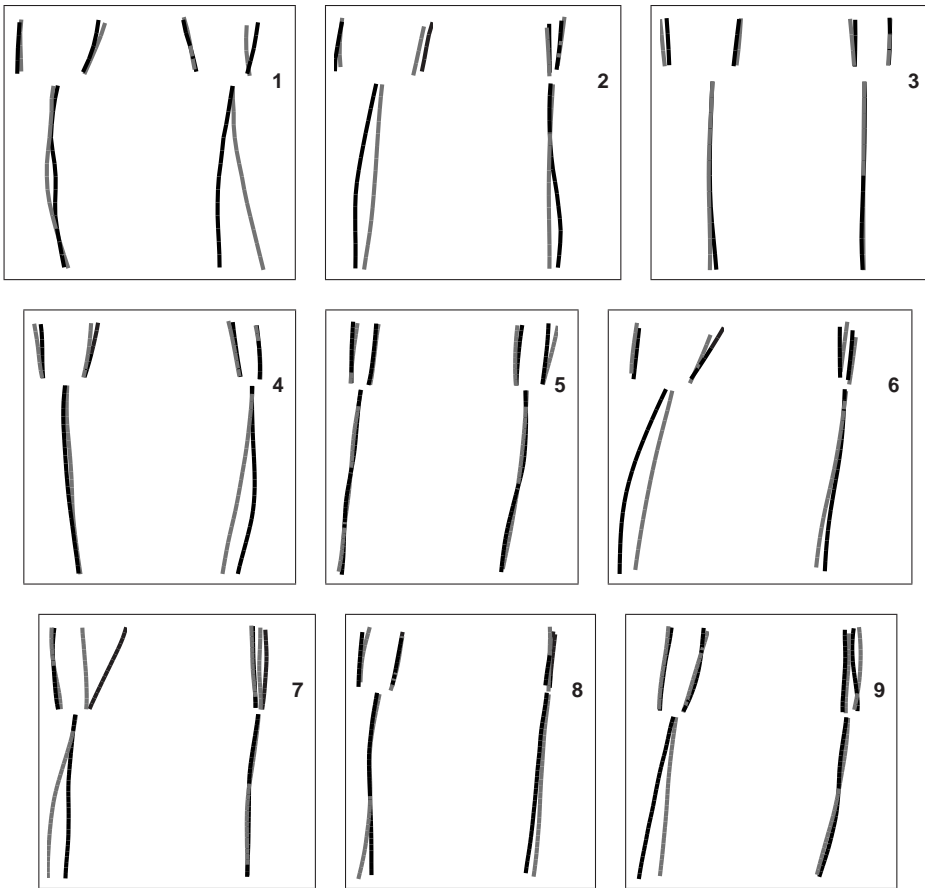
Figure XI.4.: Vessel centrelines for all subjects. Black: Straight scan, Grey: Turned scan. For each subject, two views are presented, rotated by 90° with respect to each other. The gravity point of the triangle formed by the most distal CCA centroid and the most proximal ICA and ECA centroid was used for aligning the centrelines. Subject number in top right corner.

Parameter	Hypothesis	tailed	p-value
z_{DIST}	$<0\mu$m	one	$3.3\ 10^{-5}$
NP difference	$=0\%$	two	0.57
NP difference CCA	$>0\%$	one	$5.3\ 10^{-3}$
NP difference ICA	$=0\%$	two	0.99
NP difference ECA	$=0\%$	two	0.31
L difference CCA	$=0\%$	two	0.33
L difference ICA	$=0\%$	two	0.42
L difference ECA	$=0\%$	two	0.12

Table XI.3.: p-values from Student test for centreline agreement parameters. 'difference' stands for the signed value of the difference between the Turned and the Straight position. (n=9)

Artery	Straight [cm/s]	Turned [cm/s]	diff [%]
CCA	23.91±5.09	21.19±5.91	-12.89±25.51
ICA	19.39±4.77	17.49±5.90	-11.80±28.00
ECA	21.41±8.14	21.52±11.03	-2.93±36.02
CCA	25.18±4.89	24.74±3.73	-0.98±8.65
ICA	22.17±4.13	22.39±3.24	1.68±9.11
ECA	19.40±3.63	19.29±3.98	-1.16±8.84

Table XI.4.: Mean $\pm$ standard deviation (n=9) of the velocity-dependent parameter V_{max} [cm/s]. diff: The difference in percentage is the fraction of the difference in V_{max} and the mean V_{max}. The last three lines return the results in case the same boundary conditions (a.i. the same flow rate) were imposed in the two head positions instead of using the flow rate calculated in each head position. The standard deviation on the difference can be regarded as an RMSE.

the subjects (mean±standard deviation) in each of the arteries and each of the head positions. Similarly, the last three rows are the results obtained when the same boundary conditions (i.e. the same flow rate) were imposed in the two head positions. Therefore, Table XI.4 quantifies the change in V_{max}, and, with results given in the last three rows, suggests how much of the change can be attributed to the change in mean flow rate. Table XI.5 provides the statistical analysis of the velocity related parameter V_{max}. Similar to Table XI.3, the studied parameter is in the first column, the hypothesis can be found in the second column, and the last column gives the p-value for this hypothesis using a Student test. Whether the Student test was one- or two-tailed, is reported in the third column. A previous study[118] showed that the V_{max} was reproducible within 10%.

In order to acquire an overall feel for the haemodynamic effect of head rotation on the distribution of vessel wall parameters, the WSS and OSI distribution in all subjects and all scans are shown in Figures XI.6 and XI.7. Note that low values of WSS ($<\ 0.4\ N/m^2$) have been associated with intima-media complex thickening, an early marker of atherosclerosis. WSS values above the threshold of $400\ N/m^2$ can cause direct endothelial cell damage.[171] It is well known that shear affects many functions of the arterial wall, but the exact thresholds for pathologically low and high WSS are disputable. Similarly, it is known that areas where the OSI is elevated are prone to intimal thickening. No clear thresholds for 'good' or 'bad' OSI values have been defined in literature.

The average WSS and OSI values in the vicinity of the apex are shown in Figure XI.5 (e-f). The 'vicinity of the apex' is defined here as 10 mm above and 20 mm below the apex. In Figure XI.8, the differences in WSS and OSI in different regions of the arteries are given.

(a)

(b)

(c)

(d)

(e)

(f)
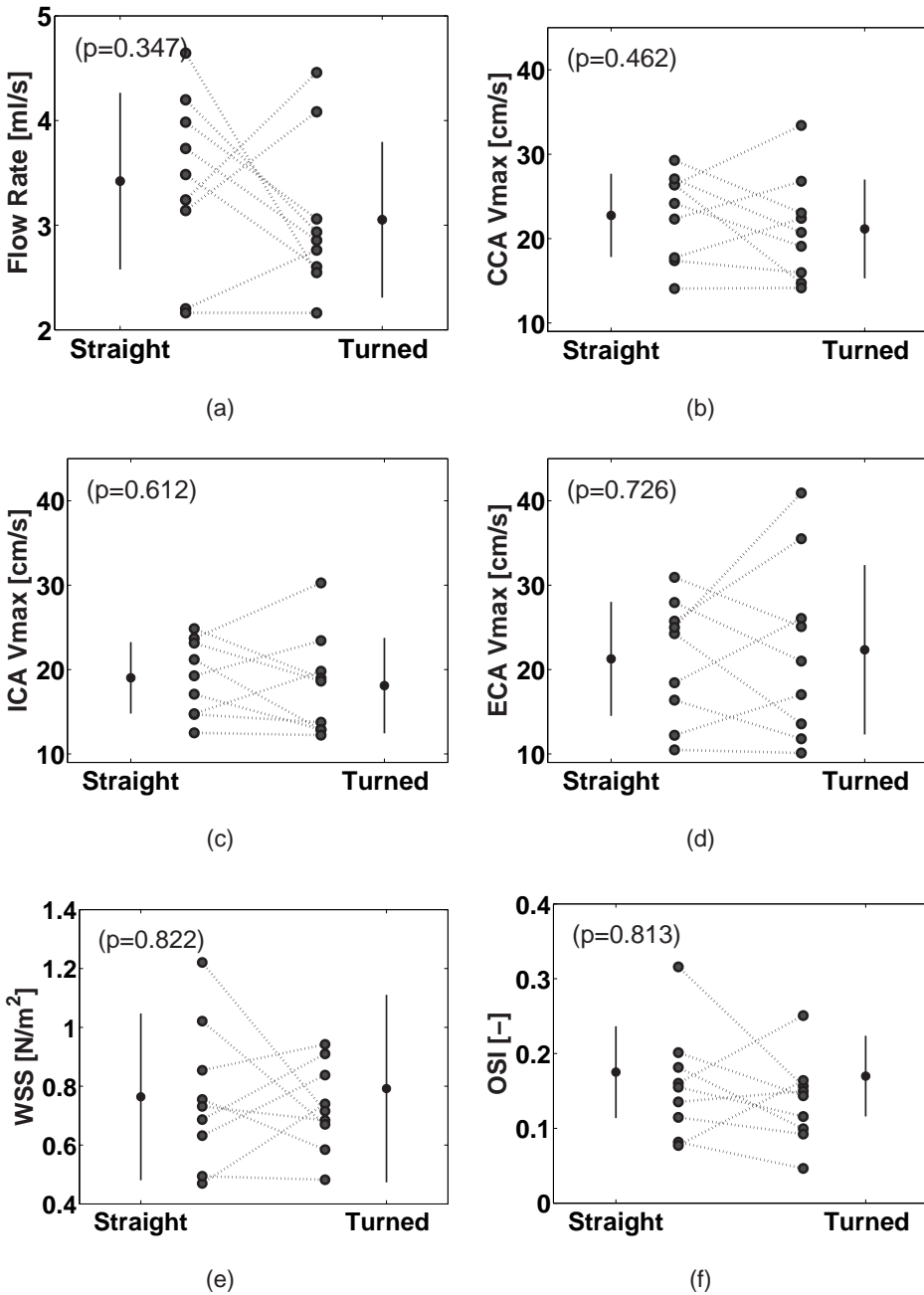
Figure XI.5.: a: Mean flow rate in the CCA calculated using pulsed-Doppler ultrasound. b-d: Velocity parameter V_{max} in CCA, ICA and ECA. e: Mean WSS. f: Mean OSI. The black dot on the vertical line gives the sample-averaged mean±standard deviation. Each of the dotted lines corresponds to a single subject. d: Non-Planarity (NP). The p-value tests the hypotheses that the sample-averaged means in the two head positions are different (paired Student test).

(a) S1   (b) T1   (c) S2   (d) T2

(e) S3   (f) T3   (g) S4   (h) T4

(i) S5   (j) T5   (k) S6   (l) T6

(m) S7   (n) T7   (o) S8   (p) T8

(q) S9   (r) T9
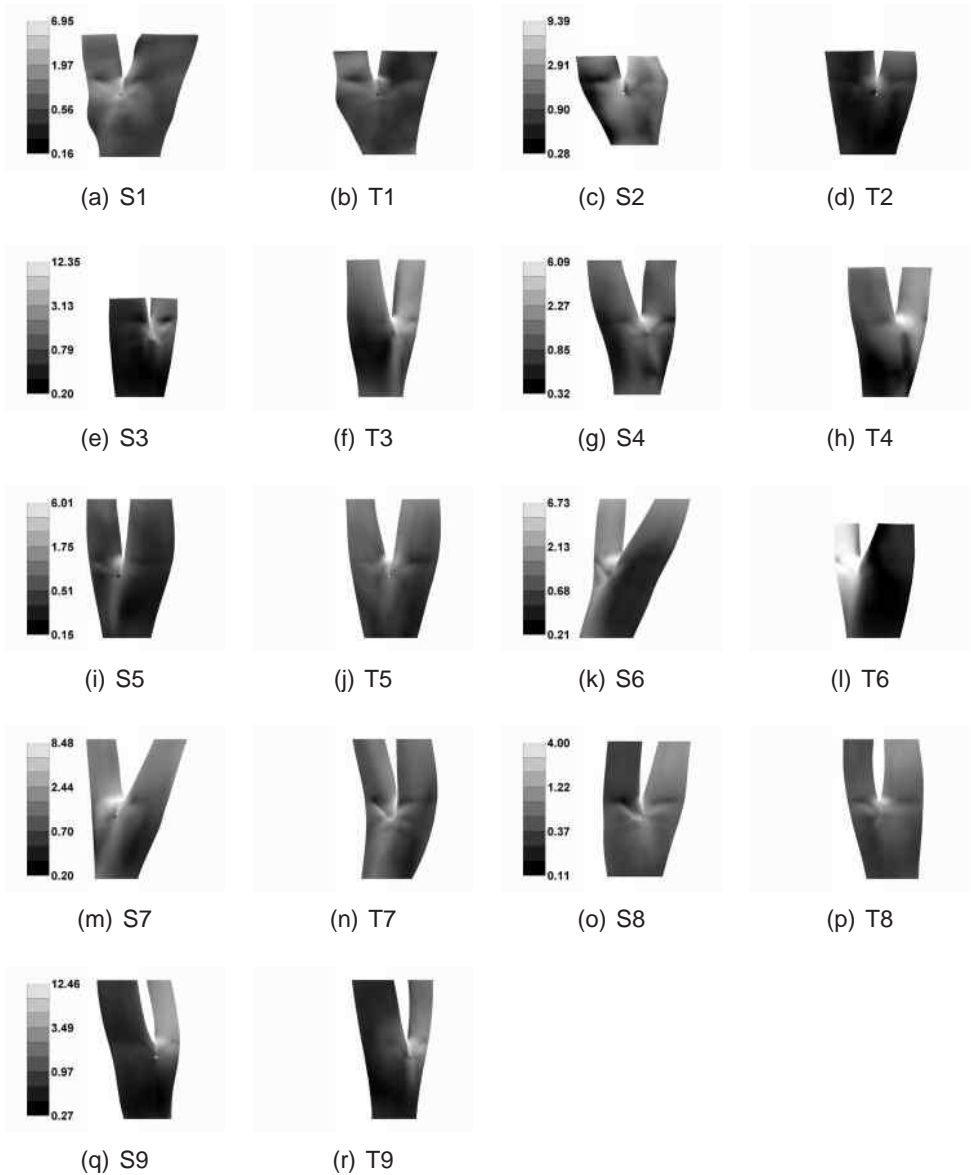
Figure XI.6.: Overview of Time-averaged WSS for all subjects and both head positions. Units are N/m^2 on a logarithmic scale. S: Straight; T: Turned; the number after the S or T stands for the subject number.

Figure XI.7.: Overview of the OSI for all subjects and both head positions. The OSI is dimensionless. S: Straight; T: Turned; the number after the S or T stands for the subject number.
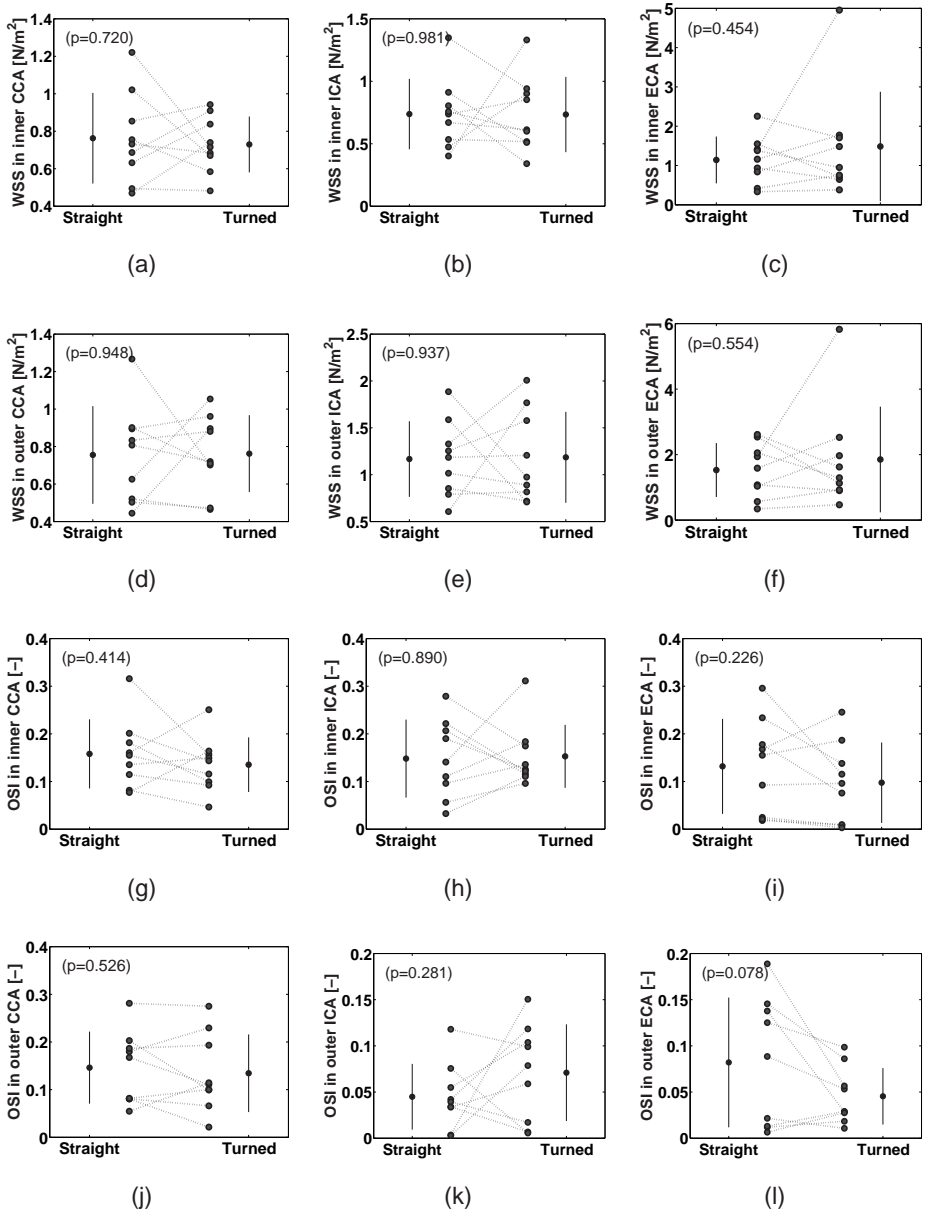
Figure XI.8.: Haemodynamic Parameters averaged over specific regions of the carotid vessel wall. The black dot on the vertical line gives the sample-averaged mean±standard deviation. Each of the dotted lines corresponds to a single subject. d: Non-Planarity (NP). The p-value tests the hypotheses that the sample-averaged means in the two head positions are different (paired Student test).

Parameter	Hypothesis	tailed	p-value
Change in CCA V_{max}	<10%	one	0.016
Change in ICA V_{max}	<10%	one	0.0053
Change in ECA V_{max}	<10%	one	0.0010
Difference in CCA V_{max}	=0%	two	0.30
Difference in ICA V_{max}	=0%	two	0.42
Difference in ECA V_{max}	=0%	two	0.98
Change in CCA V_{max}	<10%	one	0.95
Change in ICA V_{max}	<10%	one	0.93
Change in ECA V_{max}	<10%	one	0.94

Table XI.5.: p-values from Student test for flow and velocity parameters (n=9). 'Difference' stands for the value in the Turned position subtracted from the value in the Straight position. The difference in percentage is the fraction of the difference in V_{max} and the mean V_{max}. 'Change' stands for the absolute value of the difference. The last three lines return the results in case the same boundary conditions (a.i. the same flow rate) were imposed in the two head positions instead of using the flow rate calculated in each head position.

XI.4. Discussion

XI.4.1. Geometrical and Haemodynamic differences

XI.4.1.1. Geometry

In Figure XI.3 (a-c), it can be seen that the sample-averaged mean of the arterial cross-sectional area did not change significantly (p>0.05). Individual area changes were considered insignificant given that the 3DUS reproducibility in measuring cross-sectional area was around 10% for the CCA and ICA, and 15% for the ECA. In a separate validation study,[120] it was similarly shown that the shape factor was reproducible to within 10% for the CCA and ICA, and 15% for the ECA. Table XI.1 shows that all values for the shape factor are lower than these thresholds, therefore changes in cross-sectional shapes are considered as insignificant.

Although cross-sectional areas and shapes were little affected by head rotation, the vessel centrelines showed marked differences. Figure XI.4 gives a general impression of how much the centrelines changed with head rotation, noting the large changes for subjects 1, 2, 6 and 7. Interestingly, this observation was consistent with the values of z_{DIST} in Table XI.2. Conversely, the non-planarity parameter NP seemed to be less of an indicative parameter, supporting the statement that z_{DIST} is a better measure of centreline agreement than a non-planarity parameter. Figure XI.3(d) shows that individual changes in non-planarity can be significant (i.e. > 1%), but the sample-

averaged mean is not affected (p=0.565, see both Figure XI.3(d) and Table XI.3). Table XI.3 also provides the non-planarity and linearity in each of the three branches (CCA, ICA and ECA) separately with the paired Student test. It was seen that the CCA became more planar (overall Straight CCA non-planarity > overall Turned CCA non-planarity, p=0.0053, one-tailed paired Student test) with head rotation, but this was the only general observation (p<0.05).

XI.4.1.2. Haemodynamics

From Figure XI.5 (a), it can be seen that the individual time-averaged flow rate in the right CCA changed considerably when the head was turned to the left. Examining the data at an individual level, subjects 3, 4 and 5 showed sharp increase in mean flow rate from the straight head to head turned position (+26.7 $\pm$ 4.5%), whereas subjects 1, 2, 6, 7 and 9 showed a considerable reduction in flow rate (-35.1 $\pm$ 13.5%). However, the sample-averaged common carotid flow rate showed a relatively small change (-10.6 $\pm$ 31.8%).

In Table XI.4, it can be seen that change in V_{max} with turning of the head should not be ignored: the RMSE exceeded the 10% uncertainty found in a previous study.[118] Figure XI.5 (b-d) and the first three lines of Table XI.5 confirmed this statement: the average change in V_{max} was found to be greater than 10% with a significance p<0.05 (one-tailed paired Student-test). Again, there was certainty of change in the velocity profile, but it was impossible to predict whether the velocity parameter would increase or decrease: in Table XI.5 (rows 4-6), the sample-averaged means proved to be equal (mean difference in V_{max}=0%, p>0.05). The question of what causes the V_{max} to change is raised. With little differences in areas and shapes of carotid artery cross-sections, the change has to be caused by the altered centreline or flow rate. The simulations were repeated with identical flow rates as boundary conditions for both head positions in order to address this point more thoroughly. From Table XI.4, it can be seen that here, the V_{max} RMSE here did not exceed the 10% uncertainty. This was confirmed in Table XI.5, where the change in V_{max} proved smaller than 10% (p>0.9 for all arteries, one-tailed paired Student-test), which suggested that the difference in flow rate contributed more to the changes in velocities than the centreline changes. A Gauss-Newton non-linear data-fit also revealed more important dependence of the velocity on the flow rate rather than the centreline.

It is clear from Figures XI.5 (e-f), XI.6, XI.7 and XI.8 that WSS and OSI

patterns can change significantly with head rotation. In some cases, these changes were only quantitative: subject 6 had a high OSI zone in the Straight position (Figure XI.7 (k)), and when the head was turned, this high OSI zone was still present at almost the same location (Figure XI.7 (l)). In other subjects, patches of high OSI either changed positions (subject 2, Figure XI.7 (c-d)) or magnitude (subject 3, Figure XI.7 (e-f)). The largest WSS differences were found in the daughter vessels (high variance in Figure XI.8 (b-c and e-f)), whereas the inner walls of the ICA and ECA were the most affected by changes in OSI (Figure XI.8 (h-i)). The first question arising from this finding, was whether or not the change in haemodynamic parameter distributions could be correlated to head rotations. Subjects 2, 6, 7 and 9 all experienced a reduction in OSI in the vicinity of the apex (Figure XI.5 (f)), suggesting that turning the head to the left might produce a more advantageous haemodynamic environment in the right carotid arteries. The opposite was true for subjects 1, 3, 4, 5 and 8, whose right carotid OSI increased (Figure XI.5 (f)). Similar findings were made for the WSS (Figure XI.5 (e)). Therefore, there was no straightforward relationship between head position and the haemodynamic effect.

XI.4.1.3. Correlations between geometric and haemodynamic changes

The second question arising from the differences in haemodynamic wall parameter distributions, was whether or not these differences could be correlated to changes of flow rate, centreline or any other geometric property. Unsurprisingly, the change in the velocity parameter was directly related to the change in flow rate (linear correlation R of 0.97, 0.95 and 0.75 for the correlation between change in flow rate and change in velocity-parameter in CCA, ICA and ECA, respectively). This correlation can also be seen in Figure XI.5 (a-d) where a rise in flow rate (Figure XI.5 (a)) is accomplished by an increase in V_{max} (Figure XI.5 (b-d)). The WSS correlated with the flow rate in the CCA (R=0.77 and 0.87 for the CCA on the ICA and ECA sides respectively) and inner part of the ICA (R=0.81). Furthermore, the flow rate was correlated to the OSI (Figure XI.9 (a-b)): with an increase in flow rate, the OSI decreased. This was not surprising since high OSI occurs in regions of slow and recirculating flow, thus, slightly elevated flow rate is likely to discourage flow recirculation. This effect was highly noticeable in the part of the CCA from where the ECA emerges (R=0.81, Figure XI.9 (a)) and in the outer wall of the carotid bulb (R=0.78, Figure XI.9 (b)). The mean
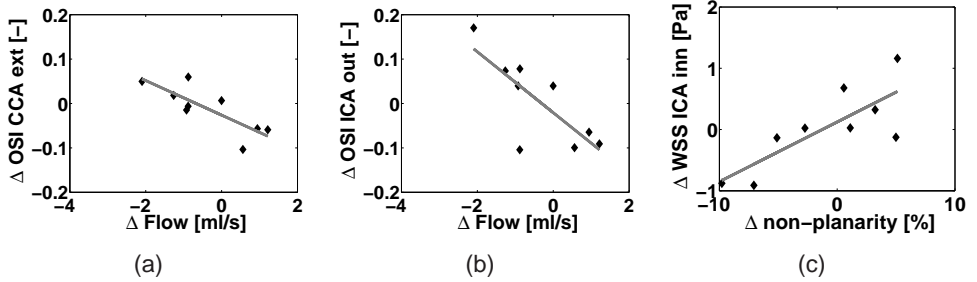
Figure XI.9.: a: Correlation between flow rate difference and difference in mean OSI in CCA part from which ECA emerges. b: Correlation between flow rate difference and difference in mean OSI in outer part of ICA. c: Correlation between overall non-planarity and difference in mean WSS in inner part ICA. 'Δ' stands for the true difference between the Straight and Turned position.

flow rate did not correlate with any of the described geometric parameters: cross-sectional areas and shapes, z_{DIST}, NP and L.

The velocity-parameter, the WSS and OSI correlated to certain geometric parameters. Apart from the dependence on the flow rate, V_{max} in the ECA correlated to the CCA non-planarity (R=0.81): with planarification of the CCA, the V_{max} was lowered in the ECA. This means that the flow profile in the ECA was less peaked when the CCA became more planar. The change in overall non-planarity influenced the WSS on the inner wall of the ICA (R=0.79, Figure XI.9 (c)), i.e. the high shear rate region at the apex and inner wall of the bulb was reduced with overall planarification. Furthermore, z_{DIST}, the parameter linked to centreline changes, correlated to V_{max} in the ICA (R=0.77), with the WSS on the inner wall of the ICA (R=0.83) and more importantly with the WSS on the outer wall of the ICA (R=0.78), which is the region prone to plaque formation.[324] When the centreline difference was large, values of WSS on the outer wall of the bulb were lowered. This meant that when the head was turned from a straight position to the left, a larger region of the bulb was exposed to a WSS lower than 0.4 N/m^2, the suggested threshold for atherogenic cellular behaviour.[208]

XI.4.1.4. Reports of atherogenic carotid geometries

The number of studies examining the atherogenic geometric features of a carotid geometry is not overwhelming. Caro[46] made the first suggestion saying that non-planarity was an important factor influencing arterial flows. Figure XI.9 (c), which shows the correlation between non-planarity and high shear regions, provide further evidence for this statement. Thomas[334] inves-

tigated the effect of planarity and curvature on carotid haemodynamics and concluded that *overall vessel curvature* rather than *(non-)planarity* had a more important effect as a potential geometric risk for atherogenesis. Here, the constatation that the overall centreline difference (z_{DIST}) correlated better to haemodynamic changes than the overall non-planarity, agreed with Thomas's results.

XI.4.2. Summary and Implications

The first outcome of this study was the quantification of the changes in geometry in the carotid bifurcation. In a second step, the effect of these changes in geometry on the flow have been investigated. Finally, correlations between changes in geometry and haemodynamic effect have been suggested.

Cross-sectional areas and shapes were only slightly influenced by head rotation, but the positions of the vessels changed. The only general observation, was a planarification of the CCA. Other geometrical changes in nonplanarity, linearity or overall centreline agreement were subject-dependent. Similar findings were made for the mean CCA flow rate: the sample-averaged mean CCA flow rate changed only slightly from one head position to another, but significant changes in individual flow rates were observed.

The changes in geometry and flow rate were mirrored in haemodynamic changes: flow profiles, WSS and OSI distributions were affected in various ways. The change in OSI distribution appeared to be linked to the change in flow rate, especially on the outer wall of the bulb (Figure XI.9 (a-b)).

Our data suggested the following relations between geometrical and haemodynamic changes:

- When the bifurcation became more planar with head rotation, the WSS at the apex decreased. Conversely, when the bifurcation curled up with head rotation, the WSS at the apex increased.

- The WSS on the outer wall of the bulb decreased when centreline difference between head positions was large. The change in WSS was correlated with the change in centreline.

Considering that the centreline difference is relatively large in most of the subjects, and that WSS reduction on the outer wall of the bulb is usually an

adverse haemodynamic phenomenon, one could conclude that the straight head position is haemodynamically preferable to the left-turned head position for the right carotid arteries. However, the large variety of possible haemodynamic conditions following head rotation undermines such a generic statement.

The fact that haemodynamic situations can be very different in the studied head positions, sheds a new light on 3DUS scan protocol. Until recently, the ultrasound operator positions the patient in order to find a head position yielding a good US signal and good coverage of the bifurcation. The chosen head position is very subject- and operator-dependent, thus the recorded anatomical and flow data may differ substantially from the physiologically normal case. As elucidated in section IX.5 on 267, two suggestions can be made: (1) scan patients in an Straight position *by convention*, and (2) scan patients in different positions and take a weighted mean. The first suggestion assumes the Straight head position to be overwhelmingly more common than any other positions, the second recommendation accounts for possibilities that patients may adopt other positions that are comfortable to them, such as sleeping in the prone position.

The fact that the present study did not show noticeable changes in cross-sectional area, means that either there were indeed no changes, or the technique was not sensitive enough to measure the changes in cross-sectional area. Nevertheless, the study was sensitive enough to quantify changes in WSS and OSI in the specified zones (see section VII.4.3 for a detailed description of the sensitivity of all geometrical and haemodynamic parameters). This has as an important implication that 3DUS-based CFD offers sufficient sensitivity for vascular studies such as this one.

The altered haemodynamic conditions in different head positions has an effect on studies concerning the potential pitfalls of carotid implants such as carotid stents[130] or carotid emboli diverters:[321] the carotid stent could work as planned in a certain head position, but could, for a particular patient, be subjected to low WSS values in a different head position, yielding a situation prone to restenosis. Similar lessons can be learned for studies on the vulnerability of carotid plaque. Apart from the composition of the carotid plaque,[212] the haemodynamic forces acting on the plaque are the main parameters when predicting plaque rupture.[94] Plaque can be harmless in one head position, but could be undergoing severe shear forces in another head position. Therefore, plaque can rupture in altered head positions and this could be the cause of 'Telephone Strokes'.

XI.4.3. Conclusion

With the important incidence of atherosclerosis on one hand, and the correlation between regional haemodynamics and the atherosclerotic process on the other hand, carotid flow behaviour becomes a topical subject. Here, the right carotid arteries of nine subjects were investigated in supine position with straight and left turned head positions respectively.

The 3D geometry was reconstructed using 3DUS and the carotid haemodynamics were calculated by combining 3DUS with CFD. The centreline was the only geometrical feature that showed noticeable change, whereas cross-sectional shape and area were altered little by head rotation. The planarification of the CCA with head rotation was the only general feature. The overall centreline difference proved to have a more powerful effect on the flow than non-planarity on its own. It was shown that haemodynamic differences between two head positions were important: flow rate, WSS and OSI distribution changed significantly. Therefore, unnatural, long lasting head positions cannot be left out in the search for possible causes for telephone strokes. Correlations between geometrical changes and changes in flow properties were suggested. Based on this likely relationship between geometry and flow, defining atherogenic carotid geometries may become feasible. Furthermore, this study showed that there is a need for standardisation considering the choice of head position in the 3DUS scan protocol. Finally, it was shown that carotid plaque and carotid stents need to be studied in several head positions before they can be considered safe.

XII. Acute Effect of Anti-Hypertensive Drugs

Many pharmacological compounds aim to influence the patient's haemodynamics and/or the morphology, structure or function of the vessel wall. When such compounds are in the research stage, their haemodynamic effect needs, among other things, to be investigated and well understood. For the pharmacological industry, a technique that visualises and quantifies the blood flow in the carotid arteries may yield valuable information on top of standard haemodynamic parameters.

In this particular study, the haemodynamic effect of two antihypertensive drugs was studied in a double-blind, placebo-controlled crossover comparison. A group of hypertensive patients was treated with amlodipine, lisinopril and a placebo in a random sequence. The follow-up of each patient was 1 week for each drug, which is why the study is referred to as an **'(sub-)acute'** study. Among other parameters, the distribution of haemodynamic wall parameters such as the WSS and the OSI as a result of the intake of a compound was quantified using a combination of TOF MRI or 3DUS and CFD, which is why the study is sometimes referred to as a **'CFD'** study.

In the first section (section XII.1), the treated pathology of hypertension will be explained. The currently commonly used antihypertensive drugs are discussed briefly, with a clear focus on Angiotensin Converting Enzyme (ACE) inhibitors (such as lisinopril) and calcium channel blockers (such as amlodipine). It is important to understand the function of ACE inhibitors and calcium channel blockers in order to acquire the broadest possible view over all factors influencing the vessel wall. The following section (section XII.2) focusses on the motivation of this study. In the third section (section XII.3), the used study protocol will be explained. In that same section, the imaging parameters and computational details used in this particular study are described. Sections 4 (section XII.4) and 5 (section XII.5) present the results and the discussion, respectively. The study is summarised in the final section (section XII.6).

XII.1. Hypertension

XII.1.1. Pathology

Blood pressure (BP) rises with age, but the term **hypertension** is only used when pressure remains above 140/90 mmHg (systolic/diastolic blood pressure). Mean arterial blood pressure (MAP) increases either due to an increased blood flow rate or an increased flow resistance.

$$\Delta P = Q \times R \qquad\qquad (XII.1)$$

Here, ΔP is the pressure drop from aorta to vena cava, Q is the blood flow rate and R is the resistance of the entire vascular tree. When the total arterial compliance changes, the pulse pressure[a] will increase, but the mean arterial pressure is not affected. In these cases, the high systolic blood pressure will be referred to as *isolated systolic hypertension*. Currently, the increased vascular resistance, i.e. vascular constriction, is the cause of hypertension in most cases. The cause of the arteriolar constriction is known only in a few cases. In the case of *renal hypertension*, the blood flow to the kidneys is limited (due to a stenosis in the renal artery) or the kidneys are dysfunctional. In both cases, renin will be released by the kidneys, causing a systemic vasoconstriction aimed at establishing a correct flow rate towards the kidneys. Renal hypertension is only one of the causes of hypertension; in more than 95% of the cases, the cause of hypertension is unknown and this is then called **primary** or **essential** hypertension.

Several hypotheses for the cause of vasoconstriction have been investigated. It is believed that an excessive *salt retention* in salt-sensitive subjects is one of the main causes.[254,310] Although the relationship remains controversial, a decrease in blood pressure is seen after salt-poor diets.[218] A *diet enriched in calcium* (Ca) seems to attribute to a pressure drop in patients with essential hypertension, because Calcium suppresses vitamin D, a substance that increases the uptake of calcium in the vascular smooth muscle cells[b] and thus a substance that constricts vessels.[381] *Obesity* is also a risk factor for hypertension: sports and weight loss are frequently effective at lowering the blood pressure. Besides salt retention, low calcium diets and obesity, cigarette *smoking* is also a risk factor.

---

[a]Pulse Pressure PP=systolic blood pressure SBP - diastolic blood pressure DBP

[b]Muscle tissue includes 3 types of tissue: *skeletal muscles*, also called voluntary muscle, *smooth muscles*, such as the muscles that surround the stomach, and *cardiac muscles*.

Hypertension may induce an important number of subsequent pathologies. The left ventricle of a hypertensive person has to pump the blood against a higher pressure. The heart muscle will increase in mass (**left ventricular hypertrophy**) in order to be able to generate enough power to obtain the pressure required. In the early stage of the disease, this helps the heart to maintain its role as a blood pump. In a later stage, the heart muscle cells (myocard cells) may show a reduced contractility[c] which can lead to heart failure. As stated in section II.2.1, hypertension can be the cause or the accelerating factor of **atherosclerosis**. Furthermore, hypertension has a detrimental effect on **kidney** function and increases the chance for a **cerebrovascular accident** (haemorrhagic[d] or thrombotic[e] stroke) and **brain damage**.[340]

XII.1.2. Anti-Hypertensive drugs

Anti-Hypertensive drugs are classified in 5 groups. All the drugs lower the flow rate, the total vascular resistance, or both (see equation XII.1).

1. **Diuretics** increase the secretion of salt and water through the urine. Diuretics reduce the blood volume contained in the cardiovascular system.

2. **Beta-blockers** block the receptors which, when activated, increase heart rate, contractility and cardiac conductivity[f] (beta receptors).[340] The antihypertensive effect is due to a decrease in heart rate.

3. **Calcium channel blockers** or **calcium antagonists** limit the calcium flow to the vascular smooth muscle cells, with vasodilatation as a consequence. This reduces the vascular resistance. The detailed cardiac and other effects of calcium antagonists is explained in section XII.1.2.1.

4. **ACE inhibitors** inhibit the angiotensin converting enzyme (ACE). The decrease in ACE will consequently decrease the production of angiotensin II, which is a vasoconstrictor. As a consequence, ACE inhibitors lower blood pressure by a decrease in vascular resistance. The detailed cardiac and other effects of ACE inhibitors is explained

---

[c]**Contractility**: intrinsic ability of the cardiac muscle to contract and generate force.
[d]Haemorrhagic stroke involves bleeding within the brain, damaging adjacent brain tissue.
[e]Thrombotic stroke is an obstruction of a cerebral vessel by aggregated blood.
[f]**Conductivity**: the ability of a nerve or muscle cell to transmit a wave of excitation.

in section XII.1.2.2. Similarly, **Angiotensin II receptor blockers** lower blood pressure by blocking the receptors to which angiotensin II needs to bind to cause vasoconstriction. Note that ACE inhibitors, as opposed to angiotensin II receptor blockers, lower blood pressure through several other pathways, including the elevation of bradykinin plasmaconcentration, a powerful vasodilator. Another important difference between ACE inhibitors and angiotensin II receptor blockers lies in the fact that angiotensin II can be formed via other events not requiring the presence of ACE. Thus angiotensin II is formed despite the presence of the ACE-inhibitor. Therefore, the angiotensin II receptor blockers can be more effective at eliminating the effects of angiotensin II.

5. Drugs that interfere with one or more components of the **sympathetic nervous system**. The most important effect of these drugs is the reduction of sympathetic mediated stimulation of the vascular smooth muscle cells. This has a reduction of the total vascular resistance as a consequence. These substances include centrally acting drugs that activate certain sympathetic centra in the brain and peripherally acting drugs such as alfa-receptor-blockers (alpha-receptors cause vascular constriction when excited with (nor)adrenaline).

Amlodipine is a calcium channel blocker produced by Pfizer (Sandwich, UK). It can be used in combination with other antihypertensive drugs. **Lisinopril** is an ACE inhibitor, a product of AstraZeneca (London, UK). The function of Ca-channel blockers and ACE inhibitors is explained in the following sections.

XII.1.2.1. Calcium Antagonists

Calcium for the muscles   Calcium antagonists are a heterogenous group of drugs which have one thing in common: they all limit the transmembrane flux of calcium into the smooth muscle cells. Their impact can be lifted by increasing the concentration of extra-cellular calcium. They also have several effects on the heart: they weaken the excitation-contraction coupling among other things. The **excitation-contraction coupling** is a number of sequential events, involving an action potential reaching a muscle cell leading to its contraction. Both in cardiac, smooth as in skeletal muscles, the contraction is initiated by an increase in *intra*-cellular calcium. The process starts when the action potential reaches the muscle cell (see (1) in Figure XII.1). This activation can be due to a membrane depolarisation caused by an exciting
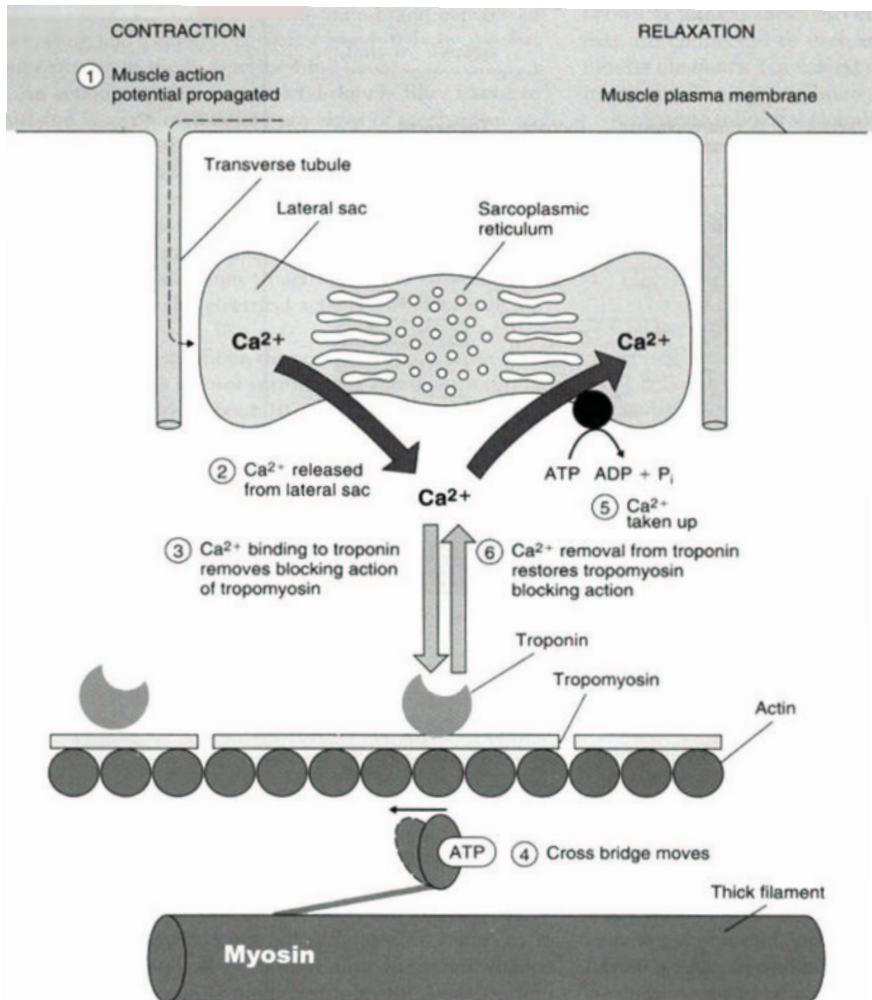
Figure XII.1.: Calcium for Muscle Contraction.[340]

neurotransmitter. This opens calcium channels in the muscle membrane. Consequently, Ca^{2+} ions flow into the cell through these channels. The penetrated calcium causes an additional release of calcium from intra-cellular storages, especially from the sarcoplasmatic reticulum ('lateral sac' in Figure XII.1). As a consequence of all this inflow of calcium, the intra-cellular calcium concentration will have increased ((2) in Figure XII.1). The free Ca^{2+} radicals will bind to a regulating peptide ((3) in Figure XII.1): **troponin C** in skeletal or cardiac muscles, and **calmodulin** in vascular muscles. This binding starts a chain of reactions, leading to a mechanical interaction between **actin** and **myosin fibres**, causing the contraction of the muscle ((4) in Figure XII.1). The role of calcium in this chain of events is crucial, and it is

clear that a lack of intra-cellular calcium will weaken the muscle contraction, both in the heart as in the vascular smooth muscle cells. Note that there are 2 sources of intra-cellular Ca: (1) extra-cellular calcium coming through the cell membrane, and (2) calcium released from the sarcoplasmatic reticulum.

Cardiac and smooth muscle cells contain less intra-cellular stored calcium than skeletal muscle cells. As a consequence, an important fraction of the calcium required for contraction needs to enter the cell through the cell membrane.

Cardiac Calcium   Apart from being required for the contraction of cardiac muscle cells, calcium is required in the process which causes automatic depolarisation of cardiac pacemaker cells, and in the conductivity of the heart. A shortage of extra-cellular free Ca^{2+}-ions will impede the pacemaker activity, and initially slow down the heart rate. Note that a systemic reflex can annihilate the drop in heart rate[129] Furthermore, contractility will decrease.

Muscle Selectivity   In order to assess the consequences of the intake of calcium blockers, it is important to find out how dependent each muscle cell is on extra-cellular calcium. The *vascular smooth muscle cells* of small arteries depend more on extra-cellular calcium than large arteries. This means that the tonus of precapillary arterioles (the smallest muscular arteries) is highly dependent on calcium influx, whereas the large vessels, such as the carotid arteries, are less sensitive to the extra-cellular calcium concentration. In general, vascular smooth muscle cells are more dependent on calcium influx than smooth muscle cells in the *gastric-intestinal* and the *respiratory tractus*. The role played by calcium influx in *skeletal* muscle cells is minimal, thus calcium antagonists do not influence the function of skeletal muscle cells substantially.

Since different cells are dependent on the calcium influx to different levels, the impact on different cells is different. Moreover, certain calcium antagonists are known to have a more important impact on cardiac cells than on vascular cells. Note that calcium influx plays an important role in the secretion of exocrine and endocrine glands, and in the release of neurotransmitters, but calcium antagonists do not seem to interfere there.

In summary, calcium blockers lead to a decrease in heart contractility, heart rate and conductivity. In the arteries, gastric-intestinal and respiratory sys-

tem, there is an overall relaxing effect. The level of relaxation is different for every cell and depends on the used drug.

Based on their effects on myocard contraction, on the heart rate and conductivity, and on vascular smooth muscle cells, calcium antagonists have a broad range of applications in cardiovascular pharmacology.

Classification of Calcium Antagonists   There are different ways to classify calcium antagonists. A chemical classification is given in Table XII.1.[360]

Group	Extension	Drug
fenylalkylamines	-pamil	verapamil, gallopamil, tiapamil
dihydropyridines	-dipine	nifedipine, nicardipine, nitrendipine, nisoldipine, felodipine, isradipine, **amlodipine**, lercanidipine, nisoldipine nimodipine, lacidipine
benzothiazepines	-zem	dilitiazem
difenylpiperazine derivatives	-zine	cinnarizine, lidoflazine, flunarizine
tetralol derivatives	-adil	mibefradil

Table XII.1.: Chemical classification of calcium antagonists.[360]

Calcium antagonists can also be classified pharmacologically: Fenylalkylamines, dihydropyridines and benzothiazepines have an influence on the calcium uptake by both smooth muscle cells and cardiac cells. These are used against hypertension, chest pain and arrythmia. Dihydropyridines can be recognised by their '-DIPINE' extension. They act mainly on the arterial vasculature, whereas the fenylalkylamines and benzothiazepines have an influence on the heart muscle as well. Difenylpiperazine derivatives are regarded as a separate pharmacological class. They are used to combat migraine and dizziness. Mibefradil has mainly antihypertensive and anti-ischaemic effects.

XII.1.2.2. ACE inhibitors and angiotensin II-receptor antagonists

The Renin Angiotensin Aldosterone System   The **Renin-Angiotensin-Aldosterone-System** (RAAS, Figure XII.2 by Wesseling[360]) is a complex regulatory system which is both enzymatic and hormonal. It plays an important role in the regulation of the electrolyte balance, fluid volume and blood pressure. Note that there is a difference between the Renin-Angiotensin-Aldosterone-System (RAAS) in blood plasma and the Renin-Angiotensin-
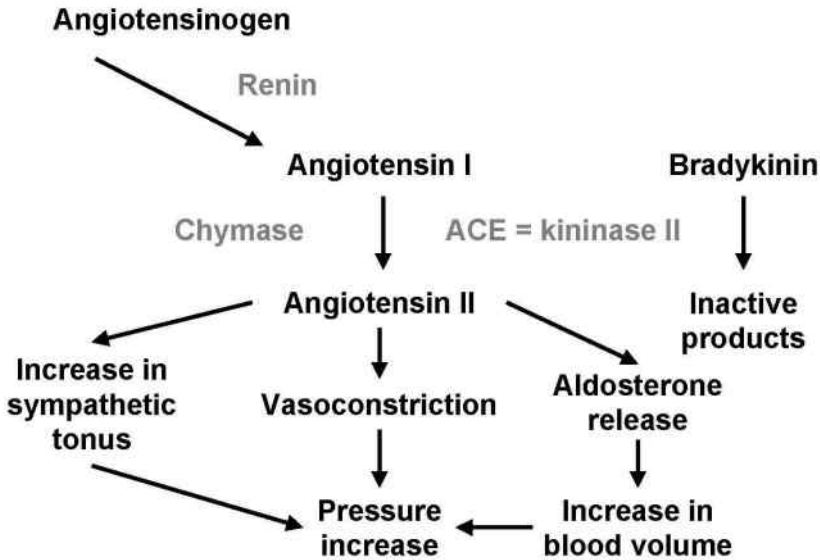
Figure XII.2.: Renin-Angiotensin-Aldosterone-System (RAAS).[360]

System (RAS) in certain tissues such as vessel, lung, myocard, brain, kidney and testes tissue. Stimulation of the RAAS and the subsequent salt and water retention forms, together with an increased sympathetic tonus, one of the most important aspects of the pathophysiology of patients with heart failure.

Renin is an enzyme that is secreted in the kidney by the juxtaglomerular apparatus[g], but several other organs produce renin as well, including the brain, the arterial wall, the adrenal gland, the salivary glands and the genitals. Renin separates a decapeptide from **angiotensinogen**, a product of the liver circulating in the blood plasma. This decapeptide is **angiotensin I** or A-I. It is as such biologically inactive, but it is converted into a biologically active octapeptide, **angiotensin II** or A-II. The conversion is done by the **angiotensin converting enzyme** (ACE), a carboxypeptidase. ACE is a membrane enzyme which can be found on vascular endothelial surfaces, especially in the lung circulation. A-I can also be converted to A-II by other enzymes, **chymase** among others. A-II is further converted to **angiotensin III** (A-III) by **angiotensinase A**. Finally, A-II and A-III are converted into inactive fragments by **angiotensinases**.

---

[g]juxtaglomerular apparatus is a group of specialised smooth muscle cells, located in the tunica media of the afferent glomerular arterioles. They contain granules for renin secretion.

Angiotensin II   Angiotensin II has the following effects (numbers between brackets referring to Figure XII.3 by Klabunde[158]): vasoconstriction (1), stimulation of aldosterone secretion (2), sodium- and water retention (3), cardiac and vascular hypertrophy (5) and activation of the sympathetic nervous system (6). All the effects together are aimed at raising the blood pressure.

Vasoconstriction (1): angiotensin II is very effective at increasing blood pressure. There is a direct interaction between A-II and vascular smooth muscles. This causes a vasoconstriction, which consequently causes blood pressure to rise. The mechanism is initiated when the kidneys are hypoperfused: the rise in blood pressure will increase the blood flow to the kidneys, recovering the required perfusion. This recovery is established at the cost of an increased work load for the heart.

Aldosterone secretion (2): A-II stimulates the secretion of aldosterone by the cells in the **zona glomerulosa** in the adrenal gland. This effect is noticeable at very low A-II concentrations, and occurs before any blood pres-
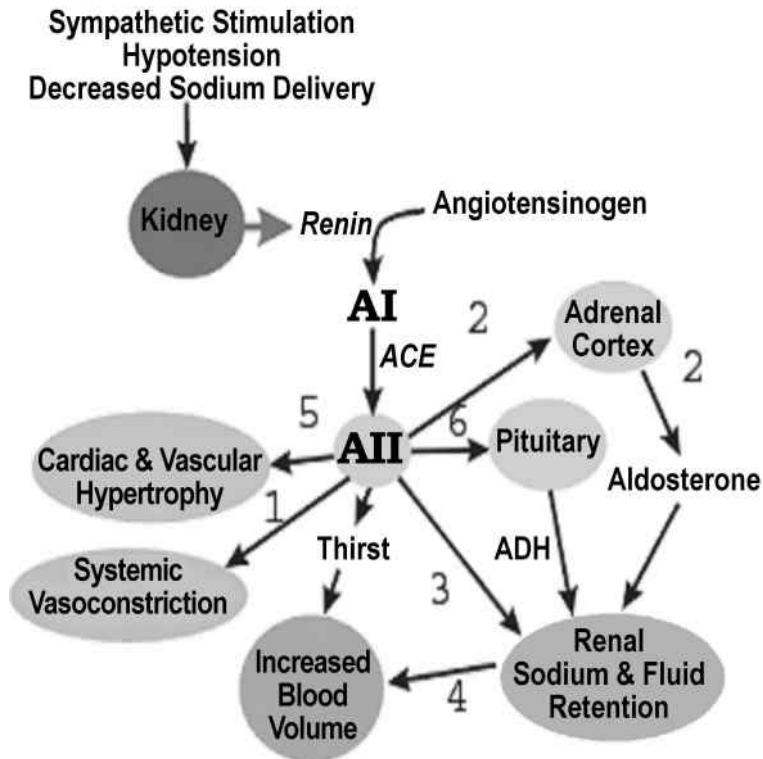
Figure XII.3.: The effect of Angiotensin II (AII). ADH: anti-diuretic hormone, takes care of the resorption of water in the kidneys; AI: angiotensin I; pituitary: hypophyses; adrenal cortex: adrenal gland outer wall.[158]

sure change has taken place. Aldosterone increases the sodium retention by the renal distal tubuli. As a consequence, there is an additional water reabsorption and thus an increase in blood volume. This helps to restore the perfusion of vital organs. However, an increased blood volume is more demanding on the heart.

Sodium- and water retention (3): A-II causes an additional sodium and water retention in the kidneys by contracting the afferent[h] arterioles. This reduces the perfusion of the kidneys. Moreover, A-II contracts the efferent renal arterioles, which causes a low peritubular renal capillary pressure. Low capillary pressure will keep the water in the blood, as opposed to forcing it through the vessel wall. The result is an additional increase of the blood volume and blood pressure.

The cardiovascular system (5): A-II stimulates the growth of myocytes (cardiac cells) and vascular smooth muscle cells. On the long-term, A-II causes vascular and ventricular hypertrophy. These long-term effects have an important impact on the pathogenesis in hypertensive cardiovascular patients.

Activation of the sympathetic nervous system (6): A-II releases catecholamine from the adrenal gland, stimulates autonomous ganglion cells, facilitates noradrenalin release from nervous cell extremities, blocks the uptake of noradrenaline and stimulates the activation of tyrosine hydroxylase. All these events excite the autonomous (sympathetic) nervous system, which causes vasoconstriction and heart rate increase. This means that A-II causes an additional vasoconstriction through the nervous system.

Furthermore, A-II causes the subject to be thirsty through a centrally mediated system. It also causes the secretion of ADH [i] from the pituitary. These events cause an additional, nervous system mediated, water retention.

Bradykinin   ACE is also called **kininase II**. In that context, it is known to be involved in the conversion of bradykinin, a powerful vasodilator, into an inactive heptapeptide (Figure XII.4).[169] Bradykinin has a relaxing effect on the vascular smooth muscle cells. Furthermore, it stimulates the excretion of sodium, urine and renal prostaglandins (vasodilators). Thus, A-II and bradykinin have outspoken opposite effects. The effect of ACE inhibitors

---

[h]**Afferent** renal arterioles bring blood from the heart to the kidney. **Efferent** renal arterioles are blood vessels between 2 different parts of the kidney.

[i]ADH: anti-diuretic hormone, a vasopressin, takes care of the resorption of water in the kidneys
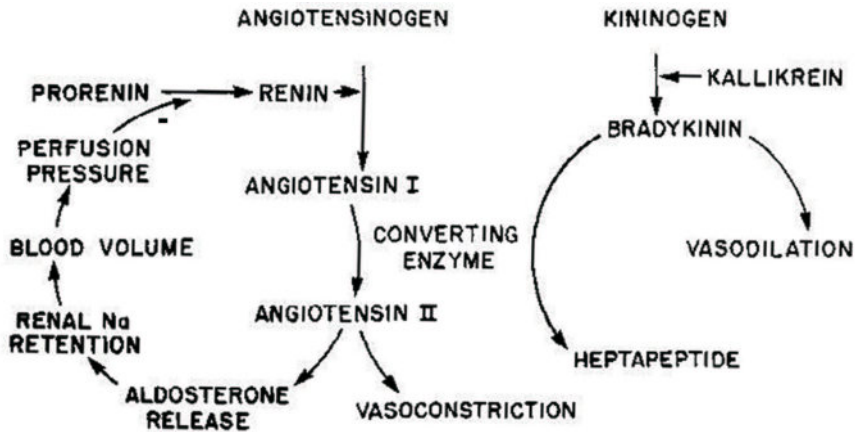
Figure XII.4.: Bradykinin and angiotensin II have opposite effects.[169]

can therefore also be explained by the fact that they limit the conversion of bradykinin.

Total effect of ACE inhibitors   ACE inhibitors inhibit the enzymatic conversion of A-I to A-II. As a consequence, the plasma concentration of A-I increases and that of A-II decreases. The effects of A-II, summarised in Figure XII.3, will be impeded. Less aldosterone will be released, thus less sodium and water will be retained. The decrease in A-II plasma concentration will relax the vascular smooth muscle cells. The total effect is a blood pressure drop. A-II is not only present in plasma, but also in tissue. In the long-term, the reduction of A-II in the tissues is the main reason for the sustained pressure drop.

ACE inhibitors also inhibit the conversion of bradykinin into inactive products. This causes an increased concentration of bradykinin in the tissues with vasodilatation and pressure drop as a consequence. In addition, the increased bradykinin concentration will stipulate the production of more NO and prostacyclin by endothelial cells. These products are vasodilators, causing an additional pressure drop. Moreover, NO and prostacyclin work against vascular smooth muscle cell proliferation and decrease platelet adhesion. This way, ACE inhibitors have a positive influence on the endothelial function. Note that although the higher concentration of bradykinin undoubtedly causes an additional pressure drop, it is believed that this contribution to the pressure drop is very small in comparison with the pressure drop due to the inhibition of A-II.

Summary   ACE inhibitors have the following effects. They decrease the concentration of angiotensin II, which causes directly a vasodilation and indirectly a loss of sodium and blood volume. The concentration of bradykinin and subsequently those of NO and prostacyclin rise, which all cause a vasodilation. The latter also results in a regression of vascular hypertrophy. The loss of blood volume and the vasodilation have a pressure drop as a consequence.

XII.2. Motivation

Stanton[302] has shown that 52 weeks of active treatment with either amlodipine or lisinopril yields (i) differences in the rates of regression of the intima-media complex and (ii) structural remodelling of the common carotid artery occur. Stanton's results are summarised in Figure XII.5 (a): the IMT showed important regression for the patients using the amlodipine regimen. Important IMT regression with calcium blockers such as amlodipine is a common feature in literature.[326] This drop in IMT was not accompanied by a significant change in lumen diameter (LD). The decrease in IMT was less spectacular in the lisinopril regimen, but the LD decreased significantly here. The intima-media area (IMA) decreased significantly for both compounds, without differences between compounds. These morphological differences occurred despite a similar blood pressure reduction. The striking difference in the morphological changes to the common carotid artery (Figure XII.5 (b)) raises the question as to whether the differences may relate to varying influences of the drugs on local carotid haemodynamics.

The aims of this study are therefore twofold. In the first place, the aim was to *compare* the acute effects of amlodipine and lisinopril on local carotid artery haemodynamics using CFD combined with MRI or ultrasound. The second aim was to *relate* the findings of the acute study *to the observations made in the 52 week study* with amlodipine and lisinopril. The present study investigates whether the changes in CCA morphology are a result of different haemodynamic situations.
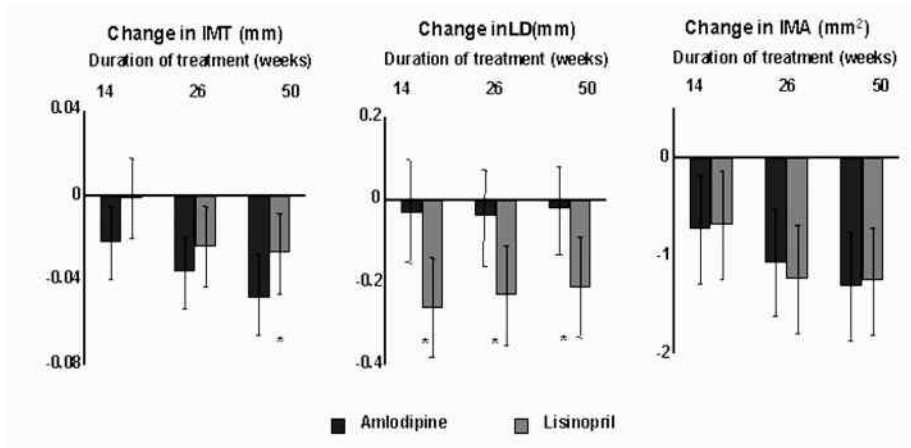
(a) IMT, LD and IMA
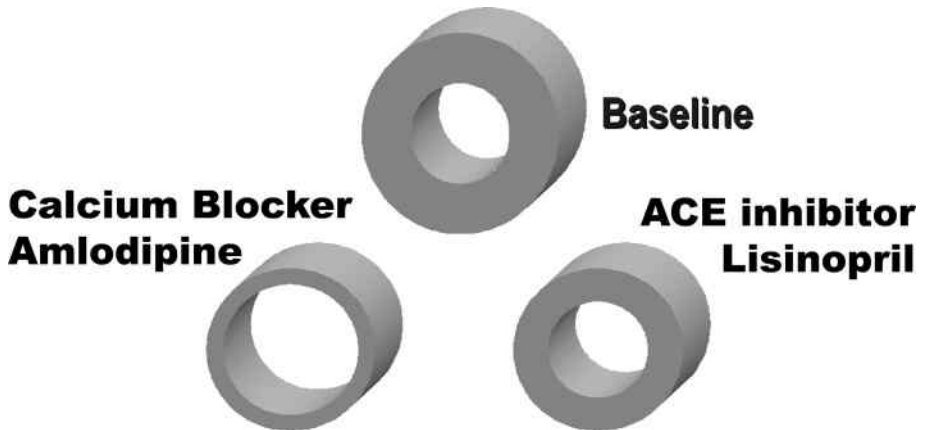
(b) Schematic Representation of Stanton's results

Figure XII.5.: Summary of the results found by Stanton[302] in a 52 weeks active treatment with either an amlodipine or a lisinopril based regimen. a: Changes in intima-media thickness (IMT), lumen diameter (LD) and IMA. '*' is significant at $p = 0.05$. b: Schematic Representation of Stanton's results. The cylinder section shown here represents a cross-section of the CCA. The cylinder wall thickness represents the IMT whereas the diameter visualises the CCA lumen diameter.

XII.3. Materials and Methods

XII.3.1. Patient & study design

Both male and female patients with untreated hypertension (office systolic BP 150[j]-220 and / or diastolic BP 90-120mmHg) were recruited into this double-blind, placebo controlled, randomised, 3 way crossover clinical trial. Individuals were excluded if they had evidence of accelerated or malignant hypertension; major organ dysfunction identified clinically or with blood sampling; a previous cardiovascular event; contraindications to the study drugs; diabetes mellitus; familial hypercholesterolaemia; glaucoma; cataracts; or plaque in their right common, internal or external carotid artery. All participants were recruited from a single clinical centre, the Peart-Rose Hypertension and Cardiovascular Disease Prevention Clinic at St Mary's Hospital, London, U.K. All subjects gave written informed consent, the local research committee approved the study protocol, and the research was carried out in accordance with the Declaration of Helsinki (1989) of the World Medical Association. Eligible patients were randomised to receive placebo, amlodipine (5mg oral dose (OD)) or lisinopril (10mg OD). The baseline characteristics of the study group are summarised in Table XII.2.

A full physical examination including 24 hour ambulatory blood pressure, ECG, baseline blood tests and screening carotid ultrasound were performed to ensure eligibility prior to randomisation. The office blood pressure recorded at the start of the study served as the comparison blood pressure for subsequent visits. Each subject was taught to record his or her own blood pressure using a validated semi-automated blood pressure cuff. After three doses of their randomised treatment, patients were required to record their

---

[j]Note that this recruiting parameter is more severe than the 'definition' of systolic hypertension on page 294

Male / Female	7 / 3
Age (years)	42 (35-52)
SBP (mmHg)	151 ± 12
DBP (mmHg)	96 ± 10
IMT (mm)	0.54 ± 0.09
LD (mm)	6.56 ± 0.58
IMA (mm^2)	12.1 ± 2.3

Table XII.2.: Baseline characteristics for the study group.
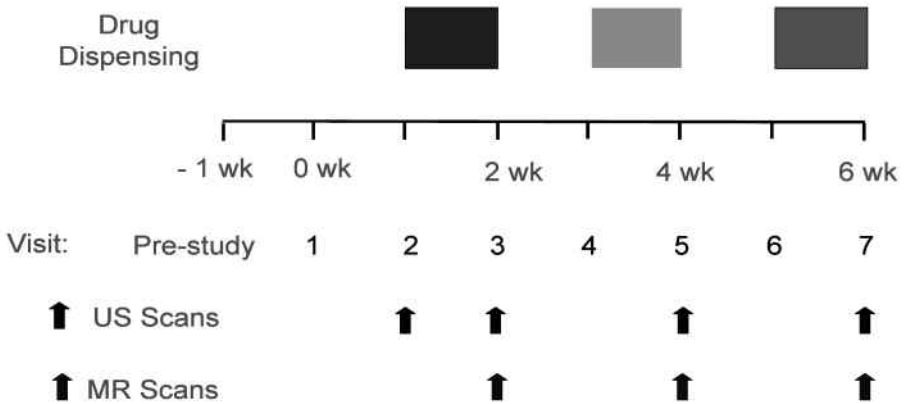
Figure XII.6.: Acute study setup. The study lasted for 6 weeks, divided into three times two weeks. Each of these two weeks consisted of a washout period of a week and a week of drug intake. The grey rectangles at the top represent a period of drug dispensing: each drug has a different colour, but the subjects and physicians were blinded. The arrows show when US and MRI scans were performed.

Subject	Visit 3	Visit 5	Visit 7
1	placebo	amlodipine	lisinopril
2	placebo	amlodipine	lisinopril
3	placebo	lisinopril	amlodipine
4	placebo	amlodipine	lisinopril*
5	placebo	lisinopril	amlodipine
6	placebo	amlodipine	lisinopril*
7	placebo	amlodipine*	lisinopril*
8	placebo	lisinopril	amlodipine
9	placebo	lisinopril	amlodipine
10	placebo	amlodipine	lisinopril

Table XII.3.: Order in which the compounds were administered to the subjects. The time-lines can be found in Figure XII.6. '*' means that the dose was up-titrated.

blood pressure prior to taking the fourth dose and inform the study physician of these results. A decision was made to up-titrate the dose to amlodipine (10mg OD) or lisinopril (20mg OD) if a target of 10 mmHg systolic blood pressure reduction compared to baseline was not achieved. MRI, Doppler ultrasound, IMT measurement and applanation tonometry of the right carotid artery and blood pressure data were collected on day seven of each treatment. This was followed by a period of a week for washout and then crossover to another treatment. Figure XII.6 represents the drug study schematically. Table XII.3 shows the order in which the different compounds were administered to the subjects. Note that all subjects started on

a placebo treatment. This reduces variability and makes the results more significant, but it also indicates that the study was in fact only randomised towards amlodipine and lisinopril, i.e. the changes seen between the placebo and amlodipine or placebo and lisinopril treatment could be influenced by sequence effects.

XII.3.2. Blood Pressure Measurements

Blood pressure was measured from the right arm using a validated fully automated sphygmomanometer (Omron HEM-705-CP, West Sussex, UK), which works according to the principles explained in section II.3.1.1 on page 47. Five pre-dose readings of BP and pulse were taken after 5 minutes rest and with at least one-minute interval between readings. The two extreme values (highest and lowest) were discarded, and BP was calculated as the average of the remaining three values.

XII.3.3. Ultrasound of the Right Distal CCA

All carotid scans were performed on the right carotid artery using a 7.5 MHz ultrasound transducer (12-5 scan head probe) with an HDI 5000 ultrasound scanner (ATL-Philips Medical Systems, WA, USA). Ten subjects were examined in the supine position with the neck extended and rotated 45 degrees towards the contra-lateral side. Common carotid artery B-mode images were obtained from the anterior, antero-lateral and posterior planes. The bulb dilatation served as a landmark indicating the border between the distal vessel and the bifurcation area. Images focussed on the far wall were recorded as cine loops with concomitant ECG traces to allow retrospective gating of images. At least 6 cardiac cycles were recorded and saved to a PC for subsequent analysis. Stored images were viewed using HDI Lab, (Software version 1.86, ATL, WA, USA) and analysed 'off-line'. Images obtained during diastole (peak of the R-wave), and systole (end of the T-wave) from each of the three planes were analysed using a validated semi-automated IMT analysis package (AMS V6 Chalmers University, Gothenburg, Sweden). Average common carotid and bulb IMT and lumen diameter (LD) were measured over a 5-15 mm segment for each projection of the right carotid artery. The mean value of all 3 projections was used as measurement for each subject. This technique has shown to have a reproducibility of 10 ± 45 μm on IMT measurements.[214]

Carotid blood flow velocity was measured using pulsed Doppler. Recordings were made in the centre of the right common carotid artery at a distance of 2 cm proximal to the bulb using a sample volume of 1.5 mm^2, and ultrasound beam positioned at 60° to the direction of blood flow. The pulsed Doppler data and simultaneous ECG trace were acquired continuously for 10 cardiac cycles and saved to hard disk for subsequent analysis. Peak velocity wave forms were analysed using HDI Lab, (Software version 1.86, ATL, WA, USA) and custom software written in MATLAB. At least 6 Doppler wave forms were ensemble averaged to give a representative wave form for measurement and further analyses. Volumetric blood flow in the carotid artery was calculated from the lumen diameter of the common carotid artery in diastole and by analytical solution of Womersley flow conditions using the peak velocity wave form, as explained in section II.3.3.1.

XII.3.4. Applanation Tonometry

Applanation tonometry was used to record arterial pressure wave forms from the right common carotid artery using a high fidelity strain-gauge tipped pencil probe (SPT 301, Millar instruments Inc, Houston, Texas, USA). The signal generated was amplified (TCB-500 pre-amplifier, Millar instruments Inc, Houston, Texas, USA), and at least 20 cardiac cycles were digitised at 200Hz and transferred to a PC for subsequent analysis. Minimum 6 contiguous pressure wave forms were ensemble averaged using custom software within the MATLAB programming environment. The ensemble averaged wave form was calibrated to diastolic and mean arterial pressure, and used to provide carotid systolic pressure measurements.

XII.3.5. MRI Protocol and coupling with CFD

The MRI protocol and the technique for coupling MRI with CFD was the same as the one applied in the study comparing BB MRI to TOF MRI. Here, the TOF scans were used in accordance with the same study, presented in section VI.5.

XII.3.5.1. Time Of Flight MRI protocol

All MRI scans involved were carried out on a Siemens Magnetom Sonata 1.5T scanner. The images were acquired using a purpose-built 2-element phased-array coil. For the acquisition of the 3D carotid geometry, axial cross-sections of the carotid arteries were imaged using a 2D time-of-flight protocol. The TOF scan parameters used 28 contiguous slices of 2mm thickness, a Field of View (FOV) of 130 x 100mm and in-plane resolution of 0.52 x 0.52 mm pixels. Other scan parameters include T_R 28 ms and T_E 7 ms.

XII.3.5.2. 3D Cine PC MRI

The velocity and flow measurements were performed using a 3D cine PC MRI sequence. MRI flow measurements were carried out in the CCA at a slice position in line with geometry scans as close to the first slice as signal to noise ratio (SNR) would allow ('inlet' scan). A second scan was taken in the CCA for a slice relatively close to the bifurcation, but far enough to ensure undisturbed flow ('midpoint' scan). ECA and ICA flow were measured as far distal as possible but before any ECA branching occurred ('outlet' scan). The in-plane resolution was 1.1 x 0.75 mm with a slice thickness of 6 mm. The first scan, close to the first slice, will be referred to as the 'inlet' scan, the other two scans as 'midpoint' and 'outlet' scan. For the outlet and midpoint scan, temporal resolution was 29 ms. The inlet flow was measured in 3 orthogonal directions (1 reference and 3 velocity encoded images) thereby reducing the temporal resolution by a factor of 1.5 to 2, depending on heart rate. The velocity encoding (V_{enc}) was 100 cm/s for axial velocities and 20 cm/s for in-plane (or secondary) velocities.

XII.3.5.3. Image Segmentation and 3D reconstruction

Each TOF MR image was segmented using the region growing method (see section VI.2.1, page 108) and snake method (see section VI.2.2, page 110). This results in a contour for each TOF MR image. The contours were superimposed on the image and shown to the operator. At this point, the operator was allowed to edit the contours if deemed necessary.

After segmentation, MRI resulted in serial contours in equidistance planes. With the knowledge of the position of the contours in 3D space, the con-

tours can be positioned adequately to produce a 3D vessel surface geometry. Smoothing was performed in two steps as discussed in section VI.3.1. First, the areas of consecutive cross-sections were smoothed using a cubic smoothing spline (p = 0.1). In a second step, the centrelines, i.e. the line that goes through the centroids of vessel cross-sections in the transverse plane, were smoothed using cubic splines (p = 0.5). This was achieved by shifting the centroids and associated contours until a smooth centreline was obtained.

XII.3.5.4. Mesh generation and computational details

The mesh was generated using the mesh generator explained in section III.2.2 (page 76). The mesh generator constructs a multi-block structured meshes of hexahedral cells (Figures III.1 and III.2). Figure VI.22 (page 143) shows a mesh reconstructed from TOF MRA for subject 5, scan 2.

The Navier-Stokes equations for laminar flow were discretised using the 'QUICK' (Quadratic Upwind Interpolation Convective Kinematics) differencing scheme explained in section III.4.1.1 and then solved using the SIMPLEC algorithm implemented in CFX4™.[3] Based on previous experience, two cardiac cycles of 80 equally spaced time-steps were simulated. The length of the time-step varied according to the measured heart rate. Blood density was considered 1176 kg/m^3. The Quemada-model was used for modelling the non-Newtonian behaviour of blood.[42] The wall was modelled as a rigid, no-slip surface. The velocities measured with cine PC MRI in the inlet plane were filtered and scaled for mass flow rate as explained in section VIII.1.1. The mass flow rate used in the scaling was obtained from the midpoint scan. Flow rate measurements were performed using CMRTools (Imperial College London, London, UK). The outflow cine series was used to compute a time-dependent ICA and ECA flow rate. From the calculated outflow rates, a time-dependent mass outflow ratio was deduced and set as boundary condition on the model outlets.

XII.3.6. 3DUS Protocol and coupling with CFD

In 2 of the 10 cases, the subjects could not be imaged using MRI due to claustrophobia. Here, the scans were performed using a 3DUS protocol. The 3D, time-varying flow profiles were obtained by performing the steps explained in section XI.2.2.

XII.3.6.1. Ultrasound imaging and Slice Positioning Information

The 3DUS imaging protocol is explained in section VII.1.4. The protocol results in 2D B-mode cross-sections of the carotid bifurcation on one hand and the position of these slices on the other hand. In addition, velocity wave forms were obtained using pulsed-wave Doppler from the centre-stream of the CCA, approximately at the location corresponding to that of the most proximal slice of the 3DUS scan. Similarly, centreline velocities were measured in the ICA and ECA. These velocities were used to calculate the mass flow rate using the technique described in section II.3.3.1.

XII.3.6.2. Image Segmentation and Carotid Reconstruction

Acquired images were segmented using purpose-built software in a MAT-LAB environment. The software was used to manually select points on the vessel wall to which a smooth cubic spline or ellipse was fitted. The final lumen contours, combined with the positioning information from the EPOM device, allowed reconstruction of a smooth 3D geometry of the carotid bifurcation.

XII.3.6.3. Mesh Generation and computational details

The mesh was generated using the in-house purpose-built mesh generator described in section III.2.2. The vessel wall was assumed to be rigid with no mass transfer and zero-velocity (no-slip condition). At the inlet, Womersley profiles derived from the measured flow wave form in the common carotid were imposed. The flow wave form was acquired from the centreline velocity, assuming developed Womersley flow in the CCA.[368] At the outlet, a time-dependent outflow ratio was imposed. To calculate the outflow ratio, the flow rates were calculated in CCA, ICA and ECA using centreline measurements and the Womersley assumption. Then, outflow ratio can be calculated from the ICA and ECA, CCA and ICA and even CCA and ECA. The ratio was calculated using the flow rates yielding a division ratio closest to the expectable 55:45 (ICA:ECA). This allows to filter out major acquisition errors. See section VIII.1.2 (page 216) for a discussion on the use of these boundary conditions.

With the knowledge of vessel geometry and boundary conditions, the partial differential equations describing the movement of the fluid (mass conservation law and Navier-Stokes equation) were solved numerically using the same settings as for the simulations performed using MRI as a basis, explained in section XII.3.5.4.

XII.3.7. Measured Parameters

For each visit, the following set of parameters were measured or calculated. They can be subdivided into pressure-related parameters, direct geometry parameters, 3D reconstruction parameters, flow parameters and haemodynamic parameters. Eight patients were scanned using MRI, 2 claustrophobic patients were examined with 3DUS.

XII.3.7.1. Pressure Parameters

The pressure parameters included clinically measured blood pressure at diastole (DBP) and systole (SBP), mean arterial pressure (MAP = SBP/3 +2×DBP/3) and pulse pressure (PP= SBP-DBP).

XII.3.7.2. Direct geometry parameters

The direct geometry parameters are called 'direct' because they do not require 3D reconstruction of the carotid bifurcation in order to be quantified. The parameters include the IMT and LD, both in systole and in diastole. The cyclic difference in IMT and LD (largest value-smallest value) were also calculated. The IMT was also measured in the carotid bulb. Furthermore, IMT/LD ratio and IMA were calculated. For more information concerning the rationale of these parameters, see section II.2.2.1.

When geometry and pressure parameters are combined, the compliance C can be calculated as in equation II.8 (page 51). Other derived parameters include the distensibility coefficient (DC, equation II.10, page 52), Young's modulus (E, equation II.9, page 51), mean and peak wall tension (T_m and T_p, equation II.12, page 52) and mean and peak tensile stress (σ_m and σ_p, equation II.14, page 52).

XII.3.7.3. 3D reconstruction parameters

The 3D reconstruction parameters are geometry parameters which necessitate the 3D reconstruction of the carotid bifurcation. They include the mean cross-sectional area (A_{art} with art=CCA, ICA or ECA), area ratio (A_R), mean individual shape factor ($SF_{i\ art}$), overall (NP) and arterial (NP_{art}) non-planarity, arterial linearity (L_{art}), arterial tortuosity (T_{art}) and bifurcation angle (α_{BIF}). For elabourate definitions of these parameters, see section II.3.2.2, page 53.

XII.3.7.4. Flow parameters

Flow parameters are measures that require a velocity or mass flow rate measurement in order to be quantified. The heart rate is conventionally part of the flow parameters. The basis of all other flow parameters is a flow rate measurement, either using 3D cine PC MRI or Pulsed Doppler ultrasound. See section II.3.3.1 for the derivation of a flow rate using these measurement techniques. Other flow parameters include the Reynolds number (Re, equation II.28, page 64) and the Womersley number (α, equation II.29, page 65).

XII.3.7.5. Haemodynamic parameters

The haemodynamic parameters are calculated from the 3D CFD simulation. They include the velocity parameter V_{MAX} (see page 67) and the wall parameters WSS, OSI, WSSGs, WSSGt and WSSAG. These parameters are explained in section II.3.3.3 which starts on page 67. The wall parameters are averaged over the entire bifurcation, and over 10 other zones: (i) the CCA half adjacent to the ICA (marked 'iCCA'); (ii) the CCA half closer to the ECA; (iii) the inner ICA, i.e. the half of the ICA which contains the apical region; (iv) the outer ICA; (v) the inner and (vi) outer ECA; (vii) the entire CCA; (viii) ICA; (ix) ECA and (x) the outer part of the bulb, i.e. part of the outer ICA and iCCA.

Figure XII.7 (a) shows an alternative way of displaying WSS information. The WSS values can be found on the horizontal axis. The time, represented as a percentage of the cardiac cycle, is found in the vertical axis. The vessel wall area, represented as a percentage of the total carotid bifurcation wall
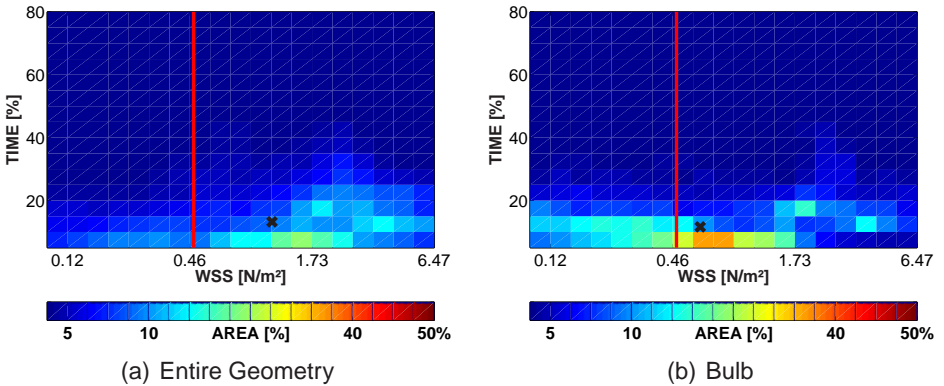
Figure XII.7.: 'Time and Area' representation of the WSS. The WSS values can be found on the horizontal axis. The time, represented as a percentage of the cardiac cycle, is found in the vertical axis. The vessel wall area, represented as a percentage of the total carotid bifurcation wall area, is colour coded in the legend and mapped on the graph. The black cross is the gravity point.

area, is colour coded in the legend and mapped on the graph. The cross on the image represents the center of gravity when the colours are used as weight factors. The cross in Figure XII.7 (a) lies in a blue area at approximate 1.2 N/m^2 and 10%. This means that approximately 8% of the carotid wall area (blue) undergoes a WSS in the range of 1.2 N/m^2 for 10% of the time. Because Figure XII.7 gives information on the *value* of WSS, its *duration* and *importance* with respect to the involved area, these images are called 'Time and area' representations of the WSS.

The presented example was obtained by considering the entire vessel wall. This can be performed for the bulb area as well. See Figure XII.7 (b) for an example from the same set of data as Figure XII.7 (a).

The red vertical line in Figures XII.7 is drawn at a threshold of 0.4 N/m^2. This is the threshold for 'atherogenic' WSS values as defined by Malek.[208] The further to the right the gravity points lies, the better. The distance between the gravity point and the red line has been quantified for all subjects in all visits.

The higher the gravity point lies in a Time and Area image, the less fluctuations occur in the WSS. This distance, subsequently referred to as the **steadiness**, has been quantified for all subjects in all visits.

315

XII.3.8. Statistical analysis

The performed statistics are summarised in Figure XII.8 which gives the results for the heart rate measurements. Figure XII.8 (a) shows all the data in one plot. The black dots represent the general means, e.g. with amlodipine, the mean heart rate was approximately 73 bpm. The black line through the general mean shows the standard deviation. The grey dots represent the individually measured values. Figure XII.8 (b) performs a 2-way anova (10 subjects, 3 compounds) followed by the 'Least Square Difference' ('LSD') post hoc test. The blue dots represent the means of the considered parameter using a particular compound. The line through the point denotes *half* of the confidence interval using a significance level of 0.05. The advantage of showing half instead of the entire confidence interval lies in the fact that a 'significant' difference between means is now represented as a lack of overlap between the presented lines. In the current example, there was no difference between the heart rate measured using the placebo or any of the drugs, but there was a significant difference between the heart rate in the lisinopril compared to the amlodipine regimen.

XII.4. Results

Each patient required up-titration of the placebo. One patient required a doubling of amlodipine dose (i.e. 10mg) to reach target blood pressure, and three patients required a doubling of lisinopril dose (20mg) to reach target
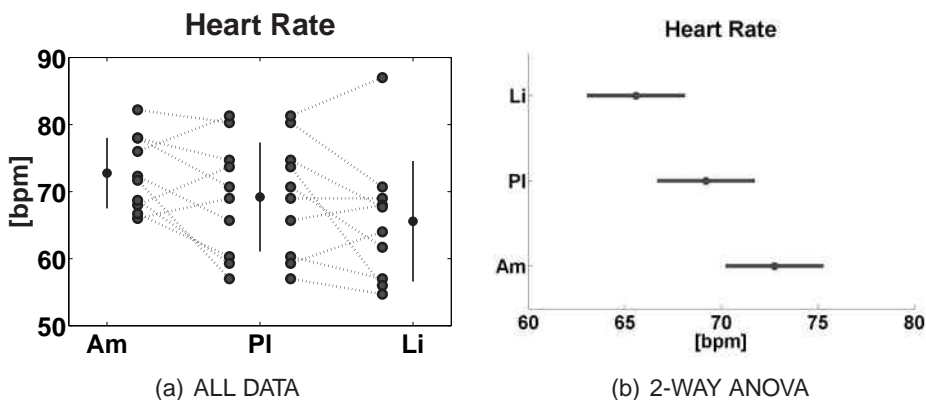
Figure XII.8.: Statistics used in Acute CFD study. Illustration using the heart rate as compared parameter. Am: amlodipine; Pl: placebo; Li: lisinopril.

Parameter	amlodipine Calcium blocker	placebo	lisinopril ACE inhibitor	ANOVA
Diastolic Pressure [mmHg]	85.6 ± 5.1 **	95.6 ± 9.9	83.2 ± 9.0 ++	0.002 ◊◊
Systolic Pressure [mmHg]	138.1 ± 10.2 ** †	150.6 ± 12.4	130.2 ± 14.5 ++ †	0.000 ◊◊
Pulse Pressure [mmHg]	52.5 ± 8.9 †	55.0 ± 5.7	47.1 ± 8.1 ++ †	0.031 ◊◊
Mean Arterial Pressure [mmHg]	103.1 ± 5.9 **	113.9 ± 10.4	98.8 ± 10.4 ++	0.000 ◊◊
Heart Rate [bpm]	72.8 ± 5.6 ††	69.2 ± 8.6	65.6 ± 9.5 ††	0.027 ◊◊

Table XII.4.: Statistical Analysis of 'Pressure' parameters considered in the Acute CFD Study. Values are mean ± standard deviation. '*' denotes significant difference between amlodipine and placebo; '+' denotes significant difference between lisinopril and placebo; '†' denotes significant difference between lisinopril and amlodipine; a single sign denotes $p<0.1$, if the sign is doubled, significance is $p<0.05$. '◊' denotes significant difference between compound means ($p<0.1$ or $p<0.05$ if double sign).

blood pressure. The patients requiring up-titration are marked with a star in Table XII.3.

Tables XII.4 to XII.13 show the mean ± standard deviation for all variables using the amlodipine, placebo or lisinopril. The statistics are performed as explained in section XII.3.8. The column ANOVA returns the p-value for the hypotheses that all compound-means are equal. For clarity, this means that p close to 0 casts doubt on the hypothesis and suggests that at least one of the means, using placebo, lisinopril or amlodipine, is different from the others. If p is sufficiently low (e.g. <0.2), a post hoc test can be performed in order to learn which of the means is significantly different from the others. Here, the 'lsd' post hoc test was used to identify the compound yielding a mean value different from the other compounds. The signs '*', '+', '†', '◊' have been used to emphasise on significance as explained in Table XII.4.

Finally, Figure XII.9 shows the time-averaged wall shear stress (WSS) distribution for three subjects after each week of treatment.

XII.5. Discussion

The reader is reminded that the aims of this study were double: in the first place, the aim was to *compare* the acute effects of amlodipine and lisinopril on local carotid artery haemodynamics, and in a second step, the goal was to *relate* the findings of the acute study to the observations made in the 52 week study with amlodipine and lisinopril performed by Stanton.[302] The discussion contains two section, each section deals with one of the aims of this study.

Parameter	amlodipine Calcium blocker	placebo	lisinopril ACE inhibitor	ANOVA
Diastolic IMT [mm]	0.570 ± 0.087 **	0.541 ± 0.085	0.563 ± 0.101 +	0.076 ◊
Systolic IMT [mm]	0.520 ± 0.080	0.507 ± 0.077	0.521 ± 0.092	0.419
IMT Difference [mm]	0.049 ± 0.034	0.033 ± 0.025	0.042 ± 0.024	0.423
Bulb IMT [mm]	0.678 ± 0.082	0.645 ± 0.094	0.668 ± 0.102	0.315
Diastolic LD [mm]	6.57 ± 0.57	6.56 ± 0.58	6.47 ± 0.72	0.694
Systolic LD [mm]	6.96 ± 0.62	7.02 ± 0.65	6.84 ± 0.88	0.511
Diameter Difference [mm]	0.39 ± 0.12 **	0.45 ± 0.11	0.37 ± 0.19 +	0.180
Diastolic IMT/Diastolic LD [-]	0.087 ± 0.012 *	0.083 ± 0.014	0.087 ± 0.014 +	0.097 ◊
Systolic IMT/Systolic LD [-]	0.075 ± 0.011	0.073 ± 0.012	0.077 ± 0.014	0.169
Diastolic IMA [mm^2]	12.8 ± 2.7 *	12.1 ± 2.3	12.5 ± 3.2	0.284
Systolic IMA [mm^2]	12.3 ± 2.5	12.0 ± 2.3	12.1 ± 3.2	0.866
Compliance [$\frac{mm^2}{kPa}$]	0.594 ± 0.172	0.670 ± 0.200	0.682 ± 0.495	0.771
Distensibility Coefficient [1/MPa]	17.02 ± 4.59	18.92 ± 4.18	18.62 ± 10.88	0.809
Young's Modulus [kPa]	749 ± 319	682 ± 176	876 ± 525	0.485
Peak Wall Tension [Pa.m]	64.0 ± 7.6 ** ††	70.6 ± 9.3	59.5 ± 11.0 ++ ††	0.000 ◊◊
Mean Wall Tension [Pa.m]	45.1 ± 4.1 **	49.9 ± 6.8	42.7 ± 7.3 ++	0.001 ◊◊
Peak Tensile Stress [kPa]	126.1 ± 27.1 ** †	141.9 ± 28.3	117.9 ± 34.2 ++ †	0.001 ◊◊
Mean Tensile Stress [kPa]	81.0 ± 16.1 **	94.3 ± 19.5	78.1 ± 20.2 ++	0.001 ◊◊

Table XII.5.: Statistical Analysis of 'Direct Geometry' parameters considered in the Acute CFD Study. Values are mean $\pm$ standard deviation. See Table XII.4 for a legend.

Parameter	amlodipine Calcium blocker	placebo	lisinopril ACE inhibitor	ANOVA
CCA Mean Area [mm^2]	50.7 ± 13.1	49.3 ± 9.7	51.0 ± 15.0	0.716
ICA Mean Area [mm^2]	29.2 ± 11.1	28.6 ± 10.4	29.1 ± 12.3	0.787
ECA Mean Area [mm^2]	18.8 ± 5.4	17.9 ± 3.9	18.5 ± 5.4	0.530
Area Ratio [-]	0.808 ± 0.099	0.884 ± 0.127	0.809 ± 0.119	0.062 ◊
CCA Shape [-]	0.967 ± 0.011 ††	0.971 ± 0.016	0.960 ± 0.015 ++ ††	0.015 ◊◊
ICA Shape [-]	0.973 ± 0.023 **	0.981 ± 0.018	0.972 ± 0.020 +	0.046 ◊◊
ECA Shape [-]	0.964 ± 0.032	0.965 ± 0.040	0.961 ± 0.045	0.761
Non-Planarity [%]	3.9 ± 1.6	4.2 ± 1.9	4.0 ± 1.9	0.227
Non-Planarity CCA [%]	0.4 ± 0.3	0.5 ± 0.3	0.4 ± 0.3	0.367
Non-Planarity ICA [%]	0.9 ± 0.9	1.0 ± 0.9	0.9 ± 1.0	0.143
Non-Planarity ECA [%]	0.8 ± 0.8	0.9 ± 0.7	1.0 ± 1.1	0.705
Linearity CCA [%]	93.2 ± 2.5	92.9 ± 2.2	92.9 ± 2.5	0.225
Linearity ICA [%]	92.4 ± 1.3	91.8 ± 1.7	92.0 ± 1.7	0.166
Linearity ECA [%]	91.8 ± 2.1	91.0 ± 2.7	91.0 ± 3.4	0.188
alpha BIF [°]	138.1 ± 23.2	145.3 ± 17.1	146.8 ± 7.4	0.317
Tortuosity CCA [%]	1.2 ± 0.8	1.2 ± 1.0	1.4 ± 0.9	0.616
Tortuosity ICA [%]	4.3 ± 4.8	4.6 ± 5.0	4.1 ± 5.6	0.641
Tortuosity ECA [%]	4.0 ± 5.3	4.1 ± 4.0	3.8 ± 5.9	0.875

Table XII.6.: Statistical Analysis of '3D Reconstruction' parameters considered in the Acute CFD Study. Values are mean $\pm$ standard deviation. See Table XII.4 for a legend.

Parameter	amlodipine Calcium blocker	placebo	lisinopril ACE inhibitor	ANOVA
Heart Rate [bpm]	72.8 ± 5.6 ††	69.2 ± 8.6	65.6 ± 9.5 ††	0.027 ◇◇
CCA Flow Rate [ml/s]	7.8 ± 1.7 ††	7.8 ± 2.8	6.3 ± 1.3 ††	0.135
ICA Flow Rate [ml/s]	4.6 ± 1.1 ††	4.7 ± 1.7	3.7 ± 0.6 ††	0.218
ECA Flow Rate [ml/s]	3.2 ± 0.7 †	3.1 ± 1.3	2.6 ± 0.9 †	0.160
Reynolds CCA [-]	362 ± 37 ††	366 ± 144	297 ± 32 ††	0.196
Reynolds ICA [-]	299 ± 33 ††	313 ± 113	250 ± 26 ††	0.199
Reynolds ECA [-]	256 ± 32 ††	246 ± 91	206 ± 47 ††	0.126
Womersley CCA [-]	5.91 ± 0.64	5.69 ± 0.41	5.69 ± 0.89	0.393
Womersley ICA [-]	4.46 ± 0.86	4.32 ± 0.87	4.30 ± 1.10	0.453
Womersley ECA [-]	3.60 ± 0.52	3.44 ± 0.47	3.44 ± 0.65	0.349

Table XII.7.: Statistical Analysis of 'Flow' parameters considered in the Acute CFD Study. Values are mean $\pm$ standard deviation. See Table XII.4 for a legend.

Parameter	amlodipine Calcium blocker	placebo	lisinopril ACE inhibitor	ANOVA
CCA Mean Vmax [m/s]	0.44 ± 0.06 ††	0.39 ± 0.11	0.36 ± 0.03 ††	0.163
ICA Mean Vmax [m/s]	0.40 ± 0.06 †	0.39 ± 0.12	0.33 ± 0.04 †	0.177
ECA Mean Vmax [m/s]	0.38 ± 0.04	0.38 ± 0.14	0.33 ± 0.11	0.341

Table XII.8.: Statistical Analysis of 'Vmax' parameters considered in the Acute CFD Study. Values are mean $\pm$ standard deviation. See Table XII.4 for a legend.

Parameter	amlodipine Calcium blocker	placebo	lisinopril ACE inhibitor	ANOVA
WSS ALL [N/m^2]	1.378 ± 0.492 ††	1.354 ± 0.665	1.138 ± 0.375 ††	0.192
WSS CCA [N/m^2]	0.754 ± 0.245	0.735 ± 0.406	0.628 ± 0.164	0.542
WSS iCCA [N/m^2]	0.807 ± 0.286	0.787 ± 0.424	0.688 ± 0.259	0.646
WSS eCCA [N/m^2]	0.688 ± 0.241	0.672 ± 0.387	0.552 ± 0.110	0.418
WSS ICA [N/m^2]	1.705 ± 0.681 †	1.702 ± 0.936	1.390 ± 0.549 †	0.263
WSS outer ICA [N/m^2]	1.376 ± 0.586	1.390 ± 0.778	1.118 ± 0.485	0.285
WSS inner ICA [N/m^2]	2.283 ± 0.856 ††	2.248 ± 1.221	1.836 ± 0.701 ††	0.200
WSS ECA [N/m^2]	2.275 ± 1.051 †	2.276 ± 1.318	1.891 ± 0.999 †	0.269
WSS outer ECA [N/m^2]	1.482 ± 0.648	1.455 ± 0.830	1.299 ± 0.672	0.417
WSS inner ECA [N/m^2]	2.275 ± 1.051 †	2.276 ± 1.318	1.891 ± 0.999 †	0.269
WSS bulb [N/m^2]	1.103 ± 0.400 †	1.138 ± 0.595	0.904 ± 0.316 †	0.239
Area with Low WSS [%]	20.561 ± 26.859	21.003 ± 27.172	23.894 ± 22.802	0.481
Area with High WSS [%]	15.277 ± 9.025 ††	14.394 ± 12.497	9.757 ± 6.516 ††	0.161
Dist from 0.4 [N/m^2]	0.609 ± 0.054 ††	0.601 ± 0.032	0.585 ± 0.055 ††	0.278
Dist from 0.4 BULB [N/m^2]	0.553 ± 0.053 ††	0.543 ± 0.026	0.522 ± 0.054 ††	0.139

Table XII.9.: Statistical Analysis of 'WSS' parameters considered in the Acute CFD Study. Values are mean $\pm$ standard deviation. See Table XII.4 for a legend.

Parameter	amlodipine	placebo	lisinopril	ANOVA
	Calcium blocker		ACE inhibitor	
OSI ALL [-]	0.084 ± 0.083 *	0.078 ± 0.083	0.084 ± 0.082	0.275
OSI CCA [-]	0.120 ± 0.086	0.122 ± 0.097	0.120 ± 0.086	0.974
OSI iCCA [-]	0.107 ± 0.078	0.106 ± 0.089	0.112 ± 0.087	0.703
OSI eCCA [-]	0.140 ± 0.102	0.143 ± 0.111	0.131 ± 0.095	0.733
OSI ICA [-]	0.056 ± 0.076 **	0.043 ± 0.068	0.052 ± 0.073 ++	0.020 ◇◇
OSI outer ICA [-]	0.070 ± 0.095 **	0.056 ± 0.085	0.069 ± 0.089 ++	0.025 ◇◇
OSI inner ICA [-]	0.024 ± 0.025 *	0.015 ± 0.021	0.021 ± 0.039	0.361
OSI ECA [-]	0.044 ± 0.068 *	0.023 ± 0.039	0.040 ± 0.065	0.234
OSI outer ECA [-]	0.082 ± 0.098	0.057 ± 0.069	0.082 ± 0.091 +	0.096 ◇
OSI inner ECA [-]	0.044 ± 0.068 *	0.023 ± 0.039	0.040 ± 0.065	0.234
OSI bulb [-]	0.098 ± 0.084	0.093 ± 0.091	0.103 ± 0.085	0.117
Area with High OSI [%]	16.646 ± 20.055 **	13.961 ± 19.782	18.091 ± 19.548 ++	0.003 ◇◇
Steadiness [%]	10.749 ± 2.526	11.066 ± 2.711	10.380 ± 2.282	0.298
Steadiness BULB [%]	10.494 ± 2.621	10.845 ± 2.763	10.476 ± 2.480	0.535

Table XII.10.: Statistical Analysis of 'OSI' parameters considered in the Acute CFD Study. Values are mean $\pm$ standard deviation. See Table XII.4 for a legend.

Parameter	amlodipine	placebo	lisinopril	ANOVA
	Calcium blocker		ACE inhibitor	
WSSGs ALL [N/m^3]	420 ± 104 ††	397 ± 157	368 ± 97 ††	0.375
WSSGs CCA [N/m^3]	231 ± 56	222 ± 89	210 ± 51	0.761
WSSGs iCCA [N/m^3]	228 ± 56	220 ± 93	209 ± 63	0.830
WSSGs eCCA [N/m^3]	235 ± 64	226 ± 84	213 ± 45	0.679
WSSGs ICA [N/m^3]	461 ± 196	429 ± 209	387 ± 161	0.522
WSSGs outer ICA [N/m^3]	347 ± 161	328 ± 166	298 ± 143	0.666
WSSGs inner ICA [N/m^3]	659 ± 248 †	606 ± 287	534 ± 200 †	0.327
WSSGs ECA [N/m^3]	819 ± 284	784 ± 298	728 ± 197	0.530
WSSGs outer ECA [N/m^3]	476 ± 154	462 ± 183	453 ± 180	0.885
WSSGs inner ECA [N/m^3]	819 ± 284	784 ± 298	728 ± 197	0.530
WSSGs bulb [N/m^3]	293 ± 100	284 ± 124	258 ± 94	0.646

Table XII.11.: Statistical Analysis of 'WSSGs' parameters considered in the Acute CFD Study. Values are mean $\pm$ standard deviation. See Table XII.4 for a legend.

Parameter	amlodipine	placebo	lisinopril	ANOVA
	Calcium blocker		ACE inhibitor	
WSSGt ALL [N/(m$^2 \times s$)]	10.65 ± 3.82	9.94 ± 3.66	10.20 ± 4.00	0.788
WSSGt CCA [N/(m$^2 \times s$)]	7.61 ± 3.09	7.09 ± 2.80	7.13 ± 2.89	0.709
WSSGt iCCA [N/(m$^2 \times s$)]	7.58 ± 3.16	7.12 ± 2.81	7.09 ± 2.94	0.771
WSSGt eCCA [N/(m$^2 \times s$)]	7.66 ± 3.09	7.07 ± 2.85	7.20 ± 2.91	0.614
WSSGt ICA [N/(m$^2 \times s$)]	11.35 ± 7.25	10.12 ± 5.16	10.20 ± 6.39	0.814
WSSGt outer ICA [N/(m$^2 \times s$)]	9.81 ± 6.10	8.95 ± 4.58	8.77 ± 5.53	0.841
WSSGt inner ICA [N/(m$^2 \times s$)]	13.95 ± 9.03	12.19 ± 6.29	12.49 ± 7.76	0.773
WSSGt ECA [N/(m$^2 \times s$)]	16.22 ± 8.63	16.23 ± 9.84	16.86 ± 8.53	0.957
WSSGt outer ECA [N/(m$^2 \times s$)]	12.37 ± 6.04	12.13 ± 7.17	13.17 ± 6.59	0.857
WSSGt inner ECA [N/(m$^2 \times s$)]	16.22 ± 8.63	16.23 ± 9.84	16.86 ± 8.53	0.957
WSSGt bulb [N/(m$^2 \times s$)]	8.46 ± 4.05	8.02 ± 3.35	7.68 ± 3.48	0.832

Table XII.12.: Statistical Analysis of 'WSSGt' parameters considered in the Acute CFD Study. Values are mean $\pm$ standard deviation. See Table XII.4 for a legend.

Parameter	amlodipine Calcium blocker	placebo	lisinopril ACE inhibitor	ANOVA
WSSAG ALL [rad/m]	169.9 ± 43.5 ** †	151.6 ± 36.1	152.8 ± 31.0 †	0.059 ◇
WSSAG CCA [rad/m]	197.0 ± 71.1	184.1 ± 70.5	175.5 ± 42.0	0.289
WSSAG iCCA [rad/m]	188.1 ± 76.3	172.3 ± 66.0	168.4 ± 54.9	0.260
WSSAG eCCA [rad/m]	210.1 ± 68.8	201.5 ± 85.9	183.5 ± 31.4	0.450
WSSAG ICA [rad/m]	138.9 ± 55.5	118.4 ± 49.6	123.4 ± 50.3	0.204
WSSAG outer ICA [rad/m]	134.9 ± 51.2	118.5 ± 56.3	122.6 ± 53.3	0.501
WSSAG inner ICA [rad/m]	147.5 ± 79.6	117.9 ± 56.1	125.9 ± 54.3	0.268
WSSAG ECA [rad/m]	182.8 ± 79.3	160.2 ± 66.8	168.3 ± 76.9	0.573
WSSAG outer ECA [rad/m]	172.8 ± 60.7	142.2 ± 43.6	161.1 ± 60.4	0.208
WSSAG inner ECA [rad/m]	182.8 ± 79.3	160.2 ± 66.8	168.3 ± 76.9	0.573
WSSAG bulb [rad/m]	186.2 ± 47.9 *	160.0 ± 45.8	165.0 ± 31.1	0.092 ◇

Table XII.13.: Statistical Analysis of 'WSSAG' parameters considered in the Acute CFD Study. Values are mean ± standard deviation. See Table XII.4 for a legend.

XII.5.1. Acute effects

XII.5.1.1. Pressure Changes

There have been several studies comparing the effects of calcium blockers and ACE inhibitors on blood pressure. The cascade of events causing pressure drop following the intake of a calcium blocker is described in section XII.1.2.1. Figures XII.10 (a-d) show the systolic and diastolic pressure drop due to the administration of ACE inhibitors or calcium blockers in studies performed by Naidu,[231] Lorimer,[201] Lafleche,[166] Sihm[284] and Stanton.[302] The studies are sorted according to their follow-up period: Naidu's study lasted for 4 weeks, whereas the follow-up was 1 year in Stanton's study. Figures XII.10 (a,c) seem to suggest that the pressure drop is greater in studies with longer follow-ups, and that the diastolic pressure drop is a fraction smaller than the systolic. In this study a target of 10 mmHg systolic blood pressure reduction was set. When not achieved, the oral dose was doubled. The average systolic pressure drop for the calcium blocker, amlodipine, was 12.5 mmHg, which meets the target.

Figures XII.10 (b,d) show the systolic and diastolic pressure drop after administration of calcium blockers recorded in literature. The studies illustrated are those of Naidu,[231] Lorimer,[201] Mitchell,[220] Lafleche,[166] Girerd,[116] Boutouyrie[36] and Stanton,[302] again sorted according to the follow-up time. Similar trends as Figures XII.10 (a,c) are found. Lorimer[201] and Stanton[302] did a comparative study between amlodipine and lisinopril. Lorimer found that amlodipine lowered the pressure more effectively than lisinopril, whereas Stanton did not report a significant difference between the two treatments.
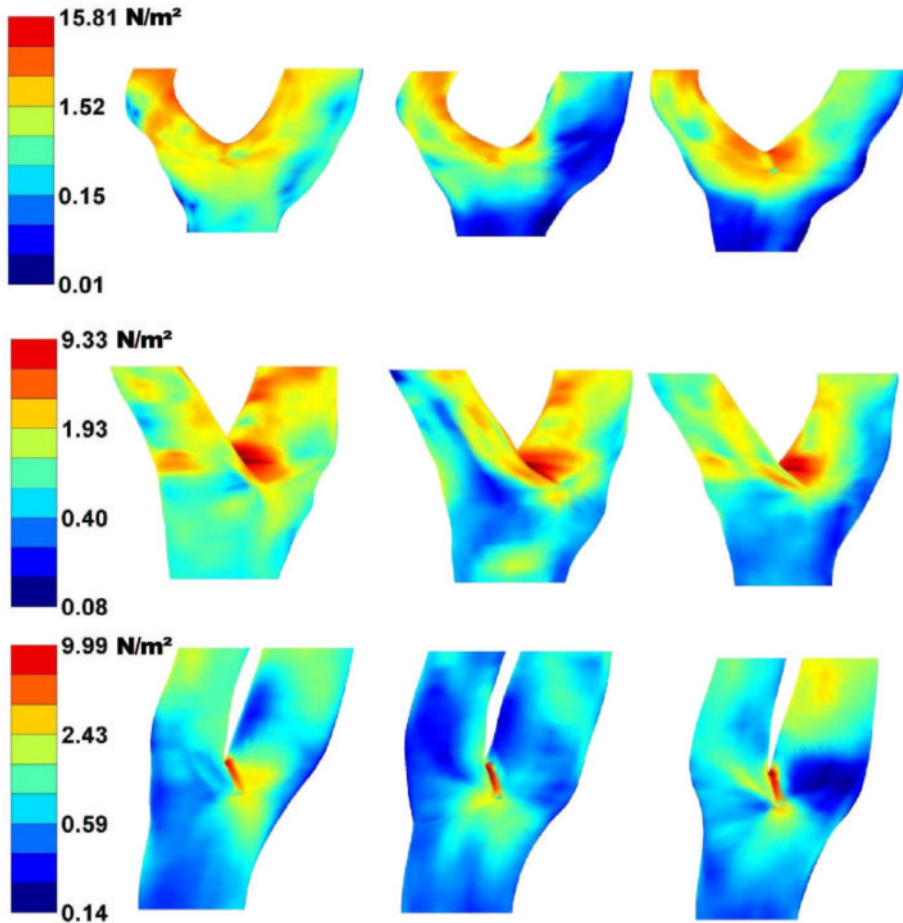
Figure XII.9.: The time-averaged wall shear stress distribution for three subjects (rows) after amlodipine (left), placebo (middle) and lisinopril (right) intake.

In our study, the systolic pressure drop with lisinopril was 20.4 mmHg, which has the tendency to be larger (p = 0.0683, LSD) than the pressure drop with amlodipine. Note that the lisinopril dose had to be doubled on three occasions, whereas the amlodipine dose was only doubled once (Table XII.3).

XII.5.1.2. Direct geometry parameters

The direct geometry parameters include IMT, LD and related parameters IMA and IMT/LD ratio. Other parameters, such as compliance, distensibility,
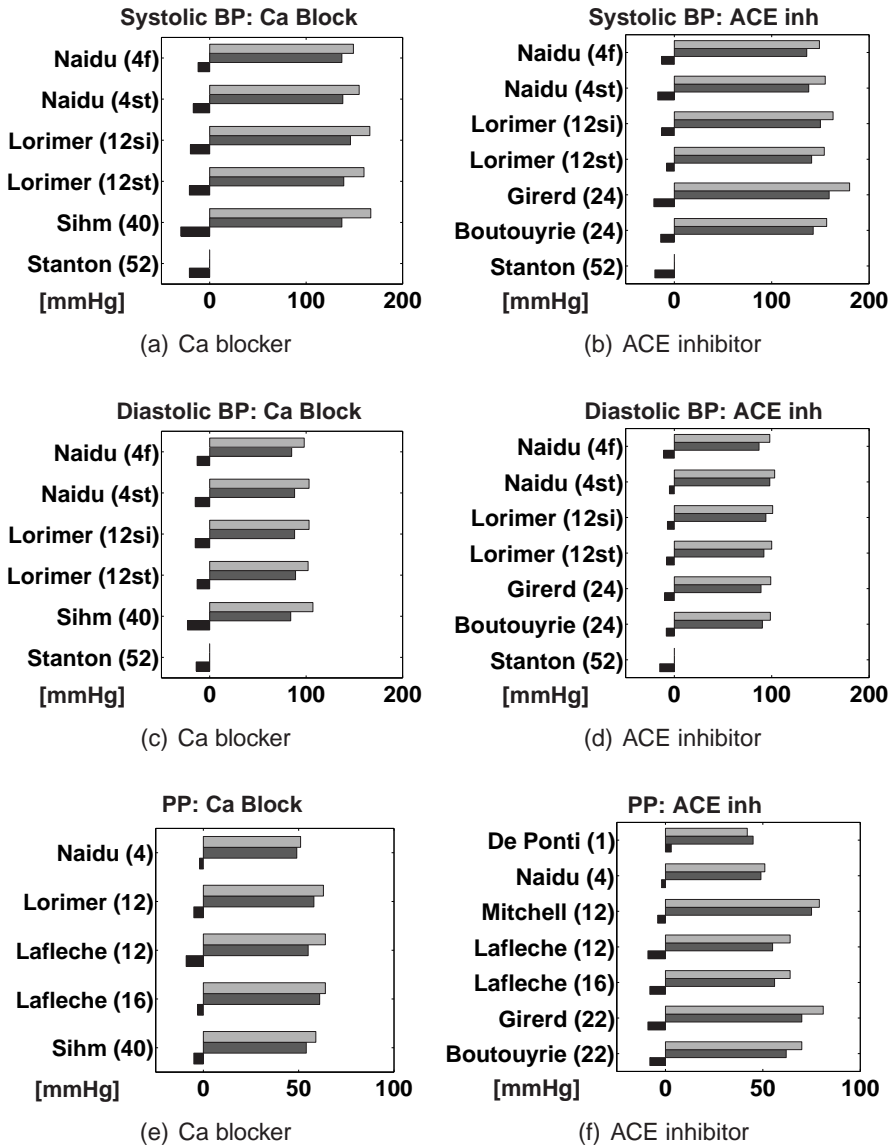
Figure XII.10.: Pressure drops using ACE inhibitors and calcium blockers in literature. The vertical axis shows the study considered. Between brackets: the number of weeks follow-up, and the position in which the subject was when blood pressure was taken. f: flat; si: sitting; st: standing. For each study, the top bar is the baseline (light grey), the middle bar is the result after treatment (dark grey) and the final bar is the difference (black). Data comes from studies by Naidu,[231] Lorimer,[201] Lafleche,[166] Sihm,[284] Mitchell,[220] Girerd,[116] Boutouyrie,[36] De Ponti[74] and Stanton[302] and are sorted according to the follow-up time. Baseline and end-study values were not stated by Stanton.[302]

young's modulus, wall tension and wall stress, are obtained when combined with the pressure data.

Lumen Diameter With the pressure drop, the vessel is expected to relax. This can be compared to a balloon which is slightly deflated. The effect of the pressure drop will thus be a decrease in carotid LD. This contradicts the fact that both compounds work as vasodilators, but since vasodilators mainly act on the arterioles, which are the smaller, pressure regulating arteries (Table I.1 on page 8), the carotid arteries are expected to be only marginally affected by this dilatation. As summarised by Figure XII.11 (a), the carotid LD has been found to decrease in other pharmacological studies by Boutouyrie,[36] Girerd,[116] Stanton,[302] Ariff[12] and Simon.[286] In this acute study, we expect the diameter to drop according to the pressure drop. Table XII.5 shows that the drop in LD occurred at very low significance. This probably means that the relaxation of the vascular smooth muscle cells due to the vasodilatory effects of the compounds are more important than originally expected. Note that the 'diameter difference', i.e. the difference in LD between systole and diastole, tends to decrease in both treatments (amlodipine: $p = 0.0378$; lisinopril: $p = 0.0856$, LSD). This decrease in cyclic LD is caused by the drop in pulse pressure, which is more important in the lisinopril group.

Figure XII.11.: Change in lumen diameter and intima-media thickness using ACE inhibitors (ACEi) and calcium blockers (CaBl) in literature. The vertical axis shows the study considered. Between brackets: the number of weeks follow-up. For each study, the top bar is the baseline (light grey), the middle bar is the result after treatment (dark grey) and the final bar is the difference (black). Data comes from studies by Boutouyrie,[36] Girerd,[116] Stanton,[302] Ariff,[12] Terpstra[326] and Simon[286] and are sorted according to the follow-up time. Baseline and end-study values were not stated by Stanton.[302]

IMT, IMA and IMT/LD   A change in LD will induce a change in IMT. The IMA can be calculated as the product of the IMT and the circumference. Changing the IMA or vessel wall mass involves vascular regression or hypertrophy which is a slow process (in the order of several weeks). It is therefore fair to assume that the IMA remains constant after a sudden pressure drop. The acute pressure drop will lead to drop in LD as mentioned earlier. When the LD decreases, the lumen circumference decreases as well, which means that the IMT has to increase if IMA is to be kept constant.

The decrease in blood pressure has an important impact on the vessel morphology in the long term as well. As explained by Laplace's law (section II.2.1, page 33), a decrease in blood pressure will lower the wall tension. In the long term, the IMT, which is exposed at smaller tensile stresses, will decrease since there is no need for a thick wall any more. All studies presented in Figure XII.11 show a decrease in IMT in long-lasting studies. Furthermore, both compounds have anti-hypertrophic effects, resulting in a decrease in myocard mass and vessel musculature.[163, 388]

Considering that this study was performed over a week, the long-term effects were not expected to occur and an increase in IMT was expected. Table XII.5 shows that the IMT indeed increases both in the CCA as in the bulb, both in diastole as in systole. The increase in IMT was the most significant (29 μm) with the amlodipine treatment (p = 0.0326, LSD). The IMA remained constant as assumed by the above reasoning. Since the LD decreased and the IMT increased, the IMT/LD ratio tended to increase (amlodipine: p = 0.0564; lisinopril: p = 0.0948, LSD).

Compliance   The compliance is estimated here as the change in cross-sectional CCA area divided by the pulse pressure (see also section II.3.2.1 on page 49). In literature, the effects of ACE inhibitors on arterial compliance have been widely investigated.[36, 116, 166, 167, 220] A very short term study (1-3 hours follow-up) conducted by Lage[167] sees a steep increase in compliance, suggesting that the arterial compliance is inversely related to the plasma angiotensin concentration. Unfortunately, Lage[167] did not provide a physiological explanation for this potential relation between ACE inhibitors and arterial compliance.

The long-term studies[36, 116, 166, 220] (6 months to 1 year) suggest a slight gain in compliance. This is mainly due to the drop in IMT which renders the vessels less stiff. Note that the variety in definitions used to quantify compliance renders it difficult to compare numerical values between studies.

In this study, a decrease in PP and 'diameter difference' was expected. What would happen with ratio of these two values was difficult to predict, but the results by Lage[167] suggest that important increases in compliance could be expected. Surprisingly, this study found that the compliance was unchanged using lisinopril (p = 0.9353, LSD). This discrepancy between our results and those of Lage[167] could be due to the difference in the definition of the compliance: $C = \frac{\pi \times LD_d}{2} \times \frac{LD_s - LD_d}{PP}$ (Lage) as opposed to equation II.8 (page 51). The compliance was recalculated using Lage's definition, but no different conclusions were drawn in comparison with the original definition (p = 0.9306, LSD). Another possible reason for the discrepancy is the fact that a different ACE inhibitor, enalaprilat, was used by Lage.[167] Moreover, Lage's results were registered after a few hours, whereas this study performed measurements after a week. A final reason for the differences found between Lage's study[167] and the present study is the fact that in Lage's study,[167] the compound was administered to patients with cardiac heart failure, whereas in the present study, young hypertensive subjects were examined.

Studies on the effect of calcium channel blockers on arterial compliance are very rare. Lafleche[166] finds an increase of arterial compliance after 12 and 16 weeks of treatment with a variety of calcium antagonists. He also states that the acute changes in compliance are minimal, and that the changes in compliance are mainly pressure-mediated and depend on the location of measurement. Van Merode[339] administered the calcium blocker Verapamil to 19 patients for 4 weeks and measured an increase in arterial compliance of 18% and 27% for respectively the left and right carotid artery. However, based on Lafleche's statements, the present study expected no change in compliance. This was confirmed by the results (p = 0.2175, LSD).

Distensibility and Young's Modulus The change in distensibility coefficient and Young's modulus are difficult to predict since studies investigating on the impact of anti-hypertensive compounds on the carotid wall's elasticity are lacking. This study found that both parameters did not change significantly with either regimen.

Wall Tension and Tensile Stress Wall tension is quantified by the product of the blood pressure and the lumen radius ($\frac{LD}{2}$). Since both values are expected to decrease for both compounds, the wall tension will decrease as well. The tensile stress (σ) is the wall tension divided by the IMT. Since the IMT is expected to increase acutely, σ will decrease. Bearing in mind
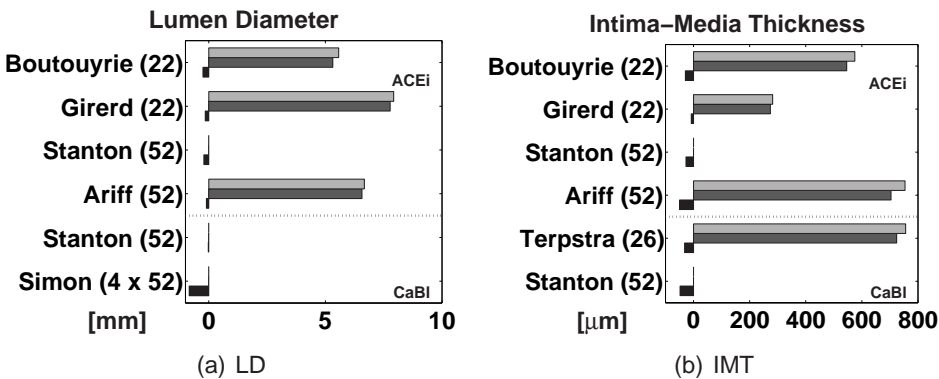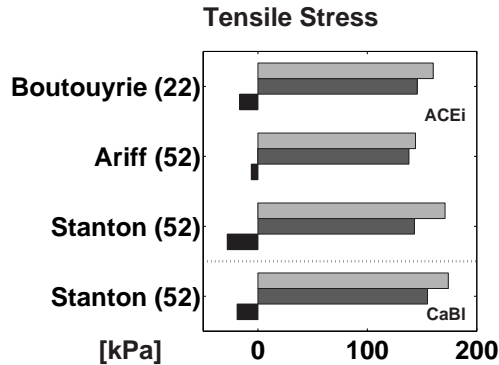
Tensile Stress

Figure XII.12.: Change in tensile stress using ACE inhibitors (ACEi) and calcium blockers (CaBl) in literature. The vertical axis shows the study considered. Between brackets: the number of weeks follow-up. For each study, the top bar is the baseline (light grey), the middle bar is the result after treatment (dark grey) and the final bar is the difference (black). Data comes from studies by Boutouyrie,[36] Ariff,[12] and Stanton[302] and are sorted according to the follow-up time. Baseline and end-study values were not stated by Stanton.[302]

that a vessel wall undergoing high tensile stress is prone to atherosclerosis,[34] it is easy to understand that the decrease in σ is a wanted effect of the drug. Figure XII.12 shows how important the decrease in σ was in studies by Boutouyrie,[36] Ariff[12] and Stanton.[302] The current results show decreases in diastolic and systolic wall tension and tensile stress with very high significance for the lisinopril treatment ($p<0.01$, LSD as opposed to $p<0.05$ for amlodipine), probably due to the higher pressure drops acquired with lisinopril.

XII.5.1.3. 3D Reconstruction parameters

The '3D reconstruction parameters' involve all parameters that require the 3D reconstruction of the carotid bifurcation for their quantification. This includes the mean arterial cross-sections and shapes, and the centreline parameters (planarity, linearity, tortuosity and bifurcation angles). To our knowledge, there have been no studies examining the change in 3D reconstruction parameters induced by anti-hypertensive compounds.

Mean area and Area ratio   Similar to the lumen diameter, one expects the average arterial cross-sectional area to decrease as a result of the pressure drop. In reality, the cross-sectional area remained unchanged throughout the study. See Figure XII.13 for a representation of all measurements. This result confirms what was found for the LD, where very small decreases with
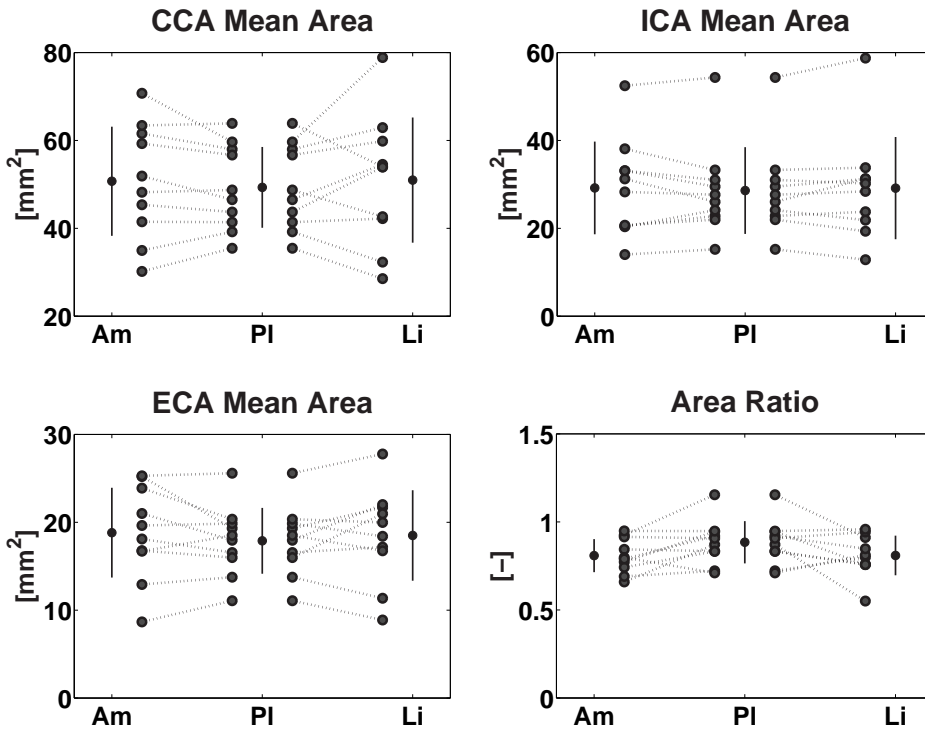
Figure XII.13.: Change in mean cross-sectional area and area ratio with both compounds. See Figure XII.8 (a) for a description of the images.

small significance were registered. Surprisingly, the area ratio, defined as $\frac{a_{ICA}+a_{ECA}}{a_{CCA}}$ where a stands for the cross-sectional area in the slice most proximal to the apex, drops approximately 0.075 with both compounds (amlodipine: p = 0.1513; lisinopril: p = 0.1625, LSD). This suggest that the CCA dilates more (or contracts less) than the ICA or ECA, probably due to (1) the fact that smaller arteries are more susceptible to systemic vasoconstriction (ACE inhibitor) or (2) the fact that the LD of smaller arteries are more sensitive to variations in extracellular calcium (calcium blocker).

Individual Shape Factor When a balloon is deflated, it loses its regular circular cross-sectional shape. The same applies for the cross-section of an artery. Mathematically, this means that the individual shape factor SF_i will decrease. This is confirmed by our findings, which include significant changes in CCA and ICA cross-sectional shape. This finding should, however, be treated with caution since the difference in mean SF_i is smaller than its variability found in part **B** of this work.
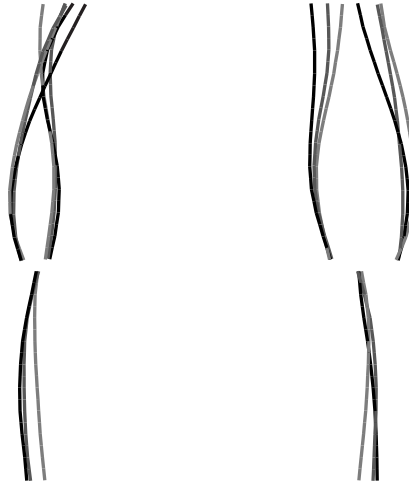
Figure XII.14.: Centrelines in subject 2 (MR scanned). Black: placebo scan; Dark grey: amlodipine scan; Light grey: lisinopril scan.

Centrelines   Figure XII.14 shows the carotid centrelines for subject 2 using the different compounds. The centrelines after each treatment were superimposed on each other using different shades of grey. Figure XII.14 illustrates a very good agreement between the centrelines. This agreement is quantified by the non-planarity, linearity, tortuosity and bifurcation angle, all of which do not change significantly (Table XII.6).

Summary for 3D reconstruction parameters   In general, the changes made on the overall carotid geometry by the anti-hypertensiva are minimal. This means that the geometry of the carotid bifurcation is robust to sudden pressure drops. It also means that any humoral or nervous reactions, initiated by the drugs and which may change the 3D geometry, take longer than one week to be effective.

XII.5.1.4. Flow parameters

The flow parameters are summarised in Table XII.7. They include blood flow rate, heart rate, Reynolds and Womersley numbers. Note that it is more common to discuss heart rate together with the pressure parameters, which are then catalogued as baseline haemodynamic parameters. Nevertheless, in this study, the impact of the heart rate is best noticeable on

the flow parameters, thus the heart rate and flow parameters are discussed simultaneously.

Heart Rate   A remarkable result from Table XII.7, is the fact that the heart rate increases with the amlodipine treatment, whereas it decreases with the lisinopril treatment (See also Figure XII.8 on page 316). This result seems to contradict literature[36, 116, 128, 166, 220, 231, 284] (Figure XII.15) which suggests that there should be no significant change in heart rate in either one of the used anti-hypertensives. For lisinopril, the ACE-inhibitor, the decrease in heart rate found here can be explained by the lack of excitation of the sympathetic nervous system when ACE is inhibited (see also section XII.1.2.2 where the effects of Angiotensin-II are elabourated). For amlodipine, the dihydropyridine (Table XII.3), there should be no change in heart rate since dihydropyridines do not interfere with the heart muscle. Despite all this, an increase in heart rate is measured with amlodipine in comparison with lisinopril (7.18 bpm, p = 0.0287, LSD).

Manzo[209] compared the effects of amlodipine and felodipine in 283 hypertensive men and found that amlodipine raised the heart rate significantly by 4.2 bpm. Grossman and Messerli[129] combined data from 63 studies in a total of 1252 hypertensive subjects on a treatment with a variety of calcium channel blockers. The effects of calcium channel blockers were divided into the effects of dihydropyridines and nondihydropyridines (see Table XII.1, page 299)), short- and long-acting compounds, and on the duration of treatment. Amlodipine is classified as a long-acting dihydropyridine. They found that in general, the dihydropyridines showed an increased heart rate in comparison with the nondihydropyridines, a constatation that agrees with the findings in the present study. Grossman and Messerli[129] pone that the increased heart rate, which is more evident in acute studies, is caused by *"the precipitous reduction in arterial pressure associated with a reflexive increase in sympathetic stimulation, heart rate, cardiac output, and left ventricular stroke work"*. This sympathetic reflex is started by the baroreceptors in the right heart, aorta and carotid bifurcation (carotid sinus reflex, see page 21). The reflex is more noticeable in short-acting calcium channel blockers (such as nifeldipine[383]) and there often causes an unwanted tachycardia[k].

One would expect this sympathetic reflex to occur for every pressure drop, whether it is induced by amlodipine or lisinopril, but this not present in pa-

---

[k]**tachycardia**: heart rate that is faster than normal
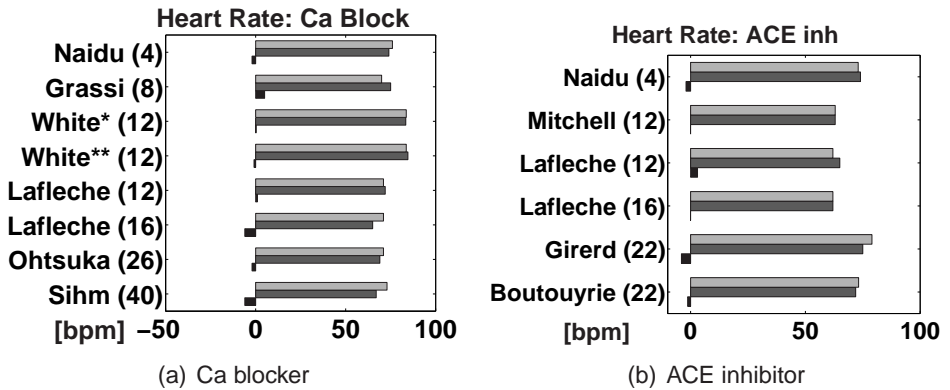
Figure XII.15.: Changes in Heart Rate (HR) using ACE inhibitors and calcium blockers in literature. The vertical axis shows the study considered. Between brackets: the number of weeks follow-up. For each study, the top bar is the baseline (light grey), the middle bar is the result after treatment (dark grey) and the final bar is the difference (black). Data comes from studies by Naidu,[231] Grassi,[128] Mitchell,[220] Lafleche,[166] Sihm,[284] Girerd,[116] Ohtsuka,[234] White[363] and Boutouyrie[36] and are sorted according to the follow-up time. White studied 2 calcium channel blockers: amlodipine (*) and nisoldipine (**).

tients on lisinopril treatment. This is due to the suppression of sympathetic activity by all ACE inhibitors.

Flow Rate and dimensionless parameters Thus, the reason for a dis- crepancies between the results for amlodipine and lisinopril lie in the fact that the reflexive increase in sympathetic tonus is suppressed with lisinopril, but unaffected by amlodipine. This explains the differences in heart rate, but also the differences in flow rate: the CCA flow rate is on average 1.5 ml/s higher (p = 0.0067, LSD) with the amlodipine treatment in comparison with lisinopril (See Table XII.7). These systemic effects are reflected in the Reynolds and Womersley numbers (equations II.28 and II.29 on page 64) which are higher for the amlodipine regimen in all branches. This means that lisinopril yields the flow more laminar (greater reduction in Reynolds numbers) and less disturbed (Womersley number kept lower than in am- lodipine treatment, Table XII.7). Both the effect on the Reynolds and on the Womersley number favour the choice for lisinopril in patients with a stenosis: the drop in these dimensionless flow parameters will decrease fluid forces on the stenosis. On the other hand, the amlodipine treatment ensures blood flow to the brain, which can be used to fight dizziness. Furthermore, a higher blood flow will increase WSS which is an atheroprotective situation.

XII.5.1.5. CFD parameters

'CFD parameters' are parameters which could not have been obtained without simulating the blood flow in the 3D geometry obtained from the *in vivo* scans. They include V_{MAX}, WSS, OSI, WSSG, WSSAG and the coordinates of the gravity point found on 'Time and Area' images (Figure XII.7): the horizontal distance from the red line at 0.4 Pa ('DIST from 0.4') and the vertical distance from the horizontal axis ('steadiness'), both in the entire bifurcation as well as in the bulb. Results are summarised in Tables XII.9 to XII.13.

It should not surprise that, with changes in the flow rate and minor changes in geometry, the changes in velocity parameter are highly correlated with the changes in flow rate. The same reasoning can be made for the WSS: the WSS is higher with the use of amlodipine, caused by the higher flow rate. This feature is most significant considering the mean WSS ('WSS ALL', p = 0.0038, LSD), 'Dist from 0.4' (p = 0.0149, LSD), 'Dist from 0.4 BULB' (p = 0.0248, LSD), 'WSS inner ICA' (p = 0.0169, LSD) and the 'area with high WSS' (p = 0.0283, LSD), suggesting that the WSS is lowered in the entire bifurcation, but it is the apical region that undergoes the most important changes. This is illustrated in Figure XII.9 where, for the three reported subjects, WSS is higher using amlodipine than under lisinopril treatment. Similar findings were made for the WSSGs (Table XII.11) and WSSAG (Table XII.13): the values found with the amlodipine treatment are higher than the values found with lisinopril, caused by the discrepancy in flow and/or heart rate. This effect is not noticeable in the WSSGt (Table XII.12), which is a parameter that appears to be more dependent on the geometry than on the flow rate.

The OSI (Table XII.10) increases slightly with both treatments. This change is best noticeable in the outer ICA (amlodipine: p = 0.0176; lisinopril: p = 0.0204, LSD), i.e. in the region where the highest OSI values are expected. This result suggests that the antihypertensive treatment destabilises endothelial function, albeit slightly.

XII.5.2. The link to Stanton's study[302]

One of the aims of this study is to explain the results from the study by Stanton summarised in Figure XII.5. It was reported that, after a follow-up of a year, hypertensive patients showed similar decrease in blood pressure us-

ing either an amlodipine or lisinopril regimen. Morphologically, the carotid vessel wall had changed in different ways. The amlodipine group showed equal luminal diameter (LD), thinner IMT and decreased IMA when compared to the baseline data. In the lisinopril group, the LD decreased, the IMT showed a less important thinning whereas the IMA had a decrease of the same order as in the amlodipine group.

Section XII.1.2 explained how both calcium channel blockers and ACE inhibitors lower the *blood pressure*. The effect of a sustained pressure drop is a drop in LD (analogy with the deflation of a balloon) and a drop in IMA (due to reduced wall tension). This explains the long-term drop in IMA and IMT occurring with both compounds, and why the LD should have decreased. Section XII.1.2 also explains how both compounds have *anti-hypertrophic* effects. This results in an additional long-term decrease in IMT and IMA.

The problem with the above reasoning lies in the fact that it does not explain the differences spotted between the amlodipine and lisinopril long-term morphology, i.e. the smaller IMT and higher LD in the amlodipine group is not explained by pressure changes or anti-hypertrophic effects.

The hypothesis at the beginning of this study was that the *acute effects on local haemodynamics* are responsible for the differences in long-term carotid morphology. Another hypothesis for the larger LD using calcium blockers could have investigated the fact that calcium blockers have more relaxing effects on the vascular muscles. This study was aimed at quantifying the change in shear stresses in the carotid arteries induced by amlodipine or lisinopril. The results show that the WSS is higher in the amlodipine than in the lisinopril regimen. The endothelium reacts to high WSS by releasing nitric oxide (NO) as explained in section II.2.3.2 (page 41). NO has a relaxing impact on the vascular smooth muscle cells. The consequent vasodilatation causes the WSS to decrease, which is the aim of the NO release. This way, the shear forces acting on the endothelium are regulated through the endothelium itself. Bearing in mind that the WSS is higher for the amlodipine treatment, it is straightforward to pone that the differences in long-term LD between amlodipine and lisinopril are due to the endothelial reflex to WSS: the higher WSS with amlodipine treatment releases NO, dilates the lumen and causes, with preservation of wall mass, a decrease in IMT. Note that NO has dilating as well as anti-hypertrophic effects, which gives further insight on the differences in IMT between amlodipine and lisinopril.

XII.6. Summary

In this chapter, the combination of MRI and CFD as well as the combination of 3DUS and CFD were used to perform a pharmacological study investigating the impact of anti-hypertensive drugs on carotid haemodynamics. Section XII.1.2 details the cascade of events caused by calcium channel blockers and ACE inhibitors, the two types of anti-hypertensiva used in this study. Ten subjects were submitted to a double-blind, placebo controlled, randomised, 3 way crossover clinical trial. The protocol involved one week of treatment with amlodipine (calcium blocker), lisinopril (ACE inhibitor) or placebo, followed by a wash-out of a week. Pressure, geometry, flow and vessel wall parameters were assessed after every treatment. Of the 10 subjects, 8 subjects were scanned using TOF MRI and 2 claustrophobic subjects were assessed with 3DUS.

The results seem to indicate that the acute pressure drop with ACE inhibitors is more important than with calcium blockers. Both compounds induce a slight decrease in LD, an increase in IMT, a conservation of IMA, a drop in wall tension and tensile stress as a result of the acute pressure drop. Compliance, distensibility and Young's modulus remain unchanged. Similarly, the period of 1 week appears to be too short for major geometry changes to occur.

Although both compounds are not intended to influence the heart rate, there was a distinct difference between the lisinopril and the amlodipine treatment. Lisinopril suppresses sympathetic activity and therefore decreases the heart rate. On one hand, amlodipine slows down pacemaker activity but on the other hand, it does not suppress the sympathetic reflex aimed at restoring the blood pressure level, causing a nett increase in heart rate. The nett result of both effects resulted in an increased heart and carotid blood flow rate. This means that amlodipine maintains the blood supply to the brain, causing less dizziness than with other anti-hypertensives. The higher blood flow rate in turn resulted in increased Reynolds and Womersley numbers, and finally increased WSS, OSI, WSSGs and WSSAG values.

The long-term effects of lisinopril include a decrease in IMT, IMA and LD. Amlodipine causes a stronger drop in IMT, an equal change in IMA and an unchanged LD. The sustained pressure drop and anti-hypertrophic effects of these compounds explain the decrease in IMT, IMA and LD. The LD decrease due to the pressure drop must be compensated by an equal increase of LD with the amlodipine treatment. In this study, it is suggested that the

higher WSS observed with the present acute amlodipine treatment, causes a reflexive NO release which dilates the LD. Simultaneously, the NO release could be stretching the IMT and intensifying anti-hypertrophic behaviour.

Part D.

Future work & Summary

XIII. Restrictions and Future work

The technique, as it is now available, still has a number of drawbacks when it is used for applications other than the study of blood flow patterns in the carotid bifurcation with no stenosis.

3DUS imaging   The biggest disadvantage of the imaging protocol in 3DUS, is that it does not allow making images of the carotid when it is hidden by the jaw-bone. Three solutions to this problem have been postulated.

1. *Extrapolation*.   Instead of ending the geometrical model at the jaw-bone, the model may be extended by extrapolating the last segment of the ICA and/or the ECA. This extrapolation can be linear.[17] This technique assumes that the area of the extended vessel does not change downstream.

2. *Longitudinal Rotation*. By using the free-hand 3DUS in different scanning planes, a *longitudinal* cross-sectional image can still be acquired. Such an image shows a longitudinal cross-section of the ICA from the bifurcation apex towards the distal end of the ICA, i.e. more distal than possible with the in-plane images. This cross-section can be used to extract a longitudinal contour along the vessel wall. This contour can then be rotated to reconstruct the ICA beyond the last segment acquired with conventional (in-plane) 3DUS.

3. *Longitudinal Reconstruction*. As in the previous method, a longitudinal segmentation could be performed on the longitudinal image. In this case, instead of only reconstructing one longitudinal vessel wall component, more components could be extracted and assembled to form an extended ICA.

The further advantage of using the longitudinal image is that it provides an estimate of the IMT along the entire bifurcation. This eliminates the errors

related to the introduction of the sixth-degree polynomial (see Figure VII.6 on page 168) used to estimate the IMT in the bifurcation.

Another important disadvantage of US, is that it cannot image carotid bifurcations with calcified plaque because the plaque will block all ultrasound waves. In those cases, and in people with carotids hidden by the jaw-bone, MRI is today still the imaging technique of choice.

MRI Segmentation   The MRI automatic segmentation program makes certain assumptions on the area ratios between proximal and distal CCA, between proximal ICA and distal CCA, between proximal CCA and ECA, and between proximal and distal ICA. For stenosed subjects, these assumptions can no longer be sustained. In early attempts, these ratios have been changed. The first results show that the operator intervention rate, which is roughly defined as the number of automatically segmented slices which need to be altered by the image processing operator and the total number of slices, increases to an extent which questions the routine use of automatic segmentation for stenosed subjects. A number of solutions have been put forward:

1. *Changes to the segmentation program.* Right now, the region growing method, which is intended to generate an initial segmentation, stops iterating when the area of the region exceeds a certain threshold A_g, preset by the operator (see page 108, section VI.2.1 on the region growing method). Instead, the iteration could stop when the difference in region found between two iterations, exceeds a certain threshold. This technique has been successful for TOF images of healthy volunteers before.[196]

2. *Functional smoothing.* In this solution, the stenosed sections are segmented on transverse sections but changed afterwards using a different geometry measurement. The diameter of the lumen at the stenosed cross-section would be measured on **MIP**'s or maximum intensity projections, similar to projections made by X-ray imaging. An example of a MIP acquired with MRI is given in Figure XIII.1. On those MIP's, the diameter of the carotid at the site of the transverse sections can be measured as done in Figure XIII.1 between the two arrowheads. The initial segmentation performed using the transverse cross-sections can now be changed using the smoothing equation VI.2 (page 114):
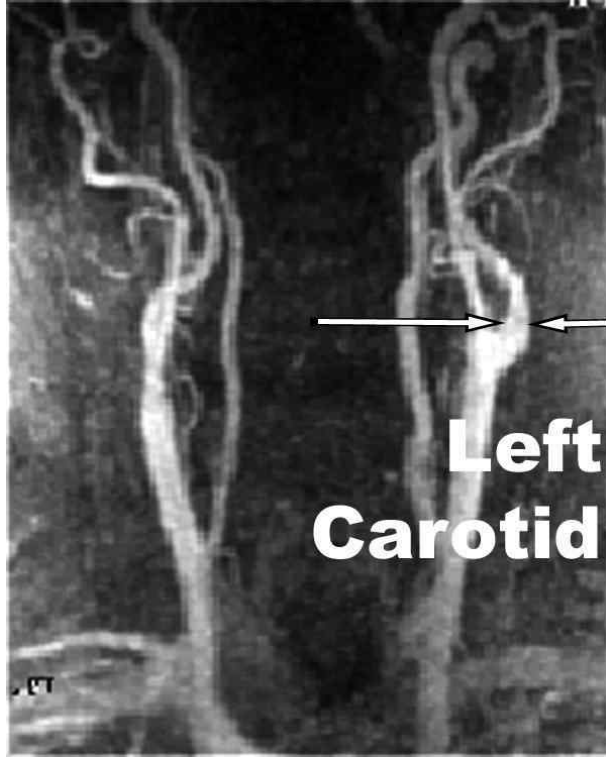
Figure XIII.1.: Example of a maximum intensity projection or MIP. The distance between the arrow tips can be used as an input in the smoothing algorithm.

$$\overrightarrow{P_{new}} \;\; = \;\; \left(\overrightarrow{P_{old}} - \overrightarrow{C_{old}}\right) \times \sqrt{a_{ratio}} + \overrightarrow{C_{new}} \qquad \text{(XIII.1)}$$

Since the functional smoothing as defined here only changes the cross-sectional area and not the centrelines, $\overrightarrow{C_{new}} = \overrightarrow{C_{old}}$. a_{ratio} would be calculated as the ratio between the cross-sectional area deduced from the diameter measurement from the MIP (Figure XIII.1) and the old cross-sectional area found after the initial segmentation.

3. *Carotid reconstruction from MIP's.* In this solution, the 3D carotid geometry is no longer reconstructed from serial transverse cross-sections, but from the MIP.

3DUS Segmentation Although it has been shown in section VII.4.3 that the operator-dependence due to manual segmentation is minor, the process of segmentation of B-mode images remains very labour-intensive. Mao[210]

and Gill[114] suggested that the segmentation could be done automatically, but they admit that the current level of image quality is not satisfactory. If the US image could be segmented automatically, either by improvements in image quality or segmentation procedure, this would induce a serious improvement of the applicability of 3DUS-based CFD since it would decrease the manual labour in the order of an hour.

3D Reconstruction using MRI The 3D reconstruction program is very flexible. This has been proven by the ability to reconstruct highly tortuous carotid bifurcations such as the ones in Figure VI.22 (page 143). Nevertheless, the program has illustrated a number of flaws:

1. *Flaws in Smoothness*. In some cases, the smoothness at the bifurcation is not satisfactory. It is not the smoothness at site of the apex that gives rise to problems, but at the interface between CCA and its branches or at the border between inner and outer ICA or ECA (see Figure VII.8, page 173 for a definition of 'inner' and 'outer'). This effect is clear in Figure VII.13 (m) (page 183), where lines of high WSS are visible. These lines originate from the points B_1 and B_2, i.e. the points where the three carotid arteries come together (see Figure VI.13, page 119, for a definition of the carotid feature points). In order to eliminate those effects in the current studies, the haemodynamic wall parameters were filtered using 3x3 median filtering, i.e. the values of e.g. the WSS in a certain point on the vessel wall was replaced by the median of the 9 values formed by the WSS of its 8 neighbours and its initial WSS value. In a smoother 3D reconstruction, this filtering would be obsolete.

   A number of solutions have been put forward:

   a) *Longitudinal spline fitting*. In the present situation, the longitudinal splines consist of piecewise linear segments. Fitting longitudinal cubic splines through the nodes of the current lines will smooth the geometry. This solution has a number of drawbacks. First, it will change the geometry at sites where no change is needed. Second, it only deals with the smoothness at the intersection of CCA and its branches, but does not assess the problem at the intersection of inner and outer ICA or ECA. Third, it could make neighbouring longitudinal splines cross each other, especially when there is a small cross-section and the longitudinal

splines thus all lie close to each other. Nevertheless, longitudinal smoothing is a common procedure in 3D reconstructions and if its drawbacks could be eliminated, it could be a good solution.

b) *Local smoothing*. This solution has been used for the smoothing at the apex. For the reader's recollection, at the apex a parabola was fitted through the apex and two points (B_1 and B_2) on the most distal CCA slice (see Figure VI.13, page 119). This parabola was the (smooth) border between ICA and ECA. For the CCA/ICA and CCA/ECA intersection, something similar can be done. Two examples are given below. In the first example, another parabola can be fitted between points C, B_1 and B_2 (see Figure VI.13, page 119, for a definition of the carotid feature points). This solution denies some data acquired in the most distal CCA slice. A second example fits a longitudinal smoothing spline through the most distal parts of the CCA and the proximal ICA or ECA *locally*, which is a difference with the longitudinal spline fitting explained in the previous section. This generates 1 longitudinal spline per point on the CCA contour. Each of this splines goes through the plane intersecting between CCA and ICA or ECA once. The line formed by these intersecting points can be used to fit a smoothing parabola. The intersections of the longitudinal splines can now be shifted towards the parabola, resulting in a smoother geometry.

c) *Circumferential smoothing*. The two previous solutions do not change the geometry at the intersection between inner and outer branch. To this purpose, the circumferential instead of the longitudinal splines could be smoothed. A circumferential spline is formed by every n^{th} point of the longitudinal spline.

2. Early tests have shown that the 3D reconstruction of stenosed arteries can be problematic when the most proximal ICA and ECA slice do not overlap with the most distal CCA slice. In this case, the vertical plane through the line $\overrightarrow{M}$ which separates ICA and ECA (see Figure VI.13 (b) on page 119) may not intersect with the most distal CCA slice (Figure VI.13 (c)). In this case, no intersection between CCA and either ICA or ECA can be defined. A possible solution to this problem is to define the intersection plane between ICA and ECA as the plane through $\overrightarrow{M}$ and two particular points on the most distal CCA contour as opposed to the present definition (through $\overrightarrow{M}$ and the I/S axis). The *particular* points on the CCA contour could be those which (1) divide the considered CCA cross-section into two equal areas and (2) can be connected by $\overrightarrow{M}$. This solution has an important drawback: since

the intersecting plane is no longer parallel with the I/S axis, it will no longer bisect the other intersecting planes (between CCA and ICA or ECA) and symmetry is lost. As a consequence, the skewness of the cells which will be fitted using the intersecting planes as a scaffold will increase. This decreases mesh quality.

3D Reconstruction using 3DUS   The 3D reconstruction program used in this study is very user-friendly, yet it shows two important flaws. Both flaws relate to the fact that longitudinal splines are being fitted and smoothed using cubic smoothing splines.

- The reconstruction procedure contains a step in which the longitudinal splines are smoothed using cubic smoothing splines (the same technique as explained in point 1a on page 343). It is important to realise that some smoothing splines originate in the CCA and end in the ICA or ECA, other splines originate in the apical region and end in the ICA or ECA. These are two separate sets of splines. When they are smoothed, it occurs that the splines of one set intersect with splines of the other set, or that the splines of one set do not have a smooth transition to the other set. This makes it impossible to generate a volume from these splines. In the cases where this intersection occurred, smoothing was kept to a minimum. Future version of the 3DUS program should question the use of longitudinal smoothing, and maybe introduce the centreline and area smoothing as performed with MRI data.

- The longitudinal splines that form the output of the 3DUS program, are polynomial (cubic) interpolations between the smoothed points (or nodes). The problem with polynomial interpolations is that it can generate high-frequency side-effects, i.e. unrealistic twists induced by the fact that the polynomial is forced to go through certain end-points. The importance of the side-effect is related to the distance between the nodes. Again, it is not possible to generate a volume from such splines. The current 3DUS reconstruction program has therefore been altered by increasing the number of nodes between which the polynomial fitting is to be performed. This reduced the distance between the nodes, and thus decreased the effect of the polynomial side-effect markedly. This is obviously not a final solution to the problem. The next version of the 3DUS reconstruction program should investigate the need for polynomial interpolation and possibly shift towards piecewise linear interpolation, which is used in the MRI reconstructions.

Meshing Program   For future use, the restriction to building structured hexahedral meshes is too limiting. In our lab, a program has been written by Ir. S. Vermeersch (unpublished) which allows to output the current 3D reconstructions to a format readable by all commercial mesh generators. This makes it possible to fit unstructured meshes in the 3D volumes created by the programs written for this thesis.

Computational Details   The current technique has been developed for studying the shear stresses in the carotid arteries without stenoses. It is plausible that the computational details should be changed if the technique is to be used in other circumstances, other applications, or at another accuracy.

- It is very likely that *turbulence* will occur in stenosed subjects. Several studies[311, 341] have investigated the use of turbulence models for blood flow simulation.

- In the present studies, the viscosity has been chosen as done by Buchanon.[42] In true life, the viscosity shows large variability and should therefore be estimated individually (e.g. using the haematocrit as done by Samijo[270]). Because this involves invasive blood tests, viscosity measurements have not been performed here. The effect of differences in viscosity values and viscosity models has been described in section VIII.2 (page 228).

- Currently, all simulations have been performed in carotid models with rigid walls. The introduction of compliant walls increases the realism of the computer model, but simultaneously increases the required processing time (approximately by a factor 10). Currently, it is therefore not possible to simulate the amount of simulations performed in this study within a reasonable time-scale. The effect of compliant walls has been studied by Zhao[384] and discussed in section VIII.1.3. If compliant walls would be used, there could be a gain in model accuracy comparable to the differences spotted in Zhao's studies.[384, 385, 387]

- Recent studies have expanded the output of a simulation from shear stresses to the LDL transport[346, 347] or blood/plasma flow through wall. These are new diagnostically important parameters which, to a different extent, all require changes to the computational details of the simulation as presented here.

XIV. Summary

XIV.1. Introduction

When this study was started in 2000, it was becoming increasingly clear that the combination of medical imaging and computational fluid dynamics (CFD) might be a technique which would allow estimation of *in vivo* shear stress using non-invasive techniques.[34, 197, 219] Despite early success, there was a substantial scepticism towards the achievable *in vivo* accuracy. Considering the amount of pathologies initiated or enhanced by certain values of shear stresses, and the effect of these pathologies on westernised societies, the quantification and increase of the accuracy of the technique was highly necessary. Before any studies could have been performed using image-based CFD, its reproducibility, accuracy and operator dependency needed to be investigated. Consequently, the first part of this thesis dealt with image-based CFD as a technique.

XIV.2. Establishing the technique

XIV.2.1. Magnetic Resonance Imaging

Magnetic Resonance Imaging (MRI) was traditionally considered the 'gold standard' in the choice of an imaging technique for combination with CFD. The process of extracting a 3D geometry of a carotid bifurcation was automated. In this context, it is noteworthy to mention that the segmentation, reconstruction and meshing of a carotid bifurcation imaged with MRI takes now less than 2 hours of which an operator is only required for 30 minutes, whereas previously it took several hours of an operator's time. The accuracy of MRI-based CFD was estimated using a carotid phantom, and the reproducibility was quantified using 8 healthy subjects. A final study compared two types of MRI protocols, black blood (BB) and time-of-flight (TOF) and

concluded that TOF MRI resulted in faster 3D reconstructions which were of superior quality.

XIV.2.2. Three-dimensional Ultrasound

Simultaneously, three-dimensional ultrasound (3DUS) was investigated as imaging technique of choice for image-based CFD. Again, the process of extracting 3D geometries suitable for CFD modelling was automated, based on ground-levelling work by Barratt[20] and Augst.[16] Although segmentation of B-mode ultrasound images still happens manually, the time-gain achieved here was in the order of several hours. Similar to the studies performed for MRI-based CFD, the accuracy of 3DUS was analysed using the same phantom used for assessing the accuracy of MRI. Subsequently, nine subjects participated in a study aimed at quantifying the reproducibility of shear stress measurements using 3DUS-based CFD. Due to the higher frequency of operator intervention for 3DUS in comparison with MRI, the operator dependency was quantified using an *in vivo* variability study in which 4 imaging operators and 3 segmenting operators participated. Overall, it was found that the accuracy and reproducibility of 3DUS-based CFD was in the same order of magnitude of MRI-based CFD.

A comparative study showed that MRI can be replaced by 3DUS without loss of accuracy. This conclusion makes it possible to replace expensive MRI investigations by the relatively cheap 3DUS alternative available in many hospitals.

XIV.2.3. Computational Details

With the eye on increasing realism, accuracy and reliability of image-based CFD, several studies investigating a number of computational details were undertaken. These studies resulted in suggestions on the use of both MRI and Doppler Ultrasound velocity measurements for the model boundary conditions. Furthermore, the effect of the use of viscosity (models) and heart rate changes on the overall shear stress distribution was investigated. Following these studies, guidelines for the setup of the most realistic CFD model were suggested.

XIV.3. Clinical Applications

Once the accuracy of image-based CFD was known, the applications were queuing up. Within the time-limit set for this thesis, two studies were finished.

A first study investigated the changes in carotid geometry and flow with head turns. It was concluded that the centrelines changed substantially from one head position to another. Together with the changes in geometry, there was a significant change in carotid blood flow rate. The two things together induced important changes in shear stress patterns.

A second study investigated the effect of two anti-hypertensive drugs in an acute, randomised, double blind, three-way cross-over study. The technique showed higher shear stresses with one of the compounds. This finding managed to relate long-term changes in carotid morphology with the acute changes measured with image-based CFD.

These two studies illustrated that the *in vivo* applications of this technique are no longer a distant dream, but have been successfully fulfilled.

Bibliography

[1] **A. Salih, Computational Fluid Dynamics**, Available at: http://www.sali.freeservers.com/engineering/cfd/, Accessed January 6, 2004.

[2] **Abrahams P**, *The Altas of the Human Body*. San Diego, CA: Thunder Bay Press, 2002.

[3] **AEATechnology**, *CFX-4.4 Programming and Operating Manual*, 1999.

[4] **Affeld K, Goubergrits L, Fernandez-Britto J, and Falcon L**, Variability of the geometry of the human common carotid artery. A vessel cast study of 31 specimens. *Pathology Research and Practice* 194: 597–602, 1998.

[5] **Agrawal Y, Talbot L, and Gong K**, Laser Anemometer Study of Flow Development in Curved Circular Pipes. *J Fluid Mech* 85: 497–518, 1978.

[6] **allrefer.com, Health, Diseases & Conditions, Stroke Secondary to Carotid Stenosis**, Available at: http://health.allrefer.com/health/stroke-secondary-to-carotid-stenosis-symptoms.html, Accessed January 4, 2004.

[7] **American Heart Association**, *Heart Disease and Stroke Statistics - 2003 Update*. Dallas, Tex.: American Heart Association, 2003.

[8] **Amersham Health, Medcyclopedia, carotid dissection**, Available at: http://www.amershamhealth.com/medcyclopaedia/Volume%20VI%201/DISSECTION%20ARTERIAL.asp, Accessed January 4, 2004.

[9] **Amersham Health, Medcyclopedia, Colour Doppler sonography**, Available at: http://www.amershamhealth.com/medcyclopaedia/Volume%20I/colour%20Doppler%20sonography.asp, Accessed January 21, 2004.

[10] **Amersham Health, Medcyclopedia, Pulsed Doppler ultrasound**, Available at: http://www.amershamhealth.com/medcyclopaedia/Volume%20I/pulsed%20Doppler%20ultrasound.asp, Accessed January 21, 2004.

[11] **Araim O, Chen AH, and Sumpio B**, Hemodynamic Forces: Effects on Atherosclerosis. *New Surgery* 1: 112–115, 2001.

[12] **Ariff B, Stanton A, Barratt D, Augst A, Glor F, Poulter N, Sever P, Xu Y, Hughes A, and Thom SA**, Comparison of the effects of antihypertensive treatment with angiotensin II blockade and beta-blockade on carotid wall structure and haemodynamics: protocol and baseline demographics. *Journal of the Renin Angiotensin Aldosterone Sys tem* 3: 116–122, 2002.

[13] **Ariff BB, Zambanini A, Mayet J, Hughes AD, and Thom SM**, Intima-medial area: A more robust method than intima media thickness for analysing non-cardiac gated common carotid images. *Circulation* 102: 3525, 2000.

[14] **Arizona Governor Janet Napolitano, Governor's Nursing Shortage Task Force Minutes**, Available at: http://www.governor.state.az.us/nurse/minutes.cfm, Accessed January 4, 2004.

[15] **Augst A, Glor F, Ariff B, Crowe L, Firmin D, Hughes A, Thom S, and Xu X**, Flow boundary conditions for CFD models in human carotid artery bifurcations: Comparison of Doppler ultrasound and MRI. *Journal of Biomechanical Engineering*, unpublished.

[16] **Augst AD, Barratt DC, Hughes AD, Glor FP, Thom SAM, and Xu XY**, Accuracy and Reproducibility of CFD predicted Wall Shear Stress using 3D Ultrasound Images. *Journal of Biomechanical Engineering Transactions of the ASME* 125: 218–222, 2003.

[17] **Augst AD, Barratt DC, Hughes AD, Thom SAM, and Xu XY**, Various issues relating to CFD simulations of carotid bifurcation flow based on models reconstructed from 3D Ultrasound images. *Journal of En gi neer ing in Med i cine Proceedings of the institue of Mechanical Engineers Part H* 217: 393–403, 2003.

[18] **Bakker SJL and Gans ROB**, About the role of shear stress in atherogenesis. *Cardiovascular Research* 45: 270–272, 2000.

[19] **Bakker SJL, Ijzerman RG, Teerlink T, Westerhoff HV, Gans ROB, and Heine RJ**, Cytosolic triglycerides and oxidative stress in central obesity: the missing link between excessive atherosclerosis, endothelial dysfunction, and beta-cell failure? *Atherosclerosis* 148: 17–21, 2000.

[20] **Barratt DC**, *Quantification of carotid disease using Three-Dimensional Ultrasound Imaging*. Ph.D. thesis, London University, 2002.

[21] **Barratt DC, Ariff BB, Humphries KN, Thom SAM, and Hughes AD**, Reconstruction and Quantification of the Carotid Artery Bifurcation from 3D Ultrasound Images. *IEEE Trans Med Imaging* , In press (May Edition), Manuscript #TMI-2003-0475.

[22] **Barratt DC, Davies AH, Hughes AD, Thom SA, and Humphries KN**, Accuracy of an electromagnetic three-dimensional ultrasound system for carotid artery imaging. *Ultrasound in Medicine and Biology* 27: 1421–1425, 2001.

[23] **Basombrio FG, Dari EA, Buscaglia GC, and Feijoo RA**, Numerical experiments in complex haemodynamics flows. Non-Newtonian effects. In *XI Congress on Numerical Methods and Their Applications ENIEF*, San Carlos de Bariloche, Argentina, 2000.

[24] **Berg S, Cole P, Hoffstein V, and Haight JSJ**, Upper airway pressures in snorers and nonsnorers during wakefulness and sleep. *J Otolaryngol* 30: 69–74, 2001.

[25] **Bergeron P, Carrier R, Roy D, Blais N, and Raymond J**, Radiation-Doses to Patients in Neurointerventional Procedures. *American Journal of Neuroradiology* 15: 1809–1812, 1994.

[26] **Berkeley University, Types and Structures of Arteries**, Available at: http://mcb.berkeley.edu/courses/mcb135e/arteries.html, Accessed January 4, 2004.

[27] **Bharadvaj BK, Mabon RF, and Giddens DP**, Steady Flow in a Model of the Human Carotid Bifurcation .1. Flow Visualization. *Journal of Biomechanics* 15: 349–362, 1982.

[28] **Biller J and Thies WH**, When to operate in carotid artery disease. *American Family Physician* 61: 400–406, 2000.

[29] **Bladin CF, Alexandrova NA, Murphy J, Alexandrov AV, Maggisano R, and Norris JW**, The clinical value of methods to measure carotid stenosis. *International Angiology* 15: 295–299, 1996.

[30] **Bland JM and Altman DG**, Measuring agreement in method comparison studies. *Stat Methods Med Res* 8: 135–160, 1999.

[31] **Blann AD, Kirkpatrick U, Devine C, Naser S, and McCollum CN**, The influence of acute smoking on leucocytes, platelets and the endothelium. *Atherosclerosis* 141: 133–139, 1998.

[32] **Blood count**, Available at: http://www.chclibrary.org/micromed/00040090.html, Accessed April 22, 2004.

[33] **Botnar R, Rappitsch G, Scheidegger MB, Liepsch D, Perktold K, and Boesiger P**, Hemodynamics in the carotid artery bifurcation: a comparison between numerical simulations and in vitro MRI measurements. *Journal of Biomechanics* 33: 137–144, 2000.

[34] **Bots ML, Hofman A, and Grobbee DE**, Increased common carotid intima-media thickness - Adaptive response or a reflection of atherosclerosis? Findings from the Rotterdam study. *Stroke* 28: 2442–2447, 1997.

[35] **Bots ML, Mulder PGH, Hofman A, Vanes GA, and Grobbee DE**, Reproducibility of Carotid Vessel Wall Thickness Measurements - the Rotterdam Study. *Journal of Clinical Epidemiology* 47: 921–930, 1994.

[36] **Boutouyrie P, Bussy C, Hayoz D, Hengstler J, Dartois N, Laloux B, Brunner H, and Laurent S**, Local pulse pressure and regression of arterial wall hypertrophy during long-term antihypertensive treatment. *Circulation* 101: 2601–2606, 2000.

[37] **Boutouyrie P, Germain DP, Tropeano AI, Laloux B, Carenzi F, Zidi M, Jeunemaitre X, and Laurent S**, Compressibility of the carotid artery in patients with pseudoxanthoma elasticum. *Hypertension* 38: 1181–1184, 2001.

[38] **Bovendeerd PHM, Vansteenhoven AA, Vandevosse FN, and Vossers G**, Steady Entry Flow in a Curved Pipe. *J Fluid Mech* 177: 233–246, 1987.

[39] **Brands PJ, Hoeks APG, Hofstra L, and Reneman RS**, A Noninvasive Method to Estimate Wall Shear Rate Using Ultrasound. *Ultrasound in Medicine and Biology* 21: 171–185, 1995.

[40] **Brands PJ, Willigers JM, Ledoux LAF, Reneman RS, and Hoeks APG**, A noninvasive method to estimate pulse wave velocity in arteries locally by means of ultrasound. *Ultrasound in Medicine and Biology* 24: 1325–1335, 1998.

[41] **British Medical Ultrasound Society, History of Ultrasound**, Available at: http://www.bmus.org/history_of_ultrasound.htm#med, Accessed January 21, 2004.

[42] **Buchanan JR and Kleinstreuer C**, Simulation of particle-hemodynamics in a partially occluded artery segment with implications to the initiation of microemboli and secondary stenoses. *Journal of Biomechanical Engineering Transactions of the ASME* 120: 446–454, 1998.

[43] **Buchanan JR, Kleinstreuer C, and Comer JK**, Rheological effects on pulsatile hemodynamics in a stenosed tube. *Comput Fluids* 29: 695–724, 2000.

[44] **Cademartiri F, Mollet N, Nieman K, Krestin GP, and de Feyter PJ**, Neointimal hyperplasia in carotid stent detected with multislice computed tomography. *Circulation* 108: E147–E147, 2003.

[45] **Caro C, Fitz-Gerald J, and Schroter R**, Atheroma and Arterial Wall Shear observation, Correlation and Proposal of a Shear Dependent Mass Transfer Mechanism for Atherogenesis. In *Proceedings of the Royal Society*, London: JSTOR, 1971, vol. 177 of *Series B, Biological Sciences*, pp. 109–133.

[46] **Caro CG, Doorly DJ, Tarnawski M, Scott KT, Long Q, and Dumoulin CL**, Non-planar curvature and branching of arteries and non-planar- type flow. *Proc R Soc London Ser A Math Phys Eng Sci* 452: 185–197, 1996.

[47] **Caro CG, Fitz-Gerald JM, and Schroter RC**, Arterial wall shear and distribution of early atheroma in man. *Nature* 223: 1159–1160, 1969.

[48] **Casiglia E, Palatini P, Da Ros S, Pagliara V, Puato M, Dorigatti F, and Pauletto P**, Effect of blood pressure and physical activity on carotid artery intima-media thickness in stage 1 hypertensives and controls. *American Journal of Hypertension* 13: 1256–1262, 2000.

[49] **Cebral J, Lohner R, Soto O, and Yim P**, On the modeling of carotid artery blood flow from magnetic resonance images. In *Proc. ASME-BED Bioengineering Conference*, 2001, vol. 50, pp. 619–620.

[50] **Cebral J, Yim P, Lohner R, Soto O, Marcos H, and Choyke P**, New Methods for Computational Fluid Dynamics of Carotid Artery From Magnetic Resonance Angiography. In *SPIE Medical Imaging*, edited by **Chin-Tu Chen AV**, San Diego, 2001, vol. 4321, pp. 177–187.

[51] **Cebral JR**, Realistic modeling of arterial hemodynamics from anatomic and physiologic image data. In *14th U.S. National Congress in Theoretical and Applied Mechanics*, edited by **Batra RC and Henneke EG**, Blacksburg, VA, 2002, p. 79.

[52] **Cebral JR, Castro M, Lohner R, Soto O, Yim PJ, and Alperin N**, Realistic cerebral circulation models from medical imaging data. In *2003 Summer Bioengineering Conference*, edited by **Soslowsky LJ, Skalak TC, Wayne JS, and Livesay GA**, Key Biscayne, FL, 2003, pp. 781–782.

[53] **Cebral JR, Castro MA, Soto O, Lohner R, and Alperin N**, Blood-flow models of the circle of Willis from magnetic resonance data. *Journal of En gi neer ing Mathematics* 47: 369–386, 2003.

[54] **Cebral JR and Lohner R**, From medical images to anatomically accurate finite element grids. *Int J Numer Methods Eng* 51: 985–1008, 2001.

[55] **Cebral JR, Lohner R, Choyke PL, and Yim PJ**, Merging of intersecting triangulations for finite element modeling. *Journal of Biomechanics* 34: 815–819, 2001.

[56] **Cebral JR, Yim PJ, Lohner R, Soto O, and Choyke PL**, Blood flow modeling in carotid arteries with computational fluid dynamics and MR imaging. *Acad Radiol* 9: 1286–1299, 2002.

[57] **Cellerini M, Mascalchi M, Mangiafico S, Ferrito GP, Scardigli V, Pellicano G, and Quilici N**, Phase-contrast MR angiography of intracranial dural arteriovenous fistulae. *Neuroradiology* 41: 487–492, 1999.

[58] **Chae CU, Pfeffer MA, Glynn RJ, Mitchell GF, Taylor JO, and Hennekens CH**, Increased pulse pressure and risk of heart failure in the elderly. *Jama Journal of the American Med i cal Association* 281: 634–639, 1999.

[59] **Chatzimavroudis GP, Oshinski JN, Franch RH, Walker PG, Yoganathan AP, and Pettigrew RI**, Evaluation of the precision of magnetic resonance phase velocity mapping for blood flow measurements. *J Cardiov Magn Reson* 3: 11–19, 2001.

[60] **Chen YT, Vaccarino V, Williams CS, Butler J, Berkman LF, and Krumholz HM**, Risk factors for heart failure in the elderly: A prospective community-based study. *American Journal of Med i cine* 106: 605–612, 1999.

[61] **Cheng CP, Parker D, and Taylor CA**, Quantification of wall shear stress in large blood vessels using lagrangian interpolation functions with cine phase- contrast magnetic resonance imaging. *Annals of Biomedical Engineering* 30: 1020–1032, 2002.

[62] **Cheong PL**, *Mahnetic Resonance Imaging and Computer simulation of haemodynamics at the human aortic bifurcation*. Ph.D. thesis, London Universityn, 2004.

[63] **Cho A, Mitchell L, Koopmans D, and Langille BL**, Effects of changes in blood flow rate on cell death and cell proliferation in carotid arteries of immature rabbits. *CircRes* 81: 328–337, 1997.

[64] **Choi US, Talbot L, and Cornet I**, Experimental-Study of Wall Shear Rates in the Entry Region of a Curved Tube. *J Fluid Mech* 93: 465–489, 1979.

[65] **Chung KY, Belfort G, Edelstein WA, and Li XM**, Dean Vortices in Curved Tube Flow .5. 3-D MRI and Numerical- Analysis of the Velocity-Field. *AICHE J* 39: 1592–1602, 1993.

[66] **Clarkson P, Celermajer DS, Donald AE, Sampson M, Sorensen KE, Adams M, Yue DK, Betteridge DJ, and Deanfield JE**, Impaired vascular reactivity in insulin-dependent diabetes mellitus is related to disease duration and low density lipoprotein cholesterol levels. *J Am Coll Cardiol* 28: 573–579, 1996.

[67] **Clowes AW and Berceli SA**, Mechanisms of vascular atrophy and fibrous cap disruption. In *Atherosclerosis V: the Fifth Saratoga Conference*, New York: New York Acad Sciences, vol. 902 of *Annals of the New York Academy of Sciences*, pp. 153–162, 2000.

[68] **Colin Europe**, Available at: http://www.colin-europe.com/pages/tonometry.html, Accessed December 31, 2003.

[69] **Collins WM and Dennis SCR**, Steady Motion of a Viscous-Fluid in a Curved Tube. *Q J Mech Appl Math* 28: 133–156, 1975.

[70] **Cross MM**, Rheology of non-Newtonian fluids: a new flow equation for pseudo-plastic system. *Journal of Colloid Science* 20: 417–437, 1965.

[71] **Crowe LA, Gatehouse P, Yang GZ, Mohiaddin RH, Varghese A, Charrier C, Keegan J, and Firmin DN**, Volume Selective 3D Turbo Spin Echo Sequence For Vascular Wall Imaging and Distensibility Measurement. *Journal of Magnetic Resonance Imaging* 17: 572–580, 2003.

[72] **Darovic GO**, *Hemodynamic monitoring: invasive and noninvasive clinical application*. Philadelphia: W.B. Saunders Company, 2nd ed., 1995.

[73] **De Ley G**, *Physiology and Anatomy*. Gent: Universiteit Gent, 1996.

[74] **De Ponti F, Marelli C, D'Angelo L, Caravaggi M, Bianco L, Lecchini S, Frigo GM, and Crema A**, Pharmacological activity and safety of trandolapril (RU 44570) in healthy volunteers. *European Journal of Clinical Pharmacology* 40: 149–153, 1991.

[75] **DeBakey ME and Glaeser DH**, Patterns of atherosclerosis: Effect of risk factors on recurrence and survival-analysis of 11,890 cases with more than 25-year follow-up. *American Journal of Cardiology* 85: 1045–1053, 2000.

[76] **Delfino A, Stergiopulos N, Moore JE, and Meister JJ**, Residual strain effects on the stress field in a thick wall finite element model of the human carotid bifurcation. *Journal of Biomechanics* 30: 777–786, 1997.

[77] **Denarie N, Gariepy J, Chironi G, Massonneau M, Laskri F, Salomon J, Levenson J, and Simon A**, Distribution of ultrasonographically-assessed dimensions of common carotid arteries in healthy adults of both sexes. *Atherosclerosis* 148: 297–302, 2000.

[78] **Dicom Standards Committee**, Available at: http://medical.nema.org/, Accessed January 7, 2004.

[79] **Dimitriou G, Greenough A, Pink L, McGhee A, Hickey A, and Rafferty GF**, Effect of posture on oxygenation and respiratory muscle strength in convalescent infants. *Arch Dis Child* 86: 147–150, 2002.

[80] **Donis J, Graf M, and Sluga E**, Carotid-Artery Flow Measurements by Means of Duplex Sonography (Results in Normal Persons). *Ultraschall in Der Medizin* 9: 216–222, 1988.

[81] **Draney MT, Herfkens RJ, Hughes TJR, Pelc NJ, Wedding KL, Zarins CK, and Taylor CA**, Quantification of vessel wall cyclic strain using cine phase contrast magnetic resonance imaging. *Annals of Biomedical Engineering* 30: 1033–1045, 2002.

[82] **Dussik K**, On the possibility of using ultrasound waves as a diagnostic aid. *Neurol Psychiat* 174: 153–168, 1942.

[83] **Ebbers T, Wigstrom L, Bolger AF, Engvall J, and Karlsson M**, Estimation of relative cardiovascular pressures using time- resolved three-dimensional phase contrast MRI. *Magnetic Resonance in Medicine* 45: 872–879, 2001.

[84] **Eckstein HH**, Surgical therapy for extracranial stenosis of the carotid. *Chirurg* 75: 93–109, 2004.

[85] **Eichler F, Ipsiroglu O, Arif T, Popow C, Heinzl H, Urschitz M, and Pollak A**, Position dependent changes of cerebral blood flow velocities in premature infants. *Eur J Pediatr* 160: 633–639, 2001.

[86] **Electromagnetic Spectrum**, Available at: http://www.electro-optical.com/bb_rad/emspect.htm, Accessed December 31, 2003.

[87] **Electronics Modern Magic, Paul Langevin**, Available at: http://mediatheek.thinkquest.nl, Accessed January 21, 2004.

[88] **Eloot S, De Wachter D, Van Tricht I, and Verdonck P**, Computational flow modeling in hollow-fiber dialyzers. *Artificial Organs* 26: 590–599, 2002.

[89] **Elzinga G and Westerho.N**, Pressure and Flow Generated by Left Ventricle against Different Impedances. *Circulation Research* 32: 178–186, 1973.

[90] **emedicine, carotid dissection**, Available at: http://www.emedicine.com/emerg/byname/dissection-carotid-artery.htm, Accessed January 4, 2004.

[91] **Ene-Iordache B, Mosconi L, Remuzzi G, and Remuzzi A**, Computational fluid dynamics of a vascular access case for hemodialysis. *Journal of Biomechanical Engineering Transactions of the ASME* 123: 284–292, 2001.

[92] **Fahrig R, Fox AJ, Lownie S, and Holdsworth DW**, Use of a C-arm system to generate true three-dimensional computed rotational angiograms: Preliminary in vitro and in vivo results. *American Journal of Neuroradiology* 18: 1507–1514, 1997.

[93] **Fayad ZA, Fuster V, Fallon JT, Jayasundera T, Worthley SG, Helft G, Aguinaldo JG, Badimon JJ, and Sharma SK**, Noninvasive in vivo human coronary artery lumen and wall imaging using black-blood magnetic resonance imaging. *Circulation* 102: 506–510, 2000.

[94] **Feldman CL and Stone PH**, Intravascular hemodynamic factors responsible for progression of coronary atherosclerosis and development of vulnerable plaque. *Current Opinion in Cardiology* 15: 430–440, 2000.

[95] **Ferrara LA, Mancini M, Iannuzzi R, Marotta T, Gaeta I, Pasanisi F, Postiglione A, and Guida L**, Carotid Diameter and Blood Flow Velocities in Cerebral Circulation in Hypertensive Patients. *Stroke* 26: 418–421, 1995.

[96] **Fitzgerald DE, Oshaughnessy AM, and Keaveny VT**, Pulsed Doppler - Determination of Blood Velocity and Volume Flow in Normal and Diseased Common Carotid Arteries in Man. *Cardiovascular Research* 16: 220–224, 1982.

[97] **Fortune JB, Bock D, Kupinski AM, Stratton HH, Shah DM, and Feustel PJ**, Human Cerebrovascular Response to Oxygen and Carbon-Dioxide as Determined by Internal Carotid-Artery Duplex Scanning. *Journal of Trauma Injury Infection and Critical Care* 32: 618–628, 1992.

[98] **Frayne R, Gowman LM, Rickey DW, Holdsworth DW, Picot PA, Drangova M, Chu KC, Caldwell CB, Fenster A, and Rutt BK**, A Geometrically Accurate Vascular Phantom For Comparative-Studies of X-Ray, Ultrasound, and Magnetic-Resonance Vascular Imaging - Construction and Geometrical Verification. *Med Phys* 20: 415–425, 1993.

[99] **Friedman MH**, A Biologically Plausible Model of Thickening of Arterial Intima under Shear. *Arteriosclerosis* 9: 511–522, 1989.

[100] **Friedman MH and Ding ZH**, Variability of the planarity of the human aortic bifurcation. *Medical Engineering Physics* 20: 469–472, 1998.

[101] **Friedman MH, Obrien V, and Ehrlich LW**, Calculations of Pulsatile Flow through a Branch - Implications for Hemodynamics of Atherogenesis. *Circulation Research* 36: 277–285, 1975.

[102] **Fry DL**, Acute vascular endothelial changes associated with increased blood velocity gradients. *Circulation Research* 22: 165–197, 1968.

[103] **Gage KL, Gartner MJ, Burgreen GW, and Wagner WR**, Predicting membrane oxygenator pressure drop using computational fluid dynamics. *Artificial Organs* 26: 600–607, 2002.

[104] **Gariepy J, Massonneau M, Levenson J, Heudes D, and Simon A**, Evidence for in-Vivo Carotid and Femoral Wall Thickening in Human Hypertension. *Hypertension* 22: 111–118, 1993.

[105] **Gariepy J, Salomon J, Denarie N, Laskri F, Megnien JL, Levenson J, and Simon A**, Sex and topographic differences in associations between large- artery wall thickness and coronary risk profile in a French working cohort - The AXA Study. *Arteriosclerosis Thrombosis and Vascular Biology* 18: 584–590, 1998.

[106] **GE systemas medicos, Ultrasonido, cursos online, Imgen de Doppler Carotideo**, Available at: http://www.gemedicalsystems.com/laes/rad/us/education/msucmecd.html, Accessed January 4, 2004.

[107] **General anaesthetic versus local anaesthetic for carotid surgery (GALA trial), General anaesthetic versus local anaesthetic for carotid surgery**, Available at: http://www.dcn.ed.ac.uk/gala/June%2002.htm, Accessed January 4, 2004.

[108] **Georgia State University, Department of Physics and Astronomy, Hyperphysics, Wall Tension**, Available at: http://hyperphysics.phy-astr.gsu.edu/hbase/ptens.html, Accessed January 4, 2004.

[109] **Germain DP, Boutouyrie P, Laloux B, and Laurent S**, Arterial remodeling and stiffness in patients with pseudoxanthoma elasticum. *Arteriosclerosis Thrombosis and Vascular Biology* 23: 836–841, 2003.

[110] **Gianaros PJ, Jennings JR, Olafsson GB, Steptoe A, Sutton-Tyrrell K, Muldoon MF, and Manuck SB**, Greater intima-media thickness in the carotid bulb is associated with reduced baroreflex sensitivity. *American Journal of Hypertension* 15: 486–491, 2002.

[111] **Giannattasio C, Failla M, Stella ML, Mangoni AA, Turrini D, Carugo S, Pozzi M, Grassi G, and Mancia G**, Angiotensin-Converting Enzyme-Inhibition and Radial Artery Compliance in Patients with Congestive-Heart-Failure. *Hypertension* 26: 491–496, 1995.

[112] **Gibson CM, Diaz L, Kandarpa K, Sacks FM, Pasternak RC, Sandor T, Feldman C, and Stone PH**, Relation of Vessel Wall Shear-Stress to Atherosclerosis Progression in Human Coronary-Arteries. *Arteriosclerosis and Thrombosis* 13: 310–315, 1993.

[113] **Gijsen FJH, van de Vosse FN, and Janssen JD**, The influence of the non-Newtonian properties of blood on the flow in large arteries: steady flow in a carotid bifurcation model. *Journal of Biomechanics* 32: 601–608, 1999.

[114] **Gill JD, Ladak HM, Steinman DA, and Fenster A**, Accuracy and variability assessment of a semiautomatic technique for segmentation of the carotid arteries from three- dimensional ultrasound images. *Med Phys* 27: 1333–1342, 2000.

[115] **Gill RW**, Measurement of Blood-Flow by Ultrasound - Accuracy and Sources of Error. *Ultrasound in Medicine and Biology* 11: 625–641, 1985.

[116] **Girerd X, Giannattasio C, Moulin C, Safar M, Mancia G, and Laurent S**, Regression of radial artery wall hypertrophy and improvement of carotid artery compliance after long-term antihypertensive treatment in elderly patients. *Journal of the American College of Cardiology* 31: 1064–1073, 1998.

[117] **Glor FP, Ariff B, Augst AD, Barratt DC, Hughes AD, Thom SA, Verdonck PR, and Xu XY**, 3D Ultrasound-based CFD for carotid flow prediction: a reproducibility study. In *2nd MIT Conference on Computational Fluid and Solid Mechanics*, edited by **Bathe KJ**, Cambridge, MA: Elsevier, 2003, vol. 2 of *Computational Fluid and Solid Mechanics*, pp. 1701–1704.

[118] **Glor FP, Ariff B, Augst AD, Barratt DC, Hughes AD, Thom SAM, Verdonck PR, and Xu XY**, 3D ultrasound-based CFD for carotid flow prediction: a reproducibility study. *Ultrasound in Medicine and Biology* , unpublished.

[119] **Glor FP, Ariff B, Crowe LA, Firmin D, Hughes AD, Thom SAM, Barratt DC, Verdonck PR, and Xu XY**, CFD-based carotid flow reconstruction: a comparison between MRI and Ultrasound. *Journal of Biomechanics* , unpublished.

[120] **Glor FP, Ariff B, Crowe LA, Hughes AD, Cheong PL, Thom SA, Verdonck P, Firmin DN, Barratt DC, and Xu XY**, Carotid geometry reconstruction: a comparison between MRI and ultrasound. *Medical Physics* 30: 3251–3261, 2003.

[121] **Glor FP, Long Q, Hughes AD, Augst AD, Ariff B, Thom SA, Verdonck P, and Xu XY**, Reproducibility study of MR-image based CFD prediction of carotid bifurcation flow. *Annals of Biomedical Engineering* 31: 142–151, 2003.

[122] **Glor FP, Westenberg JJM, Vierendeels J, Danilouchkine M, and Verdonck P**, Validation of the coupling of magnetic resonance imaging velocity measurements with computational fluid dynamics in a U bend. *Artificial Organs* 26: 622–635, 2002.

[123] **Gnasso A, Motti C, Irace C, Carallo C, Liberatoscioli L, Bernardini S, Massoud R, Mattioli PL, Federici G, and Cortese C**, Genetic variation in human stromelysin gene promoter and common carotid geometry in healthy male subjects. *Arteriosclerosis Thrombosis and Vascular Biology* 20: 1600–1605, 2000.

[124] **Goonasekera CDA and Dillon MJ**, Random Zero Sphygmomanometer Versus Automatic Oscillometric Blood-Pressure Monitor Is Either the Instrument of Choice. *Journal of Human Hypertension* 9: 885–889, 1995.

[125] **Goubergrits L, Affeld K, Fernandez-Britto J, and Falcon L**, Atherosclerosis in the human common carotid artery. A morphometric study of 31 specimens. *Pathology Research and Practice* 197: 803–809, 2001.

[126] **Goubergrits L, Affeld K, Fernandez-Britto J, and Falcon L**, Atherosclerosis and flow in carotid arteries with authentic geometries. *Biorheology* 39: 519–524, 2002.

[127] **Goubergrits L, Affeld K, Fernandez-Britto J, and Falcon L**, Geometry of the human common carotid artery. A vessel cast study of 86 specimens. *Pathology Research and Practice* 198: 543–551, 2002.

[128] **Grassi G, Seravalle G, Turri C, Bolla G, and Mancia G**, Short-versus long-term effects of different dihydropyridines on sympathetic and baroreflex function in hypertension. *Hypertension* 41: 558–62, 2003.

[129] **Grossman E and Messerli FH**, Effect of calcium antagonists on plasma norepinephrine levels, heart rate, and blood pressure. *American Journal of Cardiology* 80: 1453–1458, 1997.

[130] **Grube E, Colombo A, Hauptmann E, Londero H, Reifart N, Gerckens U, and Stone GW**, Initial multicenter experience with a novel distal protection filter during carotid artery stent implantation. *Catheterization and Cardiovascular Interventions* 58: 139–146, 2003.

[131] **H. S. Khaira, Atherosclerosis**, Available at: http://gensurg.co.uk/atherosclerosis.htm, Accessed January 4, 2004.

[132] **Hamada T, Takita M, Kawano H, Nohtomi A, and Okayama M**, Difference in Blood-Flow Volume of the Common Carotid-Artery between Vascular and Nonvascular Dementia Detected by Color Duplex Sonography. *Journal of Neurology* 240: 191–194, 1993.

[133] **Hamakiotes CC and Berger SA**, Fully-Developed Pulsatile Flow in a Curved Pipe. *J Fluid Mech* 195: 23–55, 1988.

[134] **Hamakiotes CC and Berger SA**, Periodic Flows Through Curved Tubes - the Effect of the Frequency Parameter. *J Fluid Mech* 210: 353–370, 1990.

[135] **Haynes MJ, Cala LA, Melsom A, Mastaglia FL, Milne N, and McGeachie JK**, Vertebral arteries and cervical rotation: Modeling and magnetic resonance angiography studies. *Journal of Manipulative and Physiological Therapeutics* 25: 370–383, 2002.

[136] **Haynes WM**, Viscosity of Saturated Liquid Methane. *Physica* 70: 410–412, 1973.

[137] **He XJ and Ku DN**, Pulsatile flow in the human left coronary artery bifurcation: Average conditions. *Journal of Biomechanical Engineering Transactions of the ASME* 118: 74–82, 1996.

[138] **HeartCenterOnline For Patients, Aneurysm overview**, Available at: http://www.heartcenteronline.com/myheartdr/common/articles.cfm?ARTID=551, Accessed January 4, 2004.

[139] **Hofmann W, Balashazy I, and Heistracher T**, The relationship between secondary flows and particle deposition patterns in airway bifurcations. *Aerosol Sci Technol* 35: 958–968, 2001.

[140] **Holdsworth DW, Norley CJD, Frayne R, Steinman DA, and Rutt BK**, Characterization of common carotid artery blood-flow waveforms in normal human subjects. *Physiological Measurement* 20: 219–240, 1999.

[141] **Humphrey JAC, Iacovides H, and Launder BE**, Some Numerical Experiments On Developing Laminar-Flow in Circular-Sectioned Bends. *J Fluid Mech* 154: 357–375, 1985.

[142] **Hyun S, Kleinstreuer C, and Archie JP**, Computer simulation and geometric design of endarterectomized carotid artery bifurcations. *Crit Rev Biomed Eng* 28: 53–59, 2000.

[143] **Hyun S, Kleinstreuer C, and Archie JP**, Hemodynamics analyses of arterial expansions with implications to thrombosis and restenosis. *Med Eng Phys* 22: 13–27, 2000.

[144] **Indus Instruments, Carotid Arterial Flow Velocity Spectrogram of a Mouse**, Available at: http://www.indusinstruments.com/oldWebsite, Accessed January 22, 2004.

[145] **Iternational Society of Magnetic Resonance in Medicine, Press Releases, The 2003 Nobel Prize in Physiology or Medicine**, Available at: http://www.nobel.se/medicine/laureates/2003/press.html, Accessed January 12, 2004.

[146] **James M, Watt P, Potter J, Thurston H, and Swales J**, Pulse pressure and resistance artery structure in the elderly. *Hypertension* 26: 301–306, 1995.

[147] **Jondeau G, Boutouyrie P, Lacolley P, Laloux B, Dubourg O, Bourdarias JP, and Laurent S**, Central pulse pressure is a major determinant of ascending aorta dilation in Marfan syndrome. *Circulation* 99: 2677–2681, 1999.

[148] **Jou L, vanTyen R, Berger A, and Saloner D**, Calculation of the magnetization distribution for fluid flow in curved vessels. *Magnetic Resonance in Medicine* 35: 577–584, 1996.

[149] **Kadowaki C, Hara M, Numoto M, Takeuchi K, and Saito I**, Cine Magnetic-Resonance-Imaging of Aqueductal Stenosis. *Childs Nerv Syst* 11: 107–111, 1995.

[150] **Kamarck TW, Everson SA, Kaplan GA, Manuck SB, Jennings JR, Salonen R, and Salonen JT**, Exaggerated blood pressure responses during mental stress are associated with enhanced carotid atherosclerosis in middle-aged Finnish men - Findings from the Kuopio Ischemic Heart Disease Study. *Circulation* 96: 3842–3848, 1997.

[151] **Karino T and Goldsmith HL**, Particle Flow Behavior in Models of Branching Vessels .2. Effects of Branching Angle and Diameter Ratio on Flow Patterns. *Biorheology* 22: 87–104, 1985.

[152] **Kass DA, Shapiro EP, Kawaguchi M, Capriotti AR, Scuteri A, deGroof RC, and Lakatta EG**, Improved arterial compliance by a novel advanced glycation end-product crosslink breaker. *Circulation* 104: 1464–1470, 2001.

[153] **Kass M, Witkin A, and Terzopoulos D**, Snakes - Active Contour Models. *International Journal of Computer Vision* 1: 321–331, 1987.

[154] **Keller HM, Meier WE, Anliker M, and Kumpe DA**, Noninvasive Measurement of Velocity Profiles and Blood-Flow in Common Carotid-Artery by Pulsed Doppler Ultrasound. *Stroke* 7: 370–377, 1976.

[155] **Kessler M**, Section III. Biocompatibility. *Nephrol Dial Transplant* 17: 32–44, 2002.

[156] **Keynton RS, Evancho MM, Sims RL, Rodway NV, Gobin A, and Rittgers SE**, Intimal hyperplasia and wall shear in arterial bypass graft distal anastomoses: An in vivo model study. *Journal of Biomechanical Engineering Transactions of the ASME* 123: 464–473, 2001.

[157] **King E, Xu XY, Hughes AD, Long Q, Thom SA, and Parker KH**, Quantification of the nonplanarity of the human carotid bifurcation. *Biorheology* 39: 419–424, 2002.

[158] **Klabunde RE**, Cardiovascular physiology concepts, 1999.

[159] **Kleinstreuer C, Hyun S, Buchanan JR, Longest PW, Archie JP, and Truskey GA**, Hemodynamic parameters and early intimal thickening in branching blood vessels. *Critical Reviews in Biomedical Engineering* 29: 1–64, 2001.

[160] **Kleinstreuer C, Lei M, and Archie JP**, Flow input waveform effects on the temporal and spatial wall shear stress gradients in a femoral graft-artery connector. *Journal of Biomechanical Engineering Transactions of the ASME* 118: 506–510, 1996.

[161] **Köhler U, Marshall I, Robertson MB, Long Q, Xu XY, and Hoskins P**, MRI measurement of Wall Shear Stress Vectors in Bifurcation Models and Comparison With CFD Predictions. *Journal of Magnetic Resonance Imaging* 14: 563–573, 2001.

[162] **Krams R, Wentzel JJ, Oomen JAF, Vinke R, Schuurbiers JCH, deFeyter PJ, Serruys PW, and Slager CJ**, Evaluation of endothelial shear stress and 3D geometry as factors determining the development of atherosclerosis and remodeling in human coronary arteries in vivo - Combining 3D reconstruction from angiography and IVUS (ANGUS) with computational fluid dynamics. *Arterioscler Thromb Vasc Biol* 17: 2061–2065, 1997.

[163] **Kwoon SM, Ru TF, and Guang XX**, Effects of des-aspartate-angiotensin I on neointima growth and cardiovascular hypertrophy. *Regulatory Peptides* 117: 213–217, 2004.

[164] **Ladak HM, Milner JS, and Steinman DA**, Rapid three-dimensional segmentation of the carotid bifurcation from serial MR images. *Journal of Biomechanical Engineering Transactions of the ASME* 122: 96–99, 2000.

[165] **Ladak HM, Thomas JB, Mitchell JR, Rutt BK, and Steinman DA**, A semi-automatic technique for measurement of arterial wall from black blood MRI. *Medical Physics* 28: 1098–1107, 2001.

[166] **Lafleche A, Gautier S, Topouchian J, Wilmet CS, Girerd X, Safar ME, and Benetos A**, Differential responses of the heart and vasculature to chronic blood pressure reduction in essential hypertension. *Clinical Pharmacology Therapeutics* 64: 96–105, 1998.

[167] **Lage SG, Kopel L, Medeiros CCJ, Carvalho RT, and Creager MA**, Angiotensin II contributes to arterial compliance in congestive heart failure. *American Journal of Physiology Heart and Circulatory Physiology* 283: H1424–H1429, 2002.

[168] **Laogun AA and Gosling RG**, In vivo arterial compliance in man. *Clin Phys Physiol Meas* 3: 201–212, 1982.

[169] **Laragh JH and Brenner BM**, *Hypertension Pathophysiology, Diagnosis and Management*, vol. 1. Raven Press New York, 1990.

[170] **Lee VS, Hertzberg BS, Kliewer MA, and Carroll BA**, Assessment of stenosis: Implications of variability of Doppler measurements in normal-appearing carotid arteries. *Radiology* 212: 493–498, 1999.

[171] **Lei M, Kleinstreuer C, and Archie JP**, Geometric design improvements for femoral graft-artery junctions mitigating restenosis. *Journal of Biomechanics* 29: 1605–1614, 1996.

[172] **Lei M, Kleinstreuer C, and Truskey GA**, Numerical Investigation and Prediction of Atherogenic Sites in Branching Arteries. *Journal of Biomechanical Engineering Transactions of the ASME* 117: 350–357, 1995.

[173] **Lei M, Kleinstreuer C, and Truskey GA**, A focal stress gradient-dependent mass transfer mechanism for atherogenesis in branching arteries. *Med Eng Phys* 18: 326–332, 1996.

[174] **Lentner C**, *Geigy Scientific Tables: Heart and Circulation*, vol. 5 of *Geigy Scientific Tables*. Basel, Switzerland: Ciba-Geigy Corporation, 8 ed., 1990.

[175] **Leopold PW, Shandall AA, Feustel P, Corson JD, Shah DM, Popp AJ, Fortune JB, Leather RP, and Karmody AM**, Duplex Scanning of the Internal Carotid-Artery - an Assessment of Cerebral Blood-Flow. *British Journal of Surgery* 74: 630–633, 1987.

[176] **Lerner Research Institute, The Cleveland Clinic, Vascular Imaging**, Available at: http://www.tmc.edu/thi/carotida.html, Accessed January 1, 2004.

[177] **Leuprecht A, Kozerke S, Boesiger P, and Perktold K**, Blood flow in the human ascending aorta: a combined MRI and CFD study. *Journal of En gi neer ing Mathematics* 47: 387–404, 2003.

[178] **Leuprecht A, Perktold K, Kozerke S, and Boesiger P**, Combined CFD and MRI study of blood flow in a human ascending aorta model. *Biorheology* 39: 425–429, 2002.

[179] **Leverett LB, Lynch EC, Alfrey CP, and Hellums JD**, Red Blood-Cell Damage By Shear-Stress. *Biophys J* 12: 257–271, 1972.

[180] **Levesque MJ and Nerem RM**, The Elongation and Orientation of Cultured Endothelial-Cells in Response to Shear-Stress. *Journal of Biomechanical Engineering Transactions of the ASME* 107: 341–347, 1985.

[181] **Li JKJ**, *The arterial Circulation. Physical principles and clinical applications.*. Totowa, New Jersey: Humana Press Inc., 2000.

[182] **Liang YL, Shiel LM, Teede H, Kotsopoulos D, McNeil J, Cameron JD, and McGrath BP**, Effects of Blood Pressure, Smoking, and Their Interaction on Carotid Artery Structure and Function. *Hypertension* 37: 6–11, 2001.

[183] **Liauw L, van Buchem MA, Spilt A, de Bruine FT, van den Berg R, Hermans J, and Wasser M**, MR angiography of the intracranial venous system. *Radiology* 214: 678–682, 2000.

[184] **Liepsch D**, Study of Flow Processes in Branching Models of Coronary Vessels with a Laser Doppler Probe. *Chemie Ingenieur Technik* 47: 347–347, 1975.

[185] **Liepsch D**, Pressure Measurements at Wall after Bifurcation and Visual Observation of Streaming Fluid in Glass Models of Bifurcations. *South African Mechanical Engineer* 28: 143–148, 1978.

[186] **Liepsch D and Zimmer R**, Method for Preparation of True-to-Scale Inflexible and Natural Elastic Human Arteries. *Biomedizinische Technik* 23: 227–230, 1978.

[187] **Liepsch D and Zimmer R**, The dynamics of pulsatile flow in distensible model arteries. *Technology and Health Care* 3: 185–199, 1995.

[188] **Lindsay JJ, DeBakey ME, and Beall AC**, Diagnosis and Treatment Of Diseases of the Aorta. In *Hurst's The Heart*, edited by **Schlant RC**, New York: McGraw Hill, p. 2168, 8 ed., 2001.

[189] **Linfante I, Hirsch JA, Selim M, Schlaug G, Caplan LR, and Reddy AS**, Safety of latest-generation self-expanding stents in patients with NASCET-ineligible severe symptomatic extracranial internal carotid artery stenosis. *Archives of Neurology* 61: 39–43, 2004.

[190] **Liu KC and Margosian P**, Multiple contrast fast spin-echo approach to black-blood intracranial MRA: Use of complementary and supplementary information. *Magn Reson Imaging* 19: 1173–1181, 2001.

[191] **Liu Y, Lai Y, Nagaraj A, Kane B, Hamilton A, Greene R, McPherson DD, and Chandran KB**, Pulsatile flow simulation in arterial vascular segments with intravascular ultrasound images. *Med Eng Phys* 23: 583–595, 2001.

[192] **Lohner R and Parikh P**, Generation of 3-Dimensional Unstructured Grids By the Advancing-Front Method. *International Journal of Numerical Methods in Fluids* 8: 1135–1149, 1988.

[193] **Long Q**, *Numerical investigation of blood flow in human arterial bifurcation model by the combination of CFD and MRI*. Phd, City University, London, 1998.

[194] **Long Q, Ariff B, Thom SA, Hughes AD, and Xu XY**, Reproducibility study of 3D geometrical reconstruction of the human carotid bifurcation from magnetic resonance images. *Magnetic Resonance in Medicine* 49: 665–674, 2003.

[195] **Long Q, Xu XY, Ariff B, Thom SA, Hughes AD, and Stanton AV**, Reconstruction of blood flow patterns in a human carotid bifurcation: A combined CFD and MRI study. *Journal of Magnetic Resonance Imaging* 11: 299–311, 2000.

[196] **Long Q, Xu XY, Bourne M, and Griffith TM**, Numerical study of blood flow in an anatomically realistic aorto-iliac bifurcation generated from MRI data. *Magnetic Resonance in Med i cine* 43: 565–576, 2000.

[197] **Long Q, Xu XY, Collins MW, Bourne M, and Griffith TM**, Magnetic resonance image processing and structured grid generation of a human abdominal bifurcation. *Comput Meth Programs Biomed* 56: 249–259, 1998.

[198] **Long Q, Xu XY, Collins MW, Griffith TM, and Bourne M**, The combination of magnetic resonance angiography and computational fluid dynamics: A critical review. *Crit Rev Biomed Eng* 26: 227–274, 1998.

[199] **Longest PW**, *Computational Analyses of Transient Particle Hemodynamics with Applications to Femoral Bypass Graft Designs*. Ph.D. thesis, NC State University, Raleigh, NC, 2002.

[200] **Longest PW and Kleinstreuer C**, Computational haemodynamics analysis and comparison study of arterio-venous grafts. *J Med Eng Technol* 24: 102–110, 2000.

[201] **Lorimer AR, Lyons D, Fowler G, Petrie JC, and Rothman MT**, Differences between amlodipine and lisinopril in control of clinic and twenty-four hour ambulatory blood pressures. *Journal of Human Hypertension* 12: 411–416, 1998.

[202] **Lovett JK and Rothwell PM**, Site of carotid plaque ulceration in relation to direction of blood flow: An angiographic and pathological study. *Cerebrovascular Diseases* 16: 369–375, 2003.

[203] **Luo H, Baum JD, and Lohner R**, An accurate, fast, matrix-free implicit method for computing unsteady flows on unstructured grids. *Comput Fluids* 30: 137–159, 2001.

[204] **Luo XY and Kuang ZB**, Non-Newtonian Flow Patterns Associated with an Arterial-Stenosis. *Journal of Biomechanical Engineering Transactions of the Asme* 114: 512–514, 1992.

[205] **Lyne WH**, Unsteady viscous flow in a curved pipe. *J Fluid Mech* 45: 13–31, 1970.

[206] **Mackiewich B**, *Intracranial Boundary Detection and Radio Frequency Correction in Magnetic Resonance Images*. Msc, Simon Fraser University, 1995.

[207] **Malek AK, Hilgertner L, and Szostek M**, The Effect of Internal Carotid-Artery Elongation On Intracranial Blood-Flow. *European Journal of Vascular Surgery* 8: 677–681, 1994.

[208] **Malek AM, Alper SL, and Izumo S**, Hemodynamic shear stress and its role in atherosclerosis. *J Am Med Assoc* 282: 2035–2042, 1999.

[209] **Manzo BA, Matalka MS, and Ravnan SL**, Evaluation of a therapeutic conversion from amlodipine to felodipine. *Pharmacotherapy* 23: 1508–1512, 2003.

[210] **Mao F, Gill J, Downey D, and Fenster A**, Segmentation of carotid artery in ultrasound images: Method development and evaluation technique. *Med Phys* 27: 1961–1970, 2000.

[211] **Marchand B, Hernandez-Hoyos M, Orkisz M, and Douek P**, Diagnosis of renal artery stenosis with magnetic resonance angiography and stenosis quantification. *J Mal Vasc* 25: 312–320, 2000.

[212] **Maseri A and Fuster V**, Is there a vulnerable plaque? *Circulation* 107: 2068–2071, 2003.

[213] **Mayberg MR, Wilson SE, Yatsu F, Weiss DG, Messina L, Hershey LA, Colling C, Eskridge J, Deykin D, and Winn HR**, Carotid Endarterectomy and Prevention of Cerebral-Ischemia in Symptomatic Carotid Stenosis. *Jama Journal of the American Medical Association* 266: 3289–3294, 1991.

[214] **Mayet J, Stanton AV, Sinclair AM, Mackay J, Shahi M, Foale RA, Nicolaides A, Poulter NR, Sever PS, Thom SAM, and Hughes AD**, The Effects of Antihypertensive Therapy on Carotid Vascular Structure in Man. *Cardiovascular Research* 30: 147–152, 1995.

[215] **Medasys, the medical imaging company, definition M-mode**, Available at: http://www.medasys.co.jp/page/deff.htm, Accessed January 21, 2004.

[216] **van der Meer IM, del Sol AI, Hak AE, Bots ML, Hofman A, and Witteman JCM**, Risk factors for progression of atherosclerosis measured at multiple sites in the arterial tree - The Rotterdam Study. *Stroke* 34: 2374–2379, 2003.

[217] **Merril EW**, Rheology of Blood. *Physiological Reviews* 26: 863–888, 1969.

[218] **Milan A, Mulatero P, Rabbia F, and Veglio F**, Salt intake and hypertension therapy. *Journal of Nephrology* 15: 1–6, 2002.

[219] **Milner JS, Moore JA, Rutt BK, and Steinman DA**, Hemodynamics of human carotid artery bifurcations: Computational studies with models reconstructed from magnetic resonance imaging of normal subjects. *J Vasc Surg* 28: 143–156, 1998.

[220] **Mitchell GF, Izzo JL, Lacourciere Y, Ouellet JP, Neutel J, Qian CL, Kerwin LJ, Block AJ, and Pfeffer MA**, Omapatrilat reduces pulse pressure and proximal aortic stiffness in patients with systolic hypertension - Results of the conduit hemodynamics of Omapatrilat International Research Study. *Circulation* 105: 2955–2961, 2002.

[221] **Mitchell GF, Lacourciere Y, Ouellet JP, Izzo JL, Neutel J, Kerwin LJ, Block AJ, and Pfeffer MA**, Determinants of elevated pulse pressure in middle-aged and older subjects with uncomplicated systolic hypertension - The role of proximal aortic diameter and the aortic pressure-flow relationship. *Circulation* 108: 1592–1598, 2003.

[222] **Mitchell GF, Tardif JC, Arnold JMO, Marchiori G, O'Brien TX, Dunlap ME, and Pfeffer MA**, Pulsatile Hemodynamics in congestive heart failure. *Hypertension* 38: 1433–1439, 2001.

[223] **Moore JA, Rutt BK, Karlik SJ, Yin K, and Ethier CR**, Computational blood flow modeling based on in vivo measurements. *Annals of Biomedical Engineering* 27: 627–640, 1999.

[224] **Moore JA, Steinman DA, and Ethier CR**, Computational blood flow modelling: Errors associated with reconstructing finite element models from magnetic resonance images. *Journal of Biomechanics* 31: 179–184, 1998.

[225] **Moore JA, Steinman DA, Holdsworth DW, and Ethier CR**, Accuracy of computational hemodynamics in complex arterial geometries reconstructed from magnetic resonance imaging. *Annals of Biomedical Engineering* 27: 32–41, 1999.

[226] **MRI on the web**, Available at: http://members.lycos.nl/themerlin/Nieuw/flowmraeng.htm, Accessed January 10, 2004.

[227] **MSCD Biology Department Faculty, The circle of Willis**, Available at: http://www.mscd.edu/ biology/2320course/2320images/Willis.gif, Accessed January 4, 2004.

[228] **Mullin T and Greated CA**, Oscillatory Flow in Curved Pipes .1. the Developing-Flow Case. *J Fluid Mech* 98: 383–395, 1980.

[229] **Nagai Y, Kemper MK, Earley CJ, and Metter EJ**, Blood-flow velocities and their relationships in carotid and middle cerebral arteries. *Ultrasound in Medicine and Biology* 24: 1131–1136, 1998.

[230] **Nagasaki University school of medicine, Department of Radiology, Introduction to MRI - History**, Available at: http://www.med.nagasaki-u.ac.jp/radiolgy/MRIhistory.html, Accessed January 12, 2004.

[231] **Naidu MUR, Usha PR, Rao TRK, and Shobha JC**, Evaluation of amlodipine, lisinopril, and a combination in the treatment of essential hypertension. *Postgraduate Med i cal Journal* 76: 350–353, 2000.

[232] **Nichols WW and O'Rourke MF**, *The nature of flow of a fluid*. McDonalds's Blood Flow in arteries, London: Hodder and Stoughton Limited, 1990.

[233] **Norris JW, Zhu CZ, Bornstein NM, and Chambers BR**, Vascular Risks of Asymptomatic Carotid Stenosis. *Stroke* 22: 1485–1490, 1991.

[234] **Ohtsuka S, Yamazaki A, Oyake Y, and Yamaguchi I**, Amlodipine improves vascular function in patients with moderate to severe hypertension. *Journal of Cardiovascular Pharmacology* 42: 296–303, 2003.

[235] **Okahara M, Kiyosue H, Yamashita M, Nagatomi H, Hata H, Saginoya T, Sagara Y, and Mori H**, Diagnostic accuracy of magnetic resonance angiography for cerebral aneurysms in correlation with 3D-digital subtraction angiographic images - A study of 133 aneurysms. *Stroke* 33: 1803–1808, 2002.

[236] **O'Leary DH and Polak JF**, Intima-media thickness: A tool for atherosclerosis imaging and event prediction. *Am J Cardiol* 90: 18L–21L, 2002.

[237] **Olson DE and Snyder B**, The Upstream Scale of Flow Development in Curved Circular Pipes. *J Fluid Mech* 150: 139–158, 1985.

[238] **PAM System International, S.A.**, *PAM FLOW™ Solver Theory Manual*. Paris, 1999.

[239] **PAM System International, S.A.**, *PAM GEN3D™ Theory Manual*. Paris, 1999.

[240] **Papaharilaou Y, Doorly DJ, and Sherwin SJ**, Assessing the accuracy of two-dimensional phase-contrast MRI measurements of complex unsteady flows. *Journal of Magnetic Resonance Imaging* 14: 714–723, 2001.

[241] **Parmar MS**, Telephone stroke. *Canadian Medical Association Journal* 167: 1104–1104, 2002.

[242] **Pellicer A, Gaya F, Madero R, Quero J, and Cabanas F**, Noninvasive continuous monitoring of the effects of head position on brain hemodynamics in ventilated infants. *Pediatrics* 109: 434–440, 2002.

[243] **Peripheral Vascular Surgery Society, The Steps in the conduct repairing a Giant Internal Carotid Aneurysm**, Available at: http://www.pvss.org/ICA/ICA1.htm, Accessed January 4, 2004.

[244] **Perktold K and Hilbert D**, Numerical-Simulation of Pulsatile Flow in a Carotid Bifurcation Model. *J Biomed Eng* 8: 193–199, 1986.

[245] **Perktold K, Hilbert D, and Siekmann J**, Numerical-Analysis of Pulsatile Flow of a Non-Newtonian Fluid in an Elastic Tube. *Zeitschrift Fur Angewandte Mathematik Und Mechanik* 72: T373–T377, 1992.

[246] **Perktold K, Peter RO, Resch M, and Langs G**, Pulsatile Non-Newtonian Blood-Flow in 3-Dimensional Carotid Bifurcation Models - a Numerical Study of Flow Phenomena Under Different Bifurcation Angles. *J Biomed Eng* 13: 507–515, 1991.

[247] **Perktold K and Rappitsch G**, Mathematical modeling of arterial blood flow and correlation to atherosclerosis. *Technology and Health Care* 3: 139–151, 1995.

[248] **Perktold K, Resch M, and Florian H**, Pulsatile Non-Newtonian Flow Characteristics in a 3-Dimensional Human Carotid Bifurcation Model. *Journal of Biomechanical Engineering Transactions of the Asme* 113: 464–475, 1991.

[249] **Perktold K, Thurner E, and Kenner T**, Flow and Stress Characteristics in Rigid Walled and Compliant Carotid-Artery Bifurcation Models. *Medical Biological En gi neer ing Computing* 32: 19–26, 1994.

[250] **Pickett JP**, *The American Heritage Dictionary of the English Language*. Boston: Houghton Mifflin Company, 4 ed., 2000.

[251] **Pignoli P, Tremoli E, Poli A, Oreste P, and Paoletti R**, Intimal Plus Medial Thickness of the Arterial-Wall - a Direct Measurement with Ultrasound Imaging. *Circulation Merate HospDept SurgMerateItaly Ente Osped Niguarda Ca GrandeInst PatholMilanItaly* 74: 1399–1406, 1986.

[252] **Powell J**, Vascular Biology. In *Comprehensive Vascular and Endovascular Surgery*, edited by **Hallett JW, Earnshaw JJ, and Reekers JA**, Mosby, p. 728, 2003.

[253] **Prakash S and Ethier CR**, Requirements for mesh resolution in 3D computational hemodynamics. *Journal of Biomechanical Engineering Transactions of the ASME* 123: 134–144, 2001.

[254] **Preuss HG**, Diet, genetics and hypertension. *Journal of the American College of Nutrition* 16: 296–305, 1997.

[255] **Quemada D**, Rheology of Concentrated Suspensions and Blood - Discussion of a Concentration-Dependence of Viscosity, Deduced from an Extremal Energy Dissipation Principle. *Comptes Rendus Hebdomadaires Des Seances De L Academie Des Sciences Serie B* 280: 793–795, 1975.

[256] **Quemada D**, Rheology of Concentrated Suspensions and Blood - Thixotropy of Red Blood-Cell Suspensions and Viscosity Shear Rate Relation. *Comptes Rendus Hebdomadaires Des Seances De L Academie Des Sciences Serie B* 281: 69–72, 1975.

[257] **Quemada D**, New Method of Characterizing Blood-Viscosity. *Comptes Rendus Hebdomadaires Des Seances De L Academie Des Sciences Serie D* 282: 1905–1908, 1976.

[258] **Quemada D**, Rheology of Concentrated Disperse Systems .2. Model for Non-Newtonian Shear Viscosity in Steady Flows. *Rheologica Acta* 17: 632–642, 1978.

[259] **Quemada D**, Rheology of Concentrated Disperse Systems .3. General Features of the Proposed Non-Newtonian Model - Comparison with Experimental-Data. *Rheologica Acta* 17: 643–653, 1978.

[260] **Ranganath S**, Contour Extraction From Cardiac Mri Studies Using Snakes. *IEEE Trans Med Imaging* 14: 328–338, 1995.

[261] **Redaelli A, Boschetti F, and Inzoli F**, The assignment of velocity profiles in finite element simulations of pulsatile flow in arteries. *Comput Biol Med* 27: 233–247, 1997.

[262] **Redaelli A, Rizzo G, Arrigoni S, Di Martino E, Origgi D, Fazio F, and Montevecchi F**, An assisted automated procedure for vessel geometry reconstruction and hemodynamic simulations from clinical imaging. *Computerized Medical Imaging and Graphics* 26: 143–152, 2002.

[263] **Refshauge KM**, Rotation - a Valid Premanipulative Dizziness Test - Does It Predict Safe Manipulation. *J Manip Physiol Ther* 17: 15–19, 1994.

[264] **Reneman RS, Hoeks A, and Westerhof N**, Non-invasive assessment of artery wall properties in humans - methods and interpretation. *J Vasc Invest* 2: 53–64, 1996.

[265] **Riley WA, Barnes RW, Applegate WB, Dempsey R, Hartwell T, Davis VG, Bond MG, and Furberg CD**, Reproducibility of Noninvasive Ultrasonic Measurement of Carotid Atherosclerosis - the Asymptomatic Carotid-Artery Plaque Study. *Stroke* 23: 1062–1068, 1992.

[266] **Rivett DA, Sharples KJ, and Milburn PD**, Effect of premanipulative tests on vertebral artery and internal carotid artery blood flow: A pilot study. *J Manip Physiol Ther* 22: 368–375, 1999.

[267] **Roubin GS, New G, Iyer SS, Vitek JJ, Al-Mubarak N, Liu MW, Yadav J, Gomez C, and Kuntz RE**, Immediate and late clinical outcomes of carotid artery stenting in patients with symptomatic and asymptomatic carotid artery stenosis - A 5-year prospective analysis. *Circulation* 103: 532–537, 2001.

[268] **Saber NR, Gosman AD, Wood NB, Kilner PJ, Charrier CL, and Firmin DN**, Computational flow modeling of the left ventricle based on in vivo MRI data: Initial experience. *Annals of Biomedical Engineering* 29: 275–283, 2001.

[269] **Salonen JT and Salonen R**, Ultrasonographically Assessed Carotid Morphology and the Risk of Coronary Heart-Disease. *Arteriosclerosis and Thrombosis* 11: 1245–1249, 1991.

[270] **Samijo SK, Willigers JM, Brands PJ, Barkhuysen R, Reneman RS, Kitslaar P, and Hoeks APG**, Reproducibility of shear rate and shear stress assessment by means of ultrasound in the common carotid artery of young human males and females. *Ultrasound in Medicine and Biology* 23: 583–590, 1997.

[271] **Sander D and Klingelhofer J**, Early carotid atherosclerosis of the internal and external carotid artery related to twenty-four-hour blood pressure variability. *Cerebrovascular Diseases* 7: 338–344, 1997.

[272] **Sander D, Kukla C, Klingelhofer J, Winbeck K, and Conrad B**, Relationship between circadian blood pressure patterns and progression of early carotid atherosclerosis - A 3-year follow- up study. *Circulation* 102: 1536–1541, 2000.

[273] **Sass C, Herbeth B, Chapet O, Siest G, Visvikis S, and Zannad F**, Intima-media thickness and diameter of carotid and femoral arteries in children, adolescents and adults from the Stanislas cohort: effect of age, sex, anthropometry and blood pressure. *Journal of Hypertension* 16: 1593–1602, 1998.

[274] **Sauve JS, Thorpe KE, Sackett DL, Taylor W, Barnett HJM, Haynes RB, and Fox AJ**, Can Bruits Distinguish High-Grade from Moderate Symptomatic Carotid Stenosis. *Annals of Internal Medicine* 120: 633–637, 1994.

[275] **Scheel P, Ruge C, and Schoning M**, Flow velocity and flow volume measurements in the extracranial carotid and vertebral arteries in healthy adults: Reference data and the effects of age. *Ultrasound in Medicine and Biology* 26: 1261–1266, 2000.

[276] **Schlichting H**, *Boundary-Layer Theory*, vol. 17 of *McGraw-Hill Series in Mechanical Engineering*. New York; London: McGraw-Hill, 1979.

[277] **Sch oning M, Walter J, and Scheel P**, Estimation of Cerebral Blood-Flow through Color Duplex Sonography of the Carotid and Vertebral Arteries in Healthy-Adults. *Stroke* 25: 17–22, 1994.

[278] **Schulz UGR and Rothwell PM**, Major variation in carotid bifurcation anatomy - A possible risk factor for plaque development? *Stroke* 32: 2522–2529, 2001.

[279] **Schulz UGR and Rothwell PM**, Sex differences in carotid bifurcation anatomy and the distribution of atherosclerotic plaque. *Stroke* 32: 1525–1531, 2001.

[280] **Selzer RH, Hodis HN, Kwongfu H, Mack WJ, Lee PL, Liu CR, and Liu CH**, Evaluation of Computerized Edge Tracking for Quantifying Intima-Media Thickness of the Common Carotid-Artery from B-Mode Ultrasound Images. *Atherosclerosis* 111: 1–11, 1994.

[281] **Sherwin S, Shah O, Doorly D, Peir J, Papaharilaou Y, Watkins N, Caro CG, and Dumoulin C**, The influence of Out-of-Plane Geometry on the Flow Within a Distal End-to-Side Anastomosis. *Journal of Biomechanical Engineering* 122: 86–94, 2000.

[282] **Shipkowitz T, Rodgers VGJ, Frazin LJ, and Chandran KB**, Numerical study on the effect of secondary flow in the human aorta on local shear stresses in abdominal aortic branches. *Journal of Biomechanics* 33: 717–728, 2000.

[283] **Siauw WL, Ng EYK, and Mazumdar J**, Unsteady stenosis flow prediction: a comparative study of non-Newtonian models with operator splitting scheme. *Med Eng Phys* 22: 265–277, 2000.

[284] **Sihm I, Schroeder AP, Aalkjaer C, Mulvany MJ, Thygesen K, and Lederballe O**, Effect of antihypertensive treatment on cardiac and subcutaneous artery structure - A comparison between calcium channel blocker and thiazide-based regimens. *American Journal of Hypertension* 11: 263–271, 1998.

[285] **Simon A, Gariepy J, Chironi G, Megnien JL, and Levenson J**, Intima-media thickness: a new tool for diagnosis and treatment of cardiovascular risk. *Journal of Hypertension* 20: 159–169, 2002.

[286] **Simon A, Gariepy J, Moyse D, and Levenson J**, Differential effects of nifedipine and co-amilozide on the progression of early carotid wall changes. *Circulation* 103: 2949–2954, 2001.

[287] **Simons W**, *Atherosclerosis ans Shear Stress*. Msc biomedical engineering, Ghent University, 2001.

[288] **Singh MP, Sinha PC, and Aggarwal M**, Flow in Entrance of Aorta. *J Fluid Mech* 87: 97–120, 1978.

[289] **Sitzer M, Puac D, Buehler A, Steckel DA, von Kegler S, Markus HS, and Steinmetz H**, Internal carotid artery angle of origin - A novel risk factor for early carotid atherosclerosis. *Stroke* 34: 950–955, 2003.

[290] **Skadberg BT and Markestad T**, Infant behaviour in response to a change in body position from side to prone during sleep. *Eur J Pediatr* 155: 1052–1056, 1996.

[291] **Slager CJ, Wentzel JJ, Schuurbiers JCH, Oomen JAF, Kloet J, Krams R, von Birgelen C, van der Giessen WJ, Serruys PW, and de Feyter PJ**, True 3-dimensional reconstruction of coronary arteries in patients by fusion of angiography and IVUS (ANGUS) and its quantitative validation. *Circulation* 102: 511–516, 2000.

[292] **Smith FT**, Pulsatile Flow in Curved Pipes. *J Fluid Mech* 71: 15–42, 1975.

[293] **Smith FT, Purvis R, Dennis SCR, Jones MA, Ovenden NC, and Tadjfar M**, Fluid flow through various branching tubes. *Journal of En gi neer ing Mathematics* 47: 277–298, 2003.

[294] **Smith RF, Rutt BK, Fox AJ, and Rankin RN**, Geometric characterization of stenosed human carotid arteries. *Academic Radiology* 3: 898–911, 1996.

[295] **Smith RF, Rutt BK, and Holdsworth DW**, Anthropomorphic carotid bifurcation phantom for MRI applications. *Journal of Magnetic Resonance Imaging* 10: 533–544, 1999.

[296] **Soh WY and Berger SA**, Laminar Entrance Flow in a Curved Pipe. *J Fluid Mech* 148: 109–135, 1984.

[297] **Soh WY and Berger SA**, Numerical-Solution For Entry Flow in Curved Pipes of Arbitrary Curvature Ratio. *Lecture Notes in Physics* 218: 526–530, 1985.

[298] **Soh WY and Berger SA**, Fully-Developed Flow in a Curved Pipe of Arbitrary Curvature Ratio. *Int J Numer Methods Fluids* 7: 733–755, 1987.

[299] **Song HK, Wright AC, Wolf RL, and Wehrli FW**, Multislice double inversion pulse sequence for efficient black-blood MRI. *Magnetic Resonance in Medicine* 47: 616–620, 2002.

[300] **South Florida Vascular Associates, Carotid Stenting**, Available at: http://sfva.vasculardomain.com/images/uploaded/sfva/carotid_stenting.cfm, Accessed January 4, 2004.

[301] **Southern California Mobile Imaging, History of Ultrasound**, Available at: http://www.scmobileimaging.com/history.html, Accessed January 21, 2004.

[302] **Stanton AV, Chapman JN, Mayet J, Sever PS, Poulter NR, Hughes AD, and Thom SAM**, Effects of blood pressure lowering with amlodipine or lisinopril on vascular structure of the common carotid artery. *Clinical Science* 101: 455–464, 2001.

[303] **Starmans-Kool MJ, Stanton AV, Zhao SZ, Xu XY, Thom SAM, and Hughes AD**, Measurement of hemodynamics in human carotid artery using ultrasound and computational fluid dynamics. *Journal of Applied Physiology* 92: 957–961, 2002.

[304] **Steinman DA**, Image-based computational fluid dynamics modeling in realistic arterial geometries. *Annals of Biomedical Engineering* 30: 483–497, 2002.

[305] **Steinman DA**, Image-based Computational Fluid Dynamics: A New Paradigm for Monitoring Hemodynamics and Atherosclerosis. *Current Drug Targets Cardiovascular and Haematological Disorders* , in press.

[306] **Steinman DA, Milner JS, Norley CJ, Lownie SP, and Holdsworth DW**, Image-based computational simulation of flow dynamics in a giant intracranial aneurysm. *American Journal of Neuroradiology* 24: 559–566, 2003.

[307] **Steinman DA and Rutt B**, On the nature and reduction of plaque-mimicking flow artefacts in black blood MRI of the carotid bifurcation. *Magnetic Resonance in Medicine* 39: 635–641, 1998.

[308] **Steinman DA, Thomas JB, Ladak HM, Milner JS, Rutt BK, and Spence JD**, Reconstruction of carotid bifurcation hemodynamics and wall thickness using computational fluid dynamics and MRI. *Magnetic Resonance in Med i cine* 47: 149–159, 2002.

[309] **Stemerman DH, Krinsky GA, Lee VS, Johnson G, Yang BM, and Rofsky NM**, Thoracic aorta: Rapid black-blood MR imaging with half-Fourier rapid acquisition with relaxation enhancement with or without electrocardiographic triggering. *Radiology* 213: 185–191, 1999.

[310] **Strazzullo P, Galletti F, and Barba G**, Altered renal handling of sodium in human hypertension - Short review of the evidence. *Hypertension* 41: 1000–1005, 2003.

[311] **Stroud JS, Berger SA, and Saloner D**, Numerical analysis of flow through a severely stenotic carotid artery bifurcation. *Journal of Biomechanical Engineering Transactions of the Asme* 124: 9–20, 2002.

[312] **Sugawara M, Niki K, Furuhata H, Ohnishi S, and Suzuki S**, Relationship between the pressure and diameter of the carotid artery in humans. *Heart Vessels* 15: 49–51, 2000.

[313] **Suh JS, Jeong EK, Shin KH, Cho JH, Na JB, Kim DH, and Han CD**, Minimizing artifacts caused by metallic implants at MR imaging: Experimental and clinical studies. *American Journal of Roentgenology* 171: 1207–1213, 1998.

[314] **Sulek CA, Gravenstein N, Blackshear RH, and Weiss L**, Head rotation during internal jugular vein cannulation and the risk of carotid artery puncture. *Anesth Analg* 82: 125–128, 1996.

[315] **Sun P, Dwyer KM, Merz CNB, Sun W, Johnson CA, Shircore AM, and Dwyer JH**, Blood pressure, LDL cholesterol, and intima-media thickness - A test of the "response to injury"hypothesis of atherosclerosis. *Arterioscler Thromb Vasc Biol* 20: 2005–2010, 2000.

[316] **Sun Y, Lin CH, Lu CJ, Yip PK, and Chen RC**, Carotid atherosclerosis, intima media thickness and risk factors-an analysis of 1781 asymptomatic subjects in Taiwan. *Atherosclerosis* 164: 89–94, 2002.

[317] **Sunagawa K, Maughan WL, and Sagawa K**, Stroke Volume Effect of Changing Arterial Input Impedance over Selected Frequency Ranges. *American Journal of Physiology* 248: H477–H484, 1985.

[318] **Suto Y, Ohuchi Y, Kimura T, Shirakawa T, Mizuuchi N, Takizawa O, Yamane T, Kamba M, Moriyama S, and Ohta Y**, 3-Dimensional Black Blood Mr-Angiography of the Liver During Breath-Holding - a Comparison With 2-Dimensional Time-of-Flight Mr-Angiography. *Acta Radiol* 35: 131–134, 1994.

[319] **Swanson JC, Stalp SR, and Donnelly R**, Expirimental investigation of periodic flow in curved pipes. *Journal of Fluid Mechanics* 256: 69–83, 1993.

[320] **Talbot L and Gong KO**, Pulsatile Entrance Flow in a Curved Pipe. *J Fluid Mech* 127: 1–25, 1983.

[321] **Tanne D, Nishri B, Oz O, Harris D, Assaf Y, Yodfat O, and Grad Y**, The diverter - a novel permanent arterial filtration-diversion device for embolic stroke prevention. *Stroke* 34: 306–307, 2003.

[322] **Tasciyan TA, Banerjee R, Cho YI, and Kim R**, 2-Dimensional Pulsatile Hemodynamic Analysis in the Magnetic-Resonance Angiography Interpretation of a Stenosed Carotid Arterial Bifurcation. *Medical Physics* 20: 1059–1070, 1993.

[323] **Taylor CA**, Simulation-based medical planning for cardiovascular disease: challenges and opportunities. In *2003 Summer Bioengineering Conference*, edited by **Soslowsky LJ, Skalak TC, Wayne JS, and Livesay GA**, Key Biscayne, FL, 2003, pp. 791–792.

[324] **Taylor CA, Hughes TJR, and Zarins CK**, Finite element modeling of blood flow in arteries. *Comput Meth Appl Mech Eng* 158: 155–196, 1998.

[325] **Taylor DW**, Beneficial Effect of Carotid Endarterectomy in Symptomatic Patients with High-Grade Carotid Stenosis. *New England Journal of Medicine* 325: 445–453, 1991.

[326] **Terpstra WF, May JF, Smit AJ, De Graeff PA, and Crijns H**, Effects of nifedipine on carotid and femoral arterial wall thickness in previously untreated hypertensive patients. *Blood Pressure* 12: 22–29, 2003.

[327] **Texas Heart Institute, Carotid Artery Disease**, Available at: http://www.lerner.ccf.org/bme/ip/vascular/ivuslab.php, Accessed January 4, 2004.

[328] **The Math Works Inc.**, *The Student Edition of MATLAB*. New Jersey: Prentice Hall, 1992.

[329] **The Mathworks Inc.**, *Image Processing Toolbox for use with MATLAB - User's Guide*. Image Processing Toolbox for use with MATLAB - User's Guide, Natick, MA: The Mathworks Inc., 2002.

[330] **The Mathworks Inc.**, *Statistical Toolbox for use with MATLAB - User's Guide*. Statistical Toolbox for use with MATLAB - User's Guide, Natick, MA: The Mathworks Inc., 2002.

[331] **Thomas JB, Che SL, Milner JS, Antiga L, Rutt BK, Spence D, and Steinman DA**, Geometric characterization of the normal and mildly diseased human carotid bifurcation. In *2003 Summer Bioengineering Conference*, edited by **Soslowsky LJ, Skalak TC, Wayne JS, and Livesay GA**, Key Biscayne, FL, 2003, pp. 323–324.

[332] **Thomas JB, Milner JS, Rutt BK, and Steinman DA**, Reproducibility of Image-Based Computational Fluid Dynamics Models of the Human Carotid Bifurcation. *Annals of Biomedical Engineering* 31: 132–141, 2003.

[333] **Thomas JB, Milner JS, and Steinman D**, On the reproducibility of computationally imaged carotid bifurcation models. In *ASME Bioengineering Conference*, 2001, vol. 50, pp. 559–560.

[334] **Thomas JB, Milner JS, and Steinman DA**, On the influence of vessel planarity on local hemodynamics at the human carotid bifurcation. *Biorheology* 39: 443–448, 2002.

[335] **Thury A, Wentzel JJ, Janssen EH, Krams R, Oomen JA, Schuurbiers JCH, Ligthart JMR, Serruys PW, and Slager CJ**, Novel method for in vivo calculation of absolute sheer stress at any location of a stented human coronary artery. *Journal of the American College of Ccardiology* 37: 298A–299A, 2001.

[336] **Tricot O, Mallat Z, Heymes C, Belmin J, Leseche G, and Tedgui A**, Relation between endothelial cell apoptosis and blood flow direction in human atherosclerotic plaques. *Circulation* 101: 2450–2453, 2000.

[337] **Tvinnereim M, Cole P, Haight J, Mateika S, and Hoffstein V**, Postural changes in respiratory airflow pressure and resistance in nasal, hypopharyngeal, and pharyngeal airway in normal subjects. *Ann Otol Rhinol Laryngol* 105: 218–221, 1996.

[338] **Uematsu S, Yang A, Preziosi TJ, Kouba R, and Toung TJK**, Measurement of Carotid Blood-Flow in Man and Its Clinical-Application. *Stroke* 14: 256–266, 1983.

[339] **Van Merode T, Van Bortel L, Smeets FAM, Böhm R, Mooij J, Rahn KH, and Reneman RS**, The Effect of Verapamil on Carotid Artery Distensibility and Cross-Sectional Compliance in Hypertensive Patients. *Journal of Cardiovascular Pharmacology* 15: 109–113, 1989.

[340] **Vander A, Sherman J, and Luciano D**, *Human Physiology*. Mc Graw-Hill Education, 7 ed., 1998.

[341] **Varghese SS and Frankel SH**, Numerical modeling of pulsatile turbulent flow in stenotic vessels. *Journal of Biomechanical Engineering Transactions of the Asme* 125: 445–460, 2003.

[342] **Verdonck P and Perktold K**, eds., *Intra- and extracorporeal cardiovascular fluid dynamics: Fluid-Structure interaction*, vol. 2 of *Advances in Fluid Dynamics*. Southampton: WITPress, 2000.

[343] **Verma S and Anderson TJ**, Fundamentals of endothelial function for the clinical cardiologist. *Circulation* 105: 546–549, 2002.

[344] **Waddell TK, Dart AM, Medley TL, Cameron JD, and Kingwell BA**, Carotid pressure is a better predictor of coronary artery disease severity than brachial pressure. *Hypertension* 38: 927–931, 2001.

[345] **Walburn FJ and Schneck DJ**, Constitutive Equation for Whole Human-Blood. *Biorheology* 13: 201–210, 1976.

[346] **Walker PG, Turner JG, Frund T, Wu S, Ringgaard S, and Pedersen EM**, MRI guided CFD simulations of LDL transport in subject specific carotid arteries: an initial methodology. In *2003 Summer Bioengineering Conference*, edited by **Soslowsky LJ, Skalak TC, Wayne JS, and Livesay GA**, Key Biscayne, FL, 2003, pp. 507–508.

[347] **Walker PG, Turner JG, Frund T, Wu S, Ringgaard S, and Pedersen EM**, MRI guided CFD simulation of species transport in subject specific carotid arteries: effect of wall reaction mechanism. In *International Bio-Fluid Mechanics Symposium and Workshop*, edited by **Einav S**, Pasadena, CA, USA: US National Committee on Biomechanics, 2003.

[348] **Wang X and Stoltz JF**, Blood Non-Newtonian Behavior and Red-Cells Transport. *Journal Des Maladies Vasculaires* 19: 137–141, 1994.

[349] **Wang X and Stoltz JF**, Characterization of Pathological Bloods with a New Rheological Relationship. *Clinical Hemorheology* 14: 237–244, 1994.

[350] **Wang X and Stoltz JF**, Influence of Non-Newtonian Properties of Blood on the Global Transport of Red-Blood-Cells. *Clinical Hemorheology* 14: 789–796, 1994.

[351] **Warlow C**, Mrc-European-Carotid-Surgery-Trial - Interim Results for Symptomatic Patients with Severe (70-99-Percent) or with Mild (0-29-Percent) Carotid Stenosis. *Lancet* 337: 1235–1243, 1991.

[352] **Weaver JPA, Evans A, and Walder DN**, The effect of increased fibrinogen content on the viscosity of blood. *Clinical Science* 36: 1–10, 1969.

[353] **Weber KT, Janicki JS, Hunter WC, Shroff S, Pearlman ES, and Fishman AP**, The Contractile Behavior of the Heart and Its Functional Coupling to the Circulation. *Progress in Cardiovascu lar Diseases* 24: 375–400, 1982.

[354] **Wells DR, Archie JP, and Kleinstreuer C**, Effect of carotid artery geometry on the magnitude and distribution of wall shear stress gradients. *Journal of Vascular Surgery* 23: 667–678, 1996.

[355] **Wendelhag I, Gustavsson T, Suurkula M, Berglund G, and Wikstrand J**, Ultrasound Measurement of Wall Thickness in the Carotid-Artery - Fundamental Principles and Description of a Computerized Analyzing System. *Clinical Physiology* 11: 565–577, 1991.

[356] **Wentzel JJ, Janssen E, Vos J, Schuurbiers JC, Krams R, Serruys PW, de Feyter PJ, and Slager CJ**, Extension of Increased Atherosclerotic Wall Thickness Into High Shear Stress Regions Is Associated With Loss of Compensatory Remodeling. *Circulation* 108: 17–23, 2003.

[357] **Wentzel JJ, Krams R, Schuurbiers JCH, Oomen JA, Kloet J, van der Giessen WJ, Serruys PW, and Slager CJ**, Relationship between neointimal thickness and shear stress after wallstent implantation in human coronary arteries. *Circulation* 103: 1740–1745, 2001.

[358] **Wentzel JJ, Whelan DM, van der Giessen WJ, van Beusekom HMM, Andhyiswara I, Serruys PW, Slager CJ, and Krams R**, Coronary stent implantation changes 3-D vessel geometry and 3-D shear stress distribution. *Journal of Biomechanics* 33: 1287–1295, 2000.

[359] **Weskott HP and Holsing K**, US-based evaluation of hemodynamic parameters in the common carotid artery: A nomogram trial. *Radiology* 205: 353–359, 1997.

[360] **Wesseling H, Neef C, de Graeff PA, Dupont AG, Henning RH, Lefebvre R, Lekkerkerker JFF, Seegers AJM, and Zaagsma J**, *Algemene Farmacotherapie Het geneesmiddel in theorie en praktijk*. Bohn Stafleu Van Loghum, 7th edition ed., 1999.

[361] **Westenberg JJM, Wasser M, van der Geest RJ, Pattynama PMT, de Roos A, Vanderschoot J, and Reiber JHC**, Variations in blood flow waveforms in stenotic renal arteries by 2D phase-contrast cine MRI. *Journal of Magnetic Resonance Imaging* 8: 590–597, 1998.

[362] **Weston SJ, Wood NB, Tabor G, Gosman AD, and Firmin DN**, Combined MRI and CFD analysis of fully developed steady and pulsatile laminar flow through a bend. *Journal of Magnetic Resonance Imaging* 8: 1158–1171, 1998.

[363] **White WB, Saunders E, Noveck RJ, and Ferdinand K**, Comparative efficacy and safety of nisoldipine extended-release (ER) and amlodipine (CESNA-III study) in African American patients with hypertension. *American Journal of Hypertension* 16: 739–745, 2003.

[364] **Whitmore RL**, The Influence of Erythrocyte Shape and Rigidity on the Viscosity of Blood. *Biorheology* 18: 557–562, 1981.

[365] **Whitmore RL**, The Influence of Particle-Shape and Rigidity on the Viscosity of a Dispersed Suspension. *Journal of Rheology* 28: 656–656, 1984.

[366] **Wiebers DO, Whisnant JP, Sandok BA, and Ofallon WM**, Prospective Comparison of a Cohort with Asymptomatic Carotid Bruit and a Population-Based Cohort without Carotid Bruit. *Stroke* 21: 984–988, 1990.

[367] **Willink R and Evans DH**, Volumetric Blood-Flow Calculation Using a Narrow Ultrasound Beam. *Ultrasound in Medicine and Biology* 21: 203–216, 1995.

[368] **Womersley J**, Method for the calculation of velocity, rate of flow and viscous drag in arteries when pressure gradient is known. *J Physiol* 127: 553–563, 1955.

[369] **Wong ML, Edelstein J, Wollman J, and Bond MG**, Ultrasonic Pathological Comparison of the Human Arterial-Wall - Verification of Intima Media Thickness. *Arteriosclerosis and Thrombosis* 13: 482–486, 1993.

[370] **Wood N, Weston S, Kilner P, Gosman A, and Firmin D**, Combined MR imaging and CFD simulation of flow in the human descending aorta. *Journal of Magnetic Resonance Imaging* 13: 699–713, 2001.

[371] **World Health Organisation Regional Office for Europe**, *Atlas of health in Europe*. Copenhagen: World Health Organisation Regional Office for Europe, 2003.

[372] **Xu CY and Prince JL**, Generalized gradient vector flow external forces for active contours. *Signal Processing* 71: 131–139, 1998.

[373] **Xu CY and Prince JL**, Snakes, shapes, and gradient vector flow. *Ieee Transactions on Image Processing* 7: 359–369, 1998.

[374] **Xu XY, Long Q, Collins MW, Bourne M, and Griffith TM**, Reconstruction of blood flow patterns in human arteries. *Proc Inst Mech Eng Part H J Eng Med* 213: 411–421, 1999.

[375] **Xu Y**, *Numerical Analysis of 3D Blood Flow in Arterial Bifurcations.*. Phd, London Universityn, 1992.

[376] **Yao JF, van Sambeek M, Dall'Agata A, van Dijk LC, Kozakova M, Koudstaal PJ, and Roelandt J**, Three-dimensional ultrasound study of carotid arteries before and after endarterectomy - Analysis of stenotic lesions and surgical impact on the vessel. *Stroke* 29: 2026–2031, 1998.

[377] **Yellin E**, The momentum of mass, the momentum of ideas, and diastolic function. In *Systolic and diastolic function of the heart*, edited by **Ingels NB, Daughters G, and Baan J**, Amsterdam: IOS Press, 1995.

[378] **York Neurosurgical Associates, Carotid Endarterectomy**, Available at: http://www.yna.org/New%20Pages/CarotidEndarterectomy.html, Accessed January 4, 2004.

[379] **YourSurgery.com, Arterial Surgery of the Leg**, Available at: http://www.yoursurgery.com/ProcedureDetails.cfm?BR=5&Proc=33, Accessed January 4, 2004.

[380] **Zarins CK, Giddens DP, Bharadvaj BK, Sottiurai VS, Mabon RF, and Glagov S**, Carotid Bifurcation Atherosclerosis Quantitative Correlation of Plaque Localization with Flow Velocity Profiles and Wall Shear- Stress. *Circulation Research* 53: 502–514, 1983.

[381] **Zemel MB**, Calcium modulation of hypertension and obesity: Mechanisms and implications. *Journal of the American College of Nutrition* 20: 428S–435S, 2001.

[382] **Zhang JB and Kuang ZB**, Study on blood constitutive parameters in different blood constitutive equations. *Journal of Biomechanics* 33: 355–360, 2000.

[383] **Zhang WG and Wang ZY**, Resetting baroreceptors to a lower arterial pressure level by enalapril avoids baroreflex mediated activation of sympathetic nervous system by nifedipine. *Life Sciences* 68: 2769–2779, 2001.

[384] **Zhao SZ, Ariff B, Long Q, Hughes AD, Thom SA, Stanton AV, and Xu XY**, Inter-individual variations in wall shear stress and mechanical stress distributions at the carotid artery bifurcation of healthy humans. *Journal of Biomechanics* 35: 1367–1377, 2002.

[385] **Zhao SZ, Papathanasopoulou P, Long Q, Marshall I, and Xu XY**, Comparative study of magnetic resonance imaging and image-based computational fluid dynamics for quantification of pulsatile flow in a carotid bifurcation phantom. *Annals of Biomedical Engineering* 31: 962–971, 2003.

[386] **Zhao SZ, Xu XY, Collins MW, Stanton AV, Hughes AD, and Thom SA**, Flow in carotid bifurcations: effect of the superior thyroid artery. *Med Eng Phys* 21: 207–214, 1999.

[387] **Zhao SZ, Xu XY, Hughes AD, Thom SA, Stanton AV, Ariff B, and Long Q**, Blood flow and vessel mechanics in a physiologically realistic model of a human carotid arterial bifurcation. *Journal of Biomechanics* 33: 975–984, 2000.

[388] **Zhou MS, Jaimes EA, and Raij L**, Inhibition of oxidative stress and improvement of endothelial function by amlodipine in angiotensin II-infused rats. *American Journal of Hypertension* 17: 167–171, 2004.

[389] **Zhu H and Friedman MH**, Relationship between the dynamic geometry and wall thickness of a human coronary artery. *Arteriosclerosis Thrombosis and Vascular Biology* 23: 2260–2265, 2003.

Need a hand?

Newton said he was standing on the shoulders of giants. I believe every researcher has to rely on his colleagues if he wants to achieve some results. The days in which a scientist sat in his room for ages and still managed to perform outstanding research are probably over. Admittedly, you save a lot of time not having to shave, but the input of colleagues with skills other than your own can reach high levels of productivity. Many people contributed to this manuscript, I would just want to mention following individuals:

- By far the largest contributions to this research were performed by **Dr. B. Ariff**. Not only was he a key figure in the recruitment of healthy or hypertensive subjects, he also generated a vast amount of 3DUS data. Discussions with Dr. Ariff were edifying. In the study on the variability of 3DUS-based CFD (section VII.4.3), he was assisted by **Dr. S. Byrd**, **Dr. A. Zambadini** and **Dr. M. Jackson**.

- **Dr. Ir. A. D. Augst** has made enormous contributions to the mathematical CFX model. He shared his numerical codes which worked inspiring in writing my own user defined functions. More notably, Dr. Augst programmed the non-Newtonian model. His experience in the mesh generation for carotid bifurcations based on segmented 3DUS images was an excellent source of inspiration when automating the process. The study on generating boundary conditions from Doppler ultrasound measurements (VIII.1.2) was for a large part performed by Dr. Augst: he performed the simulations and wrote the discussion; my contribution here lies in generating the meshes and boundary conditions, and in the post-processing.

- **Dr. Ir. D. C. Barratt** is the 3DUS-based reconstruction *king*. In his PhD, he wrote a MATLAB-based code for the segmentation of axial B-mode ultrasound images and the reconstruction of carotid bifurcations. Although the reconstruction protocol needed to be altered on a number of points before they could be used for numerical simulations, he has done far more than paving the way for this manuscript. After his graduation, he was always present for solving reconstruction problems we encountered.

- **Ms. M. Bol** has been very elucidating in the study on anti-hypertensive drugs (Chapter XII). Her literature study was indispensable for understanding the function of amlodipine and lisinopril.

- **Dr. Ir. P.-L. Cheong** wrote the original code for the region growing and the snake model (sections VI.2.1 and VI.2.2).

- **Dr. Ir. L. A. Crowe** (from the group of **Prof. Dr. Ir. D. N. Firmin**) has performed almost all MRI-scans. By doing this, she was one of the biggest contributors to this research. The MRI scans for the study on the use of MRI-based boundary conditions were performed by **Dr. Ir. J. J. M. Westenberg** in Leiden (section VIII.1.1).

- **Ir. M. Hosp** has performed excellent post-processing for the study on MRI-based boundary conditions (section VIII.1.1).

- The first names that come to mind with the word 'statistics' have to be **Dr. A. D. Hughes** and **Prof. Dr. Ir. P. Segers**. They were extremely demystifying in their views on the statistics.

- **Dr. Ir. Q. Long** generated the meshes for the MRI-based CFD reproducibility study (section VI.4.2). At my arrival in London, he was an invaluable MRI-based CFD instructor.

- **Prof. Dr. Ir. K. Parker** is one the founding fathers of the non-planarity parameter. Whenever he switched to 'teaching-mode', his patience and clarity were very much appreciated.

- The natural leadership of **Dr. S. McG. Thom** is one of the main reasons why the group at Imperial College is achieving the results they can look back on. His efforts at redirecting research paths and advice on presentation contents are gratefully acknowledged.

- The merit of **Prof. Dr. Ir. P. Verdonck** lies in the leadership displayed at the Cardiovascular Mechanics and Biofluid Dynamics Unit, and his ability to take important political decisions. He provided the idea and the guidelines for many studies.

- **Dr. Ir. X. Y. Xu** is an extremely knowledgable supervisor, always there with good answers for scientific questions. Many of the text written in this manuscript are based on discussions with her. The role she played in the manuscript review process was of an impressive quality.

A sincere "thank you" to all of you!

Integratie van medische beeldvorming en numerieke stromingsmechanica voor het meten van de bloedstroom in de halsslagaders

Ir. Fadi Paul Glor

2003-2004